



The Seventh Asian School-Conference
on Physics and Technology of
Nanostructured Materials

Vladivostok, Russia, July 11 – July 15, 2025

P R O C E E D I N G S

**Vladivostok
Far Eastern Federal University
2025**

The Seventh Asian School-Conference on Physics and Technology of

Nanostructured Materials: Proceedings. – Vladivostok, Dalnauka, 2025. – 243 p.

ISBN 978-5-8044-1757-5

Copyright © 2025 by Institute of Automation and Control Processes FEB RAS. All rights reserved. No part of this publication may be multiple copied, stored in a retrieval system or transmitted in any form or by any means, electronic, mechanical, photocopying, recording or otherwise, without the written permission of the publisher. Single photocopies of single articles may be made for private study or research.

The Proceedings include extended abstracts of invited talks and contributed papers of the school-conference. The abstracts reflect the new results and scientific achievements in the field of new materials, nanotechnology and surface science. This proceedings volume is intended for scientist, teachers and post-graduate students.

The Seventh Asian School-Conference on Physics and Technology of Nanostructured Materials

Organizers

**Institute of Automation and Control
Processes FEB RAS, Russia**

**Presidium of Far Eastern Branch of
Russian Academy of Sciences, Russia**



Zhengzhou University, China



郑州大学
ZHENGZHOU UNIVERSITY

The school-conference official website

<http://ntc.dvo.ru/conf/nanomat2025/>

General Sponsor

LLC "Active photonics", Russia



NTEGRA PRIMA KEY FEATURES

VERSATILE TOOL FOR SCANNING PROBE MICROSCOPY

NTEGRA Prima integrates more than 40 techniques commonly used in Scanning Probe Microscopy (SPM), spectroscopy and lithography. Consequently, NTEGRA Prima is an ideal SPM tool for thoroughly investigating the physical and chemical properties of samples with the highest possible precision and performing high-resolution scans.

SIMULTANEOUS OPTICAL CONTROL AND SCALABLE POSSIBILITIES

An integrated optical viewing system with a resolution of up to 1 μm allows targeting the tip and controlling the measurement process in real time. The NTEGRA Prima system supports all types of scanning required for various samples. It can be used for scanning by sample, by probe or simultaneously by both methods. This also increases the scanning range to up to 200 μm in the XY plane and up to 20 μm along the Z axis.

PRECISE AND ACCURATE

NTEGRA Prima has built-in closed-loop capacitive sensors for all axes (X, Y, Z). These sensors measure the actual scanner displacement and compensate for parasitic piezoceramics properties including non-linearity, hysteresis and creep with extremely low noise level. This enables closed-loop control on the small fields — just what you need for precise lithography with perfect and accurate linearity.

MODULAR DESIGN

The NTEGRA Nanolab is designed with an open hardware and software architecture. This allows various compatible assemblies and components to be used in the instrument using a simple plug&play method. Due to the modular organization, the specialization of the basic atomic force microscope can be easily changed or expanded. This design provides the unique ability to configure the instrument for specific applications and specific research techniques.

LARGE SELECTION OF OPTIONAL FEATURES

Thanks to its open architecture, the functionality of the NTEGRA Prima can be significantly expanded. The modular design allows the system to be supplemented with external magnetic field measurements, sample temperature experiments, near-field optical microscopy, Raman spectroscopy, and many other options.



NT-MDT GROUP
INNOVATIVE TECHNOLOGIES.
OWN RESEARCH, DEVELOPMENT & PRODUCTION
+7 499 390 66 78 | www.ntmdt-russia.com
info@ntmdt-russia.com | sale@ntmdt-russia.com
10, Pr. Panfilovsky, Zelenograd, Moscow, 124498



NTEGRA PRIMA

- Universal scanning probe microscope
- More than 40 methods of atomic force and tunneling microscopy
- Significantly extended functionality
- Easy integration with other analytical methods

APPLICATIONS

Materials science: electrical, magnetic and mechanical properties; polymers and thin organic films; biology/biotechnology; nanomaterials/nanostructures; nanomachining/nanomanipulation



Chair of ASCO-NANOMAT 2025

Professor **Nikolay GALKIN** (Institute of Automation and Control Processes FEB RAS and Far Eastern Federal University, Vladivostok, Russia)

Honour chairpersons

Academician RAS, professor **Yuri KULCHIN** President Far Eastern Branch of RAS, Vice-President Far Eastern Branch of RAS, Vladivostok, Russia

INTERNATIONAL PROGRAMME COMMITTEE

Chair: Corr. Memb. RAS A.A. Saranin
(Vladivostok, Russia)

Academician MAS. E. Arushanov (Chisinau,
Moldova)

Prof. R.Z. Bakhtizin (Ufa, Russia)

Prof. V.E. Borisenko (Minsk, Belarus)

Prof. A. Chuvilin (San Sebastian, Spain)

Corr.-member RAS A.V. Dvurechenskii
(Novosibirsk, Russia)

Prof. V.G. Dubrovskii (S.-Petersburg, Russia)

Prof. A.V. Filimonov (S.-Petersburg, Russia)

Prof. Y. Gao (Hubei, Peoples R China)

Prof. N.V. Gaponenko (Minsk, Belarus)

Prof. S.A. Gavrilov (Moscow, Russia)

Prof. H.-F. Guo (Beijing, China)

Corr.-member RAS S.V. Gnedenkov
(Vladivostok, Russia)

Prof. D.G. Gromov (Moscow, Russia)

Prof. S. Hasegawa (Tokyo, Japan)

Prof. J. Hu (Zhengzhou, China)

Prof. M. Imai (Tsukuba, Japan)

Prof. Y.K. Kim (Seul, Korea)

Prof. V.V. Khovaylo (Moscow, Russia)

Academician RAS A.V. Latyshev (Novosibirsk,
Russia)

Prof. D. Migas (Minsk, Belarus)

Prof. M.M. Mikhailov (Tomsk, Russia)

Prof. Y. Miyazaki (Tohoku, Japan)

Prof. A.A. Naberezhnov (S.-Petersburg, Russia)

Prof. V.V. Neshchymenko (Blagoveshchensk,
Russia)

Prof. S.G. Ovchinnikov (Krasnoyarsk, Russia)

Prof. D. Pavuna (Lausanne, Switzerland)

Prof. B. Pecz (Budapest, Hungary)

Prof. R. Perez-Jimenez (San Sebastian, Spain)

Prof. V.S. Plotnikov (Vladivostok, Russia)

Prof. O.P. Pchelyakov (Novosibirsk, Russia)

Prof. S.A. Pyachin (Khabarovsk, Russia)

Corr.-member RAS R.V. Romashko
(Vladivostok, Russia)

Prof. A. Rogach (Hong-Cong, Peoples R China)

Prof. T.S. Shamirzaev (Novosibirsk, Russia)

Prof. A.A. Shklyaev (Novosibirsk, Russia)

Prof. U.V. Stukova (Blagoveshchensk, Russia)

Prof. T. Suemasu (Tsukuba, Japan)

Prof. H. Tatsuoka (Hamamatsu, Japan)

Prof. Y. Terai (Kyushu, Japan)

Prof. S.P. Timoshenkov (Moscow, Russia)

Prof. S.B. Vakhrushev (S.-Petersburg, Russia)

Prof. D. Vyalikh (San Sebastian, Spain)

Prof. O.B. Vitrik (Vladivostok, Russia)

Prof. H. Udono (Ibaraki, Japan)

Prof. N. Usami (Nagoya, Japan)

Corr. Memb. RAS A.V. Zotov (Vladivostok,
Russia)

ORGANIZING COMMITTEE

Chair: Prof. N.G. Galkin (IACP FEB RAS, FEFU)

Vice-chair: PhD. K.N. Galkin (IACP FEB RAS)

Secretary: PhD. S.V. Chusovitina (IACP FEB RAS)

Dr. Sci. D.L. Goroshko (IACP FEB RAS)

Prof. J. Hu (Zhengzhou, China)

PhD. I.M. Chernev (IACP FEB RAS)

PhD. A.N. Galkina (IACP FEB RAS)

PhD. O.A. Goroshko (IACP FEB RAS)

PhD. S.O. Gurbatov (IACP FEB RAS)

PhD. K.V. Ignatovich (IACP FEB RAS)

PhD B. Jinjin (Beijing, China)

PhD. A.A. Kuchmijak (IACP FEB RAS)

PhD. A.M. Maslov (IACP FEB RAS)

PhD. E.Y. Subbotin (IACP FEB RAS)

Mr. O.V. Kropachev (IACP FEB RAS)

Mrs. Yu.L. Brekhman (Presidium of the FEB RAS)

Mrs. M.B. Shtets (Presidium of the FEB RAS)

Mrs. A.S. Trifonova (IACP FEB RAS)

PUBLISHING COMMITTEE

Chair: Prof. N.G. Galkin (Vladivostok, Russia)

Vice-chair: Prof. D.L. Goroshko (Vladivostok, Russia)

Prof. J. Hu (Zhengzhou, China)

Prof. Huan-fang Guo (Beijing, China)

Prof. A.V. Filimonov (S.-Petersburg, Russia)

Prof. P.A. Karasev (S.-Petersburg, Russia)

Prof. S.A. Gavrilov (Moscow, Russia)

Prof. H.-F. Guo (Beijing, China)

Prof. J. Hu (Zhengzhou, China)

PhD B. Jinjin (Beijing, China)

Prof. S. Suemasu (Tsukuba, Japan)

Prof. Y. Nakamura (Osaka, Japan)

Prof. D.G. Gromov (Moscow, Russia)

Prof. S.G. Ovchinnikov (Krasnoyarsk, Russia)

Contents

Plenary lectures

Plenary 01	Nano- and microparticulation for remote controlled drug delivery systems <i>Sindeeva O.A., Kozyreva Z.V., Proshin P.P., Abdurashitov A.S., Sukhorukov G.B.</i>	15
Plenary 02	Non-hermitian singularities in all-dielectric metastructures: from bound states in the continuum to exceptional points and bulk fermi arcs <i>Bogdanov A.A.</i>	18
Plenary 03	Research progress on Ba-Si compound thin films for energy applications <i>Suemasu T.</i>	19
Plenary 04	Desing of nanomaterial and nanostructure for thin film thermoelectric generator <i>Nakamura Y.</i>	21
Plenary 05	Nano- and microstructured materials and photonics work together for biomedical applications <i>Gorin D.A.</i>	22
Plenary 06	Novel development in silicide application <i>Junhua Hu, Guoqin Cao</i>	23
Plenary 07	3D, 2D and 1D in silicon, silicides, III-V compounds and transition metal oxides: <i>ab initio</i> prediction of unexpected properties <i>Migas D.B.</i>	24
Plenary 08	Group IV heterostructures for quantum technologies and silicon photonics <i>Novikov A.V., Yablonskiy A.N., Yurasov D.V., Stepihova M.V., Peretokin A.V., Shmagin V.B., Demidov E.V., Shaleev M.V., Shengurov D.V., Zaharov V.E., Shmyrin D.A., Pankratov E.L., Revin L.S., Krasilnik Z.F., Dyakov S.A., Gippius N.A., Sitnikov S.V., Sheglov D.V.</i>	26

I. Physics of nanostructures and interfaces: self-organization processes, two dimensional materials and metrology

I.i.01	Initial stage of ultrathin film growth in metal-silicon systems: from surface phases to solid wetting layers <i>Plushin N.I.</i>	29
I.i.02	Monoatomic lead layer: exploring the interplay between atomic arrangement, electronic structure, and superconductivity <i>Bondarenko L.V., Tupchaya A.Y., Vekovshinin Yu.E., Utas T.V., Denisov N.V., Mihalyuk A.N., Gruznev D.V., Zotov A.V., Saranin A.A.</i>	32
I.o.01	<i>In situ</i> UHV REM observation of structural transitions on Si(111) surface induced by III-V group metals adsorption <i>Petrov A.S., Gumbarg V.V., Rogilo D.I., Sheglov D.V., Latyshev A.V.</i>	34
I.o.02	Ab initio calculations of the effect of lattice strain on the band structure of Cr ₂ CFBr MXene <i>Mushtuk P.S., Iliushin I.G., Afremov L.L.</i>	36
I.o.03	Controlling of 6H-SiC surface graphitization by RHEED <i>Durakov D.E., Petrov A.S., Rogilo D.I., Makeeva A.A., Nikiforov D.F., Kurus N.N., Milekhin A.G., Sheglov D.V., Latyshev A.V.</i>	38
I.o.04	Ising model on Fibonacci lattices: sphere, ring topologies of the sphere and torus. <i>Pochinok A.S., Molochkov A.V., Chernodub M.N., Chepak A.K.</i>	40
I.o.05	Surface reconstructions in a submonolayer system La/Si(111) <i>Burkovskaya P.V., Kotlyar V.G., Utas T.V., Mihalyuk A.N., Zotov A.V., Saranin A.A.</i>	42
I.o.06	Structural and morphological Bi ₂ Se ₃ (0001) surface transformations under Indium deposition <i>Ponomarev S.A., Rogilo D.I., Golyashov V.A., Nasimov D.A., Kokh K.A., Sheglov D.V., Latyshev A.V.</i> ...	43
I.o.07	New possible structure of magnesium based germanium-silicon alloys: first-principles evolution search results <i>Luniakov Yu.V.</i>	45
I.p.01	Self-organization of Ag and Au nanoparticle array on an inert surface during PVD and annealing <i>Gromov D.G., Volkov R.L., Dubkov S.V., Grishin T.S., Novikov D.V., Borgardt N.I.</i>	47

I.p.02	3D/nanodots/2D growth in Sb-mediated Ge epitaxy on Si(111) Petrov A.S., Gumbarg V.V., Rogilo D.I., Sheglov D.V., Latyshev A.V.	49
I.p.03	Growth of two-dimensional Si layers on CrSi ₂ (0001): quantum mechanical modeling Zavodinsky V.G., Plusnin N.I., Gorkusha O.A.	51
I.p.04	Ab initio calculation of Si(111)2/3√3×2/3√3-Mg models Ryzhkova M.V., Tsukanov D.A.	53
I.p.05	Monte Carlo simulations of stable topological structures Vasiliev E.V., Kapitan V.Yu., Makarov A.G., Nefedev K.V.	55
I.p.06	Atomic structure and electronic properties of Bi monolayers on ultra-thin films of rare-earth silicides Zhdanov V.S., Sevryukov D.K., Vekovshinin Yu.E., Bondarenko L.V., Tupchaya A.Y., Mihalyuk A.N., Olyanich D.A., Gruznev D.V., Zotov A.V., Saranin A.A.	56
I.p.07	Morphological features of ultrathin films of β-FeSi ₂ on Si(100) Kotlyar V.G., Utas T.V., Burkovskaya P.V., Olyanich D.A., Saranin A.A., Zotov A.V.	58

II. Physics and technology of semiconductor materials and devices

II.i.01	Synthesis of silicide- and silicate-based nanostructures, thin films, and bulk crystals via reactive interdiffusion Tatsuoka H.	60
II.i.02	Electrical and photoresponse properties of ternary silicide semiconductor Ru-doped β-FeSi ₂ Terai Y., Sakurai Y., Takahashi T.	62
II.i.03	Recent advances in short wavelength infrared sensors using single crystalline Mg ₂ Si Udono H.	63
II.i.04	Recent progress in optical characterization of silicon micro- and nanostructures Bandarenka H.V.	64
II.o.01	Formation of p-type and n-type Si doped (Ga,Al)As nanowires Shtrom I.V., Sibirev N.V., Ilkiv I.V., Soshnikov I.P., Gridchin V.O., Reznik R.R., Alekseev P.A., Cirlin G.E.	66
II.o.02	Thermoelectric potential of Ge ₂ Sb ₂ Te ₅ phase change thin films for energy harvesting of low-grade heat Terekhov D.Yu., Al-Khadge L.A., Yakubov A.O., Lazarenko P.I., Sherchenkov A.A.	68
II.o.03	III-V semiconductor nanostructures of different dimensionality: MBE growth and physical properties Reznik R.R., Ilkiv I.V., Gridchin V.O., Kotlyar K.P., Khrebrov A.I., Kryzhanovskaya N.V., Baretin D., Akopian N., Cirlin G.E.	70
II.o.04	The influence of heat treatment on the characteristics of composite thermoelectric materials based on Bi ₂ Te _{2.8} Se _{0.2} and Bi _{0.5} Sb _{1.5} Te ₃ Voloshchuk I.A., Babich A.V., Kiselev A.V., Mikhalevsky V.A., Sherchenkov A.A.	72
II.o.05	<i>In-situ</i> bonding reorganization and self-reinforcement of Si-Zr-O amorphous under high temperature marine environment Guoqin Cao, Junhua Hu	74
II.o.06	<i>In-situ</i> formation of a metal–organic interphase for interfacial kinetic reconstruction in low-temperature aqueous aluminum–air batteries Jinjin Ban, Junhua Hu	75
II.o.07	Diffusion-driven photovoltaic effect in Mn/SiO ₂ /n-Si Bondarev I.A., Rautskii M.V., Volkov N.V., Lukyanenko A.V., Yakovlev I.A., Varnakov S.N., Tarasov A.S.	76
II.o.08	Mg ₂ Si _x Sn _{1-x} film growth by ultra-fast deposition of Mg onto (Si-Sn)/Si structure with gradT Gouralnik A.S., Subbotin E.Yu., Chernev I.M., Kitan S.A., Gerasimenko A.V., Ustinov A.Yu., Kozlov A.G., Volkova L.S., Dudin A.A., Poliakov M.V.	78
II.o.09	Thermoelectric properties of Mg ₃ Bi ₂ flexible films Subbotin E.Yu., Khoroshilov D.A., Goroshko D.L., Prokopeva G.A., Kozlov A.G., Prihodchenko A.V., Chernev I.M., Lisenkov O.E., Sinotova S.A., Galkin N.G.	80
II.p.01	Nonlinear resistance drift kinetics in Ge ₂ Sb ₂ Te ₅ thin films Ermachikhin A.V., Vorobyov Y.V., Trusov E.P., Litvinov V.G.	82

II.p.02	Thermoelectric properties of a nanocomposite with embedded α -FeSi ₂ NCs in the silicon matrix Galkin K.N., Kropachev O.V., Goroshko O.A., Subbotin E.Yu., Goroshko D.L., Galkin N.G. 84
II.p.03	Single-phase formation of Ca ₅ Si ₃ films on Si(111), electronic and phonon structure and optical properties: experiment and theory Galkin N.G., Galkin K.N., Kropachev O.V., Migas D.B., Fogarassy Z., Cora I., Pécz B. 86
II.p.04	Influence of protective transparent covering on lateral photovoltaic effect in the cover/Bi ₂ Te ₃ /n-Si(111) multilayer structure Pisarenko T.A., Yakovlev A.A., Mararov V.V., Tsukanov D.A. 88
II.p.05	Optical and electronic properties of magnesium silicide films formed on silicon Polyakov A.V., Fomin D.V., Sholygin I.O., Galkin N.G., Galkin K.N. 90
II.p.06	Optical spectra and surface morphology of magnesium silicide nanofilms Fomin D.V., Ryabov I.A., Polyakov A.V., Sholygin I.O., Shemetov D.A., Galkin N.G., Galkin K.N. 92
II.p.07	Structural properties of Mg ₂ Si films formed on Si(111) Sholygin I.O., Fomin D.V., Polyakov A.V., Galkin N.G., Galkin K.N. 94
II.p.08	Resistance drift in GeTe–Sb ₂ Te ₃ system Trusov E.P., Vorobyov Y.V., Ermachikhin A.V. 96
II.p.09	The origin of the lateral photovoltaic effect in the SiO ₂ /TeO ₂ /Bi ₂ Te ₃ /n-Si(111) structure: by varying laser illumination Yakovlev A.A., Pisarenko T.A., Tsukanov D.A., Mararov V.V., Balashev V.V., Ignatovich K.V. 98
II.p.10	Synthesis of Mg ₂ Si core-shell nanowires by solid-phase epitaxy Subbotin E.Yu., Kozlov A.G., Pavlov D.V., Lisenkov O.E., Udilov A.D., Prokopeva G.A., Goroshko D.L., Chernev I.M., Khoroshilov D.A., Sinotova S.A., Galkin N.G. 100

III. Advanced optical materials, technologies and devices

III.i.01	Up-scaling of perovskite solar cell technology for terrestrial and space energy systems Luchnikov L.O., Ilicheva E.A., Gren D.A., Le T.S., Gostishchev P.A., Sukhorukova P.K., Luponosov Yu.N., Saranin D.S. 102
III.i.02	Femtosecond laser nanopatterning for IR photodetection and sensing empowered by bound states in the continuum Pavlov D.V., Cherepakhin A.B., Zhizhchenko A.Yu., Kuchmizhak A.A. 104
III.i.03	Monodisperse silica microspheres for reducing friction in lubricating oil Lei Pan, Jianrong Xin, Yao Li, Jiupeng Zhao 105
III.i.04	Phase change materials and their application Lazarenko P.I., Kovalyuk V.V., Kitsyuk E.P., Prokhodtsov A.I., Nevzorov A.A., Menshikov E.V., Sinev I.S., Kozlyukhin S.A., Goltsman G.N., Svetukhin V.V. 106
III.o.01	Femtosecond laser modification of amorphous silicon films for photovoltaic and polarization applications Shuleiko D.V., Sokolovskaya O.I., Martyshov M.N., Serdobintsev A.A., Volkovoyanova L.D., Venig S.B., Pakholchuk P.P., Kuzmin E.V., Zaboltnov S.V., Kashkarov P.K. 107
III.o.02	Laser-pulsed patterning of BaGa ₄ Se ₇ crystals for on-demand anti-reflective surface nanoengineering Kuchmizhak A.A., Cherepakhin A.B., Shevlyagin A.V., Isaenko L.I., Syubaev S.A. 109
III.o.03	Formation of 2D laser-induced periodic surface structures on metal and semiconductor thin films Fedyaj V.E., Bronnikov K.A., Simanchuk A.E., Lazarenko P.I., Yakubov A.O., Zhizhchenko A.Yu., Kuchmizhak A.A., Dostovalov A.V. 111
III.o.04	Laser-assisted fabrication of materials for electrochemical applications Levshakova A.S., Kaneva M.V., Ninayan R., Satymov E.T., Kuchmizhak A.A., Khairullina E.M. 113
III.o.05	Si LIPSS/Mg ₂ Si platform for polarization-selective infrared detection Borodaenko Yu.M., Banniy D.E., Bozhok A.V., Shevlyagin A.V., Gurbatov S.O., Kuchmizhak A.A. 115
III.o.06	High-resolution femtosecond laser coloring of titanium films: diversity of nanotexturing regimes analyzed by neural network Lapidus V.S., Zhizhchenko A.Yu., Kuchmizhak A.A. 117
III.o.07	IR transparent semimetal CaSi ₂ electrodes for thermal switching of VO ₂ phase change thin films Pavlov D.V., Banniy D.E., Bozhok A.V., Il'yaschenko V.M., Cherepakhin A.B., Zhou H., Dou S., Li Y., Kuchmizhak A.A.^{1,2}, Shevlyagin A.V. 119

III.o.08	Switching platform for tunable metasurfaces based on phase change materials <i>Pestova V.B., Pestov G.N., Kitsyuk E.P., Smayev M.P., Saurov M.A., Lazarenko P.I.</i> 121
III.o.09	Charge-transfer plasmons in non-periodic and periodic systems <i>Fedorov A.S., Eremkin E.V., Teplinskaya A.S., Gerasimov V.S.</i> 123
III.o.10	Lasing generation in disordered ZnO resonators <i>Sibirev N.V., Serov A.Yu., Labzovskaya M.E., Kadinskaya S.A., Kondratev V.M., Mikushev S.V., Agekyan V.F., Bolshakov A.D., Shtrom I.V.</i> 125
III.o.11	New erbium-activated oxyfluoroniobate glasses <i>Ignatieva L.N., Polyantsev M.M., Galkin K.N., Savchenko N.N., Marchenko Yu.V., Mashchenko V.A., Pikalov D.O.</i> 127
III.o.12	Monolithic integration of bismuth-substituted yttrium iron garnet on a silicon nitride platform for nonreciprocal photonic devices <i>Sgibnev Y.M., Shelaev A.V., Tananaev P.N., Buzaverov K.A., Baburin A.S., Rodionov I.A., Baryshev A.V.</i> 130
III.o.13	Tuning the optical properties of bound states in the continuum in photonic crystal slabs with embedded Ge nanoislands by symmetry reduction <i>Yurasov D.V., Dyakov S.A., Smagin I.A., Tikhodeev S.G., Gippius N.A., Stepikhova M.V., Peretokin A.V., Shaleev M.V., Smagina Zh.V., Utkin D.E. and Novikov A.V.</i> 131
III.o.14	Observation of bound states in the continuum of different types in the luminescence response of silicon photonic crystal slabs with Ge(Si) nanoislands <i>Peretokin A.V., Stepikhova M.V., Dyakov S.A., Yurasov D.V., Shaleev M.V., Shengurov D.V., Smagina Zh.V., Rodyakina E.E., Novikov A.V.</i> 133
III.o.15	Photoluminescence from functionalized single-walled carbon nanotubes <i>Maksimov F.M., Goldt A.E., Dozmorov S.A., Kalachikova P.M., Vildanova A.R., Morozov A.V., Gladush Yu.G., Nasibulin A.G., Chernov A.I.</i> 135
III.p.01	Model of orthogonal two-wave mixing in photorefractive crystal of cubic symmetry with optical activity <i>Bezruk M.N., Romashko R.V., Efimov T.A., Storozhenko D.V.</i> 136
III.p.02	Comparison of phase-shifting properties of MoSiON and TaSiON layers formed by magnetron sputtering <i>Gromov V.D., Lebedev E.A., Volkov R.L., Borgardt N.I., Anikin A.V., Komlenok M.S., Kurochitskiy N.D., Pavlikov A.V., Gromov D.G.</i> 138
III.p.03	Effect of different gas media, temperature and UV-visible irradiation on the volt-ampere characteristics of TiO ₂ nanopowder layer <i>Kruzhalina M.D., Sorokina L.I., Yakubov A.O., Fedyanina M.E., Dubkov S.V., Gromov D.G.</i> 140
III.p.04	Surface analysis of laser-irradiated Ge ₂ Sb ₂ Te ₅ films <i>Rybina N.V., Kunkel T.S., Ermachikhin A.V., Rybin N.B., Vorobyov Y.V.</i> 142

IV. Formation and properties of ferromagnetic and ferroelectric materials, spintronics

IV.i.01	Magnetic nanocomposites for terranostic applications: diagnostics (MPI, MPI) and magneto-hyperthermic treatment (MHT) <i>Kamzin A.S.</i> 145
IV.i.02	Dynamics of domain walls in thin magnetic films with perpendicular magnetic anisotropy <i>Chernousov N.N., Kozlov A.G., Turpak A.A., Pashenko A.S., Davydenko A.V.</i> 147
IV.o.01	The influence of interface roughness induced by Cu bottom layer on dynamics of domain walls in Cu/Pd/Co/Pd system <i>Chernousov N.N., Silina S.K., Pashenko A.S., Turpak A.A., Kozlov A.G., Davydenko A.V.</i> 149
IV.o.02	Magnetic structure of bilayered thin films Pt/Co/(CoO) <i>Kuznetsova M.A., Turpak A.A., Prihodchenko A.V., Kozlov A.G.</i> 151
IV.o.03	Motion of the ground state of the Edwards-Anderson spin system in the state space under the action of an external field <i>Lobanova E.A., Makarov A.G., Nefedev K.V.</i> 153
IV.o.04	SOT and DMI in WTe _x /Pt/Co/MgO <i>Namsaraev Zh.Zh., Turpak A.A., Kuznetsova M.A., Wang Y., Kozlov A.G.</i> 155

IV.o.05	Influence of structure on magnetic properties of Pt/Co/MgO and WTe _x /Pt/Co/MgO films <i>Prihodchenko A.V., Kuznetsova M.A., Meng F.Y., Feng Y., Wang Y. and Kozlov A.G.</i> 157
IV.o.06	Improvement magnetic properties through transition metal alloying in Fe-Si-B amorphous matrices <i>Sapovskii I.M., Rakhmatullaev T.R., Pinchuk K.E., Komogortsev S.V., Kraynova G.S.</i> 159
IV.p.01	Magnetic multilayer thin films on nanorelief with modulated curvature <i>Rogachev K.A., Samardak A.Yu., Bazrov M.A., Shishelov A.F., Samardak A.S., Ognev A.V.</i> 161
IV.p.02	Magnetic state of BiFeO ₃ compounds co-doped with Sm- and Ti at the morphotropic phase boundary <i>Silibin M.V., Mikhailova M.S., Zhaludkevich D.V., Latushka S.I., Karpinsky D.V.</i> 163
IV.p.03	Electrophysical properties of the Rochelle salt / asbestos nanocomposite material <i>Matveeva T.G., Ivanova M.S., Solovyev V.G.</i> 165
IV.p.04	Interfacial ferromagnetism in sputtered Pt/Gd/Pt system at room temperature <i>Turpak A.A., Pashenko A.S., Chernousov N.N., Ognev A.V., Davydenko A.V.</i> 167

V. Nanostructured coverages, nanocomposites, functional hybrid materials: formation, structure and properties

V.i.01	Tuning properties of carbon nanocomposite coatings formed by accelerated C ₆₀ ions <i>Karaseov P.A., Pukha V.E., Kabachkov E.N., Karaseov K.P., Strizhkin D.A., Shakhmin A.L.</i> 170
V.i.02	Synthesis, structure and electronic properties of epitaxial thin films of MAX phases <i>Tarasov A.S., Lyaschenko S.A., Rautskii M.V., Fedorova N.A., Andryushchenko T.A., Lukyanenko A.V., Yakovlev I.A., Bondarev M.A., Bondarev I.A., Solovyov L.A., Maximova O.A., Tomilin F.N., Varnakov S.N., Ovchinnikov S.G.</i> 172
V.i.03	Prospects of using hollow particles of oxide powders in thermal control systems of spacecraft <i>Mikhailov M.M., Neshchimenko V.V., Morev N.G., Lapin A.N.</i> 174
V.i.04	Ferroelectric nanocomposites on base of porous glasses with modified interfaces <i>Alekseeva O.A., Koroleva E.Yu., Molokov A.Yu., Naberezhnov A.A., Sysoeva A.A., Gorshkova E.Yu.</i> 176
V.o.01	Hydrochemical synthesis of nanostructured metal-oxide compound of the Nb-Bi-Fe-O system <i>Gorokh G.G., Fiadosenka U.S., Chaeusky V.V., Em M., Taratyn I.A.</i> 178
V.o.02	Heterostructured TiO ₂ -CuO _x layers: electrophoretic deposition approach to efficient photocatalysis <i>Sorokina L.I., Volkova L.S., Zhurina E.S., Dubkov S.V., Gromov D.G.</i> 180
V.o.03	Electron spectroscopy of MAX phase (Cr _{1-x} Mn _x) ₂ GeC and Cr ₂ (Ge _{1-x} Si _x)C thin films <i>Andryushchenko T.A., Lyaschenko S.A., Yakovlev I.A., Kriukov R.N., Lukyanenko A.V., Solovyov L.A., Varnakov S.N., Ovchinnikov S.G.</i> 182
V.o.04	Stearic acid as green corrosion inhibitor of MA8 bioabsorbable magnesium alloy: <i>in vitro</i> coating characterization <i>Marchenko V.S., Gnedenkov A.S., Sinebryukhov S.L., Gnedenkov S.V.</i> 184
V.o.05	Effects of silver nanoparticle array degradation on SERS and SICM measurements of living cells by ion-conducting nanopipette <i>Novikov D.V., Chumachenko J.V., Dubkov S.V., Kolmogorov V.S., Gorelkin P.V., Erofeev A.S., Parkhomenko Yu.N., Volkova L.S., Zheleznyakova A.V., Popenko V.F.</i> 186
V.o.06	Periodically spallated Ag+Au films for SERS-detection of polydopamine and chemosensing applications <i>Mitsai E.V., Pilnik A.A., Borodaenko Yu.M., Kuchmizhak A.A.</i> 188
V.o.07	Structure and optical properties of epitaxial Cr ₂ AC MAX-films (A - Ge, Si, Al and Ga) <i>Lyaschenko S.A., Andryushchenko T.A., Yakovlev I.A., Lukyanenko A.V., Varnakov S.N., Ovchinnikov S.G.</i> 190
V.o.08	Amorphous and crystallized tungsten trioxide: structural and optical responses in H ₂ -rich atmosphere <i>Kulikova D.P., Shelaev A.V., Lotkov E.S., Baburin A.S., Rodionov I.A., Baryshev A.V.</i> 191
V.o.09	Hybrid fumarate-containing protective coatings for MA8 magnesium alloy <i>Nomerovskii A.D., Gnedenkov A.S., Marchenko V.S., Sinebryukhov S.L., Gnedenkov S.V.</i> 192
V.o.10	Specifics of sample fabrication for studying high-resistivity thin films of phase-change materials <i>Al-Khadge L.A., Nikitin K.G., Terekhov D.Yu., Ermachikhin A.V., Kiselev A.V., Goroshko O.A., Goroshko D.L.</i> 194

V.o.11	Features of the formation SERS-substrates as a result of the combustion of multilayer thermite structures Al/CuO + Ag <i>Novoselcev A.I., Novikov D.V., Ryazanov R.M., Kruzhalina M.D., Dubkov S.V., Lebedev E.A.</i> 196
V.o.12	Electron paramagnetic resonance of Fe-doped NASICON <i>Saritsky D.A., Grishchenko D.N., Medkov M.A., Ziatdinov A.M.</i> 198
V.p.01	Investigation of electric current influence on properties and morphology of SERS-active Ag-Nb-N-O film for photonic sensorics <i>Chumachenko J.V., Novikov D.V., Dubkov S.V., Gromov D.G., Volkova L.S., Gavrilov S.A.</i> 200
V.p.02	Synthesis of boron and aluminium-based ligatures in a low-frequency arc discharge plasma <i>Churilov G.N., Glushenko G.A., Nikolaev N.S., Shalygina T.A., Elesina V.I., Lopatin V.A., Vnukova N.G., Zhyzhaev A.M., Ivaneeva A.D., Loktev A.N., Tomashevich Y.V.</i> 202
V.p.03	Obtaining and investigation of properties of C, Ni and Pd-based nanocomposites <i>Churilov G.N., Elesina V.I., Isakova V.G., Vnukova N.G., Glushenko G.A., Nikolaev N.S., Tomashevich Y.V., Lopatin V.A.</i> 204
V.p.04	Development of technology for formation of SERS-active nanostructures on Ag/Mo and Ag/Nb alloys <i>Dubkov S.V., Tarasov A.M., Medenkov G.A., Gromov D.G., Novikov D.V., Chumachenko J.V., Volkova L.S., Gavrilov S.A.</i> 206
V.p.05	Thermal annealing of ultrathin Ag films on SiO ₂ for morphology-optimized SERS substrates <i>Grishin T.S., Volkova L.S., Dudin A.A., Dubkov S.V., Medenkov G.A., Gromov D.G.</i> 208
V.p.06	Sol-gel derived nanostructured materials for luminescence and photocatalytic applications <i>Khoroshko L.S., Baglov A.V., Yauseichyk M.A., Korolik O.V.</i> 210
V.p.07	The effect of deposition potential on the electrodeposition of platinum particles on highly-doped silicon wafer for ethanol electrooxidation <i>Volovlikova O.V., Goroshko D.L., Lazorkina E.N., Dubovitsky A.A., Gavrilov S.A.</i> 212
V.p.08	Morphology control of Al-CuO _x thermite materials combustion products due to variation of geometrical characteristics of initial multilayer structure <i>Novoselcev A.I., Ryazanov R.M., Volkova L.S., Dubkov S.V., Gromov D.G., Lebedev E.A.</i> 214
V.p.09	Application of silicon anode materials in lithium-ion full cells <i>Pustovalova A.A., Morozov A.V., Nedoluzhko A.I.</i> 215
V.p.10	Electron paramagnetic resonance of Fe-doped Na ₂ Ti ₆ O ₁₃ <i>Saritsky D.A., Zheleznov V.V., Ziatdinov A.M.</i> 217
V.p.11	Self-cleaning SERS substrates based on TiO ₂ nanopillars decorated with Ag and Cu nanoparticles <i>Volkova L.S., Grishin T.S., Dudin A.A., Nazarkina Yu.V., Dubkov S.V., Gromov D.G.</i> 219
V.p.12	Raman scattering of sp ² -hybridized carbon clusters in graphite oxide <i>Ziatdinov A.M.</i> 221
V.p.13	Magneto-optical ellipsometry for experimental studies of functional thin films of atomic-layered carbon-based MAX phases <i>Maximova O.A., Lyaschenko S.A., Yakovlev I.A., Shevtsov D.V., Tarasov A.S., Varnakov S.N., Ovchinnikov S.G.</i> 223

VI. Biomaterials and biosensors on their base, gas sensors

VI.i.01	Aptamer-conjugated biosensors <i>Kichkailo A.S., Zamay T.N., Zamay G.S., Moryachkov R.V., Shabalina A.V., Lapin I.N., Svetlichnyi V.A., Zamay S.S.</i> 225
VI.i.02	Laser-assisted fabrication of magnetic biosensors <i>Dzhun I.O., Shuleiko D.V., Nesterov V.Yu., Presnov D.E., Perova N.N., Mineev Ya.S., Nazarov A.V., Romashkina I.L., Kozin M.G., Chechenin N.G., Zaboltnov S.V.</i> 227
VI.o.01	Diffraction Pd/PdO nanostructures as a hydrogen sensor element <i>Shelaev A.V., Kulikova D.P. and Baryshev A.V.</i> 229
VI.o.02	Fe ₃ O ₄ -SiO ₂ -Au nanoparticles for combined radiation therapy and phototherapy <i>Markin N.S., Gordeev I.S., Fu H.E., Lapidis V.S., Shevlyagin A.V., Kuchmizhak A.A., Ivannikov S.I., Kim Y.B., Samardak A.Yu., Samardak A.S., Kim Y.K., Ognev A.V.</i> 230
VI.o.03	SERS-based biosensors for drug resistance testing <i>Mushenkov V.A., Nechaev A.N., Kukushkin V.I., Zavyalova E.G.</i> 232

VI.p.01	Improving the sensitivity of a gas sensor based on anodic titanium oxide nanotubes <i>Dronova D.A., Savchuk T.P., Butmanov D.D., Zheleztsov A.D.</i> 234
VI.p.02	Development of MEMS resistive gas sensors for smart nose technology <i>Kondrateva A.S., Enns Y.B., Kazakin A.N., Komarevtsev I.M., Karaseov K.P., Bakanova M.D., Karaseov P.A.</i> 236
VI.p.03	Led-based compact illuminator design for effective photodynamic therapy <i>Sain A.Yu., Abdurashitov A.S., Proshin P.I., Terentyeva D.A., Sukhorukov G.B. and Sindeeva O.A.</i> 238
	Author Index 240

Plenary lectures

Nano- and microparticulation for remote controlled drug delivery systems

Sindeeva O.A.¹, Kozyreva Z.V.¹, Proshin P.P.², Abdurashitov A.S.^{1,2}, Sukhorukov G.B.*^{1,2}

¹ Skolkovo Institute for Science and Technology, Moscow, 121205, Russia

² Life Improvement by future Technologies (LIFT) Center, Moscow Russia

*e-mail: g.sukhorukov@skoltech.ru

Abstract. The paper reviews the most recent advances in elaboration various micro- and nanoparticles particles and ultrafilm coatings for controlled drug delivery and cell stimulation. Especial attention is given to exploration of remote physical stimuli to guide and activate biological function. These physical stimuli appropriate for remote drug delivery are magnetic field, ultrasound, light and the delivery systems should contain nanostructures susceptible to these signal. We focus on two developments relevant to use polyelectrolytes capsules with carbon nanoparticles as method for cell tracking and coating of medical devices with stimuli drug release coating. Perspectives are limitations are discussed.

1. Introduction

One of the challenges in the bionanotechnology field today is development of micro or nano-sized delivery systems comprising different functionalities, presumably for local sensing, tracking and medical cargo delivery. These systems should be able to ship and to carry bioactive substances to pre-defined site and unload it in designed time and place predominantly with remote physical signalling. For decade, so called Layer-by-Layer (LbL) assembled capsules have been intensively studied owing to their ability to encapsulate a wide range of chemicals from complex biomacromolecules and for their permeability to be modified and their responsiveness to different factors and functionalities to be tailored in one capsule entity. Current research leads to the fabrication of carriers with remote guiding and activation by optical, magnetic and ultrasound addressing, what envisages unique applications as multifunctional biomaterials, including intracellular entering and in-vivo delivery with remote controlled release of (bio)-chemicals cargo. While LbL capsules gained a tremendous attention due to their flexibility to add extra functionality by incorporation of responsive polymer and/or nanoparticles. In general, there are limitation for LbL capsule application relevant to relatively low scalability and problematic large scale manufacturing. Nevertheless, these capsules find a good perspectives in cells studies. Here, we report on novel developments of use of carbon nanoparticles incorporated in capsules and enable to switch capsule fluorescence while these capsules are internalized by biological cells. Up to now there various cells lines ranging from macrophages and cancerous cells to fibroblasts and neuron capable to internalize capsules of few micron sized.

Another development the paper highlights is relevant to the area of elaboration of defined polymer structures on patterned surfaces. Polymer layers can be deposition onto widely used PDMS stamps forming, so called, microchamber arrays enabled to accommodate various biologically active molecules. These chambers can be sealed over with another thin made of polymeric layers and resulted structure is pulled off to form free standing microchambers. Entrapment of water soluble molecules into sealed chambers is performed by hydrophobic layer, such as polylactic acid and water soluble molecule make

precipitate inside wells upon drying. Sealing results on formation of micro-sized air-bubble what can keep water soluble molecules inside the chamber until it released upon remote signalling via ultrasound or light. Such microchamber film can be deposited on various medical devices including catheters, stents and implants. Thus, once the medical device coated with microchamber film with drug is placed in the body the release can be stimulated by ultrasound. Examples are given on in vivo studies and clinical trials. Also, these microchambers can be separated from the film onto individual polymer printed capsules made of hydrophobic polymers and can be of different shapes [1,2]. These capsules have the same advantages in term of encapsulation capacity as microchambers in particular small molecules entrapment, stimulating release and possibilities for cell uptake.

Elaboration of microchamber coating as well as other new developments in micro- and nanostructured materials on surface found clinical application, which are now under clinical trials.

2. Experiment

Experimental details are given in referenced works [3-5].

3. Results and discussions

3.1. Photoconvertible capsules

Photoconvertible labels for cell tracking are key approaches for solving complicated medical and biological problems (e.g., studying metastatic, embryogenesis, and tissue regeneration processes). Currently, photoconvertible membrane dyes and proteins are used for this purpose, but they usually have disadvantages such as low stability, requirement for genetic modification, etc. We explore photoswitchable labels based on capsules over tracking of mesenchymal stem cells

The markers were obtained from polyelectrolyte microcapsules using hydrothermal synthesis for the encapsulation of Rhodamine B and the formation of carbon structures serving as catalysts for conversion in the capsules. The photoconvertible effect and spectral shifts were shown using confocal microscopy figure 1. The uptake of markers into cells demonstrated no effect on cytotoxicity, morphology, proliferation and motility of cells.

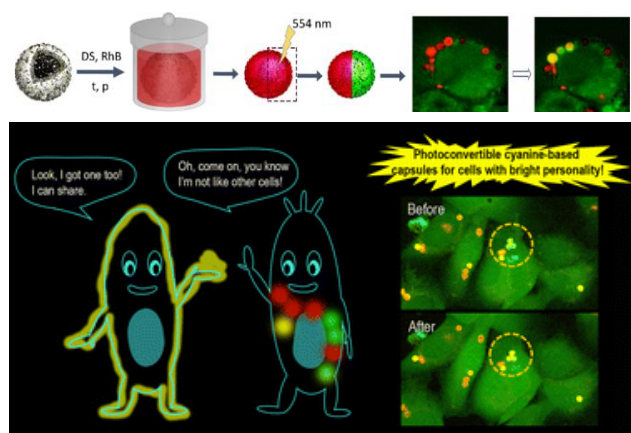


Fig. 1. Photoconversion of rhodamine containing capsules in presence of carbon nanoparticles as done in Demina et al [3]. Labelling and tracking of individual cells using cyanine dye [5].

The photoconversion efficiency of the synthesized markers depends on the irradiation wavelength, laser power density, and time of exposure and was associated with the hypochromic shift of the fluorescence peak (up to 15–40 nm). These markers are actively internalized by various types of cells (mesenchymal stromal cells, macrophages, myoblasts, etc.) without causing pronounced effects on toxicity, morphology, and mobile properties. The photoconversion of markers inside cells did not lead to death. Cells usually captured several capsules, which made it possible to assign each marked cell to its own individual color code and reliably identify each of them over time. Capsules are limited in their exchange between cells and principal of cell tracking might be used on different dyes as well [1]. The listed properties, as well as the high stability, provided the opportunity to detect a selected and labeled cell in monolayers, spheroids, and tissues after cell transplantation over few days or weeks.

3.2. Drug eluting microstructural coating of implantable medical devices

Drug-eluting coatings on implantable medical devices with programmed release of various medical components on demand is an actual task for modern development of personalized medicine. Despite of significant progress in that area there is still limited number of currently existing methods of producing coatings, which go beyond the laboratory towards clinical trials. Mainly, the problems in medical exploitation of drug eluting coatings are relevant with encapsulation efficiency and proper retention of drug in biodegradable polymer coating, programming release and appropriate scaling up facilities.

We have elaborated film fabrication and on implant deposition methods to encapsulate and retain various bioactive compounds with small molecular weight and high water solubility. The polymer used for this coating are PLA, PLGA, PCL with approval for medical use. Release of these components can be defined as polymer degradation or, if needed can be triggered on site by ultrasound. Load of active component can reach 200–400 µg/cm² of implant surface with retention in body up to several weeks. The so-called PLACE (Printed Layered Adjustable Cargo Encapsulation) technology is scalable and can be applied for coating implants with complexed shape with programmed release of drugs [5]. At present, successful preclinical studies on deposition and release of antibacterial

(Cefazolin) and/or immune-suppressor (prednisolone and its derivatives) drugs paved a way to clinical trials to treat diseases such as connective tissue growing reduction via the local suppression of inflammatory after balloon dilatation of urethral catheter with ultrasound induced release; prolonged (3–5 month) release of prednisolone from the surface of the biliary stent to minimize biliary and pancreatic stenting complications (restenosis due to overgrowth of connective tissue); prolonged release of cefazolin from 3D printed individual bone implant's surface to prevent the risk of post-surgery implant-associated infections [5].

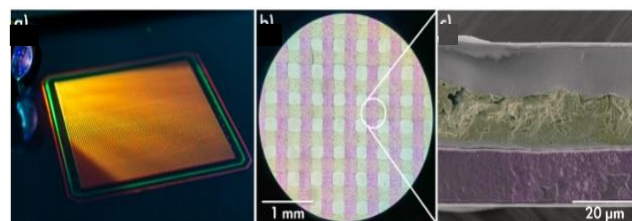


Fig. 2. PLACE technology with two different model drug (as dyes) enabling sequential release of two components [5].

At present, the developed drug-eluting coatings fulfils a number of unique clinical demands such as fully optimized to coating various medical devices, able to incorporate wide range of medical reagents with “a la carte” drug-release kinetics what is achieved by layered deposition. Competitive advantages are: adopted for encapsulation of available drug forms, used FDA approved polymers, scalable manufacturing (including additive technologies as 3D print), high payload capabilities (drug to polymer ratio is up to 10:1), sensitive to external stimulation for triggered drug release on doctor demand/

4. Conclusions

As discussed above, the modern methods of micro- and nanofabrication can enhance their use in drug delivery and tracking and sensing biologically important materials. Although we consider here two different more recent applications. Carbon nanoparticles used for photochemical reactions on dye contribute to cell tracking analysis. In this application there is no need for high production of capsules as one would not need millions of capsules. While application for coating medical devices does need scalability and automation at production. Currently, there is an intensive research for neural cell stimulation via piezo- and magnetoelectric nanoparticles, where high production and not necessary. Thus, balance of envisaged use and scalability is essential to consider while tackling new horizons in participation for biomedical use.

Acknowledgements

Russian Science Foundation grant 25-63-00019 is acknowledged for support this work

References

- [1] V. Kudryavtseva, G.B. Sukhorukov. *Adv. Mater.* 2024, 2307675.
- [2] O.A. Sindeeva, Z.V. Kozyreva, A.S. Abdurashitov, G.B. Sukhorukov. *Advances in Colloid and Interface Science* **340** (2025) 103462.
- [3] P.A. Demina, O.A. Sindeeva, A.M. Abramova, E.S. Prikhozhenko, R.A. Verkhovskii, E.V. Lengert, A. V. Sapelkin, I.Y. Goryacheva, G.B. Sukhorukov. *ACS Appl. Mater. Interfaces* **13** (2021) 19701.

- [4] Z.V. Kozyreva, P.A. Demina, O.I. Gusliakova, G.B. Sukhorukov. O.A. Sindeeva. *J. Mater. Chem. B*, **12** (2024) 12672.
- [5] P.I. Proshin, A.S. Abdurashitov, O.A. Sindeeva, A.A. Ivanova, G.B. Sukhorukov. *Polymers* **14(20)** (2022) 4318.

Non-hermitian singularities in all-dielectric metastructures: from bound states in the continuum to exceptional points and bulk fermi arcs

Bogdanov A.A.^{1,2}

¹ Qingdao Innovation and Development Center, Harbin Engineering University, Qingdao, 266000, China

² School of Physics and Engineering, ITMO University, Saint-Petersburg 197101, Russia

Non-Hermitian singularities – exceptional points (EPs), bulk Fermi arcs, Rayleigh anomalies, and bound states in the continuum (BICs) – exhibit unique wave phenomena with transformative potential in photonics [1,2]. While EPs enable extreme sensitivity, Fermi arcs bridge Hermitian and non-Hermitian topology, and BICs offer infinite radiative quality factors. Here, we theoretically and experimentally investigate these singularities within isolated dielectric and periodic metastructures. Specifically, we predict exceptional BIC (EP-BIC) states in vertically coupled dielectric metasurfaces [3], experimentally demonstrate bulk Fermi arcs in single dielectric resonators [4], and explore the previously unstudied link between EPs and anapole states [5].

References

- [1] E. J. Bergholtz et al., *Rev. Mod. Phys.* 93, 015005 (2021).
- [2] H. Zhou et al., *Science* 359, 1009 (2018).
- [3] A. Canós Valero et al., *Phys. Rev. Lett.* (in press, 2025).
- [4] N. Solodovchenko et al., *arXiv:2502.12711* (2025).
- [5] F. Zhang et al., *Sci. Adv.* 11, eadr9183 (2025).

Short bio



Andrey Bogdanov is a professor at ITMO University and Harbin Engineering University. He obtained Bachelor's and Master's degrees with honors in Solid State Physics at Saint-Petersburg State Polytechnical University. He received his PhD from Ioffe Institute in 2012. The thesis was devoted to the theoretical analysis of quantum cascade lasers. This work was awarded the “Young Scientist Award” by the European Optical Society. Andrey Bogdanov is the head of the Theoretical Nanophotonics group and specializes in studying optical nanoantennas, surface waves, nonlinear optics, metasurfaces, bound states in the continuum, and related directions. Andrey Bogdanov has authored over 200 journal papers (*Science*, *Sci. Adv.*, *Adv. Mat.*, *Phys. Rev. Lett.*, *Nano Letters*, and others), over 100 conference presentations, and two patents. He is a PI in more than 20 projects supported by National foundations in China and Russia. In 2021, he received the Leonard Euler Prize for young scientists "For research of dielectric nanoantennas and nanoresonators for localization and control of electromagnetic radiation on subwavelength scales." He is a fellow of the BASIS Foundation for Theoretical Physics and Mathematics and a laureate of the Government awards for scientific and pedagogical activities. He is the author of two online courses, the head of the international master program “Nanophotonics and Metamaterials,” the chair of the annual International Summer School on Nanophotonics and Metamaterials, and the Editor of *Photonics and Nanostructures – Fundamentals and Applications* journal.

Research progress on Ba-Si compound thin films for energy applications

Suemasu T.*

Institute of Pure and Applied Sciences, University of Tsukuba, Tsukuba, Ibaraki 305-8573, Japan

*e-mail: suemasu.takashi.gu@u.tsukuba.ac.jp

Abstract. Semiconducting BaSi₂ and Ba₂AgSi₃ are promising as thin film solar cells and thermoelectric applications, respectively. For BaSi₂, the photoresponsivity has been used as a key measure because it is proportional of carrier lifetime in materials. We will show that the photoresponsivity has been improved by more than 200 times for the past five years. In addition, a thin-film solar cell structure consisting of an electron transport layer and a hole transport layer is presented. As for Ba₂AgSi₃, the first demonstration of epitaxial thin-film growth on Si(111), evaluation of thermoelectric properties, and investigation of preferential occupation site by impurity are presented.

Semiconducting BaSi₂ and Ba₂AgSi₃ are both Zintl phases^{1,2)} and expected to be used as thin-film solar cell³⁾ and thermoelectric (TE) materials,^{4,5)} respectively. In this paper, the progress of the research in each material is presented.

BaSi₂ is an indirect bandgap semiconductor with a forbidden bandwidth of about 1.3 eV, and has a large optical absorption coefficient exceeding $3 \times 10^4 \text{ cm}^{-1}$ at energies higher than 1.5 eV.⁶⁾ In a unit cell, BaSi₂ contains Si tetrahedra as shown in Fig. 1. Both Ba and Si are abundant elements. Solar cells are being considered as an application of this material. In 2016, we achieved an energy conversion efficiency approaching 10% in a p-BaSi₂/n-Si heterojunction solar cell using BaSi₂ epitaxial films grown by molecular beam epitaxy (MBE).^{7,8)} Since then, we have been working on improving the quality of BaSi₂ film as a light absorbing layer using spectral sensitivity as an evaluation index. Compared with the photocurrent density obtained when a bias voltage (0.1 V) is applied to the BaSi₂ film in the direction directly across the film, we have achieved an improvement of about 200 times in the past years as shown in Fig. 2.⁹⁾ This is due to our improved understanding of the recombination centers of carriers formed in the forbidden band, which we have been working to avoid. Our understanding of the defect species in the sample has also advanced, and by considering the oxygen contained in the film, we have reached the stage where the experimental results obtained by the electron spin resonance method can be explained by first-principles calculations, including the defect structure,¹⁰⁻¹²⁾ and both theoretical and experimental research on BaSi₂ has advanced dramatically. In the sputtering method, the oxygen concentration in BaSi₂ films is high ($>10^{20} \text{ cm}^{-3}$), and post-annealing at high temperatures above the glass softening point is necessary to control the conduction type by impurity doping¹³⁾. Therefore, we have determined that a device structure in which an undoped BaSi₂ film with high spectral sensitivity is sandwiched between an electron transport layer (ETL) and a hole transport layer (HTL) to separate photogenerated carriers is effective.¹⁴⁾ Quite recently, we have achieved high photoresponsivity of BaSi₂ films on glass substrate.¹⁵⁾ The small electron affinity of 3.2 eV for BaSi₂ makes it a candidate for many ELT materials. On the other hand, it seems uneasy to find suitable HTL materials for BaSi₂ due to the small ionization potential (*IP*) of BaSi₂ at 4.5 eV. Several materials with *IP*s of almost the

same value as BaSi₂ will be presented and the progress of the research will be discussed.

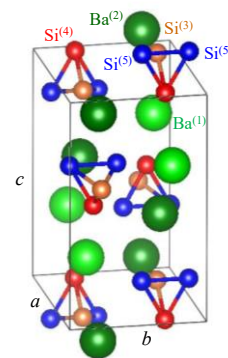


Fig. 1. Crystal structure of BaSi₂.

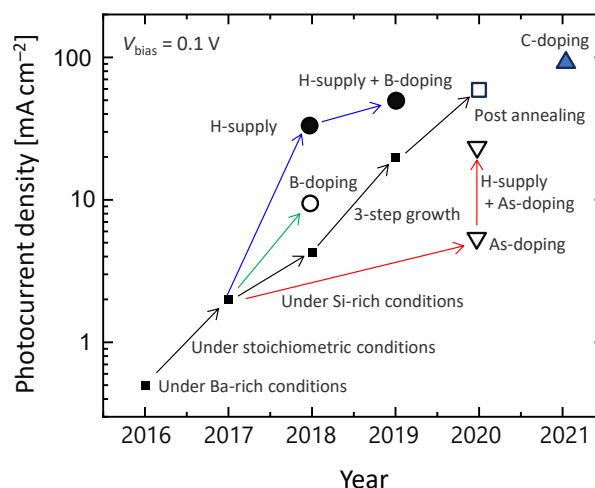


Fig. 2. Improvement in photocurrent density of BaSi₂ films calculated by integrating the product of the AM1.5 spectrum and the external quantum efficiency spectrum derived from the photoresponse spectrum when a bias voltage of 0.1V is applied between surface (ITO) and rear (Al) electrodes.⁹⁾

Ba₂AgSi₃ is also a Zintl phase with the formal charges Ba²⁺, Ag⁺, and [Si₆]¹⁰⁻ in the Ba-Ag-Si system,^{2,16)} and crystallizes with space group of *Fddd* (No. 70). Its lattice constant is $a = 1.479 \text{ nm}$, $b = 0.853 \text{ nm}$, and $c = 1.961 \text{ nm}$. The compound is described as (Ba₂AgSi₃)₁₆. Figure 3 shows the crystal structure of Ba₂AgSi₃, wherein Si forms a hexagon and is in the same *a*-*b* plane as Ag. In the *c*-axis direction, the Ag/Si and Ba planes are stacked alternately and equally spaced. Reports on the TE properties of this

material are fairly limited,^{4,16)} wherein the ZT of p-type bulk sample was very high, 0.52 at 323 K. However, there has been no report on its basic properties such as energy band gap (E_g), ionization energy, dopants for controlling its carrier type, and thin-film formatoin.

Ba_2AgSi_3 films were formed by MBE using elemental Ba, Ag, and Si sources. Since the Si forms hexagonal structure, we chose Si(111) substrates for thin-film deposition. By preciously controlling the deposition rate of each element, we have succeeded the formation of Ba_2AgSi_3 films for the first time. Figure 4 shows the (a) out-of-plane and (b) in-plane XRD patterns of the grown film. The diffractoin peak positions are perfectly matched between the Si and the grown films, meaning the epitaxial growth of Ba_2AgSi_3 films. The band gap of this material was measured to be around 0.1 eV from the temperature dependence of resistivity.⁵⁾ Regarding the preferential occupation site of group 13 and 15 elements,⁵⁾ first-principles calculation revealed that when B(P) replaces one Ba, Ag, or Si site, the formation energy becomes the smallest when the Si site is substituted, and the conductivity type becomes p-type (n-type), respectively, in terms of the position of the Fermi level. Epitaxial films exhibited an excellent performance with a high Seebeck coefficient and a high power factor ($S = 296 \mu V K^{-1}$, $PF = 250 \mu W m^{-1} K^{-2}$) near room temperature (311 K), making them highly promising for flexible TE applications.¹⁷⁾ First-principles calculations revealed that B is the most suitable p-type dopant for Ba_2AgSi_3 , while group 15 elements like P, As, and Sb are n-type dopants. Our findings pave the way for the application of this new thermoelectric material in thermoelectric power generation.

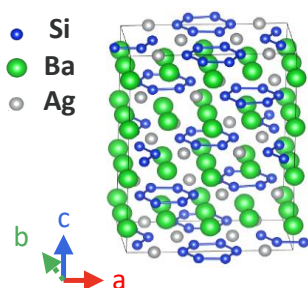


Fig. 3. Crystal structure of Ba_2AgSi_3 .

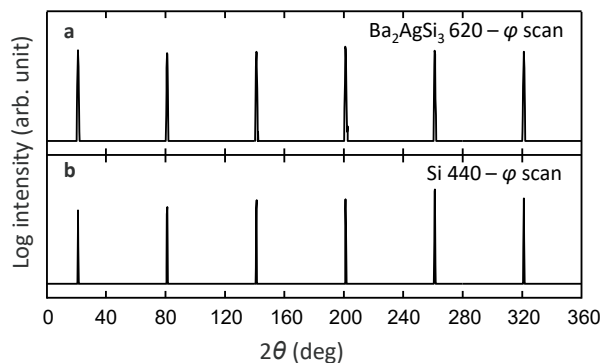


Fig. 4. ϕ scan XRD patterns obtained using (a) 620 reflection of Ba_2AgSi_3 and (b) 440 reflection of Si.

Acknowledgements

This work was financially supported in part by JSPS KAKENHI (Grant Nos. JP19KK0104, JP21H04548, and JP24KK0083). A part of this work was supported by “Advanced Research Infrastructure for Materials and Nanotechnology in Japan (ARIM)” of the Ministry of Education, Culture, Sports, Science and Technology at University of Tsukuba (JPMXP1224BA002).

References

- [1] H. K. Janson, H. Schäfer, and A. Weiss, *Z. Anorg. Allg. Chem.* **372**, 87 (1970).
- [2] G. Cardoso, W. Carrillo-Cabrera, M. Schultheiss, K. Peters, and H.G. von Schnering, *Anorg. Allg. Chem.* **625**, 285 (1999).
- [3] T. Suemasu and D.B. Migas, *Phys. Status Solidi A* **219**, 2100593 (2022).
- [4] Y. Koda, R. Akichi, and M. Mesuda, *TOSOH Res. Techno. Rev.* **65**, 63 (2021).
- [5] K. Kajihara, Y. Koda, T. Ishiyama, S. Aonuki, K. Toko, S. Honda, M. Mesuda, and T. Suemasu, *J. Appl. Phys.* **135**, 075107 (2024).
- [6] K. Morita, Y. Inomata, and T. Suemasu, *Thin Solid Films* **508**, 363 (2006).
- [7] D. Tsukahara, S. Yachi, H. Takeuchi, R. Takabe, W. Du, M. Baba, Y. Li, K. Toko, N. Usami, and T. Suemasu, *Appl. Phys. Lett.* **108**, 152101 (2016).
- [8] S. Yachi, R. Takabe, K. Toko, and T. Suemasu, *Appl. Phys. Lett.* **109**, 072103 (2016).
- [9] T. Suemasu, *Jpn. Soc. Appl. Phys. Review* 230431 (2023).
- [10] T. Sato, C. Lombard, Y. Yamashita, Z. Zu, L. Benincasa, T. Toko, S. Gambarelli, and T. Suemasu, *Appl. Phys. Express* **12**, 061005 (2019).
- [11] Y. Cao, J.-M. Mouesca, S. Gambarelli, and T. Suemasu, *Jpn. J. Appl. Phys.* **62**, SD1009 (2023).
- [12] T. Sato, J.-M. Mouesca, A. Barra, D. Gourier, M. Imai, T. Suemasu, and S. Gambarelli, *Act. Materialia* **278**, 120230 (2024).
- [13] H. Hasebe, K. Kido, H. Takenaka, M. Mesuda, K. Toko, D.B. Migas, and T. Suemasu, *Jpn. J. Appl. Phys.* **62**, SD1010 (2023).
- [14] R. Du, S. Aonuki, H. Hasebe, K. Kido, H. Takenaka, K. Toko, M. Mesuda, and T. Suemasu, *Jpn. J. Appl. Phys.* **62**, SD1015 (2023).
- [15] R. Du, H. Takenaka, T. Sato, Y. Koda, M. Mesuda, K. Toko, and T. Suemasu, *ACS Appl. Mater. Interfaces* **16**, 52595 (2024).
- [16] I. Zeiringer, E. Bauer, A. Grytsiv, P. Rogl, and H. Effenberger, *Jpn. J. Appl. Phys.* **50**, 05FA01 (2011).
- [17] K. Kajihara *et al.*, submitted.

Desing of nanomaterial and nanostructure for thin film thermoelectric generator

Nakamura Y.

Graduate School of Engineering Science, Osaka University

Abstract. Towards stand-alone power supply for IoT sensors, thin film thermoelectric generator from low temperature wasted heat has been expected. For its realization, dimensionless figure of merit zT , described as $S^2\sigma T/\kappa$, is required to be high, where S is Seebeck coefficient, σ is electrical conductivity, and κ is thermal conductivity. However, the correlation among three thermoelectric properties makes it difficult to increase zT .

Nanostructuring is one of the promising approaches to increase ZT by controlling three thermoelectric properties. Furthermore, nanomaterials are drawing much attention because their inherent low dimensionality can bring low thermal conductivity, high carrier mobility, and high Seebeck coefficient. In these strategies, nanostructure and nanomaterial design and well-controlled formation of these thin films are required.

We have developed various kinds of original well-controlled nanostructures and nanomaterials: For example, Si-based films including ultrasmall nanodots of group IV semiconductor with controlled interfaces, strains, crystal orientations, and compositions. Therein, phonon was coherently scattered on nanoscale, resulting in the ultralow κ and high σ . For power factor enhancement, we succeeded in obtaining giant power factor using semiconductor quantum well of GaAs/AlGaAs. Furthermore, we focused on quasi 2 dimensionality and formed Ca-intercalated multi-layered silicene films. By modifying the silicene bucked structure, S was enhanced with high σ . Furthermore, In this talk, we will present our nanostructuring and nanomaterial strategies for thermoelectric performance enhancement.

Nano- and microstructured materials and photonics work together for biomedical applications

Gorin D.A.*

Skolkovo Institute of Science and Technology, Bolshoy Boulevard, 30, bld. 1, Moscow 121205, Russia

*e-mail: d.gorin@skoltech.ru

Abstract. One of the trends in biophotonics is the use of multimodal diagnostic systems that combine several types of visualization in one device, such as optoacoustics (OA) and ultrasound (US), MRI and OA. This requires the creation of multimodal contrast agents. A technology for the synthesis of multimodal and multifunctional contrast agents (CA) has been developed. It has been established that the concentration of inorganic nanoparticles and / or organic dyes in the core-shell and shell structures allows varying the contrast of OA, fluorescent and MRI images. The core can be in a gaseous, liquid and solid phase. The presence of iron oxide nanoparticles in the shells allows not only to increase MRI contrast, but to use a magnetic field for their controlled aggregation and movement. External influences, such as laser radiation or low-intensity ultrasound, allow remotely triggering the therapeutic function of contrast agents. The developed technology allows the synthesizing composite particles with specified properties, which, together with modern methods of visualization and detection, can be used to create a new generation of contrast agents combining such functionalities as multimodal visualization and remotely activated therapeutic action.

Nano- and microstructured materials have good prospects for creating new type of contrast agents. A technology for scalable synthesis of MRI contrast agents based on iron oxide nanoparticles has been developed. These agents are less toxic than traditional gadolinium-based contrast agents and have therapeutic potential against tumor cells. The methods for obtaining particles with a given nanostructure include the sequential adsorption method [1-3], the freezing induced loading (FIL) method [2-5], and their combination [4]. The possibility of using optical methods for *in situ* FIL monitoring has been shown.

The presence of inorganic nanoparticles and/or organic dyes in core-shell structures and microcapsules allows them to be visualized by an optoacoustic method [6-13]. The core can be in a gaseous [6,7], liquid [8], or solid phase [9]. The presence of a liquid or gaseous core provides ultrasound (US) contrast [7,8].

It has been established that the optoacoustic signal from microcapsules is determined by the concentration of the substance absorbing laser radiation and its location in the capsule (in the polymer shell or the internal volume of the capsules) [1,3,10,13].

The presence of iron oxide nanoparticles allows for MRI visualization of nanocomposite particles [8,12]. In addition, the presence of iron oxide nanoparticles in the capsules allows using a magnetic field for their controlled aggregation and movement [5]. The MRI image contrast of microcapsules containing iron oxide nanoparticles can be changed by varying their average value between iron oxide nanoparticles in the nanocomposite shell [11], and the capsule shell can be destroyed using ultrasound exposure [12,13].

The possibility of combining encapsulated gold nanoparticles (nanozymes) and a photodynamic (PD) dye to increase the effectiveness of photodynamic therapy (PDT) has been shown. It has been shown that for capsules containing both gold particles and photodynamic dye, the efficiency of PDT is 9 times higher compared to capsules containing only PD dye, and 25 times more effective compared to non-encapsulated PD dye [14].

The possibility of using microstructured fibers with a hollow core to create optical and optoacoustic sensors has been demonstrated [15,16].

Nano- and microstructured materials together with modern photonics methods, which have already become commonplace in both preclinical and clinical studies, can be used to create new multimodal and multifunctional contrast agents that combine such functionalities as visualization, *in vivo* monitoring of biochemical processes, and remotely activated therapeutic action.

Acknowledgements

This work was supported by Skolkovo Institute of Science and Technology – Hamad Bin Khalifa Joint Projects grant No. 1-HBKU-0001.

References

- [1] M.D. Mokrousov et al, Biomedical Optical Express, **10**, (2019), 4775.
- [2] M.V. Novoselova et al, Colloids and Surface B: Biointerfaces, **181**, (2019), 680.
- [3] M.D. Mokrousov et al, Biomedical Optics Express, **12**, (2021), 3181.
- [4] S.V. German et al, Scientific Reports, **8**, (2018), 17763
- [5] E.S. Vavaev et al, ACS Applied Nano Materials, **5**, (2022), 2994.
- [6] J. Mujtaba et al, Advanced Materials, (2021), 2007456.
- [7] R.A. Barmin et al, Colloids and Surfaces B: Biointerfaces, **219**, (2022), 112856.
- [8] E.A. Maksimova et al, Laser & Photonics Reviews, (2023), 2300137.
- [9] R. E. Noskov et al, Adv. Mater., (2021), 2008484.
- [10] M.V. Novoselova et al, Photoacoustics, (2020), 100186.
- [11] S.V. German et al, Phys. Chem. Chem. Phys., **18**, (2016), 32238.
- [12] M.V. Novoselova et al, Nanomedicine: Nanotechnology, Biology and Medicine, **47**, (2023), 102612.
- [13] M.V. Novoselova et al, Colloids and Surfaces B, (2021), 111576.
- [14] I. S. Sergeev et al, Particle & Particle Systems Characterization, (2024), 2300149.
- [15] T. Ermatov et al, Light: Science & Applications, **9**, (2020), 173.
- [16] N. Kaydanov et al, ACS Photonics, **8**, (2021), 3346.

Novel development in silicide application

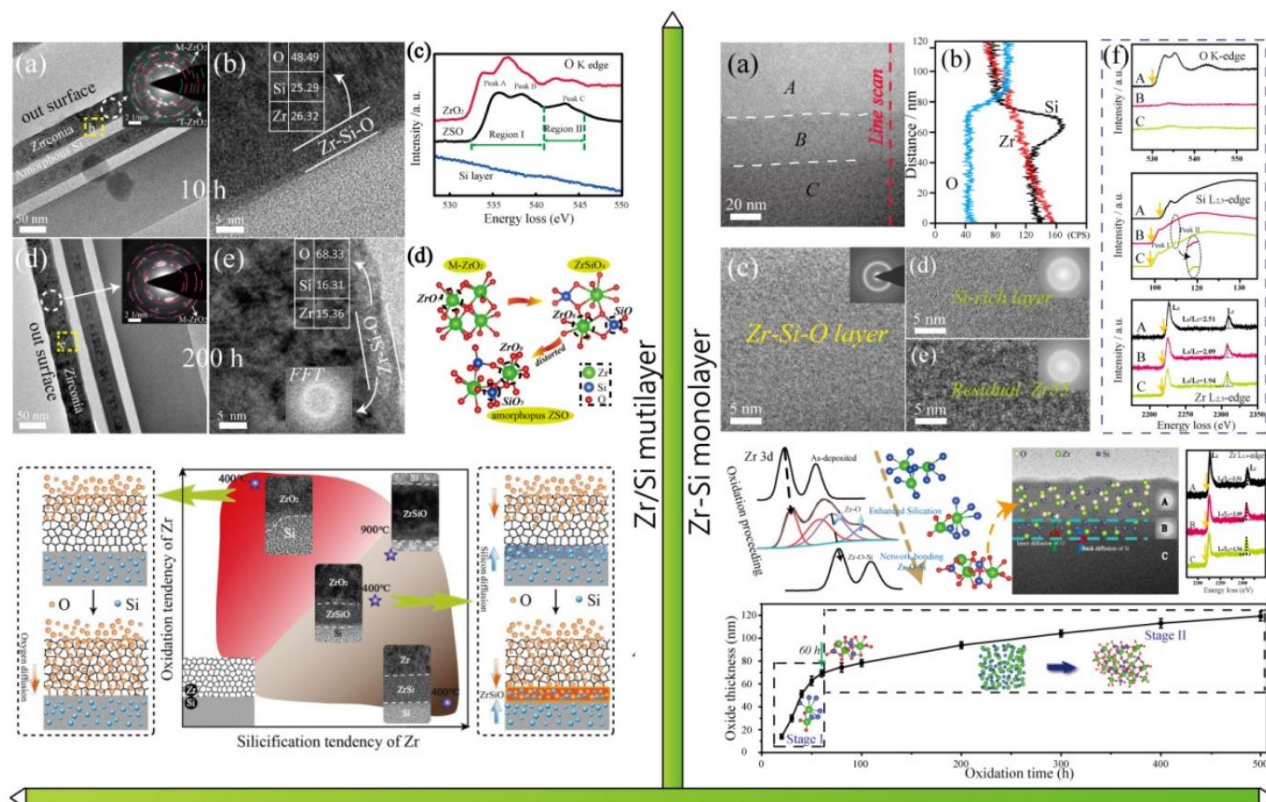
Junhua Hu*, Guoqin Cao

School of Materials Science and Engineering, Zhengzhou University, Zhengzhou 450001, China

*e-mail: hujh@zzu.edu.cn

Abstract. Silicide materials, especially zirconium silicide, have good thermal matching characteristics and chemical compatibility with zirconium alloy, as well as structural stability and oxidation resistance at high temperature. Recent advancements in thin film deposition technologies, particularly through high target utilization sputtering (HiTUS) systems, have enabled systematic investigations into the structure-property relationships of Silicide coatings. Contemporary research has focused on optimizing coating performance through innovative compositional gradient designs and nano-layered architectures, which effectively enhance their high-temperature structural integrity and oxidation resistance. The development of these functionally graded coatings has shown particular promise in nuclear applications where simultaneous requirements for interfacial compatibility and extreme environment durability must be satisfied: **1)** Based on the characterization of XPS and EELS, the oxygen-induced chemical bond reassignment (OBR) process and the formation mechanism of amorphous Zr-Si-O layer in the initial normal working condition of Zr-Si coating were established for the first time. At the initial stage of oxidation, the surface unoxidized silicon tends to further combine with Zr, resulting in enhanced hybridization between Zr and Si, which was conducive to the formation of amorphous oxide layer. The chemical bond is strengthened and the silicon-rich transition layer was formed by the OBR process. The stability of the amorphous oxides (Zr/Si atomic ratio, 2:1) was maintained. The subsequent bonding relaxation of amorphous ZSO was the key structural basis for water stability. **2)** The structure of Zr/Si multilayer films was designed, and the competitive formation and multilevel protection effect of amorphous passivation films at Zr-Si-O (ZSO) interface were confirmed. In the multilayer system, the phase selection of amorphous ZSO was a scale-dependent process determined by the competitive consumption of Zr layers by silicification and oxidation. **3)** Further, amorphous Zr-Si-O coatings with different Zr/Si atomic ratios were prepared by sputtering method. The adsorption energy of hydroxide on silicon atoms was increased by the change of amorphous bonding structure ($-\text{Si}-\text{O}-\text{Si}- \rightarrow -\text{Zr}-\text{O}-\text{Si}-$), and the reaction dissolution of silicon was inhibited in high temperature and high pressure water. On this basis, the bonding mixing enthalpy and the compact arrangement rules of amorphous atoms were combined, and the composition basis of the structural stability of amorphous ZSO coating in the service process was explored (two interfacial stability: Zr/ZSO, ZSO/H₂O). Ensuring the content of silicon was high enough was the basis of oxygen resistance, and the contribution of zirconium was reflected in inhibiting the reaction between silicon and high temperature water.

Key words: Zirconium Silicide; bonding state; phase selection; reaction dissolution; interfacial stability



3D, 2D and 1D in silicon, silicides, III-V compounds and transition metal oxides: *ab initio* prediction of unexpected properties

Migas D.B.^{*,1,2}

¹ Belarusian State University of Informatics and Radioelectronics, 6 P. Browka St., Minsk 220013, Belarus

² National Research Nuclear University MEPhI (Moscow Engineering Physics Institute), Kashirskoe Shosse 31, 115409, Moscow, Russia

*e-mail: migas@bsuir.by

Abstract. We present our recent results on ground state, electronic, optical, magnetic and transport properties of β -FeSi₂, OsSi₂, BaSi₂, CaSi₂, FeSi, CrSi, Nb₁₂O₂₉, W₁₈O₄₉ and BaFe₁₂O₁₉ as bulk materials, Mg₂Si and Ca₂Si as thin films and 2D materials, Mg₂Si and Ca₂Si as single wall nanotubes, III-V, α -FeSi₂ and TiO₂ nanowires by means of *ab initio* techniques in order to assess predictive power of theoretical calculations.

1. Introduction

Ab initio techniques are the powerful tool in predicting ground state, electronic, optical, magnetic and transport properties of various bulk materials and nanostructures on their basis. Such theoretical results are very useful not only to reproduce experimental results, but also to provide explanations of sometimes contradictory experimental data and to predict possible ways how to modify properties of system under investigation. In this talk we are going to present our recent results on properties of β -FeSi₂, OsSi₂, BaSi₂, CaSi₂, FeSi, CrSi, Nb₁₂O₂₉, W₁₈O₄₉ and BaFe₁₂O₁₉ as bulk materials, Mg₂Si and Ca₂Si as thin films and 2D materials, Mg₂Si and Ca₂Si as single wall nanotubes, III-V, α -FeSi₂ and TiO₂ nanowires.

2. Results and discussions

In the case of semiconducting β -FeSi₂ and OsSi₂ silicides we show perfect agreement between the theoretically calculated and experimentally measured dielectric function connecting features in their energy band structures with the ones in the optical spectra [1].

For BaSi₂ the main focus is on possible ways to enhance its transport properties since the ~1.3 eV band gap along with high values of the absorption coefficient near the absorption edge make this silicide promising for solar cell application. We have identified that H incorporation could significantly improve photoresposivity of BaSi₂ by eliminating traps due to Si atom vacancies and interstitials [2-4].

CaSi₂ is found to be a gapless semiconductor with peculiar transport properties defined by two types of carrier (holes and electrons) that determine the resulting conductivity, concentration and mobility of charge carriers. In addition, possible reasons of the experimentally observed optical transparency of CaSi₂ in the infra-red range are also discussed [5].

The new monoclinic ground state with the antiferromagnetic ordering is revealed for FeSi, but not the cubic one as previously thought, that was supported by data of X-ray diffraction and high-resolution transmission electron microscopy of ultrathin FeSi films as well as by resistivity versus temperature measurements within a wide temperature range (2–300 K) pointing out bad metal properties (not semiconducting ones) and by the analysis of

field and temperature dependences of the magnetic moment which showed the presence of a ferromagnetic-antiferromagnetic two-phase state [6].

Similar to FeSi, the new monoclinic ground state of CrSi has been also predicted, which turned out to a gapless semiconductor with holes as the main charge carriers and antiferromagnetic ordering [7].

In the case of Nb₁₂O₂₉ we show that it is impossible to get any adequate description of this oxide by using one crystallographic unit cell, while a larger supercell is needed increased at least 3 times along the shortest lattice parameter *b* to accommodate lattice distortions associated with polaron formation. Our results also point out the possibility of simultaneous co-existence of localized states (polaron formation) and delocalized states providing metal-like properties of Nb₁₂O₂₉, in qualitative agreement with available experimental data [8].

The existence of bipolarons in W₁₈O₄₉ is found to be an intrinsic feature of this oxide resulting in the presence of different oxidation states of W atoms (W⁶⁺ and W⁵⁺) and in the co-existence of localized and delocalized electrons. The calculated absorption and reflection coefficients of W₁₈O₄₉ confirm a transparency window in the visible region in addition to an experimentally observed shielding effect originating from transitions involving the localized bipolaronic states in the near infrared region [9].

A peculiar polarization behavior of BaFe₁₂O₁₉ in an electric field (the linear polarization is detected at temperatures below 150 K whereas at higher temperatures a hysteresis-like polarization response is observed) has been explained by a shift of specific Fe atoms through an energy barrier which height depended on the temperature change of the unit cell volume [10].

Structural changes in semiconducting Mg₂Si and Ca₂Si thin films (from 17 nm down to 0.2 nm corresponding to the 2D structure) along with band-gap variations due to quantum confinement have been investigated. It is found that cubic Mg₂Si(111) thin films being dynamically stable at thicknesses larger than 0.3 nm displayed an indirect band gap, the reduction of which with increasing thickness could be reasonably well described by the simple effective mass approximation. Only 2D Mg₂Si has a unique structure because of the orthorhombic distortion and the direct band gap. The cubic phase of Ca₂Si, being metastable in the bulk

form, in the case of thin films turned out to be preferable in total energy than any orthorhombic Ca_2Si thin film (the ground state for the bulk form) for thicknesses smaller than 3 nm because of lower values of surface energy of cubic $\text{Ca}_2\text{Si}(111)$ films with respect to any surface of the orthorhombic phase. Sizable structural distortion and the appearance of surface states in the gap region of Ca_2Si thin films with thicknesses smaller than 3 nm were revealed that could be the reason for an odd dependence of the band-gap variation on film thickness [11].

Changes in the structure and electronic properties of Ca_2Si , Mg_2Si and MgCaSi nanotubes caused by the curvature-induced effects have been investigated. The curvature-induced effects can stabilize Mg_2Si nanotubes in a phase, which is metastable for the parent 2D Mg_2Si . Moreover, an energy gain as a result of 2D to nanotube structural transformation in the case of ternary MgCaSi nanotubes is found in addition to changes in the band dispersion and band gaps for nanotubes with the diameters less than 3 nm. Mg_2Si and MgCaSi nanotubes are found to be direct band-gap (0.5–1.2 eV) materials with appreciable oscillator strength of the first direct transitions [12].

In the case of $\langle 111 \rangle$ -oriented GaP, GaAs, GaSb, InP, InAs and InSb nanowires with the zinc-blende structure their morphology is found to crucially affect nanowire electronic properties. Thus, the formation of small $\{112\}$ facets between the adjacent $\{011\}$ ones, which characterize a hexagonal cross section of nanowires, provides a more stable structure and removes surface states from the gap region. This structural model also predicts a crossover between the indirect and direct band gap in GaP, GaAs and GaSb nanowires when increasing diameters starting from 4 nm, while InP, InAs and InSb nanowires display the direct band gap at diameters of 1.5 nm and larger. Analysis of charge distribution between atoms suggests that $\{011\}$ facets are positively charged even though a (011) surface of these materials is considered to be non-polar [13].

Calculations in the case of $\alpha\text{-FeSi}_2$ nanowires reproduced the experimentally observed appearance of magnetic moments on Fe atoms and ferromagnetism even though $\alpha\text{-FeSi}_2$ in bulk is a non-magnetic material. It is revealed that only surface Fe atoms on $\{001\}$ and $\{100\}$ facets and on edges between $\{110\}$ and $\{001\}$ facets possess magnetic moments, whereas Fe atoms on $\{110\}$ facets and inside the NWs not have any magnetic moment [14].

Sizable anisotropy in electronic properties of TiO_2 nanowires in the anatase phase with respect to orientation is found: nanowires with $\langle 001 \rangle$, $\langle 100 \rangle$ and $\langle 110 \rangle$ axes are direct band-gap, indirect band-gap and degenerate semiconductor materials, respectively. The degenerate semiconducting properties of $\langle 110 \rangle$ -oriented TiO_2 nanowires are predicted to be the intrinsic features closely connected with stoichiometry. A band-gap variation with nanowire diameter is also shown to display rather complex behavior originated from a competition between quantum confinement and surface state effects that is fully compatible with the available contradictory experimental data [15].

Acknowledgements

D.B. Migas acknowledges the support from the MEPhI Program Priority 2030.

References

- [1] D.B. Migas, L. Miglio, W. Henrion, M. Rebien, F. Marabelli, B.A. Cook, V.L. Shaposhnikov, V.E. Borisenko. *Phys. Rev. B* **64**(2001)075208.
- [2] T. Deng, T. Suemasu, D.A. Shohonov, I.S. Samusevich, A.B. Filonov, D.B. Migas, V.E. Borisenko. *Thin Solid Films* **661**(2018)7.
- [3] Z. Xu, D. A. Shohonov, A. B. Filonov, K. Gotoh, T. Deng, S. Honda, K. Toko, N. Usami, D. B. Migas, V. E. Borisenko, T. Suemasu, *Phys. Rev. Mater.* **3**(2019) 065403.
- [4] D.A. Shohonov, D.B. Migas, A.B. Filonov, V.E. Borisenko, R. Takabe, T. Suemasu. *Thin Solid Films*. **686**(2019) 137436.
- [5] N. G. Galkin, S. A. Dotsenko, K. N. Galkin, A. M. Maslov, D. B. Migas, V. O. Bogorodz, A. B. Filonov, V. E. Borisenko, I. Cora, B. Pecz, D. L. Goroshko, A. V. Tupkalo, E. A. Chusovitin, E. Y. Subbotin. *J. Alloys Compd.* **770**(2019)710.
- [6] N. G. Galkin, D. B. Migas, N. V. Medvedeva, A. B. Filonov, S. A. Dotsenko, A. M. Maslov, I. M. Chernov, E. Yu. Subbotin, D. L. Goroshko, A. Yu. Samardak, A. K. Gutakovskii, I. A. Tkachenko, A. V. Gerasimenko. *Comput. Mater. Sci.* **233**(2024)112762.
- [7] N. G. Galkin, K. N. Galkin, O. V. Kropachev, S. A. Dotsenko, D. L. Goroshko, D. B. Migas, A. B. Filonov, N. V. Skorodumova, A. V. Gerasimenko, A. K. Gutakovskii. *J. Mater. Chem. C*, **13**(2025)2987.
- [8] D.B. Migas, A.B. Filonov, V.E. Borisenko, N.V. Skorodumova. *J. Alloys Compd.* **821**(2020)153527.
- [9] D.B. Migas, A.B. Filonov, N. V. Skorodumova. *Phys. Chem. Chem. Phys.* **23**(2021)25824.
- [10] D. B. Migas, V. A. Turchenko, A. V. Rutkauskas, S. V. Trukhanov, T. I. Zubar, D. I. Tishkevich, A. V. Trukhanov, N. V. Skorodumova. *J. Mater. Chem. C* **11**(2023)12406.
- [11] A. Yu. Alekseev, D. B. Migas, A. B. Filonov, N. G. Galkin, N. V. Skorodumova. *Phys. Chem. Chem. Phys.* **25**(2023)19952.
- [12] A. Yu. Alekseev, D.B. Migas, A.B. Filonov, A.G. Chernykh, V.E. Borisenko, N. V. Skorodumova. *Physica E* **128**(2021)114582.
- [13] D.B. Migas, A. B. Filonov, D. A. Yatsyna, Rusli and C. Soci. *Nano Convergence* **2**(2015)14.
- [14] N. G. Galkin, D. L. Goroshko, I. A. Tkachenko, A. Yu. Samardak, K.N. Galkin, E. Yu. Subbotin, S. A. Dotsenko, D. B. Migas, A. K. Gutakovskii. *Nanomaterials* **12**(2022)3707.
- [15] D.B. Migas, A. B. Filonov, V. E. Borisenko, N. V. Skorodumova. *Phys. Chem. Chem. Phys.* **16**(2014)9479.

Group IV heterostructures for quantum technologies and silicon photonics

Novikov A.V.^{*1}, Yablonskiy A.N.¹, Yurasov D.V.¹, Stepikhova M.V.¹, Peretokin A.V.¹, Shmagin V.B.¹, Demidov E.V.¹, Shaleev M.V.¹, Shengurov D.V.¹, Zaharov V.E.¹, Shmyrin D.A.¹, Pankratov E.L.¹, Revin L.S.¹, Krasilnik Z.F.¹, Dyakov S.A.², Gippius N.A.², Sitnikov S.V.³, Sheglov D.V.³

¹ Institute for Physics of Microstructures RAS, 7 Akademicheskaya St., Afonino v., Nizhny Novgorod 603950, Russia

² Skolkovo Institute of Science and Technology, Bolshoy Boulevard, 30, bld. 1, Moscow 121205, Russia

³ Institute of Semiconductor Physics of SB RAS, 13 pr. Lavrentieva, Novosibirsk 630090, Russia

*e-mail: anov@ipmras.ru

Abstract. The paper presents a review of literature data as well as original results on the development of light sources based on group IV heterostructures for silicon photonics. To solve this problem, both various direct gap heterostructures and indirect gap structures with Ge(Si) self-assembled nanoislands are considered. The possibility of using dielectric resonators to increase the light emission efficiency of Ge(Si) islands is discussed. As for quantum tech applications, isotopically enriched Si/SiGe structures with low fraction of non-zero nuclear spin ²⁹Si and ⁷³Ge isotopes are discussed. These structures are promising for formation of electron spin qubits with long coherence time and work temperature above 100 mK.

1. Introduction

Currently, group IV heterostructures and, first of all, SiGe heterostructures are an integral part of modern nano- and optoelectronics. They were successfully used to increase the performance of p-FET and HBT transistors, as well as photodetectors for the wavelength range of 1.3-1.55 μm in silicon integrated photonic circuits. At the same time, there is a tendency to expand the functionality of these heterostructures, the main advantage of which is compatibility with modern Si CMOS technology. This paper presents some latest results on the development of the light sources for silicon photonics and qubits for quantum computing based on group IV heterostructures.

2. Light sources based on group IV heterostructures

There are currently several approaches to formation of efficient light sources on silicon. One approach is based on the formation of direct-gap group IV heterostructures on Si(001) substrates. Such structures include:

- tensile strained n-Ge microstructures [1];
- hexagonal Ge and SiGe structures, realized in nanowires (hex-Ge) [2];
- GeSn and SiGeSn structures with high (more than 10 %) Sn content [3].

Laser action has been demonstrated for each of these types of structures at cryogenic temperatures [4-6]. Light-emitting diodes (LEDs) based on GeSn structures formed on 300 mm Si wafers operating at temperatures above room temperature were also demonstrated [7]. However, for all of these structures there is a problem of coupling their emission into a Si/SOI planar waveguide, since they either contain thick buffers (Ge and SiGeSn structures) or have a non-planar morphology (hex-Ge nanowires). In addition, these structures emit in the mid-IR range [4-7], far from the currently widely used telecommunication wavelength range of 1.3-1.55 μm .

However structures with Ge(Si)/Si(001) self-assembled nanoislands emit in this spectral range. One of the significant advantages of these structures is the possibility of their growth directly on SOI substrates, without the use of any buffers. However, the efficiency of radiative

recombination in these structures is low due to the indirect nature of the bandgap structure. In recent years, it has been demonstrated that due to the interaction of Ge(Si) islands with various modes of Mie resonator [8] or photonic crystal (PhC) [9, 10], the intensity of their luminescence signal at room temperature can be significantly increased. It was also shown that the structures with Ge(Si) islands are a convenient object for studying various optical properties of dielectric microresonators [8–10].

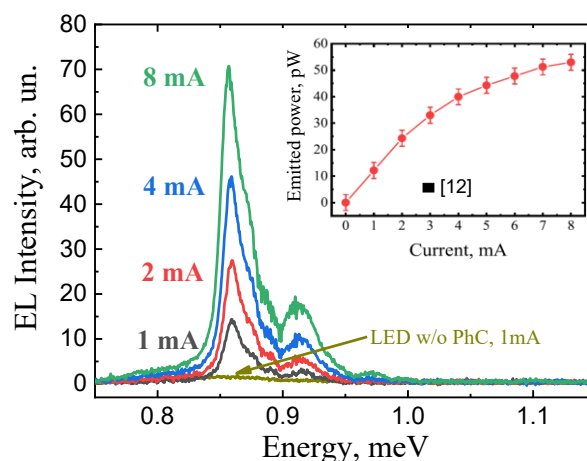


Fig. 1. Electroluminescence spectra of Ge(Si) islands LED with and without a PhC at different LED's current. The inset shows the dependence of the emitted power on the current. The data from Ref. 12 is indicated by a separate symbol for comparison.

For applications in Si photonics a technology for formation of lateral LEDs with Ge(Si) islands embedded into the PhC has been developed [11]. The output power of the obtained LEDs is an order of magnitude higher than in the previously published works for LEDs with islands [12] and is comparable to the power of Si LEDs in an integrated design [13] (Fig. 1). In addition, it was demonstrated that by applying a gate voltage to the SOI substrate, it is possible to control the emission properties of the obtained LEDs, which allows them to be considered as light-emitting transistors [14]. It was shown that the emission from Ge(Si)

LEDs can be introduced into a planar waveguide formed on the SOI substrate.

3. Isotopically enriched Si/SiGe structures for quantum computing

Currently, qubits based on silicon and SiGe heterostructures are one of the promising platforms for development of practically useful quantum computer. The advantage of silicon compared to A3B5 semiconductors is the possibility of its purification from isotopes with non-zero nuclear spin (isotopic enrichment). This allows to significantly increase the coherence time of qubits based on electron spin manipulation [15]. Among the various qubits based on Si and Ge, qubits based on Si/SiGe structures, in which electrons are localized in tensile strained Si quantum well (QW) grown on a relaxed SiGe buffer, have a number of record-breaking characteristics. These qubits demonstrate high electron spin phase coherence times and high precision in performing one- and two-qubit operations [15]. A significant disadvantage of Si/SiGe qubits is the small value of the valley splitting of the electron states, which significantly limits the possibility to increase the operating temperatures of this type of qubit. Recently, several approaches to increasing this value have been proposed, based on the controlled introduction of Ge into the Si QW [16]. The implementation of these approaches in practice is hampered by the fact that in most studies, only isotopically enriched Si is used to form the Si/SiGe structures.

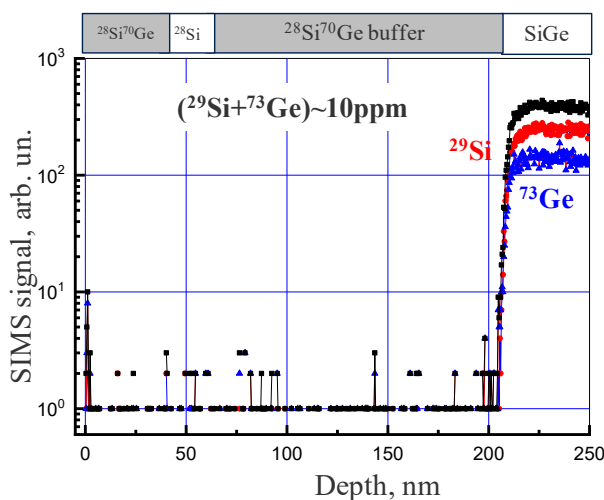


Fig. 2. Distribution of ^{29}Si and ^{73}Ge isotopes in the grown Si/SiGe structures obtained by secondary ion mass spectrometry (SIMS). The top part of the figure shows a diagram of the grown structure.

In this work, isotopically enriched Si/SiGe structures with low content of both ^{29}Si and ^{73}Ge isotopes were grown by molecular beam epitaxy (Fig. 2). The structures with the total content of these isotopes from 200 part per million (ppm) to 10 ppm were obtained (Fig. 2). The last value is close to the record values for isotopic enrichment of epitaxial structures. The structures demonstrate electron mobility at the level of $3 \times 10^4 \text{ cm}^2/(\text{V} \times \text{s})$ at low temperatures, which indicates their high quality. A system of submicron gates is formed on isotopically enriched Si/SiGe structures, which is necessary for the formation of both quantum dots themselves, in which the manipulation of electron spin is realized, and single-electron transistors, which act as spin state detectors. Effects associated with

single-electron tunneling were obtained in the transport properties of the formed quantum dots and single electron transistor at $T \leq 500 \text{ mK}$.

Acknowledgements

The studies aimed to formation of light sources based on structures with Ge(Si) nanoislands was carried out with the support of the Russian Science Foundation, project # 25-12-00367. Development of a qubit based on isotopically enriched Si/SiGe structures was supported by Rosatom within the framework of Quantum Computing Roadmap (contract # 868-1.3-15/15-2021 of 10/5/2021 and contract # P2194 of 12/14/2021). The part of results was obtained by using the equipment of Common Use Center “Physics and Technology of Micro- and Nanostructures” of IPM RAS.

References

- [1] J. Liu, X. Sun et al., Optics Express **15** (2007) 11272.
- [2] E.M.T. Fadaly, A. Dijkstra et al., Nature **580** (2020) 205.
- [3] O. Moutanabbir, S. Assali et al., Appl. Phys. Lett. **118** (2021) 110502.
- [4] F.T. Armand Pilon, A. Lyasota et al., Nature Communications (2019) 10:2724.
- [5] M.A.J. van Tilburg, R. Farina et al., Comm. Physics (2024) 7:328.
- [6] L. Seidel, T. Liu, et al., Nature Communications (2024) 15:10502.
- [7] Sh. Wu, L. Zhang et al., Photonics Research **11** (2023) 1606.
- [8] V. Rutckaia, et al., Nano Letters **17** (2017) 6886.
- [9] S.A. Dyakov, et. al, Las & Phot Reviews **15** (2021) 2000242.
- [10] M.V. Stepikhova, et. al, Nanomaterials **12** (2022) 2687.
- [11] V. B. Shmagin et. al. Nanotechnology **35** (2024) 165203.
- [12] X. Xu, T. Chiba, et al., Appl. Phys. Expr. **5** (2012) 102101.
- [13] M. de Cea, Zh. Li et al., APL Photon. **8** (2023) 081301.
- [14] A.N. Yablonskiy, et. al, Appl. Phys. Lett. **125** (2024) 0231103.
- [15] P. Stano, D. Loss, arXiv:2107.06485v9.
- [16] M.P. Losert, M.A. Eriksson et al., Phys. Rev. B **108** (2023) 125405.

**I. Physics of nanostructures and interfaces:
self-organization processes,
two-dimensional materials and metrology**

Initial stage of ultrathin film growth in metal-silicon systems: from surface phases to solid wetting layers

Plusnin N.I.*

Institute of Nanotechnology of Microelectronics, 16a Nagatinskaya, Moscow, 115487, PO Box 50, Russia

*e-mail: plusnin.n@inme-ras.ru

Abstract. The formation of surface phases (SPs) and solid wetting layers (SWLs) is the fundamental basis for the initial stage of growth of ultrathin films (UTFs) and nanostructures of micro- and nanoelectronics. This study provides a chronological overview of the author's research, which spans four decades and focuses on SPs, SWLs and, more broadly, the growth early stages of UTFs. The article identifies the main causes of phase transitions with an increase in the number of monolayers in SWL. The role of vapor pressure and temperature, as well as substrate temperature, in the structure and composition of the forming phases and the boundary layer of the substrate is demonstrated. A new method of growing with pulsed heating of a planar wall (PHPW) has been developed. This method increased the steam pressure, lowered the steam temperature and expanded the range of materials for SWL. The study also examined the early stages of UTF growth of Cr, Co, Fe, Cu and their silicides on the (111) and (001) Si faces, as well as Si on Si(111)7×7 and CrSi₂(0001). As a result, nanofilms of the corresponding substances were obtained, as well as granular nanolayers of Co, Fe and Cu on Si(001). It is shown that grown films have unique electrical, optical, and magnetic properties and are promising for use in various nanodevices.

1. Introduction

The basis for the growth of nanostructures for microelectronics is the theoretical understanding of the initial stage of thin film growth, including its interface formation. The initial stage, in fact, is the formation of composition, structure, morphology, and phase state of SPs, SWLs and UTFs, including their interfaces with the solid substrate.

However, it was only 30 years after the publication of our inaugural papers [1, 2] that it became evident to us that, subsequent to SPs, the growth of UTFs occurs through the formation of SWLs in the form of a two-dimensional and then nanophase SWLs.

Historically, up to a certain stage, two approaches to UTF growth existed independently and moved towards each other: Approach I - from bulk phases (BPs) to UTFs and Approach II - from SPs to UTFs. Moreover, the understanding of the nature of the SPs and SWLs was influenced by differences in research methods, in particular, the degree of microscopicality of these methods. For instance, the employment of optical methodologies, such as ellipsometry, has resulted in the conceptualization of SWLs as a metastable BPs [3]. Conversely, the utilization of surface-sensitive methodologies [4] has resulted in the identification of interface phases [5] or SPs [6,7], as solely SPs with their own composition, thickness, density, and lattice [4]. A more complete understanding of the nature of SWLs was obtained later (see below).

This paper presents a review of the results on the growth of metallic (Me) and silicide (MSi_x) UTFs on silicon or silicon UTFs on Si or MeSi_x. The research is founded on four decades of investigation by the paper's author, employing surface-sensitive methodologies. The results have been systematically organized according to the theory of UTF growth using Approach II and a methodology developed by the author.

2. Chronological overview

In the seminal works of [1, 2], electron energy loss spectroscopy (EELS) spectra of SWLs were obtained, which demonstrated the reduced electron density in SWLs

relative to the BPs. The SWLs were designated in this study as an "atomically similar" phase, which is essentially a low-dimensional layer. These SWL exhibited a thickness of several monolayers (>3 ML), which is not characteristic of low-dimensional or "submonolayer" SPs. Consequently, the authors of works [1, 2] referred SWLs to "extended thickness" SPs, meaning that this "thick" SPs as well as the "submonolayer" phases, have stabilized by the substrate.

The following study was focus on Me-Si intermixing and its role in the formation of SWLs and UTFs. Research in the Si(111)-Cr system has demonstrated that mixing and SWLs play a significant role in the formation of both ordered and disordered SWLs, as well as template layers and epitaxy of UTFs [1, 2, 8-10]. The data, systematized in the form of a diagram, was obtained, which show conditions of the formation of Cr and CrSi₂ UTFs [10].

The present findings have demonstrated that the thickness sets two different types (two-dimensional and with extended thickness) of "intermixed" SWLs, CrSi₂ nucleates and CrSi₂ UTFs (templates) with A- or B-type azimuthal orientation relative to Si(111). Using these CrSi₂ template has enabled the successful fabrication of a substantial (1000 Å) single-crystalline film (A-type) of semiconducting CrSi₂ with a minimal hole concentration and augmented hole mobility. This represents a significant breakthrough, as it is the first time such a film has been obtained.

However, it should be noted that these early studies were carried out at reduced vapor pressure or at elevated temperatures. In order to reduce the thickness of the films, an increased pressure and a decreased vapor temperature were required. Furthermore, a number of studies on the systems of Cr-Si(111), Co-Si(111), and Si-CrSi₂(0001) demonstrated that an enhancement in the deposition rate, concomitant with an increase in vapor pressure, results in film growth without intermixing. Consequently, a cycle of computer modelling of growth kinetic was initiated. This culminated in the formulation of a probabilistic-geometric analytical model of the growth kinetics, which elucidated the role of increased vapor pressure in the aforementioned transition [11].

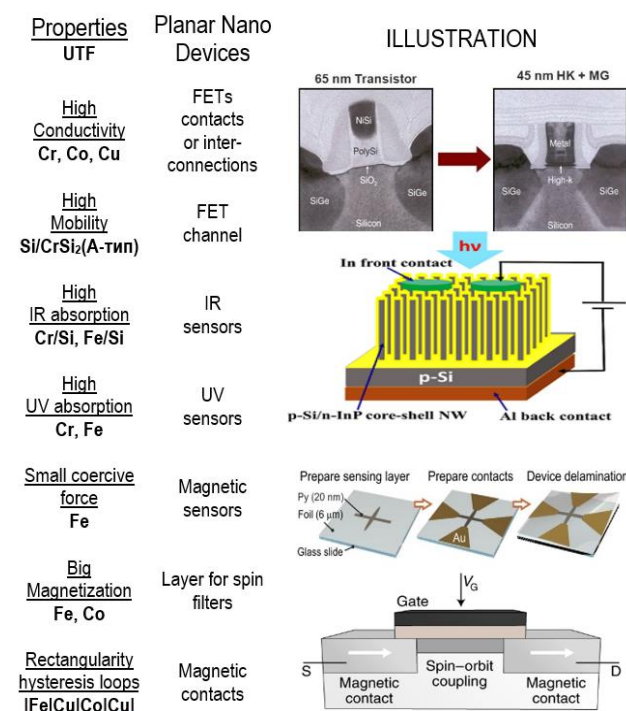


Fig. 1. Properties of the obtained nanostructures and their possible applications in nanodevices

Subsequent investigations was focused on the growth of amorphous Si on Si(111), the role of intermixing in the formation of Co UTFs on Si(111) and the growth of amorphous and epitaxial Si UTFs on CrSi₂(0001) [12].

However, it was necessary to develop a method of obtaining vapor that would provide both its high pressure and, as well as its reduced temperature. The PHPW method was thus developed [12] on the basis of the famous "hot wall" technique. This method involved the process of pulse double deposition ("overdeposition") from the adsorbate onto the wall, and subsequently from the wall onto the substrate [13].

This innovative approach resulted in the successful cultivation of SWLs comprising nearly pure Me (a solid solution of Si in Me) [12,14]. Notably, a "pseudo-three-dimensional" SWLs were identified, exhibiting heterogeneity nanosizes comparable to those of known bulk nanophases. Consequently, these SWLs were designated as thin-film (or film) nanophase layers in [15,16]. The cycle of studies was completed by the generalization of [17].

Subsequent studies focused on the growth of Cu SWLs and Cu UTFs, as well as multilayer UTFs comprising Co, Fe, and Cu. The generalisation of these and previous results with the interpretation of the surface phases of increased thickness as a solidphase wetting layers (SWLs) was made in the reviews [17-20].

The final period of the series was associated with the concept of the SWLs (or WLs) [19]. Experiments on SWL growth were performed, a phenomenological theory of its nucleation and growth was developed, and SWL modelling was carried out for a number of Me-Si systems (see references in [21-27]).

These studies revealed that the root cause of the mechanisms of SWLs and UTFs formation is change coordination of atoms and electronic structure in SWLs and UTFs with the thickness. The influence of these changes

leads to stresses in the films and the interface layer of the substrate. This, in turn, results in the destabilisation of the film-substrate systems and the transition of SWLs to the BPs, accompanied by the release of latent energy in the form of heat.

3. Prospects of application

As illustrated in Figure 1, the unique properties of the obtained nanostructures and the potential applications of the nanodevices for planar integrated microelectronics are outlined. The figure also provides a schematic representation of the applications of several nanodevices, including: nanocontacts or interconnects, channels for field-effect transistors (FETs), semitransparent contacts for infrared (IR) and ultraviolet (UV) sensors, cores for magnetic sensors, layers for spin filters, contacts (electrodes) and channels for spin transistors (for example, CrSi₂ covered by 2D Si), and numerous other applications.

4. Conclusion

This paper presents a series of works on vapor-phase growth of extremely thin layers in the metal-silicon system. The role of a solid wetting layer in this process is demonstrated. The paper goes on to identify the fundamental causes of this phenomenon. A novel method of growth has been developed. The structures obtained are promising with regard to practical application.

References

- [1] V. Lifshits, N. Plyusnin. Physics, Chemistry and Mechanics of Surfaces 1984 (9) 78. (RUS)
- [2] V. G. Lifshits, N. I. Plusnin. In: Preprint No. 18 (127). IACP FESC USSR Acad. of Sciences (Vladivostok)1984. - 35 c.
- [3] Kukushkin S. A., Osipov A. V. Technical Physics Letters 2016 (42) 175.
- [4] V. G. Lifshits. Electron spectroscopy and atomic processes on the silicon surface. Ed. S. M. Repinsky. Moscow: Nauka, 1985. 200 p.
- [5] Rossi G. Surface Science Reports 1987 (7/1-2) 1.
- [6] Linford, R. G. Chemical Society Reviews 1972 (1/4) 445.
- [7] Runnels L. K. Critical Reviews in Solid State and Material Sciences 1973 (4/1-4) 151.
- [8] N. Galkin, N. Plyusnin, V. Lifshits. Physics, Chemistry and Mechanics of Surfaces 1987 (12) 50. (RUS)
- [9] N. Plyusnin, N. Galkin, A. Kamenev, V. Lifshits, S. Lobachev. Physics, Chemistry and Mechanics of Surfaces 1989 (9) 55. (RUS)
- [10] N. Plusnin, N. Galkin, V. Lifshits, S. Lobachev. Surface Review and Letters 1995 (2) 439.
- [11] N. Plyusnin. In: Heat and Mass Transfer Processes and Growth of Single Crystals and Thin Film Structures / Proc. of the Second Rus. Symp. HT&CG'97 (Ed. by V.P. Ginkin). Obninsk, 1998. P 303. (RUS)
- [12] N. Plyusnin. Thesis of Doctor of Physic. and Mathemat. Sciences. Vladivostok, 2000 (RUS)
- [13] Lopez-Otero A. Thin solid films 1978 (49/1) 3.
- [14] N. Plusnin, A. Milenin, V. Iliyashenko, V. Lifshits. Phys. of Low-Dimens. Struct. 2002 (9-10) 129.
- [15] N. Plusnin, V. Il'yashchenko, S. Krylov. Journal of Physics: Conference Series 2008 (100/5) 052094.
- [16] N. Plyusnin, V. Il'yashchenko, S. Kitan', S. Krylov. Journal of Surface Investigation. X-Ray, Synchrotron and Neutron Techniques 2009 (3) 734.
- [17] N. Plyusnin. Bulletin of the Far Eastern Branch of the Rus. Acad. of Sci. 2010 (5/153) 26. (RUS)
- [18] N. Plusnin. In: Comprehensive Guide for Nanocoatings Technology. Vol. 2. Characterization and Reliability. N.Y.: Nova Sci. Publ. Inc., 2015 (2) 87.

-
- [19] N. Plusnin. Advances in Materials Physics and Chemistry 2016 (6/7) 195.
 - [20] N. Plusnin. Modern Electronic Materials 2017 (3/2) 57.
 - [21] N. Plusnin. Modern Electronic Materials 2017 (3/4) 131.
 - [22] N. Plyusnin. Cond. Matter and Interphases 2023 (25/4) 594.
 - [23] N. Plusnin. Solid phase wetting layer. In: "Big Russian Encyclopedia" 2024 (3) 1.
 - [24] N. Plusnin. In: Abstracts of XV Conference "Silicon-2024". Irkutsk, 2024. P. 11.
 - [25] V. Zavodinsky, N. Plusnin, O. Gorkusha. Journal of Technical Physics 2024 (94/2) 231. (RUS)
 - [26] N. Plusnin, V. Zavodinsky, O. Gorkusha. Solid State Physics 2024 (66/2) 275.
 - [27] V. Zavodinsky, O. Gorkusha, N. Plusnin. Computational nanotechnology 2024 (11/1) 121.

Monoatomic lead layer: exploring the interplay between atomic arrangement, electronic structure, and superconductivity

Bondarenko L.V.^{*1}, Tupchaya A.Y.¹, Vekovshinin Yu.E.¹, Utas T.V.¹, Denisov N.V.¹, Mihalyuk A.N.^{1,2}, Gruznev D.V.¹, Zotov A.V.¹, Saranin A.A.¹

¹ Institute of Automation and Control Processes, 5 Radio St., Vladivostok 690041, Russia

² Far Eastern Federal University, 8 Sukhanova St., Vladivostok 690950, Russia

*e-mail: bondarenko@dvo.ru

Abstract. A lead (Pb) monolayer on the Si(111) surface is known to be the thinnest superconductor. Although its transition temperature (T_c) is low, this system provides a valuable platform for exploring various aspects of superconductivity at the ultimate thickness limit, such as the effects of disorder, the role of atomic steps, and electron-phonon and spin-orbit couplings. In this study, we demonstrate the ability to tune the T_c of the Pb monolayer solely through structural reordering while keeping the total amount of Pb nearly constant. We find that transforming the so-called striped incommensurate (SIC) Pb/Si(111)-($\sqrt{3}\times\sqrt{3}$) surface into a well-ordered $14\times\sqrt{3}$ single-domain structure increases T_c . Surprisingly, further surface ordering achieved by forming a commensurate $\sqrt{3}\times\sqrt{3}$ phase decreases T_c , contrary to expectations. In this report, we investigate how these changes in T_c correlate with modifications in atomic structure and electronic properties.

1. Introduction

Single-atom Pb layers on Si(111) have proven to be a valuable prototype system for exploring various aspects of superconductivity at the ultimate thickness limit, including the effects of disorder [1], the role of atomic steps [2, 3], electron-phonon and spin-orbit couplings [4, 5], and the Berezinskii-Kosterlitz-Thouless transition [6]. Regarding the critical temperature T_c , nearly all available data pertain to the so-called striped incommensurate (SIC) Pb phase with 1.28–1.30 monolayers (ML) of Pb (where 1 ML = 7.8×10^{14} cm⁻²). As concerns the critical temperature T_c , scanning tunneling spectroscopy (STS) and four-point-probe (4PP) measurements report superconducting transition temperatures in the range of 1.1 to 1.83 K [7, 8].

In this study, we achieved an enhancement of T_c up to 2.08 K [9] by improving surface ordering through the formation of a single-domain $14\times\sqrt{3}$ structure. Surprisingly, further ordering via the formation of a commensurate $\sqrt{3}\times\sqrt{3}$ phase led to a decrease in T_c , contrary to expectations.

2. Experiment

Experiments were performed in the two separate ultrahigh vacuum (UHV) systems depending on the research tasks. In particular, characterization of the growth mode, as well as the structural and electronic properties of the Pb/Si(111) samples, was conducted in the UHV Omicron MULTIPROBE system equipped with scanning tunneling microscopy (STM), low-energy electron diffraction (LEED), and angle-resolved photoelectron spectroscopy (ARPES) facilities. The electron transport measurements of the samples at low temperatures were performed in the UNISOKU USM 1500 LT STM system, equipped with a superconducting magnet and the four-point-probe (4PP) technique. The base pressure in the both UHV systems was on the order of 1×10^{-10} Torr. To prepare the atomically clean Si(111) 7×7 surfaces, the Si(111) samples were first annealed in situ at 600°C for several hours and finally were flashed to 1280°C. Pb was deposited from a Ta tube. STM images were acquired in a constant-

current mode with a mechanically cut PtIr tip after annealing in vacuum. ARPES measurements were conducted using a VG Scienta R3000 electron analyzer and high-flux He discharge lamp with a toroidal-grating monochromator as a light source. The 4PP head mount on the STM stage instead of the tip holder was used for the in situ transport measurements. Gold wires of 0.1 mm in diameter equally spaced by 0.2 mm along the straight line were used for the probes. Low temperatures were calibrated in the special experiments with the additional temperature sensor directly attached to the sample and using the samples with thick films of materials with known superconductivity critical temperatures.

3. Results and discussions

Preparation and Atomic structure. Figure 1 illustrates the structural difference between the SIC-Pb [Figs. 1(a) and 1(c)] and the $14\times\sqrt{3}$ -Pb [Figs. 1(b) and 1(d)] phases. The former is the well-known SIC-Pb phase formed by RT deposition of Pb onto the bare Si(111) 7×7 surface followed by annealing. The SIC phase displays in the STM a triple-domain structure with meandering domain walls [Fig. 1(a)]. In the LEED patterns [Fig. 1(c)], the triple-domain structure is known to be reflected by occurrence of three smeared spots around the nominal position of the $\sqrt{3}$ reflection. The most essential peculiarity of the alternative procedure is the RT deposition of Pb onto the $\sqrt{7}\times\sqrt{3}$ -Pb (which looks up as 1×1 at RT) at the final stage, which results overall in the formation of the single-domain $14\times\sqrt{3}$ -Pb phase, as evidenced in STM and LEED observations [Figs. 1(b) and 1(d), respectively]. The $14\times\sqrt{3}$ -Pb layer uniformly covers the entire sample surface, it is free of domain walls, and its single-domain orientation is set along the direction perpendicular to the atomic steps of the Si(111) substrate.

The commensurate $\sqrt{3}\times\sqrt{3}$ -Pb ($c\text{-}\sqrt{3}\times\sqrt{3}$ -Pb) phase was formed similarly to the $14\times\sqrt{3}$ -Pb-Pb phase but with low-temperature Pb deposition. This procedure yielded large domains with sparse domain walls, dividing the surface into two domain types with an uneven area ratio (~80% preferred domain). High-resolution STM and density

functional theory simulations indicate that Pb trimers in the preferred domain are centered on H3 sites, while those in the minority domain reside on T4 sites. Total energy calculations, including spin-orbit coupling, confirm that H3 sites are slightly more stable [10].

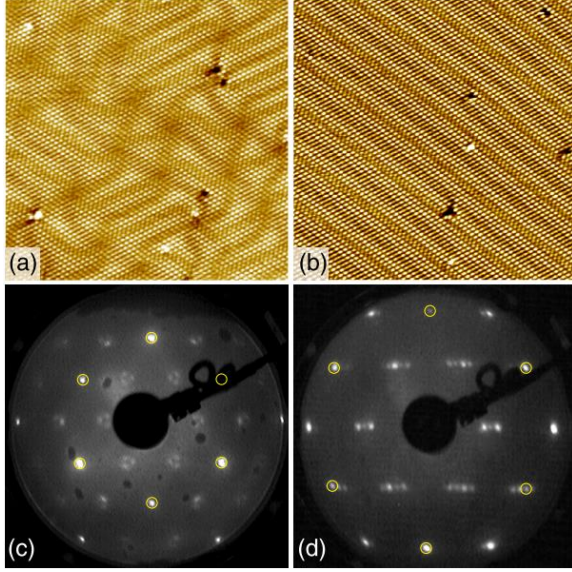


Fig. 1. STM images ($40 \times 40 \text{ nm}^2$) and LEED patterns of the densest single-atom Pb layers formed on the Si(111) surface upon growth using alternative formation procedures: (a), (c) SIC-Pb phase and (b), (d) $14 \times \sqrt{3}$ -Pb phase. The main reflections in the LEED patterns are outlined by yellow circles. LEED electron beam energies are (c) 75 eV and (d) 38 eV.

Transport Measurements. The SIC-Pb phase exhibits a superconducting transition at $\sim 1.8\text{--}1.9 \text{ K}$, while the $14 \times \sqrt{3}$ -Pb phase shows $T_c = 2.08 \text{ K}$. Surprisingly, the $c\text{-}\sqrt{3} \times \sqrt{3}$ -Pb phase shows no signs of superconductivity down to our lowest measurable temperature, indicating $T_c < 1 \text{ K}$. These results highlight the strong dependence of superconducting properties on atomic structure.

Our measured T_c of $\sim 1.8\text{--}1.9 \text{ K}$ for the SIC-Pb phase exceeds previous transport results [8] but agrees with STS data ($T_c = 1.83 \text{ K}$) [7]. The higher T_c (2.08 K) for the $14 \times \sqrt{3}$ -Pb phase likely stems from improved structural ordering. However, the suppression of T_c in the $c\text{-}\sqrt{3} \times \sqrt{3}$ -Pb phase is counterintuitive. To explain this, we examine the electronic structure.

Superconductivity arises from electron-phonon coupling, which strengthens with a higher electronic density of states (DOS) at the Fermi level [11]. ARPES experiments reveal that the SIC-Pb and the $14 \times \sqrt{3}$ -Pb phases exhibit a higher DOS near the Fermi level compared to the $c\text{-}\sqrt{3} \times \sqrt{3}$ -Pb phase. This difference originates from band-structure modifications induced by large periodicities: the $14 \times \sqrt{3}$ supercell (and the disordered SIC-Pb phase) produces electron band folding, which significantly distorts the band geometry. Our ARPES data confirm this behavior for both the SIC-Pb and the $14 \times \sqrt{3}$ -Pb phases, though the spectra for the SIC-Pb phase are more smeared due to its inherent disorder.

In contrast, the $c\text{-}\sqrt{3} \times \sqrt{3}$ -Pb phase displays simpler spectra with no evidence of band folding and a substantially lower DOS near the Fermi level. Thus, the enhanced DOS in the SIC-Pb and the $14 \times \sqrt{3}$ -Pb phases driven by band folding from their ordered/disordered domains promotes stronger superconductivity.

4. Conclusions

We enhanced T_c in single-atom Pb layer on Si(111) to 2.08 K by forming ordered a single-domain $14 \times \sqrt{3}$ -Pb structure. Contrary to expectations, further ordering via a commensurate $c\text{-}\sqrt{3} \times \sqrt{3}$ -Pb phase formation reduced T_c . This behavior is attributed to DOS variations at the Fermi level caused by electronic band folding.

Acknowledgements

The work was supported by the Russian Science Foundation (Grant No. 24-12-00181, <https://rscf.ru/en/project/24-12-00181/>).

References

- [1] C. Brun, et.al, Nat. Phys. 10, 444 (2014).
- [2] Y. Sato, et.al, Phys. Rev. Lett. 130, 106002 (2023).
- [3] H. Kim, et.al, Phys. Rev. Lett. 117, 116802 (2016).
- [4] J. Noffsinger and M. L. Cohen, Solid State Commun. 151, 421 (2011).
- [5] I. Y. Sklyadneva, et.al, Phys. Rev. B 97, 195409 (2018).
- [6] W. Zhao, et.al, Solid State Commun. 165, 59 (2013).
- [7] T. Zhang, et.al, Nat. Phys. 6, 104 (2010).
- [8] M. Yamada, et.al, Phys. Rev. Lett. 110, 237001 (2013).
- [9] L. V. Bondarenko et al. Phys. Rev. B 108, 115428 (2023).
- [10] Ren et al. Phys. Rev. B 94, 075436 (2016).
- [11] J. Bardeen, et.al, Physical Review 108 (5) (1957) 1175–1204.

***In situ* UHV REM observation of structural transitions on Si(111) surface induced by III-V group metals adsorption**

Petrov A.S.^{*1,2}, Gumbarg V.V.^{1,2}, Rogilo D.I.^{1,2}, Sheglov D.V.¹, Latyshev A.V.^{1,2}

¹ Institute of Semiconductor Physics of SB RAS, 13 pr. Lavrentieva, Novosibirsk 630090, Russia

² Novosibirsk State University, 2 Pirogova St., Novosibirsk 630090, Russia

*e-mail: alexey_petrov@isp.nsc.ru

Abstract. Using *in situ* ultrahigh vacuum reflection electron microscopy, we have visualized and studied $(7\times 7) \Rightarrow (\sqrt{3}\times\sqrt{3})R30^\circ$ structural transition on the Si(111) surface induced by deposition of In, Sn, Pb, Sb, and Bi coverages up to 1 ML at $T = 400\text{--}860^\circ\text{C}$. The way how Si(111) morphology evaluates during $(\sqrt{3}\times\sqrt{3})R30^\circ$ formation is divided according to the group of deposited metal. Group III: 2D island nucleation, their following coalescence, formation of flat terraces. Group II: 2D nucleation or preservation of initial terrace smoothness depending on substrate temperature. Group IV: Si(111) surface roughening.

1. Introduction

Metallic thin films and metal-induced reconstructions on Si surface are considered as model systems to study sharp metal/semiconductor interfaces, 2D quantum size systems, or, at least, as passivation coverages for following epitaxy. The $(\sqrt{3}\times\sqrt{3})R30^\circ$ structure (hereafter, $\sqrt{3}$) is a typical impurity-induced reconstruction forming on Si(111) surface after adsorption of such III-V group elements as In [1], Sn [2], Pb [3], Bi [4], Sb [5]. Note, that $\sqrt{3}$ structure forms after 1/3 ML (1 ML = $7.8\times 10^{14}\text{ cm}^{-2}$) adsorption of In, Sn, and Pb coverages, while for Sb and Bi cases it also forms at 1 ML (trimers are placed in the nodal positions of the $\sqrt{3}$ elementary cell). But while the structure and properties of $\sqrt{3}$ -metall reconstructions on Si(111) surface has been widely studied by such common techniques as scanning tunneling microscopy and reflection high-energy electron diffraction (RHEED), these methods do not allow us to visualize surface morphology during metal deposition directly, especially in temperature range above 300°C .

In this work we have visualized, studied and compare atomic processes on Si(111) surface during In, Sn, Pb, Bi, and Sb deposition at substrate temperatures up to 860°C by *in situ* ultrahigh vacuum reflection electron microscopy (UHV REM) being efficient technique to control structural and morphology evolutions at monatomic step level on the crystal surface during epitaxial growth in a wide range of temperatures [6].

2. Experiment

Specimens with $8\times 1.0\times 0.4\text{ mm}$ dimensions were cut from P-doped Si(111) wafers with $0.01^\circ\text{--}0.3^\circ$ miscut angles and $0.3\ \Omega\cdot\text{cm}$ resistivity. Specimens with $8\times 1.0\times 0.4\text{ mm}$ dimensions were cut from phosphorus-doped Si(111) wafers with a misorientation 0.01° and $0.3\ \Omega\cdot\text{cm}$ resistivity and cleaned with petroleum ether. The samples were treated by low-energy (5 keV) Ar⁺ ion bombardment to form round-shaped craters ($\sim 2\text{ mkm}$ deep and $\sim 100\text{ mkm}$ wide) on their surface. Next, the samples were placed into the UHV REM chamber and resistively annealed at $\sim 1300^\circ\text{C}$ for 300 s to remove the native oxide layer and contaminants, and to form an amphitheater-like surface morphology with atomically flat terraces of moderate width divided by concentric monatomic steps at the crater bottom. After the sample preparation, the substrate temperature was reduced first rapidly ($\sim 5^\circ\text{C/s}$) to 835°C and then slowly

($\sim 0.1\text{--}0.5^\circ\text{C/s}$) to 795°C to form large-scale ($\sim 10\text{--}100\text{ mkm}^2$) domains of (7×7) reconstruction on the terraces. The materials were deposited from an embeddable home made evaporator (tungsten filament wetted with molten growth material and heated by DC). All morphological and structural transformations on the Si(111) surface were observed and recorded by *in situ* REM and RHEED techniques. Due to a small angle of electron beam incidence onto the sample surface, REM images are foreshortened by ~ 50 times along beam incidence which distorts the shape of all surface morphology features.

3. Results and discussions

Recently we have studied in details the impact of Sn adsorption on Si(111) surface morphology and structure during Sn deposition, electromigration, and desorption at $200\text{--}860\text{ C}$ [7,8]. Fig. 1 shows typical *in situ* REM images of the Si(111) surface during $(7\times 7) \Rightarrow \sqrt{3}$ -Sn structural transition induced by Sn deposition. When Sn coverage increases on Si(111)- (7×7) surface, $\sqrt{3}$ -Sn domains (indicated by white arrows) nucleate along atomic steps and expanse over the terraces in all directions. In RHEED patterns this moment corresponds to the appearance of $\sqrt{3}$ reflections while the intensity of (7×7) reflections decrease. The rearrangement of the substrate top layer Si atoms from the initial (7×7) surface reconstruction to the (1×1) bulk termination during $(7\times 7) \Rightarrow \sqrt{3}$ -Sn structural transition causes the adsorption of 0.08 ML Si coverage. At $T < 650^\circ\text{C}$ where the pure 1/3 ML Sn metallic α - $\sqrt{3}$ -Sn structure forms, 0.08 ML Si coverage nucleates 2D islands on the $> 1\text{ mkm}$ terraces. At $T > 650^\circ\text{C}$, Sn adsorption induces also emission of Si atoms from the steps onto the terraces with the following step shift as it shown in Fig. 1. The 0.08 ML Si coverage and Si atoms detaching from the steps participate in the formation of the mosaic γ - $\sqrt{3}$ -Sn phase which decreases Sn coverage sufficient to form $\sqrt{3}$ -Sn structure below 1/3 ML. It was found that Pb deposition at $T > 500^\circ\text{C}$ also forms mosaic-like γ - $\sqrt{3}$ phase with reduced Pb content and induces similar ascending step shift.

A different situation is observed for In deposition onto the Si(111)- (7×7) surface relative to Sn and Pb. Fig. 2 shows consecutive *in situ* REM images of the Si(111) during $(7\times 7) \Rightarrow \sqrt{3}$ -In structural transition induced by In deposition at 550°C . Deposition of In coverages above 1/6 ML leads to appearance of a spotted contrast on the terraces (Fig. 2b). Due to depletion zones near the steps

edges (indicated by black arrows Fig. 2b) are observed in REM images, this spotted contrast is supposed to be 2D island nucleation (similar 2D nucleation was observed for 1/3 ML Sn deposition at $T < 650^\circ\text{C}$). However, following In deposition leads to disappearance (or coalescence) of 2D islands nucleated at previous stage and, when In coverage approaches the values being slightly below 1/3 ML, dark contrast appears near the step edges (Fig. 2c) and rapidly cover whole terrace area at 1/3 ML In coverage (Fig. 2c). That moment corresponds to $\sqrt{3}$ reflections maximum intensity while (7×7) reflections fully decrease. This $(7\times 7) \Rightarrow \sqrt{3}$ -In structural transition is observed in REM images for $450\text{--}750^\circ\text{C}$ temperature range. The $\sqrt{3}$ -In structure is stable and continues to exist on the surface at zero In flux and $T = 450\text{--}550^\circ\text{C}$. At $T > 600^\circ\text{C}$ and zero In flux, reverse $\sqrt{3}$ -In $\Rightarrow (7\times 7)$ transition induced by In desorption occurs: the higher the temperature, the earlier this transition begins. No step shift was observed during 1/3 ML In deposition for whole temperature range.

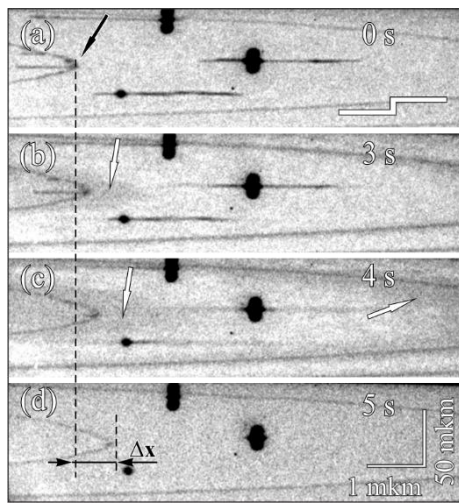


Fig. 1. In situ REM images of Si(111) surface during $(7\times 7) \Rightarrow \sqrt{3}$ -Sn structural transition induced by Sn deposition at $R_{\text{Sn}} = 0.03$ ML/s and $T = 800^\circ\text{C}$, total deposited Sn coverage is 0.15 ML. White arrows indicate $\sqrt{3}$ -Sn domains, a dashed line corresponds to the initial position of the atomic step indicated by a black arrow.

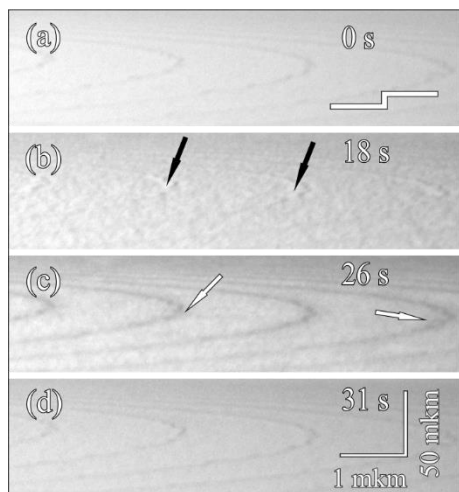


Fig. 2. In situ REM images of Si(111) surface during the $(7\times 7) \Rightarrow \sqrt{3}$ -In structural transition induced by 1/3 ML In deposition ($R_{\text{In}} = 0.01$ ML/s) at 550°C . Black arrows indicate depletion zones near step edges. White arrows indicate $\sqrt{3}$ -In phase nucleating near step edges.

In contrast to Sn/Pb/In deposition, there were no pronounced surface transformations observed in REM images during structural transitions induced by Sb or Bi adsorption. During Sb deposition at 600°C onto a clean Si(111)- (7×7) surface (Fig. 3a) the terrace color contrast to change to a darker one (Fig. 3b), which correlates with disappearing of (7×7) reflections in RHEED patterns at 0.5 ML Sb coverage. The $\sqrt{3}$ -Sb reflections appear in RHEED patterns at 0.8 ML Sb coverage and fade away when Sb coverage rises above 1 ML. A dark contrast of terraces and bright areas close to the step edges may also correspond to generation of 2D vacancies and islands with elevated concentration on the terraces and depletion zones near the steps due to an imbalance of surface Si atom induced by Sb adsorption, which are clearly observed in AFM images of Sb/Si(111) surface. Terrace and steps in REM images return their bright contrast only after Si(111) surface annealing at $T > 800^\circ\text{C}$ inducing Sb desorption.

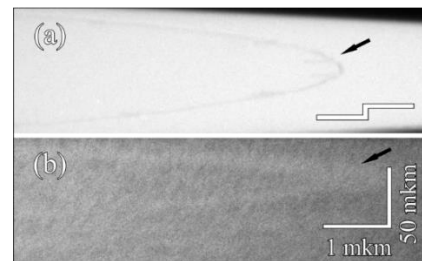


Fig. 3. In situ REM images of Si(111) surface (a) before and (b) after 1 ML Sb deposition at 600°C . White arrows indicate step edges.

4. Conclusions

Despite the fact that $\sqrt{3}$ structure forms on Si(111) surface for In, Sn, Pb, Sb, and Bi adsorption, the $\sqrt{3} \Rightarrow (7\times 7)$ transition and simultaneous transformation observed on Si(111) surface follow by different ways individual for each element. While for Sn (Pb) deposition form Si(111)- $\sqrt{3}$ morphology with atomically-flat terraces or with 2D-island on the terraces depending on substrate temperature, In deposition leads to formation of atomically-flat Si(111)- $\sqrt{3}$ interface with short-term appearance of 2D islands for all deposition temperatures. At the same time, Sb (Bi) deposition leads to roughening of Si(111) terraces.

Acknowledgements

This work was performed on the equipment of CKP “Nanostruktury” and was supported by Russian Science Foundation [grant number 19-72-30023].

References

- [1] A. V. Zotov, A. A. Saranin, O. Kubo, T. Harada, M. Katayama, K. Oura. *Appl. Surf. Sci.* **159–160**(2000)237.
- [2] T. Ichikawa. *Surf. Sci.* **140**(1984)37.
- [3] M. Hupalo, M. C. Tringides. *Phys. Rev. B.* **5**(2002)205406.
- [4] R. H. Miwa, T. M. Schmidt, G. P. Srivastava. *J. Phys.: Condens. Matter*, **15**(2003)2441.
- [5] V. K. Paliwal, A. G. Vedeshwar, S.M. Shivaprasad. *Surf. Sci. Lett.*, **513**(2002)L397.
- [6] A. V. Latyshev, A. B. Krasilnikov, A. L. Aseev. *Appl. Surf. Sci.* **60–61**(1992)397.
- [7] A. S. Petrov, D. I. Rogilo, R. A. Zhachuk, A. I. Vergules, D. V. Sheglov, A. V. Latyshev. *Appl. Surf. Sci.* **609**(2023)155367.
- [8] A. S. Petrov, D. I. Rogilo, A. I. Vergules c, V. G. Mansurov, D. V. Sheglov, A. V. Latyshev. *Surf. Sci.* **741**(2024)122418.

Ab initio calculations of the effect of lattice strain on the band structure of Cr₂CFBr MXene

Mushtuk P.S.^{*}, Iliushin I.G., Afremov L.L.

Far Eastern Federal University, 10 Ajax Bay, Russky Island, Vladivostok 690922, Russia

*e-mail: mushtuk_ps@dvfu.ru

Abstract. The band structure of the two-dimensional Cr₂CFBr MXene was investigated under biaxial compressive/tensile strain using first-principles calculations. The ground state of the MXene is semiconducting. At strains $\varepsilon < -10\%$, a transition from a semiconducting to a semimetallic state is observed.

1. Introduction

In recent years, the study of Janus two-dimensional materials has attracted significant attention due to their outstanding physical properties, such as the Rashba effect [1], tunable band gap [2], and strong Dzyaloshinskii-Moriya interaction [3]. In Janus MXenes, it is possible to control the magnetic order by varying the functional group ligands [4]. One of the approaches for tuning a material's physical properties is tunable strain. In this work, we investigate the effect of in-plane strain on the electronic band structure of the two-dimensional Cr₂CFBr MXene using first-principles calculations.

2. Methods

The first-principles calculations were performed using the Vienna *ab initio* simulation package (VASP) [5]. The exchange-correlation potential was treated within the generalized gradient approximation (GGA) in the Perdew-Burke-Ernzerhof (PBE) formulation [6]. The electron-ion interactions were described using the projector augmented-wave (PAW) method [7]. The electronic configurations of the atoms were set as follows: Cr ($3d^5 4s^1$), C ($2s^2 2p^2$), F ($2s^2 2p^5$), Br ($4s^1 4p^5$). The plane-wave cutoff energy was set to 520 eV. For Brillouin zone integration, a Gamma-centered $19 \times 19 \times 1$ Monkhorst-Pack \mathbf{k} -point mesh was employed [8]. During geometric optimization, atomic positions were relaxed until the forces on each atom became smaller than $1 \cdot 10^{-6}$ eV/Å. For electronic property calculations, the self-consistent loop was terminated when the total energy difference between successive steps fell below $1 \cdot 10^{-7}$ eV. To account for strong electron localization in chromium's d -orbitals, Hubbard corrections (DFT+U) were applied within the Dudarev formalism [9]. Following [4], the effective Hubbard parameter $U_{\text{eff}} = 3$ eV was adopted ($U_{\text{eff}} = U - J$, where U represents Coulomb repulsion and J the exchange parameter).

The crystal lattice strain was defined as $\varepsilon = \frac{a - a_0}{a_0}$, where a and a_0 – represent the lattice constants of the strained and unstrained systems, respectively [10]. To prevent boundary layer interactions, a 15 Å vacuum layer was added above the system. To investigate possible magnetic orderings in the system, we employed a $2 \times 2 \times 1$ supercell.

3. Results and discussions

Figure 1 shows the electronic band structure of Cr₂CFBr in its unstrained state. In the ground state, Cr₂CFBr exhibits bipolar magnetic semiconductor behavior [11] with a band

gap of 1.42 eV. The electronic states show no degeneracy. When spin-orbit coupling (SOC) is included, the band gap decreases by 20 meV to 1.40 eV. The transition occurs between the valence band maximum and conduction band minimum with a flip of the electron spin orientation.

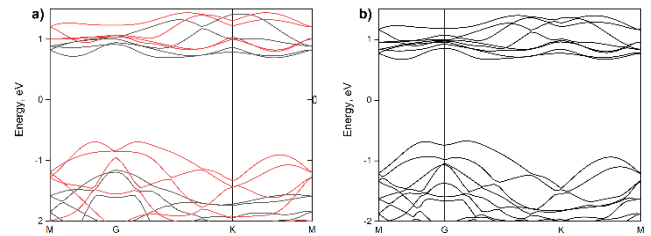


Fig. 1. Band structure of Cr₂CFBr in the unstrained state: (a) without spin-orbit coupling (SOC) (electronic states with spin-down and spin-up are shown in red and black, respectively), (b) with SOC included.

Under compressive strain (Fig. 2a), the band gap decreases progressively, reaching 0.91 eV at $\varepsilon = -10\%$. The spin-orbit coupling (SOC) effects become increasingly significant with greater strain (Fig. 2b), reducing the SOC-included band gap to 0.62 eV at $\varepsilon = -10\%$.

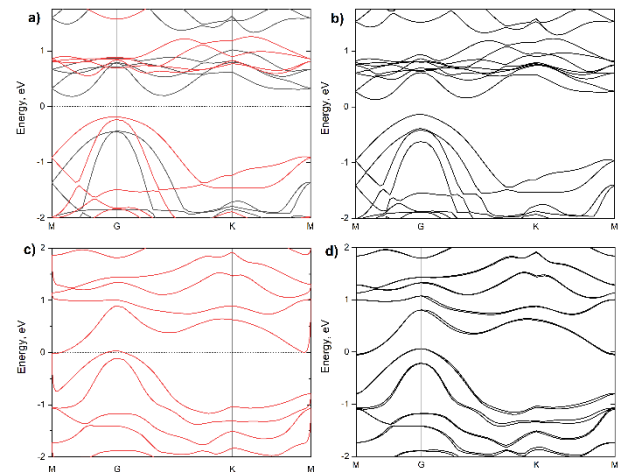


Fig. 2. Electronic band structure of Cr₂CFBr under applied strain: (a) at $\varepsilon = -10\%$ without spin-orbit coupling (SOC), with spin-down states shown in red and spin-up states in black; (b) at $\varepsilon = -10\%$ with SOC included; (c) at $\varepsilon = -11\%$ without SOC; (d) at $\varepsilon = -11\%$ with SOC.

Notably, the G-point interband transition occurs without spin flipping. When the compressive strain exceeds 10% ($\varepsilon < -10\%$), the system undergoes a semiconductor-to-semimetallic transition (Fig. 2c). In this regime, the

electronic states become degenerate, though the degeneracy is lifted by spin-orbit coupling.

Under tensile strain, the material maintains its semiconducting state (Fig. 3). When stretched to $\varepsilon = 11\%$, the band gap increases to 1.09 eV. Inclusion of spin-orbit coupling (SOC) reduces this value to 0.94 eV. Similar to the unstrained case, the valence-to-conduction band transition involves an electron spin flip.

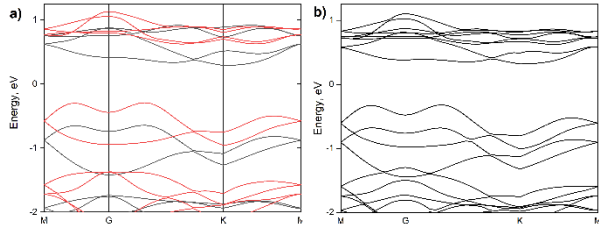


Fig. 3. Band structure of Cr_2CFBr under tensile strain: (a) $\varepsilon = 11\%$ without spin-orbit coupling (SOC), with spin-down states shown in red and spin-up states in black; (b) $\varepsilon = 11\%$ with SOC included.

4. Conclusions

Through first-principles calculations, we investigated the strain-dependent band structure of two-dimensional Cr_2CFBr MXene under compressive/tensile deformation. The study revealed that under compressive strains of $\varepsilon < -10\%$, the material undergoes a semiconductor to semimetallic transition. In contrast, tensile strains only modify the band gap magnitude while preserving the semiconducting character. This transition mechanism originates from increased distances between chromium ions and functional group.

Acknowledgements

The work by Mushtuk P.S., Iliushin I.G., and Afremov L.L. was supported by the state assignment of the Ministry of Science and Higher Education of the Russian Federation (Project No. FZNS-2023-0012).

References

- [1] Y. Wang, W. Wei, H. Wang, N. Mao, F. Li, B. Huang, Y. Dai. *J. Phys. Chem. Lett.* **10**(2019)7426.
- [2] A. Kandemir, H. Sahin. *Phys. Rev. B* **97**(2018)155410.
- [3] J. Liang, W. Wang, H. Du, A. Hallal, K. Garcia, M. Chshiev, H. Yang. *Phys. Rev. B* **101**(2020)184401.
- [4] C. Si, J. Zhou, Z. Sun. *ACS Appl. Mater. Interfaces* **7**(2015)17510.
- [5] G. Kresse, J. Furthmüller. *Phys. Rev. B* **54**(1996)11169.
- [6] J.P. Perdew, K. Burke, M. Ernzerhof. *Phys. Rev. Lett.* **77**(1996)3865.
- [7] P.E. Blöchl. *Phys. Rev. B* **50**(1994)17953.
- [8] H.J. Monkhorst, J.D. Pack. *Phys. Rev. B* **13**(1976)5188.
- [9] S.L. Dudarev, D. Nguyen Manh, A.P. Sutton. *Philos. Mag. B* **75**(1997)613.
- [10] Y. Yang, W. Ren, M. Stengel, X.H. Yan, L. Bellaiche. *Phys. Rev. Lett.* **109**(2012)057602.
- [11] X. Li, X. Wu, Z. Li, J. Yang, J.G. Hou. *Nanoscale* **4**(2012)5680.

Controlling of 6H-SiC surface graphitization by RHEED

Durakov D.E.^{*1,2}, Petrov A.S.^{1,2}, Rogilo D.I.^{1,2}, Makeeva A.A.¹, Nikiforov D.F.^{1,2}, Kurus N.N.¹, Milekhin A.G.¹, Sheglov D.V.¹, Latyshev A.V.^{1,2}

¹ Institute of Semiconductor Physics of SB RAS, 13 pr. Lavrentieva, Novosibirsk 630090, Russia

² Novosibirsk State University, 2 Pirogova St., Novosibirsk 630090, Russia

*e-mail: durakov@isp.nsc.ru

Abstract. The evolution of diffraction patterns (DPs) from the 6H-SiC(0001) surface during graphene growth was systematically investigated. Distinct DP characteristics were identified, corresponding to sequential morphological transitions: from an initially rough SiC surface to a step-terraced morphology, followed by formation of a carbon buffer layer and subsequent epitaxial graphene nucleation during thermal annealing. Complementary *ex situ* characterization via atomic force microscopy (AFM) and Raman spectroscopy confirmed strong correlations between the observed DPs and the surface's morphological evolution, stoichiometric composition, and structural perfection at each growth stage.

1. Introduction

Graphene is a two-dimensional carbon allotrope with a hexagonal lattice. It exhibits record charge carrier mobility of approximately $2 \times 10^5 \text{ cm}^2/\text{V}\cdot\text{s}$, surpassing silicon mobility by more than two orders of magnitude, high conductivity, and flexibility. Owing to these exceptional properties, various graphene-based devices have been developed, including transistors [1]. However, the fabrication of large-area, defect-free monolayers on dielectric substrates is still significant challenge in graphene electronic. This way thermal decomposition of silicon carbide is a promising synthesis approach.

Recent studies have confirmed the possibility of precisely controlled graphene growth on SiC(0001) substrates through thermal annealing in argon atmosphere [2]. Particular scientific attention has focused on graphitization processes and monolayer formation, which occur via sequential surface transformations. The key structures controlling graphene layer parameters include the $(6\sqrt{3} \times 6\sqrt{3})R30^\circ$ buffer carbon layer and the (1×1) graphene surface lattice [3]. In situ observations of reflection high-energy electron diffraction (RHEED) patterns corresponding to the given surface transformations have not been previously reported.

In this work, we have investigated the evolution of the crystalline structure in the near-surface layer of 6H-SiC(0001) during thermal processing using *in situ* methods. The obtained results establish correlations between annealing parameters, RHEED and the characteristics of obtained graphene layers, enabling precise control over their quantity and quality, that which research provides new insights into the mechanisms of graphene formation on silicon carbide substrates, contributing to the development of advanced electronic devices based on two-dimensional materials.

2. Experiment

The samples $8.0 \times 1.5 \times 0.33 \text{ mm}$ with dimensions were prepared from nitrogen-doped 6H-SiC(0001) substrates with $0.02\text{--}0.1 \text{ } \Omega\cdot\text{cm}$ resistivity. Thermal annealing procedures were conducted *in situ* within an ultra-high vacuum (UHV) chamber of a reflection electron microscope [4], utilizing direct or alternating electric current passage through the specimen for heating purposes.

Temperature monitoring was performed using an optical pyrometer, while structural evolution of the 6H-

SiC(0001) surface and graphitization processes were characterized by *in situ* through RHEED.

Ex situ morphological characterization was performed by atomic force microscopy (AFM, Bruker Multimode 8). Surface stoichiometric composition analysis was performed using Raman spectroscopy measurements (XploRa Plus, Horiba, excitation wavelength $\lambda = 532 \text{ nm}$).

3. Results and discussions

All investigated samples underwent the step-terrace surface formation stage. At temperatures below 1000°C , the 6H-SiC(0001) substrate surface displayed substantial roughness and nanoscale scratches with height of $5\text{--}15 \text{ nm}$. After heating to 1200°C , the surface gets a vicinal structure with incomplete SiC bilayer coverage on narrow terraces ($400\text{--}500 \text{ nm}$ wide) with step 0.75--nm -high, corresponding to half the (0001) lattice constant of 6H-SiC. These morphological characteristics confirmed by (AFM) profiles (Fig. 1a) correspond to the expected step height of 6H-SiC formed during low-temperature annealing, representing three Si-C bilayers [5].

The growth of high-quality graphene on 6H-SiC(0001) substrates occurs on a buffer layer having $6\sqrt{3}$ surface reconstruction, upon which graphene layers with (1×1) structure subsequently form.

Fig. 2(a) displays diffraction patterns (DP) along $[11\bar{2}0]$ direction obtained after five-minute annealing at $T = 1300^\circ\text{C}$. The rod-like reflections corresponding to the SiC structure begin to be accompanied by two satellites on either side of the rod reflections matching the $6\sqrt{3}$ reconstruction during annealing. "The appearance of satellite reflections on the diffraction pattern along the $[11\bar{2}0]$ direction indicates complete coverage of the sample surface by the buffer layer. The presence of the buffer layer is confirmed by distinct D and G peaks in the Raman spectrum (Fig. 1(c)). The sample surface exhibits large pits up to 5 nm deep (Fig. 1a) where graphene clusters form as evidenced by the weak broad feature at $\approx 2700 \text{ cm}^{-1}$ in the Raman spectrum referred to as the 2D peak.

The DP presented in Fig. 2b along $[1\bar{1}00]$ direction corresponds to the formation of the first graphene layer during 4-minute annealing at $T = 1350^\circ\text{C}$ with an electron beam incidence angle of $2\text{--}3^\circ$, enabling probe of the two uppermost surface layers. The surface exhibits (1×1) structure with rod-like reflections in the DP demonstrating the hexagonal structure. The rod-like diffraction features

associated with graphene exhibit high homogeneous intensity distribution, and continuous elongation along their entire length, being characteristic for high-quality two-dimensional graphene clusters.

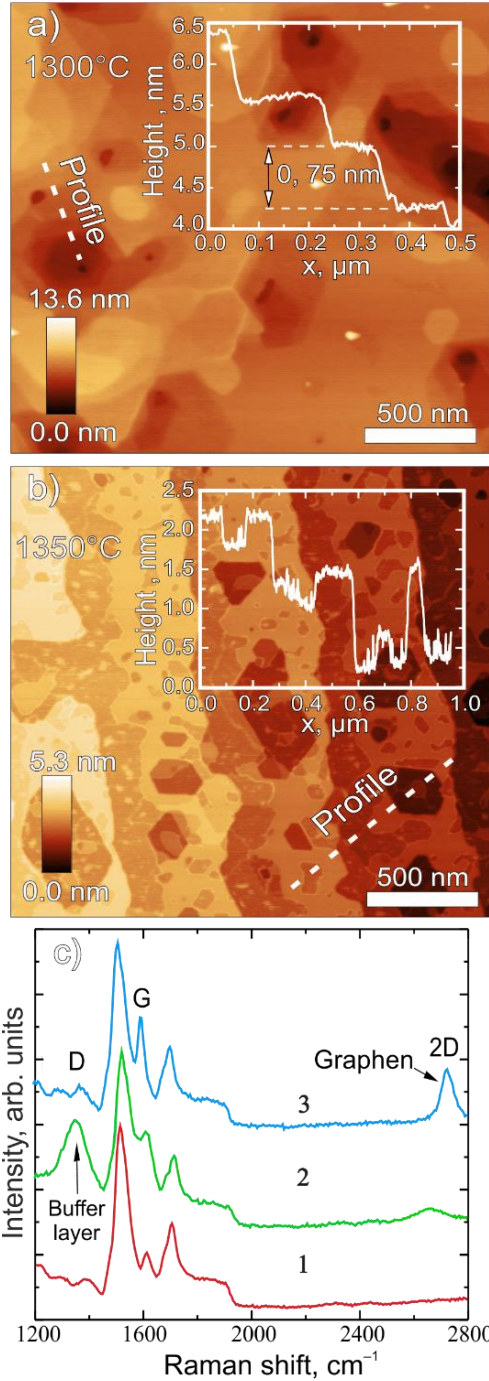


Fig. 1. AFM images of the sample surface after annealing: (a) $t = 5$ min at $T = 1300^\circ\text{C}$; (b) $t = 4$ min at $T = 1350^\circ\text{C}$; (c) Raman spectra: 1 — initial SiC, 2 — spectrum corresponds to annealing for 5 min at 1300°C , and 3 — spectrum was obtained after 4 min annealing at 1350°C . Surface profiles measured along the dashed lines are displayed in the insets.

Raman spectroscopy analysis (Fig. 1c) confirms graphene formation through significant intensity reduction of the D-peak associated with the buffer layer, along with marked increase in intensity and narrowing of the 2D-peak. The zero-order Laue zone in Fig. 2b contains unlabeled patterns (indicated by white arrows) evidencing the presence of the carbon buffer layer [15], while their presence simultaneously confirms the absence of a second

graphene layer. However, AFM image (Fig. 1b) reveals terrace segmentation onto stripe-like features along step edges and numerous polygonal pits up to 1 nm deep induced by silicon sublimation, indicating nucleation of a second graphene layer.

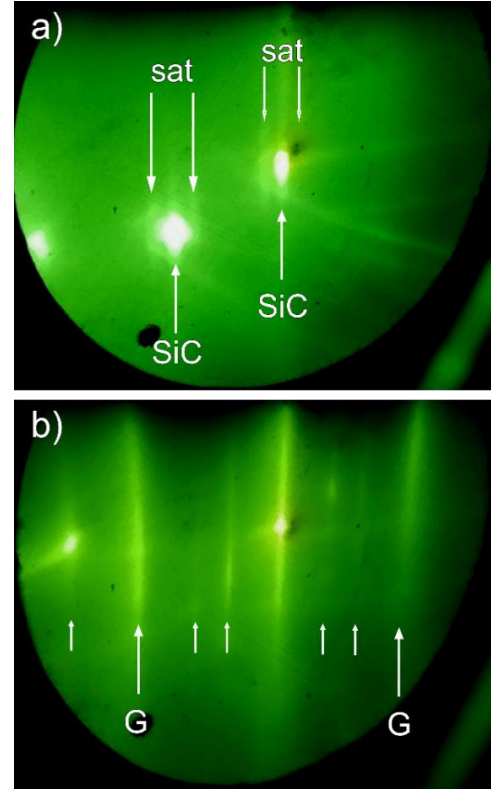


Fig. 2. (a) DP observed along $[11\bar{2}0]$ direction during annealing at $T = 1300^\circ\text{C}$; (b) DP observed along $[1\bar{1}00]$ direction during annealing at $T = 1350^\circ\text{C}$. Unmarked arrows indicate patterns of the $6\sqrt{3}$ -reconstructed buffer layer.

4. Conclusions

Our *in situ* REM investigation and *ex situ* AFM investigation and Raman spectroscopy measurements demonstrate that the formation of the buffer layer can be monitored through the appearance of satellite reflections in DP. For controlled synthesis of monolayer graphene, the annealing process must be terminated while the diffraction pattern still shows a superposition of reflections from both graphene and buffer layers. Complete disappearance of buffer layer reflections, which would indicate the formation of the second graphene layer, should be avoided to maintain monolayer coverage.

Acknowledgements

This work was performed on the equipment of CKP “Nanostruktury”. Raman spectroscopy investigations and were conducted under a state-funded research program (Project №. FWGW-2025-0014). AFM characterizations were financially supported by the Russian Science Foundation (RSF Grant №. 19-72-30023).

References

- [1] A. K. Geim, A. H. MacDonald. *Phys. Today*, **60**(2007)35.
- [2] K. V Emtsev, A. Bostwick, K. Horn, et al., **8**(2009)203.
- [3] J. B. Hannon, M. Copel, R. M. Tromp. *Phys. Rev. Lett.*, **107**(2011)166101.
- [4] D. I. Rogilo, S. V Sitnikov, et al. *Crystallography Reports*, **66**(2021)528.
- [5] S. Nakamura et al. *Applied Physics Letters*, **76**(2000)23.

Ising model on Fibonacci lattices: sphere, ring topologies of the sphere and torus.

Pochinok A.S.^{*,1}, Molochkov A.V.¹, Chernodub M.N.², Chepak A.K.¹

¹ Far Eastern Federal University, 690950 Vladivostok, Russia

² Université de Tours, 37200 Tours, France

*e-mail: pochinok.as@mail.ru

Abstract. We study the Ising model on Fibonacci-discretized 2D surfaces with Delaunay triangulation, examining sphere, ring, plane and torus topologies. Phase diagrams reveal connectivity-dependent transitions at $T_c \approx 3.33(3)J$. The characteristic 5/7-vertex defects in Fibonacci lattices cause: deviation from flat lattice critical temperature, singular connectivity transitions with increasing N, topology-dependent finite-size effects. Notably, the torus (<1% defects) shows no T_c shift, converging to the universal Fibonacci lattice limit. This demonstrates how local defects and global topology jointly determine critical behavior.

1. Introduction

The Ising model on two-dimensional lattices has long served as a paradigmatic system for studying phase transitions and critical phenomena [1]. While its properties on conventional flat lattices are well understood, its behavior on curved surfaces with complex topology presents new theoretical challenges and opportunities.

In this work, we investigate the ferromagnetic Ising model on curved surfaces discretized via the Fibonacci method with Delaunay triangulation [2]. The Fibonacci approach generates uniform coverings with approximately equal-area triangles [3], providing a natural framework for studying the thermodynamic limit on curved manifolds. A key feature of these lattices is the presence of topological defects - 5- and 7-coordinated vertices. As the number of nodes in the Fibonacci sphere increases, its triangular covering undergoes a series of singular transitions reflecting abrupt changes in connectivity properties. These changes substantially influence the system's statistical characteristics, leading to first-order-like discontinuities as the sphere's radius grows [5].

We compare phase diagrams across different topologies: sphere [5], torus, and spherical ring configurations (including ring and planar cuts). The critical temperature $T_c \approx 3.33(3)J$ remains universal in the thermodynamic limit, yet is lower than for flat triangular lattices ($T_c \approx 3.64J$) [4]. We attribute this to finite-size effects and global topology's influence on phase behavior. Notably, the torus exhibits negligible T_c shifts due to minimal connectivity defects (<1%), yet converges to the same limiting critical point as spherical topologies.

These results provide new insights into how connectivity properties, curvature, and topology collectively determine critical phenomena in curved spaces. The observed effects demonstrate nontrivial relationships between local lattice geometry and global topological constraints in statistical mechanical systems.

2. Experiment

Fibonacci lattices are characterized by an almost uniform and isotropic distribution of sites. This enables effective discretization of curved surfaces using triangles of approximately equal area.

The Fibonacci distribution on surfaces forms a structure consisting of two sets of spiral arcs [11]. In these arcs, the distance between consecutive points is determined by

Fibonacci numbers. Some spiral sets are twisted clockwise, while others are twisted counterclockwise. As the lattice radius (total number of sites) increases, the number of dominant spirals grows. It can also be demonstrated that the Fibonacci lattice essentially results from a sequential arrangement of elements along a single "generative spiral" [3]. The angular distance between elements of this generative spiral corresponds to the golden ratio. ($g \approx 1.618 \approx 137.5^\circ$).

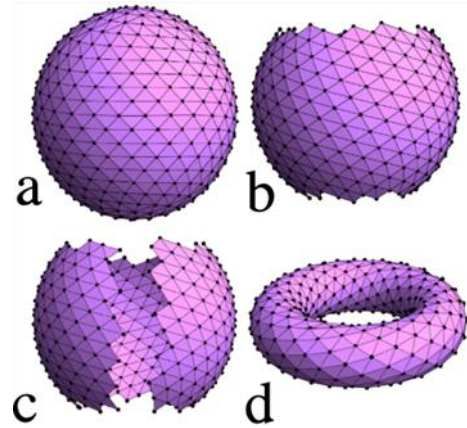


Fig. 1. Fibonacci lattices: a) sphere; b) ring; c) plane (cut ring); d) torus.

The Fibonacci spherical lattice (Fig. 1a) is generated through the coordinate transformation equations (1, 2):

$$x = r \cos \theta \sin \varphi; y = r \sin \theta \sin \varphi; z = r \cos \varphi \quad (1)$$

$$\varphi = \frac{2\pi k}{g}; \theta = \arccos \frac{k}{N} \quad (2)$$

where k runs through sites from 1 to N , and r is the radius of the sphere.

The Fibonacci ring lattice (Fig. 1b) was generated through excision of the polar regions containing 5- and 7-coordinated nodes from the spherical configuration, resulting in exclusively 6-coordinated vertices throughout the ring structure. Subsequent longitudinal sectioning of this annular geometry yielded the planar Fibonacci lattice (Fig. 1c).

The Fibonacci pattern on the torus surface (Fig. 1d) was constructed according to the mapping equations (3, 4), which preserve the uniform point distribution while adapting to the toroidal topology:

$$x = (R + r \cos \varphi) \cos \theta;$$

$$y = (R + r \cos \varphi) \sin \theta;$$

$$z = r \sin \varphi \quad (3)$$

$$\varphi = \frac{2\pi k}{g}; \theta = \frac{2\pi k}{N}. \quad (4)$$

After constructing the triangulated Fibonacci lattices, we define the Ising model with the Hamiltonian (5):

$$H = -J \sum_{\langle x,y \rangle} S_x S_y - h \sum_x S_x \quad (5)$$

The spin variable S_k represents the magnetic moment of an atom at the site k . This variable can take two values, $S_k = \pm 1$, associated, respectively, with up or down orientations of the magnetic moment with respect to the atomic crystal plane. To simplify notations, we consider dimensionful variables in units of the coupling $J = 1$.

3. Results and discussions

We used the Monte Carlo method to generate configurations using the Metropolis algorithm.

The boundary conditions for the Fibonacci ring and plane were fixed: on the original spherical lattice the spins were fixed and equal to +1, on the cut-out areas (ring and ring with a cut) the spins changed in a Monte Carlo cycle.

The magnetic susceptibility (6) was computed for all lattice configurations presented in Figure 1 (sphere, ring, plane, and torus) under zero external magnetic field conditions:

$$\chi(T, N) = \frac{\langle M^2(T, N) \rangle - \langle M(T, N) \rangle^2}{T} \quad (6)$$

where $M = \sum_x S_x$ is the total magnetic moment of the system.

The susceptibility data were fitted with a Gaussian function to determine the critical point. The following presents the distribution of critical temperatures as a function of the inverse number of lattice sites ($1/N$).

The spherical lattice undergoes a series of transitions associated with the formation of new spirals. The phase behavior exhibits segmentation of the extrapolation region into distinct intervals, similar to those observed for connectivity properties. Phase diagrams for the Fibonacci sphere are also presented in the article [5]. Comparable critical point patterns are observed for both the ring and plane (Fig. 2) configurations derived from the sphere. For the investigated high-density lattices, scaling analysis yields nearly identical critical temperatures of $T_c \approx 3.33(3)J$.

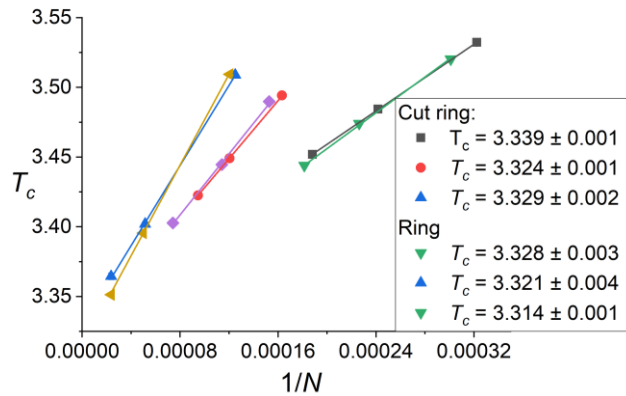


Fig. 2. The scaling of the temperature obtained from the magnetic susceptibility of Ising model at the Fibonacci ring as the function of an inverse number.

In contrast to the sphere and its ring-like topologies, the torus shows virtually no temperature shift. The

susceptibility versus temperature fitting (Fig. 3) gives a phase transition point of approximately $T_c \approx 3.32$.

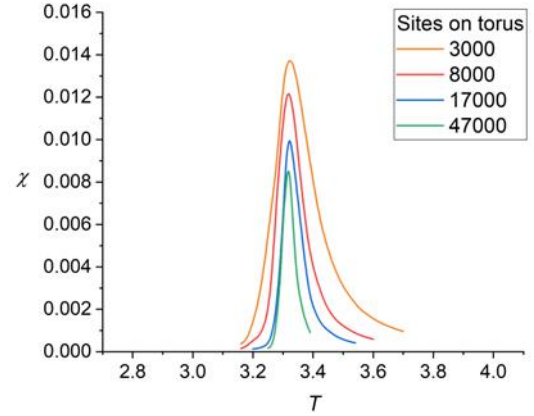


Fig. 3. Magnetic susceptibility of the Ising model on the Fibonacci torus.

4. Conclusions

The study of the Ising model on Fibonacci-Delaunay lattices (sphere, ring, plane, and torus) reveals a universal critical temperature $T_c \approx 3.33(3)J$ in the thermodynamic limit, despite topological differences. The deviation from the flat triangular lattice value ($T_c \approx 3.64J$) stems from 5/7-coordinated topological defects, inherent to spherical and ring geometries. Notably, the torus, with minimal defect density ($<1\%$), shows negligible T_c shifts, highlighting possible influence of local connectivity on phase transitions.

The segmented scaling of $T_c(1/N)$ for the sphere and derived configurations reflects abrupt connectivity changes during Fibonacci spiral growth, while the torus's smooth behavior underscores global topology's role in suppressing such singularities. However, the question remains as to how dominant a role topology plays in the observed deviations from the planar triangular lattice behavior.

Acknowledgements

The numerical simulations were performed at the computing cluster of Far Eastern Federal University.

References

- [1] L. D. Landau and E. M. Lifshitz, Statistical Physics: Volume 5, Vol. 5 (Elsevier, 2013).
- [2] B. Delaunay, Bulletin de l'Académie des Sciences de l'URSS. Classe des sciences mathématiques et naturelles 6, 793–800 (1934).
- [3] R. Swinbank and R. J. Purser, Quarterly Journal of the Royal Meteorological Society 132, 1769 (2006).
- [4] L. Zhi-Huan, L. Mushtaq, L. Yan, and L. Jian-Rong, Chinese Physics B 18, 2696 (2009).
- [5] A. Pochinok, A. Molochkov, and M. Chernodub, arXiv preprint arXiv:2301.06849 (2023).

Surface reconstructions in a submonolayer system La/Si(111)

Burkovskaya P.V.^{*,1,2}, Kotlyar V.G.¹, Utas T.V.¹, Mihalyuk A.N.^{1,2}, Zotov A.V.¹, Saranin A.A.¹

¹ Institute of Automation and Control Processes, 5 Radio St., Vladivostok 690041, Russia

² Far Eastern Federal University, 10 Ajax Bay, Russky Island, Vladivostok 690922, Russia

*e-mail: burkovskaya_pv@iacp.dvo.ru

Abstract. The details about growth conditions and surface morphologies of La-induced thin films on Si(111) substrate are observed by scanning tunneling microscopy (STM) and low-energy electron diffraction (LEED). We identify a new reconstruction $\sqrt{3}\times\sqrt{3}$ -La/Si(111) with domain walls (DWs). According to our experimental data, we report on models of unique atomic structures of the investigated compound.

1. Introduction

Rare earth metal (REM) thin films grown on silicon surface have attracted the attention of the scientific community due to their prospective for magnetic, spintronic, and electronic devices. There are three types of structures on Si(111) induced by submonolayer La (trivalent REM): 5×2 , $(2m+1)\times 6$, and 2×3 [1]. In particular, quasi-one-dimensional (1D) 5×2 -La reconstruction with $1/5$ monolayer (ML) coverage and 2×3 -La reconstruction with $1/3$ ML coverage. Recently, based on the ab-initio calculations the atomic structure of the La-induced Si(111)-($\sqrt{3}\times\sqrt{3}$)R30° surface was proposed [2]. However, there are relatively few experimental studies of this structure. In this article, we investigated growth and atomic structure of the uniform ($\sqrt{3}\times\sqrt{3}$)- La/Si(111) and domain walls (DWs) formed on it.

2. Experiment

Experiments were performed in the ultra-high vacuum system OMICRON STM-1 (with base pressure $\sim 1.8\times 10^{-10}$ Torr). ($\sqrt{3}\times\sqrt{3}$)-La and DWs were investigated by scanning tunneling microscopy (STM), low-energy electron diffraction (LEED), and ab-initio calculations. For the formation of the $\sqrt{3}\times\sqrt{3}$ -La surface, La deposition was carried out onto the preliminarily formed 2×3 -La/Si(111) surface at about 650°C.

3. Results and discussions

The $\sqrt{3}\times\sqrt{3}$ -La/Si(111) surface reconstruction with DW was found from STM and LEED measurement (Fig. 1).

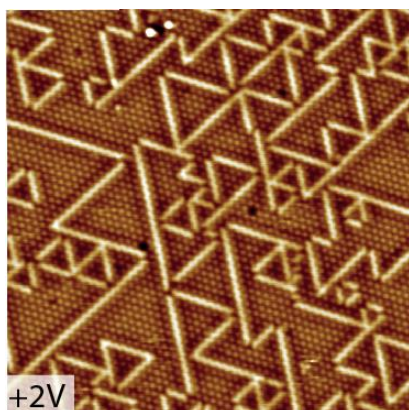


Fig. 1. Empty state (+2V) STM image ($35\times 35\text{ nm}^2$) of the $\sqrt{3}\times\sqrt{3}$ -La/Si(111) structure with DW.

One can see that the surface is built of the various sized triangular domains, which bounded by the DWs. These triangular domains contain the $\sqrt{3}\times\sqrt{3}$ -periodical hexagonal arrays (Fig. 2 a) and DW separates them (Fig. 2 b).

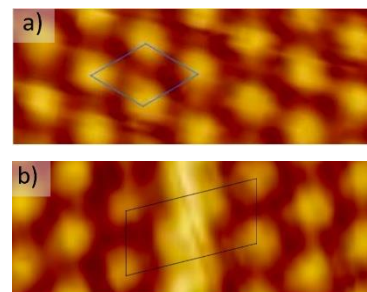


Fig. 2. Empty state (+2V) experimental high-resolution STM images of the a) $\sqrt{3}\times\sqrt{3}$ -La/Si(111) surface (the blue rhombus outlines the $\sqrt{3}\times\sqrt{3}$ unit cell) and b) domain wall at the $\sqrt{3}\times\sqrt{3}$ -La/Si(111) surface (the black shape outlines the $\sqrt{13}\times\sqrt{3}$ cell).

The La coverage estimation yields that the DWs contain excess La atoms in comparison with the triangular domains. Based on the STM observations we proposed atomic structural models of the $\sqrt{3}\times\sqrt{3}$ -La phase and DW by using ab-initio calculations. For the $\sqrt{3}\times\sqrt{3}$ -La phase it was established that La atoms occupy the H3 sites. For the heavy DWs separating the $\sqrt{3}\times\sqrt{3}$ -La domains (Fig.2 b) it was found that La atoms replace some substrate Si atoms forming double zig-zag atomic wire.

4. Conclusions

The $\sqrt{3}\times\sqrt{3}$ -La/Si(111) surface reconstruction with DWs has been investigated by STM, LEED, and ab-initio calculations. We proposed atomic structural models of the $\sqrt{3}\times\sqrt{3}$ -La phase and DW separating the $\sqrt{3}\times\sqrt{3}$ -La domains. The obtained results show that the structure of the DW is an almost ideal one-dimensional (1D) structure.

Acknowledgements

The research was carried out within the state assignment of IACP FEB RAS (Theme FFWF-2021-0002).

References

- [1] L. Liu, Z. Lin, Y. Wang, W. Wang, F. Yang, X. Zhu, J. Guo. Surface Science **674**(2018)40.
- [2] G. Yang, J.-S. Chai, L.-F. Xu, J.-T. Wang. New J. Phys. **23**(2021)123011.

Structural and morphological Bi₂Se₃(0001) surface transformations under Indium deposition

Ponomarev S.A.^{*1,2}, Rogilo D.I.^{1,2}, Golyashov V.A.¹, Nasimov D.A.¹, Kokh K.A.³, Sheglov D.V.¹, Latyshev A.V.^{1,2}

¹ Institute of Semiconductor Physics of SB RAS, 13 pr. Lavrentieva, Novosibirsk 630090, Russia

² Novosibirsk State University, 2 Pirogova St., Novosibirsk 630090, Russia

³ Institute of Geology and Mineralogy of SB RAS, 3 pr. Ac. Koptuyuga, Novosibirsk 630090, Russia

*e-mail: ponomarev@isp.nsc.ru

Abstract. We report the study of submonolayer indium deposition on Bi₂Se₃(0001) surface at room temperature and 450°C in the column of *in situ* reflection electron microscope. At room temperature indium atoms substitute bismuth in the uppermost Bi₂Se₃ layer. Subsequent annealing at ≈200°C drives displaced Bi atoms to the surface which create 0.4 nm-high Bi(111) bilayer with a labyrinth-like morphology. In contrast, deposition at 450°C (<1 ML In) leads to a surface phase appearing with 0.4 nm-high that locally suppresses Bi₂Se₃ sublimation. Ascending step flow during sublimation leads to star-shaped multilayer islands (N+0.4 nm height) formation. At higher coverages (>2 ML), In accumulates at step edges leading to intercalation into the van-der-Waals gap and further Bi substitution accompanied by the formation of 0.4-nm-high rims.

1. Introduction

One of the primary methods for fabricating high-quality van-der-Waals heterostructures and superlattices based on layered metal chalcogenides is molecular beam epitaxy (MBE) [1]. Like other epitaxial techniques, MBE does not allow to completely prevent the formation of point defects, twin domains, and various crystalline phases with identical stoichiometry (polymorphs). A significant number of defects appears at the interface during nucleation and formation of the initial film's layers. Consequently, investigating surface processes—adsorption, diffusion, nucleation, and growth of 2D islands—using *in situ* and *ex situ* techniques is crucial for advancing van-der-Waals epitaxy and addressing challenges that hinder the production of high-quality heterostructures for semiconductor applications.

In this work, we present the study of Bi₂Se₃(0001) structural and morphological surface transformations during the indium deposition, investigated using *in situ* reflection electron microscopy (REM) and *ex situ* characterization methods.

2. Experiment

To study the adsorption of indium on the Bi₂Se₃(0001) surface, *in situ* REM investigation was performed using samples with dimensions of 7×3×0.3 mm. The samples were prepared by cleaving a bulk Bi₂Se₃ single crystal grown by the Bridgman method [2]. The cleaving was performed under ambient conditions, followed by cutting the edges. High-purity indium (99.999%, Ted Pella, USA) and selenium (99.999%, Metallon, Russia) were used as deposition sources. The indium evaporator was calibrated by monitoring the formation rate of a √3×√3 surface reconstruction at 450°C on a pre-annealed Si(111) substrate following established procedures [3,4].

Ex situ diagnostics were performed by scanning electron microscopy (SEM) and atomic force microscopy (AFM). The chemical composition and electronic structure of the samples were characterized using X-ray photoelectron spectroscopy (XPS) and angle-resolved photoelectron spectroscopy (ARPES). Indium was deposited onto the Bi₂Se₃(0001) surface in ARPES camera

via electron-beam evaporation from a molybdenum crucible; the deposition rate was monitored using a quartz crystal microbalance and verified by XPS. Surface structural evolution was tracked in real time using low-energy electron diffraction.

3. Results and discussions

Indium deposition at room temperature already leads to the substitution of Bi atoms in the near-surface Bi₂Se₃ layer by In atoms — all indium atoms become covalently bonded with Se. Subsequent annealing at ≈200°C causes the displaced bismuth atoms to migrate to the surface, where they form covalent bonds with each other (Fig. 1) resulting in the formation of a Bi(111) bilayer. This bilayer exhibits a labyrinth-like morphology with no distinct faceting of boundaries and a height of 0.4 nm (Fig. 2(a)) [5].

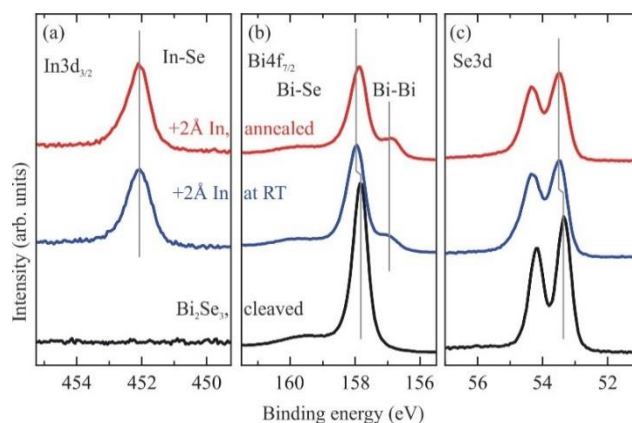


Fig. 1. XPS spectra of In3d (a), Bi4d_{7/2} (b) and Se3d(c) lines measured for a pristine Bi₂Se₃(0001) surface after cleavage in vacuum (black lines), after deposition of ≈2 Å indium at room temperature (blue lines), and after subsequent heating of the sample at 200°C (red lines).

Using backscattered electron detector sensitive to the atomic number of material's elements (Z-contrast), SEM analysis of a Bi₂Se₃(0001) surface with submonolayer In coverage (≈0.5 ML – 1 monolayer (ML) having a height ≈ 0.2 nm) revealed a morphological features consisting of three distinct regions (fig. 2(b)). Bright-contrast domains (0.4 nm height) corresponded to Bi-rich areas where

displaced bismuth formed a surface bilayer, while dark-contrast regions indicated In-substituted areas lacking Bi(111) bilayer coverage. Intermediate-contrast areas represented untransformed $\text{Bi}_2\text{Se}_3(0001)$ surface remained due to incomplete In adsorption. Quantitative analysis showed approximately equal distribution between transformed (bright/dark) and pristine (intermediate) regions. These observations corroborated by complementary AFM, XPS, and ARPES data demonstrate the competitive processes of In substitution and surface Bi aggregation during submonolayer low-temperature deposition.

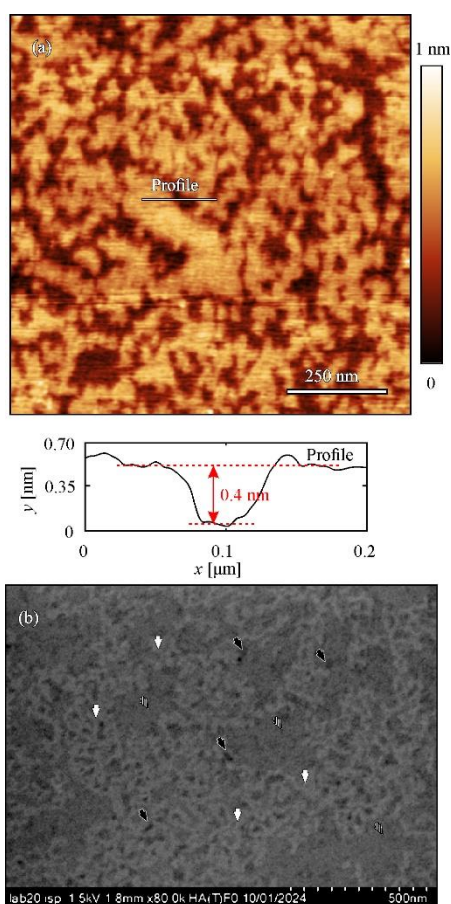


Fig. 2. (a) AFM image of the Bi_2Se_3 surface after indium deposition with 0.4-nm-high Bi(111) bilayers. (b) SEM image of the surface obtained in backscattered electron mode: white arrows indicate the regions corresponding to Bi(111) bilayers, black arrows indicate the regions of the surface reacted with indium but not covered by the Bi(111) bilayer, hatched arrows indicate the regions with the pristine $\text{Bi}_2\text{Se}_3(0001)$ surface.

Fig. 3(a) reveals $\text{Bi}_2\text{Se}_3(0001)$ sublimation at ~ 0.03 QL/sec (1 QL – quintuple layer (QL) having a height ≈ 1 nm), with dark-contrast atomic steps moving toward upper terraces [6]. The initial surface demonstrate straight 1-nm steps. Upon In deposition (0.007 ML/sec), dark step contrast intensifies (Fig. 3(b)), which indicates the incorporation of indium atoms into the step. After 500 sec of In deposition (1.25 ML), dark-contrast regions wide near step edges (Fig. 1c), which indicates the zigzag step formation. The In-induced phase at these stage of deposition covers $\sim 7\%$ of the surface. By 800 sec of indium deposition (2 ML), steps roughen further, and 0.4-nm rims form along all steps (Fig. 2d). Beyond 3 ML of In coverage under Se flux, In_2Se_3 grows via 2D nucleation (RHEED

oscillations) peocceeding to multilayer van-der-Waals epitaxy at 4 ML.

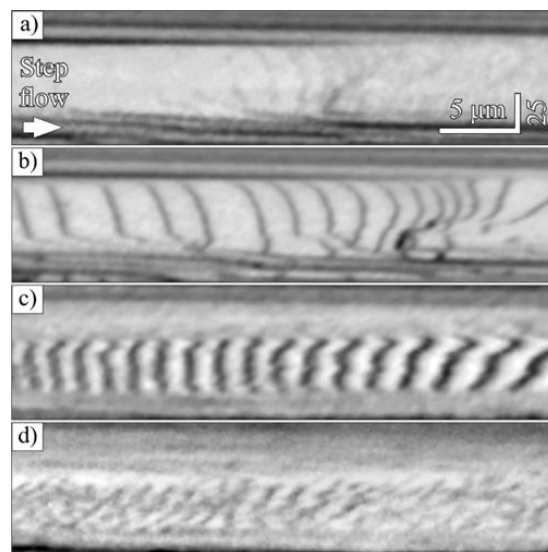


Fig. 3. *In situ* REM images of indium adsorption on the $\text{Bi}_2\text{Se}_3(0001)$ surface exposed to Se molecular beam at 450°C : (a) congruent sublimation (0 ML of indium coverage), (b) ~ 0.5 ML, (c) ~ 1.25 ML, (d) ~ 2 ML.

4. Conclusions

Using *in situ* REM, AFM, SEM, ARPES, and XPS, stages of indium deposition onto the $\text{Bi}_2\text{Se}_3(0001)$ surface at room temperature (followed by annealing at $\approx 200^\circ\text{C}$) and at 450°C were investigated. Indium deposition at room temperature induces the substitution of bismuth atoms in the near-surface Bi_2Se_3 layer. Subsequent annealing at $\approx 200^\circ\text{C}$ promotes the segregation of displaced bismuth atoms to the surface where they form a 0.4-nm-high Bi(111) bilayer exhibiting a labyrinth-like morphology. Indium deposition at 450°C (< 1 ML) induces the formation of a 0.4-nm-high surface phase that locally suppress Bi_2Se_3 sublimation. During sublimation, ascending step flow leads to formation of star-shaped multilayer islands with a height of $N+0.4$ nm (N is the number of QLs). At higher In coverages (> 2 ML), indium preferentially accumulates at step edges, then intercalates into the van-der-Waals gaps and further substitutes Bi atoms. This process is accompanied by the formation of 0.4-nm-high rims at the edges of the modified regions.

Acknowledgements

This work was performed on the equipment of CKP “Nanostruktury” and was supported by Russian Science Foundation [grant number 19-72-30023].

References

- [1] K. Lasek, P. Coelho, K. Zberecki, Y. Xin, S. Kolekar, J. Li, M. Batzill. ACS Nano **14**(2020)8473.
- [2] K. Kokh, S. Makarenko, V. Golyashov, O. Shegai, O. Tereshchenko. CrystEngComm **16**(2014)581.
- [3] A. Zotov, A. Saranin, O. Kubo, T. Harada, M. Katayama, K. Oura. Appl. Surf. Sci., **159**(2000)237.
- [4] S. Ponomarev, K. Zakhozhev, D. Rogilo, A. Gutakovsky, N. Kurus, K. Kokh, D. Sheglov, A. Milekhin, A. Latyshev. J. Cryst. Growth **631**(2024)127615.
- [5] С. Пономарев, Д. Рогило, В. Голяшов, Д. Насимов, К. Кох, Д. Щеглов, А. Латышев, ФТП **58**(2024)606.
- [6] S. Ponomarev, D. Rogilo, D. Nasimov, K. Kokh, D. Sheglov, A. Latyshev. J. Cryst. Growth **628**(2024)127545.

New possible structure of magnesium based germanium-silicon alloys: first-principles evolution search results

Luniakov Yu.V.*

Institute of Automation and Control Processes, 5 Radio St., Vladivostok 690041, Russia

*e-mail: luniakov@iacp.dvo.ru

Abstract. The search of minimal enthalpy structures of ternary magnesium alloys of different stoichiometry $Mg_xSi_yGe_z$ under pressure $P \leq 6$ GPa has been performed using the software suite USPEX implementing the evolution algorithm combined with the density functional theory (DFT) approach. The evolutionary search has yielded new possible ternary compounds of the stoichiometries $Mg_6Ge_4Si_3$, $Mg_6Ge_3Si_4$, $Mg_6Ge_3Si_3$, $Mg_4Ge_3Si_2$, Mg_2GeSi and $Mg_{12}Ge_3Si$, which have negative enthalpy of formation at pressures in the range of 0 to 10 GPa and which are not substitution solutions of Ge on Mg_2Si matrix. The stability and fabrication conditions of the resulting structures merit further investigation.

1. Introduction

Since the 1960s, Mg_2X compounds ($X = Si, Ge, Sn$) and their solid solutions have been shown to be promising materials for thermoelectric energy conversion [1, 2], since the high thermoelectric conversion efficiencies observed in these systems [3–5] make them suitable for heat recovery and energy conversion applications due to their valuable properties such as high melting point [6], narrow indirect band gaps, environmental safety and sufficient cheapness. These compounds are very promising materials as thermal elements in industrial production, infrared detectors in optical fibres, high efficiency solar cells and for use in hydrogen energy technologies for its storage and transport.

Magnesium silicide shows great compositional flexibility as evidenced by its formation of solid solutions with tin or germanium [7–9]. This flexibility allows the thermoelectric performance of these materials to be enhanced through improved electrical and thermal conductivity [10]. By varying the concentration of germanium in the compound, we can tailor the thermoelectric properties to our needs, increasing their potential for use in energy conversion applications [11].

The properties of three-component $Mg_xSi_yGe_z$ alloys over all possible stoichiometric ratios still remain unexplored. Antifluorite structure with $Fm\bar{3}m$ symmetry is the only structure considered in the analysis of magnesium stannides, as both magnesium silicide and magnesium germanide share this structural form. Furthermore, the application of evolutionary optimisation methods to the calculations of Mg_2Si [12], Mg_2Sn [13] and Mg_2Ge [14] has allowed the reproduction of known phase transitions as well as also predicting previously unknown structures under high pressures. The aim of this study is to identify optimal structures in the three-component $Mg_xSi_yGe_z$ system using modern evolutionary optimization techniques [15], and to investigate the stability of these structures both at ambient pressure conditions as well as at pressures ranging from 0 to 10 GPa.

2. Methodology of calculation

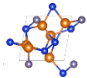
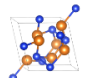
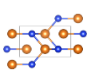

For evolutionary modeling of the three-component Mg-Si-Ge system, Universal Structure Predictor: Evolutionary Xtallography (USPEX) algorithms were applied in the variable composition mode [16–18]. During the evolutionary search, from 40 to 60 generations of structures were produced depending on the convergence, which was

considered to be achieved when the most energetically favorable structure remained unchanged for 20 consecutive generations. Each generation contained 20 structures and the first generation contained more than 120 structures, with 4 to 32 atoms per every structure. The structures of the first generation were randomly selected from the list of 230 space groups. In the following generations, 50% of the lowest-energy structures were inherited from the previous generation, 10% of the structures were produced by lattice mutation, 10% of the structures were obtained by atom transmutation, and the remaining 30% of the structures were generated randomly.

All USPEX generated structures were then relaxed using the conjugate gradient method implemented in the VASP software [19] with an energy precision of up to 0.1 meV/cell. The one-electron wave functions were expanded using a plane-wave basis with a energy cutoff of 500 eV; the exchange-correlation potential in the Perdew-Burke-Ernzerhof form [20] was used in the generalized gradient approximation. The Brillouin zones were sampled using a Monkhorst–Pack mesh with k-points resolution of $\sim 10^{-3}$ eV/Å and in the energy of $\sim 10^{-6}$ eV. The enthalpy at a zero temperature was determined using relationship $F = E + PV$, where E is the total energy, P is the external pressure, and V is the primitive cell volume.

3. Results and discussions

Table 1. Structures, corresponding to the vertices of the convex shell at pressures of 1, 4 and 6 GPa. Si atoms are shown as small blue spheres, Mg atoms as large yellow spheres and Ge atoms as large grey spheres in the unit cell in the last column.

Pressure/ Composition	Lattice parameters a, b, c (Å)	α, β, γ (°)	Symmetry	Unit cell
1 GPa Mg_6Si_3Ge	7.46×3	90, 90, 120	$R\bar{3}$ (146)	
1 GPa Mg_3Si_2	7.44, 7.44, 12.22	90, 90, 90	$R\bar{3}C$ (167)	
1 GPa Mg_2Si	4.14, 4.14, 6.90	90, 90, 90	$P4/nmm$ (129)	
4 GPa $Mg_6Si_4Ge_3$	8.4, 5.31, 5.25	93.9, 90.2, 95.3	$P1$ (1)	

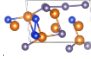
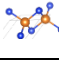
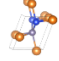
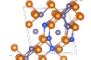
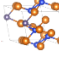

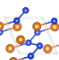
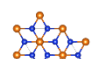
4 GPa	8.46, 5.34, 5.26	93.8, 90.4, 95.6	$P1 (1)$	
4 GPa	6.23×3	90, 90, 90	$Fm\bar{3}m (225)$	
6 GPa	4.17, 3.66, 5.00	90, 70.55, 90	$Pm (6)$	
6 GPa	5.06, 8.46, 8.04	78, 90.5, 73.3	$P1 (1)$	
6 GPa	4.95, 5.68, 6.59	76.3, 103.9, 98.1	$P1 (1)$	
6 GPa	4.52, 4.52, 5.82	90, 90, 120	$P6_3/mmc (194)$	
6 GPa	5.38, 5.25, 5.19	89.4, 79.7, 111.4	$P-1 (2)$	
6 GPa	7.62, 7.62, 15.05	90, 90, 120	$R-3m (166)$	

Table 1 shows the lattice parameters and enthalpies of formation of the most stable compounds of magnesium, silicon and germanium obtained by evolutionary methods at external hydrostatic pressures of 1, 4 and 6 GPa. At a pressure of $P = 1$ GPa, the convex hull consists of five vertices, one of which corresponds to the ternary compound Mg_6GeSi_3 (146 space group), while two others correspond to the binary silicides Mg_2Si and Mg_3Si_2 from groups 129 and 167, respectively. At a pressure $P = 4$ GPa, the convex hull includes two asymmetric ternary alloys $Mg_6Ge_4Si_3$ and $Mg_6Ge_3Si_4$, and a cubic magnesium silicide Mg_2Si of 225 space group symmetry. At a pressure $P = 6$ GPa, the convex hull is formed by three ternary alloys and three binary silicides of different stoichiometries from Mg_2Si to $MgSi_3$. The ternary alloys have symmetries 1 in the case of $Mg_4Ge_3Si_2$ and Mg_6GeSi_3 or 6 in the case of Mg_2GeSi . The binary silicides group symmetries 2 for $MgSi$, and 166 for $MgSi_3$ and 194 for Mg_2Si .

For a more detailed study of the stability of the most energetically favorable structures in different pressures, all results presented in Table 1 were recalculated in the pressure range from 0 to 10 GPa with full geometry re-optimization. Fig. 1 shows the most stable structures with negative formation enthalpy, obtained by optimizing the results of the evolutionary search at pressures $P \leq 10$ GPa as well as the results of calculations of handmade ternary compounds derived from the convex hull structures of the corresponding $Mg_xSn_ySi_z$ compounds [21] by replacing Sn atoms with Ge atoms and following optimizations. The most energetically favorable three-component alloy structure is three-component alloy Mg_6Si_3Ge of 146 space group symmetry. This structure is the most stable of all and was obtained by exchanging of Si and Ge atoms in the convex hull structure shown in Table 1. There is at least one other Mg_6Si_3Ge structure of the same composition but with a much higher enthalpy, shown on fig. 1. Next on the Enthalpy-axis is the three-component structure Mg_4SiGe , which competes with the Mg_6Si_3Ge and $Mg_{12}SiGe_3$ ones. At pressures $P < 1.5$ GPa Mg_6Si_3Ge is more energetically favorable among them, while at higher pressures it is losing to the $Mg_{12}SiGe_3$ and Mg_4SiGe structures. However, at

pressure $P=0$ their energies are comparable to those of the well-known binary silicide structure Mg_2Si .

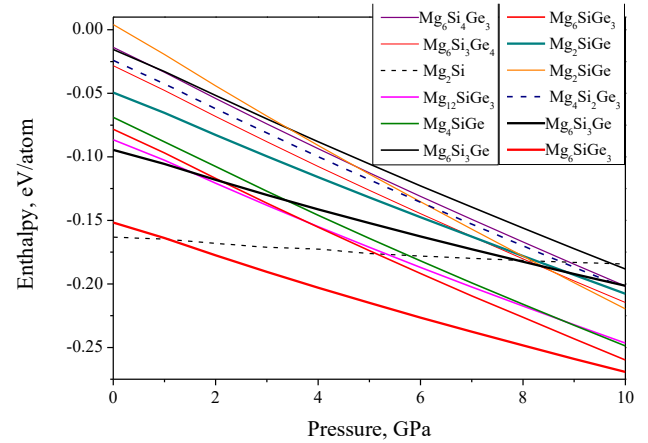


Fig. 1. Enthalpy-pressure dependence for the most energetically favorable crystal structures obtained by optimizing the results of the evolutionary search and their corresponding derivatives.

4. Conclusions

Evolutionary search allows the prediction of new unknown structures of mixed $Mg_xSi_yGe_z$ compositions. Some of them can be more stable than the known Mg_2Si at ambient pressure conditions.

Acknowledgements

All calculations were carried out using IACP FEB RAS Shared Resource Center «Far Eastern Computing Resource» equipment (<https://cc.dvo.ru>). The research was carried out within the state assignment of IACP FEB RAS (Theme FWFW-2021-0002).

References

- [1] E. N. Nikitin, V. G. Bazanov, V. I. Tarasov. Soviet Physics of Solid State 3 (1961) 2648.
- [2] R. J. Labotz, D. R. Mason, D. F. O'Kane. J. Electrochem. Soc. 110 (1963) 127.
- [3] Y. Noda, H. Kon, Y. Furukawa, N. Otsuka, I. A. Nishida, K. Masumoto. Mater. Trans. JIM 33 (1992) 851.
- [4] J. Tani, H. Kido. Physica B 364 (2005) 218.
- [5] V. K. Zaitsev et al. Phys. Rev. B 74 (2006) 4.
- [6] A.A. Nayeib-Hashemi, J.B. Clark. Bulletin of Alloy Phase Diagrams 5 (1984) 466.
- [7] H. Kamila et al. J. Mater. Chem. A, 7 (2019) 1045.
- [8] Y. Noda et al. Mater. Trans., JIM 33 (1992) 851.
- [9] Y. Noda et al. Mater. Trans., JIM 33 (1992) 845.
- [10] <https://www.iea.org>
- [11] K. Kaur, S. Dhiman, and R. Kumar. Indian J Phys 91 (2017) 1305.
- [12] Yu V. Lunyakov. Physics of the Solid State 62 (2020) 880.
- [13] Yu V. Lunyakov. Physics of the Solid State 63 (2021) 590.
- [14] Yu V. Lunyakov. Physics of the Solid State 64 (2022) 1414.
- [15] A.R. Oganov, C.J. Pickard, Q. Zhu, R. J. Needs, Nat. Rev. Mater. 4 (2019) 331.
- [16] A.O. Lyakhov, A.R. Oganov, H.T. Stokes, Q. Zhu. Comp. Phys. Comm. 184 (2013) 1172.
- [17] A.R. Oganov, A.O. Lyakhov, M. Valle. Acc. Chem. Res. 44 (2011) 227.
- [18] A.R. Oganov, C.W. Glass. J. Chem. Phys. 124 (2006) 244704.
- [19] G. Kresse, J.E. Furthmüller. Phys. Rev. B 54 (1996) 11169.
- [20] J.P. Perdew, K. Burke, M. Ernzerhof. Phys. Rev. Lett. 77 (1996) 3865.
- [21] Yu V. Lunyakov. Nanosystems: Phys. Chem. Math. 15, (2024) 621.

Self-organization of Ag and Au nanoparticle array on an inert surface during PVD and annealing

Gromov D.G.^{*1}, Volkov R.L.¹, Dubkov S.V.¹, Grishin T.S.², Novikov D.V.¹, Borgardt N.I.¹

¹ National Research University of Electronic Technology (MIET), Moscow, Russia

² Institute of Nanotechnology of Microelectronics of the Russian Academy of Sciences, Moscow, Russia

*e-mail: gromadima@gmail.com

Abstract. Understanding the processes of formation and evolution of metal nanoparticle arrays is important because it allows one to control their parameters and properties in practical applications. This paper analyzes the features of Ag and Au nanoparticle array transformation during condensation of these materials and energy exposure in a vacuum. The nanoparticles in the array were classified according to their size. It was found that small Ag nanoparticles (<3.0 nm) actually have perfect fcc structure, whereas larger diameter nanoparticles unexpectedly have predominantly icosahedral or decahedral faces. Even with a weak energy impact, the nanoparticle array evolution takes place that is caused by the simultaneously occurring processes of migration of individual atoms along the surface, coalescence of nanoparticles and evaporation. As a result, the evolution of Ag and Au nanoparticle arrays has different mechanisms. In the case of Ag, the coarsening of nanoparticles occurs through the gas phase via the Ostwald ripening mechanism. In the case of Au, it was found that the coalescence of nanoparticles depends on their mutual crystalline orientation, resulting in mechanisms being realized through the formation of a bridge or through a jump.

1. Introduction

In recent years, metallic nanoparticle arrays have attracted the interest of researchers due to the identified complex of their properties that allows to use this product of nanotechnology for various applications. For use in various devices or technological processes, an array of metallic nanoparticles must be formed on the solid state surface. Self-assembly of an array of nanoparticles with a reproducible average size and average distance between them on the surface is possible using physical vapor deposition methods. In these methods, the gas phase is formed by evaporation or sputtering, after which this vapor condenses on the solid state surface.

In this paper, we compare the features of the evolution of gold and silver nanoparticle arrays during condensation of these materials and energy exposure in a vacuum.

2. Experiment

This study utilized high-resolution transmission electron microscopy (HRTEM) to examine the structure of silver and gold nanoparticles on a thin film of amorphous carbon (a-C). A 20 nm thin film of a-C was used as a substrate because it is chemically inert towards silver and gold nanoparticles and does not affect the diffraction pattern when studying the crystal structure of the sample by TEM. To create substrates for silver and gold nanoparticles, amorphous carbon layer was deposited using magnetron sputtering on single crystals of NaCl, measuring 5×5×3 mm in size. The NaCl crystals were then dissolved in deionized water, and the resulting carbon films were transferred onto copper grids with a 3 mm diameter and 200 holes per inch using a standard procedure. Silver and gold nanoparticles were subsequently deposited onto the prepared carbon foil via vacuum thermal deposition at a distance of 20 cm from the substrates [1]. The masses of the vaporized portions of gold and silver were 1.5 and 0.8 mg, respectively. The residual pressure in the chamber was maintained at 1.5×10^{-5} Torr.

The nanoparticles were analyzed using HRTEM on a Titan Themis 200 instrument, which is equipped with a spherical aberration corrector for the objective lens. High-

resolution images of nanoparticles were obtained at an accelerating voltage of 200 kV, under consistent illumination conditions, and with nearly perfect focusing of the objective lens.

3. Results and discussions

Detailed analysis of the arrays using TEM allowed us to classify the nanoparticles by type: small monocrystalline nanoparticles, monocrystalline twin, icosahedral, decahedral, and polycrystalline nanoparticles [2]. As can be seen in Fig. 1, the proportion of small monocrystalline nanoparticles in the array was the largest.

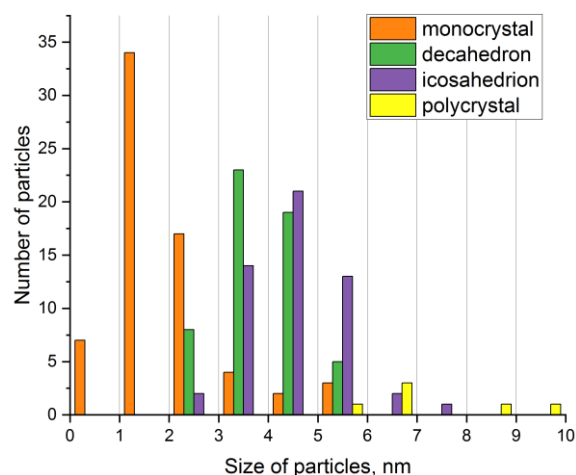


Fig. 1. Histogram of the distribution of nanoparticles in the array depending on their size and type of internal structure.

As can be seen in Fig. 1, the proportion of small monocrystalline nanoparticles in the array was the largest. The single-crystal type was predominant for particles sized 1–3 nm, decahedral for particles sized 3–4 nm, and icosahedral for particles sized 4–5 nm (Fig. 1). For particle sizes >6 nm, the polycrystalline type became predominant. Interestingly, the smallest nanoparticles had a single-crystal structure. The most of these nanoparticles with diameters of 0.8–3.0 nm exhibited a nearly perfect face-centered cubic (FCC) structure with a distinct faceted

appearance. In the size range, a significant percentage of nanoparticles with fivefold symmetry, i.e. icosahedral (Ih) and decahedral (Dh) structures, were observed.

During a weak energy impact, the nanoparticle array evolution takes place that is caused by the simultaneously occurring processes of migration of individual atoms along the surface, coalescence of nanoparticles and evaporation. As a result, the evolution of Ag and Au nanoparticle arrays has different mechanisms [3]. In the case of gold, the particles vibrate close to each other for quite a long time. But at some point, when they get a little closer, a "bridge" appears between them. This occurs in cases where the planes of the crystal lattice of nanoparticles are located either in continuation of each other or are turned at an angle (Fig. 2(a)).

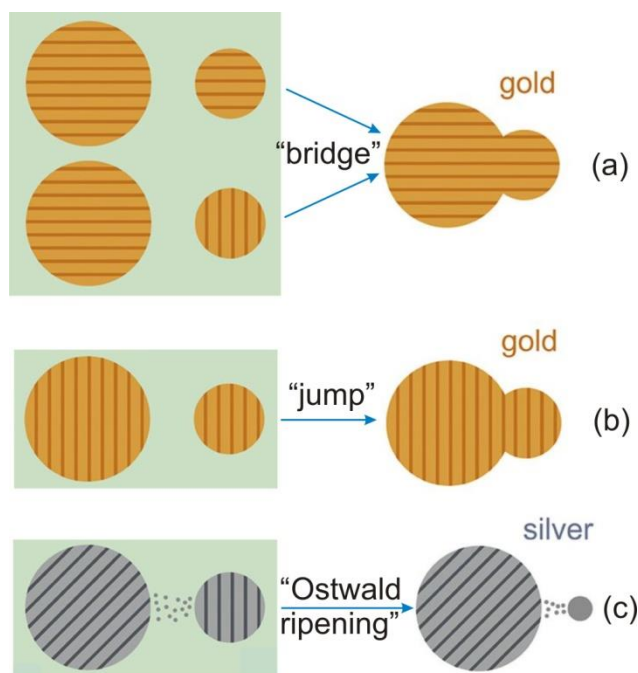


Fig. 2. Scheme of coalescence mechanisms of gold and silver nanoparticles: (a) - "Bridge"; (b) - "Jump"; (c) - "Ostwald ripening".

Then the unification occurs rapidly: the particles instantly come closer together, and the bridge instantly expands with rapidly growing crystal planes. In cases where the planes of the crystal lattice of nanoparticles are located parallel, at some point, with some convergence (in the presented case, at 0.7 nm), a sudden "jump" coalescence occurs without the formation of a bridge between them (Fig. 2(b)). At the final stage, the shape of the nanoparticles is optimized by reducing the surface.

The behavior of silver nanoparticles differs significantly from that of gold (Fig. 2(c)). The Ag particles also vibrate around each other. However, unlike Au particles, it is noticeable that they decrease in size over time. In the case of silver particles, there is no obvious abrupt coalescence or formation of chains of atoms, i.e. the particles remain at some distance from each other. Moreover, it is clear that mass transfer is observed in the space between particles. As a result, it appears as if the larger particle is "sucking" into itself the material of the smaller particle. At the final stage, a relatively smooth transition of the remains of the small nanoparticle to the large one occurs. Thus, our observations show that when an array of Ag nanoparticles is exposed to energy, two

simultaneously occurring processes take place: evaporation and coalescence. Since the vapor phase for Ag is easily formed, it is natural that the coalescence of nanoparticles in this case occurs by the Ostwald ripening mechanism, when larger particles with a larger radius and lower saturated vapor pressure absorb smaller particles with a smaller radius and higher saturated vapor pressure by directed mass transfer through the external environment due to the pressure difference.

4. Conclusions

Thus, in the initially deposited array of gold and silver nanoparticles, under energy exposure, the evolution process is observed due to the enlargement of nanoparticles and a decrease in their number in the array. Under the same conditions of energy exposure, the process of coalescence of Au and Ag nanoparticles in the array by joining neighboring particles differs significantly. In the case of Ag, the evaporation process plays a significant role. For this reason, the aggregation of Ag nanoparticles occurs by intensive mass transfer through the external environment, implementing the well-known Ostwald ripening mechanism. In the case of Au, evaporation of the material is not significant for the coalescence of nanoparticles. However, the mechanism of this process depends on the mutual spatial orientation of the atomic planes of the crystal lattices of nanoparticles. With a parallel arrangement of closely packed planes of nanoparticles, the "jump" mechanism of coalescence is realized. In all other cases, the coalescence of Au nanoparticles occurs by "bridges" formed by Au atoms.

Acknowledgements

The work was carried out within the framework of the state assignment 2023-2025. Agreement FSMR-2023-0003.

References

- [1] D.G. Gromov, L.M. Pavlova, A.I. Savitskii, A.Yu. Trifonov. *Physics of the Solid State* 57 (2015) 173.
- [2] Gafner Yu.Ya., Ryzhkova D.A., Gafner S.L., Gromov D.G., Dubkov S.V., Novikov D.V., Borgardt N.I., Volkov R.L., Poletaev G.M. *Mater. Chem. Phys.*, 2024, v.326, 129810.
- [3] Gafner Y.Y., Gromov D.G., Volkov R.L., Dubkov S.V., Ryzhkova D.A., Gafner S.L., Cherepovskaya A.A., Novikov D.V., Grishin T.S., Borgardt N.I. *Surfaces and Interfaces*, 2024, v. 54, 105165.

3D/nanodots/2D growth in Sb-mediated Ge epitaxy on Si(111)

Petrov A.S.^{*,1,2}, Gumbarg V.V.^{1,2}, Rogilo D.I.^{1,2}, Sheglov D.V.¹, Latyshev A.V.^{1,2}

¹ Institute of Semiconductor Physics of SB RAS, 13 pr. Lavrentieva, Novosibirsk 630090, Russia

² Novosibirsk State University, 2 Pirogova St., Novosibirsk 630090, Russia

*e-mail: alexey_petrov@isp.nsc.ru

Abstract. We report *in situ* ultrahigh vacuum reflection electron microscopy and *ex situ* atomic force microscopy study of Sb-mediated Ge epitaxy (0–10 BL) on Si(111) surface with Sb surfactant coverages (0–1 ML) at 500–650 C. Sb passivation of Si(111) surface does not suppress Stranski-Krastanov growth regime at 600 C for Ge coverages above 3 BL, however 3D Ge islands ($h \approx 10$ nm, area $S \sim 1$ mkm², $N \sim 10^7$ cm⁻²) nucleation on clean Si(111) surface transits to growth of Ge nanodots ($h \approx 2$ nm, and $S \sim 100$ nm², $N \sim 10^{11}$ cm⁻²) on 1 ML Sb-passivated Si(111) surface at 600 C. Ge epitaxy on 1 ML Sb-passivated Si(111) surface at 500–550 C proceeds under layer-by-layer growth mode.

1. Introduction

Semiconductor heteroepitaxial technologies mostly deal with Stranski-Krastanov growth mode where layer-by-layer growth transmits to growth of 3D islands due to relaxation of elastic strains induced by lattice parameter mismatch between growth material and substrate. Applicable to the most common hetero system Ge/Si, transition to 3D growth mode occurs at Ge coverages above 2 BL (1 BL = 2 ML = 1.56×10^{15} cm⁻²) on Si(111) surface. It is well known that application of Sb as a surfactant on Si surface allows one to suppress 3D Ge nucleation and to obtain thicker Ge pseudomorphic film under certain growth conditions [1,2]. However, according to works [1,2], exact experimental conditions for 3D/2D transition or at least for reduction of 3D Ge island sizes at Sb-mediated Ge epitaxy on Si(111) are not clear. Moreover, self-organizing Ge quantum dots density was shown to be regulated by Sb coverage varying on Si(100) surface [3]. In this work, using *in situ* ultrahigh vacuum reflection electron microscopy (UHV REM) and *ex situ* atomic force microscopy (AFM) we reveal features of Ge epitaxy via growth of 3D islands and nanodots on Sb-passivated Si(111) surface at 500–650°C.

2. Experiment

Specimens with $8 \times 1.0 \times 0.4$ mm dimensions were cut from phosphorus-doped Si(111) wafers with a misorientation 0.01° and $0.3 \Omega \cdot \text{cm}$ resistivity and cleaned with petroleum ether. The samples were treated by low-energy (5 keV) Ar⁺ ion bombardment to form round-shaped craters (~ 2 mkm deep and ~ 100 mkm wide) on their surface. Next, the samples were placed into the UHV REM chamber and resistively annealed at $\sim 1300^\circ\text{C}$ for 300 s to remove the native oxide layer and contaminants, and to form an amphitheater-like surface morphology with atomically flat terraces of moderate width (at least 10 mkm) divided by concentric monatomic steps at the crater bottom [4]. After the sample preparation, the substrate temperature was reduced first rapidly ($\sim 5^\circ\text{C/s}$) to 835°C and then slowly ($\sim 0.1\text{--}0.5^\circ\text{C/s}$) to 795°C to form large-scale ($\sim 10\text{--}100$ mkm²) domains of (7×7) reconstruction on the terraces. Sb and Ge were deposited from embeddable evaporator with two separated tungsten filaments wetted with molten Sb and Ge and heated by DC. Sb coverages (0–1 ML) were deposited onto the Si(111)- (7×7) surface at

600°C . Sb flux was calibrated by $(\sqrt{3} \times \sqrt{3})\text{-Sb} \Rightarrow "1 \times 1"\text{-Sb}$ structural transition observed by reflection high-energy electron diffraction (RHEED) when adsorbed Sb coverage θ_{Sb} rises above 1 ML at $T = 600\text{--}650^\circ\text{C}$ [5]. Ge coverages θ_{Ge} up to 10 BL were deposited onto Si(111)- (7×7) and Sb/Si(111) at $500\text{--}650^\circ\text{C}$ and $R_{\text{Ge}} = 0.01\text{--}0.1$ BL/s. All experimental stages including Sb and Ge flux calibration were observed and recorded by *in situ* REM and RHEED techniques. Due to a small angle of electron beam incidence onto the sample surface, REM images are foreshortened by ~ 50 times along beam incidence, which distorts the shape of all surface morphology features. Following analysis of obtained surface morphologies was carried out by *ex situ* AFM technique in air.

3. Results and discussions

The typical transformations observed by *in situ* REM technique on the Si(111) surface during Sb deposition and following Ge epitaxy at 600°C are presented in Fig. 1. Thin dark line indicated by white arrow in Fig. 1a correspond to concentric monatomic steps dividing atomically flat terraces with bright contrast. Ge deposition onto clean Si(111)- (7×7) at 600°C leads to 2D island nucleation (Fig. 1b) and with their following coalescence when θ_{Ge} reaches 1 and 2 BL values (we discussed these processes in detail here [6]). At Ge coverages above 2 BL, 2D growth transits to nucleation and growth of 3D Ge islands being observed in REM images as thick dark stripes (Fig. 1c). According to AFM images (Fig. 2a), these 3D islands are flat and arrow shaped with height $h \approx 10$ nm, area $S \sim 1$ mkm², and concentration $N \sim 10^7$ cm⁻². Further Ge deposition up to 10 BL do not rise the quantity of 3D islands, while 3D islands enlarge in height and area but do not coalesce with neighbors. Notice, that $(7 \times 7) \Rightarrow (5 \times 5)$ structural transition is observed in RHEED patterns when θ_{Ge} reaches 1 BL, and (5×5) structure is observed further for Ge coverages above 2 BL due to 3D islands are flat. During Sb deposition onto Si(111)- (7×7) at 600°C the terrace color contrast to change to a darker one (Fig. 1d) which correlates with disappearing of (7×7) reflections in RHEED patterns at $\theta_{\text{Sb}} \sim 0.5$ ML. The $(\sqrt{3} \times \sqrt{3})\text{-Sb}$ reflections appear at $\theta_{\text{Sb}} \sim 0.8$ ML and fade away when θ_{Sb} rises above 1 ML. A dark contrast of terraces and bright areas close to the step edges may also correspond to generation of 2D vacancies and islands on the terraces and depletion zones near the steps due to an imbalance of

surface Si atom induced by Sb adsorption [7], which is clearly observed in AFM images of Sb/Si(111) surface. Ge deposition onto Sb/Si(111) surface at 600 C leads to general brightness decrease and appearance of dark spotted contrast in REM image (Fig. 1e). Atomic steps are not resolved in REM images of Sb/Si(111) surface with $\theta_{\text{Ge}} \geq 3$ BL deposited at 600 C. At the same time, 3D diffraction spots appear in RHHED pattern at $\theta_{\text{Ge}} = 2-3$ BL. According to AFM images, with Sb coverage increasing in $\theta_{\text{Sb}} = 0-0.5$ ML range, 3D Ge island density rises up to 10^{10} cm^{-2} (Fig. 2d), while their size decreases. At $\theta_{\text{Sb}} \geq 0.5$ ML 3D Ge island growth transits to growth of a dense array of Ge grains (Fig. 2b) with $N \sim 10^{11} \text{ cm}^{-2}$, $h \approx 2 \text{ nm}$, and $S \sim 100 \text{ nm}^2$, which can be considered as Ge nanodots or Ge quantum dots due to their sizes. Ge nanodot maximum density is reached at $\theta_{\text{Sb}} = 1 \text{ ML}$ and $\theta_{\text{Ge}} = 3 \text{ BL}$. Ge nanodot density dependence on Ge deposition rate at fixed $T = 600 \text{ C}$ and $\theta_{\text{Sb}} = 1 \text{ ML}$ has been measured (Fig. 2e). Coalescence of neighboring Ge nanodots was found on Sb/Si(111) surface at $\theta_{\text{Ge}} > 3 \text{ BL}$ and 600 C.

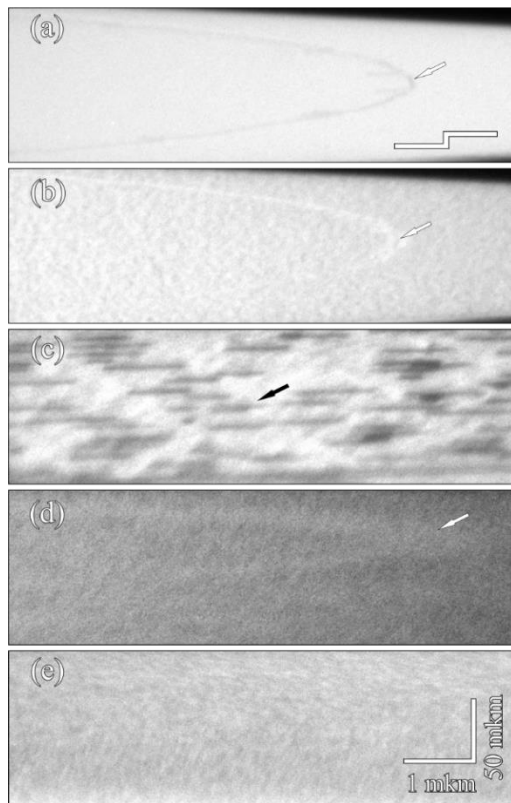


Fig. 1. Typical in situ REM images of Si(111) surface at 600 C, $R_{\text{Ge}} = 0.02 \text{ BL/s}$: (a) clean Si(111)-(7 \times 7) surface, white arrow indicates on concentric step edge; (b) after 0.5 or 1.5 BL Ge deposition; (c) after 3 BL Ge deposition, black arrow indicates on 3D Ge island; (d) after 1 ML Sb deposition; (e) after 3 BL Ge deposition onto 1 ML Sb-passivated Si(111) surface.

In contrast to Ge/Sb/Si(111) epitaxy at 600 C, there was no 3D island or grain nucleation on Sb/Si(111) surface during 3 BL Ge deposition at 500–550 C. REM images of Sb/Si(111) surface during Ge deposition from 0 to 5 BL are similar to REM images of Si(111) surface with $\theta_{\text{Ge}} = 0.5 \text{ BL}$ Ge where spotted contrast of 2D island on the terraces is observed (Fig. 2b). However, for Ge/Sb/Si(111) epitaxy at 500–550 C we do not observe coalescence of nucleated islands and clear terraces when Ge coverage reaches integer values (1, 2,..., 5 BL). Sb-induced 1 ML “1 \times 1” structure was observed in RHHED patterns during

Ge deposition and there was no appearance to 3D reflexes. AFM image of Sb/Si(111) surface with 3 BL Ge deposited at 500 C present surface morphology with clearly observed atomic steps with depletion zones near their edges and 2D islands ($N \sim 10^{10} \text{ cm}^{-2}$, $h \approx 0.6 \text{ nm}$, and $S \sim 300 \text{ nm}^2$) on the terraces (Fig. 2c). These 2D islands cover $\sim 10\%$ of surface area due to exact θ_{Ge} was slight above 3 BL. Thus, in accordance with work [2], 1 ML Sb passivation suppresses 3D nucleation and produces layer-by-layer growth (step-flow and 2D island nucleation and coalescence on the terraces above 1 μm width) of Ge film on Si(111) surface during deposition of $\theta_{\text{Ge}} > 3 \text{ BL}$ at 500–550 C.

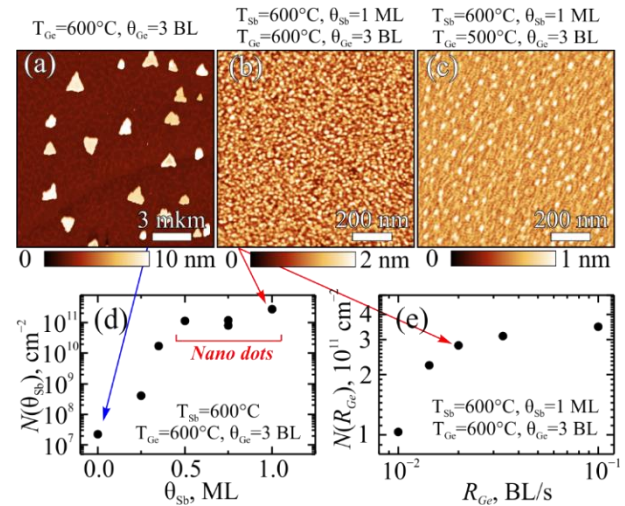


Fig. 2. AFM images of 3 BL Ge deposited on (a) clean Si(111) surface at 600 C, and on 1 ML Sb/Si(111) at (b) 600 C and (c) 500 C. (d) Dependence of 3D islands/nanodots density on θ_{Sb} deposited at 600 C. (e) Dependence of Ge nanodot density on Ge deposition rate.

4. Conclusions

We have shown, that for narrow substrate T close to 600 C, where Sb desorption is neglected, Sb adsorption does not suppress 3D growth at $\theta_{\text{Ge}} \geq 3 \text{ BL}$ — it significantly decreases 3D Ge island sizes and enhances their density. Thus, 3D islands become Ge nanodots at 600 C when Sb coverage rises on the surface. Maximum Ge nanodot density $\sim 10^{11} \text{ cm}^{-2}$ is reached at 1 ML Sb and 3 BL Ge. At $T < 600 \text{ C}$, in accordance with previous results [1,2], Sb adsorption on Si(111) surface suppress 3D growth for deposition of $\theta_{\text{Ge}} = 3-10 \text{ BL}$.

Acknowledgements

This work was performed on the equipment of CKP “Nanostruktury” and was supported by Russian Science Foundation [grant number 19-72-30023].

References

- [1] B. Voigtländer, A. Zinner. Surf. Sci. **351**(1996)L233.
- [2] A. Portavoce, I. Berbezier, A. Ronda. (2004). Mater. Sci. Eng. B., **B101**(2004)181.
- [3] A. A. Tonkikh, N. D. Zakharov, A. V. Novikov, et al. Thin Solid Films, **520**(2012)3322.
- [4] S. V. Sitnikov, A. V. Latyshev, S. S. Kosolobov. J. Cryst. Growth, **457**(2017)196.
- [5] V. K. Paliwal, A. G. Vedeshwar, S.M. Shivaprasad. Surf. Sci. Lett., **513**(2002)L397.
- [6] A. S. Petrov, D. I. Rogilo, D. V. Sheglov, A. V. Latyshev, J. Cryst. Growth, **531**(2020)125347.
- [7] S. Hasegawa, R. G. Ryland, E. D. Williams. Appl. Phys. Lett., **65**(1994)2609.

Growth of two-dimensional Si layers on CrSi₂(0001): quantum mechanical modeling

Zavodinsky V.G.¹, Plusnin N.I.^{*,1,2}, Gorkusha O.A.¹

¹ Khabarovsk Branch of Institute of Applied Mathematics FEB RAS, 60, Seryshev St., Khabarovsk 680038, Russia

² Institute of Nanotechnology of Microelectronics, 16a Nagatinskaya, Moscow, 115487, PO Box 50, Russia

*e-mail: plusnin.n@inme-ras.ru

Abstract. Quantum-mechanical modeling of the growth of two-dimensional (2D) Si layers on CrSi₂(0001) was performed using the electron density functional theory. Relaxation of non-dense (thickness <1 ML) and dense (thickness ≥1 ML) Si atomic condensate under the action of quantum mechanical forces was performed. It was found that in non-dense condensates 2D surface phases (SPs) of Si are formed. In dense condensates pseudomorphous (up to 2-3 ML) and then (after 2-3 ML) polymorphic solid wetting layers (SWLs) of Si with ABC (as in the substrate) and, accordingly, ABC → AB packing are formed.

1. Introduction

The study of the growth of 2D Si layers in a non-isostructural Si film - CrSi₂ substrate pair and the influence of the coordination of atoms in the substrate on the coordination of atoms in these layers is of significant interest for the theory of SWL growth. In addition, metallic conductivity and a significant magnitude of spin coherence can be expected in 2D Si layers on CrSi₂(0001), which allows them to be considered as new nanomaterials for spintronics. In this report, the formation of 2D SPs and SWLs of Si on CrSi₂(0001) is considered and the changes in the density and packing type of atoms with increasing thickness of these films are investigated.

2. Research Methods

As the films grew, a condensate of atoms was deposited on the substrate in 1/3 ML portions with low or 1 ML c portions with high surface density. After its deposition, the system was relaxed to a minimum of free energy. The calculations were performed using the FHI96md package [1], based on density functional theory, methods of the pseudopotential and a set of plane waves [2, 3]. One k-point of the Brillouin zone (0, 0, 0) was used. At the same time, pseudopotentials were generated using the FHI98PP package [4]. The cutoff energy of the plane wave set was 40 Ry. The exchange-correlation interaction was taken into account in the generalized gradient approximation [5]. The CrSi₂ lattice was represented in a Cartesian coordinate system and defined in a rectangular X and Y supercell with dimensions: a(X) = 18.668 a.u., b(Y) = 13.042 a.u., c(Z) = 65.0 a.u. (1 a.u. = 0.529 Å). One-sided silicon growth on CrSi₂ was performed at a CrSi₂ thickness of 3 or 4 ML, and its two-sided growth was performed at a thickness of 6 ML or 8 ML.

3. Results and discussions

In general, it was found that the loose packing of Si atoms on both sides of the CrSi₂ supercell leads to the formation of Si SPs, which consist first of an array of 2D Si clusters and then of an array of 3D Si clusters (see Fig. 1).

In dense condensates (Fig. 2), the ABC packing was still preserved at the film thickness is up to 2-3 ML, and at high thicknesses it becomes mixed: ABC - in the first 2-3 layers and AB (hexagonal packaging) – in the subsequent ones.

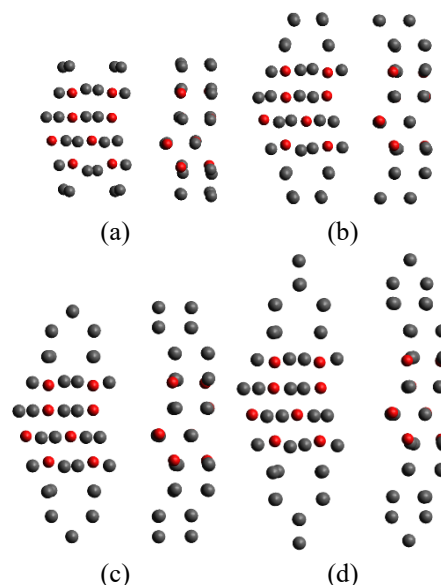


Fig. 1. Frontal and side views on Si/CrSi₂(0001)/Si with Si thicknesses: 2/3 ML (a), 4/3 ML (b), 5/3 ML (c) and 11/6 ML (d).

In order to increase the reliability of the results, we carried out studies with both single- and double-sided arrangement of Si condensate on the CrSi₂(0001) supercell with different CrSi₂ thickness, symmetry, and mutual c 2D Si rotation angle.

If the CrSi₂(0001) supercell was obtained by symmetric splicing of two halves of small thickness (3 ML), such splicing deformed the CrSi₂ supercell because of the electron density imbalance on its surface and in its volume. In the case of a mirror-asymmetric CrSi₂ cell, on one of its surfaces there was a growth of Si SWL with AB atoms packing, and on the other - with ABC packing. In general, it was found that the two-sided arrangement, maximum thickness, mirror symmetry, and angles 0° and 30° between Si and CrSi₂(0001) lattices are more consistent with the real physical heterostructure of Si on CrSi₂(0001).

At rotation angles of 2D Si relative to CrSi₂(0001) 0° and, respectively, 30°, the formation of Si SWL with higher and, respectively, lower stability occurred. Increasing the thickness of the CrSi₂(0001) substrate to 8 ML decreased the thickness threshold to 3 ML Si to change the packing from ABC to AB, which, in terms of the role of substrate screening by the film is understandable. With an even number of layers in Si SWL with AB packing, its stability

of Si SWL was more pronounced. This correlates with the packing in the $\text{CrSi}_2(0001)$ lattice through an even number of layers.

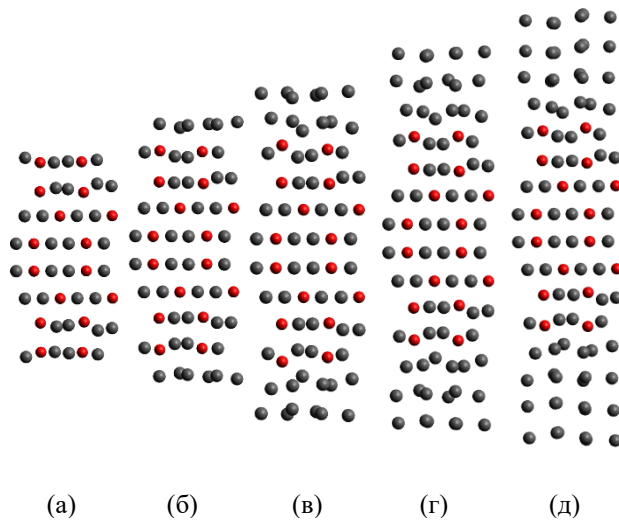


Fig. 2. Frontal view on $\text{Si}/\text{CrSi}_2(0001)/\text{Si}$ at CrSi_2 thickness of 8 ML and Si thickness: (a) - 0, (b) - 1 ML, (c) - 2 ML, (d) - 3 ML and (e) - 4 ML.

In general, the obtained results can be explained as follows. At first, during the growth of Si SWL on $\text{CrSi}_2(0001)$, up to 3 ML, a certain “screening” Si layer grows, in which ABC packing is preferred as in the substrate. Further, there is a change of packing type from ABC to AB and a mixed $\text{ABC} \rightarrow \text{AB}$ packing is formed. This is because, at higher thickness, the film is less dependent on the substrate and the independent AB packing is more favorable.

It is found that the maximum stability of Si SWL is achieved when 2 ML Si is deposited. This is in agreement with the experiment [6, 7]. Nevertheless, modeling has shown that, for a Si 3 ML thickness of SWL, the mixed packing ABC (2 ML) \rightarrow AB (+1ML) provides the highest stability.

In the experiment [6, 7], the value of the superstructural correspondence between the 2D lattice parameters of $\text{Si}(111)$ and $\text{CrSi}_2(0001)$ 30° and 0° is $\sqrt{3}/2 \approx 1.15$ and $6/7 \approx 1.16$, respectively. This approximately corresponds to the known value of the mismatch between the Si and CrSi_2 OF lattices of about -0.13 %. Therefore, with respect to CrSi_2 , 2D Si forms the superstructure $\text{CrSi}_2(0001)3\sqrt{3} \times 3\sqrt{3}$ -Si. Meanwhile, during epitaxy on $\text{Si}(111)$ substrate, the $\text{CrSi}_2(0001)$ lattice 30° and 0° are ordered into $\text{Si}(111)2 \times 2$ - $\text{CrSi}_2\text{R}30^\circ$ and $\text{Si}(111)6/7 \times 6/7$ - $\text{CrSi}_2\text{R}0^\circ$ structures [6, 7]. In this case, the $6/7 \times 6/7$ structure, in the case of $\text{R}0^\circ$ orientation, refers to the $\text{Si}(111)$ substrate-induced periodicity of $\text{CrSi}_2(0001)$ itself, and the $3\sqrt{3} \times 3\sqrt{3}$ structure, in the case of $\text{R}30^\circ$ orientation, refers to the periodicity of the two-dimensional metastable Si SWL on $\text{CrSi}_2(0001)$ itself.

4. Conclusions

Quantum mechanical modeling of Si growth on two-sided $\text{CrSi}_2(0001)$ supercell plates with different structural symmetry and dimensions has been carried out. It is determined that the symmetry and increase in thickness of the $\text{CrSi}_2(0001)$ supercell contribute to the elimination of its distortions. In the process of adsorption of loose Si condensates on CrSi_2 , the formation of: up to 1 ML - 2D

surface phases and after 1.67 ML - a two-dimensional array of 3D crystalline Si clusters with tetrahedral configuration of interatomic bonds was found. In the process of deposition of dense Si condensates on $\text{CrSi}_2(0001)$, it is shown that the growth of Si SWL, in the first layers, goes with ABC packing, and in the subsequent (after 2 ML) layers - with $\text{ABC} \rightarrow \text{AB}$ packing. At the same time, after the formation and change of packing, with each subsequent layer, the SWL becomes less stable.

References

- [1] M. Bockstedte, A. Kley, J. Neugebauer, M. Scheffler. Computer physics communications 1997 (107/1-3) 187.
- [2] P. Hohenberg, W. Kohn. Phys. Rev. 1964 (136/3B) B864.
- [3] W. Kohn, L. J. Sham. Phys. Rev. 1965 (140/4A) A1133.
- [4] M. Fuchs, M. Scheffler. Computer Physics Commun. 1999 (119/1) 67.
- [5] J. P. Perdew, W. Yue. Phys. Rev. 1986 (B 33/12) 8800.
- [6] N.I. Plusnin, N.G. Galkin, V.G. Lifshits, A.P. Milenin. Physics of low-dim. structures (PLDS) 1999 (1-2) 55.
- [7] N.I. Plusnin, N.G. Galkin, V.G. Lifshits, A.P. Milenin. Surface. X-ray, Synchrotron and Neutron Studies 2000 (16/6) 22. (RUS).

Ab initio calculation of $\text{Si}(111)\frac{2}{3}\sqrt{3}\times\frac{2}{3}\sqrt{3}\text{-Mg}$ models

Ryzhkova M.V.^{*,1}, Tsukanov D.A.^{1,2}

¹ Institute of Automation and Control Processes, 5 Radio St., Vladivostok 690041, Russia

² Far Eastern Federal University, 8 Sukhanova St., Vladivostok 690950, Russia

*e-mail: lavric@iacp.dvo.ru

Abstract. Ab initio calculation of density functional theory and pseudopotentials was applied to study $\text{Si}(111)2/3\times 2/3\text{-Mg}$ models. Structures were studied in 2×2 cell. The most favorable structure for 2×2 cell has 1.75ML of Mg and 0.75ML of Si. The best structure with $2/3\sqrt{3}$ periodicity has 2ML of Mg and 0.75ML of Si.

1. Introduction

A considerable number of studies have focused on the investigation of magnesium silicide on the $\text{Si}(111)$ surface [1-3]. However, theoretical calculations for the $\text{Si}(111)2/3\sqrt{3}\times 2/3\sqrt{3}\text{-Mg}$ (thereafter $2/3\sqrt{3}$) surface structure have not been reported yet. The present work is aimed at modeling the $2/3\sqrt{3}$ reconstruction.

A structural model of this surface phase has been proposed in [2], but no calculation was performed.

We have investigated this model [2] and some other structures in present study.

2. Computational methods

The calculation were performed using a plane-wave basis set and correlation functional projector-augmented wave pseudopotentials (PAW-PBE) with generalized gradient approximation (GGA) for the exchange-correlation energy. VASP ab initio programm package was used for this study.

Wave functions were performed using energy cutoff 250 eV. The geometry was optimized until the total energy was converged to 10^{-6} eV and the atomic forces reduced to 10^{-2} eV/Å. Γ -point $7\times 7\times 1$ grid was used.

The surface has been simulated by periodic slab with periodicity $\text{Si}(111)2\times 2$. The thickness of the slab was 6 silicon layers and vacuum region was more than 20Å to prevent interaction between surfaces in two adjacent cells. The dangling bonds of the bottom silicon layer have been saturated by hydrogen atoms. Two bottom layers and hydrogen atoms were fixed, the rest atoms were allowed to move freely.

Airss was used for random structure search calculation. Energy convergence was 10^{-5} eV and $5\times 5\times 1$ kpoints grid was set for this case.

Since the $2/3\sqrt{3}$ cell disrupts the periodicity of the silicon substrate, a 2×2 unit cell was used. 2×2 cell contains 3 subcells of $2/3\sqrt{3}$.

The formation energy was calculated following this formula:

$$E_{\text{form}/1\times 1} = \frac{E_{\text{tot}} - E_{\text{slab}} - n_{\text{Si}}\mu_{\text{Si}} - n_{\text{Mg}}\mu_{\text{Mg}}}{N} \quad (1),$$

where E_{tot} – total energy of calculated model, E_{slab} – energy of relaxed slab without silicon atoms in surface phase (usually 3 atoms), n_{Si} and n_{Mg} – number of Si and Mg atoms, respectively. μ_{Si} and μ_{Mg} – the chemical potentials for the Si and Mg, respectively, taken from bulk phases of these elements. N – the number of 1×1 cells in given structure ($N = 4$ for 2×2 , 6 for 3×2 , 3 for 3×1).

All calculations were performed using the resources of the collective center of Far-Eastern Computational Resource [4].

3. Results and discussions

There is a model of this surface phase presented in the article [2]. We calculated it in the process of relaxation. It has retained the periodicity of $2/3\sqrt{3}$. The Fourier transform of the simulated scanning tunnelling microscopy pattern at +2V gives the ratio of the reflex intensities from $2/3\sqrt{3}$ and 2×2 as $I_s/I_{2\times 2} \sim 1.4$. But it has a high formation energy - 0.153eV/ 1×1 (table 1).

Table 1. Parameters of Models and Intensity Ratio.

Model	Energy, (eV/ 1×1)	$I_s/I_{2\times 2}$	Si-Si, (Å)	Mg-Mg, (Å)
[2]	-0.153	1.4	3.95	4.9
9-3	-0.619	2.7	4.39	4.43
9-3_T4	-0.66	1.5	4.32	4.54
8-3	-0.676	1.4	4.31	4.71
7-3_random	-0.822	0.9	4.25-4.6	3.88-4.54
3x2	-0.53	-	-	-
3x1	-0.527	-	-	-

We have modified this structure and have increased the Mg coverage to 2.25, it has 9 atoms in a 2×2 cell, the number of silicon atoms remained the same 3 (0.75 ML). Model 9-3. The formation energy decreased to -0.619 eV/ 1×1 (table 1), while maintaining the periodicity of $2/3\sqrt{3}$. Fourier transform of the simulated scanning tunnelling microscopy pattern at +2V gives intensity ratio ~ 2.7 (fig. 1). Model 9-3 best fits the parameters of the bulk magnesium silicide structure. Mg_2Si has 4.48Å of Si-Si and Mg-Mg bonds.

Then, by moving the lower magnesium layer to symmetrical T4 positions, the energy again decreased to -0.66 eV/ 1×1 . Model 9-3_T4. The periodicity of $2/3\sqrt{3}$ has saved. By removing one magnesium atom, the energy was a bit reduced to -0.676 eV/ 1×1 (table 1). Model 8-3. This is the most favorable model of the structure, preserving the periodicity of $2/3\sqrt{3}$ with intensity ratio is ~ 1.5 . The structure consists of 2 MC magnesium and 0.75 MC silicon. Removing two or three magnesium atoms either led to the loss of the periodicity of $2/3\sqrt{3}$, or to higher formation energies.

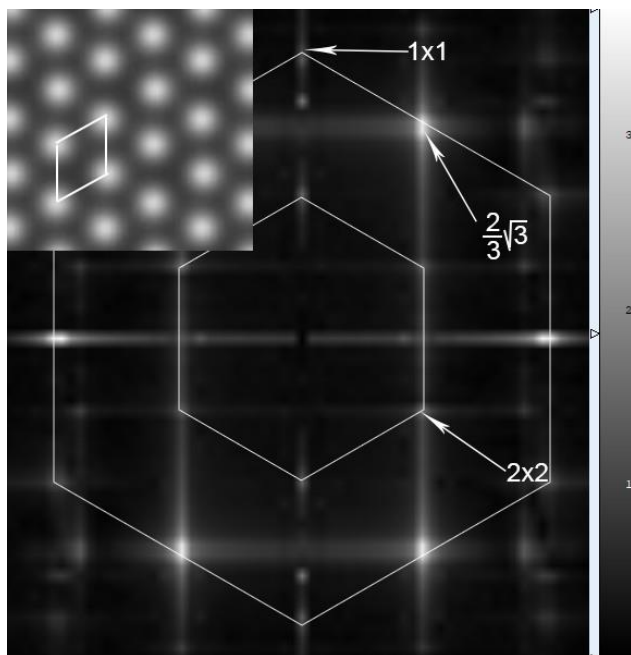


Fig. 1. 9-3 model. The Fourier transform of the simulated scanning tunnelling microscopy pattern at +2V. Simulated scanning tunnelling microscopy (in picture), $2/3\sqrt{3}$ cell is outlined.

Using Airss script, the most favorable structures were calculated for magnesium coverage of 1.75 MC (7 Mg and 3 Si atoms per 2×2 cell) and 2 MC (8 Mg and 3 Si), as well as 2 MC (8 Mg and 2 Si) and 2.25 MC (9 Mg and 1 Si). Thus, we found the model with the lowest formation energy (-0.822 eV/ 1×1). This is a structure consisting of 1.75 MC magnesium and 0.75 MC silicon. Model 7-3_random. However, such model has only a 2×2 periodicity, the $2/3\sqrt{3}$ periodicity is preserved only for silicon atoms. When considering various models of magnesium silicide, it is clear that 3 silicon atoms prefer places T4, H3 and T1, which ensures a $2/3\sqrt{3}$ periodicity. Fig. 2 shows the results of calculations of the formation energy depending on the proportion of Mg in the structure. This plot also contains reference points that relate to the calculations of the 3×2 and 3×1 surface phases. The latter structures we have also calculated based on the models of alkaline earth adsorbates presented for 3×2 and 3×1 in the article [5].

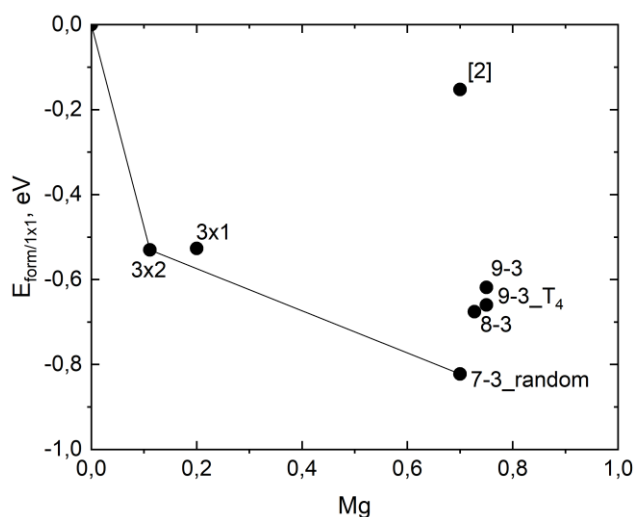


Fig. 2. The formation energy versus proportion of magnesium.

4. Conclusions

We have done ab initio calculation to study Si(111) $2/3\times 2/3$ -Mg models. The most favorable structure is 7-3_random has 1.75ML of Mg and 0.75ML of Si. The best structure with $2/3\sqrt{3}$ periodicity is 8-3 has 2ML of Mg and 0.75ML of Si. Model 9-3 with 2.25ML of Mg and 0.75ML of Si best fits the parameters of the bulk Mg_2Si structure.

Acknowledgements

The research was supported by the Government research assignment for IACP FEB RAS, project FFW-2021-0002.

References

- [1] D.Lee, G.Lee, S.Kim, Ch.Hwang, J.Phys.:Condens.Matter **19**(2007)266004.
- [2] K. N. Galkin, M. Kumar, S.M. Shivaprasad, N. G. Galkin Physics Procedia, **11**(2011)47-50.
- [3] S.A. Dotsenko, Yu.V. Luniakov, A.S. Gournik, A.K. Gutakovskii, N.G. Galkin, Journal of Alloys and Compounds **778**(2018)514-521.
- [4] <https://cc.dvo.ru/>
- [5] J. Shuai Chai, Zh. Li, L. Xu, J. Wang, Phys. Chem. Chem. Phys. **20**(2018)25235-25239.

Monte Carlo simulations of stable topological structures

Vasiliev E.V.^{*1,2}, Kapitan V.Yu.³, Makarov A.G.^{1,2}, Nefedev K.V.^{1,2}

¹ Far Eastern Federal University, 8 Sukhanova St., Vladivostok 690950, Russia

² Institute of Applied Mathematics, Far Eastern Branch, Russian Academy of Science, Vladivostok, 690041, 7 Radio St., Russian Federation

³ National University of Singapore, 21 Lower Kent Ridge Road, 119077, Singapore

*e-mail: vasilev.eva@dvfu.ru

Abstract. This study explores the emergence and stability of topological spin textures in two-dimensional ferromagnetic systems through large-scale Monte Carlo simulations. A classical Heisenberg model, incorporating exchange interactions, Dzyaloshinskii–Moriya interaction, anisotropy, and external magnetic fields, was implemented to capture the essential physics. Simulations were carried out using high-performance C++ code on a supercomputing cluster, initiating from disordered high-temperature states to ensure proper thermal equilibration over 10^6 – 10^8 Monte Carlo steps per spin. The analysis reveals the characteristic conditions under which skyrmions, bimerons, and antiskyrmions form and remain stable, offering new insights into the control of such structures for potential applications in spintronic devices.

1. Introduction

In recent years, one of the key areas of spintronics has been the study of magnetic nanostructures. Magnetic spin configurations such as skyrmions, bimerons, and antiskyrmions have attracted significant interest. Their topological protection, small size, and controllability by external stimuli make them promising candidates for the development of energy-efficient information storage and processing devices [1]. However, the stabilization and control of such structures require a deep understanding of their behavior under various conditions.

Numerical simulations based on the Monte Carlo method make it possible to study complex spin systems while accounting for the effects of exchange interaction, Dzyaloshinskii–Moriya interaction, external fields, anisotropy, and temperature. This work investigates the conditions for the formation and stability of spin configurations within the framework of the Heisenberg model using the Metropolis algorithm.

2. Model description

The classical Heisenberg model was implemented. Simulations were performed for two-dimensional ferromagnetic systems on a square lattice with periodic boundary conditions (4 nearest neighbors). The Metropolis algorithm was used to minimize the system's energy [2]. The Hamiltonian of the system was:

$$H = H_{\text{ex}} + H_{\text{DMI}} + H_{\text{B}} + H_{\text{an}}$$

where:

Heisenberg exchange:

$$H_{\text{ex}} = -J \sum_{\langle i,j \rangle} \mathbf{S}_i \cdot \mathbf{S}_j;$$

Dzyaloshinskii–Moriya interaction:

$$H_{\text{DMI}} = -D \sum_{\langle i,j \rangle} \mathbf{S}_i \times \mathbf{S}_j;$$

External magnetic field in set direction k :

$$H_{\text{B}} = -B \sum_i S_i^k;$$

Anisotropy:

$$H_{\text{an}} = -K \sum_i (S_i^z)^2.$$

The simulations were performed using C++ on a supercomputing cluster, with 10^6 – 10^8 Monte Carlo steps per spin for equilibration. The initial conditions corresponded to a high-temperature paramagnetic state (random spin distribution).

3. Conclusions

The results of the numerical simulations highlight key mechanisms that influence the formation, stabilization, and persistence of topological spin textures, including skyrmions, bimerons, and antiskyrmions, in two-dimensional ferromagnetic lattices. Various states of the system were investigated by determining the dependencies between the magnetic field, the magnitude of the DM interaction and temperature. The boundaries between the various phases of the system were determined.

A convolutional neural network (CNN) was applied to automate the analysis of simulation data, trained to recognize spin configuration types based on their spatial patterns [3]. This approach accelerated phase classification and the identification of transition regions on phase diagrams.

Acknowledgements

The research was supported by the Russian Science Foundation grant No. 24-71-10069, <https://rscf.ru/en/project/24-71-10069/>

References

- [1] Yang Y. H., Chen S. H., Chang Y. H. Evolving skyrmion racetrack memory as energy-efficient last-level cache devices //Proceedings of the ACM/IEEE International Symposium on Low Power Electronics and Design. – 2022. – C. 1-6.
- [2] Barkema G. T., Newman M. E. J. New Monte Carlo algorithms for classical spin systems //arXiv preprint cond-mat/9703179. – 1997.
- [3] Kapitan D. et al. Application of machine learning in solid state physics //Solid State Physics. – Academic Press, 2023. – T. 74. – C. 1-65.

Atomic structure and electronic properties of Bi monolayers on ultra-thin films of rare-earth silicides

Zhdanov V.S.^{*1}, Sevryukov D.K.^{1,2}, Vekovshinin Yu.E.^{1,2}, Bondarenko L.V.¹, Tupchaya A.Y.¹, Mihalyuk A.N.^{1,2}, Olyanich D.A.¹, Gruznev D.V.¹, Zotov A.V.¹, Saranin A.A.¹

¹ Institute of Automation and Control Processes, 5 Radio St., Vladivostok 690041, Russia

² Far Eastern Federal University, Campus 10, Ajax Bay, Russky Island, Vladivostok 690922, Russia

*e-mail: vzhdanov@iacp.dvo.ru

Abstract. The exploration of low-dimensional materials and their heterostructures has provided new insights into fundamental phenomena and potential applications in next-generation devices. This study investigates the growth and electronic properties of Bi monolayers on rare-earth silicide surfaces, such as HoSi₂ and GdSi₂, focusing on spin-orbit coupling and the emergence of saddle points in the electronic structure. Bi monolayers on these silicides exhibit Rashba-type spin splitting and a saddle point in the band structure, located below the Fermi level. Using scanning tunneling microscopy, photoelectron spectroscopy, and density functional theory, we reveal the formation of Bi trimers in a milkstool configuration and demonstrate how the underlying substrate influences the electronic properties. Our results suggest that the Bi/silicide interface offers a promising platform for tuning spin-orbit interactions and exploring novel electronic phenomena, with implications for spintronic applications.

1. Introduction

Recent advancements in surface physics have led to the discovery and investigation of various two-dimensional (2D) materials, both in free-standing forms (e.g., graphene, phosphorene) and as surface phases and thin films on substrates [1]. These materials exhibit unique properties such as superconductivity, magnetism, Hall effects, spin splitting (e.g., Rashba-type), and topological phenomena (e.g., topological insulators). Despite significant progress, challenges remain in fine-tuning the properties of individual 2D materials and creating materials with predefined characteristics. A promising approach to overcome these challenges is the stacking of distinct 2D materials, which can modify and complement each other's properties. For instance, twisting graphene layers at a "magic angle" induces superconductivity [2], while stacking layers of thallium and tin results in Rashba-type spin splitting [3].

In this study, we investigate a complex system consisting of monolayers bismuth (Bi) grown on mono- and multi-layer rare-earth silicides (RE = Ho, Gd, etc.) [4]. We find that, despite similar surface structures of one- and multi-layer rare-earth silicides, the growth of Bi layers at room temperature leads to notable differences. Specifically, bilayer Bi can form on monolayer RE silicides, while the monolayer exhibits highly mobile trimer vacancies. The crystalline structure of Bi monolayers is similar to the β -Bi/Si(111)-($\sqrt{3}\times\sqrt{3}$) phase, known for its significant Rashba spin splitting [5]. The electronic structure of the 1-ML-Bi / 1-ML-HoSi₂ system at the Fermi level is primarily determined by HoSi₂ states, with Bi inducing a strong bending of the bands and a saddle point appearing at the Fermi level.

2. Experiment

The STM and ARPES experiments were performed in an ultrahigh-vacuum Omicron MULTIPROBE system with a base pressure better than $\sim 2.0 \times 10^{-10}$ Torr. Atomically-clean Si(111)- 7×7 surfaces were prepared in situ by flashing to 1280°C after the samples were first outgassed at 600°C for several hours. The pristine rare-earth silicides Ho and Gd were obtained by depositing 1 monolayer (ML) for single layer and 3 ML for multilayer films onto the

Si(111)- 7×7 surface, followed by gradual direct heating to 650°C and 800°C, respectively. Bismuth was deposited from a tungsten basket onto the silicide substrates at room temperature.

STM images were acquired using Omicron variable-temperature STM-VT-XA operating in a constant-current mode. Electrochemically-etched W tips and mechanically cut PtIr tips were used as STM probes after annealing in vacuum. ARPES measurements were conducted in the ultrahigh vacuum chamber Omicron MULTIPROBE using VG Scienta R3000 electron analyzer and high-flux He discharge lamp ($h\nu = 21.2$ eV) with toroidal-grating monochromator as a light source. Our calculations were based on DFT as implemented in the Vienna ab initio simulation package VASP, using a planewave basis and the projector-augmented wave approach for describing the electron-ion interaction. The generalized gradient approximation (GGA) of Perdew, Burke, and Ernzerhof (PBE) [30] has been used for the exchange correlation (XC) potential.

3. Results and discussions

Bi growth on multilayer RE silicides proceeds in a Stranski-Krastanov regime. Initially, Bi islands of the uniform height form, and as deposition continues, these islands merge into a continuous film. This film exhibits a $\sqrt{3}\times\sqrt{3}$ periodicity, inherited from the substrate, with the underlying defects influencing the film's structure. Scanning tunneling microscopy (STM) images reveal that the surface of the multilayer silicide is composed of a buckled silicon bilayer with a 1×1 structure, which does not shift in position during Bi deposition. Notably, the Bi film adopts a "milk-stool" configuration (Fig. 1(c)), similar to that observed in β -Bi/Si(111)-($\sqrt{3}\times\sqrt{3}$), where the Bi atoms are located in the T₁ positions, and the trimers are centered over the T₄ positions of the silicon bilayer. Figure 1(a) shows an STM image of the Bi film on multilayer silicide (40×40 nm), while Figure 1(b) presents a high-resolution STM image (7×7 nm², V_t = -0.005 V) revealing the Bi trimer structure. This behavior suggests that the presence of the rare-earth silicide substrate exerts a guiding influence on the arrangement of Bi trimers, preventing the formation

of anti-phase boundaries at the junctions of merging islands.

The electronic structure of Bi on multilayer silicides, as shown by the ARPES spectrum in Figure 1(d). A detailed comparison with β -Bi/Si(111)-($\sqrt{3}\times\sqrt{3}$) and multilayer silicides indicates that the system is not simply a combination of two known spectra, but rather a unique hybrid structure with new electronic characteristics.

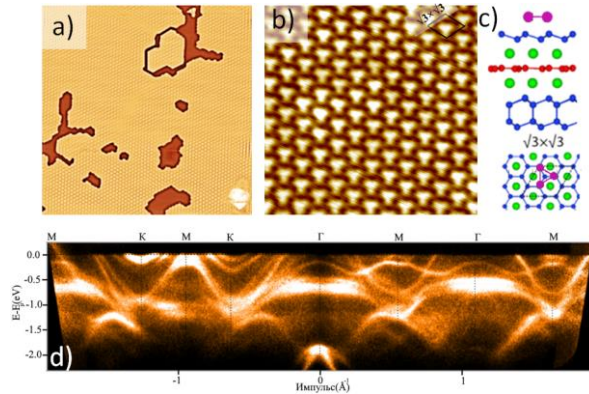


Fig. 1. STM images of the Bi film on multi-layer RE silicides: a) $40\times 40\text{ nm}^2$; $V_t = +0.1\text{ V}$, b) $7\times 7\text{ nm}^2$; $V_t = -0.005\text{ V}$, c) calculated structural model, d) band structure.

In contrast to the multilayer silicide, Bi growth on monolayer RE silicides reveals significant differences in both the growth mechanism and the resulting electronic structure. While Bi grows in a Frank–van der Merwe regime on the monolayer silicide, the islands are less well-defined compared to those on the multilayer silicide. As the coverage approaches 1 (ML), the islands merge into a continuous film, inheriting defects from the underlying silicon bilayer. However, in this case, the Bi monolayer is more susceptible to defect formation and exhibits a higher degree of noise at room temperature, as evidenced by the appearance of rapidly moving vacancies in STM images. Figure 2(a) shows an STM image of Bi on monolayer silicide ($40\times 40\text{ nm}$), including the formation of Bi on a double-layer silicide island (labeled as Bi/HoSi₂-II for the bilayer island and Bi/HoSi₂-I for the monolayer region). STM images of high-resolution Bi films reveal the same milk-stool configuration of Bi trimers centered on the silicon bilayer (Fig. 2 (b,c)), similar to the structure seen on multilayer silicides. At higher coverage, a bilayer Bi structure with a $\sqrt{7}\times\sqrt{3}$ periodicity emerges, which is distinct from all previously observed Bi phases.

The electronic structure of Bi on monolayer silicides is influenced by the underlying rare-earth silicide. Our calculations show that the states near the Fermi level in this system are primarily determined by the RE silicide, with the Bi-induced states appearing at lower binding energies. In the M-point near the Fermi level, there is a clear bending of the bands, as observed in both experimental and theoretical ARPES spectra (Figure 2(d)).

This bending is indicative of the formation of an Schottky barrier layer at the interface between the metal and the semiconductor, leading to the accumulation of electrons at the contact region. Interestingly, the saddle point in the electronic spectrum near the M-point suggests the possibility of electronic instabilities and strong electron correlations in the system, which could lead to interesting physical phenomena.

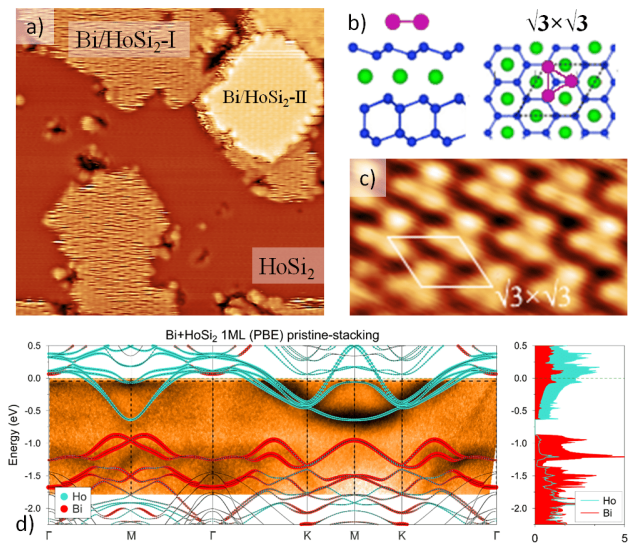


Fig. 2. STM images of the Bi film on single-layer RE silicides: a) $30\times 30\text{ nm}^2$; $V_t = -1.5\text{ V}$, b) calculated structural model, c) $2\times 3\text{ nm}^2$; $V_t = 0.01\text{ V}$, d) band structure with the overlaid calculated spectrum.

4. Conclusions

The system consisting of a bismuth monolayer and single- and multi-layer rare-earth element (RE = Ho, Gd, etc.) silicides has been investigated. Despite the similar surface structure of single- and multi-layer silicides (regarding the structure of the topmost layers), differences are observed during the growth of Bi at room temperature. On RE single-layer silicides, the formation of a bi-layer Bi film is possible, while the Bi monolayer exhibits a high concentration of mobile trimer vacancies. The Bi monolayers exhibit an atomic structure close to the β -Bi/Si(111)-($\sqrt{3}\times\sqrt{3}$), which is known for its giant Rashba splitting of surface states. The electronic structure of the 1-ML-Bi / 1-ML-HoSi₂ system at the Fermi level is dominated by states from HoSi₂, while the presence of Bi induces a significant band bending and shifts the S1 state by 0.5 eV towards higher energies, resulting in the emergence of a saddle point at the Fermi level.

Acknowledgements

The work was supported by the Russian Science Foundation (Grant No. 24-12-00181, <https://rscf.ru/en/project/24-12-00181/>). Calculations were performed using the equipment of the "Far Eastern Computational Resource" HPC center, IACP RAS (<https://cc.dvo.ru>)

References

- [1] Shanmugam V. et al. Particle & Particle Systems Characterization. **39**(2022) 2200031.
- [2] Park J. M. et al. Nature Materials. **21**(2022) 877.
- [3] Gruznev D. V. et al. Physical Review B. **91**(2015) 035421.
- [4] Mihalyuk A. N. et al. //Journal of Materials Chemistry C. **12**(2024)5926.
- [5] Gruznev D. V. et al. Scientific Reports. **4**(2014)4742.

Morphological features of ultrathin films of β -FeSi₂ on Si(100)

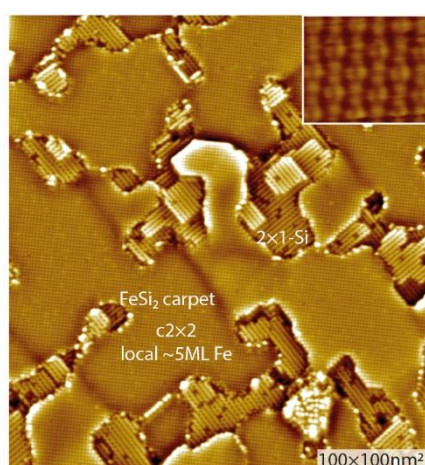
Kotlyar V.G.¹, Utas T.V.^{*1}, Burkovskaya P.V.^{1,2}, Olyanich D.A.¹, Saranin A.A.^{1,2}, Zotov A.V.¹

¹ Institute of Automation and Control Processes FEB RAS, 5 Radio Street, Vladivostok 690041, Russia

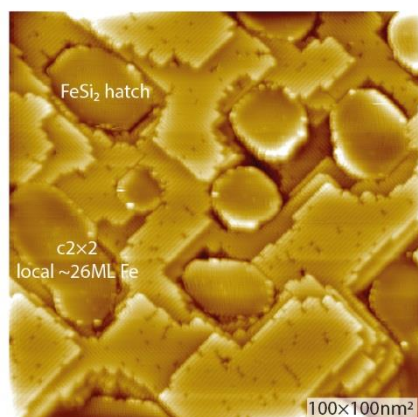
² Far Eastern Federal University, Vladivostok 690950, Russia

*e-mail: kasyanova@mail.dvo.ru

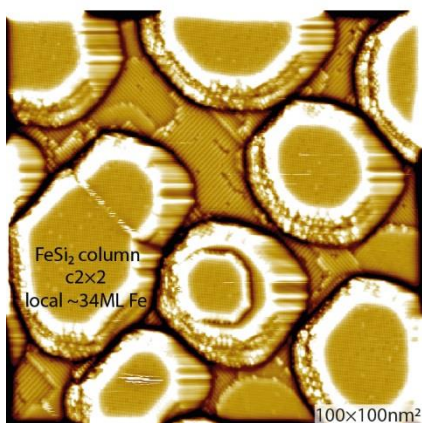
Abstract. Semiconducting iron disilicide (β -FeSi₂) is a promising material for a wide range of applications, spanning from thermoelectric to photovoltaic devices [1,2]. Nowadays, most research groups are focused on continuous epitaxial films and nanoparticles embedded in Si. However, exploring the two-dimensional limit is particularly attractive, as novel and unexplored properties may emerge [3]. Concerning silicide layers, a single-atomic-layer NiSi₂ sheet has already demonstrated advanced properties [4]. In this paper, we report on the formation and thorough characterization of single-unit-cell β -FeSi₂ layers on Si(001) substrates.



Fe (3÷3.3) ML at RT+ 455°C



Fe (3.4÷4.5) ML at RT+ 650°C÷830°C



Fe (4.5÷13) ML at RT+ 650°C÷830°C

This work was made using STM and LEED methods. Thin layers of silicide were grown on silicon surface Si(100) *in situ*.

In this work, the optimal conditions for the obtaining of a single-layer β -FeSi₂ silicide, which is a combination of Si-Fe-Si layers (height 4.9Å), were determined. The deposition of Fe atoms with subsequent heating leads to the endotaxy growth of β -FeSi₂ crystal (approximately 70 Å). However, the further adsorption doesn't allow to fabricate the silicide on the whole surface: the area of β -FeSi₂ islands remains constant, but the height increases significantly (by 40 Å). The adsorption at 450°C gives the same result.

Meanwhile, the adsorption of Si without Fe atoms results in the formation of the next layers of Si on the whole surface apart from β -FeSi₂ areas. The surface can be visualized as a Si array with a system of pits with β -FeSi₂ rods.

Acknowledgements

The research was carried out within the state assignment of IACP FEB RAS (Theme FFW-2021-0002).

References

- [1] T. Suemasu, K. Takakura, C. Li, Y. Ozawa, Y. Kumagai, and F. Hasegawa, "Epitaxial growth of semiconducting β -FeSi₂ and its application to light-emitting diodes," *Thin Solid Films*, vol. 461, no. 1, pp. 209–218, (2004).
- [2] E. Arushanov and K. G. Lisunov, "Transport properties of β -FeSi₂," *Jpn. J. Appl. Phys.*, vol. 54, no. 7S2, p. 07JA02, (2015).
- [3] M. Zeng, Y. Xiao, J. Liu, K. Yang, and L. Fu, "Exploring Two-Dimensional Materials toward the Next-Generation Circuits: From Monomer Design to Assembly Control," *Chem. Rev.*, vol. 118, no. 13, pp. 6236–6296, (2018).
- [4] L. V. Bondarenko *et al.*, "Metal Sheet of Atomic Thickness Embedded in Silicon," *ACS Nano*, vol. 15, no. 12, pp. 19357–19363, (2021).

II. Physics and technology of semiconductor materials and devices

Synthesis of silicide- and silicate-based nanostructures, thin films, and bulk crystals via reactive interdiffusion

Tatsuoka H.*

Graduate School of Integrated Science and Technology, Shizuoka University

*e-mail: tatsuoka.hirokazu@shizuoka.ac.jp

Abstract. This study explores the diffusion-driven synthesis of silicide- and silicate-based nanostructures, thin films, and bulk crystals through distinct reactive interdiffusion pathways. While lateral surface diffusion on Si substrates is known to yield nanodots such as $\text{MnSi}_{1.7}$ and $\beta\text{-FeSi}_2$, vertical interdiffusion into CaSi_2 gives rise to porous micro-rods, which are then topotactically transformed into Mg_2Si , $\text{MnSi}_{1.7}$, and Mg_2SiO_4 nanosheet bundles, while maintaining anisotropic morphology. Additionally, these silicide nano- and microstructures were successfully synthesized using pre-patterned silicon-based templates. In contrast, deep bulk diffusion into substrates like FeSi under molten salt conditions yields columnar $\beta\text{-FeSi}_2$ crystals. These structurally diverse outcomes demonstrate how diffusion dimensionality and substrate type critically influence phase selectivity, morphology retention, and interface quality, offering a design framework for functional materials in energy and electronic applications.

1. Introduction

Semiconducting silicides and silicates are promising candidates for environmentally friendly electronics, thermoelectrics, and photonics due to their composition of non-toxic, earth-abundant elements and compatibility with silicon-based technologies. A critical aspect of synthesizing these materials is understanding and controlling the diffusion processes that govern their formation. Diffusion mechanisms dictate the resulting structure from nanoscale dots to bulk crystals [1,2].

The formation of nanosheet bundle structures is particularly important, as they provide both structural anisotropy and accessible surface area while maintaining crystalline continuity. This unique architecture opens new avenues for applications in directional charge transport, thermal anisotropy control, and interface-enhanced reactivity [3]. Such nanosheet bundles are especially relevant in thermoelectric materials, interfacial layers for energy devices, and hierarchical architectures for optoelectronic applications.

This study aims to explore the relationship between diffusion dimensionality and structural development by systematically comparing distinct interdiffusion cases. The results highlight diffusion geometry as a central parameter in designing functional silicide and silicate materials.

2. Experiment

$\text{MnSi}_{1.7}$, Mg_2Si , and Mg_2SiO_4 nanosheet bundles were synthesized from CaSi_2 micro-walls or powders by thermal reaction with MnCl_2 and MgCl_2 without and with oxygen. Ca extraction from CaSi_2 facilitated the formation of silicon nanosheets, which served as templates for subsequent silicide and silicate formation. For nanodots and thin films, planar Si substrates were used. Mg_2Si -based nanowires, microrods and bulk crystals were synthesized using vapor phase technique. Bulk $\beta\text{-FeSi}_2$ crystals were synthesized using FeSi plates as the solid source in a molten salt. Structural and morphological characterizations were conducted using XRD, SEM, TEM with EDX.

3. Results and discussions

The formation of silicide and silicate structures in this study is governed by a range of reactive interdiffusion mechanisms that differ in dimensionality, substrate

configuration, and resulting morphology. On planar silicon substrates, deposited metal species diffuse laterally across

the surface and react to form discrete nanodots, as seen in the synthesis of $\text{MnSi}_{1.7}$ and $\beta\text{-FeSi}_2$. In contrast, when diffusion occurs vertically into CaSi_2 microstructures, differences in atomic flux between diffusing species give rise to Kirkendall voids, resulting in hollow or porous micro-rods. Further complexity arises when Mn or Mg atoms selectively penetrate CaSi_2 -derived silicon nanosheets. This interlayer diffusion enables topotactic transformations while preserving the anisotropic morphology, leading to the formation of $\text{MnSi}_{1.7}$, Mg_2Si , and Mg_2SiO_4 nanosheet bundles—structures that maintain crystallographic orientations and high surface accessibility. Moreover, the synthesis of silicides from Si-based frameworks revealed that the underlying geometry of the template was preserved throughout the silicide conversion process. Additionally, when diffusion proceeds into bulk substrates such as FeSi, deep volumetric interdiffusion under molten salt conditions promotes the growth of columnar $\beta\text{-FeSi}_2$ bulk structures. Together, these contrasting diffusion environments reveal how interdiffusion geometry fundamentally influences the resulting phase formation. A comprehensive understanding and precise control of these diffusion-mediated processes are critical for the rational design of functional silicide and silicate materials.

4. Conclusions

This work demonstrates that controlling diffusion geometry enables the design of silicide and silicate materials across multiple length scales. From nanosheets to bulk crystals, diffusion-driven synthesis allows for precise modulation of phase, morphology, and interface structure. The results provide a pathway toward scalable, environmentally compatible materials with applications in thermoelectrics, optoelectronics, and interfacial devices.

Acknowledgements

This work was partially supported by the Cooperative Research Project of Research Center for Biomedical Engineering, Research Institute of Electronics, Shizuoka University.

References

- [1] H. Tatsuoka, Y. Shimura, JSAP Rev. **2023**(2023)230427.
- [2] W. Li, C. Wen, M. Yamashita, T. Nonomura, Y. Hayakawa, H. Tatsuoka, J. Cryst. Growth **340**(2012)51.
- [3] H. Tatsuoka, W. Li, E. Meng, and D. Ishikawa, ECS Trans. **50**(2012)3.

Electrical and photoresponse properties of ternary silicide semiconductor Ru-doped β -FeSi₂

Terai Y.^{*}, Sakurai Y., Takahashi T.

Department of Physics and Information Technology, Kyushu Institute of Technology, 680-4 Kawazu, Izuka, Fukuoka 820-8502, Japan

*e-mail: terai@phys.kyutech.ac.jp

Abstract. Ruthenium-doped β -FeSi₂ (β -(Fe_{1-x}Ru_x)Si₂) polycrystalline thin films were grown by solid phase crystallization from Ru-Si amorphous layers. β -(Fe_{1-x}Ru_x)Si₂ polycrystalline thin films ($x = 0-0.71$) with orthorhombic structure were confirmed by XRD. The β -(Fe_{1-x}Ru_x)Si₂ thin films showed the low electron density ($\sim 10^{16}$ cm⁻³) and the high mobility (~ 290 cm²/V·s) at $x = 0-0.35$. In the photoresponse spectra, the photoresponse in the near-infrared region increased with increasing Ru composition.

1. Introduction

Semiconducting iron disilicide (β -FeSi₂) is a silicon-based semiconductor with an indirect bandgap in the near-infrared region of 0.8 eV. β -FeSi₂ is more sensitive than Si as a photovoltaic material in the near-infrared region due to its large absorption coefficient of 10^5 cm⁻¹ at 1.0 eV. In this study, we have focused on Ru-doped β -FeSi₂ [β -(Fe_{1-x}Ru_x)Si₂], in which Fe is mainly replaced by Ru, to control the band structure of β -FeSi₂ and suppress the non-radiative recombination processes at the surface [1]. The Ru concentration dependence of the electrical properties, band structure, and photoresponse properties, which have not been well understood, were investigated in detail. In the electrical properties of β -FeSi₂ polycrystalline thin film ($x = 0$), a low electron density (2×10^{16} cm⁻³) and a high electron mobility (~ 800 cm²/V·s) have been confirmed. The substitution of Fe with Ru, which is of lower purity (3N) and heavier atomic mass than Fe, is thought to affect its electron density and conduction mechanism.

2. Experiment

In the sample for electrical characterization, β -(Fe_{1-x}Ru_x)Si₂ polycrystalline thin films of 500 nm were grown on Si substrates by solid phase crystallization from Fe-Ru-Si amorphous layers. For photoresponse measurements, n -type β -(Fe_{1-x}Ru_x)Si₂/p-type Si substrate heterojunction devices were fabricated in the Ru composition of $x = 0-0.71$.

3. Results and discussions

The growth of orthorhombic β -(Fe_{1-x}Ru_x)Si₂ polycrystalline thin film ($x = 0-0.71$) was confirmed by XRD. Raman measurements also confirmed the substitution of Fe with Ru. Figure 1 shows the temperature dependence of electron density (n) and electron mobility (μ) in β -(Fe_{1-x}Ru_x)Si₂. The n -type conduction was observed in all samples, and the carrier type did not change with Ru-doping. In the electrical properties at room temperature (RT), the low electron density ($\sim 10^{16}$ cm⁻³) and the high mobility (~ 290 cm²/V·s) were observed at $x = 0-0.35$, but the electron density increased, and the mobility decreased rapidly at $x \geq 0.49$. In the temperature dependence of n and μ in the β -FeSi₂ ($x = 0$), the n decreased and the μ became large with decreasing temperature from 350 to 250 K. In the temperature region, band conduction is concluded to be the main conduction mechanism of electrons. However, the mobility decreased at low temperatures below 250 K. The

result showed the change from band conduction to localized conduction in β -FeSi₂. The change in the conduction mechanism was also observed in Ru-doped β -FeSi₂, indicating that the temperature dependence of the conduction mechanism is not significantly affected by Ru-doping. As seen in Fig. 1, the β -(Fe_{1-x}Ru_x)Si₂ with $x = 0.71$ showed a high electron density and low mobility in the band conduction region. In XRD and Raman measurements, a Ru substitution to non-Fe sites, such as Si anti-sites and interstitial positions, has been observed in the β -(Fe_{1-x}Ru_x)Si₂ with $x = 0.71$ [2]. The Ru substitution outside the Fe site is considered to act as a donor, resulting in increased electron density and low mobility at $x = 0.71$.

In the photoresponse spectra of n - β -(Fe_{1-x}Ru_x)Si₂/p-Si hetero devices the photoresponse in the near-infrared region increased with increasing Ru composition. In the dependence of photoresponse on β -(Fe_{1-x}Ru_x)Si₂ thickness, the high sensitivity was obtained with a thin device (50, 100 nm).

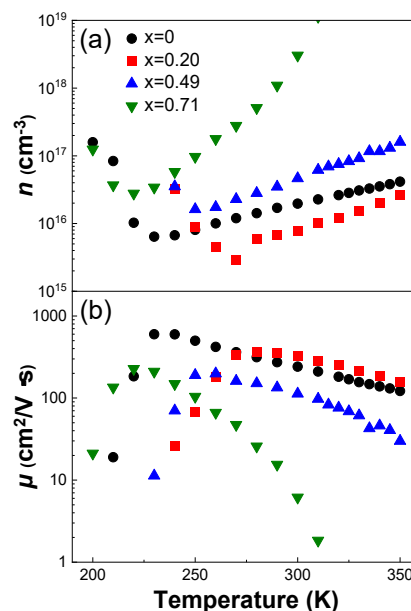


Fig. 1. Temperature dependence of (a) electron density and (b) mobility in β -(Fe_{1-x}Ru_x)Si₂ polycrystalline films.

References

- [1] Y. Terai, *et al.* J. Appl. Phys. **135**, 205302 (2024).
- [2] Y. Terai, *et al.* Jpn. J. Appl. Phys. **62**, SD1006 (2023).

Recent advances in short wavelength infrared sensors using single crystalline Mg₂Si

Udono H.*

Graduate School of Science and Engineering, Ibaraki University, 4-12-1 Nakanaruawa, Hitachi 316-8511, Japan

*e-mail: udono@vc.ibaraki.ac.jp

Abstract. We are developing short wavelength infrared (SWIR) photodetectors and image sensors on Mg₂Si single crystal substrates by simple thermal diffusion and photolithography processes. In this paper we report our recent progress in the growth of Mg₂Si bulk single crystals and the development of Mg₂Si pn-junction photodiodes and photodiode linear arrays.

1. Introduction

Short-wavelength infrared (SWIR: 0.9 – 2.5 μm) photodetectors are expected to be used as machine vision systems in a wide range of applications, such as night monitoring, automated driving, and agricultural and industrial inspection, with the recent advances in IoT and artificial intelligence (AI) technologies [1].

Semiconducting magnesium silicide Mg₂Si, with a bandgap energy of about 0.6 eV, has emerged as a promising candidate material for SWIR photodetectors due to its low environmental impact and abundance [2,3]. Single crystalline bulk ingots with 2-inch diameters have been developed by the vertical Bridgman (VB) growth method in atmospheric pressure [4,5]. The grown crystals have good crystallinity with a well-controlled carrier concentration. Photosensitivity in the SWIR range was observed from the pn-homojunction Mg₂Si diodes fabricated by thermal diffusion of Ag acceptor in the n-type Mg₂Si substrate [6], and the two kinds of Ag diffusion mechanism in Mg₂Si and their diffusion coefficients were also investigated, so far [7]. Very recently, we have developed photodiode (PD) linear arrays on the Mg₂Si single crystalline substrate [8]. In this paper, we report our recent progress in the growth of Mg₂Si bulk single crystals and the development of Mg₂Si pn-junction PDs and PD linear arrays.

2. Experiment

Single crystalline n-type Mg₂Si bulk ingots were prepared by the VB growth method. The raw materials, composed of 5N-purity Mg and 7N-purity Si flakes, were weighed in stoichiometric ratios and melted in crucibles made of pyrographite-coated graphite (PG) or boron nitride-coated pBN in an Ar atmosphere. The Mg₂Si substrates were utilized to fabricate pn-junction PDs and were obtained from the bulk Mg₂Si ingots. Single PDs and PD linear arrays were fabricated on the n-Mg₂Si substrates with various conductivity by simple thermal diffusion of Ag dopant and conventional photolithographic processes. The performance of the PDs was evaluated by IV and spectral photosensitivity measurements at precisely controlled temperatures using a Peltier-cooling unit.

3. Results and discussions

Photodetection from single PDs with inner diameters of 0.1–0.6 mm and PD linear arrays with 8 to 32 pixels were demonstrated on Mg₂Si substrates in the SWIR range below 2.1 μm . Fig. 1(a) and 1(b) show surface micrographs of a typical single PD and PD linear array, respectively. In

these devices, pn-junctions were formed on the front surface with surrounded Au contact electrodes. The peak wavelength of the photosensitivity spectrum varies from approximately 1200 nm to 1600 nm depending on the pn-junction depth controlled by the conditions of thermal diffusion.

The IV measurement revealed that the typical values of dark current density in both single PD and PD linear arrays were in the order of 10^{-3} A/cm² at 300K. The internal quantum efficiencies of more than 80% were also found to be determined from the photosensitivity measurements at 300K under -5V biased conditions. These experimental results clearly indicate that Mg₂Si PDs are promising photodetectors in the SWIR range.

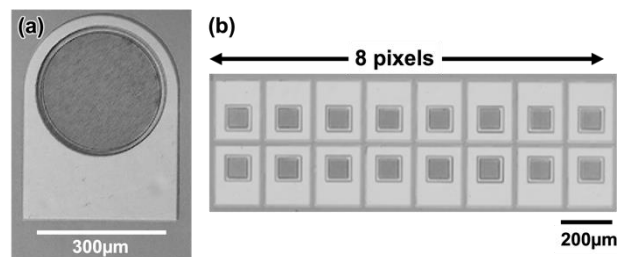


Fig. 1. Micrographs of (a) Mg₂Si pn junction single photodiode (PD) and (b) 8 pixels PD linear arrays with 200 μm pixel pitch.

Acknowledgements

This study was partially supported by JSPS KAKENHI (JP23H01440) and JST A-STEP (JPMJTR21RB and JPMJTR22R3). Part of the microfabrication was performed using the NIMS Nanofabrication Platform supported by MEXT ARIM, Japan.

References

- [1] C. Downs and T.E. Vandervelde, *Sensors*, **13** (2013) 5054.
- [2] D. Tamura, R. Nagai, K. Sugimoto, H. Udono, I. Kikuma, H. Tajima, I. J. Ohsugi, *Thin Solid Films*, **515** (2007) 8272.
- [3] H. Udono, H. Tajima, M. Uchikoshi, M. Itakura, *Jpn. J. Appl. Phys.*, **54** (2015) 07JB06.
- [4] T. Umehara, N. Mizunuma, and H. Udono, *JJAP Conf. Proc.*, **10** (2022) 011002.
- [5] Y. Kimura, X. Liu, N. Usami, S. Sakane and H. Udono, *IUMRS-ICA 2023*, A1-P304-37.
- [6] H. Udono, Y. Yamanaka, M. Uchikoshi and M. Isshiki, *J. Phys. Chem. Sol.* **74** (2013) 311.
- [7] S. Sakane, and H. Udono, *AIP Adv.*, **13**(2023) 105307.
- [8] H. Udono, K. Ojima, N. Imaizumi, H. Takei, S. Sakane, *Proc. SPIE.*, **13362** (2025) 133620I.

Recent progress in optical characterization of silicon micro- and nanostructures

Bandarenka H.V.*

Belarusian State University of Informatics and Radioelectronics, 6 Browka St., Minsk 220013, Belarus

*e-mail: h.bandarenka@bsuir.by

Abstract. Silicon remains the undisputed leader among semiconductors of micro/nanoelectronics for both general and dual purposes, since 1958, when Robert Noyce, one of the founders of Fairchild Semiconductor, created the first planar transistor on the surface of a silicon substrate. This is primarily due to the availability of silicon, its unique electrophysical properties that are well suited for electronic applications and the well-mastered technology. An integral part of the engineering/introduction of new silicon microcircuits is reliable non-destructive testing of their parameters during operation, i.e., their response to external effects like thermal/electrical fields and mechanical stress to avoid unauthorized deactivation or improper control. Optical methods are most suitable to achieve this goal. The present review collects the most recent advances in the characterization of silicon wafers and micro/nanoscale elements of silicon chips using modern optical techniques such as photoluminescence spectroscopy, third harmonic generation imaging and tip-enhanced Raman scattering, to name a few.

1. Introduction

For many years, the “more than Moore” law has been accompanied by a dramatic shrinking of integrated circuit (IC) dimensions. Current sizes of the silicon IC components vary in a wide range including 180–350 nm for the special purpose microcircuits to just a few nanometers for the high-performance computer processors. This poses a major challenge to analytical techniques for non-destructive characterization of submicron silicon structures. Addressing security and trusted electronics requires reliable spatiotemporal imaging of silicon microcircuits to probe external latent fields (pressure, temperature, electric and magnetic fields) through monitoring their structural parameters. Undoubtedly, the least invasive approaches for such an analysis are the optical ones. Here, a review of the most recent progress in application of the optical techniques for advanced characterization of silicon wafers, micro/nanoscaled elements, and microchips is presented. Photoluminescent spectroscopy including that with potentiometric dye, third harmonic generation (THG) imaging, and tip-enhanced Raman scattering (TERS) spectroscopy are reported as sufficient techniques to reveal nuances of the silicon-based structure response to external fields.

2. Photoluminescence spectroscopy

At room temperature, a band-to-band phonon-assisted photoluminescent (PL) spectrum of silicon can be obtained in the wavelength range from 900 to 1300 nm [1]. Given temperature dependent silicon bandgap, the PL signature is sensitive to the local temperature distribution. However, the prohibitively low emission from c-Si at above the room temperature has been a hurdle for the reliable “feeling” of the slight variations of its broad PL spectra at the thermal conditions typical for the ICs operating regimes. On the contrary, lower temperatures provided by liquid nitrogen or helium, open a way for more informative PL analysis of the silicon structure. One of the examples is the study of the PL spectra of silicon at 3 K, which led to the demonstration of the existence of the so-called excitonic molecules [2]. Early PL studies of silicon have resulted in determining the concentration of dopants [3], characterizing atomic size defects and dislocations [4], transition metal complexes [5].

Recently, the PL imaging has been driven by the fast development of silicon photovoltaics, where it has become essential for characterization of large area silicon wafers [6]. PL spectroscopy has also been demonstrated to be capable of measuring minority carrier lifetime free of experimental artifacts, occurring in other techniques [7]. The micro-PL spectroscopy study of the passivated c-Si solar cells revealed parasitic absorption of visible light in the silicon nitride layer and distinct emission from the heavily-doped silicon layers [8]. Combined PL spectra were collected at 79 K and 298 K, yet again proving much better sensitivity at the low temperatures. Further developments in this area demonstrated that the resistance of the silicon solar cells can be extracted from PL images with 125 mm spatial resolution for the 12.5×12.5 cm² illumination area [9]. In parallel with these studies PL imaging instrumentation has been constantly worked on to increase the sensitivity of the method [10]. In particular, an approach was proposed to bring the spatial resolution below the submicron level via silicon nanoparticles placed on top of the bulk silicon wafer. There have also been attempts to identify the effect of mechanical stress on the PL signal [11]. In [12], it was shown that potentiometric dyes routinely used for measuring transmembrane potential in live cells can be an excellent probe for sensing the local electric fields in operating silicon-based ICs. A potentiometric dye embedded in the laponite clay thin film was spread on the surface of a silicon microchip, to study the effect of local electric fields on the infrared photoluminescence (IR PL) of the dye molecules excited by near-IR laser radiation, and demonstrated that this method provides a reliable approach to sensing the local temperature and electric field in Si-based chips in real time.

3. Third harmonic generation imaging

The third harmonic generation (THG) can potentially be one the most fruitful approach to investigate silicon wafers and microchips, which is known to give an information about the bulk properties of this semiconductor. An escape depth of TH signal from silicon can be tuned in the submicron range by selecting the wavelength of high-power laser excitation. An infrared (IR) radiation at a wavelength varying from 1200 to 2100 nm makes it possible to detect the reflected TH signal from layers in

silicon at a depth of 0.1–10 μm at which functional elements are typically buried. The THG effect was studied to reveal the cubic anisotropy of the third-order nonlinear susceptibility $\chi^{(3)}$ in silicon and its linear dependence on the laser power. Moss et al. firstly reported on a doping effect on the THG signal in silicon subjected to antimony and boron ion implantation [13]. It was shown that the introduction of antimony reduces the THG intensity and anisotropy, which is associated with the amorphization of silicon. On the other hand, bombardment with boron ions had virtually no effect on the THG signal. In addition, it was found that an annealing of silicon after implantation of antimony ions up to 10^{23} cm^{-3} leads to a significant increase in the intensity of the collected TH signal due to linear optical effect of reflection enhancement. Controversial results on a significant surface contribution to the THG signal were obtained by Tsang during a study of the normalized THG in silicon of (111) and (100) crystal orientation as a function of the rotation angle of the excitation laser beam [14]. The qualitative argument indicating that the induced third order-polarization field $P(3\omega) = \chi^{(3)} E^3(\omega)$ can easily exceed the second-order polarization $P(2\omega) = \chi^{(2)} E^2(\omega)$ at an interface was taken into account. Therefore, THG in transmission from dielectric interfaces was suggested to be surface-enhanced under a rather intensive laser irradiation. The strong surface contribution to the THG signal in silicon, however, was experimentally refuted via analyzing a thinning layer of c-Si sandwiched by thick layers of silicon dioxide. Quite modest surface contribution was shown only for the 20-nm thick silicon layer. A small escape depth of the electrically induced TH radiation was shown for oxidized *n*-Si (111). The possibility of the interlayer defect inspection between silicon wafers by collection of the transmitted TH signal was demonstrated [15]. In [16], a spatial and temporal THG imaging of silicon wafers routinely used in microelectronics and microchips was demonstrated via pumping a femtosecond 1250-nm laser. The depth of the THG analysis reached nearly 100 nm taking into account the THG signal detection in a reflection mode in a range of 410–450 nm. It was experimentally shown that the THG imaging provides characterization of doping parameters of c-Si, which is more prominent for the highly doped wafers. Such a result was theoretically validated by DFT modeling. Even slight oxidation of silicon wafers enabled better contrast between areas with different dopant level and density, which was associated with the THG signal enhancement in SiO_2 layer. In addition, the THG signal was found to be sensitive to mechanical stress in the silicon wafer induced by a compression. The THG imaging of a real microchip allows confident differentiation of silicon areas formed by epitaxy and ion implantation. The most important result was probing the electric field and current in silicon. A bias voltage of 5–30 V applied to the lightly doped *p*-type silicon through a 300-nm oxide layer caused changes in the THG signal intensity dependent on the direction of the electric field strength vector (\vec{E}). The THG intensity of the non-oxidized *p*-type silicon was also tuned by \vec{E} when a bias voltage was 1–3 V. On the other hand, a higher bias voltage applied to silicon free of oxide resulted in the THG intensity decrease. This happened due to current flow in the substrate that was not detected in an absence of the pulsed IR laser excitation or upon

continuous wavelength (CW) IR radiation. Thus, the possibility of spatially and temporally resolved sensing of electrical signals in silicon micro/nanostructures including transistor channels by the THG imaging method was hypothesized.

4. Tip-enhanced Raman scattering spectroscopy

A combination of atomic force microscopy with noble metal cantilever and Raman spectroscopy (TERS spectroscopy) is a relatively new yet intriguing technique to study silicon micro/nanostructures since it has a potential to provide accurate structural analysis at submicron resolution. In [17], spatially and temporally resolved TERS-sensing and mapping to find defects in Si wafers and electric current in Si microchips were demonstrated. TERS-imaging provided revealing points of uneven doping in ion-implanted areas in contrast to spontaneous Raman scattering imaging. TERS resolution was approx. 0.15 nm to achieve relatively fast mapping (the mapping took about 1 h). The defect observed on the TERS-image was supposed to be in a few nanometers' thick surface layer, which cannot be scanned with the same sensitivity and resolution by spontaneous Raman scattering spectroscopy. TERS-imaging of Si microchip (n-p-n bipolar transistor) showed that Si Raman band shifts to lower wavenumber if the transistor is "on" because of electric current induced mechanical stress or/and local heating in the channel of transistor. An increase in the voltage biasing led to the Si Raman intensity change due to electric current induced disorder in the crystalline lattice.

5. Conclusions

The reported results on optical characterization of silicon-based substrates are extremely promising for providing precision testing of structure, function, operation and security not only at the component level, but also at the level of the entire IC.

References

- [1] E. G. Gule, Semiconductors, 39 (4), 406, 2005.
- [2] J. R. Haynes, Phys. Rev. Lett., 17 (16), 860–862, 1966.
- [3] M. Tajima, Appl. Phys. Lett., 32 (11), 719–721, 1978.
- [4] R. Sauer, J. Weber, J. Stolz, E. R. Weber, K.-H. Kusters, H. Alexander, Appl. Phys. Solids Surf., 36 (1), 1–13, 1985.
- [5] H. Conzelmann, Appl. Phys. Sol. Surf., 42 (1), 1–18, 1987.
- [6] T. Trupke, B. Mitchell, J. W. Weber, W. McMillan, R. A. Bardos, R. Kroeze, Energy Procedia, 15, 135–146, 2012.
- [7] T. Trupke, R. A. Bardos, M. C. Schubert, W. Warta, Appl. Phys. Lett., 89 (4), 044107, 2006.
- [8] H. T. Nguyen et al., Sol. Energy Mater. Sol. Cells, 145, 403–411, 2016.
- [9] T. Trupke, E. Pink, R. A. Bardos, M. D. Abbott, Appl. Phys. Lett., 90 (9), 093506, 2007.
- [10] B. I. Afinogenov et al., Opt. Lett., 46 (13), 3071, 2021.
- [11] K. Yasutake, M. Umeno, H. Kawabe, H. Nakayama, T. Nishino, Y. Hamakawa, J. Appl. Phys., 21(12), 1715, 1982.
- [12] Bandarenka H, Kuzmin A, Baev A, Gupta S, Prasad PN. ACS Omega. 2024, 23, 9(31), 34036–34045.
- [13] D. J. Moss, H. M. Van Driel, J. E. Sipe, Appl. Phys. Lett., 48 (17), 1150–1152, 1986.
- [14] T. Y. F. Tsang, Phys. Rev. A, 52 (5), 4116–4125, 1995.
- [15] Y. Gao et al., Opt. Express, 26 (25), 32812, 2018.
- [16] H. Bandarenka, D. Adinehloo, E. Oskolkov, A. Kuzmin, A. Pliss, O.D. Shaibu, J. Bird, A. Baev, V. Perebeinos, P.N. Prasad, ACS Photonics, 2025, published online.
- [17] H. Bandarenka, O. Savkina A. Kuzmin, A. Baev, P.N. Prasad, MRS Communications, 2025, accepted.

Formation of p-type and n-type Si doped (Ga,Al)As nanowires

Shtrom I.V.^{*,1,2,3}, Sibirev N.V.^{1,2}, Ilkiv I.V.^{1,2,3}, Soshnikov I.P.^{3,4}, Gridchin V.O.^{1,2,3}, Reznik R.R.^{1,2,3}, Alekseev P.A.⁴, Cirilin G.E.^{1,2,3}

¹ St. Petersburg State University, Universitetskaya Embankment 7-9, 199034 St. Petersburg, Russia

² IAI RAS, 198095 St. Petersburg, Russia

³ Alferov University, 194021 St. Petersburg, Russia

⁴ Ioffe Institute, Saint-Petersburg, 194021, Russia

*e-mail: i.shtorm@spbu.ru, igorstrohmail@mail.ru

Abstract. (Ga,Al)As nanowires (NWs) grown by molecular beam epitaxy on a Si substrate provide a promising platform for applications in photonics. A3B5 nanowire (NW)-based applications demand controllable variation of composition and doping levels. For this, it is necessary to study the doping of (Ga,Al)As NWs with p- and n-types. This study investigates the growth of GaAs NWs using arsenic-rich droplets, wherein Si serves as an acceptor and Pb,Sn act as a catalyst. First time Pb-catalyzed GaAs NW growth in different modes was demonstrated. In addition, our work investigates the properties of Si doped (Ga,Al)As core-shell NWs grown with a gold catalyst.

1. Introduction

We have previously demonstrated the opportunity of creating array of optically pumped single photon sources based on hybrid nanostructures such as GaAs quantum dots embedded into AlGaAs NWs [1]. However, for the effective use of such structures in modern cryptography and instrumentation, it is important to be able to electrically pump of single photons sources. Thus, it is important to study the controllable doping of (Ga,Al)As NWs with p- and n-types.

Traditional NW growth techniques, primarily based on Vapor-Liquid-Solid mechanism, focus on on reducing the nucleation barrier beneath the liquid [2]. Boron group metals form alloys (with the catalyst) more easily than nitrogen group elements. Therefore, commonly used catalysts easily dissolve metal but poorly dissolve arsenic. Si and other amphoteric dopants in GaAs act as donors rather than acceptors.

This study investigates the growth of GaAs NWs using arsenic-rich droplets, wherein Si serves as an acceptor. The catalyst for such growth must have at least two properties: high solubility of As and low incorporation rate in GaAs. Pb and Sn are identified as suitable catalysts. Growth of GaAs NWs with Sn-As catalyst already demonstrated via CVD [3], while growth of A3B5 NWs with Pb catalyst didn't studied previously. Yet Sn more easily incorporates in GaAs than Pb. Si shows poor solubility in liquid Pb at typical growth temperatures, so the reservoir effect is suppressed [4], which allows the formation of sharp heterointerfaces.

2. Experiment

This talk is devoted to studying the growth of GaAs NWs with Pb and Sn catalyst [4] via MBE. Our research also examines silicon doping of GaAs NWs. All growth was done in the solid-source molecular beam epitaxy system Riber Compact 21 with pre-deposited 5nm tin or lead layer.

The description of the synthesis, morphological properties and crystal structure of (Ga,Al)As arrays is demonstrated in our work [1]. The study of AlGaAs core-shell NWs electrical properties was performed with the

atomic force microscope (AFM) Ntegra Aura (NT-MDT) [6]. The IV curves of a single (Ga,Al)As NW on the Si substrate were measured using the conductive atomic force microscopy (C-AFM) by contacting the probe with one NW.

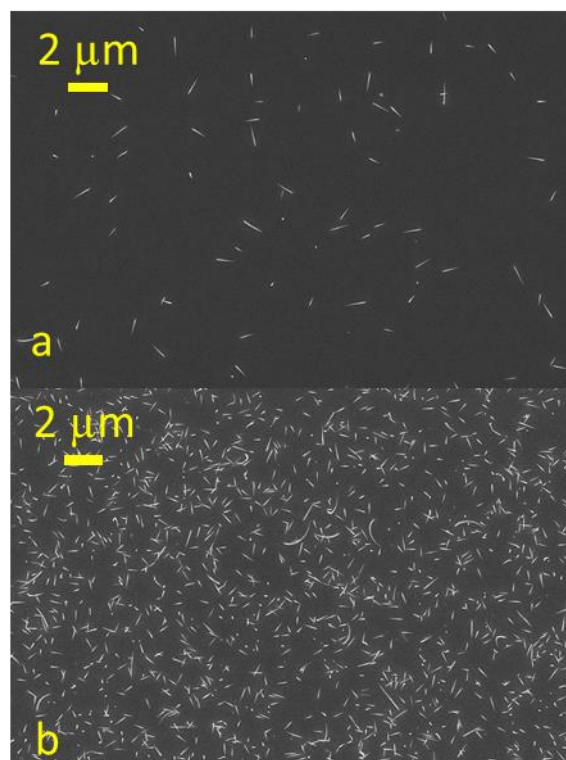


Fig. 1. SEM image of NWs grown at 410 °C on GaAs(111)B substrate (a) Sn-catalyzed; (b) Pb catalyzed.

3. Results and discussions

Most interesting temperature for GaAs NWs with tin catalyst growth is greater than 579°C eutectic temperature of Sn-As alloy. Unfortunately, we didn't reach success at this growth temperature, tin dissolves in the substrate. The growth at lower temperature about 400 °C on GaAs(111)B

was successful. Typical SEM image of Sn-catalyzed NWs is represented in Fig. 1a.

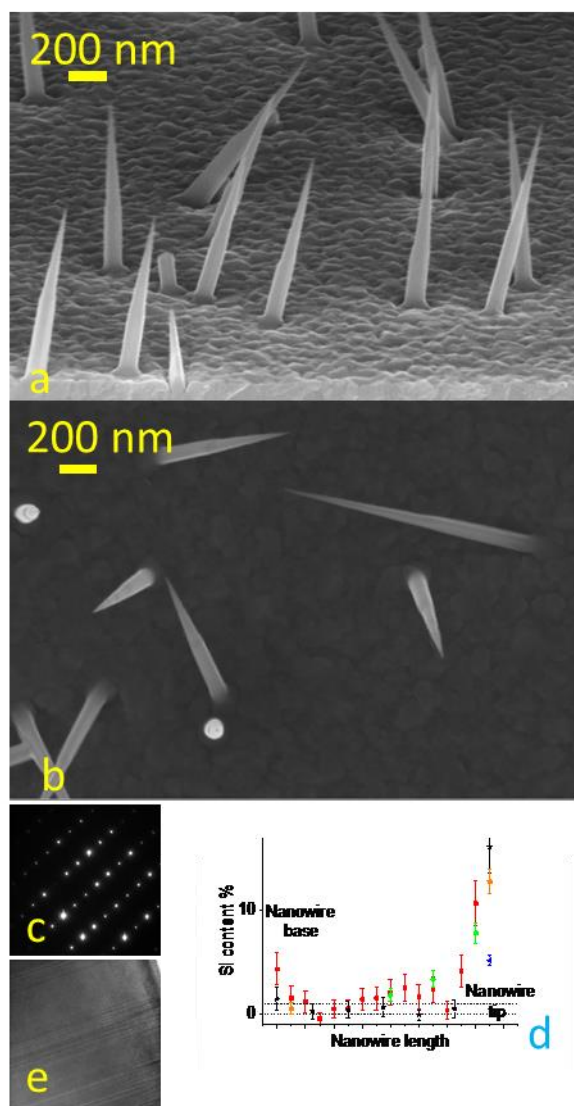


Fig. 2. (a), SEM image of NWs grown at 350 °C side-view (a); SEM image of heavily Si doped NW grown at 410 °C top-view(b); Selected area (electron) diffraction from NWs grown at 380 °C (c), Si content along the NW length for different NWs grown at 350 °C (d), A TEM image of NW grown at 380 °C (e).

Pb-catalyzed GaAs NWs were grown on Si (111) and GaAs(111)B. The growth temperature of $380 \pm 30^\circ\text{C}$ was decided upon when the As solubility in Pb was at least 20%, while Ga and Pb formed immiscible liquids. Typical SEM image of Pb-catalyzed NWs on GaAs(111)B is represented in Fig. 1b. The growth results of Pb catalyzed NWs on Si(111) substrate are illustrated in Fig. 2.

In the case of (Ga,Al)As NWs, it is important to note that NWs have a spontaneously formed "core-shell" structure in the wurtzite phase [1]. In general, the scanning maps indicates that the core and shell have different types of doping. N-type conductivity in (Ga,Al)As nanowire shell clearly demonstrated. Nanowire core conductivity is relatively small and didn't allow to determine type of doping.

4. Conclusions

The growth of GaAs NWs with Pb and Sn catalyst has been demonstrated [4]. Pb-catalyzed NW growth can occur

in various modes with a Ga-rich droplet, As-rich droplet and a depleted droplet. Rarely, NWs with solid silicon arsenide particles at their tip were found. The potential for both n-type and p-type Si doping of GaAs NWs has been established. Furthermore, the formation of metastable GaAs-Si alloy was observed. In most cases, Sn and Pb droplets were found to dissolve within NWs. The preservation of a droplet remains a subject of our studies.

N-type conductivity in (Ga,Al)As nanowire shell clearly demonstrated.

Acknowledgements

The author acknowledges St.-Petersburg State University for a research project No. 129360164.

References

- [1] L. Leandro, C. P. Gunnarsson, R. Reznik, K. D. Jöns, I. Shtrom, A. Khrebtov, T. Kasama, V. Zwiller, G. Cirlin, Nika Akopian. *Nano Lett.* **v.18, N 11.**(2018).7217.
- [2] Dubrovskii V.G., Sibirev N. V., Cirlin G.E. et. al., *Phys Rev E*, **V. 73.** (2006) 021603.
- [3] Sun R., Vainorius N., Jacobsson D., Pistol M.E., Lehmann S., Dick K.A. *Nanotechnology V. 27. Iss.21* (2016).
- [4] Dubrovskii V.G., Sibirev N.V. *Cryst. Growth Des.* **V. 16. Iss.4** (2016).
- [5] Shtrom I. V., Sibirev N. V., Soshnikov I.P., Ilkiv I. V., Ubyivovk E. V., Reznik R.R., Cirlin G.E. *Nanomaterials V. 14. Iss.23.* (2024) 1860.
- [6] Alekseev P A, Sharov V A, Borodin B R, Dunaevskiy M S, Reznik R R and Cirlin G E *Micromachines* **11** (2020) 581.

Thermoelectric potential of $\text{Ge}_2\text{Sb}_2\text{Te}_5$ phase change thin films for energy harvesting of low-grade heat

Terekhov D.Yu.^{*}, Al-Khadge L.A., Yakubov A.O., Lazarenko P.I., Sherchenkov A.A.

National Research University of Electronic Technology, Bld. 1, Shokin Square, Zelenograd, Moscow, Russia, 124498

^{*}e-mail: gsm.ads@yandex.ru

Abstract. This study investigates the thermoelectric properties of $\text{Ge}_2\text{Sb}_2\text{Te}_5$ (GST) thin films for potential application in low-power thin-film thermoelectric generators (TEGs). The films were fabricated via magnetron sputtering on ST50 glass-ceramic substrates with W/TiN electrodes. Temperature-dependent measurements of the Seebeck coefficient and electrical resistivity were performed from room temperature to 270 °C. A sharp drop in resistivity by two orders of magnitude was observed between 154 °C and 184 °C, corresponding to the amorphous-to-crystalline phase transition. This transition led to a three-order-of-magnitude increase in power factor, reaching $0.4\text{--}0.7\text{ W}\cdot\text{K}^{-2}\cdot\text{cm}^{-1}$, comparable to that of bulk thermoelectric materials. The figure of merit ZT was estimated using reported thermal conductivity data and shown to increase by two orders of magnitude upon crystallization. The effect of Ti and Bi doping (0.5 wt.%) on film properties was analyzed, revealing that Bi improves thermoelectric performance, while Ti has a detrimental impact. These results demonstrate the potential of doped GST thin films for integrated micro-TEG applications.

1. Introduction

Thin-film thermoelectric generators (TEGs) are promising primary power sources for low-power electronic devices, typically up to a few watts. However, the widespread adoption of thin-film TEGs is currently limited by the low efficiency of the thermoelectric materials used. The efficiency of converting thermal energy into electrical energy in a TEG is typically characterized by the thermal-to-electrical conversion efficiency (η). A key parameter influencing this efficiency is the thermoelectric figure of merit ZT , which plays a central role in the expression for η . Since ZT is directly proportional to the square of the Seebeck coefficient and electrical conductivity, significant improvements in these properties could lead to a long-awaited breakthrough in TEG performance. Chalcogenide glassy semiconductors in the Ge-Sb-Te system are widely used in non-volatile optical memory applications, such as CD/DVD storage, and show potential for use in non-volatile electrical phase-change memory. Previous studies [1] have demonstrated that thin films based on these materials, in both amorphous and crystalline states, exhibit high Seebeck coefficients and low thermal conductivity—characteristics that are promising for use in thin-film TEGs. Accordingly, the objective of this work was to investigate the temperature dependence of the Seebeck coefficient and electrical conductivity of $\text{Ge}_2\text{Sb}_2\text{Te}_5$ thin films for potential application in thin-film thermoelectric generators.

2. Experiment

The experimental samples were fabricated on polished glass-ceramic substrates of the ST50 grade (Figure 2). Tungsten (W) electrodes with a 100 nm TiN adhesion layer were deposited onto the substrate. $\text{Ge}_2\text{Sb}_2\text{Te}_5$ -based thin films with a thickness of 650 nm were then deposited over the electrodes by magnetron sputtering using metal shadow and photoresistivity masks. The properties of the thin films were characterized off the measurement system used to measure the Seebeck coefficient and current-voltage characteristics (I – V curves) over a temperature range from room temperature up to 400 °C. The system provides thermal gradients from 2 °C to 20 °C and heating step increments from 1 °C to 50 °C. The main specifications of the system are summarized in Table I.

Calibration of the measurement system was performed using chromel, alumel wires and lead reference standards. The measurement error for the Seebeck coefficient does not exceed $\pm 0.5\%$.

Table I. Parameters of measurement setup.

Parameters	Range
Temperature: 25 to 400 °C	Temperature: 25 to 400 °C
Temperature gradient: 2 to 20 °C	Temperature gradient: 2 to 20 °C
Step increment: 1 to 50 °C	Step increment: 1 to 50 °C
Measurement accuracy: ± 0.2 °C	Measurement accuracy: ± 0.2 °C
Soak time: 0 to ∞	Soak time: 0 to ∞
Stabilization time (1 °C step): 1.5 minutes	Stabilization time (1 °C step): 1.5 minutes
Stabilization time (50 °C step): 5 minutes	Stabilization time (50 °C step): 5 minutes
Sensitivity (with 10 M Ω load): from 0.05 mV	Sensitivity (with 10 M Ω load): from 0.05 mV

Temperature-dependent measurements of the Seebeck coefficient and electrical resistivity were carried out in the range from room temperature to 270 °C, with a controlled heating step of 5 °C and a soak time of 5 minutes at each temperature point.

3. Results and discussions

In the temperature range from 154 °C to 184 °C, a sharp drop in electrical resistivity by two orders of magnitude—to approximately $0.01\text{ }\Omega\cdot\text{cm}$ —is observed (Fig. 1). This behavior is attributed to a phase transition from the amorphous to the crystalline state. With further temperature increase, the resistivity changes only slightly. During the crystallization temperature range of the $\text{Ge}_2\text{Sb}_2\text{Te}_5$ thin film, only a minor decrease in the Seebeck coefficient is observed. Conductivity calculations for the $\text{Ge}_2\text{Sb}_2\text{Te}_5$ thin films indicate that the sharp drop in resistivity during crystallization leads to a significant increase in electrical

conductivity, resulting in a three-order-of-magnitude rise in the power factor. As a result, $\text{Ge}_2\text{Sb}_2\text{Te}_5$ thin films in the crystalline state exhibit power factor values in the range of $0.4\text{--}0.7\text{ W}\cdot\text{K}^{-2}\cdot\text{cm}^{-1}$, which are comparable to those of state-of-the-art bulk thermoelectric materials ($0.8\text{--}2\text{ W}\cdot\text{K}^{-2}\cdot\text{cm}^{-1}$).

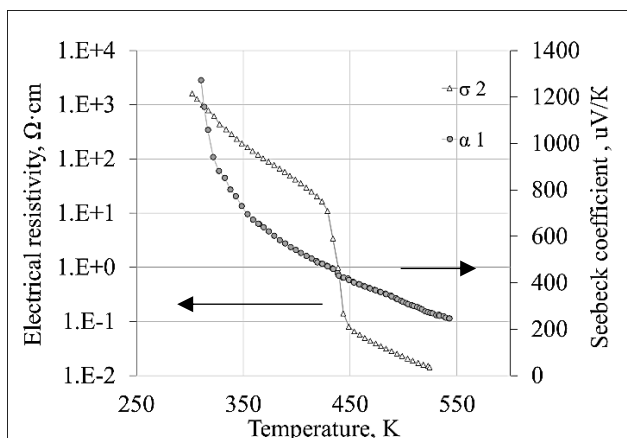


Fig. 1. Temperature dependences of the thermoelectric power coefficient and specific resistance for a thin $\text{Ge}_2\text{Sb}_2\text{Te}_5$ film.

Since the efficiency of TEGs is largely determined by the figure of merit Z of the thermoelectric materials, the temperature dependence of Z for $\text{Ge}_2\text{Sb}_2\text{Te}_5$ thin films was evaluated (Fig. 2).

The temperature-dependent values of Z were calculated using thermal conductivity (λ) data for $\text{Ge}_2\text{Sb}_2\text{Te}_5$ thin films reported by Ho-Ki Lyeo et al. [2]. The results show that upon crystallization, the thermal conductivity of the film doubles, while the figure of merit increases by two orders of magnitude, reaching approximately $0.8 \times 10^3\text{ K}^{-1}$.

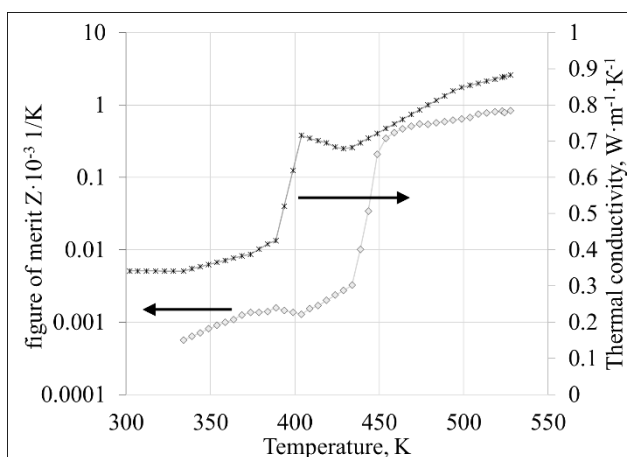


Fig. 2. Temperature dependences of the thermoelectric power coefficient and specific resistance for a thin $\text{Ge}_2\text{Sb}_2\text{Te}_5$ film.

However, current thermoelectric materials used for energy harvesting typically exhibit a figure of merit of $Z \sim 1 \times 10^{-3}\text{ K}^{-1}$, corresponding to a thermodynamic efficiency of about 15–16% of the ideal Carnot cycle [3]. Therefore, to achieve a twofold increase in efficiency compared to the current level, a figure of merit greater than $10 \times 10^{-3}\text{ K}^{-1}$ would be required—an almost unattainable value with present-day thermoelectric materials.

Enhancing the Z value of $\text{Ge}_2\text{Sb}_2\text{Te}_5$ thin films may be possible by tuning their thermoelectric and electrical properties, for example, through doping with elements such as Bi or Ti. Previous research conducted under PNIR

showed that the addition of 0.5 wt.% Ti to $\text{Ge}_2\text{Sb}_2\text{Te}_5$ thin films significantly increases the resistivity in the amorphous state and slightly increases the Seebeck coefficient (see Table II), which ultimately has a negative effect on the material's figure of merit. In contrast, doping with 0.5 wt.% Bi reduces the resistivity and increases the Seebeck coefficient, which, taken together, can positively impact the thermoelectric figure of merit of the material.

Table II. Parameters of measurement setup.

Material	Seebeck coefficient, $\mu\text{V/K}$	Resistivity, $\text{M}\Omega$
$\text{Ge}_2\text{Sb}_2\text{Te}_5$	591	6,4
$\text{Ge}_2\text{Sb}_2\text{Te}_5 + 0.5\text{ wt. \%Bi}$	826	1.0
$\text{Ge}_2\text{Sb}_2\text{Te}_5 + 0.5\text{ wt. \%Ti}$	896	12.8

4. Conclusions

The results showed that during crystallization the quality factor increases by 2 orders of magnitude and is $0.8 \times 10^3\text{ K}^{-1}$, which is a relatively small value for energy harvesting tasks. An increase in Z of $\text{Ge}_2\text{Sb}_2\text{Te}_5$ thin films can be achieved by controlling the thermoelectric and electrophysical properties, for example, by introducing dopants

The introduction of 0.5 wt. % Bi impurity into a thin $\text{Ge}_2\text{Sb}_2\text{Te}_5$ film leads to a decrease in the film resistance and an increase in the thermoelectric coefficient, which together can positively affect the thermoelectric quality factor of the material, and as a result will allow the development of a thin-film thermoelectric generator

Acknowledgements

The work was performed in the laboratory "Materials and devices of active Photonics" (Agreement 075032025266/1 dated 03/25/2025, FSMR-2025-0002).

References

- [1] Terekhov, D.Y. et al. (2017). Investigation of Temperature Dependencies of Seebeck Coefficient and Electrical Conductivity of $\text{Ge}_2\text{Sb}_2\text{Te}_5$ // 22. 518-527. 10.24151/1561-5405-2017-22-6-518-527.
- [2] Lyeo H. K. et al. Thermal conductivity of phase-change material $\text{Ge}_2\text{Sb}_2\text{Te}_5$ // Applied Physics Letters. – 2006. – T. 89. – №. 15. – C. 151904.
- [3] Громов Г. Г. Термоэлектрические микрогенераторы. Оптимизация для применений energy harvesting. // Издательские решения / ISBN 978-5-4490-1734-5 K. Oyoshi, D. Lenssen, R. Carrius, S. Mantl. Thin Solid Films **381**(2001)194.

III-V semiconductor nanostructures of different dimensionality: MBE growth and physical properties

Reznik R.R.^{*,1-3}, Ilkiv I.V.¹⁻³, Gridchin V.O.¹⁻³, Kotlyar K.P.¹⁻³, Khrebrov A.I.^{1,2}, Kryzhanovskaya N.V.⁴, Baretin D.⁵, Akopian N.⁶, Cirlin G.E.¹⁻³

¹ St. Petersburg State University, Universitetskaya Embankment 13B, 199034 St. Petersburg, Russia

² Alferov University, Khlopina street 8/3, St. Petersburg, 194021, Russia

³ IAI RAS, Ivana Chernykh street 31-33, St. Petersburg, 198095, Russia

⁴ HSE University, Souyuza Pechatnikov 16, St. Petersburg 1940121, Russia

⁵ Università degli Studi Niccolò Cusano - Telematica, via don Carlo Gnocchi 3, 00166 Rome, Italy

⁶ Technical University of Denmark, DK 2800 Lyngby, Denmark

*e-mail: r.reznik@spbu.ru

Abstract. In this work we present the results of experimental studies on the synthesis by molecular beam epitaxy and physical properties studies of new III-V hybrid semiconductor nanostructures for next-generation applications.

1. Introduction

Nowadays III-V semiconductor nanostructures attract an increasing attention due to recent advances in their use as building elements for various electronic, optical, and biological applications [1-2]. Moreover, the progress in modern synthesis methods enables nanostructures of combined dimensionality formation, such as quantum dots (QDs) in nanowires (NWs) [3]. The most studied epitaxially grown QDs are self-assembled, i.e., grown by island nucleation in the Stranski - Krastanov growth mode. In common case, the size, shape, and density of self-assembled QDs can be changed by growth parameters, but it is a strain induced process and controlling the properties of the array independently is a challenging task [4]. QDs in nanowires have in contrast shown great potential as a highly controllable system. The diameter, height, and density of the QDs are defined by the NW diameter, the growth time, and the NW density, respectively, and can be chosen more predictable. Due to the ability to accumulate for strain in two dimensions, the NW geometry is ideal for monolithic integration of semiconductor materials with different lattice mismatched substrates, which is important for achieving high performance optoelectronic devices based on Si technology [5].

2. Experiment

Nanostructures were grown using molecular-beam epitaxy (MBE) machine Riber Compact 21T equipped with Ga, Al In, Si, Be effusion sources, As and P cracking sources, N plasma source and additional chamber for high temperature heating and Au deposition. Silicon plates were used as the substrates for MBE growth. The fluxes values were pre-calibrated using GaAs(100) substrate. The physical properties of the synthesized nanostructures were studied using scanning electron microscopy (SEM), transmission electron microscopy (TEM), photoluminescence (PL) and other methods.

3. Results and discussions

In this work we present for the first time MBE growth of QDs in NWs based on (In)GaAs/AlGaAs materials system on silicon surface also studied their physical properties. Typical TEM images of single AlGaAs NW

with InGaAs QD, diffraction pattern obtained in QD location and schematic representation of AlGaAs NWs with InGaAs QDs structure are shown in figure 1. Studies results have shown that grown hybrid nanostructures are efficient single photons sources and by changing the size and composition of QDs, we can strictly control the emission energy from the QD in a wide range. It is important to note that the direction of emission from QDs in the body of NWs was studied experimentally and theoretically. Our work opens new prospects for integration of direct band-gap semiconductors and single-photon sources on silicon platform for various applications in the fields of silicon photonics and quantum information technology.

In addition, we present the results of experimental studies on the III-V nanostructures growth on silicon platform by molecular-beam epitaxy and their physical properties studies for next-generation applications.

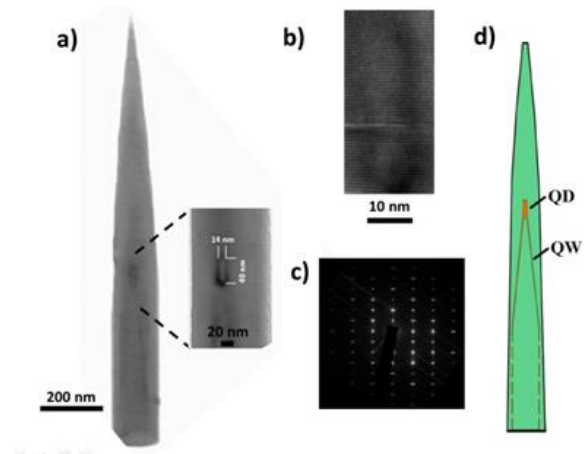


Fig. 1. a) Typical TEM image of single AlGaAs NW with InGaAs QD grown at 510°C. b) Typical HRTEM image of InGaAs QD in single AlGaAs NW grown at 510°C. c) Typical diffraction pattern obtained in QD location. d) Schematic representation of AlGaAs NWs with InGaAs QDs structure.

Acknowledgements

The authors acknowledge Saint-Petersburg State University for a research project 122040800254-4.

References

- [1] K. Oyoshi, D. Lenssen, R. Carrius, S. Mantl. Thin Solid Films **381**(2001)194.
- [2] T. Suemasu, T. Fujii, K. Takakura, F. Hasegawa. Thin Solid Films **381**(2001)209.
- [3] R. Bayazitov, R. Batalov, R. Nurutdinov, V. Shustov, P. Gaiduk, I. Dezsi, E. Kotai. Nucl. Instr. Meth. **B** **24**(2005)224.
- [4] K. Oyoshi, D. Lenssen, R. Carrius, S. Mantl. Thin Solid Films **381**(2001)202.
- [5] J. Chrost, J. J. Hinarejos, E. G. Michel, R. Miranda. Surf. Sci. **330**(1995)34.

The influence of heat treatment on the characteristics of composite thermoelectric materials based on $\text{Bi}_2\text{Te}_{2.8}\text{Se}_{0.2}$ and $\text{Bi}_{0.5}\text{Sb}_{1.5}\text{Te}_3$

Voloshchuk I.A.^{*1}, Babich A.V.¹, Kiselev A.V.², Mikhalevsky V.A.², Sherchenkov A.A.¹

¹ National Research University of Electronic Technology, 1 Shokin Square., Moscow, Zelenograd 124498, Russia

² National Research Centre «Kurchatov Institute», Moscow, 123098, Russia

* e-mail: voliriand@gmail.com

Abstract. In this work, the influence of heat treatment on the electrophysical, thermoelectric and mechanical properties of the fabricated composite thermoelectric materials based on $\text{Bi}_2\text{Te}_{2.8}\text{Se}_{0.2}$ (n-type) and $\text{Bi}_{0.5}\text{Sb}_{1.5}\text{Te}_3$ (p-type) was investigated. Power factor for the obtained composite thermoelectric materials was determined. The developed method of forming thermoelectric legs can be used for fabrication of flexible thermoelectric generators.

1. Introduction

Today, the development of flexible thermoelectric generators (TEG) is of particular interest, since the use of such TEGs can become both a serious addition and an alternative to batteries used today in portable microelectronics. The main advantage of flexible TEGs compared to classical ones is the ability to take the necessary shape within certain limits, which makes it possible to use such devices on heat sources with a developed surface, for example, to convert the heat of a living organism, including the human body. The technology of thick-film thermoelectric materials (namely composite materials) is of particular interest for the formation of flexible thermoelectric generators. This paper proposes a method for forming composite materials that include thermoelectric materials, modified by nanodispersed particles, and a matrix of aqueous alkaline solutions of sodium or potassium silicates. The introduction of nanoparticles of various natures (for example, semiconductor particles with a narrow band gap, nanosized carbon tubes or highly conductive metal oxides) to improve electrical conductivity can affect not only electron transport in the material, but also increase phonon scattering, thereby increasing the thermoelectric figure of merit of the material.

One of the most important stages in the fabrication technology of composite thermoelectric materials is heat treatment. Firstly, heat treatment allows to remove residual moisture from the composite thermoelectric material, thereby increasing its electrical conductivity [1]. Secondly, heat treatment can lead to sintering of thermoelectric material particles. It can significantly affect the electrophysical, thermoelectric and mechanical properties of the resulting composite materials. Thus, the purpose of this work is a complex study of the heat treatment effect on the properties of low-temperature composite $\text{Bi}_2\text{Te}_{2.8}\text{Se}_{0.2}$ - and $\text{Bi}_{0.5}\text{Sb}_{1.5}\text{Te}_3$ -based thermoelectric materials.

2. Experiment

Experimental samples were made using low-temperature thermoelectric materials: $\text{Bi}_2\text{Te}_{2.8}\text{Se}_{0.2}$ (n-type) and $\text{Bi}_{0.5}\text{Sb}_{1.5}\text{Te}_3$ (p-type). Copper oxide nanopowder ($\text{CuO-Cu}_2\text{O}$) in the amount of 0.1 wt.% was used as a nanostructured additive. An aqueous alkaline solution of sodium silicate was used as a binder, which acts as a matrix in the composite. To obtain a thermoelectric suspension, the

thermoelectric material was crushed to a powder state and mixed with a binder. The samples were formed by screen printing through a fluoroplastic mask, after which they were dried at room temperature for 24 hours. To remove excess moisture, the samples were annealed for 4 hours at a temperature of 110°C. To study the electrophysical and thermoelectric properties of the obtained samples, electrical contacts were formed by the method of electrochemical deposition. Ni and Cu were used as deposited materials, Ni was used as a diffusion barrier layer.

Based on the results of differential scanning calorimetry (Netzsch DSC 204 F1 Phoenix), the temperature range for heat treatment of materials was determined. The studies were carried out in the temperature range from room temperature to 400°C in an inert argon atmosphere. Thermogravimetric analysis of the obtained materials was also used.

Electrophysical and thermoelectric characteristics were studied for the formed samples. Measurements were carried out directly during the heat treatment process in an inert argon atmosphere, the heating rate was 5°C/min.

To study the thermoelectric characteristics of the manufactured samples, 2 measurements were carried out, in the first case the temperature dependence of the Seebeck coefficient was studied before heat treatment, in the second case, after the heat treatment. The measurements were carried out in the temperature range from room temperature to 100°C. The final stage was the study of the Hall effect.

3. Results and discussions

The electrophysical and thermoelectric properties of composite materials based on $\text{Bi}_2\text{Te}_{2.8}\text{Se}_{0.2}$ (n-type) and $\text{Bi}_{0.5}\text{Sb}_{1.5}\text{Te}_3$ (p-type) modified with nanodispersed copper oxides powder at a concentration of 0.1 wt.% were studied. In particular, the specific resistance, the Seebeck coefficient, and electrical conductivity were studied. The power factor was calculated based on the results obtained. The maximum power factor for the n-type legs with 0.1% $\text{CuO-Cu}_2\text{O}$ is 3.5 $\mu\text{W}/(\text{cm}\cdot\text{K}^2)$, for the p-type legs is 3.8 $\mu\text{W}/(\text{cm}\cdot\text{K}^2)$. The results of the study showed that the addition of nanopowder leads to a noticeable increase in the electron mobility in the n-type composite material and a slight decrease in their concentration. For the p-type

composite material, an increase in both the concentration and mobility of the majority charge carriers was observed.

4. Conclusions

In this work, the influence of heat treatment on the electrophysical, thermoelectric and mechanical properties of the fabricated composite $\text{Bi}_2\text{Te}_{2.8}\text{Se}_{0.2}$ - and $\text{Bi}_{0.5}\text{Sb}_{1.5}\text{Te}_3$ -based thermoelectric materials was investigated.

The obtained values of power factor for samples of composite thermoelectric materials with a matrix of aqueous alkaline sodium silicate solution are lower than for the synthesized material. However, the developed method of forming thermoelectric legs can be used for fabrication of flexible thermoelectric generators.

Acknowledgements

This work was supported by Russian Science Foundation (project number 24-19-00158).

References

- [1] I. Voloshchuk, A. Babich, S. Pereverzeva, D. Terekhov, A. Sherchenkov Journal of Central South University **30** (2023) 2906.

***In-situ* bonding reorganization and self-reinforcement of Si-Zr-O amorphous under high temperature marine environment**

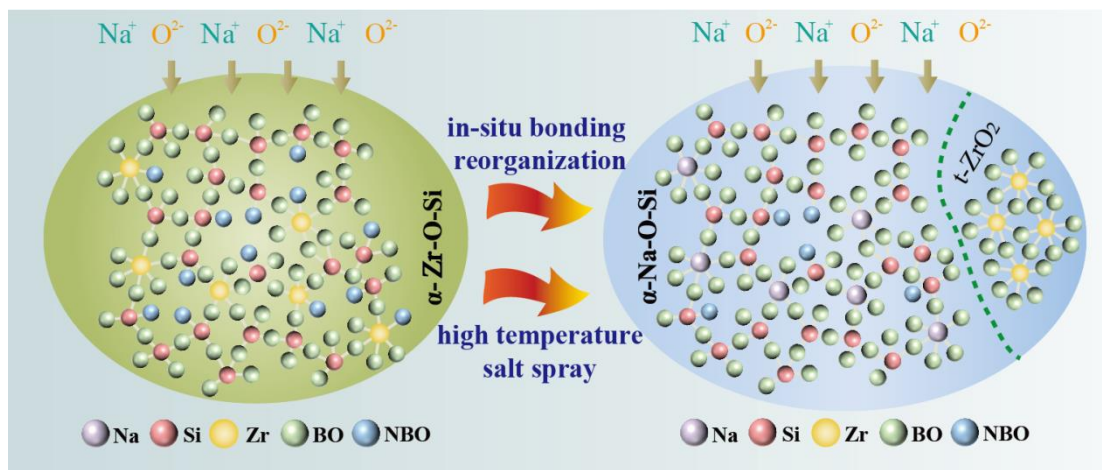
Guoqin Cao, Junhua Hu*

School of Materials Science and Engineering, Zhengzhou University, Zhengzhou 450001, China

*e-mail: hujh@zzu.edu.cn

Abstract: Material failure in high-temperature salt-spray environments predominantly aroused from the strong erosion of surface passivation layer, such as Cr_2O_3 and TiO_2 . Here, a novel amorphous Si-Zr-O (SZO) coating was designed against this extreme environment. Inspired by the biomineralization behavior, an *in-situ* atomic bonding regulation mechanism was proposed. The Na absorption coupled with *in-situ* chemical bonding reorganization was identified and the SZO coating was self-reinforced to the structure of amorphous Si-Na-O and nanocrystalline t-ZrO_2 ($\text{t-ZrO}_2/\alpha\text{-SNO}$). Molecular dynamics (MD) calculations indicated that the chemical stability and barrier property of amorphous Si-Na-O was closely related to the amount of Na content and bridging oxygen. Electron energy loss spectroscopy (EELS) analysis demonstrated that the appropriate Zr content in SZO facilitated optimal Na absorption, which ensured sufficient bridging oxygen and reduced the reactivity of the silicon site, thereby enhancing both chemical stability and barrier property. The optimized SZO coating demonstrated significant improvement in corrosion resistance, maintaining structural integrity for 100 h in a 600°C salt spray environment.

Keywords: Na absorption, *in-situ* bonding reorganization, EELS, MD calculations, Salt spray environment



***In-situ* formation of a metal–organic interphase for interfacial kinetic reconstruction in low-temperature aqueous aluminum–air batteries**

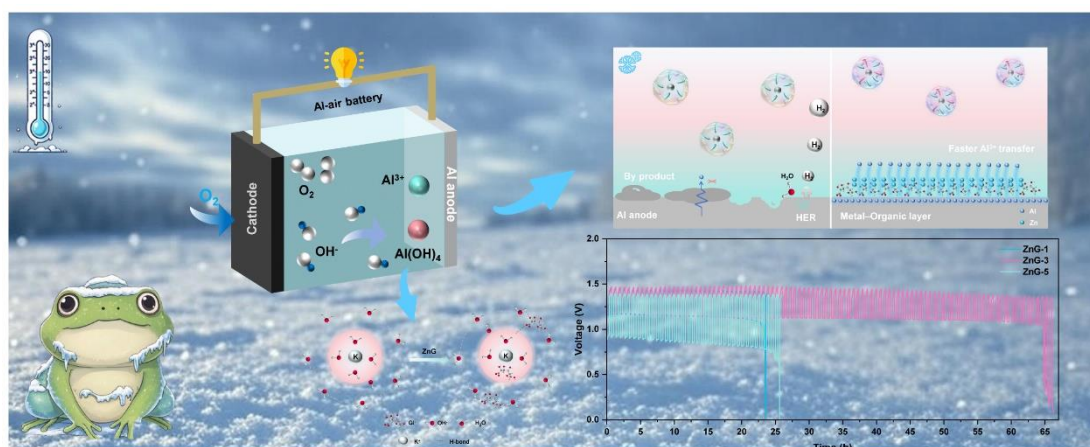
Jinjin Ban, Junhua Hu*

School of Materials Science and Engineering, Zhengzhou University, Zhengzhou 450001, China

*e-mail: hujh@zzu.edu.cn

Abstract: The operation of aluminum–air batteries (AABs) at sub-zero temperatures is significantly hindered by the poor ionic conductivity of aqueous electrolytes and sluggish Al^{3+} interfacial kinetics. Herein, a biomimetic molecular regulation strategy is proposed by introducing zinc gluconate (ZnG) as a multifunctional additive into aqueous electrolytes, enabling the construction of a robust anti-freezing system suitable for low-temperature operation. ZnG effectively reconstructs the hydrogen-bond network among water molecules, modulates the solvation structure, and lowers the freezing point while enhancing ionic conductivity. Simultaneously, ZnG facilitates the in situ formation of a metal–organic (MO) composite interfacial layer on the aluminum anode, replacing the conventional passivation film. This MO layer promotes Al^{3+} transport, accelerates interfacial charge-transfer kinetics, and alleviates low-temperature polarization. The optimized ZnG-based electrolyte exhibits excellent discharge capacity and cycling stability even at $-40\text{ }^{\circ}\text{C}$. This study elucidates, at the molecular level, a synergistic mechanism between solvation structure regulation and interfacial engineering, offering a novel theoretical framework and design strategy for high-performance aqueous aluminum batteries operating under extreme cold conditions.

Keywords: aluminum–air batteries, metal–organic (MO) composite, interfacial layer, interfacial engineering



Diffusion-driven photovoltaic effect in Mn/SiO₂/n-Si

Bondarev I.A.*, Rautskii M.V., Volkov N.V., Lukyanenko A.V., Yakovlev I.A., Varnakov S.N.,
Tarasov A.S.

Kirensky Institute of Physics, Federal Research Center KSC SB RAS, Krasnoyarsk, 660036 Russia

*e-mail: bia@iph.krasn.ru

Abstract. The study is devoted to the lateral photovoltaic effect (LPE) in a Mn/SiO₂/n-Si structure at cryogenic temperatures, revealing that carrier diffusion, rather than drift, determines the photovoltage generation due to a weak Schottky barrier. Experimental results closely match a diffusion-based model that incorporates wavelength-dependent absorption and carrier transport. Additionally, a magnetic hysteresis with a ~200 Oe coercive field suggests the formation of a weakly ferromagnetic MnSi phase at the interface. These findings highlight the potential of diffusion-driven LPE systems for position-sensitive photodetectors and magneto-optoelectronic applications, especially in low-temperature environments.

1. Introduction

The lateral photovoltaic effect (LPE) in semiconductor-based structures offers promising applications in position-sensitive photodetectors, spintronics, and magneto-optoelectronics. It is typically observed when a non-uniform illumination of a semiconductor creates a voltage difference between spatially separated contacts. This voltage, termed lateral photovoltage (LPV), arises due to the spatial separation of photogenerated carriers, which move under the influence of built-in electric fields and diffusion gradients. While LPE has been extensively studied at room temperature and under standard conditions, its behavior in complex metal/insulator/semiconductor (MIS) systems at low temperatures—especially under the influence of magnetic fields—remains insufficiently explored. Of particular interest is the role of carrier diffusion in generating LPV in systems where band bending is weak and drift effects are suppressed. This work presents a detailed investigation of a diffusion-driven LPE in a Mn/SiO₂/n-Si hybrid structure, focusing on low-temperature conditions and magnetic field influence.

2. Experiment

The experimental structure was fabricated using a phosphorus-doped n-type silicon substrate (doping level ~10¹⁵ cm⁻³), thermally oxidized to form a ~1.5 nm SiO₂ layer, and a 15 nm Mn film was deposited on top of the structure via molecular beam epitaxy (MBE). TEM image of the structure is shown on fig. 1.

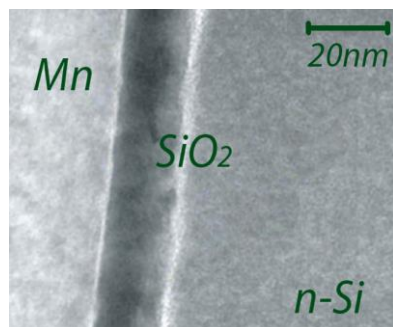


Fig. 1. Cross-sectional transmission electron microscopy (TEM) images of the Mn/SiO₂/n-Si structure.

Electrical contacts were formed both on top of the film and on backside of the substrate in order to measure photovoltage in both lateral and transverse directions.

Optical irradiation was applied using a tunable halogen lamp and semiconductor lasers. The generated photovoltages were measured across varying temperatures, wavelengths, irradiation powers, and magnetic fields. Additionally, an MnSi layer was synthesized on a similar substrate to examine potential interfacial ferromagnetic phases that could influence carrier dynamics. More detailed information about the samples can be found in [1].

3. Results and discussions

One of the most significant findings of this study is the confirmation that, in the Mn/SiO₂/n-Si structure, the LPE at cryogenic temperatures (down to 17 K) is predominantly driven by carrier diffusion rather than drift. This is a direct consequence of the low Schottky barrier height (~0.05 eV at helium temperatures), which significantly weakens the internal electric field responsible for separating photogenerated electron-hole pairs. For comparison, typical MIS structures show Schottky barriers in the range of 0.1 to 0.8 eV [2-4], creating stronger built-in fields and dominant drift currents. In the absence of such fields, photogenerated carriers move primarily due to concentration gradients—a mechanism that can be described using standard diffusion equations.

To quantify this behavior, a one-dimensional diffusion model was used, incorporating carrier generation as a function of light absorption depth and wavelength-dependent quantum efficiency. Carriers are generated at specific depths corresponding to the absorption profiles of the incident photons, and their subsequent diffusion toward the contacts results in measurable photovoltage. The absorption coefficients and quantum efficiency values for silicon were taken from literature [5,6]. The carrier movement in transverse direction was described using equations:

$$n(x) = n_i e^{-\frac{(x-x_l)^2}{L_n^2}} \text{ and } p(x) = n_i e^{-\frac{(x-x_l)^2}{L_p^2}} \quad (1)$$

Where $n(x)$ and $p(x)$ are concentrations of electrons and holes, respectively, at the vertical coordinate x . Simulation results showed that the difference in carrier concentrations between the illuminated and non-illuminated sides $\Delta[n(x) - p(x)]$ varies with wavelength, with sign reversals occurring when the dominant photogeneration shifts from one side of the substrate to the other. A comparison between the simulated LPV and experimental measurements at 28.5 K

(fig. 2) showed good agreement, validating the diffusion-dominant interpretation.

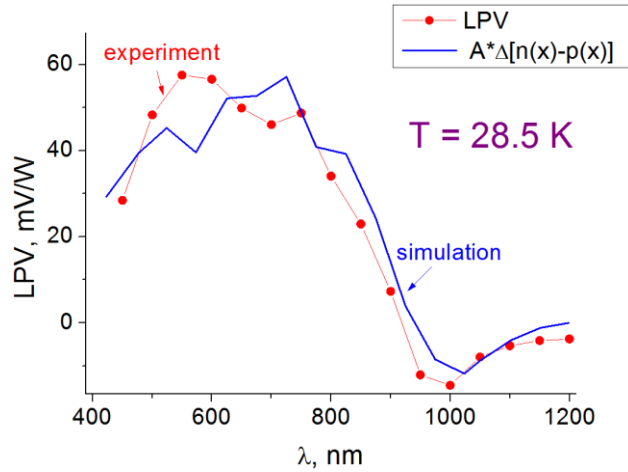


Fig. 2. Experimental $LPV(\lambda)$ curve in $Mn/SiO_2/n-Si$ at $T=28.5K$ measured from the substrate backside (blue). Simulated $LPV(\lambda)$ curve (red dots).

Another important finding involves the observation of hysteresis behavior of the magnetic field dependence of the LPV at $T = 17K$ (fig.3). It indicates the presence of a weak ferromagnetic phase at the SiO_2/Si interface with a coercive field B_c of approximately 200 Oe. Similar magnetic hysteresis behavior was observed in ferromagnetic MnSi film grown on Si. Although Mn is non-ferromagnetic, interfacial reactions during MBE growth and post-deposition annealing may lead to the formation of MnSi phase near the surface of Si substrate. The presence of this phase within or near the carrier transport region could introduce additional magnetoresistance-like effects, influencing the LPV.

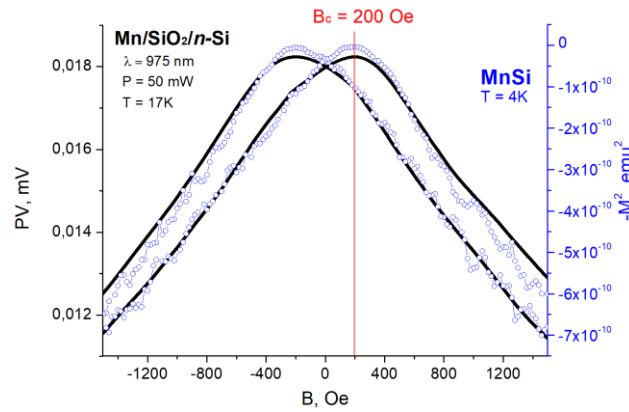


Fig. 3. Black curve represents magnetic field dependence of the LPV in $Mn/SiO_2/n-Si$ structure. Blue circles show the square of magnetization as a function of magnetic field in $MnSi/Si$.

4. Conclusions

This study demonstrates that in the $Mn/SiO_2/n-Si$ hybrid structure, the lateral photovoltaic effect at low temperatures is governed primarily by diffusion processes due to weak Schottky barrier-induced electric field. The observed photovoltage spectra are well described by a simple diffusion model, emphasizing the importance of absorption depth and carrier transport characteristics. The magnetic hysteresis in the field dependence points to the presence of interfacial ferromagnetic phase. These findings highlight the potential of diffusion-driven LPE systems in

developing advanced optoelectronic devices, particularly for cryogenic and magnetically active environments. Future work may extend this approach to explore spin-polarized transport, temperature-dependent band alignment, and integration into functional spintronic devices.

Acknowledgements

We thank M.N. Volochaev for assistance with the electron microscopy studies.

References

- [1] I.A. Bondarev, M.V. Rautskii, N.V. Volkov, A.V. Lukyanenko, I.A. Yakovlev, S.N. Varnakov, A.S. Tarasov. *Mater. Sci. Semicond. Process.* 188(2025)109237.
- [2] K. Sugiura, R. Nakane, S. Sugahara, M. Tanaka. *Appl. Phys. Lett.* 89(2006)072112.
- [3] A. Tataroglu, S. Altindal. *J. Alloys Compd.* 479(2009)893.
- [4] S.H. Kim, K.H. Han, G.S. Kim, S.G. Kim, J. Kim, H.Y. Yu. *ACS Appl. Mater. Interfaces.* 11(2019)6230.
- [5] M.A. Green, M.J. Keevers. *Prog. Photovolt.: Res. Appl.* 3(1995)189.
- [6] C.R. Osterwald, M. Campanelli, T. Moriarty, K.A. Emery, R. Williams. *IEEE J. Photovolt.* 5(2015)1692.

Mg₂Si_xSn_{1-x} film growth by ultra-fast deposition of Mg onto (Si-Sn)/Si structure with gradT

Gouralnik A.S.^{*1}, Subbotin E.Yu.¹, Chernev I.M.¹, Kitan S.A.¹, Gerasimenko A.V.², Ustinov A.Yu.², Kozlov A.G.³, Volkova L.S.⁴, Dudin A.A.⁴, Poliakov M.V.^{4,5}

¹ Institute of Automation and Control Processes FEB RAS, 5 Radio St., Vladivostok 690041, Russia

² Institute of Chemistry FEB RAS, 159, 100-letia Av., Vladivostok 690041, Russia

³ Far Eastern Federal University, 8 Sukhanova St., Vladivostok 690950, Russia

⁴ Institute of Nanotechnology of Microelectronics, Moscow, Russia

⁵ Merzhanov Institute of Structural Macrokinetics & Materials Science, Chernogolovka, Russia

*e-mail: fun_era@mail.ru

Abstract. We are demonstrating an application of two efficient original approaches, High-Temperature Ultra-Fast Deposition (HT-UFD) and sample with gradT, for pulsed growth of the Mg₂Si-based compound Mg₂Si_{1-x}Sn_x. Results of the exothermic process of compound formation at different high temperatures (HT) are directly observed by HRTEM and SEM-EDX in different zones of the Si sample with gradT. The intensity of the ultra-fast process depends on the initial local temperature; the process results in different structure and amount of the compound formed in different sample zones.

1. Introduction

Film growth and surface/interface processes are crucial in many modern technologies, including Si-based microelectronics, solar cells, thermoelectrics etc. We are demonstrating an application of two original approaches effective in film synthesis, *gradT* and HT-UFD, for growth of the Mg₂Si-based compound Mg₂Si_{1-x}Sn_x. The approaches are shown in Fig.1 and will be demonstrated in a short real time movie. The silicide Mg₂Si_{1-x}Sn_x attracts a significant attention of researchers since it is relatively light, consists of ecologic, abundant and rather cheap components and has good perspectives for applications in thermoelectric elements, solar cells etc. [1]. However, the synthesis of Mg₂Si_{1-x}Sn_x films on Si surface is not a simple task since Mg is volatile at rather low T while Sn melts and forms droplets. In addition, in certain ranges of compositions and temperatures, Mg₂Si_{1-x}Sn_x tends to decompose into precipitates [2]. To form such precipitates of supercritical size, the component atoms must be redistributed by diffusion over some distance within the mixture; this process must take a significant time. Thus, to understand the mechanism of the synthesis process and get control upon it, the investigations of the dependences of the spatial redistribution of components on temperature and time are highly required.

It has been shown by Tatsuoka e.a. that intense flows of Mg onto hot Si (due to high vapor pressure of Mg) result in Mg₂Si formation [3]. We demonstrated that HT-UFD of Mg onto Si allows to form high crystal quality Mg₂Si films within very short times ~0.1 – 20 s [4-7]; this could be used to reduce the redistribution of Sn, Si and formed compounds in the film. As we have demonstrated [7], Si samples having wedge-shaped T distributions on the surface (see Fig.1) can be used to obtain an entire T-dependence of a process in one experiment. The combination of this method with HT-UFD is easy and natural. In the present work, we apply the combination of *gradT* and HT-UHV methods to study the process of synthesis of Mg₂Si_{1-x}Sn_x by ultra-fast deposition of Mg onto Si-Sn mixture in the conditions far from equilibrium.

2. Experiment

At first the mixture Si_{1-x}Sn_x was co-deposited in UHV on the clean Si(111) in 10 portions (to reduce the diffusion in the sample heated by the long-lasting irradiation from Si and Sn sources). To synthesize Mg₂Si_{1-x}Sn_x, the sample T was risen up to the range of ~300 – 340 °C during 4 s and a large single portion of Mg was pulse-deposited onto the substrate surface. At the pulse moment, the sample heating current was reduced; in ~4 s after the pulse, the sample heating was stopped. We shall present a short real-time movie illustrating this process. Based on literature data and our analogous experiments on Mg₂Si growth on Si by Mg HT-UFD, it can be suggested that the above procedure should result in a combustion- or just explosion-like exothermic reaction of Mg₂Si_{1-x}Sn_x synthesis [4-9]. The obtained sample was cut into 5 parts to separately study the films formed within different T ranges.

3. Results and discussions

Some HRTEM and EDX results are presented in Figs.2 and 3. It is seen that for the film formed at higher T the entire Si-Sn mixture has been completely spent for Mg₂Si_{1-x}Sn_x formation and the excess Mg penetrated deeper into the Si(111) substrate where it formed Mg₂Si having lighter contrast in Fig. 2 (see the image for zone 3). For high-T sample zones, Mg, Si and Sn are relatively uniformly intermixed within the film layers. On the contrary, for lower T, relatively thinner and non-uniform film formed (see the images for zones 1 and 5). The Z-contrast evidence that some unreacted Mg remained on the surface, then it oxidized in the atmosphere. For low-T films, the Si-rich and Sn-rich compounds tend to separate mostly by the nucleation and growth mechanism (tentatively, due to Sn separation from Si during the mixture co-deposition and/or relatively longer process of Mg diffusion and compound formation in low-T zones).

It can be concluded that for higher initial T, the compound formation process reached some higher T corresponding to the higher intensity of the exothermic reaction. Then the formed compound quenched due to the rapid sample cooling. At lower initial T, the reaction was less intensive, the mixture was cooler, and the relatively

longer process of the film formation included the local redistribution of Sn concentration, which resulted in formation of Si- and Sn-rich components $\text{Mg}_2\text{Si}_{1-x}\text{Sn}_x$ visible in Figs. 2 and 3 (zones 1 and 5). Thus, it was demonstrated that the microstructure of the formed $\text{Mg}_2\text{Si}_{1-x}\text{Sn}_x$ can be tuned by the temperature of the compound formation process. This is important since the microstructure determines the electrophysical parameters, heat conductance and thermoelectric properties of the compound.



Fig. 1. Example of a sample with $\text{grad}T(x)$ (for illustration).

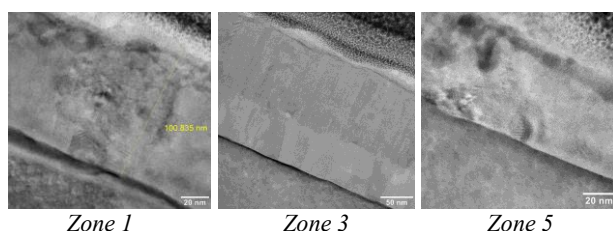


Fig. 2. Cross-sectional HRTEM images of the film.

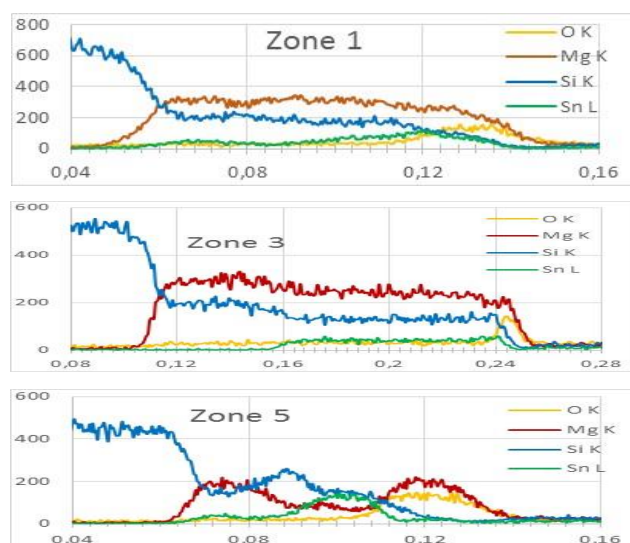


Fig. 3. In depth distribution of elements for different zones of the sample (see T distribution along the sample in Fig.1).

4. Conclusions

An easy and highly efficient way to study dependences of surface/interface processes on temperature is demonstrated. Different products of these processes obtained at different temperatures are directly observed in different points of the sample. The entire dependence of the $\text{Mg}_2\text{Si}_{1-x}\text{Sn}_x$ compound formation on temperature can be studied in one experiment. Thus, it has been demonstrated that the optimal temperature range for synthesis of the film having the required morphology can be found in a single experiment. The combination of HT-UFD with $\text{grad}T$ samples proved to be a very efficient and promising experimental approach.

Acknowledgements

This work was not supported by any grants; it was carried out within the Institute budget work (item FFWF-2021-0001). A.G.K. acknowledges the support of the Russian Ministry of Science and Higher Education (State Assignment No. FZNS2023-0012).

References

- [1] J.He, T.M.Tritt, Advances in thermoelectric materials research: Looking back and moving forward. *Science* **357** (2017) eaak9997.
- [2] Su-In Yi, R. Arroyave, Chonghoo Yu e.a. Strain-induced Suppression of the Miscibility Gap in Nanostructured Mg_2Si - Mg_2Sn Solid Solutions. [10.1039/C8TA05798B](https://doi.org/10.1039/C8TA05798B).
- [3] J. Hu, Y. Sato, T. Hosono, H. Tatsuoka. *Vacuum* **83**, 2009, 1494.
- [4] A.S. Gournalnik, A.M. Maslov, S.A. Dotsenko, A. Yu. Ustinov, A.V. Shevlyagin, I.M. Chernev, V. A. Il'iashenko, S.A. Kitan, E.A. Koblova, K.N. Galkin, N.G. Galkin, A.V. Gerasimenko. Formation of Mg_2Si at high temperatures by fast deposition of Mg on Si(111) with wedge-shaped temperature distribution. *Appl. Surf. Sci.* **439** (2018), 282. [10.1016/j.apsusc.2017.12.237](https://doi.org/10.1016/j.apsusc.2017.12.237)
- [5] Gournalnik, A.S.; S.A.; Shevlyagin, A.V.; Chernev, I.M.; Ustinov, A. Yu.; Gerasimenko, A.V., Gutakovskii, A.K. Synthesis of crystalline Mg_2Si films by ultrafast deposition of Mg on Si(111) and Si(001) at high temperatures. *Mg/Si intermixing and reaction mechanisms. MatChemPhys.* **258** (2021), 123903. [10.1016/j.matchemphys.2020.123903](https://doi.org/10.1016/j.matchemphys.2020.123903)
- [6] A.S. Gournalnik, Yu.V. Luniakov. Mg/Si interface reaction: How and Why. Towards rational technologies of Mg/Si film growth for energy conversion. *Vacuum* **196**, (2022), 110798. [10.1016/j.vacuum.2021.110798](https://doi.org/10.1016/j.vacuum.2021.110798)
- [7] A.S. Gournalnik, I.M. Chernev, A.M. Maslov, S.A. Dotsenko. A promising experimental paradigm and mechanism of Mg_2Si UHV growth on a non-uniformly heated Si(111) sample. *Vacuum* **202** (2022), 111193 [10.1016/j.vacuum.2022.111193](https://doi.org/10.1016/j.vacuum.2022.111193)
- [8] Q. Zhang, X. Tang e.a. Energy-Efficient Synthesis and Superior Thermoelectric Performance of Sb-doped $\text{Mg}_2\text{Si}_{0.3}\text{Sn}_{0.7}$ Solid Solutions by Rapid Thermal Explosion. *Materials Research Bulletin* **128** (2020) 110885
- [9] E. Godlewska, K. Mars, R. Mania, S. Zimowski, Combustion synthesis of Mg_2Si . *Intermetallics* **19** (2011), 1983. [10.1016/j.intermet.2011.06.013](https://doi.org/10.1016/j.intermet.2011.06.013)

Thermoelectric properties of Mg_3Bi_2 flexible films

Subbotin E.Yu.^{*1}, Khoroshilov D.A.¹, Goroshko D.L.¹, Prokopeva G.A.¹, Kozlov A.G.²,
Prihodchenko A.V.², Chernov I.M.¹, Lisenkov O.E.¹, Sinotova S.A.¹, Galkin N.G.¹

¹ Institute of Automation and Control Processes, 5 Radio St., Vladivostok 690041, Russia

² Far Eastern Federal University, 8 Sukhanova St., Vladivostok 690950, Russia

*e-mail: jons712@mail.ru

Abstract. In this work, a method for synthesizing Mg_3Bi_2 on a polyimide substrate was developed and thermoelectric properties of such composite were investigated. The experiment was carried out under high vacuum conditions by solid-phase epitaxy with recrystallization annealing at 300 °C. Thermoelectric properties of the material were studied in the temperature range from 80 to 450 K. The highest value of the power factor was measured at 300 K and was $3.8 \mu\text{W}/(\text{cm} \times \text{K}^2)$, the Seebeck coefficient and specific electrical conductivity were $47.8 \mu\text{V/K}$ and 1656 S/cm , respectively. The Mg_3Bi_2 film demonstrates high plasticity, retains conductivity under strong bending and a large number of bending-unbending cycles.

1. Introduction

The intensive introduction of wearable low-power electronics into everyday life has given impetus to research and development of thermoelectric converters operating in the room temperature region. In this work, Mg_3Bi_2 was chosen for a number of reasons. Firstly, Mg_3Bi_2 demonstrates competitive thermoelectric properties in the room temperature region [1]. Secondly, the chemical elements in the basis of this material are harmless to humans and the environment and are relatively cheap. Thirdly, magnesium bismuthide has plasticity [2], which allows even bulk samples to be deformed without damaging the crystal and disrupting conductivity. In other words, the material is an excellent candidate for the role of low-temperature thermoelectric converters for wearable electronics devices.

2. Experiment

The experiment was carried out under high vacuum conditions (1×10^{-6} mbar) by solid-phase epitaxy. For this purpose, magnesium and bismuth were co-deposited on a pre-cleaned polyimide substrate, followed by recrystallization annealing at 300 °C. Confirmation of the reaction of chemical material formation was carried out using Raman spectroscopy (Figure 1) and X-ray diffraction. Raman shifts at 53.4 cm^{-1} and 83.4 cm^{-1} indicate successful reaction [3].

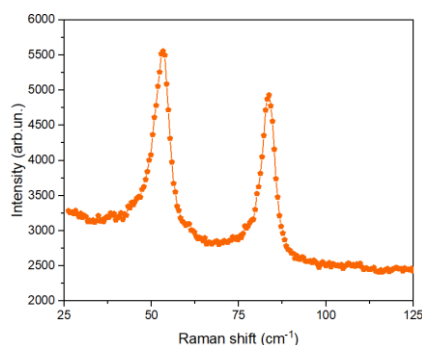


Fig. 1. Raman spectra of the sample with two peaks at 53.4 cm^{-1} and 83.4 cm^{-1} that relate to Mg_3Bi_2 .

Thermoelectrical measurements were carried out by four-probe differential method from 80 to 450K temperature range.

3. Results and discussions

It has been established that the Seebeck coefficient has positive values in the entire measured temperature range. According to literature data, the sign of the main charge carriers depends on the magnesium content in the material: with an excess of magnesium, electron conductivity is observed, and with a deficiency, hole conductivity [1].

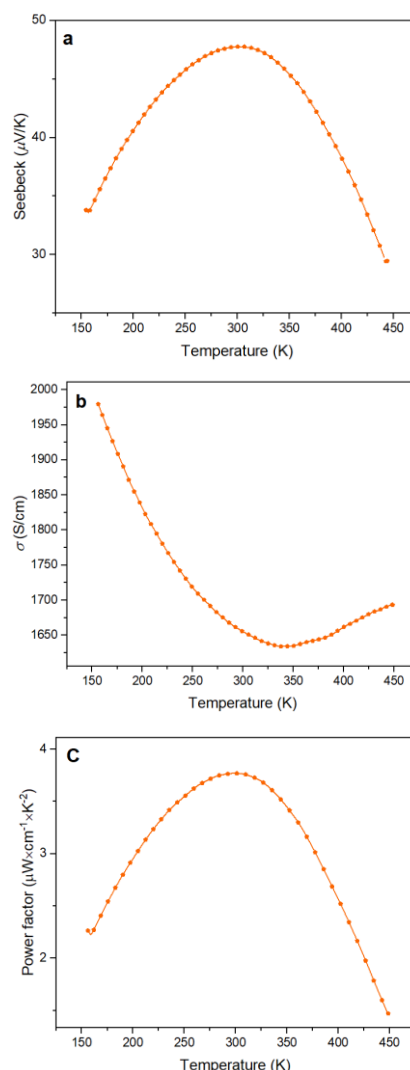


Fig. 2. Thermoelectric properties of Mg_3Bi_2 formed on polyimide tape: a – thermoelectric coefficient, b – conductivity, c – power factor.

The highest value of the power factor was measured at 301K and is $3.8 \mu\text{W}/(\text{cm}\times\text{K}^2)$, the thermoelectric coefficient and conductivity at this temperature are $47.8 \mu\text{V}/\text{K}$ and $1656 \text{ S}/\text{cm}$, respectively. It was found that the samples keep their conductivity under repeated deformation (bending cycles) and low bending angle.

4. Conclusions

In this work, the prospect of using Mg_3Bi_2 material for developing flexible planar thermoelectric converters of low-temperature range was demonstrated. Samples were formed by solid-phase epitaxy at 300°C . The highest conductive properties were demonstrated at room temperature, the power factor, thermoelectric coefficient and specific conductivity were $3.8 \mu\text{W}/(\text{cm}\times\text{K}^2)$, $47.8 \mu\text{V}/\text{K}$, $1656 \text{ S}/\text{cm}$, respectively. The sample demonstrates high plasticity and retains conductivity under high deformations.

Acknowledgements

The work was supported by the Russian Ministry of Science and Higher Education for the state task, Projects No. FZNS-2023-0012 and No. FWFW-2021-0002.

References

- [1] J. Mao, H. Zhu, Z. Ding, Z. Liu, G.A. Gamage, G. Chen, Z. Ren. *Science*, 365(2019)6452.
- [2] P. Zhao, W. Xue, Y. Zhang, S. Zhi, X. Ma, J. Qiu, Q. Zhang. *Nature*, 631(2024)8022.
- [3] W. Fang, W. Zhu, Y. Shao, P. Zheng, J. Si. *Applied Surface Science*, 596(2022)153602.

Nonlinear resistance drift kinetics in $\text{Ge}_2\text{Sb}_2\text{Te}_5$ thin films

Ermachikhin A.V.^{*1,2}, Vorobyov Y.V.^{1,3}, Trusov E.P.¹, Litvinov V.G.¹

¹ Ryazan State Radio Engineering University, Gagarin St. 59, Ryazan 390005, Russia

² Scientific-Manufacturing Complex Technological Centre, Shokin sq. 1, Zelenograd, Moscow 124498, Russia

³ National Research University of Electronic Technology, Shokin sq. 1, Zelenograd, Moscow 124498, Russia

*e-mail: al.erm@mail.ru

Abstract. This study focuses on the resistance changes in $\text{Ge}_2\text{Sb}_2\text{Te}_5$ thin films after thermal annealing. We demonstrate that after annealing at temperatures above 100°C , the resistance continues to evolve even after cooling, unlike annealing at lower temperatures. A total of seven annealing cycles (2 hours each) were performed in the range of $70\text{--}130^\circ\text{C}$. During the eighth annealing step, approximately 30 minutes after reaching 140°C , the sample began to transition into the crystalline phase. After which a strong increase in current occurred, reaching the maximum possible current for the picoammeter. Reducing the DC voltage across the film allowed the current to be measured and proved that a phase change of the film material had occurred.

1. Introduction

Phase-change materials (PCMs) are widely used for data storage. The conventional approach, where a single bit of information is encoded in the amorphous and crystalline states, limits storage density. In recent years, research has focused on increasing the stored information per cell in phase-change memory (PCM) [1, 2]. One of the major challenges in achieving multilevel storage is resistance drift over time [3], which manifests as a gradual increase in resistance, particularly at elevated temperatures. Studies have shown that this phenomenon persists even at room temperature [4]. Several approaches to mitigate resistance drift have been proposed, primarily based on device-level engineering [5-8].

However, the development of reliable multilevel PCM requires a deeper understanding of resistance drift mechanisms at the material level. A key outstanding question concerns how thermal history affects the drift kinetics. In this work, we investigate temperature thresholds for irreversible resistance changes in $\text{Ge}_2\text{Sb}_2\text{Te}_5$ (GST) thin films and analyze the relationship between resistance drift and crystallization onset at elevated temperatures. Our findings help clarify the thermal stability limits of GST's amorphous phase and provide criteria for optimizing multilevel PCM devices.

2. Experiment

For resistance measurements before and after annealing, as well as for conducting the annealing process itself, we employed a research system consisting of a closed-cycle cryostat (Janis CCS-400/204N) and a picoammeter/voltage source (Keithley 6487) [9]. Sample resistance was measured simultaneously with temperature scanning under constant voltage conditions.

The thin film was deposited by DC magnetron sputtering using a commercial polycrystalline target with 99.99% purity. X-ray diffraction confirmed the as-deposited film to be amorphous. The film thickness was approximately 130 nm.

The measurement protocol began with cooling to -160°C (Figure 1), followed by a brief temperature stabilization period and subsequent heating at a constant rate of $2^\circ\text{C}/\text{min}$. Upon reaching the target annealing temperature, the temperature was maintained with $\pm 0.01^\circ\text{C}$ precision using a LakeShore 335 temperature controller for 2 hours. In Figure 1, the horizontal parallel lines beginning

at approximately 200 minutes represent these isothermal annealing periods. This was followed by an additional cooling/heating cycle, though in this case heating was limited to 60°C . The final step involved cooling to room temperature.

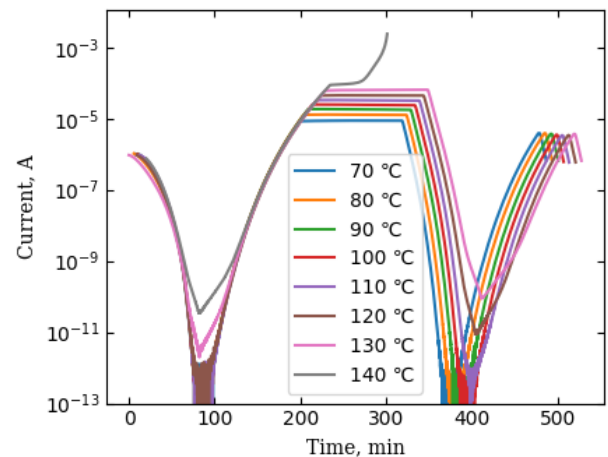


Fig. 1. Current vs. time dependence during the experiment. The current changes follow the temperature profile, which remained consistent across all experimental runs.

3. Results and discussions

As evident from Figure 1, annealing up to 120°C had minimal impact on the overall current profile, where the current at minimum temperature remained at noise level. However, above 120°C , the current increased dramatically by approximately one order of magnitude (brown curve around 400 minutes in Figure 1). Following further annealing at 130°C , an additional order-of-magnitude current increase was observed.

Interestingly, during the actual isothermal annealing periods, significant current growth only occurred at 70°C and 130°C (Figure 2). The current values were normalized by dividing each data point by the mean current during isothermal annealing at each respective temperature, enabling direct comparison of temporal current dynamics across temperature regimes. The high-temperature changes can be attributed to the onset of crystallization. The current variation at 70°C , however, may be associated with the rejuvenation phenomenon in non-crystalline materials, previously introduced in the context of resistance drift [10].

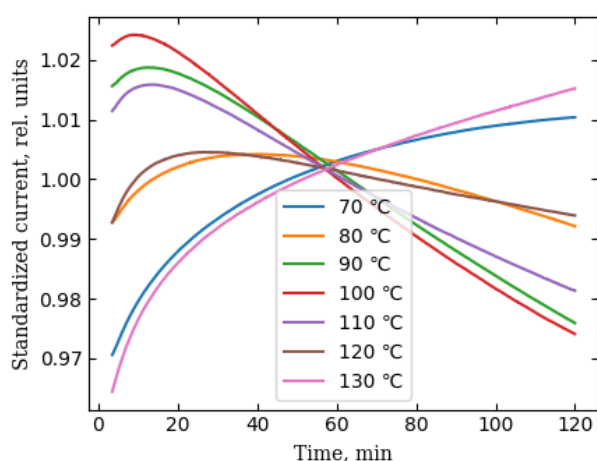


Fig. 2. Time evolution of normalized current during multi-step annealing (70–130°C).

Figure 1 clearly demonstrates that following high-temperature annealing (130°C), the measured current at low temperatures (around 400 minutes) remains substantially higher compared to the initial cooling cycle (approximately 90 minutes). This change in current indicates long-term changes in the electronic structure of the material caused by the heat treatment.

A direct comparison of these effects is presented in Figure 3, which shows two pairs of current-time (effectively current-temperature) dependencies: The first pair corresponds to measurements taken after 130°C annealing - one recorded immediately after processing and another obtained approximately 15 hours later (prior to subsequent 140°C annealing), representing an overnight aging period at room temperature. The second pair shows data following 100°C annealing, where such effects are less prominent. These comparative measurements reveal significant time-dependent evolution of electrical properties even without additional thermal processing, suggesting either progressive structural relaxation or metastable phase formation during the aging period.

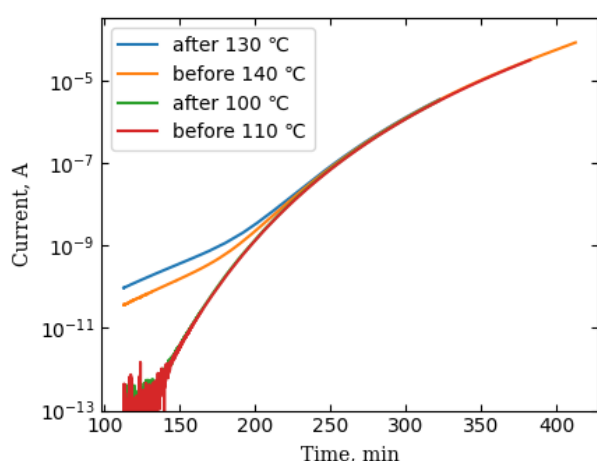


Fig. 3. Current vs. heating time dependence after different annealing treatments.

The available temperature-dependent conductivity data enables estimation of the Fermi level's thermal evolution [11]. Assuming hole-dominated band conduction in these materials [12], the observed behavior could be attributed to a nonlinear temperature dependence of the energy

separation between the Fermi level and valence band edge ($E_F - E_V$). Notably, the conductivity decrease corresponds to a widening of this energy gap.

4. Conclusions

Thermal annealing experiments on GST films revealed a nonlinear evolution of resistance drift with temperature. Initial annealing at 70°C produced resistance reduction, followed by a subsequent increase that peaked at 100°C, where the maximum resistance growth (corresponding to current decrease) was observed. Above this temperature, the rate of resistance increase gradually slowed until 130°C, where the trend reversed into resistance reduction – a clear signature of crystallization onset. Post-annealing room-temperature relaxation led to further resistance increases. These electrical changes directly correlate with changes in the Fermi level relative to the valence band, demonstrating how heat treatment tunes the electronic structure of phase change materials. The observed non-monotonic behavior reflects competing mechanisms between structural relaxation at lower temperatures (<100°C) and crystallization processes dominating at elevated temperatures (>130°C).

Acknowledgements

This work was supported by the Russian Science Foundation grant No. 24-79-10137 (<https://rscf.ru/en/project/24-79-10137/>) and utilized equipment from the Regional Centre for Probe Microscopy of Ryazan State Radio Engineering University.

References

- [1] A. Athmanathan, M. Stanisavljevic, N. Papandreou, H. Pozidis, E. Eleftheriou. *IEEE J. Emerg. Sel. Top. Circuits Syst.* **6** (2016) 87.
- [2] J. Meng, Y. Gui, B. M. Nouri, X. Ma, Y. Zhang, C.-C. Popescu, M. Kang, M. Miscuglio, N. Peserico, K. Richardson, J. Hu, H. Dalir, V. J. Sorger. *Light Sci Appl* **12** (2023) 189.
- [3] A. Pirovano, A.L. Lacaita, F. Pellizzer, S.A. Kostylev, A. Benvenuti, R. Bez. *IEEE Trans. Electron. Devices* **51** (2004) 714–9.
- [4] J. Pries, C. Stenz, S. Wei, M. Wuttig, P. Lucas. *J. Appl. Phys.* **135** (2024) 135101.
- [5] W.W. Koelmans, A. Sebastian, V.P. Jonnalagadda, D. Krebs, L. Dellmann, E. Eleftheriou. *Nat. Commun.* **6** (2015) 8181.
- [6] K. Ding, J. Wang, Y. Zhou, H. Tian, L.L. Lu, R. Mazzeo, C. Jia, W. Zhang, F. Rao, E. Ma. *Science* **366** (2019) 210–5.
- [7] R. Zhao, M. He, L. Wang, Z. Chen, X. Cheng, H. Tong, X. Miao. *Sci. China Mater.* **65** (2022) 2818–25.
- [8] Y. Lv, Q. Wang, H. Chen, C. Xie, S. Ni, X. Li, Z. Song. *Micromachines (Basel)* **12** (2021) 1085.
- [9] A.V. Ermachikhin, V.G. Litvinov, A.D. Maslov. *The measuring systems of semiconductor structures and its software.* SIBCON (2015).
- [10] J. Pries, C. Stenz, L. Schäfer, A. Gutsche, S. Wei, P. Lucas, M. Wuttig. *Adv. Funct. Mate.* **32** (2022) 2207194.
- [11] Y. Vorobyov, A. Ermachikhin, A. Yakubov, E. Trusov, M. Fedyanina, P. Lazarenko, S. Kozyukhin. *J. Phys. D: Appl. Phys.* **54** (2021) 315302.
- [12] N.F. Mott, E.A. Davis. *Electronic Processes in Non-crystalline Materials* 2nd edn (Oxford : Oxford University Press) (1979).

Thermoelectric properties of a nanocomposite with embedded α -FeSi₂ NCs in the silicon matrix

Galkin K.N.^{*}, Kropachev O.V., Goroshko O.A., Subbotin E.Yu., Goroshko D.L., Galkin N.G.
Institute of Automation and Control Processes FEB RAS, 5 Radio Street, Vladivostok 690041, Russia

^{*}e-mail: galkinkn@iacp.dvo.ru

Abstract. The technology of embedding metallic iron disilicide (α -FeSi₂) nanocrystals (NCs) with different numbers of NCs multilayers and different doping levels of silicon multilayers with holes (10^{19} cm⁻³ and 10^{13} cm⁻³) was tested on SOI substrates, and heterostructures with 4 and 8 layers of embedded α -FeSi₂ NC were grown using it. The maximum power factor of up to 1.2 mW/(m×K²) at T=450 K was observed in the heterostructure with the maximum hole concentration in the silicon interlayers, and a decrease in the hole concentration led to a decrease in the power factor to 0.25 mW/(m×K²) at T=450 K due to a sharp increase in the sheet resistance.

1. Introduction

One of the approaches to creating efficient thermoelectric materials is to embed metal nanocrystals (NC) into a semiconductor, such as germanium, which provides high matrix conductivity and an increase in the Seebeck coefficient [1]. It does not require high crystalline quality of materials with embedded nanocrystals and assumes the possibility of their random distribution in the semiconductor matrix, including silicon. NCs of transition metal silicides can be embedded into silicon, since they include both semiconductors [2] and metals [3]. It was known that embedding multilayers with one or two types of embedded NCs (CrSi₂ and β -FeSi₂) grown on an n-type silicon substrate resulted in efficient hole injection from embedded NCs, a change in the sign of the Seebeck coefficient from negative to positive, and an increase in the power factor in the temperature range from 200 K to 400 K [4]. At the same time, the incorporation of NC metal silicides into a silicon matrix with p-type conductivity and orientation (100), as well as the effect of doping silicon interlayers during the growth of multilayers on their thermoelectric parameters, remained unexplored.

In this paper, we investigated the formation of multilayers with embedded NCs of metallic iron disilicide (α -FeSi₂) in silicon-on-insulator (SOI) substrates of p-type conductivity with different numbers of NC multilayers and different doping levels of silicon multilayers, determined the phonon structure of the NCs, the conductivity and thermoelectric properties of the grown heterostructures in the temperature range of 80-450 K.

2. Experimental procedure

Multilayer heterostructures with embedded NCs of metallic α -FeSi₂ were grown in a VARIAN ultrahigh vacuum setup with a base pressure of 2×10^{-10} Torr equipped with a molecular beam source of iron (Fe), sublimation sources of silicon (Si) with different hole concentrations (p+ and p-) and a quartz thickness sensor. SOI Si(100) p-type wafers with a resistivity of (1-10) Ohm × cm were chosen as substrates and Si sources. After low-temperature cleaning of the silicon surface at a temperature of 900 °C for 10 minutes, a 50 nm thick silicon buffer layer was deposited at T=700 °C. Then, multilayer samples with embedded NCs of α -FeSi₂ were formed. This process consisted of four steps: (1) deposition of 0.5 nm Fe at room

temperature; (2) annealing at T=630 °C for 2 min and flash at T=1000 °C for 5 s; (4) growth of the silicon layer (12 nm at T=630 °C and 24 nm at T=700 °C). To form 4-layer and 8-layer structures with embedded α -FeSi₂ NCs, these four steps were repeated 3 or 7 times, followed by growth of the capping silicon layer in two steps: 12 nm at T=630 °C and 84 nm at T=700 °C. Individual multilayers were grown with doped silicon interlayers with different hole doping: 10^{19} cm⁻³ (p+) and 10^{13} cm⁻³ (p-). Test samples with 4 and 8 dummy growth stages without deposition of iron atoms, but with annealing and stopping (emulation of NC growth) with different silicon sources (p+ and p-) were grown for comparison with samples with embedded α -FeSi₂ NC multilayers. A total of 3 samples with embedded α -FeSi₂ NC and 3 samples with NC growth emulation were grown.

The morphology of the grown samples was studied using a Solver P47 scanning probe microscope in the tapping mode. The phonon structure of the grown samples was studied using an NTEGRA SPECTRA-II system in the Raman spectroscopy mode. The transport and thermoelectric properties of the samples were studied on a Kriotel (Russia) laboratory setup in a nitrogen atmosphere at temperatures of 80–450 K after preliminary formation of six Al contacts on an ADVAVAC PVD-2EB2R11 vacuum setup (T₀=450 °C for 20 minutes) to measure conductivity and thermo-emf.

3. Results and discussion

After unloading the samples with embedded NC α -FeSi₂ and the reference samples with growth emulation, their surface morphology was studied by AFM. Due to the embedding of nanocrystals with a tetragonal lattice into silicon, a process of three-dimensional overgrowth of NC was observed and punctures were formed on the surface of the capping silicon layer. However, the yield of α -FeSi₂ NCs was not observed. The root-mean-square roughness was minimal for 4-layer heterostructures both with embedded NC and without them (Table 1). Increasing the number of multilayers led to its 2-3-fold growth, but the depth of the observed punctures did not exceed 40 nm, which is less than the thickness of the capping silicon layer.

The study of the phonon structure of working samples by the Raman scattering method showed that multilayers with the supposed NC α -FeSi₂ do not have phonon peaks. This proves the absence of the semiconductor phase β -FeSi₂ [4] in the NC samples and indirectly confirms the

formation of the α -FeSi₂ phase, which does not have resolved Raman scattering phonons [5].

Table 1. Types of heterostructures, type of doping of Si interlayers, d_{HS} – total thickness of heterostructure, σ_{rms} – root mean square roughness.

Sample	Type of HS	Si interlayer doping	d_{HS} , nm	σ_{rms} , nm
A	Dummy NC Si	p ⁺	256	2.0
B	4L α -FeSi ₂	P ⁺	258	2.3
C	Dummy NC Si	p ⁺	375	7.0
D	8L α -FeSi ₂	p ⁺	371	4.6
E	Dummy NC Si	p ⁻	417	0.51
F	8L α -FeSi ₂	p ⁻	429	7.92

The grown multilayer samples with embedded NCs (Table 1) represent a structure with randomly distributed NCs [4], to which the two-layer thermoelectric model [6] cannot be applied to isolate the contribution of the modified layer. The electrical and thermoelectric properties were analyzed by comparing the temperature dependences of the sheet conductivity and the Seebeck coefficient for the SOI substrate, the emulated substrate (Dummy NC Si), and samples with embedded NCs. The data on the resistance and the Seebeck coefficient were obtained for the SOI substrate and samples A and B with 4 layers of α -FeSi₂ NCs and the emulated sample, grown with heavily doped silicon interlayers (p⁺). According to the dependences of the sheet resistance, it was found that it is minimal for a clean SOI substrate. At the same time, for embedded NCs or a Dummy NC Si sample, the sheet resistance increases by 2–10 times depending on the temperature, so the doping of the intermediate silicon layers is not felt in the resistance. The maximum Seebeck coefficient (550–600 μ V/K) is demonstrated by sample B with embedded NC α -FeSi₂ in the temperature range of 350–370 K. For the SOI substrate and the Dummy NC Si sample, the Seebeck coefficient increases approximately equally with increasing temperature and reaches 500 μ V/K at T=450 K. Calculations of the power factor showed that it remains maximum for the Dummi-NC Si sample. However, for sample D, the power factor reaches 1.2 mW/(m \times K²) at T=450 K.

Doping of silicon layers to p⁺ has a noticeable effect on the 8-layer sample D with embedded NCs (Table 1) and on the dummy-NC Si sample (C, Table 1). In this case, for the latter sample, the sheet resistance is lower than for the former, by (2–4) times with increasing temperature. According to the Seebeck coefficient, the maximum increase (400–450 μ V/K) is observed for the multilayer sample with α -FeSi₂ NCs (sample D) at temperatures of 230–320 K. Calculations of the power factor showed that it remains maximum for the dummy-NC Si sample (C, Table 1).

To determine the effect of the doping degree of silicon interlayers on the thermoelectric parameters, a multilayer sample (8 layers) with a reduced hole concentration (p⁻) was grown (Table 1, sample F). For sample F, the sheet resistance (255,000 Ohm) at T = 115 K was significantly

higher than for the SOI substrate (1000–2500 Ohm). Such behavior of the sheet resistance can be associated with a sharp increase in scattering on NCs. For the sample with built-in α -FeSi₂ NCs, the Seebeck coefficient sharply increases with decreasing temperature below 140 K and reaches values of 800 μ V/K at temperatures of 110–120 K with a subsequent decrease with increasing temperature to 200 μ V/K for the sample with α -FeSi₂ NCs. At the same time, with an increase in temperature from 150 to 450 K, an increase in the Seebeck coefficient from 300 to 600 μ V/K is observed. Calculation of the power factor from temperature for samples E and F and comparison with the SOI substrate showed that in the temperature range of 150–450 K, the most effective thermoelectric is sample F with built-in α -FeSi₂ NC multilayers.

4. Conclusions

A comprehensive technology for introducing α -FeSi₂ NCs into SOI substrates has been developed using solid-phase epitaxy with different growth temperature modes (T=630 °C and T=1000 °C) for annealing 0.5 nm thick iron layers and molecular beam epitaxy (T=630 - 700 °C) of Si interlayers. 4-layer and 8-layer samples with introduced α -FeSi₂ NCs and silicon interlayers (hole concentration: 10¹⁹ cm⁻³ and 10¹³ cm⁻³), as well as multilayer samples with emulation of NC growth on SOI-(100) substrates have been grown. It has been established that in an 8-layer heterostructure with the maximum hole concentration in silicon interlayers, a power factor of up to 1.2 mW/(m \times K²) is observed at T=450 K, which is close to the best results for thermoelectric materials at this temperature. A decrease in the hole concentration in silicon multilayers leads to an increase in the Seebeck coefficient, but the power factor decreases to 0.25 mW/(m \times K²) at T=450 K due to a sharp increase in sheet resistance and scattering at grain boundaries.

Acknowledgements

The study was carried out within the framework of the state assignment of the Institute of Atomic Energy and Control Sciences of the Far Eastern Branch of the Russian Academy of Sciences (state budget topic FFWF-2021-0002).

References

- [1] Tanusilp S., and Kurosaki K., Materials, **12**(2019)1943.
- [2] Murarka S.P., Intermetallics, **3**(3)(1995)173.
- [3] Ed. by Borisenko V.E., Semiconducting Silicides (Berlin, Springer, 2000).
- [4] Galkin N.G., Galkin K.N., Dotsenko S.A., Serhienko I., Khovailo V.V., Gutakovskii A.K., Applied Surface Science, **566**(2021)150620.
- [5] Pushkarev R.V., Fainer N.I., Katsui H., Kaichev V.V., and Goto T., Mater. Des., **137**(2018)422.
- [6] Bahk J.H., Favalaro T., Shakouri A., Annual Review of Heat Transfer, **16**(2013).

Single-phase formation of Ca_5Si_3 films on Si(111), electronic and phonon structure and optical properties: experiment and theory

Galkin N.G.¹, Galkin K.N.¹, Kropachev O.V.^{*1}, Migas D.B.², Fogarassy Z.³, Cora I.³, Pécz B.³

¹ Institute of Automation and Control Processes FEB RAS, 5 Radio Street, Vladivostok 690041, Russia

² Belarusian State University of Informatics and Radioelectronics, P. Browka 6, 220013, Minsk, Belarus

³ HUN-REN Centre for Energy Research, Institute of Technical Physics and Materials Science, EK MFA, 1525 Budapest, P.O. Box 49.

*e-mail: chernobez@gmail.com

Abstract. In this work calcium silicide films grown by MBE on a Si(111) substrate at a temperature of 500 °C with deposition rate ratios $v_{\text{Ca}}:v_{\text{Si}} = 3.49, 3.59, 3.95$, the formation of a single-phase epitaxial Ca_5Si_3 film with a thickness of up to 40 nm was detected for the first time, which was proven by HRTEM on a cross section. Reflection peaks in the region of interband transitions at 2.25, 2.75, 3.7 and 4.6 eV, a semi-metallic character of reflection at energies less than 0.5 eV and a unique phonon structure with Raman shifts at 104, 111, 125, 146, 162, 193, 220, 244, 287, 306, 349, 384, 419 and 454 cm^{-1} were detected for the first time in the reflection and Raman spectra of the Ca_5Si_3 film. The obtained experimental data are confirmed by the data of first-principles calculations of the band structure, reflection coefficient and absorption coefficient spectra.

1. Introduction

Among calcium silicides CaSi_2 , Ca_2Si and CaSi are most common displaying interesting optical and electrical properties and they have been grown as single-phase films on silicon [1-4]. However, the other calcium silicide Ca_5Si_3 has not been easily grown as films and powders [5-7], because of the peritectic reactions during its formation in addition to close energies of formation of silicides in the Ca-Si system [8]. Here we decided to closely follow the two stage method previously used for magnesium silicide formation [4]. At the first stage, a CaSi layer was formed on the atomically clean silicon surface with the (001) orientation by the MBE method with an average Ca supersaturation ($v_{\text{Ca}} : v_{\text{Si}} = 3.2$) at a temperature of 400 °C, and then, with additional step-by-step reactive deposition of calcium at temperatures of 490 °C, 600 °C and 700 °C, the transformation of the CaSi lattice into the Ca_5Si_3 lattice was ensured. However, according to the XRD data [4], the resulting film consisted of the main contribution of Ca_5Si_3 grains (narrow peaks) and a small contribution of CaSi grains (broadened peaks). The presence of two phases in the film did not allow analyzing the structure and determining their optical functions as well as the nature of optical conductivity.

In this work, we study the growth of the film by the MBE method with an increased ratio of calcium to silicon deposition rates at a temperature of 500 °C with the following identification of the structure of the Ca_5Si_3 film by the HRTEM method and investigation the optical and phonon properties in order to compare them with the data of *ab initio* calculations of bulk Ca_5Si_3 .

2. Experimental procedure and computational details

Experiments on the formation of Ca_5Si_3 films on Si(111) substrate were carried out in an OMICRON Compact ultrahigh vacuum setup with a base vacuum of 1×10^{-10} Torr, as well as a block of Si and Ca molecular beam sources and a quartz thickness gauge. A rectangular strip of n-type silicon ($4 \times 17 \text{ mm}^2$) with a resistivity of 1000 $\Omega \times \text{cm}$ (Si(111)-FZ1000) served as a sublimation

silicon source and a silicon substrate. The Knudsen cell made of pyrolytic boron nitride heated with direct current was used as a Ca source. For the grown samples, the deposition rates of Ca and Si were $(7.3\text{--}8.4) \text{ nm min}^{-1}$ and $(0.9\text{--}0.95) \text{ nm min}^{-1}$, respectively, in different experiments. The morphology of the films was examined using a Solver 47 SPM. The transmission and reflectance spectra were recorded at room temperature using Hitachi U-3010 spectrophotometers and a Bruker Vertex 80v Fourier transform spectrometer in the photon energy range of 0.05–6.50 eV. Raman spectra excited by light with wavelengths of 473 and 633 nm were recorded at room temperature using an NTEGRA SPECTRA II setup. The cross sections of the samples were analyzed using high-resolution transmission electron microscopy (HRTEM) in a THEMIS 200 F aberration corrected TEM/STEM microscope.

The full structural optimization of the Ca_5Si_3 bulk has been performed by employing the first principles total energy projector-augmented wave method (code VASP) [9]. The absorption coefficient and reflectivity have been estimated at a dense mesh of at least 700 k-points in the irreducible part of the corresponding Brillouin zone.

3. Results and discussion

Three samples (**A**, **B** and **C**) were respectively grown at different calcium to silicon velocity ratios ($v_{\text{Ca}} : v_{\text{Si}} = 3.49, 3.59, 3.95$) and the same deposition time. At the maximum ratio, a certain density of rectangular elongated nanocrystals (NC) is observed on the film surface (sample **C**), and a continuous film with roughness from 5 nm to 10 nm is observed below them. With a decrease in the ratio of calcium to silicon atom deposition rates, the number of rectangular NCs decreases and the film roughness decreases to 2 – 3 nm (sample **B**).

The studies of optical transmission and reflection spectra of Ca_5Si_3 have shown (Fig. 1) that the highest deposition ratio (3.95, sample **C**) provides a lower amplitude of reflection spectrum in the entire range of photon energies than smaller velocity ratios (samples **A** and **B**). In addition, in the reflection spectra for samples **A** and

B in the region of photon energies greater than 2 eV, peaks with energies of 2.25, 2.75, 3.7 and 4.6 eV are observed in the reflection spectra, which do not coincide with the peaks for sample **C**, being very close to the peaks for CaSi (1.95, 2.6, 3.5 and 4.4 eV) [4]. Thus, it is not excluded that in sample **C** there is an admixture of the CaSi phase (rectangular NCs) on the film surface. Calculations of the true reflectance spectrum of the calcium silicide film for sample **A** from the two-layer model [10] in the energy range of 0.1 – 1.25 eV showed (Fig. 1, curve R_0_A) that at energies below 1 eV a weak minimum with an energy of about 0.6 eV is observed [4]. Reflectance in all films below 0.5 eV increases to 0.6 – 0.8 indicating a metallic character in the films.

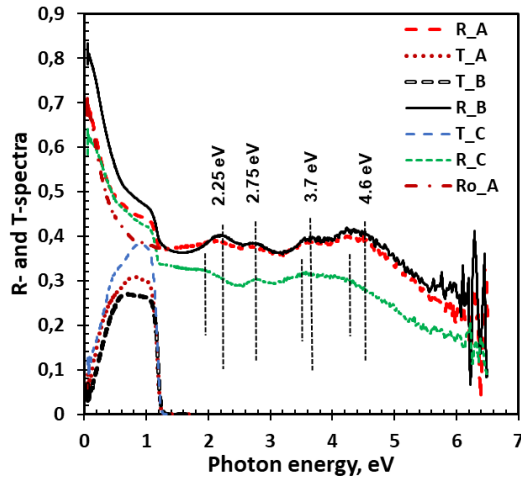


Fig. 1. Reflectance (*R*) and transmittance (*T*) spectra of samples (*A*, *B*, *C*) with grown films. The spectrum of R_0_A is the spectrum of a calcium silicide film calculated from a two-layer model [10].

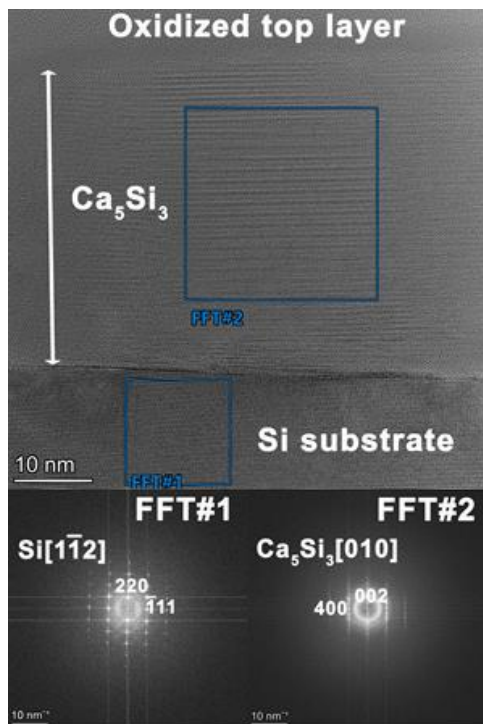


Fig. 2. HR TEM image of the cross-section in the sample **C** and FFT#1 and FFT#2 images (inserts).

First-principles calculations for Ca_5Si_3 have shown that the Fermi level crossed some bands along with an absorption coefficient to be less than $1.5 \times 10^4 \text{ cm}^{-1}$ in the

photon energy range of 0.05 – 1.0 eV. In the reflection spectrum values of 0.9–1.0 are observed at low energies (below 0.1 eV) followed by a drop to 0.3 at 0.4 eV with successive maxima at 0.8, 1.5, 2.2 and 3.6 eV.

The film structure in sample **C** was investigated by HRTEM on a cross section (Fig. 2). The FFT pattern from region 2 showed the presence of an ordered columnar NC with a Ca_5Si_3 structure and an epitaxial ratio of $\text{Ca}_5\text{Si}_3(002)//\text{Si}(220)$ in a film with a thickness of 40 nm.

The studies of the Raman spectra for the film in sample **C** with excitation at a wavelength of 633 nm showed the appearance of a strong structure of 14 peaks with Raman shifts (104, 111, 125, 146, 162, 193, 220, 244, 287, 306, 349, 384, 419 and 454 cm^{-1}), which differ greatly from the Raman spectrum for CaSi [3] and correspond to the Ca_5Si_3 phase. When the laser wavelength is reduced to 473 nm, some of the peaks below 190 cm^{-1} disappear from the spectrum, but then they repeat the peaks at large Raman shifts.

4. Conclusions

The study of the morphology, crystal structure, optical reflection and transmission spectra, and Raman spectra of calcium silicide films grown by MBE at 500°C showed that epitaxial Ca_5Si_3 grains were formed at the interface with silicon. They have reflection spectra with unique peaks at 2.25, 2.75, 3.7, and 4.6 eV and a unique phonon structure with 14 peaks in the Raman shift range from 104 to 454 cm^{-1} , which is confirmed by the band structure, reflection spectra, and absorption coefficient calculated from first principles for bulk Ca_5Si_3 . It was found that the Ca_5Si_3 film exhibits semi-metallic properties with transparency in the photon energy range of 0.5 – 1.1 eV.

Acknowledgements

The study was carried out within the framework of the state assignment of the Institute of Automation and Control Processes FEB RAS (state budget topic FFWF-2021-0002). The Hungarian authors thank the support of VEKOP-2.3.3-15-2016-00002 of the European Structural and Investment Funds. The authors gratefully thank Levente Illés for TEM sample preparations.

References

- [1] Affronte M., Laborde O., Olsece G.L., and Palenzona A., *J. Alloys Compd.* **274**(1998)68.
- [2] Wu H., Zhou W., Udovic T.J., and Rush J.J., *J. Alloys Compd.* **446–447**(2007)101.
- [3] Galkin N.G., Galkin K.N., Tupkalo A.V., Fogarassy Z., Pécz B., *J. Alloys Compd.* **813**(2020)152101.
- [4] Galkin N.G., Galkin K.N., Goroshko D.L., Dotsenko S.A., a.o., *Jpn. J. Appl. Phys.* **62**(2023)SD0803.
- [5] Uehara M., Akiyama K., Shimizu, T. Matsushima, M. Uchida, H. Kimura, Y., & Funakubo H., *Journal of Electronic Materials*, **45**(6)(2016)3121.
- [6] Inaba T., Kato A., Miura K., Akasaka M., a.o., *Thin Solid Films* **515**(2007)8226.
- [7] Brutti S., Nguyen-Manh D., Pettifor D.G., Manfrinetti P., Napoletano M., and Canepa F., *CALPHAD, Comput. Coupling Phase Diagr. Thermochem.* **33**(2009)260.
- [8] Manfrinetti P., Fornasini M.L., and Palenzona A., *Intermetallics* **8**(2000)223.
- [9] Kresse G. and Joubert D., *Phys. Rev. B* **59**(1999)1758.
- [10] Galkin N.G., A. M. Maslov, and A. V. Konchenko, *Thin Solid Films* **311**(1997)230.

Influence of protective transparent covering on lateral photovoltaic effect in the cover/Bi₂Te₃/n-Si(111) multilayer structure

Pisarenko T.A.^{*1}, Yakovlev A.A.¹, Mararov V.V.¹, Tsukanov D.A.^{1,2}

¹ Institute of Automation and Control Processes FEB RAS, 5 Radio St., Vladivostok 690041, Russia

² Far Eastern Federal University, FEPU Campus 10 Ajax Bay, Vladivostok 690950, Russia

*e-mail: tata_dvo@iacp.dvo.ru

Abstract. In this work we investigated the lateral photovoltaic effect in the cover/Bi₂Te₃/n-Si(111) multilayer structures. Topological insulator Bi₂Te₃ have been chosen as attractive candidates for the buffer layer in photovoltaic cells. To enhanced photovoltaic performances, several suggestions for the protective transparent covering material selection have been proposed.

1. Introduction

The development of optoelectronics opens up new possibilities, including current control using light [1,2]. The use of topological insulators in photovoltaic cells will allow optoelectronic devices to be transferred to spin transport [1, 3]. In such systems, diffusion spin transport is realized as a result of the interference of Rashba and Dresselhaus spin splittings [3]. 2D topological insulators based on bismuth chalcogenides are precisely the systems, in which spin orientation by current and/or light is possible.

It is known [4-7] that in order to optimize the efficiency of multilayer thin-film photovoltaic cells, it is necessary to observe the criteria for selecting materials taking into account their energy parameters [4-6], loss mechanisms [4] and recombination processes [4,5].

One of the loss mechanisms reducing the quantum efficiency of photovoltaic cells is reflection. This can be caused by light reflection at the interfaces and/or the outer surface. Another loss mechanism is the absorption of light near the surface. This problem is addressed by introducing the concept of a window/buffer/absorber heterojunction.

In addition, the generation of carriers is counteracted by the carriers' recombination [4, 5]. The recombination regions that affect the efficiency of a solar cell are the quasi-neutral recombination in the absorber layer, the recombination at space charge region, and recombination at the absorber/buffer interface. Recombination at the interface can be reduced by forming an epitaxial buffer layer [1, 2, 4].

This work presents the results of the LPE study in the multilayer structure cover/Bi₂Te₃/n-Si(111) within the electron system, i.e. without taking into account the spin states. It is known [8] that single-crystal layers of bismuth chalcogenides are oxidized to a depth of 1 quintuple layer (1QL). In this case, the kinetics of photoelectric properties is observed during natural oxidation [8]. For example, during the oxidation of 1 QL of Bi₂Se₃, the photosensitivity first increases and then decreases [8]. Since the characteristics of the Bi₂Te₃/n-Si(111) structure depend on oxidation, in order to increase the reliability of the LPE characteristics, taking into account the above criteria, we formed two versions of the top protective transparent layer: TeO₂ and SiO₂/TeO₂. In the photovoltaic cell obtained in this way, the absorber is silicon, the buffer layer is Bi₂Te₃ topological insulator, and the top protective transparent

covering is made of paratelluride (TeO₂) or a composite layer of SiO₂/TeO₂.

2. Experiment

The Si(111)-Bi₂Te₃-Te-Si multilayer structure was formed using molecular beam epitaxy in a ultrahigh vacuum (UHV) chamber with a base pressure less than 5.0×10⁻¹⁰ Torr. We used n-type Si(111) wafers (40–70 Ω·cm) as substrates. The Bi₂Te₃ films were grown at temperature of about 240°C at which the film grew in step-flow mode [9]. To reduce the amount of Te vacancies, the Bi-to-Te flux ratio was chosen close to 1:14 with the growth rate of about 0.3 QL/min. After cooling to room temperature, the Bi₂Te₃ films were covered by either 5 nm of tellurium or 2 nm of tellurium and then 1 nm of silicon. In air, the top coverings treat a natural oxidation process, resulting in the formation of tellurium and/or silicon oxides, which act as a protective transparent covering, the so-called window layer [4].

Lateral photovoltaic effect was investigated by using He-Ne laser (ML101J25 with 633 nm, 0.25 mW for incident beam on a surface, a spot diameter of 50 μm) and Keithley 2000 multimeter. The response time was defined by a digital oscilloscope (Tektronix TDS 2012B) of 150 MHz. The distance between the probes was 1 mm.

3. Results and discussions

In the work, after oxidation in air, the photovoltaic cells are made by n-Si(111) absorber, n-Bi₂Te₃ buffer and TeO₂ or SiO₂/TeO₂ window layers. To increase efficiency, we used the same elements in subsequent layers [4]. The differences are in window materials and them properties. The absorption in transparent window layer is typically low due to the sufficiently high-energy band gap of the materials used for this layer. Unfortunately, the absorption by the Bi₂Te₃ buffer layer is a significant losses source in the studied structures. Here one has to choose between performance and losses.

Figure 1 reveals the dependences of the lateral photovoltage on the light spot position, parameterized by the times of exposure of the samples to air. In the insert of Fig.1 the photoresponse dependences are presented in the LPV(t) graphical presentation format, since in this case the value of the photoresponse signal corresponds to the photosensitivity value. The photoresponse values are comparable with those presented earlier [2, 8].

The kinetics of photovoltaic characteristics allows us to analyze the oxidation processes of window layers. It is known that 1 nm Te is completely oxidized in the first 24 hours [10], however, the sample with 5 nm Te did not exhibit photovoltaic properties during the first week. Kinetic changes in the LPV(x) and LPV(t) dependences in the range of exposure in air from 10 to 120 days allow us to assume that the tellurium film is completely oxidized in 10 days. However, on the assumption of results presented in Fig. 1a, we can conclude that initially, as a result of oxidation, polymorphic phases of TeO_2 [11] and, highly likely, TeO_x can be formed. Upon subsequent exposure to air, these polymorphic phases are transformed into paratelluride, which leads to a significant increase in the resistance of the $\text{TeO}_2/\text{Bi}_2\text{Te}_3/\text{Si}$ system, bottom right insert in Fig. 1a, while the quality of the interface improves, which in turn reduces the loss of light quanta involved in photogeneration at the deeper $\text{Bi}_2\text{Te}_3/\text{Si}$ interface. One can see in Fig. 1a, an increase in the resistance of the system leads to an increase in photosensitivity (the magnitude of the photoresponse pulse, top left insert in Fig. 1a).

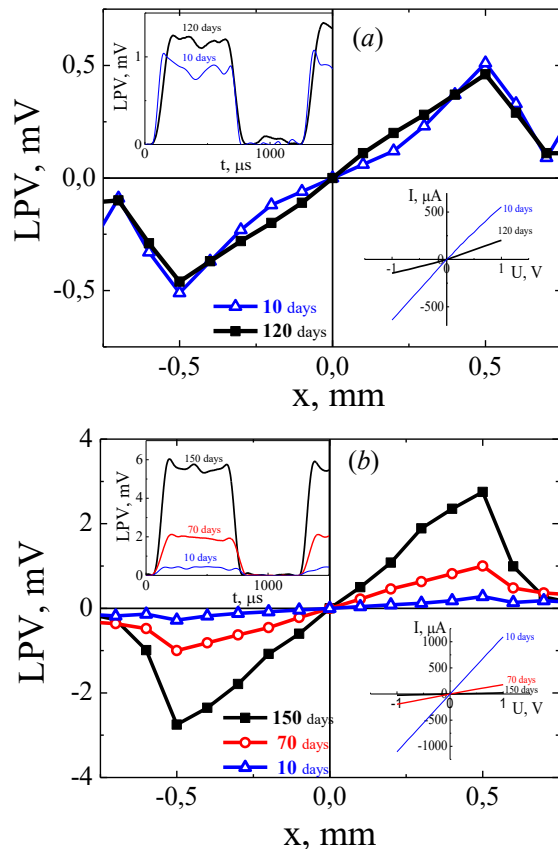


Fig. 1. Lateral photovoltage of the $\text{Bi}_2\text{Te}_3/\text{Si}$ structures with covering: a – TeO_2 ; b – $\text{SiO}_2/\text{TeO}_2$. Inserts: LPV(t) photoresponse (top left); dark I-V characteristics (bottom right).

In order to increase the resistance and transparency of the window layer, it was proposed to form a combined transparent covering $\text{SiO}_2/\text{TeO}_2$. It is natural to assume that in this case, the amorphous silicon layer formed on the surface of the thinned tellurium layer is oxidized first. Due to the high electronegativity of tellurium, the oxidation process continues until the tellurium layer is completely oxidized, which follows from the I-V characteristics, bottom right insert Fig. 1b. Such a covering improves the transport properties of the system, since its resistance increases by an order of magnitude, top left insert Fig. 1b,

but, unfortunately, requires a long formation time (120-150 days).

Comparison of Fig. 1a and 1b demonstrates the advantage of the $\text{SiO}_2/\text{TeO}_2/\text{Bi}_2\text{Te}_3/\text{n-Si}(111)$ system. Since the absorber is the silicon substrate, and photogeneration occurs at the $\text{Bi}_2\text{Te}_3/\text{n-Si}(111)$ interface, where the energy parameters of the structures are identical, the reasons for the significant improvement of photovoltaic properties in the $\text{SiO}_2/\text{TeO}_2/\text{Bi}_2\text{Te}_3/\text{n-Si}(111)$ system are an increase in the resistance of the covering layer, an increase in the transparency of the window, and a decrease in losses in the RC circuit, according to the basic scheme of the LPE, proposed by us earlier [6].

In addition, we defined the photoresponse performances of cover/ $\text{Bi}_2\text{Te}_3/\text{n-Si}(111)$ structures, top left insets in Fig. 1, although the photosensitivity of these structures were lower than those in metal-semiconductor or metal-oxide-semiconductor structures [6, 8], the response time of these structures were be faster.

4. Conclusions

The photovoltaic properties observed in cover/ $\text{Bi}_2\text{Te}_3/\text{n-Si}(111)$ structures with a protective transparent covering make them potential candidates for optoelectronics. New possibilities for light-based current control are opened up in such structures due to the diffusion spin transport, which is realized in like structures as a result of the interference of Rashba and Dresselhaus spin splittings, which provides an almost instantaneous change in the electron state using laser radiation. Thus, the obtained results show that the $\text{SiO}_2/\text{TeO}_2/\text{Bi}_2\text{Te}_3/\text{Si}$ photovoltaic cells with a buffer layer made of a topological insulator and having a compound protective transparent covering may have potential applications as high-speed polaritonic devices.

Acknowledgements

This work was financed by the budget of the Institute of Automation and Control Processes of the Far Eastern Branch of the Russian Academy of Sciences within the framework of the state assignment (No. FFW-2021-0002)

References

- [1] S. Hasegawa. Appl. Phys. Express **17** (2024) 050101.
- [2] J.Chae, S.B.Hong, D.Kim, D.K.Kim, J.Kim, K.Jeong, S.H.Park, M.H.Cho. Appl. Surf. Sci. **554** (2021) 149623.
- [3] L.E. Golub. Physics-Uspokhi **55** (2012) 814.
- [4] N. Khoshirad, N.A.M. Yunus. Nanoelectronics and materials development (2016) 41.
- [5] Wallmark J. T. Proceedings of the IRE **45** (1957) 474.
- [6] T.A. Pisarenko, V.V. Korobtsov, A.A. Dimitriev, V.V. Balashev, V.V. Zheleznev. Phys. Solid State **64** (2022) 8.
- [7] C.Yu, H.Wang. Sensors **10** (2010) 10155.
- [8] S.B.Hong, J.Chae, D.K.Kim, K.Kim, K.Jeong, J.Kim, M.H.Cho. ACS Appl. Mater. Interfaces **12** (2020) 26649.
- [9] A.V.Matetskii, I.A.Kibirev, T.Hirahara, S.Hasegawa, A.V.Zotov, A.A.Saranin. Appl. Phys. Lett. **107** (2015) 091604.
- [10] I.A. Kariper. Journal of Optics **47** (2018) 504.
- [11] A.P. Mirgorodsky, T. Merle-Méjean, J.-C. Champarnaud, P. Thomas, B. Frit. J. Phys. Chem. Solids **61** (2000) 501.

Optical and electronic properties of magnesium silicide films formed on silicon

Polyakov A.V.^{*1}, Fomin D.V.¹, Sholygin I.O.¹, Galkin N.G.², Galkin K.N.²

¹ Tsiolkovsky Scientific Research Center, Amur state university, Blagoveshchensk 675028, Russia.

² Institute of Automation and Control Processes, 5 Radio St., Vladivostok 690041, Russia

*e-mail: polyakov_a_1999@mail.ru

Abstract. The paper presents the results of investigation of the optical and electronic properties of Mg_2Si films on Si (111) by infrared (IR) spectroscopy. The samples containing these films (360 and 480 nm thick) were formed by layered reactive epitaxy. The heating temperature of the substrates was 250 °C. Based on the IR Fourier spectroscopy data, it was found that the minimum value of the transmittance coefficient at 270 cm^{-1} for the Mg_2Si film of the first sample (360 nm) is 0,02; for the second sample (480 nm) is 0,03. The analysis of the transmission spectra in the photon energy range from 0,05 to 1,4 eV revealed the presence of alternating maxima and minima (their energy position from 0,2 to 1,1 eV), which indicates the interference features of magnesium silicide films. According to the absorption spectra, as a result of geometric calculations, the value of the band gap for each of the films was determined: 0,81 eV for sample 1 and 0,83 eV for sample 2.

1. Introduction

It is indisputable that electricity is the driving force behind human progress. A wide range of electrical installations is used to provide it with electricity. Their composition is becoming more complicated every year. This increases the probability of electrical injury. To eliminate it, electrical installations are equipped with optocoupler-based relay protection. Mg_2Si belongs to one of the nanomaterials that are promising for the production of optocoupler photodetectors [1 - 7]. After all, magnesium silicide films are characterized by a wide range of photosensitivity (from 200 to 1800 nm) [4], a low far-infrared transmission coefficient (according to article [5] - 0,0056 with a photon wavelength of 272 cm^{-1}), and a small band gap (from 0,6 to 0,8 eV) [6; 7]. The purpose of this work was to determine the optical and electronic properties of magnesium silicide films formed on silicon.

2. Experiment

The experiment on the formation of magnesium silicide films was performed at the AmSU Surface Physics Laboratory in a Varian chamber with a base pressure of 10^{-7} Pa. A KEF washer (111) with a resistivity from 0,1 to 0,5 $\text{ohm}\cdot\text{cm}$ was used for the substrates. A KDB (001) washer with a resistivity from 0,001 to 0,005 $\text{ohm}\cdot\text{cm}$ was used for the Si source. The Mg source was taken with a purity of 99,999%. Before the films grew, the substrates and sources underwent standard purification steps.

The samples with films were formed by the method of reactive epitaxy at a substrate heating temperature of 250 °C. Initially, a Si buffer layer (60 nm) was formed on the substrates. Then, alternate deposition of magnesium and silicon layers (90 and 30 nm, respectively) was carried out. Precipitation was threefold for the first sample, and fourfold for the second sample. As a result, samples with films of 360 and 480 nm thicknesses were obtained. At each stage, film formation was monitored in situ by electron Auger spectroscopy, which revealed the presence of magnesium and silicon atoms in their respective layers.

3. Results and discussions

The optical and electronic properties of the formed films were studied by IR spectroscopy ex situ. The IR

Fourier transmission spectra obtained by investigation samples in the far infrared range are shown in Figure 1.

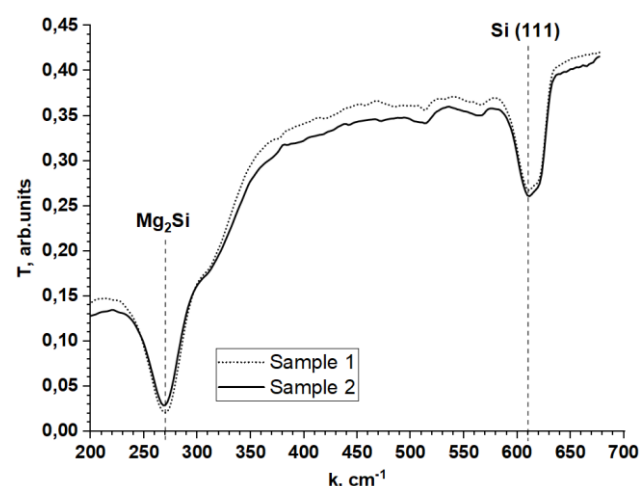


Fig. 1. IR-Fourier spectra of samples.

After analyzing the graphs of the dependence of the transmission coefficient on the photon wavenumber, it was found that a minimum peak at 270 cm^{-1} is observed in both spectra. Its presence, according to [5, 8], indicates the Mg_2Si content in both films. The presence of a reverse peak at 270 cm^{-1} , according to the source [5], is explained by the absorption of magnesium silicide in the film due to the excitation of a transverse optical phonon. At the same time, the transmission coefficient at a photon wavenumber of 270 cm^{-1} for the films of the first and second samples was 0.02 and 0.03, respectively. The minimum transmission coefficient at 610 cm^{-1} is also clearly visible on the spectra, which, according to the data [8-10], indicates the contribution of silicon (substrate) in the composition of the formed samples.

The transmission spectra obtained by examining samples in the middle and near ranges of IR radiation are shown in Figure 2. From the graphs of the dependence of the transmission coefficient on the photon energy, it can be seen that in the range from 0.2 to 1.1 eV, there is an alternation of minima and maxima. According to the data [8, 9], this indicates the interference features of Mg_2Si films.

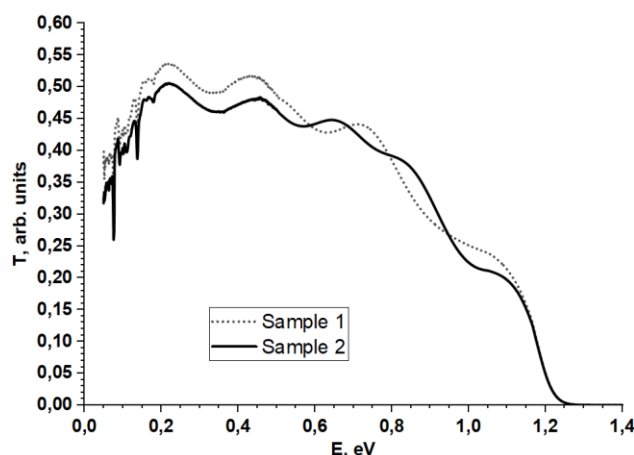


Fig. 2. Transmission spectra of samples in the near and middle IR range.

The analysis shows that in the energy range from 1.1 to 1.3 eV, there is a significant decrease in the transmission value. At energies above 1.3 eV, the transmission coefficient is close to zero, which, according to source [10], indicates a sharp increase in absorption in the film due to interband transitions, which is typical for Mg_2Si , which has semiconductor properties.

Graphs were constructed to calculate the band gap of the formed Mg_2Si semiconductor films (Figures 3 and 4).

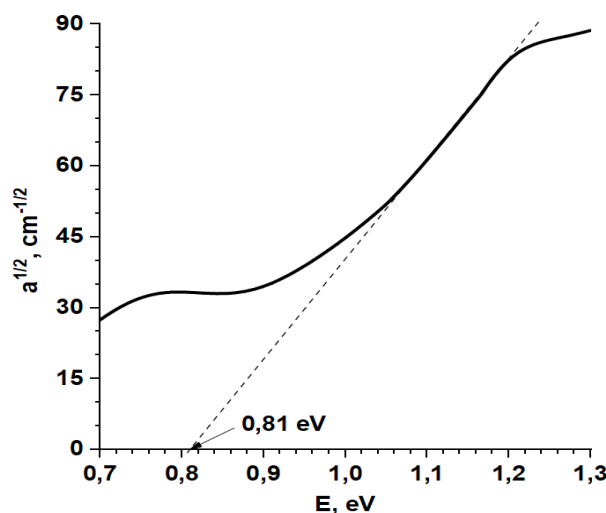


Fig. 3. The absorption spectrum of the first sample.

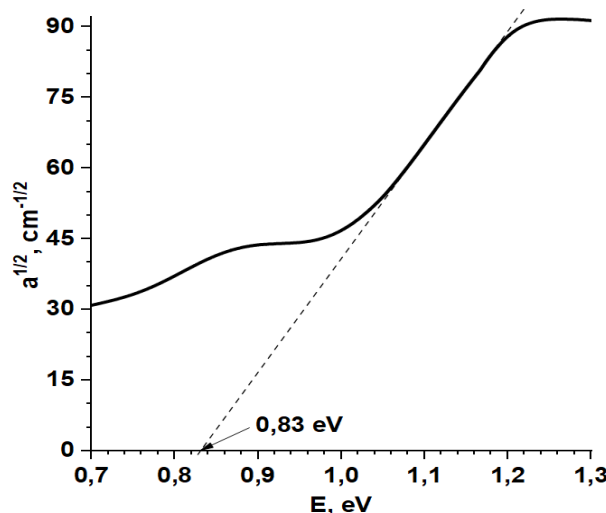


Fig. 4. Absorption spectrum of the second sample.

According to the results of geometric calculation of the band gap from absorption spectra, according to the method described in [11, 12], the following values of this parameter were obtained: 0.81 eV for the first sample (Figure 3); 0.83 eV for the second (Figure 4). The calculated values are close to the reference data (0.6-0.8 eV) [6, 7].

4. Conclusions

Thus, the method of IR-Fourier spectroscopy revealed silicification in the films of both samples (by the presence of a peak minimum transmission coefficient at a photon wave number of 270 cm^{-1}). The transmission coefficients for Mg_2Si films with thicknesses of 360 and 480 nm are 0.02 and 0.03, respectively. Based on the analysis of the IR transmission spectra, the presence of interference in both films (the presence of alternating maxima and minima at energies from 0.2 to 1.1 eV) has been established. Based on the results of geometric calculations of the band gap of Mg_2Si films, it was found that for the first sample it is 0.81 eV, for the second is 0.83 eV.

References

- [1] Synthesis and characterization of nanostructured Mg_2Si by pack cementation process / D. Stathokostopoulos, et al. // Results in Materials. – V. 13. – № 1, 2022. – P. 100252.
- [2] Simulation Study on the Effect of Doping Concentrations on the Photodetection Properties of $\text{Mg}_2\text{Si}/\text{Si}$ Heterojunction Photodetector / Hong Yu, et al. // Photonics. – 2021. – V.8. – № 11. – P. 509.
- [3] Fabrication of Mg_2Si pn-junction Photodiode with Shallow Mesa-structure and Ring Electrode / T. Akiyama, et al. // JJAP Conf. Proc. 5, 2017. – P. 011102.
- [4] Mg_2Si is the new black: introducing a black silicide with 95 % average absorption at 200 – 1800 nm wavelengths / A. Shevlyagin, et al. // Applied Surface Science. – 2022. – V. 602. – P. 154321.
- [5] Infrared spectra of semiconducting silicides nanolayers / M. Baleva, M. Marinova, A. Atanassov // Journal of Physics: Conference Series. – 2008. – V. 113. – № 1. – P. 012043.
- [6] Technology CAD (TCAD) Simulations of $\text{Mg}_2\text{Si}/\text{Si}$ Heterojunction Photodetector Based on the Thickness Effect / Hong Yu, et al. // Sensors. – 2021. – V.26. – № 16. – P. 5559.
- [7] Fabrication and Characterization of Visible to Near-Infrared Photodetector Based on Multilayer Graphene/ $\text{Mg}_2\text{Si}/\text{Si}$ Heterojunction / Hong Yu, et al. // Nanomaterials. – 2022. – V. 12. – № 18. – P. 3230.
- [8] Photoreflectance Spectra of Highly-oriented Mg_2Si (111)/ Si (111) Films / Y. Terai, et al. // JJAP Conference Proceedings. – The Japan Society of Applied Physics. – 2020. – T.8. – P. 011004-1 - 011004-4.
- [9] Optical properties of multilayer materials based on silicon and nanoscale crystallites of magnesium silicide / K.N. Galkin, A.M. Maslov, V.A. Davydov // Journal of Applied Spectroscopy. – 2006. – V. 73. – № 2. – P. 204-209.
- [10] Investigation of surface morphology, optical and electronic properties of Mg_2Si thin films on Si (111) / D.V. Fomin, et al. // Bulletin of Samara University. Aerospace engineering, technology, and mechanical engineering. – 2024. – Vol. 23. – No. 1. – pp. 203-215.
- [11] Formation and properties of $\text{Al}/\text{Mg}_2\text{Si}/\text{Si}/\text{Au}-\text{Sb}$ photodiode structures / I.O. Sholygin, et al. // Izv. vuzov. Physics. – 2025. – Vol. 68. – No. 3. – pp. 22-31.
- [12] Shalimova, K. V. Physics of semiconductors / K. V. Shalimova. Moscow: Energoatomizdat, 1985. – 392 p.

Optical spectra and surface morphology of magnesium silicide nanofilms

Fomin D.V.^{*1}, Ryabov I.A.¹, Polyakov A.V.¹, Sholygin I.O.¹, Shemetov D.A.¹, Galkin N.G.², Galkin K.N.²

¹ Tsiolkovsky Research and Education Centre, Amur State University, Blagoveshchensk, 675028, Russia

² Institute of Automation and Control Processes, 5 Radio St., Vladivostok, 690041, Russia

*e-mail: e-office@yandex.ru

Abstract: This work presents the results of the study of optical properties and surface morphology of Mg₂Si films formed on Si (111) substrates. The samples were formed by reactive epitaxy layer-by-layer (alternating magnesium and silicon) with final film thicknesses of 240 and 320 nm. The optical properties were investigated by IR-UV spectroscopy, and the films were found to have reflections at 2.2 eV corresponding to Mg₂Si. Also the presence of magnesium silicide is shown by Raman spectroscopy by the maxima at 258, 348, 693 cm⁻¹ shift. From the overall analysis of the spectra, it is found that the 320 nm thick film has higher intensity of these peaks. It was found by atomic force microscopy that the films were formed by the Vollmer-Weber growth mode, with island sizes lying in the range of 100 to 200 nm (240 nm film), 200 to 300 nm (320 nm film).

1. Introduction

Nowadays, optical nano- and microdevices are being widely developed in science and technology. Many modern researchers are obtaining materials with new properties in search of opportunities to increase the conversion efficiency of light energy into electrical energy. One of such promising materials is magnesium silicide. This material has a forbidden band width in the range of 0.6 to 0.8 eV. One of its advantages is a wide photosensitivity range: from the mid-ultraviolet (200 nm) to the short-wave infrared (1800 nm) [1-3].

The aim of the presented work is to study optical properties as well as surface morphology of magnesium silicide films formed by layer-by-layer reactive epitaxy on Si(111).

2. Experiment

The growth of magnesium silicide thin films was carried out in an ultrahigh vacuum Varian chamber at the surface physics laboratory of AmSU. The films were grown on silicon substrates made of KEF (111) wafers with resistivity of 0.1-0.5 Ohm× cm. The silicon source was FZN (111) wafer with resistivity of 50-85 Ohm× cm. The Mg source was taken of chemical purity (99.999 %). Before direct growth of films, substrates and sources underwent chemical and thermal cleaning of surfaces.

The formation was carried out by reactive epitaxy at a substrate temperature of 250 °C. In the first step, a Si buffer layer (60 nm) was formed on the substrates. In subsequent steps, silicon (20 nm) and magnesium (60 nm) layers were deposited alternately. The number of such layers was different for each sample, so for the first one - three bilayers and for the second one - four bilayers. After formation, films with thicknesses of 240 and 320 nanometres were obtained for the first and second samples, respectively. The growth was monitored in-situ by electron Auger spectroscopy, which confirmed the presence of magnesium and silicon atoms in their respective layers.

3. results and discussions

The optical properties of the formed films were investigated by IR-UV spectroscopy and Raman

spectroscopy. IR-UV reflectance spectra are presented in Figure 1.

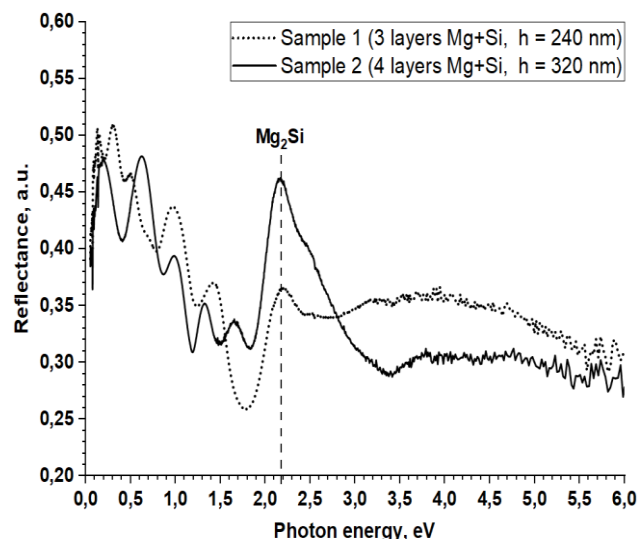


Fig. 1. Reflection coefficient spectra of IR-UV region of samples.

The spectra in the energy range from 0.2 to 1.8 eV show an alternation of interference maxima and minima, with a peak of 2.2 eV belonging to Mg₂Si [4-8] for both samples. At this photon energy, the reflection coefficient values for the films 1 and 2 are 0.37 and 0.47, respectively.

Figure 2 shows the plots obtained by Raman spectroscopy. The spectra possess all the peaks characteristic of Mg₂Si at shifts of 258, 348, 693 cm⁻¹ [4-7,9]. These peaks indicate the excitation of longitudinal optical phonons in this film material. When the spectra were compared with each other, it was found that the samples 2 has these maxima with higher intensity and also lacks the amorphous silicon peak (480 cm⁻¹). This is a consequence of the fact that the film of this sample has a greater thickness.

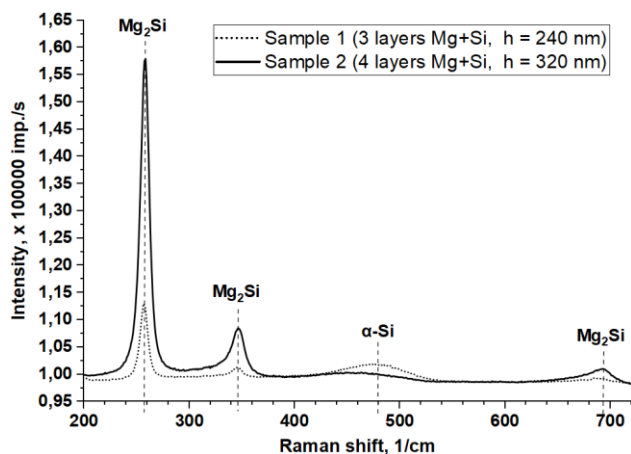


Fig. 2. Raman spectra of the samples.

The surface morphology of the films was investigated by atomic force microscopy. AFM images for the sample 1 are presented in Figure 3. Having analysed this image, it was found that the film growth proceeded according to the Vollmer-Weber mode. In this case, the size of the islets lies in the range of 100 to 200 nm. The islets coalesce to larger grains on the order of 500 nm. Inhomogeneity and height difference is also observed due to the presence of pinholes of the order of 20 nm depth in the film topography.

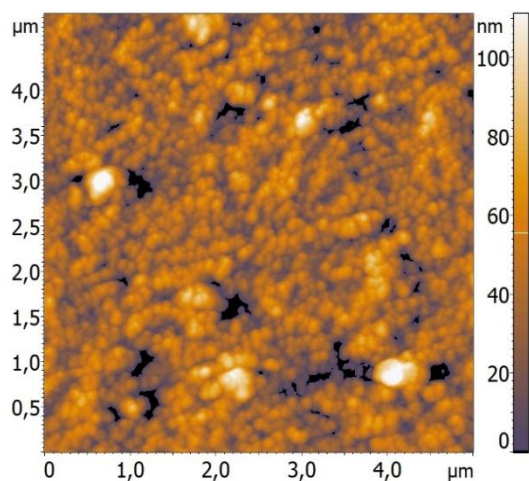


Fig. 3. AFM image of the first sample.

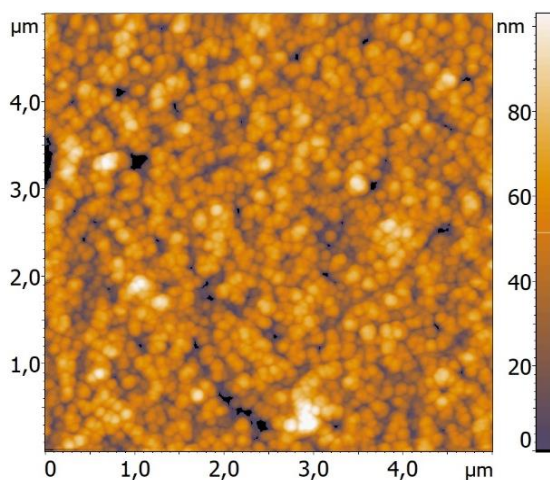


Fig. 4. AFM image of the second sample.

For the sample 2, the AFM image of which is shown in Figure 4, the size of the islands is between 200 and 300 nm. Comparing the surface images of the two samples, we can

conclude that for the second sample the size of the islands is larger than for the first sample, but the coalescence is less pronounced. Also, the second sample has practically no punctures, respectively, its film has greater continuity and homogeneity. This is due to a longer heating of the substrate of the second sample compared to the first one.

4. Conclusions

Thus, this paper presents the results of formation by reactive epitaxy of samples at a substrate heating temperature of 250 °C containing Mg₂Si films with thicknesses of 240 and 320 nm for the first and second samples, respectively. The silicide formation of Mg₂Si films in both samples was determined by IR-UV (based on the peak at photon energy of 2.2 eV) and Raman spectroscopy (based on the maxima at shifts of 258, 348, 693 cm⁻¹ due to the excitation of longitudinal optical phonons). The reflection coefficient for the 240 nm thick film is 0.37 and for the 320 nm thick film is 0.47. The atomic force microscopy method reveals the islanding mechanism of film growth. The sizes of islands for the first sample are from 100 to 200 nm and for the second sample from 200 to 300 nm. In the first sample, in contrast to the second, large grains of about 500 nm are observed due to the coalescence of islands.

References

- [1] Formation and properties of Al/Mg₂Si/Si/Au-Sb photodiode structures / I. O. Sholygin, D. V. Fomin, N. G. Galkin [et al.] // Proceedings of Higher Educational Institutions. Physics. 2025. Vol. 68, No. 3. pp. 22-31.
- [2] "Chemical and epitaxial methods of forming low-dimensional materials"/Fomin D. V., Polyakov A. V., Sholygin I. O., Ryabov I. A. // Bulletin of the Engineering School of the Far Eastern Federal University. 2025. No. 1(62). pp. 27-42.
- [3] Evolution of Structure of Multilayer Si/Mg₂Si X-Ray Mirrors at Thermal Influence / Konotopsky, L. E. [et al.] // Metallophysics and the latest technologies. Vol. 38, № 6, 2016, pp. 825-838
- [4] Buchenaur C.J., Cardona M. // Phys. Rev. B. 1971 Vol. 3, N. 8 P. 2504–2507.
- [5] Anastassakis E., Perry C.H. // Phys. Rev. B. 1971 Vol. 4, N. 4 P. 1251–1257.
- [6] Textured Stainless Steel as a Platform for Black Mg₂Si/Si Heterojunction Solar Cells with Advanced Photovoltaic Performance / A.V. Shevlyagin [et al.] // Materials. Vol.15. № 19, 2022. P. 6637.
- [7] Terai Y., Hoshida H., Kinoshita R., Shevlyagin A., Chernev I., Gournalnik A. Photorefectance spectra of highly-oriented Mg₂Si (111)/ Si (111) films // JJAP Conference Proceedings. 2020. V. 8. DOI: 10.56646/jjapcp.8.0_011004
- [8] Yu H., Deng R., Mo Zh., Ji Sh., Xie Q. Fabrication and characterization of visible to near-infrared photodetector based on multilayer Graphene/Mg₂Si/Si heterojunction // Nanomaterials. 2022. V. 12, Iss. 18.
- [9] Onari S., Cardona M., Resonant Raman scattering in the II-IV semiconductors Mg₂ Si, Mg₂ Ge, and Mg₂ Sn, Phys. Rev. B 14 (1976) 3520–3531.

Structural properties of Mg_2Si films formed on Si(111)

Sholygin I.O.^{*,1}, Fomin D.V.¹, Polyakov A.V.¹, Galkin N.G.², Galkin K.N.²

¹ Tsiolkovsky Scientific Research Center, Amur state university, Blagoveshchensk 675028, Russia.

² Institute of Automation and Control Processes, 5 Radio St., Vladivostok 690041, Russia

*e-mail: ilia.sholygin235@bk.ru

Abstract. In this work, Mg_2Si films formed on Si (111) substrates by reactive epitaxy were studied by X-ray diffraction analysis. It was found that both films are polycrystalline with values of crystal lattice constant: 6.344 - 6.354 Å for a sample with a smaller film thickness and 6.339 - 6.350 Å for a sample with a larger film thickness.

1. Introduction

Currently, metal silicides are of great interest for microelectronics. One of these silicides is Mg_2Si , which belongs to a narrow-band semiconductor with a band gap of 0.74 eV [1]. The epitaxial growth of films of this silicide is complicated by the high degree of desorption of Mg atoms from the silicon substrate at temperatures above 300°C. [2]. According to the literature data, epitaxially formed Mg_2Si films have a polycrystalline structure. Multiple interfaces between misdirected grains and the observed local defects lead to scattering of charge carriers and, as a result, deterioration of the electrical properties of the film [3]. Therefore, one of the main tasks of modern researchers for the practical application of films is to find an effective method for their formation with high crystal quality.

This paper presents the result of a study of the structural properties of two Mg_2Si films formed by reactive epitaxy on Si (111) substrates at a temperature of 250 °C.

2. Experiment

The presented samples were formed in the Varian ultrahigh vacuum chamber of the PHI-590 instrument. The plate Si (111) 65-85 ohms·cm was used as the Si source. To precipitate Mg, a resistive source made of a tantalum tube with a puncture was used, into which 99.999% magnesium powder was placed. The substrate was cut from a plate of Si (111) 2-15 ohms·cm. All materials underwent standard cleaning methods [4].

After high-temperature annealing of the substrates, a 60 nm thick Si buffer layer was deposited on them at 250 °C. Next, Mg and Si layers were deposited alternately (three layers each). The ratio of the thicknesses of Mg and Si layers for the first sample was 2.75 to 1, for the second sample 3 to 1. Deposition rates for both samples were the same: Mg: 9.4 nm/min, Si: 1.1 nm/min.

In situ, during the formation of the layers, their elemental composition was analyzed by Auger spectroscopy. From which it was established that the films contain Mg and Si atoms, while there were no impurities. The film thicknesses were measured ex situ by scanning electron microscopy by chipping samples at the $\text{Mg}_2\text{Si}/\text{Si}$ boundary. The average film thickness of the first sample was 496 nm, and that of the second sample was 682 nm.

3. Results and discussions

The formation of magnesium silicide in the films was confirmed by Raman spectroscopy using the NTEGRA

Spectra-II NT-MDT spectrometer. The Raman spectra are shown in Fig. 1.

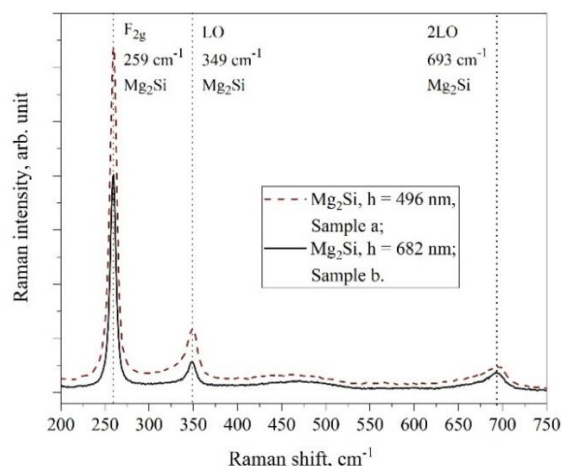


Fig. 1. Raman spectra of samples.

It can be seen from the graphs that peaks corresponding to Mg_2Si phonons are observed for all samples: F_{2g} (259 cm^{-1}), LO (349 cm^{-1}), 2LO (693 cm^{-1}) [3].

The structural properties were investigated by X-ray phase analysis, for which a Bruker D8 ADVANCE diffractometer was used. The measurements were carried out at a wavelength of $\lambda = 1.5418$ Å.

Fig. 2 and 3 show the diffractograms of the films of the first and second samples, respectively. Two reflections of the highest intensity are observed on the X-ray diffraction spectra for both samples, at angles of 2θ 28.53° and 59.03°, which correspond to the contributions of Si (111) and Si (222) from the substrate [5, 6].

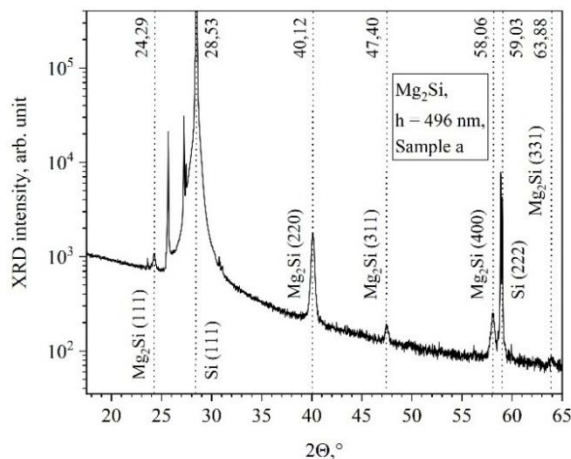


Fig. 2. X-ray diffraction spectra of the first sample.

Contributions from different Mg_2Si crystallographic planes with an Fm-3m cubic lattice are also observed at angles of 2θ 24.27-24.29° Mg_2Si (111), 40.12-40.13° Mg_2Si (220), 47.40-47.43° Mg_2Si (311), 58.06-58.09° Mg_2Si (400) and 63.94-63.88° Mg_2Si (331) [6, 7, 8]. The reflections observed on the diffraction spectra from different nonparallel Mg_2Si crystallographic planes are a sign of the formation of a polycrystalline film [8, 9].

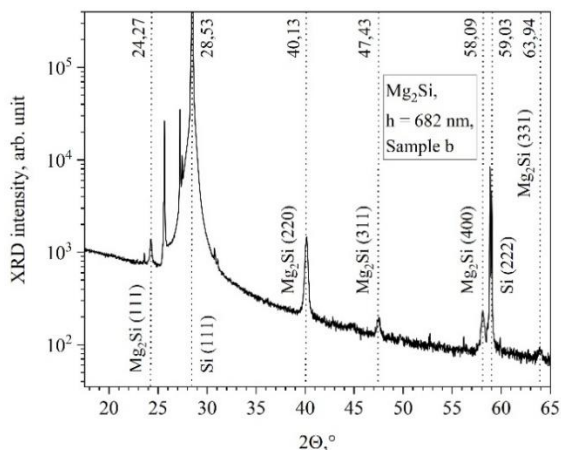


Fig. 3. X-ray diffraction spectra of the second sample.

Calculations of interplanar distances d and crystal lattice constant a were carried out using diffraction spectra. Calculations were carried out using formulas 1 and 2, the calculation results are presented in table 1.

$$d_{hkl} = \frac{m \cdot \lambda}{2 \cdot \sin \theta} \quad (1)$$

$$a = d_{hkl} \sqrt{h^2 + k^2 + l^2} \quad (2)$$

The calculated data of the permanent gratings shown in Table 1 are, on average, less than for the relaxed film [7, 8, 10, 6]. This means that compressive stresses are present in the samples, which is typical for epitaxially grown films [11, 12].

Table 1. Parameters of the crystal lattices of films Mg_2Si

Sam ple	$2\theta, ^\circ$	phase	h	k	l	$d, \text{\AA}$	$a, \text{\AA}$
A	24,29	Mg_2Si	1	1	1	3,663	6,344
	40,12	Mg_2Si	2	2	0	2,245	6,349
	47,40	Mg_2Si	3	1	1	1,916	6,354
	58,06	Mg_2Si	4	0	0	1,587	6,347
	63,88	Mg_2Si	3	3	1	1,455	6,344
B	24,27	Mg_2Si	1	1	1	3,663	6,344
	28,53	Mg_2Si	2	2	0	2,244	6,348
	40,13	Mg_2Si	3	1	1	1,914	6,350
	47,43	Mg_2Si	4	0	0	1,586	6,344
	58,09	Mg_2Si	3	3	1	1,454	6,339

4. Conclusions

Thus, it has been established in this work that Mg_2Si films formed by the method of reactive epitaxy are polycrystalline at a substrate temperature of 250 °C. The calculation of interplanar distances and permanent lattices

has shown that the data obtained correlate well with the results presented in other papers. [6, 7, 8, 10, 12]. The obtained lower values of lattice constants, in comparison with the data for relaxed films, indicate that there are compressive stresses in the formed films.

References

- [1] S.A. Dotsenko, D.V. Fomin, Galkin K.N., et al. // Chemical physics and mesoscopy. – Vol. 12, No. 3. – 2010. – pp. 376-381.
- [2] T. Akiyama, N. Hori, S. Tanigawa, et al. // APAC Silicide. – July 16 – 18, 2016. – Proc. 5. – DOI:10.7567/JJAPCP.5.011102.
- [3] I.M. Chervnev, E.Y. Subbotin, E.V. Argunov, et al. // Scientific and Technical Bulletin of St. Petersburg Polytechnic University. Physical and mathematical sciences. – 2023. – Tom. 16. – No. 3.1. – pp. 106-111. DOI: 10.18721/JPM.163.119.
- [4] Werner Kern // Journal of The Electrochemical Society, 1990. – Vol 137 No. 6. – P. 1887-1892.
- [5] D.V. Fomin, I.A. Astapov, A.V. Polykov // Sixth Asian School-Conference on Physics and Technology of Nanostructured Materials. – Vladivostok, Russia. – 25 – 29 April. – 2022. P. 105 – 106.
- [6] Septian Adi Chandra, Rahadian Roberto, Dedi Pria Utama, et al. // ACTA metallurgicaSlovaca. Vol. 29. – № 2. – 2023. – P. 108 – 112. – DOI: 10.36547/ams.29.2.1840.
- [7] A. Hong Yu, Rui Deng, Zhangjie Mo, et al. / Nanomaterials. – 2022. – Vol. 12. – P. 3230. – DOI:10.3390/nano12183230.
- [8] Kato T., Sago Y., Fujiwara H. // J Appl Phys. 2011. – Vol. 110, № 6. – P. 063723. – doi: 10.1063/1.3642965.
- [9] L. E. Konotopsky, I. A. Kopylets, V. A. Sevryukova, and et al. // Metallphys. The latest technologies. – T. 38. – № 6. – 2016. – P. 825-838.
- [10] Prem Prakash Seth, Om Parkash, Devendra Kumar // The royal society of chemistry. – 2020. – V. 10. – P. 37327-37345.
- [11] Iu. Kogut, M.C. Record // Thin Solid Films 522. – 2012. – P. 149 – 158.
- [12] S.A. Dotsenko, Yu.V. Luniakov, A.S. Gourlanik, et al. // Journal of Alloys and Compounds 778. – 2019. – P. 514.

Resistance drift in GeTe–Sb₂Te₃ system

Trusov E.P.^{*1}, Vorobyov Y.V.^{1,2}, Ermachikhin A.V.^{1,3}

¹ Ryazan State Radio Engineering University, Ryazan, Russia

² National Research University of Electronic Technology, Moscow, Russia

³ Scientific-Manufacturing Complex Technological Centre, Moscow, Russia

*e-mail: eptrusov@yandex.ru

Abstract. The effect of isothermal annealing on resistance drift and changes in the Fermi level in amorphous alloys of the GeTe–Sb₂Te₃ system is investigated. The experiments were carried out with strict control of the time between deposition and measurements to minimize the effects of aging. It is shown that the resistance drift in Ge₂Sb₂Te₅ is related to the expansion of the band gap and the shift of the Fermi level caused by structural relaxation. For compositions rich in Sb₂Te₃, such as GeSb₄Te₇, the opposite behavior is observed: the decrease in resistivity after annealing is explained by partial crystallization. GeSb₂Te₄ demonstrates resistance to drift due to the balance between relaxation and crystallization. The results obtained can be used to develop devices based on amorphous materials with a phase transition, designed for neuromorphic computing and phase memory.

1. Introduction

Artificial intelligence (AI) is one of the most relevant topics in modern computing technologies. Neuromorphic computing implemented in device memory and the development of chips with AI integration are of particular interest. These areas are being actively explored by the scientific and engineering community.

The growing demand for storage technologies for neural networks is driving the search for alternatives to traditional types of memory such as DRAM and Flash. One of the promising technologies is resistive memory [1], which stores information in the form of resistance. This property is ideal for simulating the operation of artificial neural networks, including simulating synapses.

A special place is occupied by phase transition memory (PCM). In such devices, information is recorded by changing the phase state of the material (crystalline or amorphous). The ability to adjust the volume of the material involved in the transition allows for an almost continuous change in resistance. Due to this, PCM is widely used in the development of neuromorphic devices [2], where flexibility in data management is required. One of the main problems for advanced phase memory is the phenomenon of resistance drift [3]. This is manifested in a gradual decrease in the electrical conductivity of the PCM material over time, especially at elevated temperatures.

Along with the widely used Ge₂Sb₂Te₅ material, GeSb₂Te₄ and GeSb₄Te₇ are of interest. All these materials are located on the same quasi–binary slice of GeTe–Sb₂Te₃.

2. Experiment

The experimental facility for studying the electrical conductivity of amorphous chalcogenide films consisted of a Janis CCS-400/204N closed-loop cryostat and a Keithley 6487 picoammeter with a voltage source. The sample was placed on a cooled platform inside a vacuum chamber, where the pressure was maintained below 1 mPa. To exclude the influence of photoconductivity, all measurements were carried out in complete darkness. The resistance was recorded in constant voltage mode during temperature scanning, and the conductivity was calculated taking into account the geometric parameters of the sample. The high resistance of the films minimized the effect of the electrodes. The maximum current through the samples reached 1.2 mA, which corresponds to a joule power of

60 mW. The cooling capacity of the cryostat was 12–16 watts, which significantly exceeds the value of Joule heating, completely eliminating self-heating. Thermal annealing was performed in the same vacuum chamber at a temperature change rate of 2 °C per minute to compensate for thermal inertia. Amorphous chalcogenide films are susceptible to aging even at room temperature, which can change their properties. To minimize this effect, the time interval between the application of the film and the start of measurements was strictly controlled.

The first measurements were carried out 160.9–161.9 hours after deposition. The second stage (after 362 hours) included isothermal annealing at +80°C and subsequent temperature scanning. The third stage (after 1705 hours) included annealing at +100 °C and temperature scanning. The annealing lasted 2 hours. Between the steps, the samples were stored at room temperature in the dark. This methodical approach made it possible to ensure that changes in conductivity and resistance are due to the internal properties of the material. Parameter control provided reliable data on the behavior of films during thermal annealing and aging. These results are important for the development of phase transition materials used in neuromorphic computing and resistive memory, where stability and accuracy are key characteristics.

3. Results and discussions

Resistance drift, characterized by a gradual increase in electrical resistance over time, is caused by structural relaxation processes in amorphous materials. In the Ge₂Sb₂Te₅ material, this phenomenon is associated with expansion of the band gap and shifts in the Fermi level during annealing. However, the dependence of the change in resistance on the composition in the GeTe–Sb₂Te₃ system shows a complex interaction between structural relaxation, crystallization, and other mechanisms.

Previous studies [4,5] have shown that the band gap of GeTe and Ge₂Sb₂Te₅ increases linearly relative to log(t) during annealing, which correlates with a shift in resistance (fig.1). If this expansion of the band gap leads exclusively to resistance drift, then there must be a fixed proportionality between the activation energy of the conduction and the band gap. The results confirm this relationship, demonstrating that the shift in the Fermi (E_F) level due to resistance drift is greater for Ge₂Sb₂Te₅ compared to other

compositions, which is consistent with reports of a greater increase in the band gap in materials richer in GeTe [5]. The expansion of the band gap during resistance drift is almost uniform over a wide temperature range, from the temperature of helium to 350 K. Estimates of the Fermi level position (fig. 2)

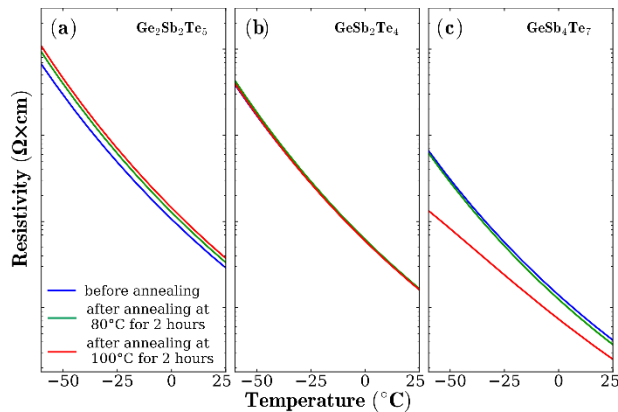


Fig. 1. Change of specific resistivity in the studied system after two anneals.

It is shown that annealing causes an almost parallel shift of E_F away from the valence band or towards the valence band, depending on whether the resistivity increases or decreases. This confirms the assumption that the proportionality between the band gap and the Fermi level remains unchanged during annealing. These results are consistent with the concept of stretching the density of states proposed in [6], which relates the resistance drift to shifts of the edges of the zones and bands of defects of the middle gap away from the Fermi level. The results indicate that an increase in the Sb_2Te_3 component in the GeTe– Sb_2Te_3 system reduces the degree of stretching of the density of states, thereby reducing the effect of resistance drift.

The composition most rich in Sb_2Te_3 in this study, $GeSb_4Te_7$, shows the opposite behavior, the resistivity decreases significantly after annealing at temperatures of 80°C and 100°C (fig. 1). This trend extends to the temperature dependence of the Fermi level (fig. 2), which also undergoes significant changes. The addition of Sb_2Te_3 accelerates the crystallization of materials in the GeTe– Sb_2Te_3 system [7,8]. Given the high Sb_2Te_3 content, $GeSb_4Te_7$ probably undergoes partial crystallization during annealing at these temperatures, which counteracts the resistance shift.

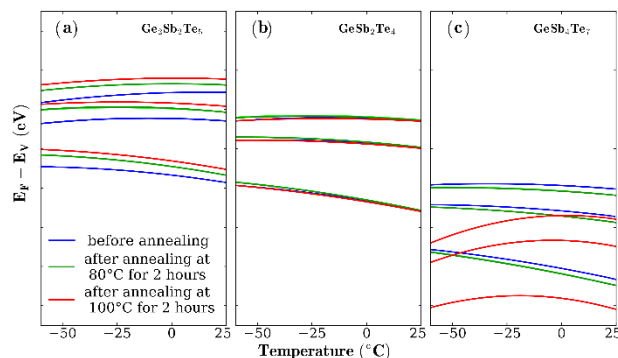


Fig. 2. Temperature dependence of Fermi level and its change after two anneals.

4. Conclusions

In this study, the resistance drift in the quasi-binary GeTe– Sb_2Te_3 system was studied during isothermal annealing at 80°C and 100°C. To ensure that the observed effects are due to differences in composition, the time between deposition and annealing was strictly controlled. Measurements of the resistivity and changes in the Fermi level revealed a gradual shift in the behavior of the material from enriched compositions to compositions enriched with Sb_2Te_3 . While $Ge_2Sb_2Te_5$ showed resistance drift, $GeSb_4Te_7$ showed the opposite behavior (resistance decreased), and $GeSb_2Te_4$ proved resistant to drift. This is explained by partial crystallization during annealing, which counteracts the drift.

Acknowledgements

This work was supported by a grant from the Russian Science Foundation No. 24-79-10137 (<https://rscf.ru/en/project/24-79-10137/>). The sample preparation was performed using equipment of the research laboratory “Active photonic materials and devices” of MIET. Measurements of conductivity and its temperature dependence were performed using equipment of the Regional Centre for Probe Microscopy of Ryazan State Radio Engineering University.

References

- [1] Wang Z, Wu H, Burr G W, Hwang C S, Wang K L, Xia Q and Yang J J Nat Rev Mater **5**(2020)173.
- [2] Xu M, Mai X, Lin J, Zhang W, Li Y, He Y, Tong H, Hou X, Zhou P and Miao X Adv Funct Mater **30**(2020)2003419.
- [3] Pirovano A, Lacaite A L, Pellizzer F, Kostylev S A, Benvenuti A and Bez R IEEE Trans Electron Devices **51**(2004)714.
- [4] Fantini P, Brazzelli S, Cazzini E and Mani A Appl Phys Lett **100**(2012)013505.
- [5] Rütten M, Kaes M, Albert A, Wuttig M and Salinga M Sci Rep **5**(2015)17362.
- [6] Krebs D, Bachmann T, Jonnalagadda P, Dellmann L and Raoux S New J Phys **16**(2014)043015.
- [7] Yamada N, Ohno E, Nishiuchi K, Akahira N and Takao M J Appl Phys **69**(1991)2849.
- [8] Rodríguez C V R, Sanchez E M, Hernández J G, Prokhorov E, Saldaña J M and Martínez G T 2012 J Surf Eng Mater Adv Techno **2**(2012)44.

The origin of the lateral photovoltaic effect in the $\text{SiO}_2/\text{TeO}_2/\text{Bi}_2\text{Te}_3/\text{n-Si}(111)$ structure: by varying laser illumination

Yakovlev A.A.^{*1}, Pisarenko T.A.¹, Tsukanov D.A.^{1,2}, Mararov V.V.¹, Balashev V.V.^{1,2}, Ignatovich K.V.¹

¹ Institute of Automation and Control Processes FEB RAS, 5 Radio St., Vladivostok 690041, Russia

² Far Eastern Federal University, FEFU Campus 10 Ajax Bay, Vladivostok 690950, Russia

*e-mail: yakovlev@iacp.dvo.ru

Abstract. In this work, we investigated the lateral photovoltaic effect in the $\text{SiO}_2/\text{TeO}_2/\text{Bi}_2\text{Te}_3/\text{n-Si}(111)$ structure by varying the wavelength and power of the illumination. It was found the lateral photovoltage increases linearly with increasing laser power, while the photosensitivity behaves in phase with the absorption spectrum of silicon. It was shown the lateral photovoltage decreases with increasing Bi_2Te_3 film thickness that is due to the shunting effect. We defined that the studied structure demonstrates promising results as photovoltaic cell when the Bi_2Te_3 buffer layer thickness of 5 nm and illumination parameters of $\lambda = 730\div 830$ nm and $W = 0.8$ mW.

1. Introduction

In the last decade, the research of two-dimensional (2D) materials has great interest in the field of optoelectronics [1]. One of the promising areas of optoelectronics development is the use of topological insulators (TI) that will increase speed [2-5]. TI are materials capable of conducting spin-polarized current on their surface and practically not conducting inside, in volume, remaining an insulator.

Bi-based TI attract attention due to their exceptional electrical and optical properties. In particular, Bi films have various combinations of properties, from superconductivity [6] to magnetotransport [7]. A study using the example of the surface of a Bi_2Te_3 crystal has shown that accelerated electrons are able to move along the surface of a TI practically without scattering — unlike movement in a conventional crystal — which means that they conduct current much faster, without heating losses [8].

The lateral photovoltaic effect (LPE), in which the surface potential difference of a certain system of materials varies linearly depending on the position of the incident laser beam, is one of the popular effects found in optoelectronics [1,9]. As a rule, in silicon-based photovoltaic cells, lateral photovoltage is generated in the space charge region of silicon. However, since in the $\text{SiO}_2/\text{TeO}_2/\text{Bi}_2\text{Te}_3/\text{n-Si}(111)$ structure both Si and Bi_2Te_3 are absorbed in the visible spectrum, it is of interest to study the origin of LPE in this structure. Due to the spin splitting in Bi_2Te_3 , when absorbing light, circular photovoltaic effect (CPE) is generated in it. Therefore, if the regions of LPE and CPE generation are separate, then photovoltaic cells based on the $\text{Bi}_2\text{Te}_3/\text{Si}$ structure will expand the functionality of optoelectronic devices.

In this work the LPE in the $\text{SiO}_2/\text{TeO}_2/\text{Bi}_2\text{Te}_3/\text{n-Si}$ structure was studied by varying parameters of wavelength and laser radiation power as well as Bi_2Te_3 thickness under continuous and pulse illumination to identify a localization of LPE generation.

2. Experiment

Thin-film growth using molecular beam epitaxy was conducted in a ultrahigh vacuum (UHV) chamber with a base pressure less than 5.0×10^{-10} Torr. We used n-type

$\text{Si}(111)$ wafers ($40\text{--}70 \ \Omega \text{ cm}$) as substrates. Atomically clean $\text{Si}(111)7 \times 7$ surface was prepared in situ by flashing to 1280°C after the wafer was first outgassed at 600°C for 6 h. Bismuth and tellur were evaporated from effusion cells with integrated shutters. The Bi_2Te_3 layers were grown at a higher temperature of about 240°C , at which the film grew in step-flow mode. To reduce the amount of Te vacancies, the Bi-to-Te flux ratio was chosen close to 1:14 with the growth rate of about 0.3 QL/min [4].

To prevent oxidation of the functional Bi_2Te_3 layer, after cooling to room temperature, the Bi_2Te_3 films were covered by 2 nm-Te and 1 nm-Si. After the samples were exposed to air, the top silicon and tellurium layers were oxidized, resulting in the formation of top transparent layers, called window layers. The lateral photovoltaic effect was therefore studied for the $\text{SiO}_2/\text{TeO}_2/\text{Bi}_2\text{Te}_3/\text{n-Si}$ structure.

Lateral photovoltaic effect was investigated by using a Ti:sapphire laser delivering 60 fs pulses with a repetition rate of 80 MHz (a spot diameter of 50 μm) and Keithley 2000 multimeter. The response time was investigated by a digital oscilloscope (Tektronix TDS 2012B) of 150 MHz. The distance between the probes was 1 mm.

3. Results and discussions

In Fig.1 we can see the lateral photovoltage dependence for photovoltaic cells with thickness of Bi_2Te_3 buffer layer of 5 and 10 nm under continuous and pulse illumination. The dependence of the lateral photovoltage on the laser spot position is parameterized by the sensitivity (κ), which also corresponds to the photopulse value. According to this parameter, the structure with a 5 nm- Bi_2Te_3 buffer layer is more promising for photodetect. A decrease of photosensitivity with increasing Bi_2Te_3 layer thickness indicates the generation of photovoltage in the near-surface silicon layer. To confirm this fact, we conducted studies with variations in such laser illumination parameters as wavelength and power.

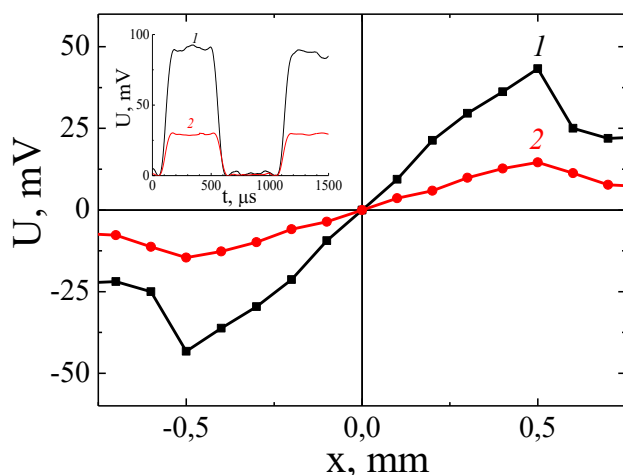


Fig. 1. Dependence of lateral photovoltage on the laser spot position in the $\text{SiO}_2/\text{TeO}_2/\text{Bi}_2\text{Te}_3/\text{n-Si}(111)$ structure with the Bi_2Te_3 buffer layer thickness: 1 – 5 nm, 2 – 10 nm. The insert shows pulsed dependences of lateral photovoltage.

Figure 2 shows the dependences of the photovoltage near the contact on the laser illumination power, the inset shows the dependence of the photosensitivity on the illumination wavelength. The linear increase in the lateral photovoltage with increasing laser power is due to the increase in the number of photogenerated carriers, which with such a significant increase in power is possible only in the space charge region of silicon. A decrease in the slope of the dependences $U_{\text{max}}(W)$ indicates significant absorption in the Bi_2Te_3 layer, which increases with increasing thickness of the Bi_2Te_3 buffer layer.

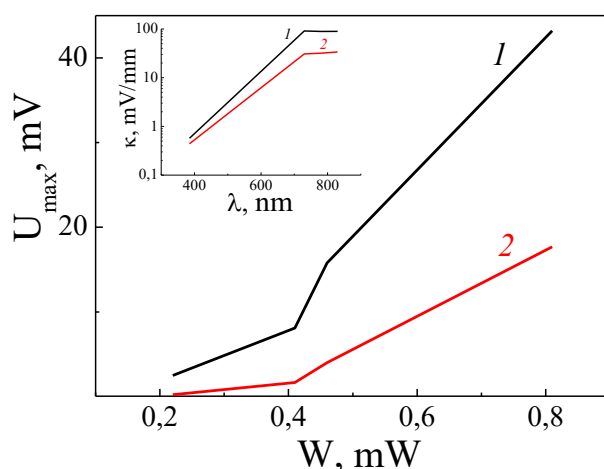


Fig. 2. Dependence of lateral photovoltage in the $\text{SiO}_2/\text{TeO}_2/\text{Bi}_2\text{Te}_3/\text{n-Si}(111)$ structure on the laser illumination power incidenting on a surface. On the insert is the dependence of photosensitivity on the laser illumination wavelength. 1 – 5 nm Bi_2Te_3 , 2 – 10 nm Bi_2Te_3 .

The most striking evidence of lateral photovoltage generation in silicon can be observed in the dependence of photosensitivity on the illumination wavelength. As can be seen in the inset in Fig. 2, the dependence inherits the nature of the absorption spectrum of silicon at both thicknesses of the buffer layer, which clearly indicates the generation of nonequilibrium photocarriers in the near-surface silicon layer.

Thus, in the $\text{SiO}_2/\text{TeO}_2/\text{Bi}_2\text{Te}_3/\text{n-Si}(111)$ structure, the absorbing layer is the silicon space charge region, the bismuth telluride layer is the buffer layer, and the tellurium

dioxide and silicon dioxide layers are protective transparent coverings, the so-called window layers.

4. Conclusions

This study revealed the role of bismuth telluride layers absorbing the visible spectrum and the silicon space charge region in the lateral photovoltaic effect. It was found that the lateral photovoltage is generated in the silicon layer at the $\text{Bi}_2\text{Te}_3/\text{Si}$ interface the bismuth telluride layer is a buffer layer that induces a heterojunction in the structure. The use of transparent window layers also allows reducing the losses of photovoltaic cells with a buffer layer of the Bi_2Te_3 topological insulator.

Acknowledgements

This work was financed by the budget of the Institute of Automation and Control Processes of the Far Eastern Branch of the Russian Academy of Sciences within the framework of the state assignment (No. FFW-2021-0002).

References

- [1] Y. Yang. J. Phys.: Conf. Ser. 2044(2021)012151.
- [2] J.M.Chae, S.B.Hong, D.Kim, D.K.Kim, J.Kim, K.Jeong, S.H.Park, M.H.Cho. Appl. Surf. Sci. 554(2021)149623.
- [3] S. Hasegawa. Appl. Phys. Express 17(2024)050101.
- [4] A.V.Matetskiiy, I.A.Kibirev, T.Hirahara, S.Hasegawa, A.V.Zotov, A.A.Saranin. Appl. Phys. Lett. 107(2015)091604.
- [5] S.B.Hong, J.Chae, D.K.Kim, K.Kim, K.Jeong, J.Kim, M.H.Cho. ACS Appl. Mater. Interfaces 12(2020)26649.
- [6] C. Granqvist and T. Claeson. Phys. Condens. Matter 18(1974)79-97.
- [7] M. Aitani, T. Hirahara, S. Ichinokura, M. Hanaduka., D. Shin and S. Hasegawa. Phys. Rev. Lett. 113(2014)206802.
- [8] Y. Chen, J. Analytis, J.-H. Chu, Z. Liu, S.-K. Mo, X.-L. Qi, H. Zhang, D. Lu, X. Dai and Z. Fang. Science 325(2009)178-181.
- [9] C.Yu, H.Wang. Sensors 10(2010)10155.

Synthesis of Mg₂Si core-shell nanowires by solid-phase epitaxy

Subbotin E.Yu.^{*1}, Kozlov A.G.², Pavlov D.V.¹, Lisenkov O.E.¹, Udilov A.D.¹, Prokopeva G.A.¹, Goroshko D.L.¹, Chernev I.M.¹, Khoroshilov D.A.¹, Sinotova S.A.¹, Galkin N.G.¹

¹ Institute of Automation and Control Processes, 5 Radio St., Vladivostok 690041, Russia

² Far Eastern Federal University, 8 Sukhanova St., Vladivostok 690950, Russia

*e-mail: jons712@mail.ru

Abstract. In this work, nanowires with a core-shell structure based on silicon and magnesium silicide were formed. Silicon nanowires, work as a substrate (core), were obtained using metal-assisted chemical etching of silicon wafers. The height of such nanowires is 10 μm , the diameter is 1.5 μm . The silicide "shell" was synthesized using solid-phase epitaxy under high vacuum conditions. The thickness of the silicide shell is 600 nm on the side walls of the silicon nanowires. According to transmission microscopy data, conjugation with a silicon core of the Mg₂Si(111)||Si(111) type is performed. The structure is polycrystalline, the film is deformed along [111] by 2.7%, along [220] by 7.6%.

1. Introduction

Micrometer-size thermoelectric converters ($\mu\text{-TEC}$) attract the significant attention due to the widespread introduction low consumption micro-watt devices [1,2] and microelectromechanical systems (so-called, MEMS). The successful development of such $\mu\text{-TECs}$ requires novel fabrication approaches and adaptation of well-developed in the past materials for these methods. In the work we have studied growth features of core-shell vertical heterostructures. In these systems nanowires with silicon core were covered by Mg₂Si shell that considered as thermoelectric active material [3]. Also, the architecture can decrease thermal conductivity that important for thermoelectric properties.

2. Experiment

The silicon core was created by anisotropy metal-assisted chemical etching (MACE). As catalytic metals thin Au film (25 – 30 nm) with thinnest Ti adhesive layer (1.5 – 2 nm) were used. As the substrate was chosen monocrystalline boron-doped Si(100) samples with 1-10 Ohm \times cm resistivity. Then these samples were etched in HF (48%, 12 ml):H₂O₂ (37%, 4 ml):H₂O (deionized, 34 ml) solution for 1 hour. Mg₂Si shell was grown by solid phase epitaxy in ultra-high vacuum conditions ($p=10^{-9}$ Torr) and by reactive epitaxy in high-vacuum chamber ($p=10^{-6}$ Torr). The silicide synthesis was confirmed by Raman-spectroscopy, linear sizes of these structures were estimate by scanning electron microscope, the material distribution was established by x-ray energy dispersive spectroscopy.

3. Results and discussions

Etched silicon vertical alignment nanowires are 10 μm height, 1.5 μm diameter and $\sim 5 \mu\text{m}$ distance between NWs that is equal $\sim 2 \times 10^7 \text{ cm}^{-2}$ arrangement density (Figure 1).

Linear sizes can be easily changed by etching conditions, the diameter and the surface density is set by lithography with high resolution or laser texturing. The Mg₂Si shell thickness is 400-600 nm on the Si-nanowires side-walls.

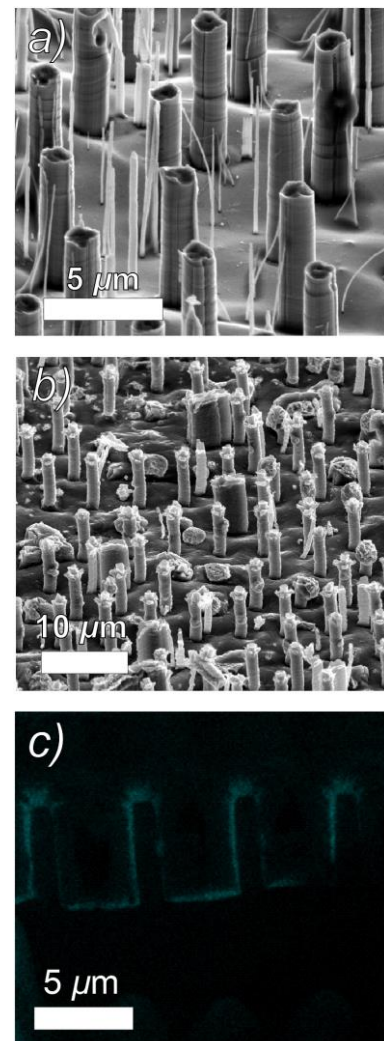


Fig. 1. Silicon/Mg₂Si-core shell structures.

References

- [1] Hu G. et.al., Nat. El. 2(7) (2019) 300-306.
- [2] Li G. et.al. Nat. El. 1(10) (2018) 555-561.
- [3] Cheng X. et.al. Jom 68 (2016) 2680-2687.

III. Advanced optical materials, technologies and devices

Up-scaling of perovskite solar cell technology for terrestrial and space energy systems

Luchnikov L.O.¹, Ilicheva E.A.¹, Gren D.A.¹, Le T.S.¹, Gostishchev P.A.¹, Sukhorukova P.K.²,
Luponosov Yu.N.², Saranin D.S.^{*,1}

¹ MISIS University, 4 Leninsky prospect., Moscow 119049, Russia

² Enikolopov Institute of Synthetic Polymeric Materials Russian Academy of Sciences, Profsoyuznaya 70, Moscow 117393, Russia

*e-mail: saranin.ds@misis.ru

Abstract. All-slot-die printing carried out in air is demonstrated for p-i-n perovskite solar cells and minimodules by coupling vacuum-assisted quenching with Cl-anion and self-assembled-monolayer (SAM) interface engineering. Compact NiOx/MA- or CsFA-based perovskite/PCBM/BCP stacks fabricated on 50 × 50 mm substrates reach 20.1 % efficiency on 0.15 cm² devices and 17.1 % on 2.1 cm² minimodules, while 64.8 cm² modules deliver 15.8 % and retain 80 % of their initial power for >3000 h under ISOS-L-2 illumination. Lattice contraction, longer carrier lifetimes, suppressed PbI₂ formation and homogenised surface wettability reveal the synergistic role of Cl doping and triphenylamine-based SAM/polymer blends in delivering large-area uniformity, high efficiency and long-term operational stability.

1. Introduction

Solution printing offers an unrivalled route to translate perovskite photovoltaics from laboratory cells to metre-scale manufacturing, yet fully ambient, additive-free printing seldom yields the film quality, interfacial perfection and stability demanded by commercialization. Slot-die coating combined with in-line vacuum quenching enables rapid deposition of micron-scale wet films, promoting controlled nucleation without a glovebox, while ionic and molecular interface engineering mitigate the defect densities that presently limit efficiency and durability. Chlorine incorporation contracts the ABX₃ lattice and passivates halide-vacancy pathways, whereas triphenylamine-based self-assembled monolayers (SAMs) align the NiOx valence band and homogenise surface wettability over tens of square centimetres[1], [2]. The present work unifies these concepts to deliver efficient, stable perovskite solar cells and modules fabricated entirely by high-throughput slot-die printing.

2. Experiment

Glass/ITO substrates were cleaned and slot-die coated with NiOx (40 nm) at 100 °C. After annealing, a dilute TPATC or blended pTPA-TDP/SAM solution was roll-coated to form a <2 nm interlayer. MAPbI₃ or CsFAPbI₃-xClx inks containing 5–10 mol % MAcl or FAcI were deposited at 25 °C; the wet web passed a 50 Pa vacuum chamber for 3 s to trigger rapid solvent extraction, then crystallised at 150 °C for 10 min. PCBM (40 nm) and BCP (11 nm) were sequentially printed and vacuum-quenched, followed by Ag evaporation. Devices (0.15–64.8 cm²) were characterised under AM 1.5 G, ISOS-L-2 stability and transient spectroscopies.

3. Results and discussions

Vacuum quenching produced compact, pin-hole-free perovskite grains ≥800 nm, reducing series resistance by 30 % relative to air-dried references. X-ray diffraction showed a 0.6 ± 0.06 % lattice contraction upon Cl inclusion, accompanied by a 0.018 eV band-gap widening and photoluminescence lifetime extension from 240 to 540 ns[3], [4], evidencing bulk defect passivation. TRMC and

impedance spectroscopy indicated a one-order-of-magnitude decrease in ionic defect density at the NiOx/perovskite contact after TPATC treatment, accounting for the improved fill factor (77 % → 81 %). Contact-angle mapping confirmed that the pTPA-TDP/SAM blend reduced the hydrophobicity gradient of pure SAM from 25° to 5°, eliminating macroscopic voids and ensuring thickness variation <20 nm over 50 × 50 mm substrates. Consequently, MAPbI₃ devices reached 16.4 % efficiency, CsFAPbI₃-xClx cells 20.1 %, and 12-sub-cell modules 17.1 %. Light-soaking at 1 sun/45 °C retained 80 % of the initial power after 3479 h, tripling the lifetime of undoped controls, while TPATC-modified modules preserved 98 % of the initial maximum power after 500 h. Degradation analysis showed suppressed PbI₂ formation and halide segregation only when the perovskite was capped with PCBM/BCP, corroborating the synergistic roles of Cl anions and organic interlayers.



Fig. 1. Photo-image of the fabricated perovskite solar panel (16 modules).

4. Conclusions

By integrating vacuum-assisted slot-die coating, Cl⁻ anion engineering and triphenylamine-based interlayers, we establish an ambient, roll-compatible route to high-performance p-i-n perovskite photovoltaics. The combined strategy simultaneously controls crystallization, passivates bulk and interfacial defects, and evens surface energy, allowing small-area efficiencies above 20 %, 2.1 cm² minimodules at 17 %, and 64.8 cm² modules at 15.8 %. Operational tracking under ISOS-L-2 demonstrates T₈₀ lifetimes beyond 3000 h—among the longest reported for printed modules—while maintaining a fully printable stack (NiOx/perovskite/PCBM/BCP). Mechanistically, Cl incorporation contracts the lattice and suppresses iodide migration, whereas TPATC or pTPA-TDP/SAM layers reorder trap energetics and block interfacial ion exchange. These insights offer a transferable toolbox for scaling perovskite photovoltaics, bridging the efficiency gap between lab and factory and providing a viable pathway toward low-cost, terawatt-scale solar energy.

Acknowledgements

Authors gratefully acknowledge the financial support from Strategic Technological project "Energy of Materials", №B523019, Program Priority 2030, STP3.

References

- [1] E. A. Ilicheva *et al.*, “Double-side integration of the fluorinated self-assembling monolayers for enhanced stability of inverted perovskite solar cells,” *Mater Today Energy*, vol. 47, p. 101741, Jan. 2025, doi: 10.1016/j.mtener.2024.101741.
- [2] T. S. Le *et al.*, “Tailoring Wetting Properties of Organic Hole-Transport Interlayers for Slot-Die-Coated Perovskite Solar Modules,” *Solar RRL*, Sep. 2024, doi: 10.1002/solr.202400437.
- [3] A. A. Vasilev, D. S. Saranin, P. A. Gostishchev, S. I. Didenko, A. Y. Polyakov, and A. Di Carlo, “Deep-level transient spectroscopy of the charged defects in p-i-n perovskite solar cells induced by light-soaking,” *Optical Materials: X*, vol. 16, p. 100218, Oct. 2022, doi: 10.1016/j.omx.2022.100218.
- [4] A. S. Shikoh *et al.*, “On the relation between mobile ion kinetics, device design, and doping in double-cation perovskite solar cells,” *Appl Phys Lett*, vol. 118, no. 9, Mar. 2021, doi: 10.1063/5.0037776.

Femtosecond laser nanopatterning for IR photodetection and sensing empowered by bound states in the continuum

Pavlov D.V., Cherepakhin A.B., Zhizhchenko A.Yu., Kuchmizhak A.A.*

Institute of Automation and Control Processes, 5 Radio St., Vladivostok 690041, Russia

*e-mail: alex.iacp.dvo@mail.ru

Abstract. Plasmonic metasurfaces with high-Q resonances offer exceptional capabilities for nanoscale light manipulation. However, their widespread adoption in practical applications—such as advanced optoelectronic devices and sensors—has been limited by costly and time-consuming fabrication methods. In this work, we present a scalable approach for direct femtosecond laser printing of plasmonic metasurfaces. By irradiating a 50-nm-thick glass-supported Au film with focused laser pulses, we induce localized melting and reshaping, forming hollow protruding nanostructures (nanobumps and nanojets). Through pulse-by-pulse printing, we fabricate ordered nanobump arrays that support symmetry-protected plasmonic quasi-bound states in the continuum (qBIC) with measured Q-factors up to 40 within a spectral range spanning from 1 to 8 μm . Optical simulations and experiments reveal that resonant excitation enhances localized electromagnetic fields, significantly boosting nonlinear optical effects, particularly third-harmonic generation (THG). We demonstrate that angled excitation optimizes radiative and nonradiative loss balance, leading to a 10^5 -fold enhancement in THG yield under critical coupling conditions. Furthermore, we apply these laser-printed qBIC metasurfaces to modulate quantum dot emission and realize optical sensors and short-wave infrared (SWIR) photodetectors.

Monodisperse silica microspheres for reducing friction in lubricating oil

Lei Pan^{1,2}, Jianrong Xin², Yao Li³, Jiupeng Zhao¹

¹ MIT Key Laboratory of Critical Materials Technology for New Energy Conversion and Storage, School of Chemistry and Chemical Engineering, Harbin Institute of Technology, Harbin, 150001, P. R. China

² Hunan Tongqiuleidun Technology Co., Ltd, Zhuzhou, 412006, China

³ National Key Laboratory of Science and Technology on Advanced Composites in Special Environments, Harbin Institute of Technology, Harbin, 150001, China

Abstract. The rapid advancement of high-speed and heavy-load mechanical systems has revealed significant performance limitations of conventional lubricant additives under extreme operating conditions. Leveraging the mechanical advantages and surface tunability of silica (SiO₂) microspheres, this study develops a novel lubrication strategy through the synthesis of monodisperse SiO₂ microspheres (mean diameter: 135 nm) via the Stöber method, followed by surface modification with a silane coupling agent (KH570) to optimize their colloidal stability in polyalphaolefin (PAO) base oil. Comprehensive characterization employing scanning electron microscopy (SEM) and Fourier-transform infrared spectroscopy (FTIR) verified the successful covalent grafting of carbon-carbon double bonds onto the SiO₂ surface.

Tribological evaluations demonstrated that incorporating 2 wt% surface-modified SiO₂ microspheres achieved a 30% reduction in the friction coefficient in standardized four-ball tests. Mechanistic analysis of wear scar topography revealed a synergistic lubrication mechanism: (1) microspheres function as nanoscale rolling elements to minimize direct asperity contact between friction pairs, and (2) in situ formation of a tribochemical Si-O-Fe boundary film that effectively repairs surface microdefects. Large-scale vehicular testing confirmed consistent fuel efficiency enhancements of 5%–14% across both light-duty and heavy-duty applications. These findings provide fundamental insights and practical methodologies for engineering next-generation nanolubricant additives, with promising implications for extending service life of mechanical components and advancing energy-efficient tribological systems.

Keywords: silica microspheres; lubricant additive; tribological mechanism; friction reduction and anti-wear; surface modification; fuel economy.

Phase change materials and their application

Lazarenko P.I.^{*,1}, Kovalyuk V.V.², Kitsyuk E.P.³, Prokhodtsov A.I.^{1,2}, Nevzorov A.A.^{1,2},
Menshikov E.V.⁴, Sinev I.S.⁵, Kozyukhin S.A.⁶, Goltsman G.N.⁷, Svetukhin V.V.³

¹ National Research University of Electronic Technology, Zelenograd, Russia

² University of Science and Technology MISIS, Moscow, Russia

³ Scientific-Manufacturing Complex "Technological Centre", Zelenograd, Russia

⁴ ITMO University, St. Petersburg, Russia;

⁵ Ecole Polytechnique Federale de Lausanne, Lausanne, Switzerland

⁶ Kurnakov Institute of General and Inorganic Chemistry of the RAS, Moscow, Russia

⁷ National Research University Higher School of Economics, Moscow, Russia

*e-mail: aka.jum@gmail.com

Abstract. The ability of phase-change materials to quickly and reversibly transform between crystalline and amorphous phases made it possible to implement various reconfigurable devices and applications. Here, we report the results of fabrication and investigation of fully optical reconfigurable devices based on the chalcogenide materials, in particular Ge₂Sb₂Te₅.

1. Introduction

Phase-change materials (PCMs) have attracted considerable attention in recent decades. One of the prominent features of PCM is that their phase transition can be induced by optical stimuli, which opens the opportunity for all-optical modulation and local in-situ engineering of the optical response. Their ability to quickly and reversibly switch between crystalline and amorphous phases, which are characterized by significant difference in electrical conductivity, refractive indices, extinction coefficients and other physical parameters [1], made it possible to implement various reconfigurable devices and applications.

2. Results and discussions

Here, we report the results of fabrication and investigation of fully optical reconfigurable on-chip nanophotonic devices, including Mach-Zehnder interferometers, balance splitters and O-ring resonators. The e-beam lithography and lift-off process were used to fabricate PCM cells atop silicon nitride rib waveguides. Each sample included devices with different lengths of PCM thin coatings along the waveguide, which varied from 0.1 to 20 μm . By varying the pump pulse power, we were able to reversibly switch the fabricated devices. The 9 nonvolatile different levels (3 bits) for the nanophotonic samples based on the PCM thin films were demonstrated [2].

Next we considered the fabrication PCM thin films with a spatial pattern of amorphous and crystalline states written by using the direct laser writing technique. We propose a method to generate a vortex beam with post fabrication variable topological charge using inherently two-dimensional structures based on phase change materials. We verify that the mechanical rotation of the films leads to a change in the topological charge of the output beam. We demonstrate an erase-and-rewrite modification of the pattern, that results in the change of the topological charge

of the generated beam, when optical elements are fixed, i.e. no mechanical displacement takes place [3].

Also we demonstrate the direct laser patterning of phase change material films that leads to formation of laser-induced periodic surface structures (LIPSS). Due to the unique properties of PCM such fabricated structures provide strong spatial modulation of the optical properties. In stark contrast to LIPSS in standard materials, phase change LIPSS can be reverted to the original state using the same laser emission, which greatly expands the scope of their applications. We demonstrate reversible and re-writable formation of phase change LIPSS on different substrates and highlight possible application for active elements in integrated photonic circuits [4].

4. Conclusions

So, we envision modification of phase change materials, in particular LIPSS, as a powerful toolkit for improving and complementing the performance of photonic integrated circuits and other photonic devices. The developed concept opens the way for applications in all-optical signal modulation and tunable integrated devices.

Acknowledgements

The fabrication and investigation of reconfigurable on-chip nanophotonic devices was supported by the Russian Science Foundation (№ 25-49-00103). The PCM were fabricated with contributions from the research laboratory "Materials and devices for active photonics" (FSMR-2025-0002).

References

- [1] Kozyukhin, S. et. al. Russ. Chem. Rev **91**(2022)RCR5033.
- [2] Lazarenko, P. et. al. Acta Materialia **234**(2022)117994.
- [3] Solomonov, A. et. al. Applied Materials Today **37**(2024)102135.
- [4] Menshikov, E. et. al. ACS Appl. Mater. Interfaces **16**(2024)38345.

Femtosecond laser modification of amorphous silicon films for photovoltaic and polarization applications

Shuleiko D.V.¹, Sokolovskaya O.I.^{*1}, Martyshev M.N.¹, Serdobintsev A.A.², Volkovoyanova L.D.², Venig S.B.², Pakholchuk P.P.^{1,3}, Kuzmin E.V.^{1,3}, Zaboltnov S.V.¹, Kashkarov P.K.^{1,4}

¹ Lomonosov Moscow State University, Faculty of Physics, 1/2 Leninskie Gory, Moscow 119991, Russia

² Saratov State University, 83 Astrakhanskaya St., Saratov 410012, Russia

³ P.N. Lebedev Physical Institute of RAS, 53 Leninsky Ave., Moscow 119991, Russia

⁴ National Research Center "Kurchatov Institute", 1 Akademika Kurchatova Sq., Moscow 123182, Russia

*e-mail: oi.sokolovskaja@physics.msu.ru

Abstract. The perspectives of amorphous silicon (a-Si) films employment as a basis for heterojunction solar cells and waveplates are demonstrated. The possibility to achieve surface crystallization of the 1 μm -thick a-Si film with crystalline layer thickness of $45 \pm 5 \text{ nm}$ is demonstrated by depth-resolved Raman spectroscopy and optical microscopy, when the irradiating laser fluence of 0.1 J/cm^2 is used, which is lower than a-Si ablation threshold. The electrical measurements indicate formation of a heterojunction between nanocrystalline Si and a-Si phases in such samples. Femtosecond laser irradiation of a-Si films with fluence of 0.15 J/cm^2 leads to formation of LIPSS with low spatial period and optical retardance of $280 \pm 40 \text{ nm}$.

1. Introduction

Advances in the ultrafast laser-assisted creation of polarization-sensitive optical elements for the visible and near-infrared range based on amorphous silicon (a-Si), as well as heterojunction "crystalline silicon (c-Si) – a-Si" on thin a-Si films open up prospects for further improvement of technologies for obtaining a-Si-based heterojunctions and submicron surface structures with optical and electrophysical anisotropy. Application of ultrafast laser pulses leads to well-known phenomenon of laser-induced periodic surface structures (LIPSS) formation that allows fabricating integrated optical elements by selective irradiation of layered structures without photoresists and lithography. Such integrated optical elements may be of interest both for polarization optical measurements or creating structured light beams, and for field of telecommunications, for example, to conduct polarized signals in fiber-optic communication lines [1].

Also of interest is the possibility of increasing the efficiency of solar cells based on a-Si layers due to its laser-induced crystallization, with the creation of a "c-Si – a-Si" heterojunction in the a-Si layer. This approach seems relevant, first of all, for HIT structures (Heterojunction with Intrinsic Thin-layer solar cells), where layers of amorphous silicon are deposited on a c-Si wafer by the PECVD method. The maximum achievable efficiency for solar cells based on heterojunctions is 26.7% [2], and the maximum limit of thermodynamic efficiency for fully silicon solar cells is estimated at about 33% [3]. Thus, it seems necessary to search for technologies to increase the efficiency of Si-based solar cells in order to increase their competitiveness. The use of laser-induced crystallization can increase the efficiency of batteries based on HIT structures by creating additional "c-Si – a-Si" heterojunctions, which promotes more efficient charge separation, as well as due to higher charge mobility in nanocrystalline silicon, compared to a-Si.

2. Experiment

To obtain a heterojunction "amorphous-crystalline silicon" by laser-induced a-Si crystallization, at the first stage, 1 μm thick a-Si layers were magnetron-sputtered

(Robvac VSM 300) at direct current on glass substrates with pre-deposited contacts made of chromium or ITO.

To determine laser radiation parameters required for nonuniform-over-depth crystallization of amorphous silicon layers as well as to determine the depth of such crystallization, a test irradiation of single scan lines was performed at the second stage. The film surface was irradiated with Satsuma femtosecond laser (515 nm, 50 μm , 300 fs, 1 kHz, scan speed 300 $\mu\text{m/s}$). The employed fluence E varied from 0.01 to 0.1 J/cm^2 , corresponding to the minimum fluence at which structural changes were visually observed in the a-Si film, and the maximum fluence at which a-Si ablation was not yet observed. As a result of irradiation, a structure in the form of a meander (Fig. 1) was formed on the surface of the a-Si layer.

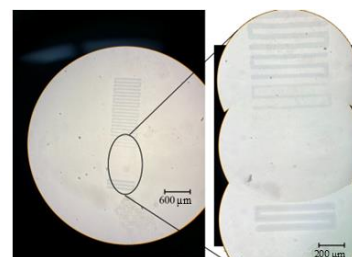


Fig. 1. An optical image of the meander resulted from femtosecond processing of a-Si film.

The irradiated regions were then subjected to ion beam etching, to create a uniformly deepening profile. After that, Raman spectra were measured at various points of the etched profile using a Renishaw Raman spectrometer (excitation 532 nm), and obtained Raman signal distribution maps were then analyzed to determine the Si crystalline phase volume fraction f_c and its distribution along the film depth.

Based on the crystallinity distribution in meanders the fluence 0.1 J/cm^2 was selected to heterojunction fabrication on the area of $5 \times 10 \text{ mm}^2$. The samples volt-ampere characteristics measurement was performed in air at room temperature using a Keithley 6487 picoammeter (under dark and white light 100 mW/cm^2 , -2 – 2 V .)

To analyze polarizing properties of LIPSS, prototypes of $0.5 \times 0.5 \text{ cm}^2$ a-Si films-based waveplates were

fabricated. For this purpose, the same magnetron-sputtered a-Si films on glass substrates, but without pre-deposited contacts were irradiated by Avesta femtosecond laser (1250 nm, 150 fs, 10 Hz). The periods of LIPSS formed on the sample surface were determined from SEM images analysis. Optical delay measurements were performed in the near and middle infrared (IR) range using a Bruker IFS 66v/S infrared Fourier spectrometer in transmission geometry with different polarizations of the transmitted radiation.

3. Results and discussions

Depth-resolved Raman spectroscopy measurements (Fig. 2) of irradiated layered Si samples revealed the optimal depth of a-Si laser-induced crystallization that is 45 ± 5 nm in the case of femtosecond laser pulses with fluence of 0.1 J/cm^2 . Within this region the volume fraction f_c of the Si crystalline phase obtained from the Raman spectra data is $86 \pm 4\%$ in the near-surface region and does not change until the etching depth is 20 ± 5 nm, and then decreases rapidly with depth to zero. Lowering the laser fluence causes the decrease in crystallized Si volume fraction in the near-surface region.

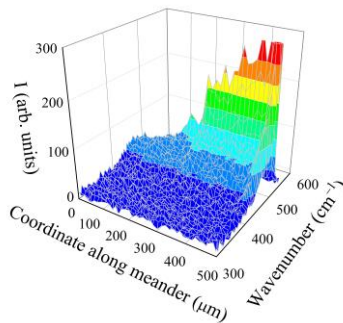


Fig. 2. Depth dependent Raman spectra of meander area.

Based on the obtained f_c distribution data, the following optimal laser irradiation parameters were determined for c-Si/a-Si heterostructures fabrication: 0.1 J/cm^2 , 1 kHz, 300 $\mu\text{m/s}$. Using these parameters, heterostructures with an area of $0.5 \times 1 \text{ cm}^2$ were made on the surface of a-Si layers in raster scanning mode with a step of 40 μm between the scan lines, which is smaller than beam diameter.

The volt-ampere characteristics for laser-crystallized a-Si layer with a bottom ITO contact demonstrate a pronounced diode character, indicating the presence of a potential barrier in the structure. It also should be noted that the overall resistance of the film is decreased about 500 times after laser irradiation, as a result of partial crystallization of the upper layer and the formation of nanocrystalline silicon, which is known to have a lower resistivity compared to amorphous silicon. The volt-ampere characteristic of the sample demonstrates "rectifying" character with the rectification coefficient k , calculated as the ratio of the current strength in the forward and reverse directions, increasing from 2.7 to 13.6 at a voltage of $U = 2 \text{ V}$ after laser irradiation. This can be attributed to the formation of an additional potential barrier for free charge carriers in the form of a nc-Si/a-Si (nanocrystalline Si/amorphous Si) heterojunction produced by femtosecond laser crystallization.

Laser irradiation of a-Si film with fluence $E = 0.15 \text{ J/cm}^2$, higher than ablation threshold lead to formation of low spatial frequency LIPSS (LSFL) with period of

$1100 \pm 20 \text{ nm}$. These structures demonstrate high regularity. The IR transmission spectra (Fig. 3) demonstrate alternating maxima and minima in the spectra of both the initial and irradiated films, which are due to interference. The decrease in the transmission coefficient and the intensity of the interference after laser surface structuring is associated with the formation of a crystalline phase in the subsurface layer as a result of the laser-induced phase transition, as well as the surface relief, which leads to more intense diffuse scattering of the transmitted light. The determined anisotropy axis orientation is parallel to the ridges of the formed LSFL. For the laser-processed a-Si film a difference in refractive indices of ordinary and extraordinary waves was determined as 0.47 ± 0.07 from near and middle IR spectra analysis. Thus, the manufactured waveplate prototype based on a-Si demonstrates an optical retardance value of $280 \pm 40 \text{ nm}$. The observed optical retardance in the laser-irradiated film can be attributed to the anisotropic surface relief of LSFL in a form of alternating crystalline-air sub-nanoscale areas.

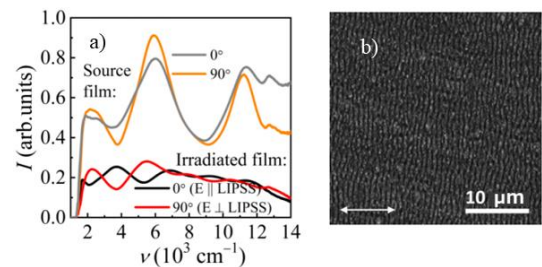


Fig. 3. a) IR transmission spectra for the initial a-Si film, as well as b) the irradiated region.

4. Conclusions

The nanoscale laser-induced crystallization of a-Si layers caused by their irradiation by femtosecond laser pulses with fluence lower than ablation threshold was demonstrated. The formed structures are promising for fabricating photovoltaic cells due to the formation of an additional nc-Si/a-Si heterojunction barrier for the carriers. Irradiating a-Si films by femtosecond laser pulses with the fluence higher than a-Si ablation threshold allows fabrication of LSFL possessing the optical retardance. Such optically anisotropic structures could be used as a basis for creating polarization-sensitive optic elements, for example, quarter-wave plates for the near-infrared range.

Acknowledgements

This research was funded by the Russian Science Foundation, grant number 22-19-00035-II, <https://rscf.ru/en/project/22-19-00035/>.

References

- [1] K. Kikuchi. J. Light. Technol. **34**(2015)157.
- [2] K. Yoshikawa, H. Kawasaki, W. Yoshida, T. Irie, K. Konishi, K. Nakano, T. Uto, D. Adachi, M. Kanematsu, H. Uzu & K. Yamamoto. Nat. Energy. **2**(2017), 17032.
- [3] T. Tiedje, E. Yablonovitch; G.D. Cody; B.G. Brooks. IEEE Trans. Electron Devices. **31**(1984)71.

Laser-pulsed patterning of BaGa₄Se₇ crystals for on-demand anti-reflective surface nanoengineering

Kuchmizhak A.A.¹, Cherepakhin A.B.¹, Shevlyagin A.V.¹, Isaenko L.I.², Syubaev S.A.^{*,1}

¹ Institute of Automation and Control Processes, 5 Radio St., Vladivostok 690041, Russia

² V.S. Sobolev Institute of Geology and Mineralogy, 3 Ac. Koptyuga ave., Novosibirsk 630090, Russia

*e-mail: trilar@bk.ru

Abstract. Anti-reflective (AR) surfaces, operating in the near-infrared (NIR) spectral range, are of great interest to improve performance of broadband coherent radiation sources, for which common AR coatings struggle with this task owing to inherent limiting factors. This work reports the formation of laser-induced periodic surface structures (LIPSS) on the nonlinear IR-transparent BaGa₄Se₇ (BGSe) crystal under its processing with 257 and 513 nm femtosecond laser pulses wavelength. Fourier-transform infrared spectroscopy revealed the excellent AR properties of produced subwavelength gratings within visible-to-NIR spectral range. Specifically, 513-nm wavelength laser patterning was applied to fabricate LIPSS on both crystal facets, yielding in 1.22-fold increased BGSe NIR transmission approved by direct power measurements of optical radiation transmitted through bulk crystal. These results suggest the potential of LIPSS-based AR interfaces to improve optical properties of nonlinear crystals.

1. Introduction

Coherent optical radiation, delivered by the optical parametric oscillator (OPO) systems, with tunable wavelength in the visible and near-infrared range demonstrates the special usefulness in spectroscopic, remote sensing and biomedical researches [1,2]. This is mainly ensured due to significant development in the synthesis technologies of nonlinear optical single-crystals, which in turn are OPO vital component. Such frequency converters are represented by diverse crystals, that differ in chemical composition, laser-induced damage threshold (LIDT), optical linear and nonlinear characteristics, but all are characterized by high (>2) refractive index [3].

Optical radiation, propagating across the interface between air and high-index medium, undergoes a high refractive jump with associated significant Fresnel reflection losses ($\approx 20\%$ for $n=2.5$), that suppresses the efficiency of OPO devices. Conventional attempts to resolve this problem typically involve film deposition on the crystal surface to provide gradient index change and minimize the reflection losses. However, such approaches suffer from adhesion problems, reduced LIDT and limited spectral bandwidth due to specific film thickness [4]. A more beneficial approach consists of the intermediary-free formation of gradient index profile directly on the crystal surface. As an example, such scenario can be realized via high-resolution UV laser engraving of micropillars mesh arrays [5]. However, strict focusing conditions obstruct the industrial-scale (mm sized) AR microstructures fabrication.

Over the short time, laser-induced periodic surface structures (LIPSS) have become the attractive fundament for frontier research applications, ranging from nanostructural coloration and multifunctional bio-replicated metasurfaces to advanced lab-on-chip devices and broadband anti-reflective interfaces [6-10]. The latter is of exceptional interest, since LIPSS present rival counterpart to mentioned AR coatings and microstructures owing to unpretentious self-assembling processes, allowing easy to achieve macroscopic areas of AR nanostructures on nonlinear crystals surface, suitable for practical application.

In this work, multi-pulse femtosecond (fs) laser ablation of BaGa₄Se₇ nonlinear crystal was applied to produce LIPSS with characteristic periodicity $\Lambda = 200$ and 380 nm

at corresponding laser radiation wavelength $\lambda_{\text{pulse}} = 257$ and 513 nm. The morphology and anti-reflection performance of produced LIPSS were shown to also be governed by applied laser pulse wavelength. Fourier-transform infrared (FTIR) spectra analysis revealed that LIPSS-patterning of both BGSe facets at $\lambda_{\text{pulse}} = 513$ nm led to 1.22-fold improvement in NIR transmittance of BGSe crystal.

2. Experiment

BaGa₄Se₇ crystals were synthesized in accordance with Bridgman growth protocol. LIPSS formation on BGSe surface was accomplished using Yb:KGW laser system (Pharos by Light Conversion), delivering linearly polarized femtosecond (~ 230 fs) laser pulses at the second harmonic wavelength $\lambda_{\text{pulse}} \sim 513$ nm with repetition rate $f = 50$ kHz. Easy-to-integrate portable fourth harmonic module was integrated into the optical system to generate 257 nm wavelength laser pulses. Laser radiation was focused onto the sample surface by means of objectives, having NA = 0.42 and 0.1 for $\lambda_{\text{pulse}} = 513$ and 257 nm, respectively. PC-controlled 3-axis motorized nanopositioners (ANT130 by Aerotech) transferred the BGSe along snake-like trajectory with translation speed of 2.5 mm/s and lateral shift of 300 nm. Laser structuring of BGSe surface was accompanied by side air blowing to minimize the amount of ablation products. Laser-processed BGSe topography was inspected by scanning electron microscopy (SEM). LIPSS transmission spectra were measured using Fourier-transform infrared spectrometer (FTIR, Vertex-80 by Bruker), equipped with IR microscope (Hyperion 1000 by Bruker). Optical radiation with tunable wavelength in the visible-to-NIR spectral range was generated by femtosecond OPO (TOPOL-1050 by Avesta) at 80 MHz pulse repetition rate and its power was measured by thermopile sensor (PM10 by Coherent).

3. Results and discussions

The multi-pulse laser fabrication of AR relief on BGSe surface was undertaken taking into account laser-induced self-nanoorganization processes, underlying LIPSS formation. The initial part of laser pulses creates surface inhomogeneities to premise the photoexcited subsurface layer, transiently manifesting metallic properties on a 10 - 100 ps time interval, to convert the part of laser radiation

into the surface plasmon polariton. The interference pattern of incident laser pulse and plasmon-coupled one is gradually imprinted onto the laser-irradiated BGSe site as periodical one-dimensional subwavelength grating with periodicity $\Lambda = \lambda_{\text{pulse}}/n_{\text{eff}}$ and orientation, orthogonal to the laser pulse polarization. Fig. 1 illustrates SEM image of LIPSS produced on BGSe facet under UV (257 nm) and visible (513 nm) laser pulse wavelength and hereinafter will refer to UV-LIPSS and VIS-LIPSS, respectively. While fabrication of both LIPSS types was accompanied with air-blowing, ablation products are almost absence in UV-LIPSS comparing to VIS-LIPSS. Since such BGSe nanoparticles were ejected from the laser-ablated surface site in the molten phase, UV-LIPSS formation apparently proceeds in a more stable manner owing to superficial penetration of UV laser radiation into material and corresponding thin layer formation of melted BGSe pool, which in its turn completely redistributed in LIPSS without nanodroplets ejection. Contrary, VIS-LIPSS demonstrate deeper nanotrenches, indicating the increased volume of involved melted material and ablation products generation.

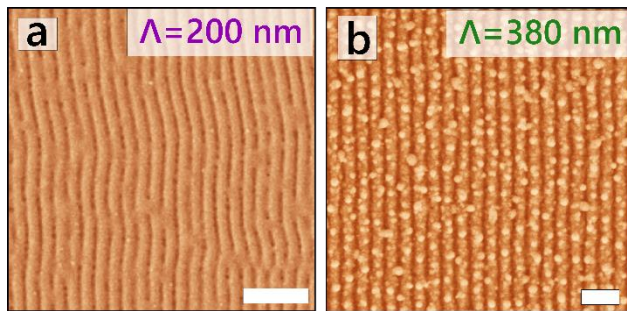


Fig. 1. Top-view SEM-images of LIPSS fabricated on BGSe surface under (a) 257 and (b) 513 nm laser pulse wavelength. LIPSS characteristic periodicities (Λ) are linked in the top of corresponding images. Scale bars in all images equal 1 μm .

LIPSS can be considered as an intermediate layer between air and BGSe bulk crystal with gradual change in their relative proportions. This property provides depressed refractive index jump on the air-crystal interface, that allows LIPSS to be applied in AR application. Large-scale ($250 \times 250 \mu\text{m}^2$) arrays of both LIPSS types were produced on BGSe surface in a notably fast fabrication procedure, requiring less than 1 min. BGSe, containing VIS-LIPSS on the input facet, demonstrates enhanced integral transmission in NIR spectral range with 1.12-fold increased local maximum near 1300 nm (Fig. 2a). In the case of UV-LIPSS, the spectral position of transmission window is shifted towards the shortwave region. However, amorphous subsurface layer, formed during LIPSS fabrication, leads to increased absorption in this spectral range, suppressing AR performance. Along with it, UV-LIPSS exhibits moderate modulation of nanotrenches depth, that reflects in the reduced NIR transmission level, compared to VIS-LIPSS.

VIS-LIPSS fabricated on both crystal facets was found to achieve 1.22-fold boosted transmittance maxima (Fig. 2b). Analogous conclusions of LIPSS AR properties can be drawn via power measurements of OPO-generated optical radiation, incident on and transmitted through the crystal (P_{inc} and P_{tran} , respectively). Dependence of $P_{\text{inc}}/P_{\text{tran}}$ relation, implying transmission coefficient, was systematically acquired for the optical radiation with wavelengths, ranging from 750 to 2000 nm, after its propagation across pristine BGSe and double-sided LIPSS.

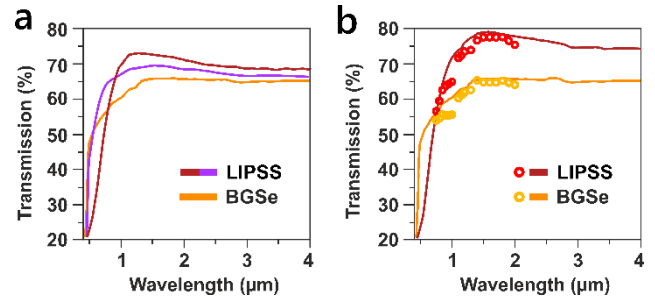


Fig. 2. FTIR transmission spectra measured from pristine crystal (orange curve) and: (a) one-sided LIPSS with periodicity $\Lambda = 200$ (purple curve) and 380 (red curve) nm; (b) Double-sided LIPSS with $\Lambda = 380$ nm (red curve). Markers indicate the measured transmission coefficient of OPO-generated optical radiation at specific wavelengths after its propagation through untreated crystal (yellow data) and double-sided LIPSS (red data).

4. Conclusions

This research highlights high-performing fs multi-pulse laser processing of BGSe single-crystal to fabricate LIPSS with periodicity $\Lambda = 200$ and 380 nm at corresponding laser radiation wavelength $\lambda_{\text{pulse}} = 257$ and 513 nm. FTIR spectroscopy was used to analyze the anti-reflective properties of both mentioned subwavelength gratings, unveiling the increased visible and NIR transmittance of LIPSS-patterned BGSe crystal. BGSe with VIS-LIPSS produced at both crystal facets was demonstrated to achieve 1.22-fold enhanced transmission maximum, spectrally located near 1300 nm. The obtained FTIR spectra are in good agreement with systematic studies results, aimed at power measuring of OPO-generated optical radiation transmitted through pristine and LIPSS-patterned crystal.

Acknowledgements

This research was supported by the Russian Science Foundation grant No. 25-79-20014.

References

- [1] V. Petrov, V. Badikov, D. Badikov, K. Kato, G. Shevyrdyaeva, K. Miyata, M. Mero, L. Wang, Z. Heiner, V. Panyutin. *J. Opt. Soc. Am. B* 38(2021)B46.
- [2] Y. Ma, H. Kong, H. Shao, J. Zou, B. Liu, Y. Wang, B. Shi, F. Li, K. Wang, Y. Chen. *Opt. Express* 32(2024)40695.
- [3] N. Kostyukova, E. Erushin, A. Boyko, G. Shevyrdyaeva, D. Badikov. *Photonics* 11(2024)281.
- [4] E. Erushin, A. Boyko, G. Shevyrdyaeva, D. Badikov, N. Kostyukova. *Opt. Mater.* 157(2024)116275.
- [5] S. Syubaev, E. Modin, S. Gurbatov, A. Cherepakhin, A. Dostovalov, A. Tarasova, P. Krinitsin, A. Yelissev, L. Isaenko, A. Kuchmizhak. *Appl. Phys. Lett.* 123(2023) 061108.
- [6] V. Lapidis, A. Cherepakhin, A. Kozlov, A. Shevlyagin, K. Kolonica, S. Shevlyagina, A. Kokhanovskiy, J. Zhang, A. Zhizhchenko, A. Kuchmizhak. *ACS Appl. Mater. Interfaces* 17(2025)16122.
- [7] A. Visan, G. Popescu-Pelin. *Coatings* 14(2024)1290.
- [8] Y. Borodaenko, A. Cherepakhin, S. Gurbatov, E. Modin, A. Shevlyagin, A. Kuchmizhak. *Surf. Interfaces* 56(2025)105568.
- [9] S. Gurbatov, Y. Borodaenko, E. Mitsai, E. Modin, A. Zhizhchenko, A. Cherepakhin, A. Shevlyagin, S. Syubaev, A. Porfirev, S. Khonina, A. Yelissev. *J. Phys. Chem. Lett.* 14(2023)9357.
- [10] S. Syubaev, A. Dostovalov, A. Tarasova, A. Shevlyagin, L. Isaenko, A. Kuchmizhak. *Bull. Russ. Acad. Sci.: Phys.* 88(2024)S439.

Formation of 2D laser-induced periodic surface structures on metal and semiconductor thin films

Fedyaj V.E.^{*,1,2}, Bronnikov K.A.³, Simanchuk A.E.¹, Lazarenko P.I.⁴, Yakubov A.O.⁴, Zhizhchenko A.Yu.⁵, Kuchmizhak A.A.^{5,6}, Dostovalov A.V.^{1,2}

¹ Institute of Automation and Electrometry of the SB RAS, Novosibirsk, Russia

² Novosibirsk State University, Novosibirsk, Russia

³ ITMO University, Saint-Petersburg, Russia

⁴ National Research University of Electronic Technology, Zelenograd 124498, Russia

⁵ Institute of Automation and Control Processes of the FEB RAS, 5 Radio St., 690041 Vladivostok, Russia;

⁶ Far Eastern Federal University, 690041 Vladivostok, Russia;

*e-mail: fedajvlad@gmail.com

Abstract. The laser-induced periodic surface structures (LIPSS) represent an effective technique to modify optical, mechanical, and chemical surface characteristics. While most studies focus on one-dimensional (1D) LIPSS formation on bulk and thin-film materials with orientation direction depending on laser polarization state, more complex morphologies are needed for advanced applications. Here, we demonstrate the formation of two-dimensional (2D) square and hexagonal LIPSS on titanium (Ti) and phase-change material (Ge₂Sb₂Te₅) thin films, driven by thermochemical and plasmonic mechanisms, respectively. These findings expand the potential for applications in tunable photonic devices, diffractive optical elements, and structurally colored metals with 2D anisotropic optical properties.

1. Introduction

Laser-Induced Periodic Surface Structures (LIPSS) represent micro- and nano-scale surface relief patterns formed on material surfaces under laser irradiation. The period of these structures is determined by both laser parameters (wavelength, polarization, pulse energy) and the properties of the processed material. The ability to precisely tailor optical, mechanical, and chemical surface properties—combined with a cost-effective fabrication process that eliminates the need for vacuum systems or multi-step treatments—enables the application of LIPSS in photonics, sensing, biomedicine, and related fields [1].

Traditionally one-dimensional (1D) LIPSS was studied on metals, semiconductors, and dielectrics, which exhibit anisotropy along a single direction [2]. However, expanding LIPSS morphological diversity to two-dimensional (2D) structures with bi-directional anisotropy provides the way to cover the new applications fields. Such structures can be produced, by using circular or elliptical laser polarization, resulting in more complex patterns like triangular lattices [3]. There are also studies demonstrating 2D LIPSS formation using linear polarization and double-pass approach [4].

Here, we report on the formation of square and hexagonal thermochemical 2D LIPSS on Ti films. We also demonstrate the formation of similar 2D structures on film of phase change material Ge₂Sb₂Te₅ despite a different mechanism of LIPSS formation in this case.

2. Experiment

Experiments on formation LIPSS on amorphous Ge₂Sb₂Te₅ 200 nm thick films and Ti 30 nm thick films were performed under the impact of linearly polarized laser radiation with a wavelength of $\lambda = 1026$ nm and a pulse duration of 232 fs. The size of the astigmatic beam was 15×150 microns, the pulse repetition rate $f = 200$ kHz. The pulse energy E and scanning speed was altered to acquire structures with the best regularity. The formation of 2D structures was carried out using 2 scans with perpendicular

polarization direction and two types of pass orientation relative to each other: parallel and perpendicular.

TLIPSS surface morphology were investigated via atomic force microscope (AFM) and scanning electron-microscopy (SEM).

3. Results and discussions

The formation of 2D structures on Ti 30 nm thick films was carried out using 2 scans with perpendicular polarization direction and two types of pass orientation relative to each other: parallel and perpendicular. We found that in the case of parallel tracks, square 2D structures are formed, whereas in the case of orthogonal tracks, hexagonal 2D structures are observed (Fig. 1).

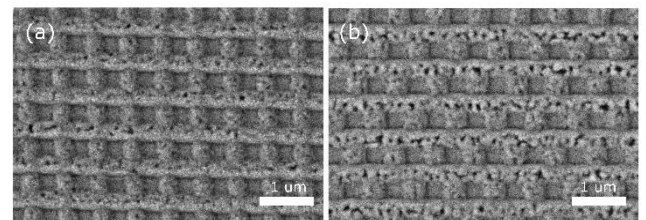


Fig. 1. AFM image of square (a) and hexagonal (b) TLIPSS structures produced on the 30-nm thick Ti at energy $E = 0.95 \mu\text{J}$ and scanning speed $10 \mu\text{m/s}$. (c, d).

The LIPSS on the GST film are oriented perpendicular to the polarization direction of the incident laser radiation. Fig. 2 illustrates these structures, produced at an energy of $E = 125$ nJ and a scanning speed of $100 \mu\text{m/s}$. As observed, the surface relief has a height of 3–4 nm and a period of approximately $1 \mu\text{m}$. These groove-like structures result from the crystallization of the amorphous film in the intensity modulation maxima.

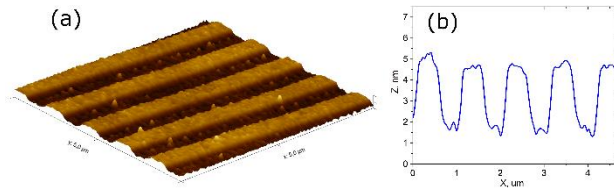


Fig. 2. AFM image (a) and profile (b) of TLIPSS structures produced on the 200-nm thick GST at energy $E = 125$ nJ and scanning speed $100 \mu\text{m/s}$.

On the surface of the GST film, as with titanium, two-dimensional structures of both square (Fig. 3 a) and hexagonal (Fig. 3 b) types are formed. However, for both parallel and crossed tracks, a square grating initially appears at the intersection of the two tracks. Later, the hexagonal LIPSS dominate, eventually occupying the entire area.

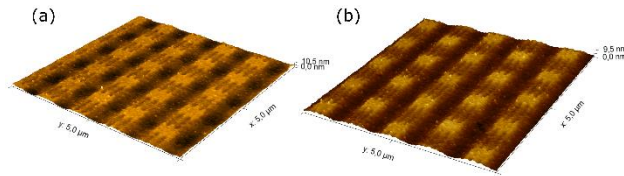


Fig. 3. AFM images of the square (a) and the hexagonal (b) 2D structures formed on the 200-nm thick GST at energy $E = 105$ nJ and scanning speed $400 \mu\text{m/s}$.

4. Conclusions

We demonstrate the formation of square and hexagonal thermochemical 2D LIPSS on Ti films. Additionally, highly regular 1D LIPSS were observed on $\text{Ge}_2\text{Sb}_2\text{Te}_5$ (GST) phase-change films, exhibiting a periodicity and orientation perpendicular to the laser polarization direction. Notably, we also report the first observation of two-dimensional square and hexagonal LIPSS patterns on GST thin film. These findings expand the range of demonstrated surface morphologies and open new possibilities for practical applications, including tunable photonic devices, diffractive optical elements, and structural coloration of metals.

Acknowledgements

The work was funded by the Russian Science Foundation grant (No. 21-72-20162-II). In the research, we used the equipment of the following Multiple-Access Centres (MAC): MAC of the Far Eastern Federal University (FEFU), MAC “High-resolution spectroscopy of gases and condensed matters” at IAE SB RAS.

References

- [1] J. Bonse, S. V. Kirner, S. Höhm, N. Epperlein, D. Spaltmann, A. Rosenfeld, and J. Krüger. Laser-Based Micro- and Nanoprocessing XI **10092**(2017)114.
- [2] Y. Borodaenko, A. Cherepakhin, S. O. Gurbatov, E. Modin, A. V. Shevlyagin, A. A. Kuchmizhak. Surfaces and Interfaces **56**(2025)105568.
- [3] J. M. Romano, A. Garcia-Giron, P. Penchev, S. Dimov. Triangular laser-induced submicron textures for functionalising stainless steel surfaces. Applied Surface Science **440**(2018)162.
- [4] Q. Ibrahim, Y. Andreeva, A. Suvorov, D. Khmelenin, E. Grigoryev, A. Shcherbakov, D. Sinev. Optics & Laser Technology **174**(2024)110642.

Laser-assisted fabrication of materials for electrochemical applications

Levshakova A.S.¹, Kaneva M.V.¹, Ninayan R.¹, Satymov E.T.¹, Kuchmizhak A.A.²,
Khairullina E.M.^{*,2}

¹ St. Petersburg State University, 26 Universitetskii pr. St. Petersburg 199034, Russia

² Institute of Automation and Control Processes, 5 Radio St., Vladivostok 690041, Russia

*e-mail: evgeniia.khairullina@gmail.com

Abstract. Deep eutectic solvents (DES), recognized for their low toxicity and tunability, offer sustainable platforms for nanomaterial synthesis. This study introduces a one-step laser-assisted pyrolysis technique to functionalize commercial screen-printed electrodes (SPEs) using a DES comprising choline chloride, tartaric acid, nickel acetate, and graphene. A 532 nm laser facilitated the in situ generation of nickel-decorated graphene nanocomposites (Ni-G/SPE) directly on electrode surfaces. Key synthesis parameters (laser power, graphene concentration) were optimized via the Nelder-Mead algorithm to maximize electrochemical response of the Ni-G/SPE to dopamine. Electrochemical analysis revealed a wide linear detection range (0.25–100 μ M) and a low detection limit (0.095 μ M) using differential pulse voltammetry. These findings demonstrate the efficacy of laser-driven DES processing in fabricating advanced sensors for biogenic amine detection.

1. Introduction

Deep eutectic solvents (DES), formed via hydrogen bonding between donors and acceptors, offer sustainable, low-toxicity media for nanomaterial synthesis [1]. DESs enable eco-friendly synthesis of various nanomaterials, including noble metal nanoparticles and transition metal compounds. Nevertheless, the non-electrochemical production of pure transition metal nanoparticles remains limited [2]. Laser-assisted synthesis addresses this limitation by leveraging localized high temperatures to rapidly decompose DES components, significantly accelerating reactions compared to conventional methods. While previous studies have primarily focused on fabrication of conductive patterns for electronics [3], the potential of laser-assisted synthesis in electrochemical sensing—offering surfactant-free fabrication and enhanced material purity—remains underexplored.

Biogenic amines (BAs), such as dopamine, play critical roles in physiological processes but pose health risks when present at abnormal levels. Elevated dopamine levels are associated with neurological disorders, including Parkinson's disease etc. [4]. Current BA detection methods often lack portability or suffer from interference, highlighting the need for advanced, reliable sensors. This study employs laser pyrolysis of a DES (composed of choline chloride, tartaric acid, nickel acetate, and graphene) to functionalize screen-printed electrodes (SPEs). The results demonstrate that laser-DES synthesis is a scalable and efficient approach for developing sensors capable of monitoring BAs in healthcare, food safety, and other applications.

2. Experiment

DES was prepared by mixing choline chloride, tartaric acid, and nickel acetate in a 1:1:1 molar ratio. Graphene (3–50 wt%) was dispersed into the DES, followed by heating at 110°C to melt the mixture and stirring at 120–140°C to form a homogeneous viscous liquid. SPEs were functionalized by applying 5 μ L of the DES onto the working area, drying at 50°C, and laser-scribing using a 532 nm Nd:YAG laser (100–1200 mW power, 1.4 mm/s scan speed).

The morphology and composition of the electrodes were analyzed using SEM-EDX, XPS and XRD techniques. Electrochemical performance was evaluated in 0.1 M PBS (pH 7.0) using a three-electrode system: Ni-G/SPE (working), Ag/AgCl (reference), and Pt/carbon (counter). Cyclic voltammetry (CV, –0.1 to 0.8 V, 50 mV/s) and differential pulse voltammetry (DPV: 0.05 V amplitude, 0.004 V step) were employed for dopamine detection.

3. Results and discussions

The Nelder-Mead optimization method was employed to determine the optimal laser power (500–1500 mW) and graphene concentration (3–50 wt%) in the DES to maximize the electrochemical response of the screen-printed electrodes to dopamine [5]. Electrodes fabricated under optimized conditions were characterized using SEM, XRD, and XPS (Figure 1). XRD analysis revealed reflections corresponding to graphite from the unmodified SPE and metallic nickel, confirming the laser-driven reduction of nickel ions into nanoparticles (Figure 1f). XPS survey spectra confirmed the presence of Ni, C, N, and O (Figure 1d,e). High-resolution Ni 2p spectra exhibited peaks at 873.4 and 855.8 eV (spin–orbit separation: 17.6 eV), indicative of nickel nanoparticles, alongside Ni²⁺ contributions from surface oxidation (Figure 1e).

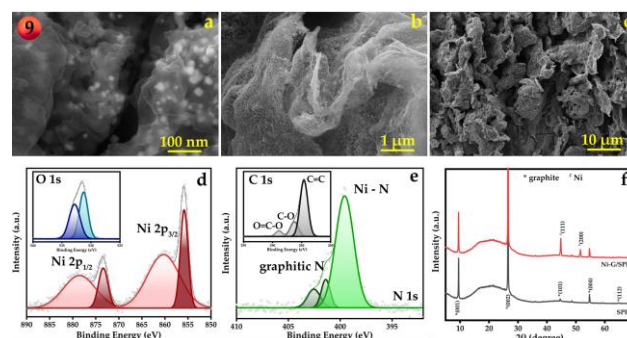


Fig. 1. SEM images showing the morphology of the optimized Ni-G/SPE electrode (a–c), X-ray photoelectron spectra of the Ni 2p and O 1s (d), N 1s and C 1s (e) XRD spectra of SPE and Ni-G/SPE electrodes (f) [5].

The O 1s spectrum showed peaks at 531.3 eV (Ni–O/OH bonds) and 532.8 eV (C–O groups on graphene), suggesting partial nickel oxidation and the presence of oxygenated graphene functionalities. Nitrogen species included N–Ni (399.6 eV), graphitic N (401.4 eV), and trapped N₂/N–O (402.5 eV), formed during high-temperature laser processing. The C 1s spectrum confirmed presence of sp² carbon (284.6 eV) and oxygen-containing groups (286.3, 288.9 eV).

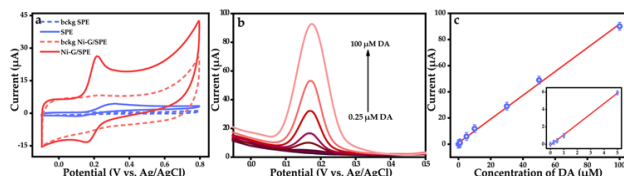


Fig. 2. (a) CV curves of SPE and Ni-G/SPE in 0.1 M PBS without additives (dashed line) and in the presence of 50 μM DA (solid line), (b) DPV of the Ni-G/SPE electrode measured with the addition of various concentrations of DA, (c) Correlations of DA oxidation currents with respective concentrations [5].

Cyclic voltammetry (CV) in 0.1 M PBS with 50 μM dopamine revealed a well-defined redox pair for Ni-G/SPE, corresponding to dopamine oxidation and reduction (Figure 2a). The modified electrode exhibited a 4.5-fold higher current response compared to the bare SPE, attributed to the increased active surface area of graphene and the catalytic role of nickel in accelerating electron transfer. Differential pulse voltammetry (DPV) demonstrated a linear dopamine detection range (0.25–100 μM) with a sensitivity of 0.91 $\mu\text{A } \mu\text{M}^{-1}$ and a detection limit of 0.095 μM (S/N = 3) (Figure 2b,c). Moreover, the sensor exhibited excellent repeatability (RSD = 3.3%, $n = 8$), reproducibility (RSD = 4.5%, $n = 3$), and stability (95% signal retention after 3 months), underscoring its reliability for practical applications.

4. Conclusions

This study demonstrates the potential of laser-driven synthesis in deep eutectic solvents for the development of nickel-graphene nanocomposite-modified screen-printed electrodes for biogenic amine detection. By combining computational optimization (Nelder-Mead algorithm) with laser processing, a high-performance dopamine sensor was achieved, offering a linear detection range of 0.25–100 μM , a detection limit of 0.095 μM , and a sensitivity of 0.91 $\mu\text{A } \mu\text{M}^{-1}$. The approach highlights the scalability, efficiency, and eco-friendliness of laser-DES synthesis for creating advanced electrochemical sensors, with promising applications in healthcare, food safety, and beyond.

Acknowledgements

This research was funded by the Russian Science Foundation, grant N° 24-19-00541. <https://rscf.ru/project/24-19-00541/>

References

- [1] Santana-Mayor, Á.; Rodríguez-Ramos, R.; Herrera-Herrera, A.V.; Socas-Rodríguez, B.; Rodríguez-Delgado, M.Á. *TrAC Trends Anal. Chem.* **134**(2021)116108.
- [2] 19. Cherigui, E.A.M.; Sentosun, K.; Mamme, M.H.; Lukaczynska, M.; Terryn, H.; Bals, S.; Ustarroz, J. J. *Phys. Chem. C* **122**(2018)23129.

- [3] Shestakov, D.; Khairullina, E.; Shishov, A.; Khubezhov, S.; Makarov, S.; Tumkin, I.; Logunov, L. *Opt. Laser Technol.* **167**(2023)109777.
- [4] Lakshmanakumar, M.; Nesakumar, N.; Kulandaisamy, A.J.; Rayappan, J.B.B. *Measurement* **183**(2021)109873.
- [5] A Levshakova, M Kaneva, R Ninayan, E Borisov, E Satymov, A Shmalko, L Logunov, Al Kuchmizhak, Y Kulchin, A Manshina, E Khairullina, *Materials* **18**(2025)425.

Si LIPSS/Mg₂Si platform for polarization-selective infrared detection

Borodaenko Yu.M.^{*1}, Banniy D.E.^{1,2}, Bozhok A.V.^{1,2}, Shevlyagin A.V.¹, Gurbatov S.O.^{1,2},
Kuchmizhak A.A.^{1,2}

¹ Institute of Automation and Control Processes, 5 Radio St., Vladivostok 690041, Russia

² Far Eastern Federal University, 8 Sukhanova St., Vladivostok 690950, Russia

*e-mail: borodaenko_yu@mail.ru

Abstract. Here, we demonstrate a novel approach to enhance the infrared photoresponse of vertical p-n junction Si photodetectors by their laser-induced periodic surface structuring (LIPSS) with optically anisotropic nanogratings ($\Lambda \approx 270$ nm) followed by deposition of a narrow-bandgap Mg₂Si nanolayer. The resulting patterned surface exhibit ultralow broadband reflectance below 1.5% within 450–1500 nm, as well as polarization-dependent reflectivity within 1500–2500 nm. The modified photodetector exhibits enhanced and spectrally expanded photoresponse up to 2000 nm, justifying cost-effective, CMOS-compatible fabrication method for scalable SWIR optoelectronic devices.

1. Introduction

Silicon (Si) photodetectors are widely used in optoelectronics due to their excellent charge carrier mobility, mature fabrication technology, and cost-effectiveness for mass production. Their reliability in the 400–1100 nm range (visible to near-IR) stems from silicon's bandgap (~ 1.12 eV). However, performance declines sharply beyond 1100 nm limiting applications in short-wave infrared (SWIR).

Nanostructuring techniques can extend silicon's photoresponse into the SWIR region, as the tailored optical properties of nanostructures promote interaction with longer wavelengths beyond the material's fundamental absorption edge. Femtosecond (fs) laser processing offers a rapid, non-lithographic approach for controlled fabricating nanostructures. For example, this technique generates laser-induced periodic surface structures (LIPSS) — uniform antireflective subwavelength gratings formed in a single processing step without requiring costly masks. Processing in liquid media (e.g., methanol) further reduces the structure periodicity and suppresses surface oxidation. However, despite enhanced light absorption in Si LIPSS, the IR photoresponse remains limited by insufficient charge separation and rapid carrier recombination [1].

To improve the infrared sensitivity of Si LIPSS-based photodetector, the deposition of narrow-bandgap materials has been investigated. Magnesium silicide (Mg₂Si), with its adjustable bandgap (~ 0.7 eV), forms a heterojunction with silicon that facilitates sub-bandgap photon absorption while maintaining low dark currents [2]. The combination of LIPSS and an thin Mg₂Si coating presents a promising approach to achieving broadband photodetection.

In this study, fs laser fabrication in methanol allow to obtained subwavelength Si LIPSS with periodicity $\Lambda \sim 270$ nm ($\sim \lambda/2$) that serve as optical antennas, increasing light-matter interaction, while the Mg₂Si layer extends photodetection into the SWIR range. The spectral photoresponse of the device was characterized under zero-bias conditions (self-powered mode), revealing a significant improvement in responsivity at wavelengths beyond silicon's bandgap. The results indicate that this approach offers a viable pathway for developing Si-based photodetectors with extended spectral range and improved

efficiency in the SWIR regime by CMOS-compatible fabrication method.

Moreover, the periodic nature of LIPSS introduces a strong optical anisotropy, making the nanostructured surface inherently polarization-sensitive [3]. The Mg₂Si coating partially maintains this anisotropy while boosting photoconductivity, thereby enabling functionality unattainable in conventional planar Si photodetectors. This effect is particularly advantageous for applications requiring polarization dependence, such as security communications, polarimetric imaging, and polarization bioanalysis.

2. Experiment

A 6 mm \times 6 mm sample was cut from a commercially available, (001)-oriented, n-type silicon wafer featuring a 2 μ m epitaxially grown p-type silicon layer. Then, room-temperature magnetron sputtering was used to deposit a 100 nm aluminum film, which was patterned via a shadow mask to create a square-loop top electrode with a 1 mm border. The bottom electrode consisted of a 2 nm antimony film overcoated with 100 nm of gold. Subsequent vacuum annealing (5×10^{-6} Torr, 400 °C, 30 min) enhanced electrode adhesion and reduced contact resistance.

The resulting sample was immersed in a quartz cuvette filled with methanol and processed using 200 fs linearly polarized laser pulses (wavelength $\lambda = 515$ nm). The laser radiation was focused through a 4 mm layer of methanol onto the silicon surface using a dry microscope objective (NA = 0.13), resulting in a focal spot diameter of ≈ 5 μ m. Laser processing parameters (fluence $F = 0.12$ J/cm², scan speed $V = 50$ μ m/s, repetition rate $\nu = 1$ kHz, spacing between scan lines $l = 3$ μ m) were selected to induce a surface morphology characterized by quasi-regular LIPSS with a periodicity of 270 nm; the electric-field polarization vector was oriented parallel to the scan direction. After laser fabrication, the sample was removed from the solution and successively washed in methanol and neutral-pH deionized water, then air-dried. Next, a nanolayer of Mg₂Si was deposited on the nanostructures using vacuum evaporation.

The reflectance spectra (500–1600 nm range) of the sample were acquired using a Fourier-transform infrared spectrometer (Vertex 80, Bruker) coupled with an infrared

microscope (Hyperion 2000, Bruker). Scanning electron microscopy (Ultra 55+, Carl Zeiss) was employed to characterize the surface morphology. The spectral photoresponse was measured under ambient temperature and zero-bias conditions using circularly polarized, wavelength-tunable laser radiation (80 MHz repetition rate) generated by a femtosecond optical parametric oscillator (TOPOL, Avesta Project Ltd.). Multiple measurement sites were analyzed to obtain statistically averaged results.

3. Results and discussions

Optically anisotropic nanogratings LIPSS with a periodicity $\Lambda \sim 270$ nm were fabricated on the active area of a vertical p-n junction Si photodetector using direct fs laser patterning. Subsequent vacuum evaporation preserved the LIPSS geometry while enabling flake-like epitaxial growth of Mg_2Si on the nanograting surface. Representative top-view SEM images show the morphology of both bare LIPSS and LIPSS coated with an Mg_2Si nanolayer (figure 1a,b).

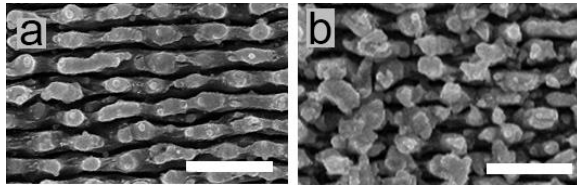


Fig. 1. Top-view SEM images showing (a) bare and (b) Mg_2Si -coated Si LIPSS morphology. Scale bar is 1 μm .

The FTIR reflectance spectra (figure 2) reveal ultralow reflectance (1-1.5%) in the obtained Mg_2Si -coated LIPSS structures across the 450-1000 nm range and. This can be attributed to several mechanisms: the LIPSS nanogaps act as efficient Mie resonators for visible light while simultaneously functioning as diffraction gratings for IR photons; the Mg_2Si coating creates additional nanoscale roughness, further reducing reflection.

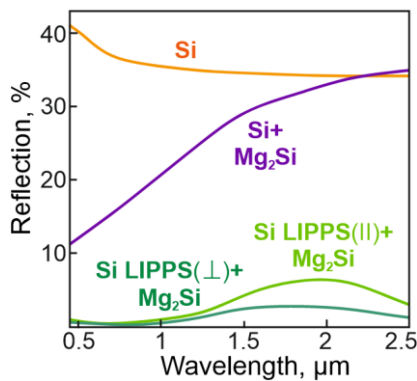


Fig. 2. Representative FTIR reflectance spectra of pristine Si surface, Mg_2Si -coated Si surface, and Mg_2Si -coated Si LIPSS ($\Lambda \approx 270$ nm). LIPSS \perp and LIPSS \parallel correspond to cases where the incident polarization is perpendicular or parallel to the LIPSS nanogaps, respectively.

Furthermore, the reflectance spectra reveal significant polarization-dependent optical behavior in the Mg_2Si -coated Si LIPSS structures. As can be seen, light polarization parallel and perpendicular to nanogaps provides antireflection performance with average values below 6% and 3%, respectively, within the 1500-2500 nm spectral range. These results demonstrate that the synergistic effects of antireflection anisotropic LIPSS

geometry and Mg_2Si coating can effectively tailor the infrared optical response of silicon.

The LIPSS morphology does not significantly deteriorate the zero-bias photoresponse of the photodetector to unpolarized light within the typical operational range (<1100 nm) of Si-based devices under zero-bias conditions (figure 3). The observed reduction in sensitivity at shorter wavelengths appears to be laser-induced defects in surface Si nanostructures. Notably, these defects simultaneously with Mg_2Si nanolayer enable the patterned device to demonstrate marked sensitivity to sub-bandgap photons, with detectable photoresponse extending up to 2000 nm.

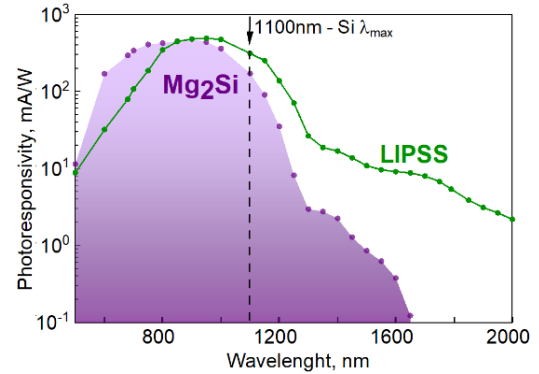


Fig. 3. Zero-bias photoresponse spectra of p-n junction silicon photodetectors: with an Mg_2Si nanolayer, and with LIPSS morphology coated by an Mg_2Si nanolayer.

Thus, a Si LIPSS with Mg_2Si coating photodetector featuring optically anisotropic morphology demonstrates excellent room-temperature photoresponse characteristics.

4. Conclusions

To conclude, we developed a high-performance silicon-based SWIR photodetector by combining Si LIPSS with an Mg_2Si nanolayer. Key achievements include broadband antireflection (at 450-2500 nm range), polarization-selective response (up to 2-fold difference in reflection at 1500–2500 nm range), extended SWIR sensitivity that enable sub-bandgap photodetection up to 2000 nm, while maintaining compatibility with zero-bias operation. The demonstrated platform paves the way for low-cost Si-based detectors with customizable optical properties, addressing needs in surveillance, scientific instrumentation and material imaging/analysis.

Acknowledgements

This work was supported by the Russian Science Foundation (Grant no. 23-49-10044).

References

- [1] Yu. Borodaenko, D. Pavlov, A. Cherepakhin, E. Mitsai, A. Pilnik, S. Syubaev, A. Kuchmizhak. *Adv. Mat. Tech.* **9.8.**(2024)2301567.
- [2] A. Shevlyagin, V. Il'yaschenko, A. Kuchmizhak, E. Mitsai, A. Sergeev, A. Amosov, A. Gutakovskii. *Appl. Surf. Science* **602**(2022)154321.
- [3] Yu. Borodaenko, A. Cherepakhin, S. Gurbatov, E. Modin, A. Shevlyagin, A. Kuchmizhak. *Surf. and Interf.* **56**(2025)105568.

High-resolution femtosecond laser coloring of titanium films: diversity of nanotexturing regimes analyzed by neural network

Lapidas V.S.¹, Zhizhchenko A.Yu.¹, Kuchmizhak A.A.^{*1,2}

¹ Institute of Automation and Control Processes, 5 Radio St., Vladivostok 690041, Russia

² Far Eastern Federal University, 8 Sukhanova St., Vladivostok 690950, Russia

*e-mail: alex.iacp.dvo@mail.ru

Abstract. Pulsed laser radiation effectively modifies material interfaces, creating various nanostructures. These structures can permanently change the optical properties of surfaces through interference, scattering, absorption, or diffraction, resulting in stable, vivid structural coloration. Despite advancements in laser-assisted techniques, there is still a need for methods that offer easy implementation, high resolution beyond current inkjet printers, and multiple color patterns in one sample. This study examined a Ti-TiO₂-Ti sandwich structure, revealing the coexistence of femtosecond laser processing techniques that generate subwavelength ripples, regular thermo-chemical laser-induced periodic surface structures, and uniform oxide films. This combination produces isotropic and anisotropic polarization-dependent colors. We developed a neural network to analyze the link between processing parameters and color appearance, allowing for predictable multi-color printing. Additionally, we achieved a remarkable printing resolution of up to 20,000 dpi, with potential applications in marking, labeling, and anti-counterfeiting.

1. Introduction

Structural coloration has emerged as a cutting-edge technique for high-resolution color marking, anti-counterfeiting, optical filtering, and display technologies [1]. These artificial colors result from the interaction of visible light with various photonic structures, such as multi-layer films, gratings, and nanoparticles, leading to durable optical properties that outperform traditional pigments in UV and thermal resistance.

The smallest color pixel size is constrained by the nanostructure dimensions, necessitating complex nanofabrication processes. Recent advancements in laser technologies enable precise structural coloration through surface nanopatterning, allowing localized modifications of optical properties. The tightly focused laser energy induces local heating, resulting in morphological transformations via phase transitions and chemical reactions [2].

Laser-driven self-organization can create periodic surface structures (LIPSS) that produce vibrant colors dependent on light diffraction [3]. Additionally, lasers can facilitate additive printing by depositing functional nano-layers or inducing structural transformations through oxidation, enhancing color modulation.

In our study, we produced diverse isotropic and anisotropic morphologies on a thin titanium film using femtosecond laser processing achieving high-resolution color applications suitable for marking and anti-counterfeiting.

2. Experiment

A multilayer coating was fabricated on a silica glass substrate, featuring a 30-nm thick titanium (Ti) top layer, a 60-nm thick titanium dioxide (TiO₂) spacer, and a 200-nm thick Ti back reflecting mirror, using an e-beam evaporation instrument (Kurt Lesker). The samples were patterned using second-harmonic (515 nm) radiation from an Yb:KGW laser system (Light Conversion, Pharos) with a pulse duration of 200 fs and a maximum repetition rate of 200 kHz. Laser pulses were focused using dry microscope objectives with numerical aperture (NA) of 0.1. The

patterning setup included a Glan-Taylor polarizer, a half-wave plate, a PC-driven attenuator, and 3D nanopositioning stages for precise control over pulse energy and scanning trajectory.

The morphology of the laser-patterned sites was examined using scanning electron microscopy (Ultra 55+, Carl Zeiss) to correlate properties with processing parameters like average laser power and scanning speed. Cross-sectional samples were prepared via focused ion beam milling (Thermo Fischer) through a protective 500-nm thick platinum layer.

Reflection spectra were analyzed using a home-built microspectroscopy setup, integrating a bright-field optical microscope with a grating spectrometer (Shamrock 303i, Andor) and a cooled CCD camera. The spectra were normalized to a monocrystalline silicon bulk and converted to CIE 1931 color space coordinates.

A multi-layer feed-forward neural network (MFFNN) was designed using an MSI laptop (Intel Core i5, Nvidia RTX 3060) and MATLAB 2021b, comprising an input layer, three hidden layers, and an output layer representing RGB coordinates.

3. Results and discussions

Figure 1a depicts the proposed method of directly processing a Ti-TiO₂-Ti (30-60-200 nm) multilayer structure using first (1030 nm) and second (515 nm) harmonic femtosecond laser pulses (220 fs) at a maximum repetition rate of 200 kHz. By varying the scanning speed (*v*) and average laser power (*P*), the material texturing pathways are controlled through ultrafast thermalization, phase transitions, and thermo-mechanical effects.

The interaction of femtosecond laser pulses with the titanium film involves several processes: electron thermalization during the pulse, electron-phonon relaxation on a picosecond scale, and solid-to-liquid or solid-to-vapor transitions at the nanosecond scale. This ultrafast thermal expansion generates pressure waves that help remove material as liquid nanoparticles. Additionally, titanium reacts with oxygen at temperatures above 600 K,

transforming the top layer into titanium dioxide (TiO_2), with thickness increasing with laser exposure.

Different processing parameters yield distinct patterns, including ablative ripples and thermally induced LIPSS (TLIPSS), as shown in Figure 1a. The ripples 150 nm deep with periodicity around 320 nm, contrast with the shallower (30–40 nm) TLIPSS, which have a period of approximately 450 nm [4]. The differing orientations of these features suggest varied self-organization mechanisms, with ripples likely resulting from interference patterns due to light scattering and surface plasmon coupling, while TLIPSS grow through interference feedback from protruding TiO_2 defects.

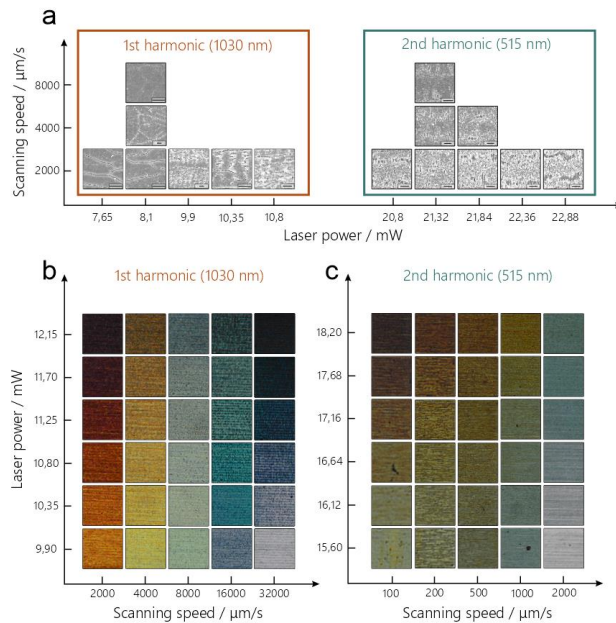


Fig. 1. (a) Series of SEM images showing morphology variation versus average laser power P (at 200 kHz repetition rate) and scanning speed v . Scale bar is 1 μm . (b,c) Bright-field optical images of the patterned surface areas obtained with white light.

Figure 1a presents a summary linking the ablative and additive patterning methods to key processing parameters, specifically average laser power (P) at a constant repetition rate of 200 kHz, and scanning speed (v). Red and yellow hues can be generated using the first harmonic (1030 nm) of a femtosecond laser at speeds of 2000 and 4000 $\mu\text{m/s}$, respectively. As the laser power increases, these colors transition to black and brown. Scanning speeds of 16000 and 32000 $\mu\text{m/s}$ can create green and dark blue colors, which also fade with higher laser power. In contrast, using the second harmonic (515 nm) results in no significant color variations, as all conditions appear similar in dark green and brown, regardless of scanning speeds and laser intensity.

Figure 1(b,c) examines the visual characteristics ($\text{NA} = 0.3$) of the laser-patterned regions ($200 \times 200 \mu\text{m}^2$) by comparing bright-field optical images. This color change is attributed to the progressive oxidation of the top titanium layer, leading to the formation of a TiO_2 layer above the underlying titanium film, with an effective thickness of up to 150 nm (considering the Pilling and Bedworth ratio of approximately 1.8 for the Ti to TiO_2 conversion). This thickness is adequate for reflectivity modulation via the Fabry-Perot effect. Numerical simulations of the surface reflectivity change due to oxidation are showing good

agreement with experimental data; however, surface roughness, defects, and pores introduce additional losses that diminish color purity in the experiments. It's important to note that excessive laser power can lead to surface ablation and shock wave formation instead of promoting oxidation, resulting in surface blackening (not depicted in the images). Additionally, the oxidation efficiency decreases as the TiO_2 layer thickens, limiting further oxygen penetration and interaction with the underlying titanium film. Figure 2 displays optical and SEM images of the printed parrot drawing, showcasing the capability to produce vibrant images using the suggested structural coloration technology.

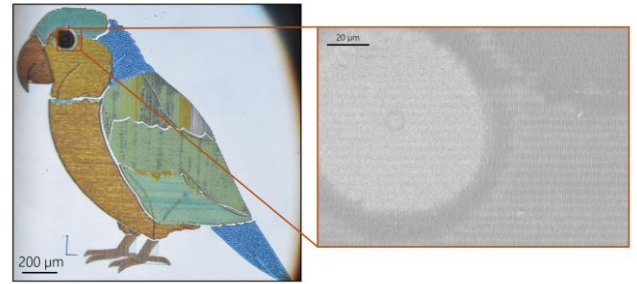


Fig. 2. Example of the structural color image produced and visualized at $\text{NA}=0.1$. SEM image demonstrates variations in surface morphology that enable modulation of surface color.

4. Conclusions

In conclusion, we demonstrated high-resolution structural coloring of a thin Ti film using laser-induced oxidation and self-organization regulated by femtosecond laser parameters. For a Ti- TiO_2 -Ti sample, we achieved parameter-controlled processing regimes that produced ripples, thermochemical LIPSS, and uniform oxide films. We developed a neural network to analyze the correlation between processing parameters and color appearance, enabling predictable printing of free-form images with high reproducibility. Additionally, leveraging ultrashort pulse duration and a multi-layer design, we achieved exceptional color printing resolution of up to 20,000 dpi, surpassing traditional technologies like ink-jet printing. This method has promising applications in multi-level marking, labeling, and anti-counterfeiting.

Acknowledgements

This work was supported by the Russian Science Foundation (Grant No. 24-19-00541; <https://rscf.ru/project/24-19-00541/>).

References

- [1] X. Zhiyi, et al. The Innovation 2(2021)1.
- [2] K. Frederik, et al. Opt. Laser Technol. 168(2024)109882.
- [3] J. Bonse et al. Handbook of laser micro- and nano-engineering (2020).
- [4] V. Lapidis et al. ACS Appl. Mater. Inter. 17(2025)16122.

IR transparent semimetal CaSi_2 electrodes for thermal switching of VO_2 phase change thin films

Pavlov D.V.¹, Banniy D.E.^{1,2}, Bozhok A.V.^{1,2}, Il'yaschenko V.M.¹, Cherepakhin A.B.¹, Zhou H.³, Dou S.³, Li Y.³, Kuchmizhak A.A.^{1,2}, Shevlyagin A.V.^{*1}

¹ Institute of Automation and Control Processes, 5 Radio St., Vladivostok 690041, Russia

² Far Eastern Federal University, Vladivostok, Russia, 10 Ajax Bay, Russky Island, Vladivostok 690091, Russia

³ Center for Composite Material and Structure, Harbin Institute of Technology, Harbin 150001, P. R. China

*e-mail: shevlyagin@iacp.dvo.ru

Abstract. Semimetal calcium disilicide thin film (CaSi_2) acting as a transparent microheater was used as the underlying substrate layer to grow thin film of phase change vanadium dioxide (VO_2). Room-temperature optical measurements and Raman study revealed insignificant deterioration of infrared (IR) transparency of the resulting structure and crystallinity of the grown layers, respectively, compared with bare VO_2 and CaSi_2 films. This allowed realizing optical switching of the designed structure in the atmospheric window (3–5 μm) with modulation depth of 60% by supplying a DC voltage of 4V to CaSi_2 electrode, which triggered metal-insulator transition of the VO_2 layer by the electrothermal stimuli.

1. Introduction

The Stefan-Boltzmann law dictates that infrared (IR) radiation can be regulated by either temperature or emissivity of the object. Vanadium dioxide (VO_2) is a potential material for smart thermal emitter and optical limiter and switch technologies due to metal-insulator transition (MIT) taking place near the 70°C [1]. There are three possible types to switch IR optical properties of the VO_2 : thermochromic, all-optic and electro-optic regulations. The latter has gained interest since electrically triggered phase transition is more preferable for practical uses. Generally, the intrinsic electrical resistivity of VO_2 is too high in the low-temperature insulating state, which requires high threshold voltage to be switched. Alternatively, instead of making electrical contacts for creating the electric field inside the phase change material, VO_2 films can be grown directly on the electrode material acting as a resistive element for uniform heating by appropriate voltage supply [2]. This method is referred to as electrothermally switching. However, existing electrically controlled microheaters are usually opaque, limiting practical applications. As a solution, transparent conducting oxides are used to dynamically regulate IR transparency of the VO_2 . However, popular choice as indium-tin oxide demonstrates not enough temperature stability to resist during the deposition of the VO_2 atop requiring 600°C for high quality films.

Calcium disilicide (CaSi_2) electrodes have attracted growing interest due to high electrical conductivity with simultaneously high optical transparency especially in the IR spectral range up to 7 μm [3], which enables the realization of the transparent microheater on their base [4]. In addition, CaSi_2 is composed of abundant and non-toxic chemical elements, while high growth temperature (500–800 °C) assumes its suitability for VO_2 films overgrowth. Thus, realization of the phase-changing VO_2 films integrated with transparent in the wide spectral range microheater made of CaSi_2 is of great demand, which prospects for electrically driven optical filters and limiters.

In this work, VO_2 films were successfully grown atop CaSi_2 thin films, which allowed electrothermally switching of the IR transparency of the samples under supply of the

DC voltage through CaSi_2 thin film electrode. It was shown that a voltage of 2V is enough to trigger the MIT of the VO_2 as efficiently as in the case of traditional thermochromic switching by the change in the ambient temperature. Of importance, that optical modulation could be tuned by applied voltage exceeding 60% in the atmospheric window (3–5 μm) at 4V.

2. Experiment

CaSi_2 film of 60 nm in thickness was grown by solid phase epitaxy on sapphire substrate in the vacuum chamber with basic pressure 10^{-6} Torr as described elsewhere [3]. After that, magnetron sputtering was used to form gold pads atop silicide film followed by the covering of the CaSi_2 with protective 30 nm thick amorphous Al_2O_3 film. Finally, 80 nm thick VO_2 film by a high-power impulse magnetron sputtering at 400°C and post growth annealing in a tube furnace at 400 °C for 2 h under Ar atmosphere [5]. As a reference, thin films of uncovered CaSi_2 and VO_2 were grown in the same manner. Crystal quality of the grown VO_2 and CaSi_2 layers was investigated by the Raman micro-spectroscopy with 473 nm CW laser pump and dry objective with NA=0.9. Optical properties were studied within Fourier-Transform IR spectrometer coupled to the IR microscope. For the temperature dependent optical measurements either a Peltier element or DC voltage source were used as a heaters for thermal and electrothermal switching of the VO_2 , respectively, while the samples temperature was monitored by the IR camera.

3. Results and discussions

Figure 1 shows the evolution of the optical properties of the samples with every new grown layers starting from the pure CaSi_2 and VO_2 thin films acting as transparent conducting and phase-changing materials, respectively, to Al_2O_3 -coated CaSi_2 film with Au pads serving as transparent microheater and finally to the end samples of electrothermally switched IR optical limiter with integrated heater consisting of $\text{VO}_2/\text{Al}_2\text{O}_3/\text{CaSi}_2$ structure grown on transparent substrate. Of importance, that despite the multilayer structure including semimetal (CaSi_2) and insulating in low-temperature state (VO_2), both the end sample and all the constituent structures demonstrates semitransparent properties in the visible spectral range

obvious for the naked eyes as can be deduced from the inset photos in Figure 1, where one can see the word “transparency” through all the samples. As expected, optical transmittance is gradually reduced within the each grown layer compared to pure VO₂ films due to semimetal related semitransparency of the CaSi₂. Nevertheless, an average transmittance exceeding 55% is preserved in the (1–4 μm) spectral range indicating that CaSi₂ indeed can be used as a transparent microheater, which does not interfere much with VO₂ intrinsic optical properties.

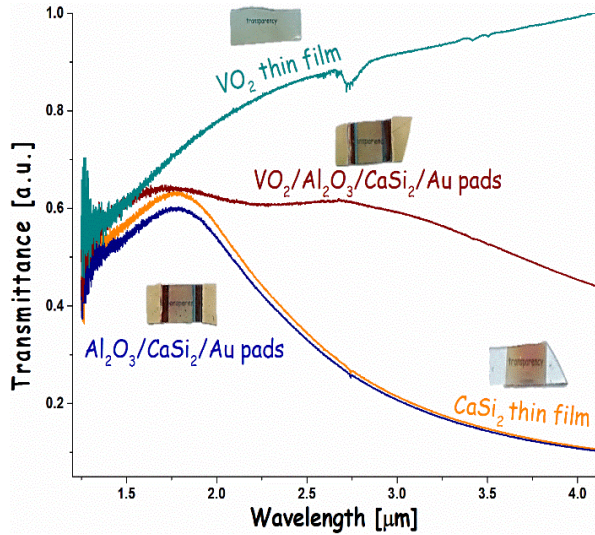


Fig. 1. Room-temperature optical transmittance of the grown samples from the near to middle infrared range. The insets show the sample photos to illustrate their partial transparency.

As crystallinity of the VO₂ has an impact on MIT transition, Raman study was conducted to verify the influence of the underlying layers on the quality of the VO₂ film. Figure 2 demonstrates that the VO₂/Al₂O₃/CaSi₂ multilayer structure was successfully grown as both the VO₂ (♣) and CaSi₂ (♠) related phonons contribute to its Raman spectrum. However, the intensity and the width of the former suggest the deterioration compared to bare VO₂ film being the common issue of the growth on the non-lattice-matched substrates.

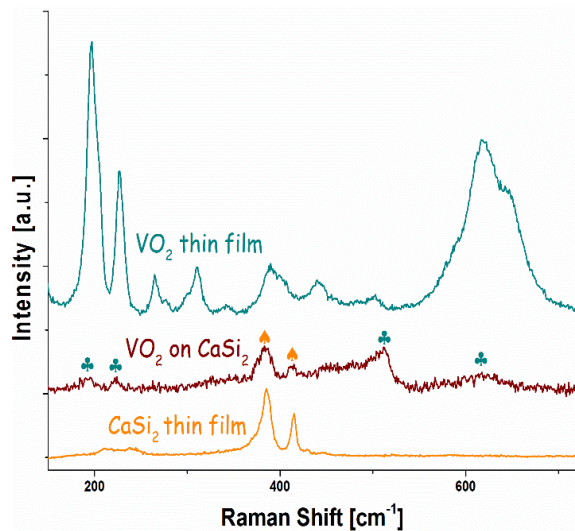


Fig. 2. Raman spectra of the bare VO₂ and CaSi₂ thin films as well as the spectrum of the multilayer VO₂/Al₂O₃/CaSi₂ structure with denoted by the ♣ and ♠ symbols phonon signatures contributed from VO₂ and CaSi₂.

Finally, VO₂/Al₂O₃/CaSi₂ sample with Au pads was tested as an electrically driven IR optical limiter. For this purpose, first, MIT induced change in the transmittance was evaluated through the standard scheme with Peltier heating. Despite the lower crystal quality of the VO₂ film grown on Al₂O₃/CaSi₂ underlayer it still could demonstrate optical switching (navy and wine colored curves in Figure 3) at the transition temperature estimated as 75°C compared to that of about 68°C for bare VO₂. Next, electrothermal switching was performed by applying a DC voltage between Au pads. It was observed that the same optical modulation depth could be reached at relatively low voltage of 2V (Figure 3, dark cyan curve), approving the efficiency of the CaSi₂ layer as a transparent microheater. Moreover, voltage doubling (Figure 3, orange curve) could further tune the drop in transparency, which allows reducing the transmittance from 70 down to 30% at the wavelength of 5 μm.

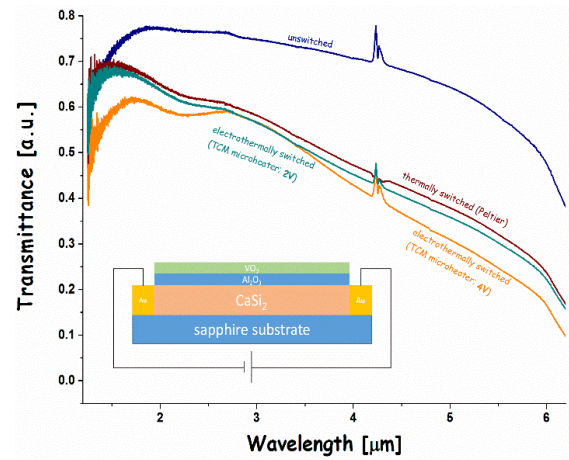


Fig. 3. Temperature-dependent optical transmittance spectra of the VO₂/Al₂O₃/CaSi₂ sample. MIT of the VO₂ was triggered either by thermal heating from the Peltier element or resistive heating by the integrated CaSi₂ microheater.

4. Conclusions

To conclude, successful growth of VO₂ thin films on Al₂O₃/CaSi₂ underlayer was realized. It enabled the electrically driven modulation of the IR transparency of the resulting VO₂/Al₂O₃/CaSi₂ system where CaSi₂ acts as integrated microheater for electrothermally regulation of the VO₂ metal-insulator transition. Results obtained have bright perspectives to be applied in the dynamic optical limiter applications.

Acknowledgements

The research is founded by the Russian Science Foundation, grant No 24-79-00185 (<https://rscf.ru/project/24-79-00185/>).

References

- [1] Y. Ke et al. *Small* **14**(2018)1802025.
- [2] Z. Xu, G. Qin, A. Bernussi, Z. Fan. *J. Alloys Compd.* **381**(2021)157640.
- [3] A.V. Shevlyagin et al. *J. Alloys Compd.* **910**(2022)164893.
- [4] D.V. Pavlov et al. *Bull. Russ. Acad. Sci. Phys.* **88** Suppl.3(2024)S418-S422.
- [5] J. Gu et al. *ACS Appl. Mater. & Inter.* **14**(2022)2683-2690.

Switching platform for tunable metasurfaces based on phase change materials

Pestova V.B.^{*,1}, Pestov G.N.^{1,2}, Kitsyuk E.P.², Smayev M.P.³, Saurov M.A.², Lazarenko P.I.¹

¹ National Research University of Electronic Technology, 1 Shokin Sq., Moscow 124498, Russia

² Scientific-Manufacturing Complex "Technological Centre", Zelenograd, Russia

² Lebedev Physical Institute of the RAS, Leninsky pr. 53, Moscow, Russia

*e-mail: Kapakycek2009@yandex.ru

Abstract. A switching platform has been developed to enable the writing and erasing of extended two-phase periodic laser-induced surface structures on $\text{Ge}_2\text{Sb}_2\text{Te}_5$. Writing is achieved using femtosecond (fs) laser pulses, while erasing is performed with electric current pulses. The results demonstrate the feasibility of employing a thin-film resistive heating element of the proposed design for the creation of non-volatile, active integrated optical and optoelectronic devices, such as tunable diffraction gratings.

1. Introduction

Phase-change materials like $\text{Ge}_2\text{Sb}_2\text{Te}_5$ (GST) can rapidly and reversibly switch between crystalline and amorphous states, each exhibiting unique optical properties, such as high optical contrast ($\sim 30\%$) and fast switching times (< 500 ps) [1]. This makes GST suitable for dynamic photonic applications. Femtosecond laser irradiation of GST surfaces can create laser-induced periodic surface structures (LIPSS), with their morphology and periodicity controlled by laser parameters.

LIPSS act as metasurfaces-engineered structures capable of manipulating light propagation, including direction, polarization, phase, and wavelength. These metasurfaces are essential for tunable diffraction gratings and versatile optical devices. However, achieving reversible recording and erasure of LIPSS remains a challenge.

This study demonstrates the formation of femtosecond laser-induced LIPSS on GST films and their erasure using resistive heating. The approach highlights the potential of dynamic metasurfaces for photonics and optoelectronic applications.

2. Experiment

The structure was fabricated on a glass substrate using a three-step contact lithography process (Fig. 1). In the first stage – the metal heater formation: Ni (150 nm) was deposited on a Ti adhesive sublayer (20 nm). In the second stage – the contact pad formation: Ni (250 nm) was layered on the same Ti sublayer. In the third stage – functional layer deposition: a 30 nm $\text{Ge}_2\text{Sb}_2\text{Te}_5$ (GST) layer was coated with a 20 nm protective SiO_2 film. The thin films of this heater structure were deposited by the magnetron sputtering.

The LIPSS were generated using femtosecond (fs) pulsed laser exposure (wavelength: 1030 nm, repetition rate: 50 kHz, pulse duration: 250 fs) in scanning mode with a diverging beam [2]. This process resulted in the formation of LIPSS across the entire GST surface.

Electrical switching of the fabricated structure was performed using a probe station with an Agilent E3647A power supply and a Keysight B2912A pulse generator operated in pulse mode. Structural analysis before and after switching was conducted by Raman spectroscopy ($\lambda = 532$ nm, $P_{\text{max}} = 10$ mW) in a scanning mode.

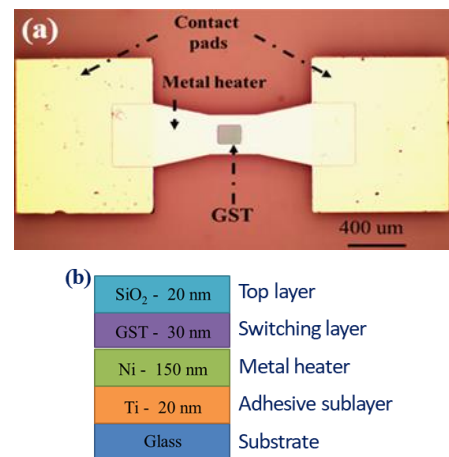


Fig. 1. Formed structure: (a) schematic top view; (b) cross section of switching area.

3. Results and discussions

The operating principle of the developed structure (Fig. 1) is based on the crystallization of the GST layer induced by the absorption of Joule heat generated by the resistive heater when an electric current flows through it. The design of this optoelectronic platform for LIPSS erasure is patented in the [3].

Before switching, the formed LIPSS consists of two-phase amorphous-crystalline periodic stripes with varying optical contrast (Fig. 2a). When U-shaped current pulses with a duration of 450 ms and an amplitude of 2 V are applied to the heater, the LIPSS is erased, and the periodic structure is no longer observed (Fig. 2b).

After switching, the surface becomes optically homogeneous due to the elimination of optical contrast. This is confirmed by Raman mapping of the LIPSS area before and after switching, which indicates that the amorphous stripes crystallized under the influence of electrical pulses (Fig. 2c,d).

The crystallization of amorphous stripes is accompanied by changes in the spectral characteristics, specifically $n(\lambda)$ and $k(\lambda)$. At a wavelength of $\lambda = 650$ nm, the refractive index change is $\Delta n \approx 1$, and the extinction coefficient change is $\Delta k \approx 0.5$. These changes are further confirmed by alterations in the Raman spectrum profile.

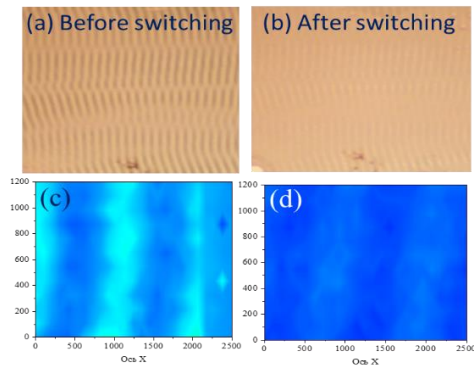


Fig. 2. GST area before (a) and after (b) switching; Raman mapping in the ripple area (12 lines \times 30 spectra) before (c) and after (d) switching.

The observed optical transformations are attributed to the crystallization of amorphous LIPSS stripes into an fcc crystalline structure. The identified structural modifications are consistent with the X-ray phase analysis results of thermally treated GST films, as reported in [4]. The amount of Joule heat generated by the metal heater during the crystallization process was approximately 0.11 J.

4. Conclusions

The obtained results demonstrated the possibility of using a thin-film resistive heating element of the developed design to create elements of non-volatile active integrated optical and optoelectronic devices, for example, tunable diffraction gratings.

Acknowledgements

This work was supported by Russian Science Foundation (project №23-79-10309).

References

- [1] Joo Hwan Ko, Young Jin Yoo, *iScience Review*, **25**, (2022), pp. 1-25.
- [2] Patent for invention №2786788.
- [3] Patent for invention №2825198.
- [4] P. Lazarenko et al, *Chalcogenide Letters*, **15** (2018), pp. 25-33.

Charge-transfer plasmons in non-periodic and periodic systems

Fedorov A.S.^{*,1,2}, Eremkin E.V.^{1,2}, Teplinskaia A.S.^{1,2}, Gerasimov V.S.^{2,3}

¹Kirensky Institute of Physics, Federal Research Center KSC SB RAS, 660036, Krasnoyarsk, Russia

²International Research Center of Spectroscopy and Quantum Chemistry – IRC SQC, Siberian Federal University, 660041, Krasnoyarsk, Russia

³Institute of Computational Modeling, Federal Research Center KSC SB RAS, 660036, Krasnoyarsk, Russia

*e-mail: gchem99@yandex.ru

Abstract. We have investigated both theoretically and experimentally charge-transfer plasmons (CTP) implemented in different systems. An original quantum-classical models are presented that describes CTP in systems consisting of non-periodic or periodic arrays of metal nanoparticles (MNPs) connected by narrow conducting linkers (polymer molecules), or located on the graphene surface. These techniques allow to describe CTP properties at 3-4 orders of magnitude faster than calculations using standard Finite Element (FEM) or Finite Difference Time Domain (FDTD) methods and provide possibilities to predict CTP properties in very large systems for different applications. The results of experimental synthesis of dimers consisting of gold MNPs adjacent by conducting molecules also presented. They show an intense absorption peak with a wavelength of ~780 nm, which is connected with CTP mode. This CTP mode may be of interest to hyperthermia in medicine due to its position in the transmission window of biological tissues.

1. Introduction

In recent years, researchers have devoted considerable attention to the processes of absorption and scattering in planar systems composed of closely spaced MNPs, where plasmons can be generated. These structures are relatively easy to synthesize, and their plasmon spectra can be tuned by adjusting the coupling (distance) between individual MNPs [1]. CTPs can be generated in systems consisting of two or more MNPs connected by a conducting linkers (bridges). In such systems free charges flow through the bridges between MNPs, resulting in the formation of CTPs with frequencies typically lie in the visible or infrared (IR) range [2–3]. In recent years, plasmonic effects have been intensively studied also for systems consisting of MNPs on the surface of graphene. The plasmon frequencies in these systems lie in the THz range, which has recently become more and more in demand in practice [4].

2. CTP Calculation models

Here the family of original hybrid quantum-classical models are developed to describe the properties of CTP plasmons in systems consisting of arrays of MNPs connected by narrow conducting linkers, consisting, for example, of conducting polymer molecules [6]. The models accounted quantum effects, with the parameters obtained from first-principles density functional theory (DFT) simulations. The models are based on assumption that the total energy of the systems is divided into two parts: the electrostatic potential energy E_{pot} of charged MNPs, expressed by the quadratic function of their charges Q_j as well as the kinetic energy E_{kin} of the ballistic current of electrons through the conductive bridges:

$$E_{\text{pot}} = \sum_{j \neq k} \frac{Q_j Q_k}{R_{jk}} + \sum_j \{a_j Q_j^2 + b_j Q_j + c_j\}$$

$$E_{\text{kin}} = -\frac{e}{L} \sum_{jk} \frac{\alpha_{jk} I_{jk}(t)^2}{2}, \quad \alpha_{jk} = \frac{L^2 m^*}{2 n_f e^2}$$

where R_{jk} is the distance between the particle centers, α_{jk} describes the conductive properties of the linker between the j -th and k -th MNPs (simplified to α for identical linkers), n_f is the number of carriers at the Fermi level of

the linker, L denotes the linker's length, and m^* is the effective electron mass in the linker.

The main equation is assumed to be the equation of conservation of total energy in addition to the continuity equation, showing that the oscillating charge of every particle with index j : $Q_j(t) = Q_j \exp(i\omega t)$ can be changed only by the current through the linkers that are in contact with it $\dot{Q}_j = \dot{Q}_j - \sum_k I_{jk}$. These equations lead to the differential system of equations sufficient to solve the charge dynamics in nanoparticles and to find the CTP frequencies ω_j as well as the eigenvectors of these oscillations:

$$\ddot{Q}_j = -\frac{1}{\alpha} \sum_k \left\{ \sum_{s \neq j, k} Q_s \left(\frac{1}{R_{sj}} - \frac{1}{R_{sk}} \right) + (Q_j - Q_k) \left(\frac{1}{R} - \frac{1}{R_{jk}} \right) \right\}$$

It is shown that CTP frequencies lies in the near infrared region and strongly depends on the conductivity and length of the linkers. This approach makes it possible to describe CTP properties on 3-4 orders of magnitude faster compared to commercial electromagnetic solvers based on FEM or FDTD methods.

The model can be adapted to the case of periodic arrays of connected MNPs. It is assumed that the oscillating MNP charges are characterized by a wave vector q and a cell number j .

$$Q_i(\vec{R}_j + \vec{R}_n) = Q_j e^{iq\vec{R}_n}$$

Using Bloch's theorem and using the transition to reciprocal space, it is possible also to obtain a system of linear equations for finding ω_j and CTP eigenvectors. The similarity of band structures of phonons in crystals and CTP of connected NPs regular arrays is demonstrated.

Based on these models, it is developed also the model for CTP properties calculating in systems of non-periodic or periodic MNPs array located on the graphene surface [6]. It are shown the CTPs frequencies in these systems lie in the THz range and they are factorized, i.e. represented as the factor depending on the Fermi energy, multiplied by the factor depended on the geometry of MNPs array. It is

demonstrated also the CTP frequencies are consistent with experiments and FDTD calculations.

Using FDTD/FEM calculations, CTP plasmons are studied in systems consisting of gold MNPs located on the surface of thin film of gold or heavily doped silicon. It is shown that CTP frequencies lie in the near-IR range and can be effectively changed by changing the geometry of the system or by electrostatic doping of the silicon film.

2. Experiments to prove the CTP existence

We also carried out a synthesis of gold nanoparticles dimers adjacent by conducting 1,2-bis(2-pyridyl)ethylene (BPE) molecules in an aqueous solution[7]. The formation of stable dimers with 22 nm diameter of MNPs has been confirmed by TEM microscopy. The possibility of charge transfer through the BPE linkers has been proven by the density functional theory (DFT) calculations. In addition to localized plasmon resonance of solitary nanoparticles in the solution that has a peak at a wavelength of 530 nm, the optical spectra exhibit a new intense absorption peak in the near-infrared range with a wavelength of ~ 780 nm, which is attributed to the CTP mode, see Fig.1:

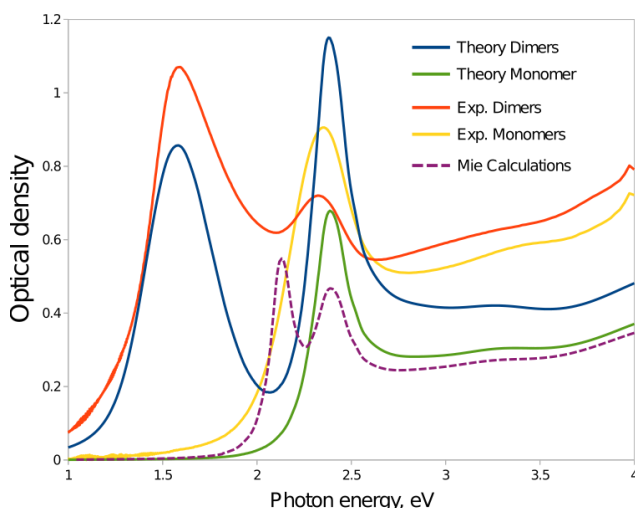


Fig. 1. Experimental and calculated absorption spectra of gold MNP dimers and monomers in water solution.

At the same time the spectra simulated within the developed model agree with the experimental ones. This resonant absorption by CTPs may be of interest to biomedical applications due to its position in the so-called transmission window of biological tissues. The in-vitro heating of CTP dimer solution by a laser diode with a wavelength of 792 nm proved the efficiency of CTP dimers for achieving a temperature increase of $\Delta T = 6$ °C, which is sufficient for hyperthermia treatment of malignant tumors.

3. Conclusions

Highly efficient models for calculating of CTP frequencies and their eigenvectors for regular and irregular arrays of MNPs bound either by conducting linkers or located on graphene are proposed. It is shown the CTP frequencies lie in the near-IR range for MNPs connected by conductive bridges and they can be effectively changed by changing the system geometry or by conductivity of the bridges.

It is also shown the CTP frequencies of MNP complexes on graphene lie in the THz range that are consistent with experiments and FDTD calculations.

At the same time, they are factorized, i.e. represented as the factor depending on the Fermi energy, multiplied by the factor depended on the geometry of MNPs array. The similarity of band structures of phonons in crystals and that for MNPs regular array on graphene is demonstrated.

The adequacy of the proposed models was proven by synthesizing dimers of gold MNPs adjacent by conducting BPE molecules and measuring the CTP frequencies in the water solution containing the dimers.

Acknowledgements

This study was supported by the Russian Science Foundation, Agreement No. 23-12-20007, and the Government of the Krasnoyarsk Territory and the Krasnoyarsk Territorial Foundation for Support of Scientific and R & D Activities, Agreement No. 256.

References

- [1] Y. Cheng and M. Sun, New J. Phys. **24**(3), (2022) 033026.
- [2] F. Wen, Y. Zhang, S. Gottheim, et al., ACS Nano **9**(6), (2015) 6428–6435.
- [3] A. N. Koya and J. Lin. Appl. Phys. Rev. **4**(2), (2017) 021104.
- [4] Tonouchi M. Nature Photon., **1** (2007) 97–105.
- [5]] A. S. Fedorov, P.O. Krasnov, M.A. Visotin, et al. J. Chem. Phys. **151** (2019) 244125
- [6] A.S. Fedorov, E.V. Eremkin, P. O. Krasnov et al, J. Chem. Phys. **160** (2024) 044117
- [7] A.S. Fedorov, M. A. Visotin, A.V. Lukyanenko, V.S. Gerasimov and A.S. Aleksandrovsky, J. Chem. Phys. **160**, (2024) 084110.

Lasing generation in disordered ZnO resonators

Sibirev N.V.^{*1}, Serov A.Yu.¹, Labzovskaya M.E.¹, Kadinskaya S.A.^{3,4}, Kondratev V.M.^{3,4}, Mikushev S.V.¹, Agekyan V.F.¹, Bolshakov A.D.^{3,5}, Shtrom I.V.^{1,2}

¹ St. Petersburg State University, Universitetskaya Embankment 7-9, 199034 St. Petersburg, Russia

² IAI RAS, 198095 St. Petersburg, Russia

³ Alferov University, 194021 St. Petersburg, Russia

⁴ Moscow Institute of Physics and Technology, 9 Institutskiy Lane, 141701 Dolgoprudny, Russia

⁵ Laboratory of Advanced Functional Materials, Yerevan State University, Yerevan 0025, Armenia

*e-mail: n.sibirev@mail.spbu.com

Abstract

The lasing generation in ZnO whiskers has been described. The spatially reproducible lasing generation from the use of whiskers was observed. While the strongest lasing mode shifted nearly randomly in each experiment, the distance between the lines demonstrates a tendency to increase with wavelength. The optical length of lasing resonators lies in the range between 400 and 600 micrometers, while sizes of whiskers are less than 3 micrometers. The energy is transferred inside the bush because of the whisker coupling. The existence of laser generation strongly depends on the shape of the whisker tip. Laser generation requires that the shape of whisker tip looks like corner retroreflector. The big refractive index of ZnO allows the existence of ZnO corner retroreflectors with small dihedral angles $\pi/4$ and $\pi/6$.

1. Introduction

Zinc oxide is of great interest for various applications. The large exciton binding energy of 60 meV and the wide forbidden bandgap of 3.37 eV [1] make zinc oxide (ZnO) interesting for use in UV optoelectronic devices. In addition, zinc oxide is non-toxic.

Recently, a large number of zinc oxide nanostructures of different dimensions, possibly even fractal, have been synthesized. Most often 'one-dimensional' structures are investigated. The variety of fractal structures of zinc oxide like flowers, snow flakes, hedgehogs are available to study.

Usually, samples with clear and understandable geometry, whose properties are relatively easy to calculate, are used for research. This paper investigates the properties of randomly grown nanostructures with a wide variation of parameters.

2. Experiment

In this work, we employ a conventional synthesis protocol using equimolar concentration $\text{Zn}(\text{NO}_3)_2$ and HMTA aqueous solutions. Synthesis is carried out on Si (111) substrates, which were preliminarily purified in acetone and then in isopropanol [2].

Typical images of the synthesized ZnO nanostructures obtained using a JSM 7001F scanning electron microscope are shown in Figure 1.

For the convenience of the study, a marking was applied to the sample. The marking allows you to compare the object that glows with the SEM image.

The Photoluminescence (PL) spectra of the synthesized samples were studied using an MDR-204-2 monochromator (LOMO-Photonics) [3]. The samples were placed in a closed-cycle helium cryostat (Janis Research Company). The PL was excited by a He-Cd laser (excitation wavelength $\lambda = 325$ nm, maximum radiation power of $13\text{ W} = 50\text{ kW}\cdot\text{cm}^{-2}$).

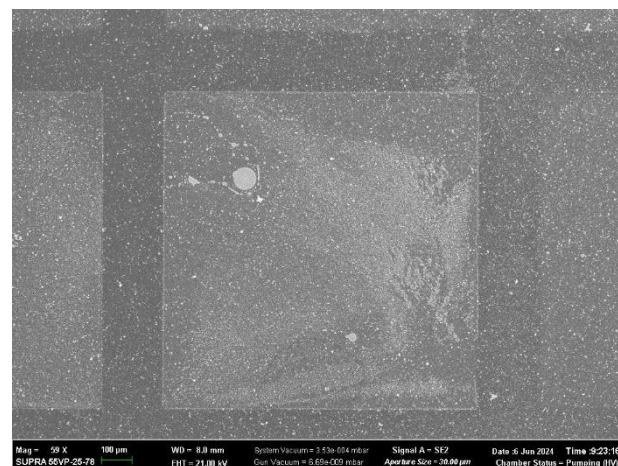


Fig. 1. SEM Image of the square.

On the most part of the surface, the PL spectra are rather monotonous and correspond to the usual emission of ZnO under strong pumping. A broad smooth band with a maximum $\lambda \sim 371$ nm was observed in the emission. At some selected points of the sample situation is different. At the long-wavelength edge of the 371 nm band, narrow ($\sim 1.6 - 1.9$ meV), peaks appear in the region starting at 372 nm, at some points from 372 nm onwards, see Figure 2.

Usually, the laser generation was well reproducible [3], but there were rare exceptions. Spectrum from top left angle of square, see figure 1, demonstrate laser generation, which is not reproducible. The spectra from this point measured at different times are presented in figure 2. Another interesting feature of this spectrum is the fast increase of distance between lines with wavelength.

3. Results and discussions

We assume that in this case we can talk about the Fabry-Perot resonator [3]. Calculation by the optical resonator formula. Fabry-Perot (1) allows us to determine the optical length of the resonator - S and to estimate the first derivative of the optical length from the wavelength - $dS/d\lambda$. The line spacing varies approximately from 0.37 nm to 0.25 nm.

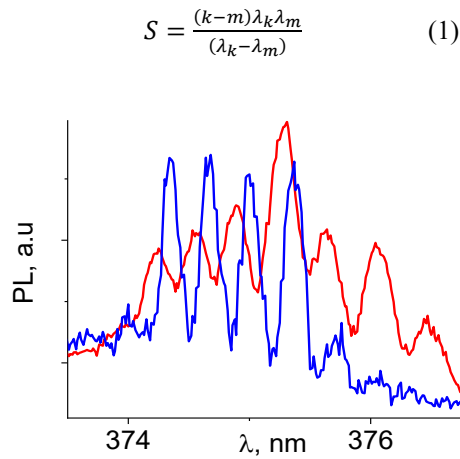


Fig. 2. Photoluminescence spectrum of the top left angle.

For the resonator with spectra shown in Figure 2, the optical length was $S=430\pm 15 \mu\text{m}$ and its derivative $dS/d\lambda=-120\pm 30 \mu\text{m}/\text{nm}$ or $d(\ln S)/d\lambda=-0.279 \text{ nm}^{-1}$. This means that our entire resonator is inside ZnO. It is easy to see that in Figure 1 there is only one region where we can place the resonator entirely in ZnO, the bush is in the upper left corner. A magnified image of the bush is given in Figure 3. It can be seen that the bush consists of numerous small whiskers.

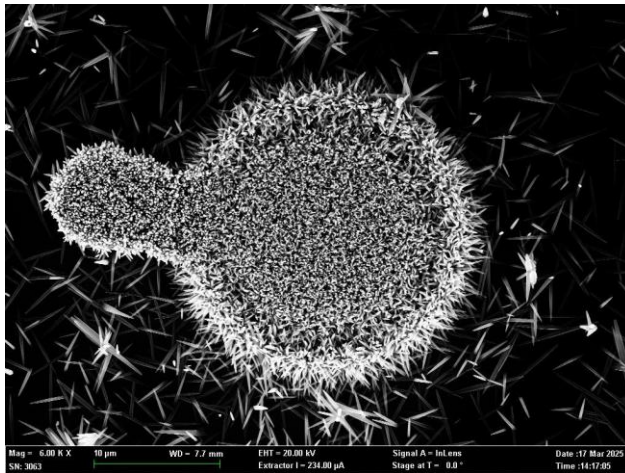


Fig. 3. SEM Image of the bush.

ZnO has a relatively large refractive index of 2.5 [1]. So, the phenomenon of total internal reflection is possible even for relatively small incident angle. The critical incident angle is 0.41 radian only. This makes possible the formation of retroreflectors with sharp angles $\pi/6$ and $\pi/4$. Typical whisker tip in bush with laser generation is represented in figure 4. The whisker tip is formed by six faces converging at a sharp angle smaller than $\pi/4$, most probably $\pi/6$. So, whisker tips in the bush forms reverse corner reflectors. Before light leaves the bush, it reflects from the tips of the whiskers and bounces back and forth between them. Because many laser generation modes are confined in the bush, the spectrum is not reproduced in the experiments.

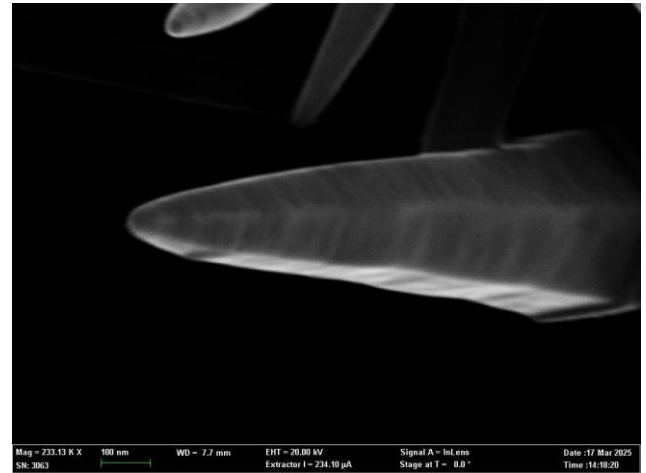


Fig. 4. SEM Image of whisker tip.

In some parts of sample whiskers have flat tips. Even the bushes with huge number of such whiskers demonstrates only stimulated emission without laser generation. It's not excluded other mechanism of lasing generation from whiskers.

4. Conclusions

The lasing generation in the bush of ZnO whiskers has been shown. The increasing distance between the lines on PL spectrum with the wavelength shows that lasing represents a collective effect. For light propagating along the whisker axis, the conditions of total internal reflection are realized. The whisker tip's configuration is hypothesized to resemble a corner retroreflector with dihedral angles of $\pi/6$. Such corner retroreflector could be formed by (2,-1,-1,6) and (2,-2,0,7) facets. Lasing generation is explained by whisker coupling inside the bush.

Acknowledgements

The author acknowledges St.-Petersburg State University for a research project No. 129360164.

References

- [1] Ü. Özgür, Y.I. Alivov, C. Liu, A. Teke, M.A. Reshchikov et. al. *J. Appl. Phys.* **98** (2005) 1.
- [2] S.A. Kadinskaya, V.M. Kondratev, I.K. Kindyushov, O.Y. Koval, D.I. Yakubovsky et. al. *Nanomaterials* **13** (2023) 58.
- [3] Labzovskaya M.E., Novikov B.V., Serov A.Yu., Mikushev S.V., Kadinskaya S.A. et. al. *Physics of the Solid State* **7** (2024) 1184.

New erbium-activated oxyfluoroniobate glasses

Ignatieva L.N.¹, Polyantsev M.M.¹, Galkin K.N.², Savchenko N.N.¹, Marchenko Yu.V.¹,
Mashchenko V.A.¹, Pikalov D.O.^{*1}

¹ Institute of Chemistry, FEB RAS, Prosp 100-letia, 159 Vladivostok 690022, Russia

² Institute of Automation and Control Processes, FEB RAS, 5 Radio St., Vladivostok 690041, Russia

*e-mail: dimpiks95@gmail.com

Abstract. New glasses in the $\text{ZnNbOF}_5\text{-BaF}_2\text{-InF}_3\text{-ErF}_3$ systems have been obtained and studied. The glass networks of all glasses are formed with NbO_nF_m polyhedra linked via oxygen bridges. The InF_3 component forms its own polyhedra and modifies the glass networks by attaching to oxyfluoroniobates via -Nb-F-In- bridges. The transparent glass ceramics has been obtained. The glasses of $\text{ZnNbOF}_5\text{-BaF}_2\text{-InF}_3$ can be promising for obtaining materials with high fluoride-ion mobility. In the $\text{ZnNbOF}_5\text{-BaF}_2\text{-InF}_3$ glasses, photoluminescence (542, 573 nm) was recorded. The glasses in the $\text{ZnNbOF}_5\text{-BaF}_2\text{-InF}_3\text{-ErF}_3$ system show luminescence of Er-ion, 543, 550 nm. The luminescence intensity increases synchronously up to 1 mol.% ErF_3 , with a further increase of ErF_3 it gradually decreases due to concentration quenching. The appearance of crystalline phases in the glasses leads to a decrease in the luminescence intensity.

1. Introduction

Niobium oxyfluoride is a successful progenitor for the creation of oxyfluoride glasses [1], which combine the properties of oxide glasses (mechanical strength, thermal and chemical stability) and fluoride glasses, characterized by a wide range of transparency and the possibility of introducing into the systems composition of fluorides with high polarizability of cations (BiF_3 , InF_3 , FeF_3) and doping with Rare Earth ions [2-5]. Such a combination is the path to the creation of ionic conductors, magneto-optical and luminescent materials. The works [3-5] consider glasses, based on the complex compounds of MNbOF_5 ($M = \text{Mn}$, Cd , Cu). These glasses differ in a number of characteristics from glasses based on NbO_2F , and differ from each other and within the same system, different REEs can have different effects on the properties of glass. These factors determine the importance of studying each specific system.

This paper presents the results of a study of glass-formation, structure, the possibility of obtaining glass-ceramics, and the dynamic and luminescent properties of new glasses in the $\text{ZnNbOF}_5\text{-BaF}_2\text{-InF}_3\text{-ErF}_3$ system.

2. Experiment

Monocrystals of $\text{ZnNbOF}_5\cdot 6\text{H}_2\text{O}$, synthesized by the method [6], BaF_2 , InF_3 , and ErF_3 were used to synthesize glasses in the $\text{ZnNbOF}_5\text{-BaF}_2\text{-InF}_3\text{-ErF}_3$ system. $\text{ZnNbOF}_5\cdot 6\text{H}_2\text{O}$ dehydrates with the formation of ZnNbOF_5 which decomposes at 650 °C to ZnF_2 и NbO_2F . To obtain indium trifluoride, indium acetate was calcined at 600-700 °C to obtain indium oxide. Indium oxide was dissolved with ammonium fluoride addition to the solution salt of $(\text{NH}_4)_3\text{InF}_6$ was obtained. This salt, calculated for the required amount of InF_3 , was introduced into the batch to obtain glass. Glass synthesis was carried out in closed platinum crucibles in a muffle furnace at a temperature of 900-950 °C in an air atmosphere. The obtained glasses were studied by X-ray phase analysis, calorimetry, IR and Raman spectroscopy, SAXS, ^{19}F NMR, luminescence.

3. Results and discussions

X-ray measurements showed the absence of crystalline phases in the obtained samples, and the DSC curves show the presence of a glass transition region (T_g), so all the discussed samples are glasses. Crystallization begins at

temperatures above 350°C. The compositions and heat treatment modes were determined, in which the samples retain the glass phase in the presence of crystalline phases (glass ceramics).

The IR absorption spectra of $\text{ZnNbOF}_5\text{-BaF}_2\text{-InF}_3\text{-ErF}_3$ glasses show a great similarity with the IR spectra of the oxyfluoroniobate glasses studied earlier. It indicates the similarity of the structure of their glass networks. In the IR spectra of the $\text{ZnNbOF}_5\text{-BaF}_2\text{-InF}_3\text{-ErF}_3$ glasses, bands are observed in the regions of 920-960, 800 and 500-400 cm^{-1} which characterize vibrations of the non-bridging bond Nb=O , bridging bonds -Nb-O-Nb-, Nb-F and In-F, respectively. Consequently, in the glasses under discussion, the glass networks are formed by polyhedra of NbO_nF_m connected by oxygen bridges. The components of ErF_3 have a stabilizing effect. Fluoroindate polyhedra modify the general glass network, joining the NbO_nF_m polyhedra by -Nb-F-In- bridges, and with a high content of InF_3 , they can also form layers of InF_6 , possibly, InF_7 polyhedra connected by fluorine bridges. The appearance of highly coordinated fluoroindate polyhedra in the structure increases the number of non-bridging fluorines, potential carriers of F-ionic mobility. This is consistent with the conclusions made on the basis of NMR ^{19}F studies of glasses of $\text{ZnNbOF}_5\text{-BaF}_2\text{-InF}_3$.

NMR data (Fig. 1) indicate the absence of ionic motions with frequencies above 10^4 Hz in the fluoride sublattices of glasses at temperatures of 150–300 K ("rigid" lattice). The development of dynamic processes involving fluorine ions for all the glasses discussed begins in the region of 300–320 K and ends at 520 K. The degree of spectrum narrowing at a temperature of 520 K, associated with the intensity of translational-diffusion movements of fluorine, depends on the concentration of InF_3 . The lowest activation energy of local motions ($E_{\text{NMR}} \approx 0.48$ eV) is recorded for glass with the largest amount of InF_3 .

It has been established that glasses of the $\text{ZnNbOF}_5\text{-BaF}_2\text{-InF}_3$ system are characterized by luminescence upon excitation by radiation with $\lambda = 470$ and 480 nm. In the luminescence spectra of its, bands are observed at 542, 573, 658 and 751 nm, the intensity of these bands is sensitive to the InF_3 content in the glasses (Fig. 2).

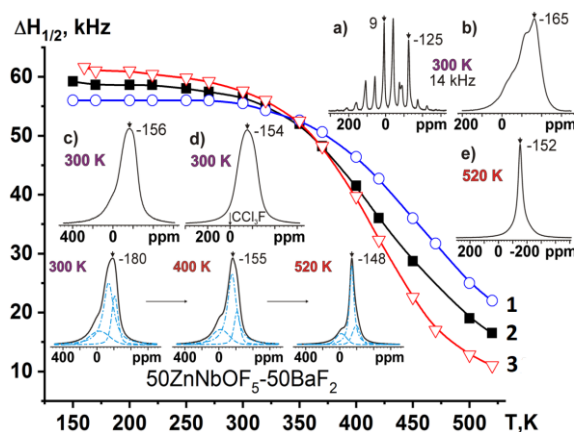


Fig. 1. Temperature dependences of the half-widths $\Delta H_{1/2}(F)$ of the ^{19}F NMR spectra of the glasses 1 - $50\text{ZnNbOF}_5\text{-}50\text{BaF}_2$, 2 - $40\text{ZnNbOF}_5\text{-}50\text{BaF}_2\text{-}10\text{InF}_3$, 3 - $20\text{ZnNbOF}_5\text{-}30\text{BaF}_2\text{-}50\text{InF}_3$. Inserts: ^{19}F NMR spectra: 1-(300-520 K), MAS ^{19}F NMR spectra of $\text{ZnNbOF}_5\cdot 4\text{H}_2\text{O}$ (a), glass 1 (b), glass 2 (c, 300 K), and glass 3 (d, 300 K; e, 520 K).

The luminescence spectra do not depend on the wavelength of the exciting light. This indicates the presence of a single luminescence center. When studying these glasses using SAXS, the presence of nanosized inclusions of ~ 9 nm in size was revealed in the glasses. Nanoparticles were not detected in glasses that did not contain InF_3 , and these glasses did not show luminescent properties. Taking into account the revealed relationship, it can be assumed that the nature of the observed photoluminescence is associated with quantum-size effects in the nanoparticles present in the glasses, nanoparticles contain Zn and In.

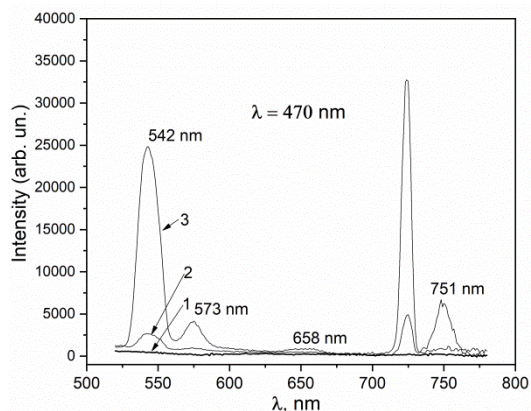


Fig. 2. Photoluminescence spectra of glasses in the $\text{ZnNbOF}_5\text{-BaF}_2\text{-}x\text{InF}_3$ systems: 1 - 0 InF_3 , 2 - 10 mol.% InF_3 , 3 - 40 mol.% InF_3 .

The luminescence spectra of the glasses in the system of $\text{ZnNbOF}_5\text{-BaF}_2\text{-InF}_3\text{-ErF}_3$ are characterized by the presence of intense bands in the region of 500–575 nm. These bands are characteristic of the luminescence spectra of Er-containing glasses and compounds. They correspond to the transitions: $^4\text{S}_{3/2} \rightarrow ^4\text{I}_{15/2}$ (543 nm), $^2\text{H}_{11/2} \rightarrow ^4\text{I}_{15/2}$ (550 nm). The luminescence intensity increases with an increase in the ErF_3 content in the range of 0.1–1 mol.%, a further increase in the content of one in the glass leads to a gradual decrease in the luminescence intensity. This effect is associated with concentration quenching. The optimal content of ErF_3 in glass, from the point of view of luminescent properties, is 1 mol.%. The appearance of crystalline phases in the glasses leads to a noticeable decrease in the luminescence intensity (Fig.3). It is

assumed that the observed quenching of luminescence in the $\text{ZnNbOF}_5\text{-BaF}_2\text{-ErF}_3$ glasses during heat treatment is associated with a common phenomenon in glass-ceramic materials known as “squeezing in” luminescence centers to glass matrix.

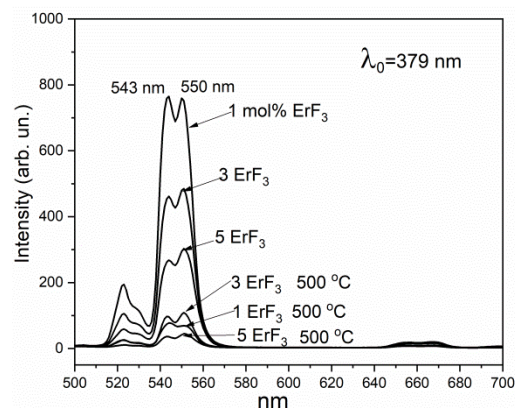


Fig. 3. luminescence spectra of glasses in the $\text{ZnNbOF}_5\text{-BaF}_2\text{-}x\text{ErF}_3$ system.

4. Conclusions

Using specially synthesized $\text{ZnNbOF}_5\cdot 6\text{H}_2\text{O}$ and InF_3 , and (high-purity) reagents BaF_2 and ErF_3 we synthesized new glasses in the $\text{ZnNbOF}_5\text{-BaF}_2\text{-InF}_3\text{-ErF}_3$ system with the content of ErF_3 from 0 to 5 mol.% and InF_3 from 0 to 50 mol.%. The transparent glass ceramics has been obtained under thermal treatment. Glasses are formed by polyhedra of NbO_2F_4 or NbO_3F_3 , connected by oxygen bridges. These are the main structural elements forming the glass networks. The InF_3 forms its own polyhedra and modifies the glass network by attaching to oxyfluoronibates via -Nb-F-In- bridges. According to the results of the study of the temperature behavior of the ^{19}F NMR spectra, glasses in the $\text{ZnNbOF}_5\text{-BaF}_2\text{-InF}_3$ system may be promising for obtaining materials with high mobility of fluorine ions and, as a consequence, ionic conductivity. In the $\text{ZnNbOF}_5\text{-BaF}_2\text{-InF}_3$ glasses, a photoluminescence (542, 573 nm) was recorded. Based on SAXS data, it is suggested that the nature of this effect is associated with the presence of nanosized inclusions containing In and Zn. The glasses in the $\text{ZnNbOF}_5\text{-BaF}_2\text{-InF}_3\text{-ErF}_3$ system show luminescence of Er^{3+} , corresponding to the transitions: $^4\text{S}_{3/2} \rightarrow ^4\text{I}_{15/2}$ (543 nm), $^2\text{H}_{11/2} \rightarrow ^4\text{I}_{15/2}$ (550 nm). The intensity of luminescence depends on the concentration of ErF_3 . The appearance of crystalline phases in the glasses leads to a noticeable decrease in the luminescence intensity.

Acknowledgements

The work was supported by the Russian Science Foundation Grant No. 24-13-00133, https://rscf.ru/prjcard_int?24-13-00133.

References

- [1] Mi. Poulain., Ma. Poulain Oxyfluoride glasses. Mater. Sci. Forum, 1991, 67–68, P. 129–136.
- [2] P.P. Fedorov, A.A. Luginina, A.I. Popov. Journal of Fluorine Chemistry – 2015. V. 172 – P. 22–50.
- [3] S.A. Polyshchuk, L.N. Ignatieva, Yu.V. Marchenko, V.M. Buznik. Physics and Chemistry of Glass 2011. Vol. 37. No. 1. pp. 3–27.

-
- [4] S.A. Polyschuk, L.N. Ignatyeva, S.L. Sinebryukhov, S.V. Gnedenkov, A.B. Podgorbunsky, N.N. Savchenko, V.M. Buznik, J. Inorganic Chemistry 2013, 58, No. 4, 387–391.
- [5] L.N. Ignatieva, N.N. Savchenko, Yu.V. Marchenko, S.A. Sarin. Ceramics International 45 (2019) 17737–17741. <https://doi.org/10.1016/j.ceramint.2019.05.343>.
- [6] R L Davidovich, T F Levchishina, T A Kaidalova, V I Sergienko *Less Common Metals* **27** 35 (1972).

Monolithic integration of bismuth-substituted yttrium iron garnet on a silicon nitride platform for nonreciprocal photonic devices

Sgibnev Y.M.^{*1}, Shelaev A.V.¹, Tananaev P.N.¹, Buzaverov K.A.^{1,2}, Baburin A.S.^{1,2}, Rodionov I.A.^{1,2}, Baryshev A.V.¹

¹ Dukhov Automatics Research Institute (VNIIA), 22, ul. Sushchevskaya, Moscow 127055, Russia

² FMN Laboratory, Bauman Moscow State Technical University, Moscow 105005, Russia

*e-mail: sgibnevem@yandex.ru

Abstract. We propose and experimentally demonstrate a new approach for monolithic integration of bismuth-doped yttrium iron garnet on silicon nitride photonic platforms. The approach combines metal-organic decomposition garnet deposition with localized laser-induced crystallization and selective chemical etching of the amorphous oxide layer. Experimental results confirm that degradation performance of Si₃N₄ waveguide structures does not occur, paving the way for fabrication of efficient nonreciprocal photonic devices.

1. Introduction

Bismuth-substituted yttrium iron garnet (Bi:YIG) is a highly versatile magneto-optical material widely employed in photonic applications. High-temperature annealing and need in a seeding undoped YIG layer are significant challenges for fabricating high-performance nonreciprocal photonic devices, including on-chip components and magneto-photonic crystals. [1]

In this work, we propose a novel approach for monolithic integration of Bi:YIG on Si₃N₄ waveguide platform. The approach is based on deposition of an amorphous oxide layer via MOD technique followed by local laser-induced crystallization of Bi:YIG and selective chemical etching of unirradiated oxide layer.

2. Experiment

Yttrium iron garnet with the composition Y_{2.5}Bi_{0.5}Fe₅O₁₂ was deposited on Si wafer with Si₃N₄ waveguide structures [2] via the MOD technique as described in details in [3]. Continuous-wave laser irradiation ($\lambda=405$ nm) was focused by an objective (10 \times , NA = 0.25) onto the sample placed on an XYZ piezo stage for garnet crystallization. [4] The fabricated samples were characterized by Raman spectroscopy, atomic force microscopy (AFM), scanning electron microscopy, and optical spectroscopy.

3. Results and discussions

To realize on-chip magneto-optical isolators, Bi:YIG must be crystallized either laterally (for TE mode) or on top (for TM mode) of a waveguide. Due to the similar refractive indices of the garnet and Si₃N₄, Bi:YIG layer must be significantly thinner than the waveguide to prevent light leakage into the Bi:YIG. Simulations in COMSOL Multiphysics revealed that for 220 nm-thick Si₃N₄ waveguides, the Bi:YIG thickness must be below 130 nm to maintain optical confinement. Initial experiments yielded a Bi:YIG laser-crystallized thickness of 180 nm, which led to attenuation light in waveguide resonators. AFM images of the side- and top-crystallized Bi:YIG are shown in Fig. 1. On the other hand, measurements of resonators without the garnet showed that the Bi:YIG deposition process and subsequent chemical etching of the oxide layer in nitric acid did not cause any degradation in

performance of the Si₃N₄ resonators. Current efforts include waveguide structure fabrication and garnet deposition process optimization to improve control of garnet film thickness.

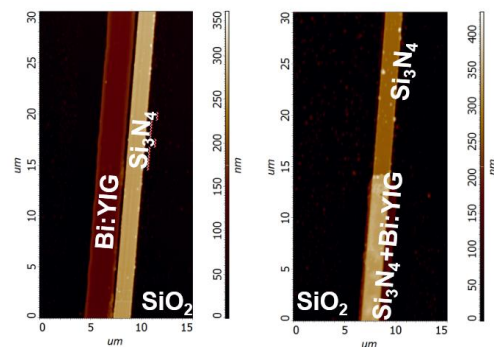


Fig. 1. AFM images of the Bi:YIG crystallized from the side and on the top of a Si₃N₄ waveguide.

4. Conclusions

The proposed approach based on MOD-deposited Bi:YIG and laser-induced crystallization followed by selective chemical etching enables monolithic integration of the garnet on silicon nitride waveguide platform. This paves the way for fabricating high-efficient on-chip magneto-optical isolators and circulators without high-temperature annealing.

Acknowledgments

Si₃N₄ waveguide samples were fabricated and studied at the BMSTU Nanofabrication Facility (FMN Laboratory, FMNS REC, ID 74300).

References

- [1] K. Srinivasan, B.J.H. Stadler. Optical Materials Express **12**(2022)697.
- [2] K. A. Buzaverov, A. S. Baburin, E. V. Sergeev, S. S. Avdeev, E. S. Lotkov, S. V. Bukatin, I. A. Stepanov, A. B. Kramarenko, A. S. Amiraslanov, D. V. Kushnev, I. A. Ryzhikov, I. A. Rodionov. Laser & Photonics Reviews **18**(2024)2400508.
- [3] P. Tananaev, A. Shelaev, Y. Sgibnev, D. Kulikova, S. Efremova, A. Voennov, A. Baryshev. Ceramics International **49**(2023)38921.
- [4] A. Shelaev, Y. Sgibnev, P. Tananaev, A. Baryshev. Optics & Lasers Technology **155**(2022)108411.

Tuning the optical properties of bound states in the continuum in photonic crystal slabs with embedded Ge nanoislands by symmetry reduction

Yurasov D.V.^{*1}, Dyakov S.A.², Smagin I.A.³, Tikhodeev S.G.³, Gippius N.A.², Stepikhova M.V.¹, Peretokin A.V.¹, Shaleev M.V.¹, Smagina Zh.V.⁴, Utkin D.E.⁴ and Novikov A.V.¹

¹ Institute for Physics of Microstructures RAS, GSP-105, Nizhny Novgorod, 603950, Russia

² Skolkovo Institute of Science and Technology, Bolshoy Boulevard 30, str. 1, Moscow 143025, Russia

³ Lomonosov Moscow State University, Moscow 119991, Russia

⁴ Institute of Semiconductor Physics of SB RAS, 13 pr. Lavrentieva, Novosibirsk 630090, Russia

*e-mail: Inquisitor@ipmr.ru

Abstract. Bound states in the continuum (BIC) have attracted a lot of attention in all-dielectric nanophotonics due to their ability to provide spectral features with a very high Q-factor. An ideal BIC cannot be observed in the far field because of the symmetry mismatch with the free space modes and so it has infinitely large Q-factor. However, in real structures BICs transform into quasi-BICs with non-infinite but very high Q-factor which could be detected. In this work, using the photonic crystal (PhC) slabs with embedded Ge nanoislands as a light source, we have shown the ability to control their light emission features by symmetry breaking. It was demonstrated that it provides independent tool to alter the spectral position of PhC modes, their dispersion, and degeneracy and so it offers additional way to manage the light emission of active media in PhC slabs.

1. Introduction

Nowadays, all-dielectric microstructures draw enormous attention in photonics due to their low material losses and also thanks to the advancements of modern fabrication technologies. Photonic crystals (PhCs) are among the most intensively studied kinds of such structures because their manufacturing is rather well-developed and they provide a number of possibilities for light management and control. Moreover, they could support special interesting states - bound states in the continuum (BIC) - whose symmetry prohibits their coupling to propagating modes in free space. If symmetry is slightly reduced such restriction is softened resulting in the appearance of high Q-factor spectral features related to BICs in the system optical response. In this work we utilize the idea of a controllable symmetry reduction of the PhC slab in order to modify its modal structure and, consequently, its optical properties.

2. Experiment

Samples under investigation were PhC slabs fabricated on samples with Ge nanoislands grown by molecular beam epitaxy on a silicon-on-insulator substrate. The grown structure consisted of 5 layers of Ge islands separated by Si interlayers and capped by top Si layer. The PhCs were created using the e-beam lithography followed by the dry etching. The air holes were etched down to the SiO₂ layer. Optical properties of the fabricated samples were studied using the micro-PL spectroscopy at 300K. Excitation was carried out using the laser ($\lambda=532$ nm) and 10x objective (NA=0.26). The PL response was collected using the same objective and detected by the Bruker FTIR spectrometer with a cooled Ge detector. The details of the fabrication and measurements can be found in [1]. The geometric parameters of the fabricated PhCs were evaluated using scanning electron microscopy (SEM).

3. Results and discussions

In this work we realize a reduction in the symmetry of the PhC lattice in two ways – the 1-st one was tilting one of the basis vectors of a PhC unit cell while the 2-nd one was reshaping the circular holes into ellipses. These changes could be characterized by the angle α between the lattice's basis vectors and the ratio of the ellipse's vertical-to-horizontal radii (r_y to r_x ratio). The schematic of these modifications is illustrated in Fig. 1a and the corresponding SEM images of fabricated samples with lattice modifications along with the initial highly symmetric reference sample are shown in Figs.1b-d.

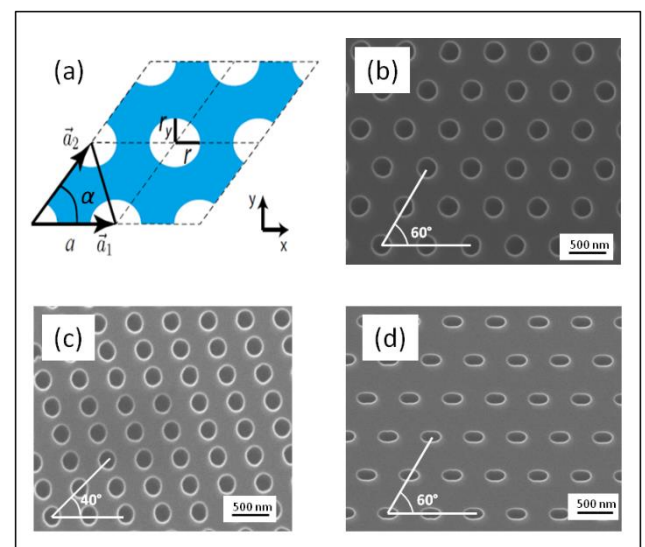


Fig. 1. (a) – schematic of PhC unit cell. SEM images of fabricated PhCs with symmetrical (b), distorted (c) and symmetrical, but with elliptical holes (d) lattices.

In order to demonstrate the influence of symmetry breaking by tilting one of the basis vectors of PhC unit cell (changing the angle α , see Fig. 1c) we calculate the photon energy and in-plane wavevector dependencies of the emissivity of point sources, gradually decreasing the angle

α from 60° to 35° (Fig. 2a). One can see that with the decrease in the parameter α , the number of BIC modes in the Γ -point is reduced, while the degeneracy for all doublet modes is lifted. These changes occur due to the symmetry reduction from a highly symmetric C_{6v} to the less symmetric C_2 point group. In addition to the above-mentioned changes in the modal structure, the number of modes that fall within the Ge nanoisland PL spectral range is reduced, and for $\alpha=35^\circ$ the only one mode remains in this energy range (Fig. 2b). This mode, however, exhibits a relatively strong dispersion, which results in a moderate Q-factor for this peak ($Q \sim 1000$ in this case, the PL collection angle was taken to be 3° during this estimation). Additionally, this peak displays an asymmetrical profile due to the shape of the dispersion curve.

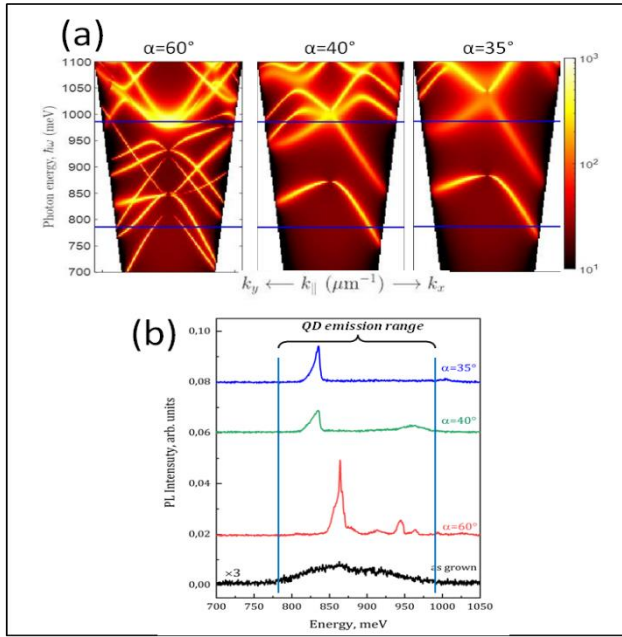


Fig. 2. (a) – band structure modification caused by varying the angle α . (b) – corresponding PL spectra at 300K.

Consider the other type of PhC unit cell modification where the shape of air holes was gradually transformed from circular to elliptical but the PhC unit cell was undisturbed. Such a change is characterized by the decrease of r_y value keeping the r_x value fixed and equal to $0.2a$ (a is the PhC period) (see Fig. 1d). One can see that seemingly similar symmetry reduction from C_{6v} to C_2 nevertheless lead to different results. In contrast to the previous case of deformed lattice, in the case of elliptical holes, several modes are seen in PL spectra, and no “single-mode emission” is observed (Fig. 3). One can also notice that for the value of $r_y=0.14$ the peak PL enhancement is 2–5 times higher than for the other r_y values. This could be used for the fine-tuning of the PhC parameters in order to maximize the optical response of the PhC. The measured Q-factor in the case of a PhC slab with elliptical holes was ~ 1750 , which is higher than in the case of a deformed PhC lattice due to the flatter dispersion curve.

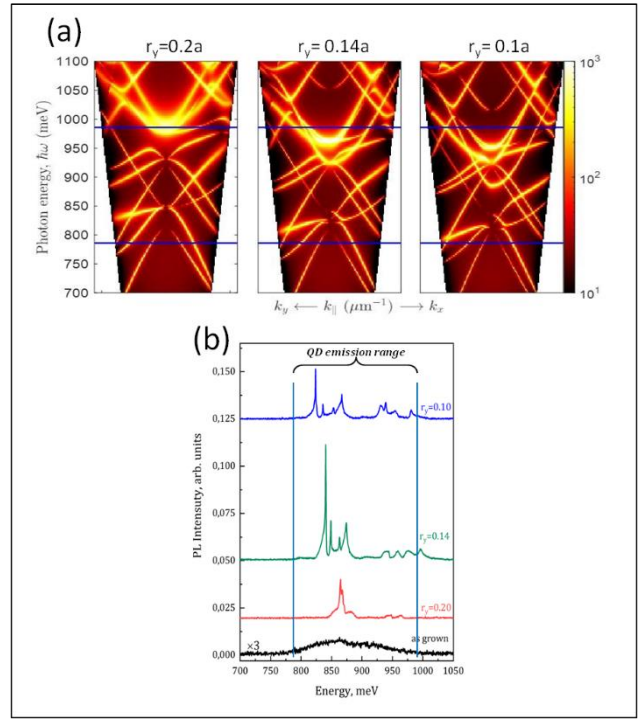


Fig. 3. (a) – band structure modification caused by transforming the circular holes to elliptical. (b) – corresponding PL spectra at 300K.

4. Conclusions

To conclude, we have studied the influence of the controllable symmetry breaking with various types and strengths of asymmetry of a PhC slab on its light-emitting properties. We have shown that by reducing the symmetry of the PhC lattice by changing its basis vectors, it is possible to spectrally isolate one of the modes within the desired energy range, resulting in the “single-mode” emission. We have also changed the symmetry by making the PhC holes elliptical. Such a type of symmetry reduction preserved the number of modes involved in the emission process but allowed us to break the degeneracy of doublet modes, resulted in the energy splitting of the initially degenerate modes. Therefore, controllable symmetry reduction is a powerful tool to alter the PhC features that could be used also in combination with other approaches to alter the systems optical properties.

Acknowledgements

This work was supported by Russian Science Foundation (grant #25-12-00367).

References

- [1] D.V. Yurasov *et.al.*, Appl. Phys. Lett. **125** (2024) 021105.

Observation of bound states in the continuum of different types in the luminescence response of silicon photonic crystal slabs with Ge(Si) nanoislands

Peretokin A.V.^{*1}, Stepikhova M.V.¹, Dyakov S.A.², Yurasov D.V.¹, Shaleev M.V.¹, Shengurov D.V.¹, Smagina Zh.V.³, Rodyakina E.E.^{3,4}, Novikov A.V.¹

¹ Institute of Physics of Microstructures RAS, st. Akademicheskaya, 7, Afonino, Kstovsky district, Nizhny Novgorod region 603087, Russia

² Skolkovo Institute of Science and Technology, st. Nobelya, 3, Moscow 121205, Russia

³ Institute of Semiconductor Physics of SB RAS, 13 pr. Lavrentieva, Novosibirsk 630090, Russia

⁴ Novosibirsk State University, 1 Pirogova St., Novosibirsk 630090, Russia

*e-mail: aperetokin@ipmras.ru

Abstract. In this work, we demonstrate the possibility to observe bound states in the continuum (BIC) in two-dimensional photonic crystal slabs (PCS) formed on Si structures with Ge(Si) nanoislands. To observe the BICs, an original method of the micro-photoluminescence measurements with angular resolution was applied. This method allowed us to distinguish different types of BICs, both localized at the Γ -point of the first Brillouin zone (symmetry-protected BICs) and beyond it (accidental BICs). The conditions for the formation of BICs are analyzed taking into account the symmetry and polarization of the modes arising in the photonic crystal slabs studied. The use of high-Q bound states in the continuum opens up new possibilities for the implementation of efficient radiation sources, including those integrated into silicon photonic circuits.

1. Introduction

To date, the problem of creating efficient silicon-based sources for the near-infrared range remains unsolved. A possible key to solving this problem is photonic crystal slabs (PCS) with Ge(Si) nanoislands. In such structures, efficient luminescence is observed in the wavelength range of 1.2-1.6 μm at room temperature [1]. The introduction of Ge(Si) nanoislands into PCSs makes it possible to enhance their luminescent response by more than two orders of magnitude due to the interaction with distinct photonic modes [2].

The most interesting feature of PCSs is the presence of bound states in the continuum (BIC) in them. BICs can be divided into two main types: i) localized at the Γ point of the Brillouin zone (also known as symmetry-protected BICs – SP-BICs), and ii) localized outside the Γ -point of the Brillouin zone (also known as the off- Γ BICs, accidental (A-BICs), parametric, or Friedrich-Wintgen (FW) BICs). Both types of these states are interesting from an applied point of view [3], in particular for the creation of lasers [4], compact unidirectional light sources [5], etc.

In this work, we experimentally demonstrate the possibility to observe BICs in two-dimensional photonic crystal slabs with Ge(Si) nanoislands. For these purposes, an original method for measuring micro-photoluminescence (micro-PL) with angular resolution is proposed. The method allows us to study bound states in the continuum in the PCSs both at the Γ point of the Brillouin zone and beyond it. The measurement results are discussed together with the data of theoretical calculations. In the work, the emissivity of PCSs, as well as electromagnetic fields and polarization characteristics of the modes participating in their luminescent response, are calculated. The data obtained are analyzed in the context of the features and conditions for BIC's formation.

2. Samples and methods

Photonic crystal slabs under study were formed on a structure with Ge(Si) nanoislands grown by molecular beam epitaxy. The structure was grown on an SOI substrate with 70 nm top Si layer and 2 μm buried SiO_2 layer, and contained a buffer Si layer, 5 layers of Ge(Si) nanoislands separated by 17 nm thick Si layers, and a 135 nm thick Si cap layer. The total thickness of the structure above the buried SiO_2 layer was 335 nm.

Electron beam lithography and plasma-chemical etching techniques were used to form photonic crystal slabs with a hexagonal lattice of holes. For the studies, two PCSs with the following parameters were selected: lattice period $a=575$ nm, ratio of the hole radius to the lattice period $r/a=0.25$, hole etching depth $h=135$ nm - parameters of PCS-1; and lattice period $a=550$ nm, $r/a=0.2$, $h=250$ nm – parameters of PCS-2. In more detail, the conditions for the growth of a structure with Ge(Si) nanoislands and the formation of photonic crystals are described in [6].

In the experiment, we used an original technique for micro-PL measurements with angular resolution. This method is based on the standard micro-PL technique. To provide angular resolution, we used a diaphragm placed in a parallel beam formed by the objective. In this case, changing the diaphragm diameter is equivalent to changing the PL signal collection angle. By using sufficiently small collection angles, the diaphragm can be moved in a parallel beam relative to the main symmetry axes of PCS. The displacement of the diaphragm corresponds to a change in the signal detection angle, and therefore the wave vector. Using the set of spectra obtained in this way, it is possible to construct the dispersion characteristics of the studied PCS and compare them with those obtained numerically (see Figs. 1 and 2).

The dispersion characteristics of the PCS emissivity (PhC's band structure) were numerically modelled by means of the Fourier modal method in the scattering matrix form [7].

3. Results and discussions

It can be shown that in PCS with a hexagonal lattice there are 8 fundamental modes at the Γ -point of the Brillouin zone, 6 of which should be characterized by the presence of BIC [2]. Fig. 1 shows the band structure of the studied PCS-1. The red circles in the Figure denote the modes for which SP-BICs were observed. These are modes A_2, B_1, B_2 and E_2 (mode A_1 is located higher in energy and is not shown in this band structure). The BICs arising in these modes at the Γ point are caused by the mismatch of their symmetry with the symmetry of the modes in free space. In the luminescence spectra, such BICs appear as narrow, high-Q, intense lines [2,6]. They are present in all spectra measured in the conventional micro-PL schema and become more pronounced in angular-resolved micro-PL measurements, when the small-aperture diaphragm is located exactly in the center of the parallel beam formed by the objective, i.e. at the Γ point of the Brillouin zone. The intensity of these lines can be more than two orders of magnitude higher than the intensity of PL signal measured in the original, unprocessed structure.

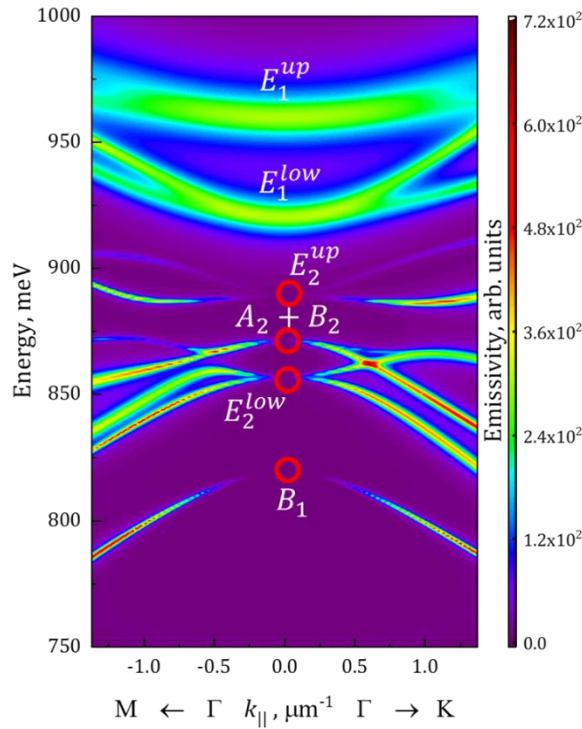


Fig. 1. Band structure of the PCS-1. The color in the figure shows the emissivity of PCS-1 in the far field, the letters indicate the designations of modes according to the irreducible representations of the group theory, the red circles mark the SP-BICs observed at the Γ -point of the Brillouin zone.

In the case of PCSs with a small etching depth, a larger number of lines can be observed in their luminescence spectra compared to the number of modes localized at the Γ -point of the Brillouin zone. This is explained by the fact that at small etching depths the modes are located closer to each other, and their dispersion branches cross and interact more strongly with each other (see Fig. 2). Mode anti-crossings can also cause BICs, but in this case the BICs are located far from the Γ -point (red circles in Fig. 2). They can also appear in the luminescence spectra as narrow, intense lines.

BICs that arise at the anti-crossing of modes are referred to as the so-called Friedrich-Wintgen BICs. In this report

we will take a closer look at the conditions of their formation and observation. The relationship between the symmetry of modes beyond the Γ -point of the Brillouin zone and their polarization will also be shown.

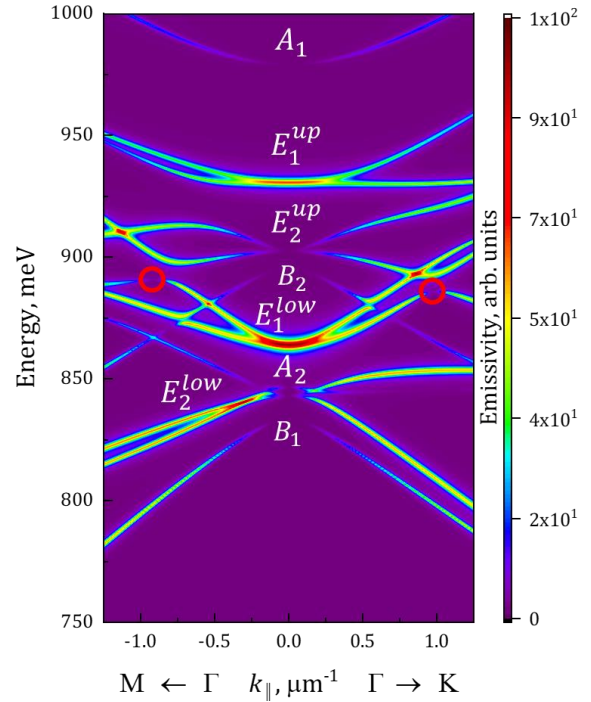


Fig. 2. Band structure of the PCS-2., the color reflects the far field emissivity. The designations in the figure are similar to those in Figure 1.

4. Conclusions

In this work, we show the possibility to observe bound states in the continuum of various types in the luminescent response of PCS. The conditions for the formation of BICs located both at the Γ -point of the Brillouin zone and outside it are considered. These states are of interest for realization effective radiation sources, including those on silicon.

Acknowledgements

The work was funded by the Russian Science Foundation (grant # 25-12-00367).

References

- [1] V. Aleshkin, N. Bekin, N. Kalugin, Z. Krasilnik, A. Novikov, V. Postnikov, H. Seyringer. JETP Letters **67**(1998)48.
- [2] S. Dyakov, M. Stepikhova A. Bogdanov, A. Novikov, D. Yurasov, M. Shaleev, Z. Krasilnik, S. Tikhodeev, N. Gippius Laser & Photonics Reviews **15**(2021)2000242.
- [3] M. Kang, T. Liu, C.T. Chan M. Xiao. Nature Reviews Physics **5**(2023)659.
- [4] A. Kodigala, T. Lepetit, Q. Gu, B. Bahari, Y. Fainman, B. Kanté. Nature **541**(2017)196.
- [5] X. Yin, J. Jin, M. Soljačić, C. Peng, B. Zhen. Nature **580**(2020)467.
- [6] A.V. Peretokin, D.V. Yurasov, M.V. Stepikhova, M.V. Shaleev, A.N. Yablonskiy, D.V. Shengurov, S.A. Dyakov, E.E. Rodyakina, Z.V. Smagina, A.V. Novikov. Nanomaterials **13**(2023)1678.
- [7] S. G. Tikhodeev, A.L. Yablonskii, E.A. Muljarov. N.A. Gippius, T. Ishihara. Phys. Rev. B **66**(2022)045102.

Photoluminescence from functionalized single-walled carbon nanotubes

Maksimov F.M.^{*,1,2}, Goldt A.E.³, Dozmorov S.A.³, Kalachikova P.M.³, Vildanova A.R.³,
Morozov A.V.³, Gladush Yu.G.³, Nasibulin A.G.³, Chernov A.I.^{1,2}

¹ Russian Quantum Center, Skolkovo Innovation City, Moscow, Russia

² Center for Photonics and 2D Materials, Moscow Institute of Physics and Technology, Dolgoprudny, Russia

³ Skolkovo Institute of Science and Technology, Moscow, Russia

*e-mail: maksimov.fm@phystech.edu

Abstract. Single-walled carbon nanotubes (SWCNTs) are promising low-dimensional material which can be used as a basis for a single photon source. The main advantages of such emitters are the possibility of obtaining single photons at room temperature, as well as the possibility of choosing the wavelength of emission in the near infrared range by selecting the chirality of the nanotube, which allows, for example, to tune the emitters to the wavelength of telecom-munication networks 1550 nm [1]. Single photon source is an important component of the element base for the creation of quantum communication and quantum computing devices. Functionalized single-walled carbon nanotubes are one of the solid-state platforms for its creation. This requires developing synthesis methods with the ability to control optical properties [2], functionalizing the nanotubes, protecting them from the external environment [3], and enhancing the single-photon properties with a metasurface. Here, we investigate the effect of SiO₂ protective coating on the optical properties of functionalized single-walled nanotubes. The (6,5) nanotubes were modified with aryl diazonium salt, and demonstrate a PL peak in the 1100-1300 nm region. Which corresponds to the ortho+ geometry of the sp³ defect attachment. The shell strongly changes the local dielectric environment and this is expressed in the appearance of a red-shifted peak, which corresponds to a different geometry of the sp³ defect attachment (ortho++). This approach of SiO₂ protecting coating of nanotubes opens the possibility of their application as a source of single photons at room temperature and at the telecommunication wavelength.

Acknowledgements

This work was supported by the Ministry of Science and Higher Education of the Russian Federation, Agreement 075-15-2024-680.

References

- [1] He X. et al. Tunable room-temperature single-photon emission at telecom wavelengths from sp³ defects in carbon nanotubes //Nature Photonics. – 2017. – T. 11. – №. 9. – C. 577-582.
- [2] Ilatovskii D. A. et al. Photophoretic deposition and separation of aerosol-synthesized single-walled carbon nanotubes //Carbon. – 2024. – T. 218. – C. 118725.
- [3] Dozmorov S. A. et al. Photoluminescence from Pristine and Functionalized SWCNTs Coated by Silica //Surfaces and Interfaces. – 2025. – C. 106674.

Model of orthogonal two-wave mixing in photorefractive crystal of cubic symmetry with optical activity

Bezruk M.N.*, Romashko R.V., Efimov T.A., Storozhenko D.V.

Institute of Automation and Control Processes, 5 Radio St., Vladivostok 690041, Russia

*e-mail: bezmisha@iacp.dvo.ru

Abstract. We presented a physical model describing the process of two-wave vectorial mixing in optically active photorefractive crystal of cubic symmetry for an orthogonal scheme of interaction. Using the model, we calculated the two-wave interaction in a gyrotropic photorefractive crystal of bismuth titanate Bi₁₂SiO₂₀ at wavelength of 633 nm. We have determined conditions at that polarization changes don't affect on result of two-wave mixing. It was found that it is possible to select the parameters of the crystal and interacting waves for the quasi-polarization independence mode, when changes of interferometer output signal caused by polarization instability of the signal wave is reduced to a minimum (no more than 3%).

1. Introduction

The continuous updating of the hologram within the PRC stabilizes the interferometer's operation, preserving its high sensitivity and providing strong immunity to external noise [1-3]. However, similar to traditional interferometers, the sensitivity of adaptive interferometers is affected by the polarization of the light beams. Polarization fluctuations can significantly reduce or even eliminate the signal, highlighting the need for an interferometer design whose output is unaffected by polarization. This paper introduces and investigates a physical model that describes vectorial two-wave mixing in a gyrotropic PRC, specifically in an orthogonal configuration. The model considers how the polarization of the waves changes not only due to the PRC's gyrotropy, but also as a result of the two-wave mixing process itself within the PRC. This model enables a more precise selection of the interacting waves' polarization parameters and the dimensions of the PRC, considering the crystal's material properties and the light's wavelength that can lead to polarization-independent operation of the adaptive interferometer.

2. Model Overview

The developed model builds upon the theory of vector wave interaction in cubic photorefractive crystals for the transmission geometry described by Sturman et al. [4]. Unlike collinear wave interaction, the orthogonal geometry involves signal and reference waves propagating at right angles, resulting in varying polarization states throughout the PRC. To overcome this difficulty, the proposed physical and mathematical model of vectorial two-wave mixing divides the intersection region of the signal wave **As** and the reference wave **Ar** within the PRC into an M x N grid of cells. The signal and reference waves entering the cells of the first layer are defined as follows:

$$\mathbf{As}_{m1}^{\text{in}} = \mathbf{As}/N, \quad \mathbf{Ar}_{1n}^{\text{in}} = \mathbf{Ar}/M \quad (1)$$

Lets consider a cell, denoted as (m, n) where m ranges from 0 to M and n ranges from 0 to N (as illustrated in Fig. 1). The amplitudes of the interacting waves entering this cell are equivalent to the amplitudes of the waves exiting the preceding cell:

$$\mathbf{As}_{mn}^{\text{in}} = \mathbf{As}_{m-1,n}^{\text{out}}, \quad \mathbf{Ar}_{mn}^{\text{in}} = \mathbf{Ar}_{m,n-1}^{\text{out}}. \quad (2)$$

Within each cell, a calculation of two-wave vector mixing is performed. The polarization states of the **As** and

Ar waves are altered both by the crystal's optical gyrotropy and by the vectorial interaction itself. Subsequently, the **As** and **Ar** waves propagate to the next cells, (m+1, n) and (m, n+1) respectively, where this process is repeated. Since the measured information is encoded in the phase modulation φ of the signal wave **As**, its amplitude is represented as $\mathbf{As} \cdot e^{i\varphi}$. Following the two-wave mixing process, the amplitude of the signal wave at the output of cell (m, n) is given by [4]:

$$\mathbf{As}_{mn}^{\text{out}}(\varphi) = (\hat{\mathbf{T}}_+(y) \mathbf{As}_{m-1,n}^{\text{out}} e^{i\varphi} + e^{\pm i\varphi_0} \hat{\mathbf{T}}_-(y) \mathbf{Ar}_{m,n-1}^{\text{out}}) e^{-\alpha \Delta L/2}, \quad (3)$$

where y represents the propagation direction of the signal wave **As**, ΔL is the cell size, and α denotes the optical absorption coefficient of the PRC. The terms $\hat{\mathbf{T}}_+$ and $\hat{\mathbf{T}}_-$ are transformation matrices that account for the diffraction of wave **As** in the direction of **As** (zero-order diffraction) and the diffraction of reference wave **Ar** in the direction of **As**, respectively. The interferometer's output signal S is defined as the change in the intensities of the signal wave **As** at the exit of the "final cell layer" (where $m = M$), summed along the N direction:

$$S = \sum_{n=1}^N \mathbf{As}_{Mn}^{\text{out}}(\varphi)^2 - \mathbf{As}_{Mn}^{\text{out}2} \quad (4)$$

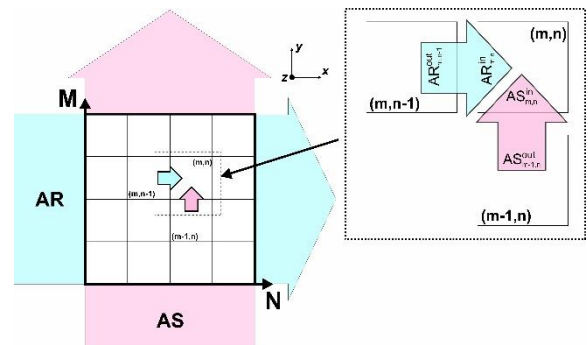


Fig. 1. Scheme of propagation of signal and reference waves in a photorefractive crystal.

3. Results and discussions

A physical and mathematical model was investigated using a gyrotropic photorefractive crystal of bismuth silicate B₁₂SiO₂₀ (BSO) of cubic symmetry. Numerical simulations were performed to study vectorial two-wave mixing within the PRC at a wavelength of 633 nm (rotation of polarization is 220 deg/cm). A linearly polarized signal wave **As** and an elliptically polarized reference wave **Ar**

were used at the input of the PRC. The developed model allowed for the investigation of the polarization independence of the BSO crystal. Fig. 2 presents experimental data demonstrating the dependence of the interferometer output signal on the azimuthal angle γ of the signal wave **As** for BSO crystal of varying thicknesses (from 1 to 30 mm).

During the simulation, the reference wave had circular polarization. The results show that for crystal thicknesses L_p the influence of the polarization of the signal wave **As** on the output signal is minimized. Thus, L_p values correspond to 8.7 mm, 17.4 mm, 26 mm, and so on (multiples of 8.7 mm). At these points, the variations in the output signal are, on average, only 3% of the maximum possible. Thus, a regime close to polarization independence (PI-mode) is achieved at a crystal thickness of L_p . However, complete polarization independence, where the output signal does not depend on the parameters of the interacting waves and the crystal, cannot be attained, which is likely due to the nonlinear nature of light interaction within the PRC.

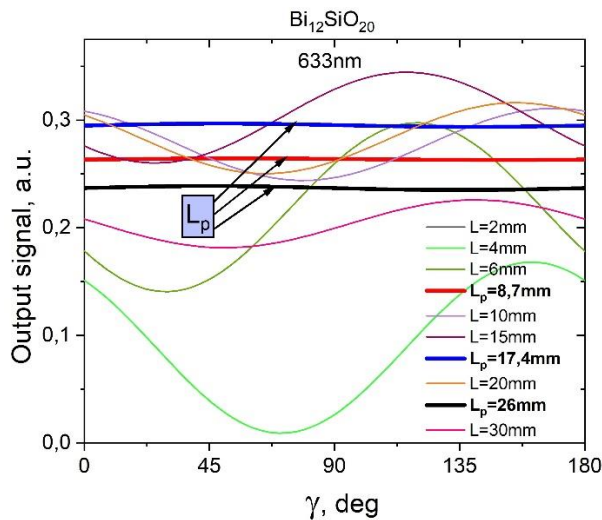


Fig. 2. Dependences of the output signal on the azimuthal angle of the signal wave, obtained for the BSO crystal at wavelength $\lambda = 633$ nm.

Fig. 3 illustrates the dependences of the interferometer output signal on the size of PRC BSO, at various angles γ of the signal wave **As**. The maximum and minimum achievable signal levels are indicated by red and blue lines, respectively. The plot reveals that increasing the PRC's size leads to an increase in both the minimum and maximum signal. The output signal peaks when the crystal length is $L_{opt} = 13$ mm, achieved with a linearly polarized signal wave **As** oriented at $\gamma = 140^\circ$. At crystal lengths of $L_p = 8.7$ mm and 17.4 mm, the difference ΔS between the maximum and minimum possible output signals is minimized, representing only 3% of the maximum possible signal. This implies that regardless of the input polarization state of the signal wave **As**, the output signal will only vary within this narrow range.

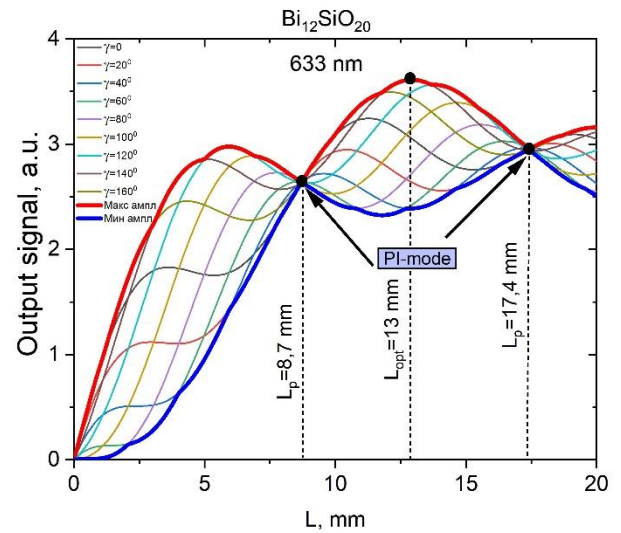


Fig. 3. Dependences of the interferometer output signal on the crystal length, obtained at different azimuthal angles of the signal wave $\lambda = 633$ nm.

4. Conclusions

This paper introduces a physical model to describe vectorial two-wave mixing in optically active photorefractive crystals with cubic symmetry, specifically within an orthogonal interferometer setup. Using this model, two-wave interaction in a gyrotropic bismuth titanate ($\text{Bi}_{12}\text{SiO}_{20}$) photorefractive crystal at a wavelength of 633 nm was simulated. Our simulations indicate that complete polarization independence is not attainable. However, by selecting crystal and wave parameters, signal variations due to polarization instability of the signal wave can be minimized to less than 3%. It was discovered that quasi-polarization independence mode occurring at a photorefractive crystal length of 8.7 mm for a 633 nm wavelength. Furthermore, it was identified optimal parameters for the photorefractive crystal and interacting waves that maximize the efficiency of two-wave mixing, finding a crystal length of 13 mm to be optimal at 633 nm.

Acknowledgements

The study was supported by the Russian Science Foundation (project No. 24-22-00413).

References

- [1] S.I. Stepanov. In International Trends in Optics, Chap. 9. (New York: Academic, 1991).
- [2] A. Kamshilin, R. Romashko, Y. Kulchin. J. Appl. Phys. 105(2009)031101.
- [3] L. Solymar, D. Webb, A. Grunnet-Jepsen. The Physics and Applications of Photorefractive Materials (Oxford: Clarendon Press, 1996).
- [4] B. Sturman, E. Podivilov, K. Ringhofer, E. Shamonina, V. Kamenov, E. Nippolainen, V. Prokofiev, A. Kamshilin, Phys. Rev. E., 60(1999)3332.

Comparison of phase-shifting properties of MoSiON and TaSiON layers formed by magnetron sputtering

Gromov V.D.^{*1}, Lebedev E.A.¹, Volkov R.L.¹, Borgardt N.I.¹, Anikin A.V.¹, Komlenok M.S.², Kurochitskiy N.D.², Pavlikov A.V.³, Gromov D.G.¹

¹ National Research University of Electronic Technology (MIET), Moscow, Russia

² Prokhorov General Physics Institute of the Russian Academy of Sciences, 38 Vavilova St., Moscow 119991, Russia

³ Faculty of Physics, Moscow State University, Moscow, Leninskie gory, 1, bld. 2, 119991 Russia

*e-mail: grovla2002@mail.ru

Abstract. Diffraction effects that occur when topological elements of integrated circuits are reduced to nanometer sizes negatively affect the resolution during the lithography process. To overcome these effects, phase-shifting layers are used in photomasks. The properties of Mo-Si-O-N and Ta-Si-O-N phase-shifting layers formed by reactive magnetron sputtering of Si and Mo or Ta targets in a nitrogen-containing environment were investigated. The change in the layer composition parameters depending on the partial pressure of nitrogen in the sputtering environment was studied. For the selected compositions and thicknesses of the Mo-Si-O-N and Ta-Si-O-N layers, the optical characteristics were measured: transmission, refractive index, extinction coefficient and phase shift of the electromagnetic wave. These layers were exposed to different doses of deep ultraviolet radiation from a KrF excimer laser with a wavelength of 248 nm. It has been demonstrated that both materials show insignificant change in their optical properties in the dose range from 0 to 2.5 kJ/cm², which makes them suitable for use in the photomask production. During irradiation degradation of optical properties caused by partial oxidation of the layers begins. For the obtained optical characteristics of the Mo-Si-O-N and Ta-Si-O-N layers, modeling photomask diffraction pattern with a set of 120-nm-wide stripes and slits for a wavelength of 248 nm was simulated, which showed the possibility of obtaining a high (close to 1) optical contrast.

1. Introduction

One of the methods for increasing resolution in photolithography is the use of phase-shifting photomasks. In addition to the standard absorbing chromium layer, such photomasks contain a phase-shifting layer, which allows not only to modulate the amplitude of the working radiation, but also to change its phase. This contributes to a significant increase in resolution and focus depth in projection photolithography in comparison to binary photomasks. Such photomasks are called halftone phase-shifting photomasks or Embedded Attenuated Phase-Shift Masks (EAPSM).

The main requirement for the photomask phase-shifting layer is a 180° phase shift of the light wave when passing through it, which is determined by the optical properties of the material and its thickness. Among the optical properties of the material, transmission is also an important parameter.

In this work, MoSiON and TaSiON materials were studied for comparison as phase-shifting layers. A comparison of the optical characteristics of these materials was made for a radiation wavelength of 248 nm. In particular, the change in optical characteristics was investigated under the effect of deep ultraviolet radiation at different exposure doses.

2. Experiment

To deposit the thin films, two magnetron systems were used with Si and Mo or Ta targets, the sputtering of which was carried out in a mixture of inert Ar and N₂ reactive gases with varying the partial pressure of the latter. Both Si and Mo (or Ta) targets were sputtered simultaneously depending on the material being produced. The source of oxygen in the layers was the residual atmosphere in the vacuum chamber.

Quartz glass with a thickness of 6.35 mm and overall dimensions of 15×20 mm was used as a substrate for studying optical properties. Preliminary the substrates were washed in an ultrasonic bath with acetone and then in

Caro's solution. After this, the substrates were thoroughly washed in deionized water and dried in isopropyl alcohol vapor.

Titanium foil was used as a substrate for measuring the elemental composition. The choice of titanium foil is explained by the fact that titanium is not included in the composition of the film, which allows for an accurate assessment of the composition of the film. The titanium foil was pre-washed in acetone in an ultrasonic bath, and to remove the natural oxide layer, it was etched in a solution of HF:HNO₃:H₂O = 1:2:6. After this, the substrates were thoroughly washed in deionized water and dried in isopropyl alcohol vapor.

Silicon with partially covered areas of chemically resistant varnish was used as a substrate for studying the layer thickness and, consequently, the deposition rate. The varnish was removed after the film was applied.

Thickness control was performed using an atomic force microscope. The composition was controlled using X-ray energy-dispersive spectroscopy, and the composition distribution across the layer thickness was determined using a transmission electron microscope. Optical characteristics were investigated using a spectroscopic ellipsometer.

3. Results and discussions

Detailed studies of the composition, thickness and distribution of elements across the thickness of the films were performed using transmission electron microscopy. TEM examination of the cross-section of the samples showed that the original Mo-Si-O-N and Ta-Si-O-N films do not contain any crystalline inclusions and are completely amorphous. Cross-section mapping of the elements using energy-dispersive X-ray microanalysis showed their uniform distribution (Fig. 1). As can be seen, it was possible to obtain thin films based on Mo-Si-O-N and Ta-Si-O-N that are quite close in composition and thickness,

which makes it possible to compare them with each other in terms of optical properties.

The formed phase-shifting layers Mo-Si-O-N and Ta-Si-O-N were exposed to different doses of deep ultraviolet (DUV) radiation from a KrF excimer laser with a wavelength of 248 nm. As a result, the dependences of optical properties, in particular transparency and phase shift on the composition and film thickness and their changes under the influence of different doses of excimer laser radiation were obtained.

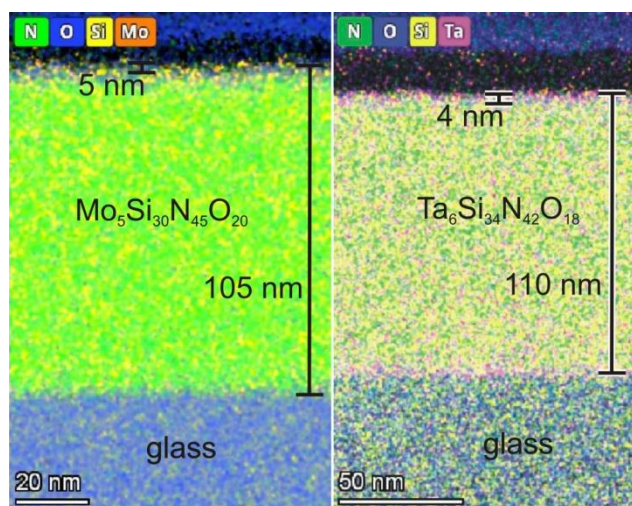


Fig. 1. Maps of element distribution on the cross section of Mo-Si-O-N and Ta-Si-O-N thin films.

It was found that both materials slightly change their optical properties in the range of radiation doses from 0 to 2.5 kJ/cm², which is demonstrated in Fig. 2 using the example of a phase shift change. This makes them suitable for use in the production of photomasks.

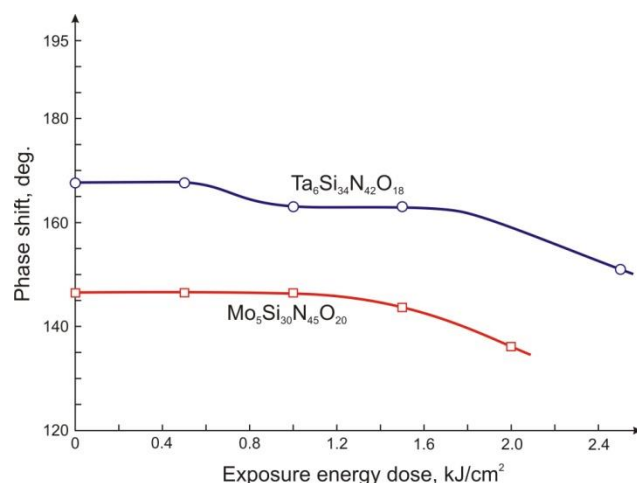


Fig. 2. Change in the phase shift of radiation when passing through layers based on Mo-Si-O-N and Ta-Si-O-N during the accumulation of the energy dose of radiation from a KrF excimer laser with a wavelength of 248 nm.

It was found that the change in optical properties is caused by partial surface oxidation of the layers. A simulation of the diffraction pattern was carried out when radiation with a wavelength of 248 nm passed through a photomask with a set of stripes of these materials, showing that when using the obtained phase-shifting materials based on Mo-Si and Ta-Si, it is possible to obtain a high (close to

1) optical contrast for the width of the stripes and gaps between them of 120 nm.

4. Conclusions

Overall, based on the results of the study, it can be concluded that photomasks based on both MoSiON and TaSiON layers allow, when using a radiation wavelength of 248 nm and an off-axis source, to obtain images with a resolution of 120 nm with high optical contrast. Although radiation with a wavelength of 248 nm affects the optical characteristics of the materials under consideration, these changes are not critical, i.e. they do not have a noticeable effect on the optical contrast of the diffraction pattern. At the same time, the Ta-Si-O-N film demonstrates characteristics that are somewhat superior to Mo-Si-O-N for use in photomasks.

Acknowledgements

The work was carried out within the framework of the state assignment (Agreement FSMR-2025-0006).

References

- [1] K. Oyoshi, D. Lenssen, R. Carrius, S. Mantl. *Thin Solid Films* **381**(2001)194.
- [2] T. Suemasu, T. Fujii, K. Takakura, F. Hasegawa. *Thin Solid Films* **381**(2001)209.
- [3] R. Bayazitov, R. Batalov, R. Nurutdinov, V. Shustov, P. Gaiduk, I. Dezs, E. Kotai. *Nucl. Instr. Meth. B* **24**(2005)224.
- [4] K. Oyoshi, D. Lenssen, R. Carrius, S. Mantl. *Thin Solid Films* **381**(2001)202.
- [5] J. Chrost, J. J. Hinarejos, E. G. Michel, R. Miranda. *Surf. Sci.* **330**(1995)34.

Effect of different gas media, temperature and UV-visible irradiation on the volt-ampere characteristics of TiO₂ nanopowder layer

Kruzhalina M.D.^{*}, Sorokina L.I., Yakubov A.O., Fedyanina M.E., Dubkov S.V., Gromov D.G.

National Research University of Electronic Technology – MIET, Bld. 1, Shokin Square, Zelenograd, Moscow, 124498 Russia

^{*}e-mail: kruzhalina43@gmail.com

Abstract. Nanopowder oxide semiconductors such as TiO₂ in 0d-, 1d-, and 2d- configurations are widely used in microelectronics, including sensors, optoelectronics, and photovoltaics. However, there is a problem related to the stability of TiO₂: its electrophysical properties change significantly under the influence of a gaseous medium, light and temperature, which requires taking these factors into account in its practical application. For effective operation of TiO₂-based microelectronic devices, it is important to understand the mechanisms occurring on its surface and the influence of external factors on electrophysical characteristics. In this paper, the complex effect of the gaseous atmosphere, temperature, and irradiation on the properties of TiO₂ nanopowder layers is investigated. The temperature dependences of the electrophysical parameters of TiO₂ in oxidizing and reducing gases under periodic UV-visible irradiation and without it are shown. The presented results allow us to better understand the mechanisms of changing the properties of TiO₂ and optimize its use in functional devices.

1. Introduction

TiO₂ is well known as an n-type semiconductor material with advantages such as non-toxicity, high stability, and electronic transport, which makes it an attractive candidate for widespread use in chemical sensors, including gas, photocatalysts, lithium batteries, solar cells, and photodetectors [1]. Various factors can affect the stable operation of any device using TiO₂ as an active material. It is known that the TiO₂ resistance is affected by the interaction of gas in the atmosphere with chemisorbed oxygen on the semiconductor surface [2]. In addition to the effect of adsorbed gas molecules, water vapor also affects the electrical conductivity by changing the number of oxygen atoms on the surface involved in the capture of molecules of the gas under study. The influence of humidity can be reduced by increasing the operating temperature; however, this may contribute to the reproducibility of properties [3]. UV-irradiation activates the generation of electron-hole pairs, where holes participate with chemisorbed oxygen, which will cause oxygen desorption from the semiconductor surface. Because of this, there is an excess of electrons in the conduction band, which will increase the conductivity [4]. Therefore, the aim of this work is to combine factors such as gas adsorption, temperature, and UV-visible irradiation to better understand their effect on the electrical conductivity of TiO₂.

2. Experiment

A series of samples was produced according to the following procedure. First, a 100 nm thick Ti layer was formed on a 2×2 cm silicon substrate by magnetron sputtering. The formation of a TiO₂ P25 nanopowder layer was carried out by electrophoretic deposition (EPO) for 3 minutes in a potentiostatic mode, the area of the deposited layer was 2.25 cm². Gold contact pads were formed through a mask on top of the deposited layer by vacuum-thermal evaporation. In this way, two gold electrodes with a size of 1.5×1.5 mm and a thickness of 100 nm were obtained, the distance between which was 2.5 mm (Fig. 1).

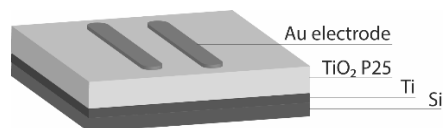


Fig. 1. Schematic image of sample.

To eliminate the influence of the conductive substrate layer, the formed samples were thermally treated in air in a muffle furnace at 200 °C for 1 hour, which allowed the lower Ti layer to be oxidized to TiO₂.

To study the effect of UV-visible radiation on the electrical conductivity of the TiO₂ semiconductor layer in a gaseous atmosphere, the sample was irradiated with a xenon lamp for 2 hours before measurement. Next, it was placed in a measuring cell consisting of a heating table with probes (Fig. 2).

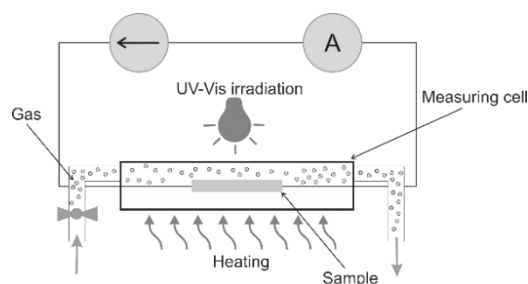


Fig. 2. Schematic representation of the measuring stand.

A constant voltage of 20 V was applied to the sample and the current was continuously measured, first in air, then in vacuum. Next, the sample was heated to 120 °C, after which the test gas (CO₂ or O₂) was injected. The current strength was measured first in the dark, then when UV-visible radiation was applied for 5 minutes, which made it possible to register a photoresponse (Fig. 3).

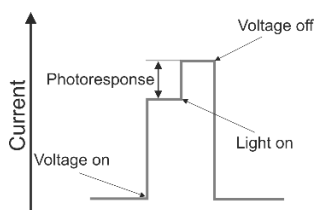


Fig. 3. Measuring conductivity in the dark and the photoresponse.

Next, the sample was cooled, and the current was measured in the same way at temperatures from 120 °C to 30 °C in increments of 15 °C.

3. Results and discussions

Layers of TiO₂ P25 nanopowder with a specific gravity of 1 mg/cm² were deposited by the EPO method. The uniformity of the deposited layer of nanoparticles is confirmed by an image obtained using scanning electron microscopy (SEM). The thickness of the TiO₂ P25 layer was about 7 μm (Fig. 4).

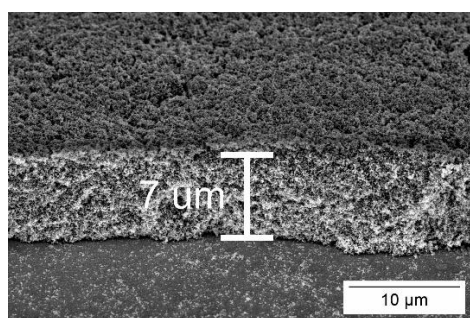


Fig. 4. SEM image of the formed TiO₂ layer with specific mass layer 1 mg/cm².

The study of the effect of temperature, the gaseous atmosphere, and periodic UV-visible irradiation on the electrical conductivity of the TiO₂ layer was accompanied by recording cycloramas of current values from time to time. Two types of measurements were performed. In the first case, the sample was not pretreated with UV-visible irradiation for 2 hours, and the electrical conductivity of the samples was measured in CO₂ and O₂ atmospheres. In the second case, the electrical conductivity was measured in the same way in the same gases, but the samples were previously irradiated with UV-visible light, as described in paragraph 2. Based on the results obtained, histograms of the values of the photoresponse of the sensitive layer from temperature were constructed for the untreated (Fig. 5) and processed (Fig. 6) samples.

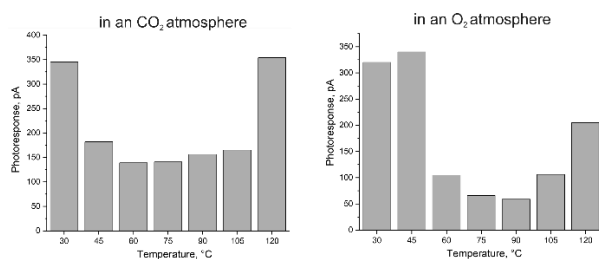


Fig. 5. Histogram of the difference in electric current in light and in darkness depending on the cell temperature of the untreated by UV-visible irradiation TiO₂ layer.

From the histograms in Figure 5, the maximum photoresponse of the TiO₂ layer is reached at temperatures of 30 °C and 120 °C in a CO₂ atmosphere and at a

temperature of 45 °C in an O₂ atmosphere, equal to approximately 350 pA.

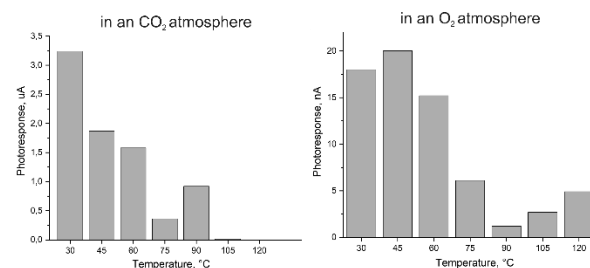


Fig. 6. Histogram of the difference in electric current in light and in darkness depending on the cell temperature of the pretreated by UV-visible irradiation TiO₂ layer.

At the same time, Figure 6 shows that the maximum photoresponse of the TiO₂ layer in the CO₂ atmosphere is reached at a temperature of 30 °C, whereas in the O₂ atmosphere the maximum photoresponse is observed at a temperature of 45 °C, equal to 3,25 μA and 20 nA, respectively. The increased response at low temperature (approximately equal to room temperature) is explained by the sensitivity of the TiO₂ layer to humidity due to the adsorption of water molecules on Ti defects, which is especially evident at room temperature [5], therefore, it is necessary to compensate for the influence of humidity when studying the electrical conductivity of TiO₂ in a gaseous atmosphere, too.

4. Conclusions

As a result of experiments, it was found that the photoresponse of TiO₂ in an atmosphere of CO₂ and O₂ is higher, the higher its electrical conductivity. UV-visible pre-irradiation for 2 hours reduces the electrical resistance of TiO₂ by several orders of magnitude, which significantly increases the photoresponse. However, the lower the cell temperature, the more pronounced the photoresponse becomes. It is noteworthy that the difference between photoresponses in an O₂ atmosphere for samples pretreated and untreated with ultraviolet radiation is less than one order of magnitude, while for samples measured in a CO₂ atmosphere, the difference is significant and is about six orders of magnitude.

Acknowledgements

This work was supported by State Assignment № FSMR-2023-0003.

References

- [1] Z. Li, Z. Li, C. Zuo, X. Fang. *Advanced Materials* **34**(2022)2109083.
- [2] J.M. Rzaizj, A.M. Abass. *Chem. Rev.* **2**(2020)114.
- [3] M. Shooshtari, A. Salehi, S. Vollebregt. *Nanotechnology* **32**(2021)325501.
- [4] D. Nunes, E. Fortunato, R. Martins. *Discover Materials* **2**(2022)2.
- [5] P. Pascariu, M. Homocianu, F. Tudorache, A. Bele, D. Rusu. *Journal of Materials Science* **59**(2024)2712.

Surface analysis of laser-irradiated Ge₂Sb₂Te₅ films

Rybina N.V.^{*1}, Kunkel T.S.¹, Ermachikhin A.V.^{1,2}, Rybin N.B.¹, Vorobyov Y.V.^{1,3}

¹ Ryazan State Radio Engineering University, Gagarin St. 59, Ryazan 390005, Russia

² Scientific-Manufacturing Complex Technological Centre, Shokin sq. 1, Zelenograd, Moscow 124498, Russia

³ National Research University of Electronic Technology, Shokin sq. 1, Zelenograd, Moscow 124498, Russia

*e-mail: pgnv@mail.ru

Abstract. Analysis of AFM images of Ge₂Sb₂Te₅ films irradiated with femtosecond laser pulses was performed using methods of average mutual information and detrended fluctuation analysis. The scaling exponent and average mutual information increased with rising radiation energy density, reaching their maximum values at the boundary of film reamorphization, then decreased again in the center of the laser spot. After reamorphization, the information-correlation parameters of the surface did not return to the values characteristic of the amorphous surface prior to crystallization. The study demonstrates the potential of using information-correlation characteristics of Ge₂Sb₂Te₅ film surfaces for creating multilevel memory elements.

1. Introduction

Currently, various designs and prototypes of reconfigurable metasurfaces and metamaterials are being actively developed based on phase-change materials (PCMs) [1,2]. Phase-change materials show great promise for photonic applications [3] as well as data storage technologies [4].

Femtosecond laser irradiation holds a special place in the field of solid-state material surface modification, enabling the creation of nanostructured surfaces with tailored properties.

To evaluate the surface topography features of both amorphous regions and crystallized areas with complex structures in PCMs, specialized surface analysis techniques are required. In this context, our study employs two-dimensional detrended fluctuation analysis (2D DFA) and average mutual information (AMI) methods, which were specifically developed for analyzing heterogeneous material surfaces [5,6].

We performed a comprehensive analysis of atomic force microscopy (AFM) images of Ge₂Sb₂Te₅ (GST225) films irradiated with femtosecond laser pulses using 2D DFA and AMI techniques.

2. Experiment

Amorphous GST225 films were irradiated with laser pulse series under the following parameters:

- Wavelength: 1030 nm.
- Pulse duration: 185 fs.
- Repetition rate: 200 kHz.
- Beam diameter: ~70 μm (measured using an Ophir Spiricon SP620U CCD-based beam profiler).
- Incidence: normal to sample surface.
- Polarization: linear.
- Gaussian beam intensity profile.

Figure 1 presents the surface topography of the modified region produced with 512 pulses per sequence. The non-uniform radiation intensity distribution induced the formation of both crystalline and amorphous domains on the film surface [7]. Reamorphization occurred in the center of the Gaussian beam (region 1), then regions with crystallites of different sizes were formed (regions 2-5). Region 6 had the minimum energy density, maintained the film remained in the initial amorphous state.

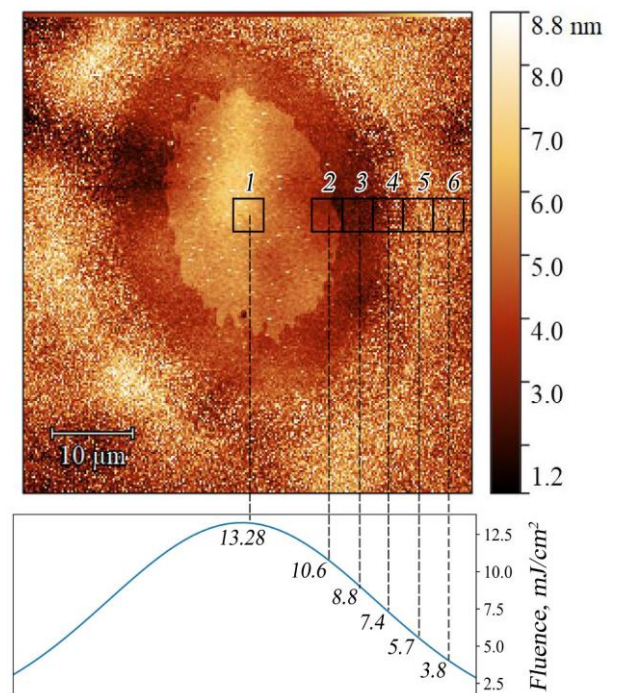


Fig. 1. AFM image of the modified structure with identified regions analyzed using 2D DFA and AMI methods. The profile at the bottom of the figure shows the energy density distribution that formed the structure and the local energy density values corresponding to different regions.

3. Results and discussions

The surface topography was analyzed using AFM data through 2D DFA and AMI methods. The 2D DFA method provides the fluctuation function's scale dependence, from which two key parameters are derived: the correlation distance d (corresponding to the period of surface harmonic components) and the scaling exponent α (indicating correlation types). The AMI method quantifies both surface ordering degree and topography complexity through the maximum mutual information value.

For all samples, multiple correlation distances d were obtained, corresponding to the spatial periods of harmonic surface structures. Notably, correlation distances were also observed in amorphous regions, indicating the existence of specific pattern formation mechanisms in their surface topography.

The calculated α values for amorphous region 6 and partially crystallized region 5 ranged from 0.58 to 0.59, corresponding to an intermediate state between noise and several superimposed periodic signals with different periods [6]. When a crystalline phase became clearly visible on the surface (region 4), α increased to slightly above 0.65. For the fully crystalline surface (region 3), α reached 0.96. The highest scaling exponent value of 1.06 was observed for the surface with a sharp boundary between crystalline and amorphous phases (region 2).

The AMI values exhibited a similar dependence on laser pulse energy density. Higher energy densities led to increased surface ordering and the formation of self-organized structures.

The AMI values ranged between 0.4-0.523, falling into both low ($\text{AMI} < 0.5$) and medium ($0.5 < \text{AMI} < 0.7$) information capacity categories according to reference [6].

Laser irradiation of GST225 films leads to modification of their surface topography. Figure 2 shows an AFM image of a GST225 area modified by femtosecond laser pulses. The crystallized region exhibits more developed surface roughness compared to the amorphous one. There is also reason to believe that surface morphology depends on the degree of crystallinity of the GST material. Furthermore, it is known that the crystallinity degree affects the optical properties of GST films [8], which can be evaluated, for example, through surface optical contrast. Extrapolating these findings to amorphization processes, we can conclude that GST films with different degrees of amorphization will also demonstrate different surface morphologies and optical properties.

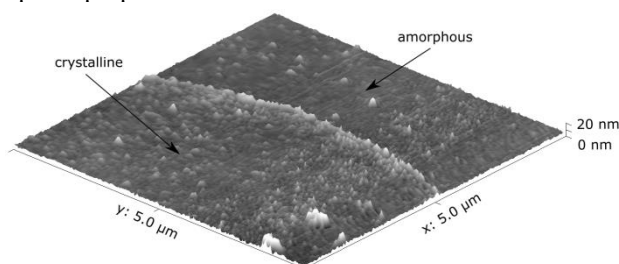


Fig. 2. AFM image of laser-modified GST225 film, demonstrating distinct surface topography changes induced by femtosecond laser irradiation.

The results of this work could be useful for designing multilevel non-volatile memory elements based on GST225 films. Under specific laser irradiation conditions, the GST film develops distinct surface topographies. Each surface morphology can be characterized using 2D DFA and AMI methods. Since each surface topography type possesses unique optical characteristics (such as optical contrast and reflectivity), different information states can be assigned based on these optical properties. Furthermore, the laser irradiation affects not only the surface but also the bulk GST material structure. At specific irradiation parameters, the GST film will exhibit particular degrees of amorphization or crystallization. For instance, the amorphization degree can be determined by measuring the film's electrical resistance, enabling assignment of a second information state to the structure. This dual-state structure can be utilized either for independent information storage (with data encoded separately in each state) or for data duplication to enhance reliability.

4. Conclusions

Femtosecond laser surface modification of phase-change materials opens up diverse application possibilities for these materials.

The results of this study demonstrate that data storage can be implemented in GST225 films using periodic surface patterns as an information capacity medium. Different surface topographies exhibit distinct information capacities, enabling each specific pattern type to serve as a storage medium for unique information states. The AMI and 2D DFA methods provide effective characterization tools for these states while also facilitating investigation of self-organization processes [9] in chalcogenide film nanostructures.

The AMI and MMI data revealed that both the initial amorphous surface and reamorphized surface exhibit the lowest information capacity. In contrast, the presence of well-defined boundaries between crystalline and amorphous phases within a single region significantly enhances these parameters, which gradually decrease as the crystalline phase fraction diminishes. Utilizing surfaces containing multiple boundaries appears particularly promising for boosting information storage capacity. Reference [10] demonstrates the feasibility of fabricating rewritable data storage devices using periodically patterned GST225 surfaces.

Acknowledgements

This work was supported by the Russian Science Foundation grant No. 24-79-10137 (<https://rscf.ru/en/project/24-79-10137/>) and utilized equipment from the Regional Centre for Probe Microscopy of Ryazan State Radio Engineering University.

References

- [1] M. Xu, X. Mai, J. Lin, W. Zhang, Y. Li, Y. He, H. Tong, X. Hou, P. Zhou, X. Miao. *Adv. Funct. Mat.* **30** (2020) 2003419.
- [2] Y. Meng, T. Cao, Y. Long. *J. Appl. Phys.* **128** (2020) 140904.
- [3] O.A.M. Abdelraouf, Z. Wang, H. Liu, Z. Dong, Q. Wang, M. Ye, X. R. Wang, Q.J. Wang, H. Liu. *ACS Nano* **16** (2020) 13339.
- [4] A. Lotnyk, M. Behrens, B. Rauschenbach. *Nanoscale Advances* **1** (2019) 3836.
- [5] A.V. Alpatov, S.P. Vikhrov, N.V. Grishankina. *Semiconductors* **47** (2013) 365.
- [6] A.V. Alpatov, S.P. Vikhrov, N.V. Vishnyakov, S.M. Mursalov, N.B. Rybin, N.V. Rybina. *Semiconductors* **50** (2016) 22.
- [7] T. Kunkel, Y. Vorobyov, M. Smayev, P. Lazarenko, V. Veretennikov, V. Sigaev, S. Kozyukhin. *Journal of Alloys and Compounds* **851** (2021) 156924.
- [8] M.E. Fedyanina, P.I. Lazarenko, Yu.V. Vorobyev, S.A. Kozyukhin, A.A. Dedkova, A.O. Yakubov, V.S. Levitskii, I.V. Sagunova, A.A. Sherchenkov. *Proc. Univ. Electronics* **25** (2020) 203.
- [9] T. Kunkel, Y. Vorobyov, M. Smayev, P. Lazarenko, A. Kolobov, S. Kozyukhin. *Applied Surface Science* **624** (2023) 157122.
- [10] S. Zaboltnov, A. Kolchin, D. Shuleiko, D. Presnov, T. Kaminskaya, P. Lazarenko, V. Glukhenkaya, T. Kunkel, S. Kozyukhin and P. Kashkarov. *Micro* **2** (2022) 88.

IV. Formation and properties of ferromagnetic and ferroelectric materials, spintronics

Magnetic nanocomposites for terranostic applications: diagnostics (MPI, MPI) and magneto-hyperthermic treatment (MHT)

Kamzin A.S.*

Ioffe Physical-Technical Institute RAS, 26 Polytechnicheskaya st., Saint-Petersburg 194021, Russia

*e-mail: ASKam@mail.ioffe.ru

Abstract. Magnetic nanocomposites (MNCs) provide a new highly effective approach to visualization (diagnosis) and treatment of human diseases, including malignant tumors (cancer). Thus, MNCs can significantly increase the contrast of magnetic resonance imaging (MRI). MNCs are promising for magnetic hyperthermic treatment (destruction) of cancer tumors due to relaxation heating of particles by an external alternating magnetic field without the use of radiation methods. In 2000 was proposed for using MNPs in a new highly sensitive method of magnetic particle imaging (MPI) of disease foci. To implement these methods, MNPs with certain magnetic parameters are required. The paper presents the results of studies of MNCs $M_x\text{Fe}_{3-x}\text{O}_4$, (where $M^{2+} = \text{Zn, Ni, Mn}$) and $\text{Ni}_{1-x}\text{Cu}_x\text{Fe}_2\text{O}_4$ synthesized by different methods, doped with different amounts of divalent metals ($x=0, 0.25, 0.5, 0.75$, and 1) and then functionalized with polyacrylic (PAA), citric (CA) or oleic (OA) acids. The created MNCs meet the requirements for composites intended for diagnostics (MRI and MPI), targeted drug delivery and treatment of diseases by magnetic hyperthermia (MHT).

1. Introduction

Magnetic iron oxide nanoparticles, namely magnetite (Fe_3O_4), due to their biocompatibility, biodegradability and low toxicity, are widely studied for biomedical applications such as organ imaging (diagnostics) (MRI, MPI), targeted drug delivery, magnetic hyperthermia (MHT) treatment including cancer. They are used in MRI for increasing contrast of pictures, but the negative contrast effects of iron oxide can lead to errors in diagnostic. These errors are eliminated in a new unique highly sensitive magnetic powder imaging (MPI) diagnostic method proposed in 2000 [2].

Particles for biomedicine consist of a magnetic core (MNP) coated with inorganic and/or organic layers (e.g., dextran, chitosan, silicon, etc.) to prevent aggregation and improve physicochemical stability in various physiological environments. In addition, appropriate surface functionalization of MNPs allows highly selective chemical interaction with biological systems. The insignificance of the magnetic background from the biological environment allows MNCs to be used as highly sensitive visualizers (markers/tracers) in MPI.

In recent years, the researchers has been aimed at the synthesis of Fe_3O_4 nanoparticles doped with divalent ions ($M^{2+} = \text{Zn, Ni, Mn, Co, etc.}$). The magnetic properties of Fe_3O_4 can be controlled by doping with M^{2+} . The synthesis technology determines the distribution of cations over sublattices, particle size and shape, which are important parameters of MNCs. In addition, water-dispersible MNCs are required for biomedicine.

The paper presents new MNCs with characteristics that meet the requirements of modern biomedical technologies, which is crucial for the transition from the experimental stage of MNC use to clinical practice. New MNCs for theranostic use (diagnostics + treatment), are also described.

2. Experiment

The $M_x\text{Fe}_{3-x}\text{O}_4$ (where $M = \text{Ni, Zn or Mg}$) samples with $x = 0, 0.25, 0.5, 0.75$, and 1 were prepared using a two-step model. In the first step, MNPs were obtained by the hydrothermal method. In the second step, the synthesized

MNPs were functionalized with polyacrylic (PAA), citric (CA) or oleic (OA) acids using coprecipitation methods. Comprehensive studies of the properties of the obtained nanocomposites and the effect of particle modification or functionalization with acids were carried out using X-ray, magnetic and Mössbauer measurements.

To study the properties of MNCs, Mössbauer spectroscopy was used, which allows one to reliably establish the phase composition, distribution of iron ions over nonequivalent positions of the crystal lattice and their number, which is inaccessible to other methods. Modeling of experimental Mössbauer spectra (MS) was carried out using a special program. In the procedure of minimization of the functional χ^2 the program searches for the optimal values of widths, intensities and positions of spectral lines. The values of hyperfine interactions (HFI) are calculated from the positions of spectral lines: IS - isomer shift, QS - quadrupole splitting, Heff - effective magnetic field.

3. Results and discussions

Fig. 1 shows examples of the MS of $\text{Ni}_x\text{Fe}_{3-x}\text{O}_4$ MNPs and $\text{Ni}_x\text{Fe}_{3-x}\text{O}_4@\text{PAA}$ and $\text{Ni}_x\text{Fe}_{3-x}\text{O}_4@\text{CA}$ MNCs obtained at 300K. These MS of $\text{Ni}_x\text{Fe}_{3-x}\text{O}_4$ MNPs differ significantly from the spectra of NiFe_2O_4 bulk crystals [3]. With decreasing size, the MS of NiFe_2O_4 MNPs acquires a relaxation character. An important requirement for MNCs for MPW is the superparamagnetic state that occurs at small sizes of MNPs, when thermal energy overcomes the anisotropy energy of the particle and the magnetization jumps from the direction of one easy axis to another, which significantly complicates the analysis of MS (Fig. 1). Therefore, for fitting of the experimental MS of $M_x\text{Fe}_{3-x}\text{O}_4$ MNPs, a complex procedure of fitting and restoring the probability functions $P(\text{Heff})$ of the Heff distribution from MS was also used. The obtained $P(\text{Heff})$ curves allow us to establish that the model lines belong to the corresponding iron oxides and positions of Fe ions in the crystal lattice [3-5].

The accuracy of MS fitting is determined by the deviation of the experimental values from the models (χ^2), which in our cases is in the range from 1.1 to 1.2, which indicates good agreement between the models and the

experimental data and, consequently, the reliability of processing the obtained MS. The model spectra are shown in Fig. 1 by solid lines. The HFI parameters are given in Table 1. MS allows to reliably identify the lines belonging to Fe^{2+} and Fe^{3+} ions by the IS values, which are 0.2 ± 0.5 mm/s for Fe^{3+} and 0.9 ± 1.1 mm/s for Fe^{2+} [3-5]. As can be seen from Table 1, the IS values correspond only to Fe^{3+} ions, and values correspond to Fe^{2+} ions are absent in the studied MNCs. In NiFe_2O_4 @CA MNCs, a slight decrease in the line intensity and the H_{eff} value of the Z sextuplet is observed. The intensity of the R component also decreases, and doublet lines of paramagnetic particles appear. In the MS of NiFe_2O_4 @PAA MNCs, the intensity of the R component does not change, but the line widths have increased. The Z component is absent, and the intensity of the D doublet has increased. These changes can be explained by the fact that in the case of uncoated NiFe_2O_4 MNPs, the particles are linked to each other by strong interactions and agglomerates are formed that have the properties of larger, medium, and smaller particles. In NiFe_2O_4 @CA MNCs, the CA surface layer isolates the particles from each other, agglomerates are eliminated, and the MNC exhibits the properties of superparamagnetic particles. The molecular weight and density of PAA are higher than those of CA, and, in addition, PAA forms strong complexes with transition metal ions. Therefore, in the case of NiFe_2O_4 @PAA MNCs, a significantly greater destruction of agglomerates occurs compared to CA, and a greater number of NiFe_2O_4 particles separated by PAA are formed, as a result of which a greater number of NiFe_2O_4 MNPs in the MNCs exhibit superparamagnetic and paramagnetic properties.

When NiFe_2O_4 MNPs are functionalized by CA, doublet lines appear on the MS, the areas of which are significantly smaller than the area of the sextuplets. This means that the blocking temperature (T_B) in these particles is higher than 300 K. On the MS of NiFe_2O_4 @PAA MNCs, the doublet line intensities are significantly higher, which means a decrease in the T_B temperature to ~ 300 K.

4. Conclusions

$\text{Ni}_{1-x}\text{Cu}_x\text{Fe}_2\text{O}_4$ and $\text{M}_x\text{Fe}_{3-x}\text{O}_4$ (where M= Ni, Zn or Mg) MNP (where $x = 0, 0.25, 0.5, 0.75$, and 1), doped with different amounts of divalent metals were synthesized using various methods and than functionalized (coated) with polyacrylic (PAA), citric (CA) or oleic (OA) acids. Comprehensive studies of the properties of the obtained MNCs and the effect of particle functionalization with acids were carried out using X-ray, magnetic and Mössbauer measurements. It was found that the synthesized MNCs are single-phase, do not have foreign impurities and are in a superparamagnetic state. Coating of the MNPs leads to a decrease in the blocking temperature (T_B), and T_B of MNCs coated with PAA is lower than that of CA coating, which is explained by different densities and molecular weights of PAA and CA, leading to different degrees of isolation of particles by CA and PAA from each other, changes in agglomeration and interactions of particles. Based on the Mössbauer spectroscopy data, the sizes of the studied MNPs were estimated.

New multifunctional biocompatible MNPs were obtained for MRI and MPI diagnostics, drug delivery and magnetic hyperthermia treatment. The created NiFe_2O_4 @CA MNCs are superparamagnetic at room

temperature, which is required for MPI, the latest method for diagnosing human diseases.

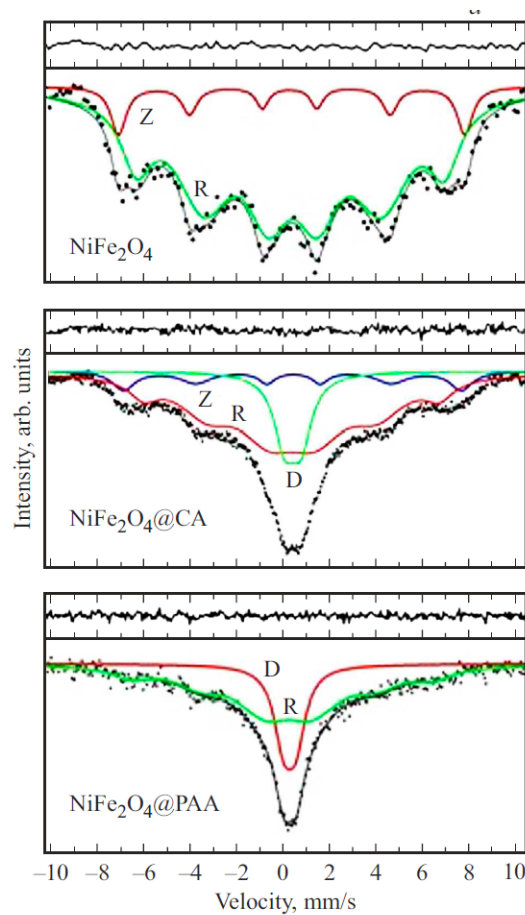


Fig. 1. Experimental MS of NiFe_2O_4 , NiFe_2O_4 @CA and NiFe_2O_4 @PAA MNCs at 300 K and their model representations. Sextuplet - Z belong to Fe ions in magnetically ordered particles, R - Fe ions in superparamagnetic particles, D - Fe ions of particles in the paramagnetic phase.

Table 1. HFI parameters for NiFe_2O_4 , NiFe_2O_4 @CA and NiFe_2O_4 @PAA MNCs obtained from MS: Zeeman sextuplet (Z), superparamagnetic component (R) and paramagnetic doublet (D). Line widths (G_1) and component areas (I_n).

Sample	Comp	G_1 (mm/s)	IS (mm/s)	Q_2 (mm/s)	$H_{\text{eff}}(T)$	I_n (%)
NiFe_2O_4	Z	0.772 ± 0.259	0.298 ± 0.048	0.084 ± 0.099	46.21 ± 0.41	10
	R	1.575 ± 0.276	0.341 ± 0.045	0.091 ± 0.074	41.09 ± 0.82	90
NiFe_2O_4 @/K	Z	1.121 ± 0.126	0.342 ± 0.023	0.045 ± 0.048	45.04 ± 0.24	8
	R	1.476 ± 0.162	0.294 ± 0.020	0.028 ± 0.033	39.45 ± 0.42	72
	D	1.124 ± 0.068	0.335 ± 0.008	0.701 ± 0.021	—	18
NiFe_2O_4 @/AK	R	1.891 ± 0.685	0.116 ± 0.083	0.256 ± 0.145	40.42 ± 1.01	72
	D	0.998 ± 0.161	0.292 ± 0.015	0.522 ± 0.050	—	28

References

- [1] Y.Q. Meng, Y.N. Shi, Y.P. Zhu, Y.Q. Liu, L.W. Gu, D.D. Liu, A. Ma, F. Xia, Q.Y. Guo, C.C. Xu, J.Z. Zhang, C. Qiu, J.G. Wang. *J. Nanobiotechnology*. **22**(2024)24.
- [2] B. Gleich and J. Weizenecker, *Nature*. **435**(2005)1214.
- [3] A.S. Kamzin, N. Dogan, L.S. Kamzina, A.V. Kopilov. *Physics Solid State*. **67**(2025)356.
- [4] A.S. Kamzin, N. Dogan, O.M. Dogan, V.G. Semenov, *Physics Solid State*. **65**(2023)1373.
- [5] N. Dogan, O.M. Dogan, M. Irfan, F. Ozel, A.S. Kamzin, V.G. Semenov, I.V. Buryanenko. *JMMM* **561**(2022)169654.

Dynamics of domain walls in thin magnetic films with perpendicular magnetic anisotropy

Chernousov N.N., Kozlov A.G., Turpak A.A., Pashenko A.S., Davydenko A.V.*

Far Eastern Federal University, pos. Ajax 10, Vladivostok 690922, Russia

*e-mail: davydenko.av@dvfu.ru

Abstract. Dynamics of domain walls (DWs) was investigated in the Si(111)/Cu(2 nm)/Pd(d_{Pd})/Co(0.7 nm)/Pd(3 nm) epitaxial system with different thickness of the Pd bottom layer. It was found that the mobility of DWs is sensitive both to the distribution of strains in the Co layer and amplitude of interface roughness in the layers. The dependence of the mobility of DWs on their chirality became more pronounced in the samples with thick bottom Pd layers. The ratio of mobilities of DWs with opposite chiralities was as large as 6600 in the samples with $d_{Pd} = 12.5$ nm. Chirality of mobility of DWs was maximal in the low-speed creep regime and gradually disappeared with an increase of the velocity of DWs and switching to the depinning and flow regimes.

1. Introduction

Magnetic DWs in thin films are of interest for investigation because they can be used to store and process information [1]. One needs to control the direction of DWs propagation under the influence of magnetic fields or preferably currents that pass along magnetic tracks to use DWs as information carriers. Current-induced DW motion in magnetic tracks is possible due to a combination of two physical effects: a spin-orbit torque (SOT) effect and a Dzyaloshinskii-Moriya interaction (DMI) [2]. DMI induces certain chirality in magnetic DWs. Spin moment is transferred from conduction electrons to the electrons in magnetic layers via SOT effect and hence, it influences the orientation of the magnetization in magnetic medium.

Recently, it was found that chirality of magnetic DWs may influence their mobility via chiral damping mechanism [3]. Therefore, in some systems with the chiral damping, it is necessary to induce DMI with certain sign to fix the certain chirality of DWs with larger mobility. We investigate a Pd/Co/Pd system with extreme sensitivity of the mobility of DWs to their chirality. Our results indicate that the chiral damping is not responsible for the observed effect in the investigated system.

2. Experiment

The samples were evaporated in an Omicron ultrahigh vacuum system, which consisted of a molecular beam epitaxy chamber and an analysis chamber interconnected with each other. We used Si(111) substrates misoriented towards [11-2] by 0.1° . Before loading into the chamber, Si(111) substrates were rinsed in isopropyl and distilled water. The substrates were then heated at 800 K by indirect heating for 12 h. Just before deposition, the substrates were flash-heated by direct current at 1400 K three times for 10 s and slowly cooled down to 300 K. All the metals were evaporated from high temperature effusion cells.

The growth rates of Cu, Co and Pd were 0.9, 0.28 and 0.26 nm/min, respectively. The deposition rates were monitored by a quartz crystal microbalance, which was calibrated by means of reflection high energy electron diffraction (RHEED).

Epitaxial Pd(d_{Pd})/Co(0.7 nm)/Pd(3 nm) trilayers were grown on a Si/Cu(2 nm) surface. The thickness of the bottom Pd layer, d_{Pd} , was varied from 0 to 12.5 nm. The Pd(d_{Pd})/Co(0.7 nm)/Pd(3 nm) samples will be denoted simply as Pd(d_{Pd}) for clarity. Magnetic hysteresis loops of

the samples were measured using a vibrating sample magnetometer (Lakeshore) with applied magnetic fields of up to 2.2 T. The magnetic structure was investigated by a magneto-optical Kerr effect (MOKE) microscope (Evico-Magnetics). The MOKE microscope was equipped with hand-made coils applying out-of-plane (OOP) magnetic fields and an in-plane (IP) electromagnet. The OOP coils were used in a pulse mode and produced magnetic fields with an amplitude of up to 150 mT and a width down to 10 μ sec. Artificial nucleation centers with a diameter of 10 μ m were prepared on the samples by means of a focusing ion beam etching method. The scheme for the measurement of the DW velocity was as follows. A stable nucleating circular domain was found. A constant IP magnetic field was switched on. The pulse of the OOP magnetic field of the calibrated time-length was applied. The distance at which the DW propagated was measured from a snapshot of differential magnetic contrast made by the Kerr microscope.

3. Results and discussions

An increase in the thickness of the bottom Pd layer influenced the structure of the samples. A gradient of strains in the Co layer increased with an increase in the d_{Pd} thickness from 0 to 3 nm while a toughness of the interfaces remained nearly constant. In the thickness interval from 3 to 12.5 nm, the gradient of strains in the Co layer remained nearly constant while the toughness of the interfaces increased greatly with an increase in the d_{Pd} thickness.

We measured the dependencies of the velocities of DWs on the applied IP magnetic field $v(H_x)$ in constant driving OOP magnetic fields. OOP magnetic fields were used to shift DW in a creep regime – low speed thermally activated regime of DWs propagation. The dependencies of the velocities of $\downarrow\uparrow$ DWs on the IP magnetic field in the samples with different thickness of the Pd bottom layer are shown in Fig. 1. $v(H_x)$ dependencies of the Pd(0) sample are symmetric relative to $H_x = 10$ mT axis. With an increase in the thickness of the Pd bottom layer, $v(H_x)$ dependencies become asymmetric. It means that mobility of the left-handed and right-handed DWs are different in the samples with thick bottom Pd layers. The ratio of mobilities of DWs with opposite chiralities was as large as 6600 in the samples with $d_{Pd} = 12.5$ nm in $H_x = 150$ mT. An increase in the asymmetry of the $v(H_x)$ dependencies with increasing of the thickness of the Pd bottom layer is related with stronger

pinning of the DWs on the structural defects such as misfit dislocations and roughness of the interfaces. Our results indicate that roughness of the interfaces influences the asymmetry of the $v(H_x)$ dependencies stronger than misfit dislocations since the asymmetry in the $v(H_x)$ dependencies increases more in the thickness interval of the Pd bottom layer from 3 to 12.5 nm, in which roughness of interfaces largely increases. The aforementioned assumption is corroborated by an observed large increase in the coercive force from 11 to 27 mT with an increase in the thickness of the bottom Pd layer from 3 to 12.5 nm.

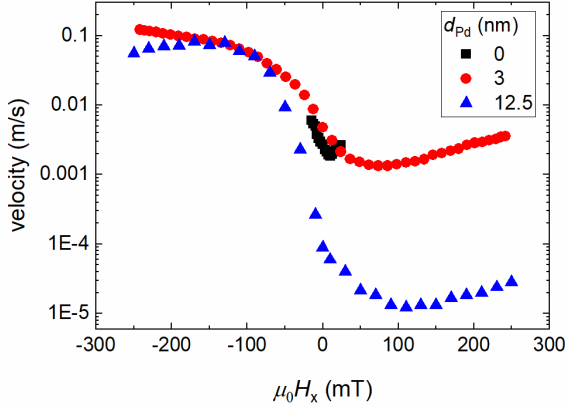


Fig. 1. The dependencies of the velocities of DWs on the IP magnetic field in the samples with different thickness of the Pd bottom layer.

The asymmetry in the $v(H_x)$ dependencies may be related with the chiral damping effect. To investigate the origin of the observed asymmetry in the $v(H_x)$ dependencies we measured $v(H_x)$ dependencies in the Pd(10) sample in different OOP magnetic fields. With an increase in the driving OOP magnetic field, a regime of DWs propagation changes from the low-speed creep to a high-speed flow regime in which DWs less interact with defects. Asymmetry coefficient is calculated by the following expression

$$A(\mu_0 \Delta H_x) = \frac{v(\mu_0 H^* + \mu_0 \Delta H_x) - v(\mu_0 H^* - \mu_0 \Delta H_x)}{v(\mu_0 H^* + \mu_0 \Delta H_x) + v(\mu_0 H^* - \mu_0 \Delta H_x)} \quad (1)$$

where H^* corresponds to the magnetic field, in which minimum in the $v(H_x)$ dependencies in the flow regime was observed. The dependencies of the asymmetry coefficients on the IP magnetic fields measured in different OOP driving magnetic fields are shown in Fig. 2.

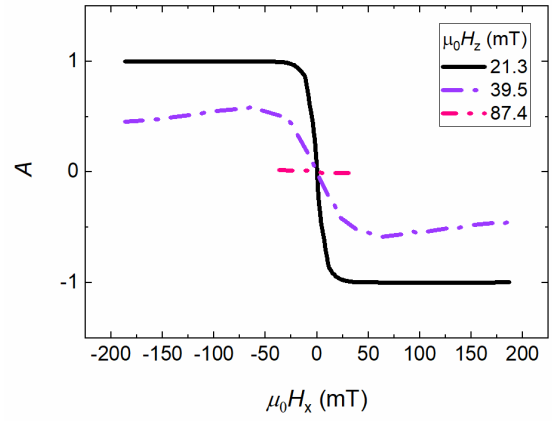


Fig. 2. The dependencies of the asymmetry coefficient on the IP magnetic field in the Pd(10) sample in different OOP magnetic fields.

It appeared that asymmetry in the $v(H_x)$ dependencies of the Pd(10) sample almost completely disappeared in the flow regime. This result indicates a paramount significance of a chiral pinning of the DWs on defects. The chiral damping cannot be the reason of the observed asymmetry in the $v(H_x)$ dependencies because damping equally influence the mobility of DWs both in the creep and flow regimes.

4. Conclusions

The dependence of the mobility of DWs on their chirality was investigated in the Pd/Co/Pd system. The difference in the mobilities of the left-handed and right-handed DWs in the creep regime increased with an increase in the thickness of the bottom Pd layer. With an increase in the driving OOP magnetic field and transition to the high-speed flow regime of the DWs propagation, the asymmetry in the $v(H_x)$ dependencies almost completely disappeared. The observed results cannot be explained by the chirality of the magnetic damping factor.

Acknowledgements

The research was supported by the Ministry of Science and Higher Education of the Russian Federation (project No. FZNS-2023-0012).

References

- [1] S. Parkin, S.-H. Yang. *Nature Nanotech.* **10**(2015)195.
- [2] S. Emori, U. Bauer, S.-M. Ahn, E. Martinez, G.S.D. Beach. *Nat. Mater.* **12**(2013)611.
- [3] C.A. Akosa, I.M. Miron, G. Gaudin, A. Manchon. *Phys. Rev. B.* **93**(2016)214429.

The influence of interface roughness induced by Cu bottom layer on dynamics of domain walls in Cu/Pd/Co/Pd system

Chernousov N.N., Silina S.K., Pashenko A.S., Turpak A.A., Kozlov A.G., Davydenko A.V.*

Far Eastern Federal University, pos. Ajax 10, Vladivostok 690922, Russia

*e-mail: davydenko.av@dvfu.ru

Abstract. Domain wall propagation in the creep regime was studied in $\text{Cu}(d_{\text{Cu}})/(\text{Pd}(3\text{ nm})/\text{Co}(0.7\text{ nm})/\text{Pd}(3\text{ nm}))$ epitaxial structures in simultaneously applied in-plane and out-of-plane magnetic fields in the creep regime. The thickness of the Cu layer was varied from 2 to 12 nm. The interface Pd/Co roughness increased with increasing of the thickness of the Cu layer. Asymmetry of the dependencies of the velocity of domain walls on the applied in-plane magnetic field, $v(H_x)$, almost disappeared with an increase in the thickness of the Cu bottom layer and interface roughness. The obtained results indicate that large interface roughness is not the only necessary condition for the observing large asymmetry in the $v(H_x)$ dependencies in the investigated system.

1. Introduction

Investigation of dynamics of magnetic domain walls (DWs) is important since dynamics of DWs determines performance of memory, magnetic logic devices and magnetic sensors based on DWs propagation [1]. The dynamics of DWs is influenced by magnetic phenomena such as magnetic anisotropy, symmetric and asymmetric interactions, and the pinning potential distribution, which are determined by the properties of interfaces and the materials.

In our previous work, we studied how the dynamics of DWs in out-of-plane (OOP) and in-plane (IP) magnetic fields changed with different Pd bottom layer thicknesses in $\text{Cu}(2)/\text{Pd}(3\text{--}10\text{ nm})/\text{Co}(0.7\text{ nm})/\text{Pd}(3\text{ nm})$ system [2]. As a result, with an increase in the thickness of the Pd bottom layer, its surface roughness increased, which led to an increase in the asymmetry of the dependencies of DWs velocities on the applied IP magnetic fields, $v(H_x)$. The open question remains what influences this asymmetry: the growing interface roughness in the structures or thickness of the Pd layer itself. To find out whether the interface roughness is the origin of the asymmetry in the Pd/Co/Pd system in this work, we change the thickness of the Cu layer, thereby changing the roughness of the Pd/Co interface without changing the thickness of the bottom Pd layer. We investigate the influence of the thickness of the Cu layer on the magnetic properties of the system and dynamics of DWs in the creep regime.

2. Experiment

The samples were evaporated in an Omicron ultrahigh vacuum system, which consisted of a molecular beam epitaxy chamber and an analysis chamber interconnected with each other. Si(111) was used as a substrate, which was washed with isopropyl alcohol and distilled water before being loaded into the chamber. Then, the substrates were heated in situ to 800 K by indirect heating for 12 h. Immediately before deposition, the substrates were subjected to instantaneous direct current heating at 1400 K seven times for 5 s and slowly cooled down to 300 K. All the metals were evaporated from high temperature effusion cells.

The deposition rates were monitored by a quartz crystal microbalance, which was calibrated by means of reflection high energy electron diffraction (RHEED). The lattice period of the metal layers during growth and their structure

were analyzed using RHEED. The thickness of the Cu layer d_{Cu} was varied from 2 to 12 nm. The roughness of the Cu layer was evaluated using scanning tunneling microscopy.

Magnetic hysteresis loops of the samples were measured using a vibrating sample magnetometer with applied magnetic fields of up to 2 T. The magnetic structure was investigated by a magneto-optical Kerr effect (MOKE) microscope. The MOKE microscope was equipped with a handmade coil applying OOP magnetic fields and an IP electromagnet. The OOP coil was used in a pulse mode and produced magnetic fields with an amplitude of up to 60 mT and a width down to 2 ms. The scheme for the measurement of the DW velocity was as follows. Using focused ion etching, an artificial defect was made on the surface of the sample, on which a circular domain was stably nucleated. A constant IP magnetic field was switched on. The pulse of the OOP magnetic field of the calibrated time-length was applied. The distance at which the DW propagated was measured from a snapshot of differential magnetic contrast made by the Kerr microscope. The velocities of the left and right DWs were measured separately, after which the results were averaged.

3. Results and discussions

The RHEED streaks confirm the well-ordered crystalline structure of the layers. Increasing the thickness of the Cu layer did not affect the crystal structure, as judged by RHEED (Fig. 1). However, as the thickness of Cu layer increases, the mechanism of film growth changes from Frank-van der Merwe (layer-by-layer) to Stranski-Krastanov (layered-island), which is accompanied by an increase in the surface roughness. A root-mean-square (RMS) roughness of the Cu layer increases from 105 to 712 pm in the thickness interval of the Cu layer from 2 to 12 nm.

Magnetic hysteresis loops are shown in Figure 2. As the Cu layer thickness increases, the perpendicular anisotropy field slightly decreases from 1.24 at 2 nm to 1.13 at 12 nm. The coercive force increases from 10 to 26.5 mT. The increase in the coercive force with an increase in the thickness of the Cu layer is explained by stronger pinning of domain walls on roughness-induced pinning centers.

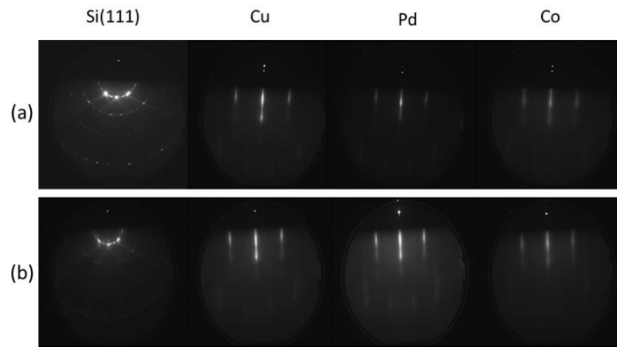


Fig. 1. RHEED patterns of Si, Cu, Pd and Co layers in (a) Cu(2)/Pd(3-10 nm)/Co(0.7 nm)/Pd(3 nm), Cu(2-12)/Pd(3 nm)/Co(0.7 nm)/Pd(3 nm) (b) samples.

$v(H_x)$ dependencies of the sample with the thickness of the Cu layer of 2 nm demonstrate strong asymmetry as shown in Fig. 3. With increasing of the Cu thickness, $v(H_x)$ dependencies change significantly. The minima in the velocity dependencies of DWs are observed in the near zero in-plane magnetic fields. In large values of H_x , we observe a maximum in the $v(H_x)$ dependencies with further decrease in the velocity in the largest IP magnetic fields. There is a strong decrease in the asymmetry of the $v(H_x)$ dependencies if compare the samples with the thickness of the Cu layer of 2 and 12 nm.

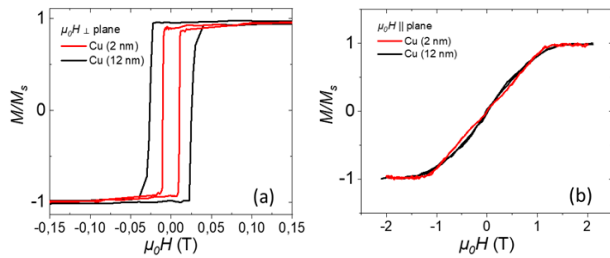


Fig. 2. (a) The OOP and (b) IP magnetic hysteresis loops for the samples with the thickness of the Cu layer of 2 and 12 nm.

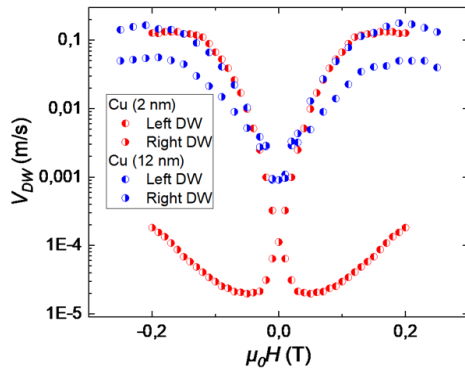


Fig. 3. The dependencies of the velocity of DWs on IP magnetic fields at different Cu thickness in the Pd/Co/Pd epitaxial system.

4. Conclusions

As the thickness of the Cu layer increases from 2 to 12 nm, the RMS roughness of the surface of Cu layer increases from 105 to 712 pm. An increase in roughness leads to a slight decrease in the effective magnetic anisotropy field from 1.24 to 1.13 T and an increase in the coercive force from 10 to 26.5 mT. The asymmetry of the $v(H_x)$ dependencies depends in a complex way on the roughness of the interfaces, and in the Cu/Pd(d_{Pd})/Co/Pd system, the asymmetry increases with increasing roughness, while in

the Cu(d_{Cu})/Pd/Co/Pd system under study, on the contrary, it disappears.

Acknowledgements

The work of Turpak A.A., Pashenko A.S. and Davydenko A.V. was supported by the Russian Science Foundation, grant No. 25-22-20079, <https://rscf.ru/project/25-22-20079/>. Chernousov N.N., Kozlov A.G. acknowledge the state assignment of the Ministry of Science and Higher Education of the Russian Federation (project No. FZNS-2023-0012).

References

- [1] S. Parkin, S.-H. Yang. Nature Nanotechnology **10**(2015)195-8.
- [2] A.V. Davydenko, A.G. Kozlov, N.N. Chernousov et al. ACS Applied Electronic Materials **6**(2024)1094.

Magnetic structure of bilayered thin films Pt/Co/(CoO)

Kuznetsova M.A.^{*}, Turpak A.A., Prihodchenko A.V., Kozlov A.G.

Far Eastern Federal University, 8 Sukhanova St., Vladivostok 690950, Russia

^{*}e-mail: kuznetcova.mal@dvfu.ru

Abstract. The paper presents the results of an experimental study of thin single-layer Pt/Co, Pt/Co/CoO, and bilayer [Pt/Co/(CoO)]₂ thin magnetic films deposited by magnetron sputtering. The aim of the study was to determine how oxidation affects the magnetic parameters of the Pt/Co and Co/CoO interfaces in the case of layer repetition. The existence of perpendicular magnetic anisotropy was proven. The correlation between magnetic and structural parameters and also dependence on number of oxidation layer has been established.

1. Introduction

Pt/Co and Pt/Co/MO_x films (where M is an oxidizable metal such as Gd [1], Al [2], or Ni [3]) are of significant interest in spintronics due to the emergence of perpendicular magnetic anisotropy (PMA) [4], spin-orbit torque generation via the spin Hall effect [5], and the Dzyaloshinskii-Moriya interaction (DMI) [6]. At the Pt/Co interface, PMA arises from the hybridization between the 5d electrons of the heavy metal Pt (which exhibits strong spin-orbit coupling) and the 3d electrons of the ferromagnetic Co layer [7]. Oxidation of the ferromagnetic layer can enhance PMA and DMI strength, as demonstrated in studies of Pd/Co/CoO systems [8–9], and may also induce exchange bias at low temperatures [10].

Although the Pt/Co/CoO system remains relatively unexplored, it holds promise for the aforementioned effects, making it a potential candidate for future applications such as skyrmion-based racetrack memory [11], magnetic sensors [12], and other spintronic devices.

2. Experiment

The samples were prepared using magnetron sputtering under high vacuum conditions, with the SiO₂ substrate rotating at a speed of 40 rpm. The layer structure consisted of an initial 5 nm Pt layer, followed by a 1 nm Co layer, a 2 nm intermediate Pt layer, and a final 3 nm Pt capping layer. The Co layer was oxidized in the magnetron load chamber under a constant pressure of $P = 10^{-3}$ Torr for two minutes. The films were heated in a vacuum oven for 10 minutes at $T = 300^\circ\text{C}$.

The magnetic properties (magnetic moment, anisotropy field, coercive force) were determined by analyzing hysteresis loops measured using a vibrating sample magnetometer (VSM). Additionally, domain wall motion dynamics were studied using Kerr microscopy (EvicoMagnetics), and layer roughness was evaluated based on X-ray reflectometry (XRR) spectra.

3. Results and discussions

All samples were characterized by the presence of perpendicular magnetic anisotropy (Fig. 1 (a)). The strongest anisotropy is realized with a larger number of oxidation layers.

After heating (red dots), mainly a decrease in PMA is observed, the magnetization of the samples increased significantly (Fig. 1 (b)), which indicates the displacement of the CoO layer and the presence of a Pt-Co alloy at the interface (the proximity effect is manifested).

The magnetic parameters of the samples turned out to be different not only depending on the number of oxidized layers, but also on the order of the oxidized layer (first or second layer). This can be caused by a change in the crystal structure of the Co/(CoO) layers.

The coercivity changes as a result of the redistribution of defects (Fig. 1 (c)).

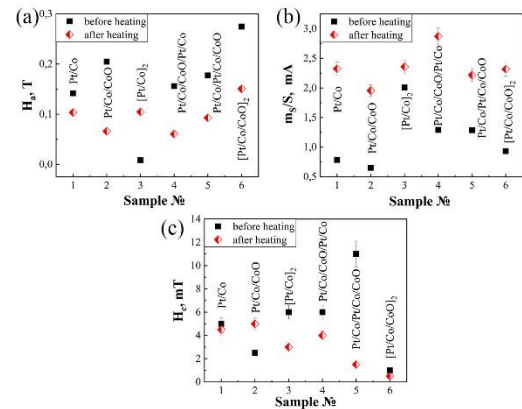


Fig. 1. Magnetic parameters of samples after and before heating (a) anisotropy field, (b) saturation magnetization per area, (c) coercive force.

The roughness in Fig. 2(a) confirms that varying the order of oxidation of the layers results in different parameters of the crystal structure.

Oxidation results in an increase in the Co/(CoO) layer, as shown in Fig. 2(b), beyond the initial cobalt thickness of 1 nm.

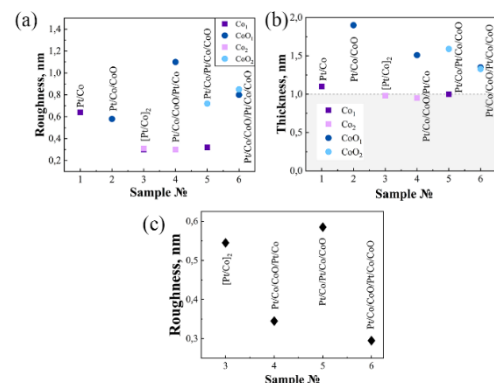


Fig. 2. XRR-measurements (a) roughness of Co/(CoO) layers, (b) thickness of Co/(CoO) layers, (c) roughness of Pt-interlayer in bilayers systems.

The presence of the oxide results in a decrease in the roughness of the intermediate Pt layer, as shown in Fig.2(c).

The domain structure, examined with a Kerr microscope, showed the presence of small and jagged domains (Fig. 3).

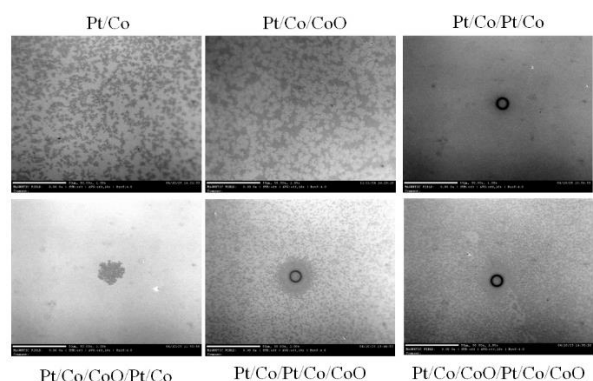


Fig. 3. Kerr-images of domain structure after the impulse of perpendicular field $H_z = 10,8 \text{ mT}$.

4. Conclusions

The study determined:

1. In polycrystalline films deposited by magnetron sputtering, the order of the oxidized layer is important;
2. Pt/Co/(CoO)/Pt films are characterized by the presence of perpendicular magnetic anisotropy, with a greater number of oxidized layers corresponding to a greater value of the anisotropy field;
3. A decrease in magnetic anisotropy and an increase in the magnetic moment is associated with the displacement of the oxide layer and the release of bulk Co;
4. According to reflectometry data, the thickness of CoO is greater than the thickness of Co.

Acknowledgements

The work was supported by the Ministry of Science and Higher Education of the Russian Federation (project No. FZNS-2023-0012).

References

- [1] Li M. et al. Magnetic properties and microstructural analyses of Pt/Co/Gd₂O₃ films //Vacuum. – 2022 – T. 205 – C. 111410.
- [2] Schott M. et al. Electric field control of interfacial Dzyaloshinskii-Moriya interaction in Pt/Co/AlO_x thin films //Journal of Magnetism and Magnetic Materials. – 2021 – T. 520 – C. 167122.
- [3] Lin K. W. et al. In-plane and perpendicular exchange bias in [Pt/Co]/NiO multilayers //physica status solidi (a). – 2007 – T. 204 – №. 12 – C. 3970-3974.
- [4] Kisielewski M. et al. Magnetic anisotropy and magnetization reversal processes in Pt/Co/Pt films //Journal of magnetism and magnetic materials. – 2003 – T. 260 – №. 1-2. – C. 231-243.
- [5] Chen S. et al. Temperature dependence of spin-orbit torques in Pt/Co/Pt multilayers //Journal of Physics D: Applied Physics. – 2018 – T. 51 – №. 9 – C. 95001.
- [6] Wells A. W. J. et al. Effect of interfacial intermixing on the Dzyaloshinskii-Moriya interaction in Pt/Co/Pt //Physical review B. – 2017 – T. 95 – №. 5 – C. 54428.

- [7] Yang H. et al. Anatomy of dzyaloshinskii-moriya interaction at Co/Pt interfaces //Physical review letters. – 2015 – T. 115 – №. 26 – C. 267210.
- [8] Kozlov A. G. et al. Effects of Interfacial Nanoengineering through an Artificial Oxidation of Epitaxial Pd/Co Ultrathin Films on Perpendicular Magnetic Anisotropy and the Dzyaloshinskii-Moriya Interaction //ACS Applied Electronic Materials. – 2024 – T. 6 – №. 7 –C. 4928-4938.
- [9] Kozlov A. G. et al. Magnetic Properties of Epitaxial [Pd/Co/CoO]_n Superlattices //Journal of Magnetism. – 2024 – T. 29 – №. 1 – C. 143-148.
- [10] Anyfantis D. I. et al. Magnetic anisotropies and exchange bias of Co/CoO multilayers with intermediate ultrathin Pt layers //Materials. – 2023 – T. 16 – №. 4 – C. 1378.
- [11] Parkin S., Yang S. H. Memory on the racetrack //Nature nanotechnology. – 2015 – T. 10 – №. 3 – C. 195-198.
- [12] Lenz J., Edelstein S. Magnetic sensors and their applications //IEEE Sensors journal. – 2006 – T. 6 – №. 3 – C. 631-649.

Motion of the ground state of the Edwards-Anderson spin system in the state space under the action of an external field

Lobanova E.A.^{*1,2}, Makarov A.G.^{1,2}, Nefedev K.V.^{1,2}

¹ Institute of Applied Mathematics, 7 Radio St., Vladivostok 690000, Russia

² Far Eastern Federal University, 10 Ajaks settlement, Russky Island, Vladivostok 690922, Russia

*e-mail: lobanova.eal@dvfu.ru

Abstract. We study the ground state of the Edwards-Anderson spin glass model with open boundary conditions in an external field using exact computations.

1. Introduction

The ground state properties of the Ising model on various lattices with competing ferromagnetic and antiferromagnetic interactions have been studied for many years [1–6]. Despite extensive research, the nature of the low-temperature phase in spin systems with a limited interaction range remains unclear [7]. Two key open questions concern the properties of spin glasses at zero temperature — specifically, the number of ground states and the nature of low-lying excitations above them [8].

The Edwards-Anderson spin glass model is one of the simplest examples of spin glass systems with short-range interactions. Despite its apparent simplicity, many of its properties in two and higher dimensions remain poorly understood, including some of the most fundamental characteristics at $T=0$ [9]. The challenge in analyzing this model stems from the fact that determining its ground state constitutes one of the most difficult problems in combinatorial optimization. In three dimensions, this problem is known to be NP-hard [10], meaning that no algorithm is currently known that can solve it in time polynomial in the system size — and it is widely believed that no such algorithm exists.

2. Numerical experiment

We introduce the notation for the minimum of the Hamiltonian:

$$H = E_{GS} - \sum_{\langle ij \rangle} J_{ij} S_i S_j - h \sum_i S_i = E_0 - hM, \quad (1)$$

where E_0 is the interaction energy, and hM is the Zeeman energy. Naturally, as the external field h increases, these two contributions must balance in such a way as to minimize the total energy and thus determine the ground state. This correlation is illustrated in Fig. 1. Therefore, the number of relevant transitions is determined solely by those states in which the spin excess M increases monotonically with increasing energy.

To characterize the influence of the density of states on the number of transitions — while excluding states that do not satisfy the monotonicity condition — we construct a transition graph between interaction energies corresponding to the minimal field values at which each state becomes the ground state.

$$E_{0n} - hM_n < E_{0(n+1)} - hM_{n+1}. \quad (2)$$

The algorithm for finding energy minima involves constructing a graph of transitions between states,

determining the minimal values of the external field at which these transitions occur, and then selecting from this graph only those transitions that are realized under a monotonically increasing field. From the graph (Table 1), it is evident that some transitions exhibit an energy difference greater than two, leading to the omission of certain intermediate transitions in subsequent rows. Furthermore, transitions corresponding to the same value of h should be grouped into a single step in the graph, since that field strength is sufficient to reach the highest-energy state within the sequence.

Table 1. Transition graph between states (from a series of states where spin excess increases monotonically with increasing energy), occurring at the minimal field values h .

$E_{0n}, M_n \rightarrow E_{0(n+1)}, M_{n+1}$	h
-82, 12 \rightarrow -80, 18	0.33
-80, 18 \rightarrow -76, 24	0.66
-78, 20 \rightarrow -76, 24	0.5
-76, 24 \rightarrow -74, 26	1.0
-74, 26 \rightarrow -72, 28	1.0
-72, 28 \rightarrow -70, 30	1.0
-70, 30 \rightarrow -68, 32	1.0
-68, 32 \rightarrow -66, 34	1.0
-66, 34 \rightarrow -64, 36	1.0
-64, 36 \rightarrow -62, 38	1.0
-62, 38 \rightarrow -54, 44	1.33
-58, 40 \rightarrow -56, 42	1.0
-56, 42 \rightarrow -54, 44	1.0
-54, 44 \rightarrow -50, 46	2.0
-50, 46 \rightarrow -46, 48	2.0
-46, 48 \rightarrow -42, 50	2.0
-42, 50 \rightarrow -38, 52	2.0
-38, 52 \rightarrow -34, 54	2.0
-34, 54 \rightarrow -28, 56	3.0
-28, 56 \rightarrow -22, 58	3.0
-22, 58 \rightarrow -16, 60	3.0
-16, 60 \rightarrow -8, 62	4.0
-8, 62 \rightarrow 0, 64	4.0

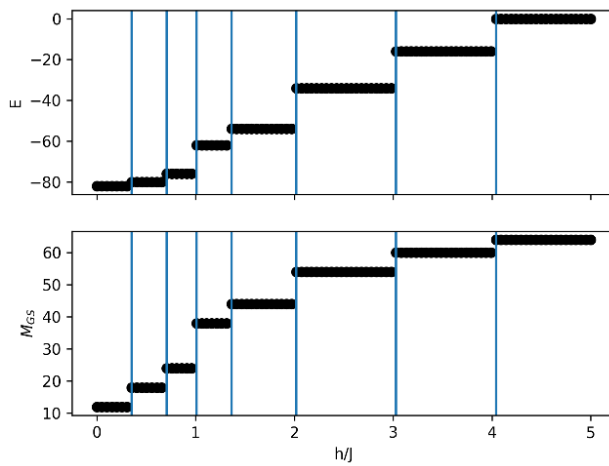


Fig. 1. Interaction energy and spin excess for ground states in different external fields. Spin glass model with $J=+1$ in 50% of cases.

3. Results and discussions

The proposed algorithm can be employed to identify symmetries in the distribution of exchange integrals across the system in linear time. The number of remagnetization events observed in the plot (Fig. 1) reflects how many spins must flip simultaneously for the system to transition between metastable states. The abundance of such states leads to a critical slowing down of Monte Carlo thermalization at low temperatures. It can be hypothesized that excluding the algorithm-defined states from the simulation may accelerate this process. In turn, this could enable a more efficient reconstruction of the density of states.

4. Conclusions

The presented numerical algorithm enables a comprehensive exploration of the system's state landscape in terms of stability. Its main limitation lies in the requirement to know the energies and spin excesses of all possible system states. Previous studies have shown that, in disordered systems, the density of states may exhibit anomalous features associated with the formation of metastable states [11]. Therefore, the ordered and disordered phases can potentially be distinguished by analyzing the number of such states across different systems.

Acknowledgements

The research was supported by the Russian Science Foundation grant No. 24-71-10069, <https://rscf.ru/en/project/24-71-10069/>.

References

- [1] Lebrecht W. et al. *Physica A: Statistical Mechanics and its Applications* **342**(2004)90-96.
- [2] Binder, K., & Young, A. P. *Reviews of Modern physics*, **58**(1986)801.
- [3] Mézard M., Parisi G., Virasoro M. A. World Scientific Publishing Company **9**(1987).
- [4] Valdés, J. F., W. Lebrecht, and E. E. Vogel. *Physica A: Statistical Mechanics and its Applications* **391.8**(2012)2585-2599.
- [5] Lebrecht, W., and J. F. Valdés *Physica A: Statistical Mechanics and its Applications* **422**(2015)89-100.
- [6] Fan, Changjun, et al. *Nature communications* **14.1**(2023)725.

- [7] Newman, C. M., N. Read, and D. L. Stein. *Physical Review Letters* **130.7**(2023)077102.
- [8] Newman, C. M., and D. L. Stein *Physical Review E* **105.4**(2022)044132.
- [9] Pál, Károly F *Physica A: Statistical Mechanics and its Applications* **223.3-4**(1996)283-292.
- [10] Barahona, Francisco *Journal of Physics A: Mathematical and General* **15.10**(1982)3241.
- [11] De Dominicis, Cirano, and Irene Giardinà. *Random fields and spin glasses: a field theory approach*. Cambridge University Press, 2006.

SOT and DMI in $\text{WTe}_x/\text{Pt}/\text{Co}/\text{MgO}$

Namsaraev Zh.Zh.^{*1}, Turpak A.A.¹, Kuznetsova M.A.¹, Wang Y.², Kozlov A.G.¹

¹ Far Eastern Federal University, 8 Sukhanova St., Vladivostok 690950, Russia

² Dalian University of Technologies, Dalian, China

*e-mail: namsaraev.zhzh@dvfu.ru

Abstract. The hysteresis loop shift method was used to measure Pt/Co/MgO and $\text{WTe}_x/\text{Pt}/\text{Co}/\text{MgO}$ thin films to evaluate the efficiency of the spin-orbit torque (SOT) and the Dzyaloshinsky-Moriya (DMI) interaction. A significant increase in the remagnetization efficiency was found when using the WTe_x sublayer, which gradually decreases as the Pt interlayer increases.

1. Introduction

Current-induced spin-orbit torque (SOT) is an efficient way of manipulating the magnetization in heavy-metal/ferromagnet (HM/FM) heterostructures. The development of SOT-MRAM devices places very serious demands on the materials on the basis of which the mechanisms of current-induced magnetization reversal are implemented. First, such materials and heterostructures should exhibit perpendicular anisotropy. Secondly, the critical switching current should be as low as possible to avoid overheating and degradation of the heterostructure, and thirdly, there should be a nonzero chiral energy of the Dzyaloshinsky-Moriya interaction to stabilize the topological structures. One of the most suitable candidates for the role of heterostructures for SOT-MRAM are films of the Pt/Co/MgO type, in which the SOT mechanism is implemented through the spin Hall effect. However, the value of the critical current density remains quite high. Reducing the critical current density is possible by including a layer in the heterostructure that would play the role of a spin generator. Heavy metal dichalcogenides, for example, WTe_2 , can be used as spin generators, since they have a strong spin-orbit coupling and, accordingly, a large angle of the spin Hall effect [1]. In our work, we investigated the effect of WTe_x added as a sublayer on the efficiency of current-induced magnetization switching of Pt/Co/MgO films.

2. Experiment

The samples for the study were multilayer polycrystalline films Pt/Co/MgO and $\text{WTe}_x/\text{Pt}/\text{Co}/\text{MgO}$ grown by magnetron sputtering. The efficiency of current-induced SOT was evaluated using the loop shift method [2]. This method allows you to simultaneously quantify the effectiveness of DL ST (damping-like spin torque) and the magnitude of the effective DMI field. A constant planar field H_x acts on the sample, which is used to reorient the domain wall moments affected by DMI. The H_z field sweep is used to obtain an out-of-plane hysteresis loop by measuring the anomalous Hall effect (AHE) at an applied direct current I_{DC} . The combination of a planar field and current creates an out-of-plane constant effective magnetic field along the z axis due to the SOT ($\pm B_z^{SOT}$) effect, which shifts the hysteresis loop to the left or right for different orientations of the current direction. The estimation of the mutual displacement between the coils at different current orientations allows us to determine the magnitude of this field, Figure 1.

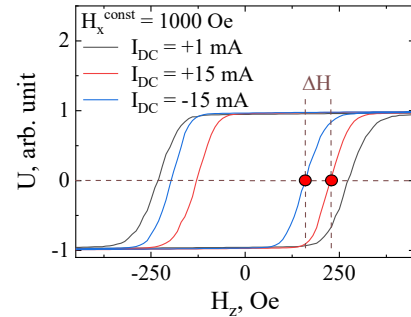


Fig. 1. The offset ΔH of hysteresis loop induced by the current in constant field H_x .

Figure 2 shows the dependences of coercive forces, highlighted in red H_c^{left} and black H_c^{right} , and the dependence, highlighted in blue, demonstrates the displacement of hysteresis loops from the magnitude and direction of I_{DC} , relative to the zero H_z field.

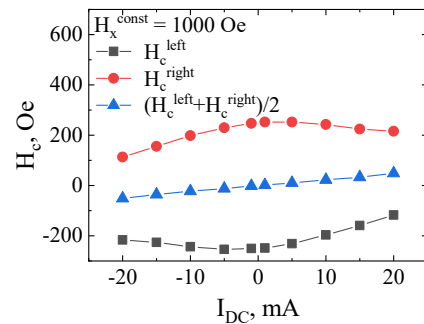


Fig. 2. Switching fields and the magnitude of the displacement of the hysteresis loops relative to zero in the H_z field from the I_{DC} current.

Having determined the value of the offset between multidirectional I_{DC} of the same magnitude, we obtain the dependence of H_{eff}^z on I_{DC} , while I_{DC} must be converted to current density J_{DC} , Figure 3. From this dependence, we can obtain the value of efficiency SOT – $\chi = H_{eff}^z / J_{DC}$.

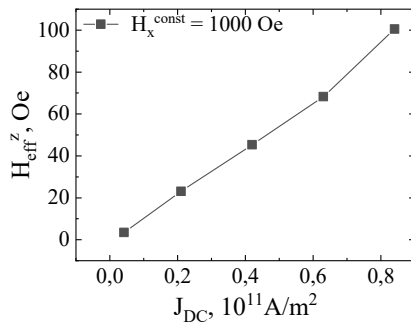


Fig. 3. The magnitude of the effective field generated by the SOT effect from the current density passed through the sample.

Further, by making similar measurements at different H_x^{const} , it is possible to build a dependence of χ on H_x^{const} . The dependence reaches saturation when the planar field overcomes the effective field generated by DMI and when the effective field generated by SOT stops growing. From this, the effectiveness of SOT and H_{DMI} can be determined.

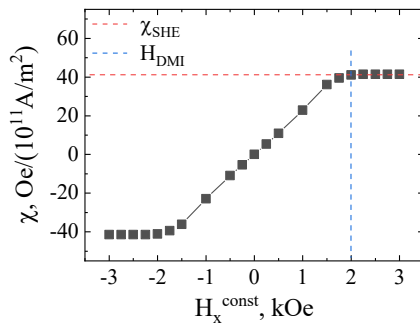


Fig. 4. SOT efficiency and effective DMI field from the planar field acting on the sample.

3. Results and discussions

For each sample, H_{eff}^z graphs from J_{DC} were plotted, Figure 5, from which χ were determined and the dependence of χ on H_x^{const} was plotted, Figure 6.

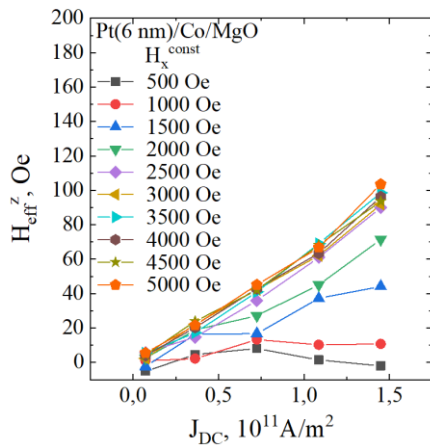


Fig. 5. Dependences of the effective field generated by the SOT effect on the current density passed through the sample at different planar fields.

Also, a similar dependence is built on a single current value, for comparison.

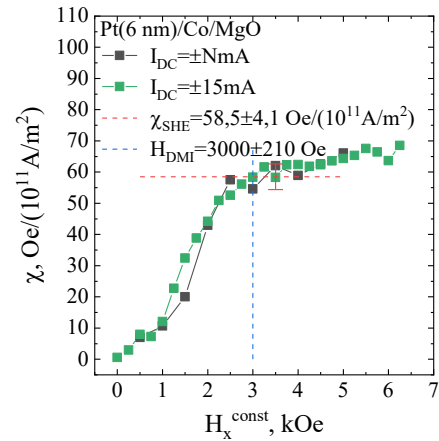


Fig. 6. The SOT efficiency and the effective DMI field depend on the planar field acting on the sample from two measurement methods – at different current values and at the same current value.

Figure 7 shows the final graphs for two series of samples.

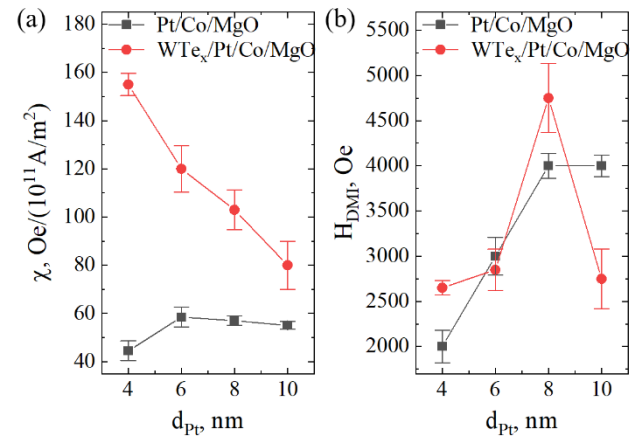


Fig. 7. (a) SOT efficiency depends on the thickness of the Pt layer. (b) Effective DMI field depends on the thickness of the Pt layer.

4. Conclusions

In this paper, the effect of the WTe_x layer on the magnetotransport properties of thin Pt/Co/MgO films is demonstrated. SOT and DMI. A significant increase in the remagnetization efficiency was shown when using the WTe_x sublayer, which gradually decreases as the Pt interlayer increases, and the largest increase in the SOT efficiency, almost four times, was found in $\text{WTe}_x/\text{Pt}(4 \text{ nm})/\text{Co}/\text{MgO}$ films compared with films without a topological sublayer.

Acknowledgements

This work was supported by Russian Scientific Foundation project №23-42-00076, <https://rscf.ru/project/23-42-00076/>.

References

- [1] Sharma P. et al. «A room-temperature ferroelectric semimetal» // Sci. Adv. 2019. Vol. 5, № 7.
- [2] Pai C.-F. et al. «Determination of spin torque efficiencies in heterostructures with perpendicular magnetic anisotropy» // Phys. Rev. B. 2016. Vol. 93, № 14. P. 144409.
- [3] Thiaville A. et al. Dynamics of Dzyaloshinskii domain walls in ultrathin magnetic films // EPL (Europhysics Lett. 2012. Vol. 100, № 5. P. 57002.

Influence of structure on magnetic properties of Pt/Co/MgO and WTe_x/Pt/Co/MgO films

Prikhodchenko A.V.^{*1}, Kuznetsova M.A.¹, Meng F.Y.², Feng Y.², Wang Y.² and Kozlov A.G.¹

¹ Far Eastern Federal University, Ajax 10, Vladivostok 690041, Russia

² Dalian University of Technology, Dalian 116024, China

*e-mail: prikhodchenko.av@dvfu.ru

Abstract. Comprehensive research of the structure and main magnetic properties of Pt/Co/MgO films on SiO₂ and Al₂O₃ substrates were performed, and the effect of the WTe_x underlayer was investigated. The thickness of the Pt layer in the films was varied, and its effect on the structural and magnetic parameters was studied. Depending on the thickness, Pt demonstrates both an amorphous and a crystalline structure. It was found that, depending on the substrate type, the growth mechanism of Pt and the upper layers changes, despite the presence of a disordered WTe_x layer. The choice of the substrate type, in turn, determines the parameters of the WTe_x interface. Differences in the roughness of the interfaces, the density of the material, and the growth rate of the average Pt grain size were revealed, which affects the growth of the Co layer.

1. Introduction

Ultrathin magnetic films are used as base materials for creating spintronic devices. The most promising are heterostructures with an ultrathin magnetic layer about 1 nm thickness and additional functional layers of non-magnetic materials, such as heavy metals. Prospects for developing information storage and recording media based on the spin-orbit torque (SOT) effect motivate the search for the materials that can meet the requirements of strong perpendicular magnetic anisotropy (PMA) and a large SOT effect simultaneously. Also, in recent years, two-dimensional materials and ultrathin magnetic films containing transition metal dichalcogenides (TMDs) have been intensively studied in the field of spintronics. Such materials have a strong spin-orbit coupling, which in turn determines the high efficiency of SOT [1], which is manifested in a significant decrease in magnetization switching currents. For example, the use of WTe₂ can provide an order of magnitude decrease in the critical current due to an increase in the spin Hall effect angle compared to heavy metals. It is known that magnetic characteristics are directly determined by the crystalline structure of the material [2]. Thus, the aim of this work was to determine the influence of the structural parameters of Pt/Co/MgO thin films on their magnetic properties. The effect of adding a WTe_x sublayer on the main magnetic properties was studied.

2. Experiment

The objects of the study were three series of samples in which the platinum thickness was varied. Series №1: SiO₂/Pt(2-10 nm)/Co(0,9 nm)/MgO(2 nm)/SiO₂ (4 nm); series №2: SiO₂/WTe_x (7 nm)/Pt(2-10 nm)/Co(0,9 nm)/MgO(2 nm)/SiO₂ (4 nm); series №3: Al₂O₃/WTe_x (7 nm)/Pt(2-10 nm)/Co(0,9 nm)/MgO(2 nm)/SiO₂ (4 nm). All samples were grown by magnetron sputtering with subsequent annealing at 300 °C. A quartz microbalance method was used to control the thickness of the layers. The topological material tungsten ditelluride was deposited from a WTe₂ target, however, with the chosen method, a violation of the stoichiometric ratio should be expected, therefore, further in the text, the topological layer is designated as WTe_x.

Structural studies were carried out using X-ray diffraction (XRD) and X-ray reflectometry (XRR) methods. Both methods were implemented using a Colibri (Burevestnik) X-ray diffractometer, where Cu(29) is used as an anode. X-ray diffraction spectra and reflectometric curves were measured. The vibrating-sample magnetometer (7410 VSM, LakeShore) was used to study the magnetic parameters of the films. Magnetic hysteresis loops were measured in a field applied perpendicular and parallel to the plane of the samples.

3. Results and discussions

According to XRD studies, Pt shows crystalline growth in the (111) plane. In thicker samples equivalent (222) plane Pt peaks were found. WTe_x obtained by magnetron sputtering is characterized by an amorphous structure [3, 4], which is confirmed by the absence of peaks in the spectra. It is expected that the diffraction peaks of Pt will be observed for the (111) plane at $2\theta = 39,239^\circ$, for the (222) plane at $2\theta = 84,371^\circ$ [5]. In our case, a shift of the spectrum line along the 2θ angle axis is observed and is fixed for the (111) plane in the range from $39,673^\circ$ to $39,931^\circ$, for the (222) plane in the range from $85,566^\circ$ to $86,144^\circ$. The difference between the reference and measured values of $\Delta 2\theta$ indicates the presence of crystalline stresses in the film caused by the compression of the crystal lattice. With an increase in the thickness of the Pt layer in series №2 and №3, the degree of deformation of the crystal lattice increases, in series №1 it decreases (Fig. 1a). However, in the selected range of thicknesses, the stresses are not completely removed. It should be noted that an increase in stress is observed in the Pt layer only in the presence of a WTe_x sublayer.

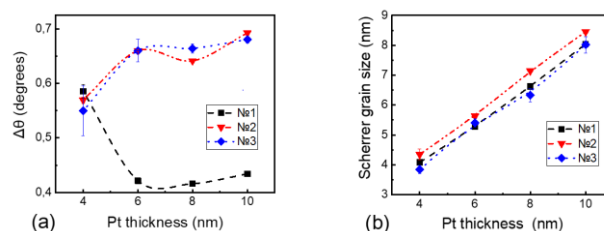


Fig. 1. Graphs of the dependences of a) $\Delta 2\theta$ and b) average crystallite sizes on the thickness of the Pt layer.

The average sizes of Pt grains were determined using the Scherrer formula [6]. It was found that the highest grain growth rate was demonstrated by a series of films grown on $\text{SiO}_2/\text{WTe}_x$ substrates (Fig.1b).

It was found that the sample series have different Pt roughness (Fig. 2). Samples of series №1 demonstrate the lowest roughness. The obtained trend (Fig. 2a) for series №1 can be associated with the linear growth of the average grain size. In series №2 and №3, Pt grows on the WTe_x layer, which has a higher roughness compared to the substrate (Fig. 2b). However, for most samples, Pt has a lower roughness than the WTe_x sublayer. This indicates that Pt first fills the surface irregularities, and after reaching a certain thickness, the roughness increases with increasing thickness in the island growth mode. On the single-crystal Al_2O_3 substrate, the WTe_x/Pt interface has the highest roughness, so smoothing is observed for all samples.

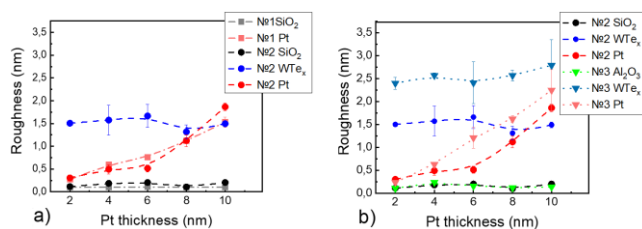


Fig. 2. Roughness of WTe_x , Pt layers and substrates from Pt thickness for series a) №1 and №2, b) №2 and №3.

Based on the measured magnetic hysteresis loops, the dependences of the coercive force (H_c) and the effective anisotropy constant (K_{eff}) on the Pt layer thickness were constructed (Fig. 3). All films with a Pt thickness of more than 2 nm demonstrate PMA, the value of which strongly depends on the thickness of the Pt underlayer. The magnetization reversal process is carried out by the nucleation and displacement of domain boundaries.

The value of H_c is affected by a lattice stress, grain size, interface roughness, etc. At small Pt thicknesses, films of all series demonstrate a small value of H_c (Fig. 3a), which is due to the small roughness and stresses of Pt. An increase in thickness is accompanied by a change in the steepness of the graphs. H_c increases by an order of magnitude with an increase in the Pt thickness. Adding a WTe_x sublayer grown on SiO_2 leads to reduce of H_c . For series №1, in the entire range of thicknesses, the values of H_c are higher than in the other series.

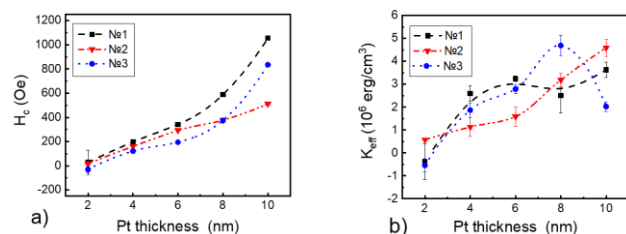


Fig. 3. Graphs of the dependences of a) the coercive force and b) the effective anisotropy constant on the thickness of the Pt layer.

Films of series №1 and №3 with a Pt thickness of 2 nm demonstrate weak in plane anisotropy (Fig. 3b). As the Pt layer thickness increases, an increase in the anisotropy field is observed, which can be explained by the improvement of the Pt crystal structure and an increase in roughness, which leads to a decrease in the effective Co thickness. Addition of the WTe_x layer leads to an increase in the effective

anisotropy energy at high Pt thicknesses. But for series №3, after 8 nm Pt, a decrease in K_{eff} is observed. Perhaps, this is due to the high roughness of Pt, which leads to a violation of the homogeneity of the Co film.

4. Conclusions

The studies of Pt/Co/MgO films with the addition of WTe_x topological material on SiO_2 and Al_2O_3 substrates were carried out. Based on the magnetic hysteresis loops, the dependences of the magnetic parameters on the Pt sublayer thickness were analyzed. The growth of crystallites leads to an increase in the roughness of film in a series of samples without the WTe_x layer. Adding a WTe_x sublayer changes the Pt growth mode, in which the surface is smoothed, after which the roughness gradually increases. The crystalline quality of the grains is somewhat better when growing on a WTe_x sublayer. This leads to improved magnetic characteristics. The coercive force decreases, the anisotropy demonstrates smoother growth, which in turn allows for more precise control. The highest anisotropy is demonstrated by films deposited on Al_2O_3 , which is determined by the crystalline nature of the substrate.

Acknowledgements

The authors thank the Russian Scientific Foundation, Project No 23-42-00076.

References

- [1] Qidong Xie, Weinan Lin, Baishun Yang et al Giant Enhancements of Perpendicular Magnetic Anisotropy and Spin-Orbit Torque by a MoS₂ Layer // Advanced Materials 2019 V.31.
- [2] В.О. Васильковский, М.Н. Волочаев, А.Н. Горьковенко Структурные особенности и магнитные свойства пленок Co-W // Физика твердого тела, 2021, том 63, вып. 7 с.915-922.
- [3] Cheng-Wei Peng, Wei-Bang Liao, Tian-Yue Chen Efficient spin-orbit torque generation in semiconducting WTe_2 with hopping transport // Applied materials & interfaces, 2021, V.13, 15950–15957.
- [4] Zheyu Ren, Ruizi Liu, Shunkong Cheung Strongly temperature-dependent spin–orbit torque in sputtered WTe_x // Journal of Applied Physics, 2024, V.135, 143904-1-7.
- [5] K. Persson, The Materials Project. Materials Data on Pt by Materials Project. United States: N.d., 2020. Web. doi:10.17188/1189002.
- [6] Patterson, A. The Scherrer Formula for X-Ray Particle Size Determination. Phys. Rev. 56 (10). (1939) P. 978–982.

Improvement magnetic properties through transition metal alloying in Fe-Si-B amorphous matrices

Sapovskii I.M.^{*1}, Rakhmatullaev T.R.¹, Pinchuk K.E.¹, Komogortsev S.V.², Kraynova G.S.¹

¹ Far Eastern Federal University, 10 Ajax Bay, Russky Island, Vladivostok 690950, Russia

² Kirensky Institute of Physics, Federal Research Center KSC SE RAS, Krasnoyarsk 660036, Russia

*e-mail: sapovskii.im@dvfu.ru

Abstract. Comprehensive studies of temperature-dependent properties of Fe-Co-Si-B-Mn amorphous alloys using differential scanning calorimetry and vibratory vibromagnetometry have been carried out. It has been established that all the studied alloys exhibit a two-stage crystallization process. The temperatures of the phase transitions and the Curie temperatures are determined. It is found that the presence of cobalt in the composition of alloys leads to a nonmonotonic character of thermomagnetic curves. The calculation of the spin-wave stiffness constant is carried out using a modified Bloch law. The results of the study are important for understanding the effect of cobalt alloying on the magnetic properties of amorphous iron-based alloys.

1. Introduction

In recent decades, research on amorphous metal alloys has attracted considerable scientific attention due to their unique physical properties and prospects for practical application in various fields of technology. Of particular interest is the study of the effect of alloying elements on the magnetic and structural characteristics of amorphous alloys [1].

This paper focuses on the study of the effect of cobalt atoms on the amorphous Fe-Si-B matrix. The relevance of the study is due to the need to understand the mechanisms of formation of magnetic properties and structural transformations in amorphous alloys with the introduction of alloying elements.

The aim of this work is to comprehensively study the phase transitions and magnetic properties of a series of amorphous Fe-Co-Si-B-Mn alloys with different concentrations of cobalt: Fe₇₈B₁₃Si₉, Fe₆₂Co₁₈B₁₄Si₆, Fe₅₅Co₂₆B₁₄Si₅, Co₇₄Fe₃Mn₃B₁₅Si₅.

2. Experiment

To study the phase transitions and thermal processes in the studied samples, thermal analysis was performed on the DSC 404 F1 Pegasus installation. The measurements were carried out in the temperature range from 300 to 973 K with a heating rate of 10 K/s. This mode made it possible to clearly record all the characteristic temperatures of the samples.

The magnetic characteristics of the alloys were studied using an induction vibration magnetometer in the same temperature range (300-973)K. The dependences of saturation magnetization on temperature at a heating rate of 10 K/s and an external magnetic field strength of 1000 E were obtained. Additionally, magnetic hysteresis loops were investigated at room temperature to evaluate the magnetic properties of the materials.

To determine the parameters of the exchange interaction, including the spin wave stiffness constant, measurements were carried out on the PPMS 9T Quantum Design installation. The dependence of saturation magnetization on an external magnetic field in the temperature range of 50-300 K at a field strength of 1000 E was studied. The data obtained allowed for a detailed analysis of the magnetic properties of the studied samples under various temperature conditions.

3. Results and discussions

X-ray diffraction analysis confirmed the amorphous state of the initial alloys, which is characterized by the presence of an amorphous halo (Fig. 1).

When studying the thermal properties of amorphous Fe-Co-Si-B-Mn alloys by differential scanning calorimetry (DSC), a two-stage crystallization process was recorded for all samples (Fig. 2). Determining the temperatures of phase transitions allowed to correlate with the magnetic characteristics of the materials.

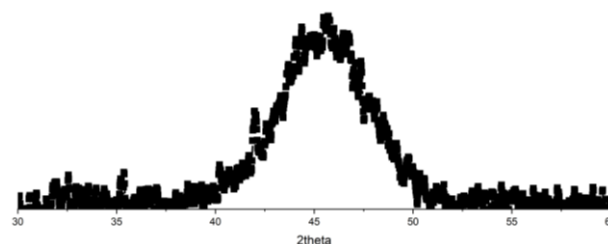


Fig. 1. Diffractogram profile of an amorphous Co₇₄Fe₃Mn₃B₁₅Si₅ alloy.

An analysis of the temperature dependences of saturation magnetization made it possible to determine the Curie temperatures and demonstrated the relationship between the nonmonotonic nature of DSC curves and thermomagnetic curves. It is noteworthy that for cobalt alloys, the saturation magnetization does not decrease to zero with increasing temperature, which indicates the presence of an additional magnetic phase with a different Curie temperature. The nature of the change in magnetization with increasing temperature corresponds to the typical behavior of amorphous alloys in the processes of structural relaxation up to the transition to a crystalline state.

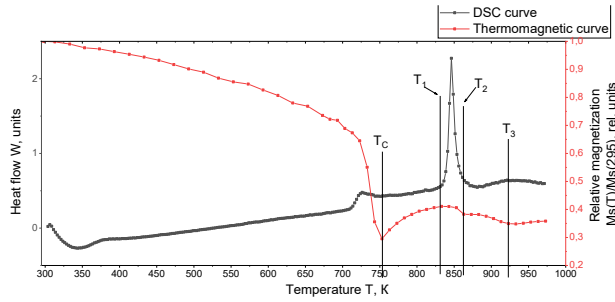


Fig. 2. DSC curve and thermomagnetic curve of the $\text{Co}_{74}\text{Fe}_3\text{Mn}_3\text{B}_{15}\text{Si}_5$ alloy.

Low-temperature studies of the saturation magnetization dependence on temperature in the range of 50-300 K (Fig. 3) revealed significant differences in the behavior of the samples. For the Fe-Si-B alloy, a standard increase in magnetization was observed with a decrease in temperature, characteristic of ferromagnets. However, cobalt alloys showed an abnormal bend in the curves in the region of 150 K.

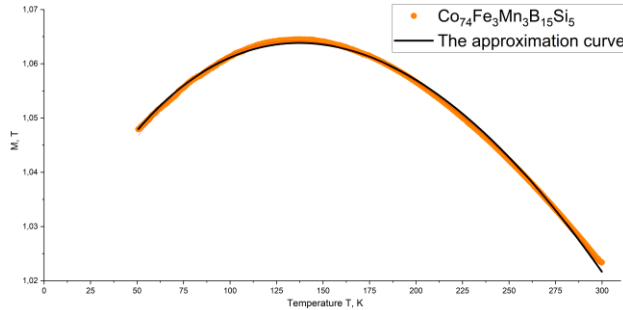


Fig. 3. Dependence of $M_s(T)$ in the temperature range from 50 to 300 K for the $\text{Co}_{74}\text{Fe}_3\text{Mn}_3\text{B}_{15}\text{Si}_5$ alloy.

For the analysis of low-temperature dependences, a modified Bloch function was used, taking into account the Holstein-Primakov correction [2]:

$$M = M_s(0) * \left(1 - B * T^{\frac{3}{2}}\right) + C' * T \quad (1)$$

$$C' = C * f_{HP} \quad (2)$$

$$f_{HP} = 3\sqrt{\mu_0 H} + \frac{M_0 + \mu_0 H}{\sqrt{M_0}} \arcsin \sqrt{\frac{M_0}{M_0 + \mu_0 H}} \quad (3)$$

Based on the obtained Bloch constant, the spin wave stiffness constant D was calculated.:

$$D = \frac{k_B}{4\pi} \left(\frac{2.612 g \mu_B \mu_0}{M_0 B} \right)^{\frac{2}{3}} \quad (4)$$

It is established that with an increase in the cobalt concentration in the Fe-Si-B matrix, an increase in the spin wave stiffness constant is observed.

4. Conclusions

The analysis of the obtained data using the modified Bloch's law made it possible to calculate the spin-wave stiffness constant, which shows a tendency to increase with increasing cobalt concentration in the Fe-Si-B matrix. The results demonstrate the prospects of modifying amorphous Fe-Si-B alloys by adding cobalt to obtain materials with modified magnetic characteristics.

References

- [1] Yu. Starodubtsev. Magnetic Properties of Amorphous and Nanocrystalline Alloys (2002).
- [2] A. Neuweiler, B. Hofmann, H. Kronmüller. Approach to magnetic saturation in nanocrystalline and amorphous $\text{Fe}_{73.5}\text{Cu}_1\text{Nb}_3\text{Si}_{13.5}\text{B}_9$ **153**(1995)28-34.

Magnetic multilayer thin films on nanorelief with modulated curvature

Rogachev K.A.^{*1}, Samardak A.Yu.¹, Bazrov M.A.¹, Shishelov A.F.¹, Samardak A.S.^{1,2},
Ognev A.V.^{1,2}

¹ Far Eastern Federal University, 8 Sukhanova St., Vladivostok 690950, Russia

² Sakhalin State University, 33, Kommunistichesky ave., Yuzhno-Sakhalinsk 693000, Russia

*e-mail: kirpers26@gmail.com

Abstract. The unique magnetic behavior of ultrathin nanostructures, whose dimensions approach atomic scales, markedly diverges from that of conventional bulk materials. This discrepancy is largely attributed to amplified quantum phenomena and surface interactions, alongside the development of specific shape anisotropy characteristics. Typically, ultrathin magnetic films exhibit in-plane magnetic alignment, where magnetization favors the film's horizontal orientation. However, under specific thickness thresholds and surface modifications, a transition to perpendicular magnetic alignment occurs, directing magnetization vertically relative to the film plane. This perpendicular alignment, combined with complex surface topography, can induce unprecedented magnetic phenomena absent in films deposited on smooth surfaces. Our research employed porous alumina matrices to engineer textured substrate surfaces, enabling detailed investigation into how such topography modulates the magnetic properties of thin films and their response to varying deposition conditions.

1. Introduction

Magnetic skyrmions are spin textures that are robust to external disturbances and are promising candidates for next-generation recording devices. However, the main challenge in implementing skyrmion-based devices is the stabilization of ordered arrays of these spin textures under ambient conditions and zero applied field. In [1], the formation and stabilization of magnetic skyrmions on arrays of self-organizing hexagonal nanodomains was demonstrated due to their curved geometry [2].

2. Experiment

In our work, we studied thin films of Pt(4 nm)/Co(0.7 nm)/Pt(2 nm) and Pt(4 nm)/[Co(0.7 nm)/Pt(2 nm)]_x/Pt(2 nm) deposited on the surface of a silicon oxide substrate and samples with a modulated nanorelief.

Matrices of anodized aluminum oxide were chosen as a method for modulating the surface relief, the synthesis of which can achieve two types of surfaces: nanodomains and nanocraters, and by varying the synthesis parameters (voltage and anodizing environment) it is possible to achieve a change in the diameters and height difference of the resulting relief. A schematic representation of the structure is shown in Figure 1.

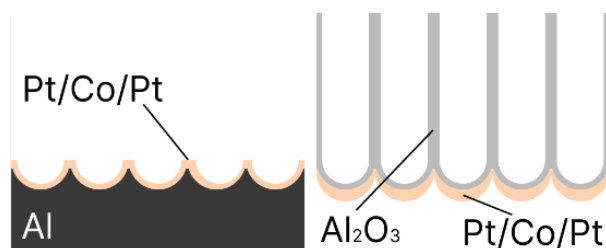


Fig. 1. Photoluminescence spectra of sample D. There is a red shift of the peak position with increasing of temperature.

The aluminum oxide matrix and the prepared aluminum surface were created by electrochemical anodizing at different voltages. Anodizing was performed using H₃PO₄ electrolyte.

The surface morphology was studied by scanning electron microscopy (SEM, ThermalScientific SCIOS 2) and atomic force microscopy (AFM, NT-MDT NTEGRA Aura). The magnetic properties of the samples were determined by vibration magnetometry (VSM, LakeShore VSM 7410). Magnetic force microscopy (AFM, NT-MDT NTEGRA Aura) was used to visualize the magnetic configuration. In addition, micromagnetic modeling of magnetization reversal processes was performed in the MuMax3 software package.

3. Results and discussions

In the first stage, a study of the surface morphology was carried out using SEM (Fig. 2), which showed that the nanodomains are a surface with nanosized protrusions, and the nanodepressions are an imprint of the nanodomains on the aluminum surface.

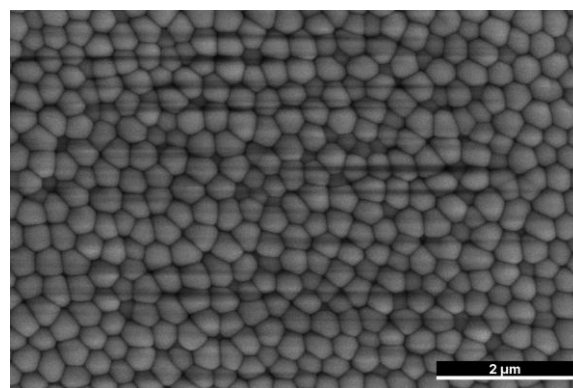


Fig. 2. SEM image of nanodomains.

Next, the surface was examined using AFM (Fig. 3). According to the results of SEM and AFM, it was found that with increasing anodizing voltage, the diameter and height of the nanorelief increase.

According to the results of studying the magnetic properties of thin multilayer films with one Co layer on the surface of the nanorelief, it was found that all samples, like the reference one, have perpendicular magnetic anisotropy. In this case, the residual magnetization and coercive force decrease with increasing diameter.

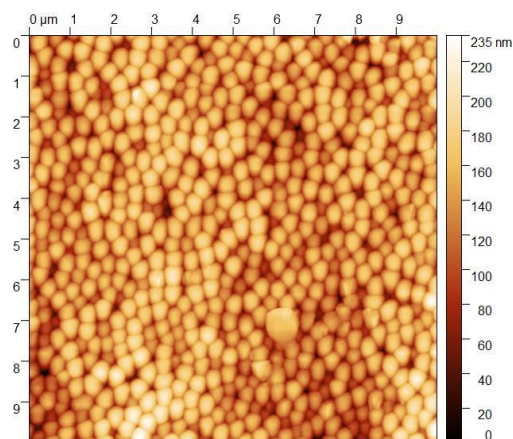


Fig. 3. Surface relief of nanodomes.

According to the results of studying the magnetic properties of thin multilayer films with 9 Co layers on the surface of the nanorelief, it was found that all samples, like the reference one and samples with one Co layer, have perpendicular magnetic anisotropy. All films obtained on the surface of the modulated nanorelief have lower residual magnetization.

To study the magnetic configuration of the samples, magnetic force microscopy was carried out, which showed that the magnetic configuration of the reference film on the surface of oxidized silicon is a labyrinthine structure. A similar structure is also observed in films obtained on a surface with a modulated nanorelief. However, films obtained on the surface of nanodomes are characterized by a greater localization of individual domains on the nanodomes. At the same time, the localization of magnetic domains on the surface of samples with nanopits was not revealed.

4. Conclusions

In this work, we investigated the magnetic properties of thin magnetic films on the surface of a modulated nanorelief of different diameters.

It was shown that the diameter and height of the nanorelief increase with increasing anodizing voltage.

The study of magnetic properties showed that all films on samples with a modulated relief have perpendicular anisotropy. In films on nanodomes, localization of magnetic domains on relief indentations is observed, which is not observed in films on nanopits.

Acknowledgements

This work was supported by the Russian Ministry of Science and Higher Education (State Task No. FZNS-2023-0012).

References

- [1] B. Tudu, A. Tiwari Vacuum. **146**(2017)329.
- [2] S. Wasef, H. Fariborzi Micromachines. **12**(2021)1345.

Magnetic state of BiFeO₃ compounds co-doped with Sm- and Ti at the morphotropic phase boundary

Silibin M.V.^{*1}, Mikhailova M.S.¹, Zhaludkevich D.V.^{1,2}, Latushka S.I.^{1,2}, Karpinsky D.V.^{1,2}

¹ National Research University of Electronic Technology "MIET", 124498 Moscow, Russia

² Scientific-Practical Materials Research Centre of NAS of Belarus, 220072 Minsk, Belarus

*e-mail: sil_m@mail.ru

Abstract. Bi_{1-y}Sm_yFe_{1-x}Ti_xO₃ ceramics with compositions at the rhombohedral- orthorhombic morphotropic phase boundary ($y \sim 0.12$, $x < 0.1$) were prepared by solid state reaction method. Crystal structure of the compounds is characterized by a coexistence of the rhombohedral and the antipolar orthorhombic phases with nearly equal volume fractions of the coexistent phases at room temperature, while the phase balance shifts towards rhombohedral phase with Ti doping and temperature decrease. Magnetization measurements demonstrate a gradual increase of remnant magnetization with Ti concentration up to $x = 0.06$ which is followed by a decrease in magnetization. Temperature decrease leads to an unexpected reduction of remnant magnetization, which is probably caused by a recovery of spatially modulated spin structure as well as an impact of unbounded spins specific for the mixed structural state of the compounds.

1. Introduction

Recent studies of the Sm doped BiFeO₃ system have clarified that the compounds at the rhombohedral-orthorhombic morphotropic phase boundary the remnant magnetization reaches its maximal value then the phase balance shifts towards the rhombohedral structural state. An evolution of the structural state of compounds Bi_{1-y}Sm_yFe_{1-x}Ti_xO₃ changes in non-trivial way with the dopants increase. The compounds Bi_{1-y}Sm_yFeO₃ with $y \sim 0.12$ are characterized by a coexistence of the dominant polar rhombohedral phase and a minor amount of the antipolar orthorhombic phase, while a complementary doping with Ti leads to stabilization of the parent rhombohedral R-phase in spite of the smaller ionic radii of the Ti ions as compared to those of the Fe ions [1]. In the present work we have focused our results on the evolution of the crystal structure and magnetic properties of Bi_{1-y}Sm_yFe_{1-x}Ti_xO₃ ceramics ($y = 0.1, 0.12$; $x \leq 0.1$) which are characterized by a dominance of the rhombohedral phase with a minor amount of the antipolar orthorhombic phase which disappears with Ti doping. The origin of non-trivial evolution of the magnetization and structural state of the compounds occurred under temperature change as well as via chemical doping are discussed.

2. Experiment

The ceramic compounds of Bi_{1-y}Sm_yFe_{1-x}Ti_xO₃ with $y = 0.12$; $0 \leq x \leq 0.1$ were prepared by a conventional solid-state reaction using high-purity oxides Bi₂O₃, Sm₂O₃, Fe₂O₃, TiO₂ (purity ≥ 99.0 %, Alfa Aesar). The mixed oxides were thoroughly mixed using a planetary ball mill RETSCH in alcohol medium for ~ 3 h. The obtained slurry was dried ($T \sim 120$ °C) and then pressed into pellets and annealed in air at $T \sim 900$ °C for ~ 20 h. After annealing, the samples were reground, pressed into pellets (10 mm in diameter, 1 mm - thickness) and sintered in air at $T \sim 960$ °C for 12 h. The crystal structure of the compounds were analyzed using X-ray diffraction data obtained with a PanAlytical X'pert Pro diffractometer with Cu-K α radiation ($\lambda = 1.5405$ Å) as well as synchrotron powder diffraction (SPD) data obtained at the BL02B2 beamline (SPring-8, $\lambda = 0.42019$ Å). The diffraction data were analyzed by the Rietveld method using FullProf software

[2]. Magnetization measurements were performed on a Physical Properties Measurement System (Cryogenic Ltd.) in magnetic fields up to 14 T in the temperature range 5–300 K.

3. Results and discussions

It is known that chemical substitution of Bi ions by Sm ions leads to structural transformation from the rhombohedral phase specific for initial BiFeO₃ to the antipolar orthorhombic phase and then to the nonpolar orthorhombic phase [3,4]. The mentioned phases having different structural symmetries can be easily distinguished by analyzing the XRD patterns, the notable difference in the metrics specific for the anti-polar orthorhombic (s.g. Pbam, $\sqrt{2}a_p \times \sqrt{2}a_p \times 2a_p$, a_p is a parameter of pseudocubic unit cell) and the non-polar orthorhombic phases (s.g. Pnma, $\sqrt{2}a_p \times 2a_p \times \sqrt{2}a_p$) also can be definitely determined as declared in the work [5]. The rhombohedral and the antipolar orthorhombic phases are coexistent in the concentration range $0.10 < y \leq 0.12$. A complementary chemical substitution of Fe ions by Ti ions in the mentioned compounds leads to a stabilization of the rhombohedral phase. Fig. 1 shows the refined diffraction pattern of the solid solution Bi_{0.88}Sm_{0.12}FeO₃ recorded using synchrotron radiation. The XRD patterns of the compounds Bi_{0.88}Sm_{0.12}Fe_{1-x}Ti_xO₃ with $0 \leq x \leq 0.10$ are presented in the inset of Fig. 1.

The XRD data confirm high phase purity of the compounds Bi_{0.88}Sm_{0.12}Fe_{1-x}Ti_xO₃ which possess a mixed structural state with a dominance of the rhombohedral phase and a minor amount of the antipolar orthorhombic phase (s.g. Pbam). The volume fraction of the orthorhombic phase gradually decreases down to local scale level as confirmed by Raman measurements.

The isothermal M(H) magnetization curves recorded for the initial compounds at room temperature are characteristic for BFO-based compounds with weak ferromagnetism [3]. At room temperature, the remnant magnetization values of the initial compound Bi_{0.88}Sm_{0.12}FeO₃ is ~ 0.16 emu/g. The magnetization loops recorded at room temperature for the compounds Bi_{0.88}Sm_{0.12}Fe_{1-x}Ti_xO₃ with $x \leq 0.4$ indicate a presence of metamagnetic transition induced by strong magnetic fields

and denoted as a mismatch in the positive part of $M(H)$ curves obtained during the first and subsequent cycles (Fig. 2).

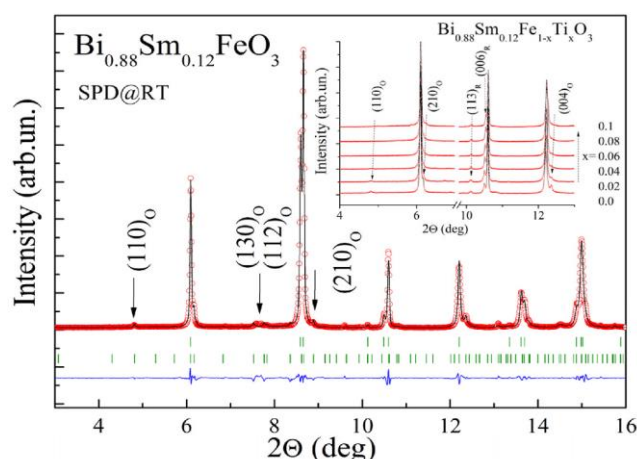


Fig. 1. Synchrotron diffraction pattern of compound $\text{Bi}_{0.88}\text{Sm}_{0.12}\text{FeO}_3$ refined using the two-phase model (upper ticks row denotes $R3c$ (R) phase, second row ticks - $P6_{3mm}$ (O) phase). The inset shows the concentration-driven changes of the structural state.

The mentioned field induced modification of the magnetic system of the compounds is most probably caused by a disruption of spatially modulated spin structure partly remained in these compounds at room temperature. The compounds with $x \geq 0.6$ denote a complete disruption of the modulated magnetic structure which is accompanied with an increase in the remnant magnetization value as well as in the magnitude of the in-field magnetization measured at $H = 14\text{ T}$.

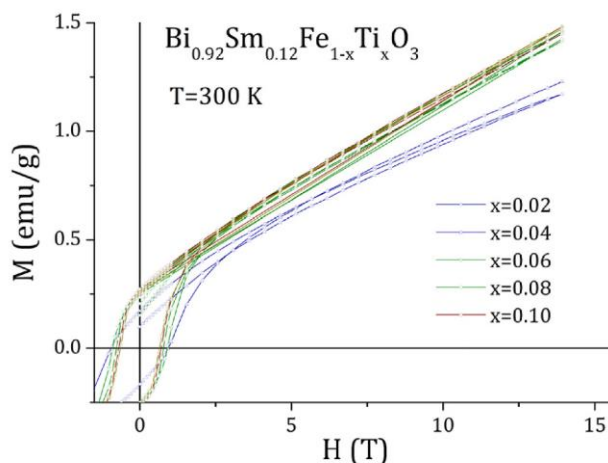


Fig. 2. Isothermal magnetization dependencies recorded at room temperatures for compounds $\text{Bi}_{0.88}\text{Sm}_{0.12}\text{Fe}_{1-x}\text{Ti}_x\text{O}_3$.

It should be noted that remnant magnetization of the compounds $\text{Bi}_{0.88}\text{Sm}_{0.12}\text{Fe}_{1-x}\text{Ti}_x\text{O}_3$ do not directly correlate with either rhombohedral or orthorhombic structural phase. The compounds with mixed structural state (i.e. $\text{Bi}_{0.88}\text{Sm}_{0.12}\text{Fe}_{1-x}\text{Ti}_x\text{O}_3$ with $x < 0.08$ as confirmed by the diffraction data) are characterized by a notable modification of the magnetic state while the magnetic state of the microscopically single phasic rhombohedral compounds ($x \geq 0.08$) does not show prominent changes. A weak if any correlation between the structural state of the compounds $\text{Bi}_{0.88}\text{Sm}_{0.12}\text{Fe}_{1-x}\text{Ti}_x\text{O}_3$ and their magnetic structure is also confirmed by magnetization measurements

performed at low temperatures. Thus, the $M(H)$ magnetization dependencies recorded at 5 K denote significant changes in the magnetic structure, which can be described as antiferromagnetic with mostly remained spatial modulation. In the compound $\text{Bi}_{0.88}\text{Sm}_{0.12}\text{Fe}_{0.94}\text{Ti}_{0.06}\text{O}_3$ the modulated magnetic structure is destroyed by magnetic fields of $\sim 8\text{--}10\text{ T}$ as denoted by an explicit deflection in the $M(H)$ curve. The compounds with larger Ti concentration are characterized by partially destroyed modulated magnetic structure occurred in low field ranges. A disruption of the modulated structure leads to a notable increase in the value of in-field magnetization which reaches 1.5 emu/g in the compound with $x = 0.06$ and it further increases with Ti content in the regime which is confirmed by nearly double value of the remnant magnetization obtained in high field measurements. Analyzing the components of remnant magnetization it should be mentioned a dominant contribution of the component associated with weak ferromagnetism as compared to that associated with the phase boundary spins having minor effect on the spontaneous magnetization as it was determined in our previous study [6].

4. Conclusions

The structural data obtained by the complementary techniques as laboratory and synchrotron X-ray diffraction allowed to conclude about a coexistence of the dominant rhombohedral phase and the antipolar orthorhombic phase in the compounds $\text{Bi}_{0.88}\text{Sm}_{0.12}\text{Fe}_{1-x}\text{Ti}_x\text{O}_3$ with $0 \leq x \leq 0.1$, wherein the volume fraction of the orthorhombic phase decreases with Ti concentration. The magnetic state of the compounds is characterized by the maximal remnant magnetization at the MPB, the evolution of remnant magnetization of the compounds is mainly caused by the unbounded spins and spatially modulated spin structure; the latter term is notably dependent on temperature and chemical homogeneity of the structural state, viz. cation vacancies, presence of the minor structural phase on local scale level etc. The component of magnetization associated with the unbounded spins is mostly pronounced in low field magnetization measurements as the magnetization caused by wF state is notably frustrated.

Acknowledgements

This research was supported by the Russian Science Foundation (project 23-19-00347).

References

- [1] R.D. Shannon, *Acta Crystallogr.* **A32**(1976)751.
- [2] J. Rodríguez-Carvajal, *Physica B* **192**(1993)55.
- [3] A. Pakalniskis, et al., *Mater. Chem. Phys.* **277**(2022) 125458.
- [4] D.V. Karpinsky, et al., *Ceram. Int.* **47**(2021)5399.
- [5] D.A. Rusakov et al., *Chem. Mater.* **23**(2010)285.
- [6] P.T. Tho, et al., *J. Alloys Compd.* **973**(2024)172873.

Electrophysical properties of the Rochelle salt / asbestos nanocomposite material

Matveeva T.G.¹, Ivanova M.S.², Solovyev V.G.^{*2,3}

¹ Pskov State University Branch in Velikiye Luki, 24 Novoslobodskaya Emb., Velikiye Luki 182100, Russia

² Pskov State University, 2 Lenin Square, Pskov 180000, Russia

³ S. M. Budyonny Military Academy of Telecommunications, 3 Tikhoretskii Ave., Saint Petersburg 194064, Russia

*e-mail: solovyev_v55@mail.ru

Abstract. Electrical conductivity, dielectric permittivity and dielectric losses of a novel nanocomposite material obtained by the infiltration of an asbestos matrix with Rochelle salt were studied in the frequency range 100 Hz – 100 kHz. A low-temperature shift of the Curie point T_C of the guest substance's upper ferroelectric transition due to the influence of confined geometry was observed.

1. Introduction

The idea of using nanoporous “host” matrices (examples include opal, zeolite, and asbestos, etc.) for fabricating three-dimensional superlattices from nanoparticles of “guest” substances within the regular systems of calibrated voids and channels of these dielectric host matrices was proposed at the end of the twentieth century [1, 2].

One of the interesting applications of regular porous dielectric matrices is their use in the creation of quantum confined nanocomposite ferroelectric materials in order to study confined geometry effects. A theoretical explanation of the Curie point T_C shift towards lower temperatures [3] is based on Landau phenomenological theory. This low-temperature shift of the T_C value has been frequently observed in experiments with ferroelectric nanoparticles in porous matrices [4–7]. However, in some cases [8, 9] a T_C value shift towards higher temperatures is also possible in systems of ferroelectric nanoparticles in host porous matrices, compared with the temperature of the phase transition in a bulk guest substance.

The aim of this study was to determine experimentally the dielectric properties of the well-researched ferroelectric substance [10–14], i. e. Rochelle salt ($\text{KNaC}_4\text{H}_4\text{O}_6 \times 4\text{H}_2\text{O}$, hereinafter referred to as RS) embedded into a chrysotile-asbestos matrix near the upper ferroelectric Curie point ($T_C = 297$ K for the bulk RS material). Chrysotile-asbestos (magnesium hydrosilicate) contains parallel channels (tubes) with an internal diameter of ~ 5 nm (Fig. 1 [15]).

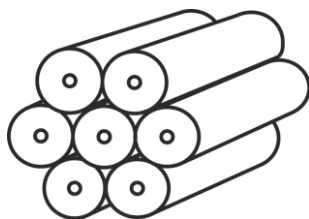


Fig. 1. Structure of asbestos porous dielectric matrix [15].

2. Experiment

The Rochelle salt was embedded into asbestos matrix from a saturated aqueous solution at room temperature; the RS / asbestos nanocomposite sample was then washed with distilled water. Then the sample was dried at $T = 300$ K, and the procedure was repeated to increase the pore filling factor. After applying graphite contacts to the sample surfaces, it was clamped between two copper electrodes of

the measuring cell. For control, similar measurements were also carried out on a bulk Rochelle salt, as well as on the asbestos host matrix. Temperature dependences of the nanocomposite electrophysical characteristics (dielectric permittivity, dielectric losses and electric conductivity) were studied using a high-precision RLC-meter MS5308 at frequencies of 100 Hz, 120 Hz, 1 kHz, 10 kHz and 100 kHz. The error bars did not exceed 5%. The temperature was measured on one of the electrodes using a two-channel thermometer GM1312 (instrument accuracy 0.1 K).

3. Results and discussions

The temperature dependences of dielectric permittivity ϵ' for the initial asbestos matrix (curve 1), for the bulk ferroelectric (curve 2) and for the RS / asbestos nanocomposite (curve 3) are presented in Fig. 2.

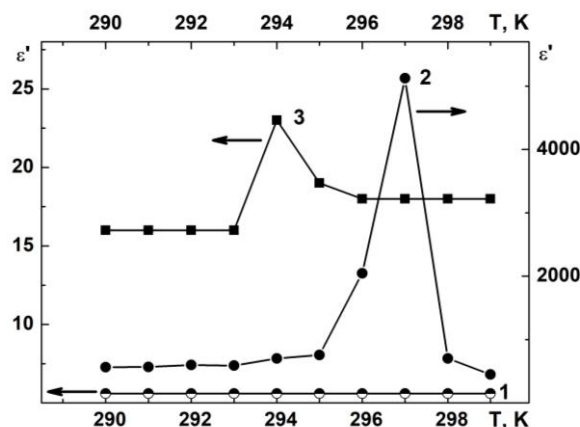


Fig. 2. Temperature dependences of the dielectric permittivity for the asbestos host matrix (curve 1), for the bulk Rochelle salt guest substance (curve 2), and for the RS / asbestos composite (curve 3) at a frequency of $f = 120$ Hz.

It is easy to see that due to the confined geometry there is a noticeable shift of T_C ($\Delta T \approx 3$ K) towards lower temperatures. This shift value is smaller than the low-temperature shift of T_C ($\Delta T \approx 5$ K) observed earlier [7] in the RS / zeolite nanocomposite since the diameters of the channels in asbestos (~ 5 nm) are larger than the diameters of the pores in NaA zeolite crystal (~ 1 nm). It should be also noted that the initial asbestos matrix has a much smaller ϵ' value ($\epsilon' \approx 6$ at 120 Hz) without any observable temperature dependence in the studied temperature range.

Arrhenius temperature dependences of the specific electrical conductivity for the initial asbestos matrix (curve 1) and for the RS / asbestos nanocomposite (curve 2) are presented in Fig 3. One can see that curve 2 has a kink near the temperature $T_C \approx 294$ K of the ferroelectric-paraelectric phase transition in composite. The composite's conductivity as well as the conductivity activation energy value $E_2 = (0.19 \pm 0.02)$ eV in the paraelectric phase are higher than those for the initial asbestos matrix (where Arrhenius plot with very small activation energy $E_1 \approx 0.04$ eV is monotonic without any features in the temperature region under study).

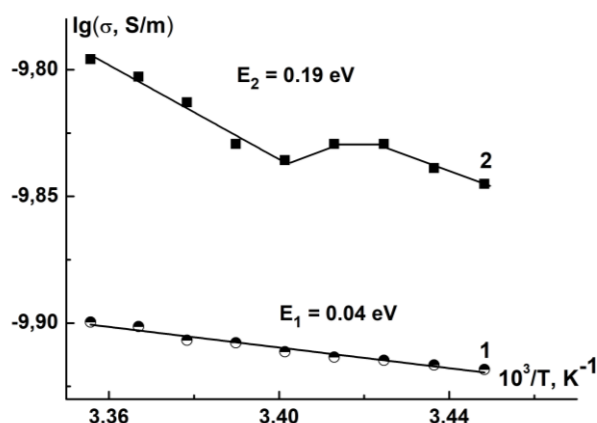


Fig. 3. Arrhenius temperature dependences of the electrical conductivity for the asbestos host matrix (curve 1), and for the RS / asbestos composite (curve 2) at a frequency of $f = 120$ Hz.

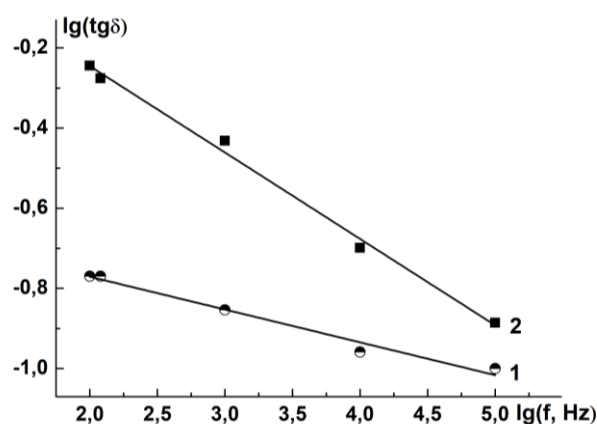


Fig. 4. Frequency dependences of dielectric losses for the asbestos host matrix (curve 1) and for the RS / asbestos nanocomposite (curve 2) at a temperature of $T = 294$ K.

Figure 4 shows, on a double logarithmic scale, the frequency dependences of dielectric losses $\text{tg}\delta$ for the initial asbestos host matrix (curve 1) as well as for the RS / asbestos nanocomposite (curve 2). In both cases, it is possible to observe a power-law dependence of dielectric losses $\text{tg}\delta$ on frequency f ($\text{tg}\delta \sim f^{-n}$), where the exponent is $n \approx 0.08$ for the initial asbestos host matrix and $n \approx 0.21$ for the RS / asbestos nanocomposite. Thus, both graphs display a smooth decrease of dielectric losses with frequency without any extremes in the studied frequency range from 100 Hz to 100 kHz which is typical for many dielectrics.

4. Conclusions

The novel nanocomposite ferroelectric / asbestos material obtained by the infiltration of a chrysotile-asbestos host matrix with a Rochelle salt guest substance demonstrates a shift of the Rochelle salt's upper ferroelectric transition Curie point T_C by ~ 3 K towards lower temperatures, compared with the temperature of the phase transition in a bulk ferroelectric. This shift value is smaller than the low-temperature shift of T_C observed earlier in the ferroelectric / zeolite nanocomposite since the diameters of the asbestos channels are larger than the diameters of the zeolite pores.

Acknowledgements

The authors are grateful to Yu. A. Kumzerov, A. A. Naberezhnov and A. I. Vanin for help and fruitful discussions.

References

- [1] V. N. Bogomolov. Soviet Physics Uspekhi **21**(1)(1978)77.
- [2] G. D. Stucky, J. E. Mac Dougall. Science **247**(4943)(1990)669.
- [3] W. L. Zhong, Y. G. Wang, P. L. Zhang, B. D. Qu. Physical Review. **B 50**(1994)698.
- [4] S. V. Pan'kova, V. V. Poborchii, V. G. Solov'ev. Journal of Physics: Condensed Matter **8**(12)(1996)L203.
- [5] C. Tien, E. V. Charnaya, M. K. Lee et al. Journal of Physics: Condensed Matter **20**(21)(2008)215205.
- [6] A. Cizman, T. Antropova, I. Anfimova et al. Journal of Nanoparticle Research **15**(8)(2013)1807.
- [7] T. G. Matveeva, M. S. Ivanova, V. G. Solovyev, A. I. Vanin. Physics of Complex Systems **5**(4)(2024)195.
- [8] O. V. Rogazinskaya, S. D. Milovidova, A. S. Sidorkin et al. Physics of the Solid State **51**(7)(2009)1518.
- [9] S. V. Baryshnikov, E. V. Charnaya, Yu. A. Shatskaya et al. Physics of the Solid State **53**(6)(2011)1212.
- [10] S. Mitani, S. Fukui, I. Shibuya et al. Ferroelectrics **8**(1)(1974)477.
- [11] X. Solans, C. Gonzalez-Silgo, C. Ruiz-Pérez. Journal of Solid State Chemistry **131**(2)(1997)350.
- [12] G. Zhou, J. Wu, A. Wang et al. Ferroelectrics **366**(1)(2008)67.
- [13] I. A. Malyshkina, N. D. Gavrilova. Ferroelectrics **268**(1)(2002)41.
- [14] S. Singaravelu, A. Uthayakumar, P. Balaji Bhargav. Ferroelectrics **550**(1)(2019)112.
- [15] A. I. Vanin, Yu. A. Kumzerov, V. G. Solov'ev et al. Glass Physics and Chemistry **47**(2021)226.

Interfacial ferromagnetism in sputtered Pt/Gd/Pt system at room temperature

Turpak A.A.^{*1}, Pashenko A.S.¹, Chernousov N.N.¹, Ognev A.V.^{1,2}, Davydenko A.V.¹

¹ Far Eastern Federal University, 10 pos. Ajax, Russian island, Vladivostok, 690922, Russia

² Sakhalin State University, 33 Kommunisticheskoy str., Yuzhno-Sakhalinsk, 693000, Russia

*e-mail: turpak.aa@dvfu.ru

Abstract. Magnetic properties of sputtered Pt/Gd(d_{Gd})/Pt ultrathin films were investigated. The thickness of the Gd layer was varied from 1 to 15 nm. A weak spontaneous magnetization was detected in Pt/Gd/Pt thin films at room temperature. The observed magnetization is mainly of an interface origin with a negligibly small bulk component. An interface magnetic moment of 14.5 $\mu\text{emu}/\text{cm}^2$ was measured at room temperature.

1. Introduction

Gd is a ferromagnetic material with a Curie temperature of 293.4 K in a bulk state. Bulk Gd fragments and thick Gd films have a hexagonal close-packed (hcp) structure, while a face-centered cubic (fcc) phase was observed in ultrathin Gd films [1]. In the fcc-Gd(10 nm) ultrathin films, the Curie temperature larger than 300 K was observed. The saturation magnetization of the fcc-Gd films was measured as near 100 emu/cm^3 at 50 K. Gd is widely used in construction of ferrimagnetic systems. $\text{Co}_x\text{Gd}_{1-x}$ alloy demonstrates ferrimagnetic properties [2]. Changing stoichiometric ratio of the $\text{Co}_x\text{Gd}_{1-x}$ alloy one may control a temperature of the magnetization cancellation, the saturation magnetization and other magnetic parameters. Antiferromagnetic alignment of the magnetic moments of interface Gd layers grown on Co surface and magnetic moments of Co layers was observed [3]. In this case, Co/Gd films may reveal complicated behavior with Gd interface layers magnetized opposite to Co layer and bulk Gd layers magnetized in the direction of the magnetization of Co layers [4]. Pt/Co/Gd system is widely investigated in recent years. It is the multilayered system with a broken inversion symmetry along the normal to the surface. A perpendicular magnetic anisotropy, spin-orbit torque effect and Dzyaloshinskii-Moriya interaction may be stabilized in the Pt/Co/Gd system. The combination of the aforementioned effects in the magnetic thin films is of great importance for the construction of racetrack or skyrmion devices. To increase the effective magnetic thickness, conserve effective perpendicular magnetic anisotropy and facilitate skyrmions formation due to a large dipolar coupling energy $[\text{Pt}/\text{Co}/\text{Gd}]_n$ superlattices may be utilized [5]. It is generally considered, that the spontaneous magnetization of Gd layers at room temperature in the $[\text{Pt}/\text{Co}/\text{Gd}]_n$ superlattices is induced in the interface Gd layers with Co. In the present study, we investigate the role of interface Pt/Gd and Gd/Pt layers in ferromagnetic properties of the Pt/Gd/Pt sputtered system.

2. Experiment

The samples were deposited by magnetron sputtering on naturally oxidized silicon SiO_2 substrates. Sputtering was performed using an Omicron vacuum chamber equipped with a rotating substrate holder and four magnetron cells, which allowed different materials to be deposited sequentially without venting the chamber. The rotating mechanism of the holder with a rotation speed of

40 rpm ensured isotropy of the magnetic properties of the samples. The layer thickness was controlled using a quartz thickness monitor with an accuracy of 1 Å. The composition of the samples was Pt(3 nm)/Gd(1-15 nm)/Pt(3 nm). The sample with the thickness of Gd layer of X nm will be denoted as Gd(X) hereinafter in the text. Magnetron sputtering was performed in an argon environment at a base pressure of $P_0 = 1 \times 10^{-8}$ Torr and an Ar working pressure in the range from 1×10^{-3} to 5×10^{-3} Torr at 300 K. The magnetic properties and magnetic anisotropy were investigated by vibration sample magnetometry (VSM) at room temperature. X-ray diffraction (XRD) was used for the determination of the structure of the samples.

3. Results and discussions

In-plane (IP) and out-of-plane (OOP) normalized magnetic hysteresis loops of Gd(1) and Gd(15) samples are shown in Fig. 1(a) and (b), respectively.

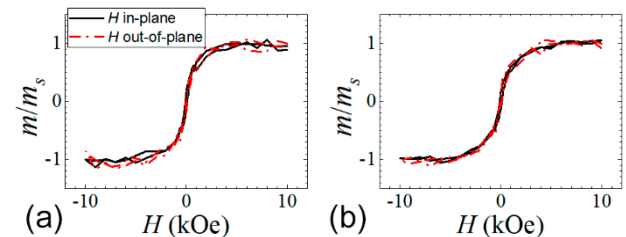


Fig. 1. Normalized magnetic hysteresis loops of (a) Gd(1), (b) Gd(15) samples.

Comparison of hysteresis loops of all the samples in the series is indicated in Fig. 2(a) and (b) for the orientation of the magnetic field IP and OOP, respectively.

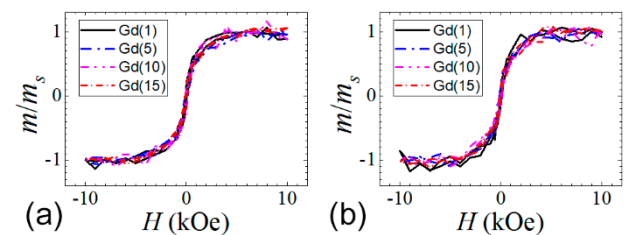


Fig. 2. Normalized magnetic hysteresis loops for the orientation of the magnetic field (a) IP, (b) OOP.

Hysteresis loops of each sample are similar: they are isotropic and without hysteresis. The shape of hysteresis loops of the samples does not change significantly with variation of the Gd layer thickness. The observed magnetic

behavior of samples resembles behavior of superparamagnetic systems that consist of ferromagnetic grains, the magnetization of which is randomly oriented due to thermal fluctuations. Such magnetic behavior may also be observed in the systems measured in temperatures close to the Curie point. However, the Curie temperature is expected to strongly depend on the thickness of the magnetic Gd layer. Therefore, the shape of hysteresis loops should depend on the thickness of Gd layer as well, that is not observed in the experiment. Moreover, the analysis of XRD spectra indicates that Gd has polycrystalline fcc structure with (111) texture only in the Gd(15) sample, while Gd is amorphous in other samples. It seems that structural changes in the Gd layer with an increase of its thickness have no effect on the magnetic properties of the samples.

The most striking result is related with the dependence of the saturation magnetic moment normalized to the unity of an area on the thickness of the Gd layer (Fig. 3).

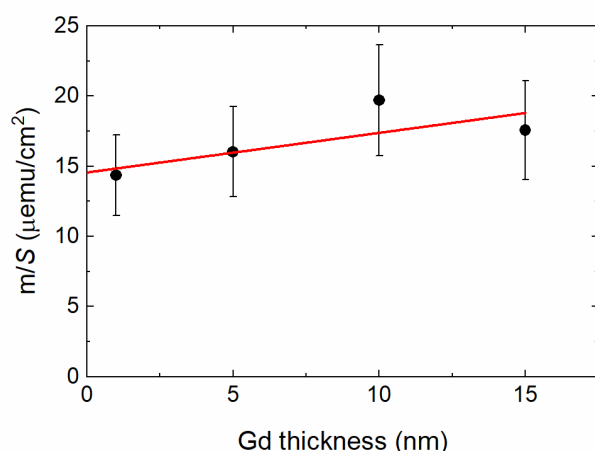


Fig. 3. The dependence of the saturation magnetic moment normalized to the unity of the area on the thickness of the Gd layer. Solid line is a linear fitting of the experimental points.

Linear fitting of the $m_s/S(d_{\text{Gd}})$ dependence gives a volume magnetization of the system and magnetic moment of interface layers. The volume magnetization that is equal to 2.8 emu/cm^3 is negligibly small. Low but non-zero value of the volume saturation magnetization may indicate that Curie temperature of the samples may be close to room temperature. Interesting that system demonstrates large interfacial magnetic moment, equal to $14.5 \text{ } \mu\text{emu/cm}^2$. The observed interfacial magnetic moment is rather large. If consider, that the interfacial magnetic moment, $m_{s \text{ int}}/S$, belongs only to two surface Gd layers: one in the bottom and other in the top, then the volume magnetization of the Gd interface layers will be $M_s = m_{s \text{ int}}/S/(2 \cdot 0.307 \text{ nm}) = 236 \text{ emu/cm}^3$. This value is even larger than the value of the saturation magnetization of fcc-Gd in 50 K.

At present moment, it is not clear what atoms in the system reveal interface ferromagnetism. It may be interface Gd atoms that are coupled with Pt atoms and possess specific electronic and magnetic properties. Also Pt atoms may reveal the magnetization due to a magnetic proximity effect [6]. However, magnetic proximity effect is attributed to induction of ferromagnetism in nonmagnetic materials that are adjacent to ferromagnetic layers. But we do not observe ferromagnetic order in the volume of Gd layer.

Additional information can be obtained by measuring X-ray magnetic circular dichroism spectra in this system, which can provide information on the distribution of magnetic moments among the atoms of different elements. It would also be beneficial to carry out measurements of hysteresis loops in low temperatures to detect the onset of the volume ferromagnetism in this system and analyze whether interfacial magnetic moment is observed in low temperatures or not. If the interfacial moment disappears in the low temperatures in which the volume magnetization appears, then the detected interfacial magnetic moment in this system at room temperatures belongs not to the Pt atoms but to the interface Gd atoms.

4. Conclusions

Isotropic superparamagnetic behavior of Pt(3 nm)/Gd(1-15 nm)/Pt(3 nm) samples was observed independently of the thickness of Gd layers. The saturation magnetic moment is predominately of interface origin in the investigated system with a small bulk component. The structure of the Gd layer is amorphous for the thickness of Gd less than 10 nm, while nanocrystalline fcc structure with (111) texture begins to develop in the sample with the thickness of the Gd layer of 15 nm.

Acknowledgements

The work of Turpak A.A., Chernousov N.N. and Davydenko A.V. was supported by the Russian Science Foundation, grant No. 25-42-00083, <https://rscf.ru/project/25-42-00083/>. Pashenko A.S. and Ognev A.V. acknowledge the state assignment of the Ministry of Science and Higher Education of the Russian Federation (project No. FZNS-2023-0012).

References

- [1] T. P. Bertelli, E.C. Passamani, C. Larica, V.P. Nascimento, A.Y. Takeuchi, M.S. Pessoa. *J. of Appl. Phys.* **117**(2015)203904.
- [2] J. Wang, B. Li, Y. An, G. Song, S. Zhang. *Appl. Phys. Lett.* **126**(2025)072401.
- [3] R. Bläsing, T. Ma, S.-H. Yang, C. Garg, F.K. Dejene, A.T. N'Diaye, G. Chen, K. Liu, S.S.P. Parkin. *Nat Commun* **9**(2018)4984.
- [4] J. Brandão, P. C. Carvalho, I. P. Miranda, T. J. A. Mori, F. Béron, A. Bergman, H. M. Petrilli, A. B. Klautau, J. C. Cezar. *arXiv:2404.04655v1* [cond-mat.mtrl-sci].
- [5] T. Nishimura, M. Haruta, D.-H. Kim, Y. Shiota, H. Iwaki, D. Kan, T. Moriyama, H. Kurata, T. Ono. *J. Magn. Soc. Jpn.* **44**(2020)9.
- [6] C. Swindells, B. Nicholson, O. Inyang, Y. Choi, T. Hase, D. Atkinson. *Phys. Rev. R.* **2**(2020)033280.

**V. Nanostructured coverages, nanocomposites,
functional hybrid materials: formation, structure
and properties**

Tuning properties of carbon nanocomposite coatings formed by accelerated C_{60} ions

Karaseov P.A.^{*1}, Pukha V.E.², Kabachkov E.N.², Karaseov K.P.^{1,3}, Strizhkin D.A.¹, Shakhmin A.L.¹

¹ Peter the Great St.-Petersburg Polytechnic University, 29 Polytechnicheskaya St., St.-Petersburg 195251, Russia

² FRC for Problems of Chemical Physics and Medicinal Chemistry RAS, 1 Ac. Semenov ave., Chernogolovka, Moscow region, 142432, Russia

³ Alferov University, 8 Khlopina St., St.-Petersburg 195220, Russia

*e-mail: platon.karaseov@spbstu.ru

Abstract. Carbon is the unique element that could form a wide variety of C-C atom bonding. Among others, irradiation of a target with accelerated fullerene C_{60} ions/molecules is a very attracting way to form a coating on its surface. Varying irradiation parameters, like ion energy and substrate temperature one can tune structure of the coating from amorphous to nanocomposite consisting of amorphous diamond-like matrix filled with graphite nanoflakes, from soft polymeric to hard diamond-like. In this contribution we consider effects of energetic keV energy C_{60} ion irradiation on carbon coating formation.

1. Introduction

Carbon-based coatings are of extreme interest as they appear in a wide variety. Indeed, this is due to the wonder ability of carbon atoms to form different C-C bonds in single film [1]. Various techniques, like, plasma-enhanced chemical vapor deposition [2], radio frequency magnetron sputtering [3], filtered cathode arc deposition [4] etc. were used to grow carbon films. It is important to note that, carbon coatings, and especially hard ones that contain large fraction of diamond-like sp^3 bonds, frequently possess high residual stress values [5]. This obstacle requires special procedures to improve adhesion.

In addition to the abovementioned, C_{60} molecules/ions could be used for coating formation. C_{60} molecule land onto a substrate intact at low energy ($E < 300$ eV) or is decomposed [6] at higher energies. The impact of such cluster ion gives rise to several collective phenomena, that, in turn, affect properties of the grown film. It could be local melting, appearance of high pressure waves, etc. Substrate temperature and C_{60} ion energy play crucial role in the processes that take place during deposition. Varying them one can tune structure of a coating from amorphous to nanocomposite consisting of amorphous diamond-like matrix filled with graphite nanoflakes [7]. Thus, using accelerated fullerene ion beams, it is possible to deposit carbon films and coatings with different structures. In this contribution, recent results of investigation of the structure and properties of carbon coatings grown by C_{60} ion irradiation are critically reviewed. that gives unique possibility to tailor properties of a growing blanket layer.

2. Experiment

In this work, deposition was performed using the home-made setup equipped with saddle-like electric field C_{60} ion source, ion beam transport system, and substrate heater. Detailed description of the experimental conditions could be found elsewhere [7]. In brief, beam transport system permit switching between magnetic mass separator and ion mirror. Ion source produces single, double and small fraction of triple charged fullerene ions. As they all are accelerated with the same voltage, we can irradiate the target either with mixed beam consisting of ions having three energies or with monoenergetic ions coming after mass separation. Fullerene C_{60} powder (99.5% purity; JSC

NeoTechProduct, St. Petersburg, Russia) was used as the starting material for the deposition of coatings. Pieces of (100) polished silicon wafer and VT1-0 titanium were used as a substrate. Structure of the coatings was studied by TEM after etching the substrate out. Carbon atom bond structure was determined by XPS and Raman scattering. Surface morphology was studied by AFM. Coefficient of friction and wear resistance of the coating were measured using stainless steel ball counter-body in dry sliding conditions at room temperature in air. In addition, before and after tribology tests surface morphology was examined by confocal microscopy.

Besides the experimental investigation, classical molecular dynamics simulations were performed using Lammmps code to get some insights into basic mechanisms of C_{60} cluster-surface interactions and carbon film formation. Silicon single crystal with open (100) surface was used as a target. Periodic boundary conditions were applied in the lateral directions of the computational cell, the 3 bottom layers of Si atoms were fixed, and next five layers were used for heat dissipation (Berendsen thermostat). The interactions between all atoms of the system (Si-Si, Si-C, C-C) were described by the Tersoff/ZBL interaction potential. Electronic energy loss were applied as a quasi-friction force to atoms with energies above 10 eV.

3. Results and discussions

Substrate temperature during the deposition significantly affects structure properties of the coating on the nanoscale. While the process proceeds with 5 keV C_{60} ions, at $T_s \leq 300$ C, halo is seen in the TEM images, which suggests amorphous structure of the film. With the temperature increase, bright rings arising from (002) graphite plane sets appear (see Fig. 1). Halo formed by amorphous fraction remains visible in the diffraction pattern. This means graphitic nanocrystal inclusions are formed in the amorphous matrix at high substrate temperature, i.e. carbon nanocomposite (CNC) is formed. On the other hand, C_{60} ion energy increase to 8 keV dramatically affects the result. In this case, coating is formed at $T_s \geq 300$ C, while no film is seen at lower substrate temperatures. Nanocrystal formation threshold shifts to lower temperature with the energy increase.

Coatings would appear on a substrate if ion energy does not exceed 10 keV (167 eV per single carbon atom).

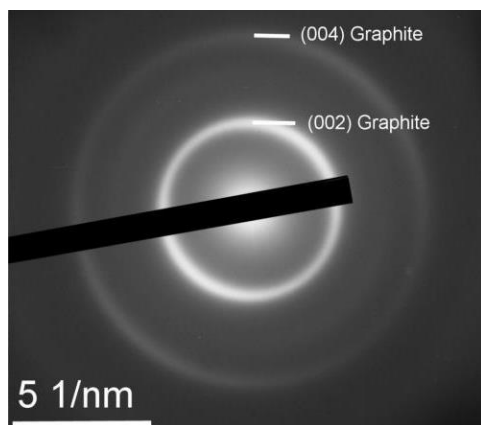


Fig. 1. TEM diffraction patterns for carbon coatings deposited by 5 keV C_{60} irradiation of Si substrate at 400°C.

XPS investigation of the sample irradiated to a low doses (initial stage of the coating formation) shows formation of carbides (either Si or Ti) together with sp^2 and sp^3 carbon bonds. Fraction of sp^3 bonded carbon atoms decreases from 60% to 50% with the temperature increase from 100 °C to 400 °C. This findings correspond well to MD data, which clearly indicate formation of covalent Si-C bonds after single C_{60} ion impact. ~5 Å thick silicon carbide layer appears after 30 successive C_{60} ion impacts, as revealed from cumulative MD simulation (see Fig. 2). Such layer provides incredibly strong film adhesion thus removing one of the main drawbacks affecting DLC and other carbon-based coatings applications.

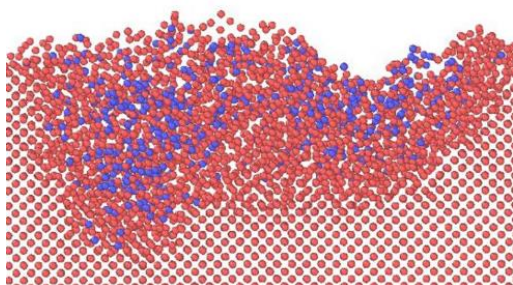


Fig. 2. MD simulated cross-section of a 20 Å thick slice of a silicon target after 30 C_{60} ions sequentially impact the surface.

Samples grown on Ti substrates were subjected to friction tests with stainless steel counter-body in ambient air conditions. Coefficient of friction of nanocomposite coatings were found as low as 0.1. The average wear-rate decreases by 2-3 orders of magnitude compare to bare Ti substrates. Counter body running over the samples during tribology tests also experienced very slight wear. This effect is due to formation of thin solid lubricating layer on the counterpart ball via transfer of graphite flakes from the coating during the tests. Such transfer was confirmed through analysis of the Raman spectra collected from the contact area of the counterpart balls.

The strength and adhesion of the coatings were measured by nanoindentation scratch tests with sphero-conical diamond tip. No carbon film delamination or cracking was observed before the CNC failure. Critical load value exceeds 50 mN, demonstrating good anti-scratching

performance and strong adhesion of the CNC coating to the metal substrate.

Interface contact resistance and anti-corrosion protective ability are very important in a wide range of applications. Contact resistance values of the CNC-coated Ti samples are as low as several mOhm·cm². Coated titanium samples exhibit stable corrosion current for a long period of time, which ensures good protection thus promoting long operation times.

4. Conclusions

In conclusion, we described technique to deposit carbon coatings on various surfaces, namely C_{60} ion irradiation. Intermixed carbonate layer formed at the coating-substrate interface at the initial stage on accelerated ion bombardment improves adhesion of the coating. Changing ion beam energy and substrate temperature, film of amorphous or nanocomposite structure could be controllably grown. Size of graphite nanocrystals embedded in sp^3 matrix could also be tuned. Presence of these nanoclusters, which are highly conductive and able to provide lubricating inclusions, provides combination of extremely attractive properties. Coatings could possess low friction and wear, high electric conductivity and good anticorrosion protection. Pretty wide range of potential applications was also discussed.

Acknowledgements

Work at StPSPU was partly supported by the State assignment for basic research (project FSEG-2023-0016).

References

- [1] J. Robertson, Mater. Sci. Eng. R. **37**(2002)129.
- [2] S. Kumar, P.N.Dixit, D.Sarangi, R.Bhattacharyya. J. Appl. Phys. **93**(2003)6361.
- [3] T. Mikami, H. Nakazawa, M. Kudo, M. Mashita. J. Thin Solid Films, **488**(2005)87.
- [4] H.Takikawa, K. Izumi, R.Miyano, T.Sakakibara. Surf. Coat. Technol. **163–164**(2003)368.
- [5] S.Zhang, H.Xie, X.Zeng, P.Hing. Surf. Coat. Technol. **122**(1999)219.
- [6] K.P.Karasev, D.A.Strizhkin, A.I.Titov, P.A.Karaseov J. Surf. Investigation **18**(2024)433.
- [7] M.Khadem, V.E.Pukha, O.V.Penkov, et al., Surf. Coat. Technol. **42425**(2021)127670.

Synthesis, structure and electronic properties of epitaxial thin films of MAX phases

Tarasov A.S.^{*,1}, Lyaschenko S.A.¹, Rautskii M.V.¹, Fedorova N.A.¹, Andryushchenko T.A.¹,
Lukyanenko A.V.¹, Yakovlev I.A.¹, Bondarev M.A.¹, Bondarev I.A.¹, Solovyov L.A.²,
Maximova O.A.¹, Tomilin F.N.¹, Varnakov S.N.¹, Ovchinnikov S.G.¹

¹ Kirensky Institute of Physics, Federal Research Center KSC SB RAS, 50 bld.38 Akademgorodok St., Krasnoyarsk 660036, Russia

² Institute of Chemistry and Chemical Technology, Federal Research Center KSC SB RAS, 50/24 Akademgorodok St., Krasnoyarsk 660036, Russia

*e-mail: taras@iph.krasn.ru

Abstract. This study investigates the growth and electronic properties of $\text{Cr}_{2-x}\text{Mn}_x\text{GeC}$ thin films synthesized via magnetron co-sputtering. By optimizing carbon content and substituting Cr with Mn, single-phase hexagonal $\text{P6}_3/\text{mmc}$ films with suppressed impurity phases (CrGe , Cr_3Ge) were achieved. Atomic force microscopy revealed grain size variations dependent on C/Cr/Mn concentrations, while X-ray diffraction confirmed enhanced phase stability at higher Mn content ($x \leq 0.86$). Transport measurements demonstrated charge carrier mobility ($\sim 125 \text{ cm}^2/\text{V}\cdot\text{s}$) comparable to single-crystal Cr_2AlC , attributed to high crystalline quality. Theoretical calculations predicted ferrimagnetic ordering in $(\text{Cr}_{4-x}\text{Fe}_x)_{0.5}\text{GeC}$ and $(\text{Cr}_{4-x}\text{Fe}_x)_{0.5}\text{AlC}$ systems and functionalized-dependent magnetism in Mn_2C , with F- and Cl-terminated structures exhibiting magnetic moments up to $5.63 \mu_B$. The results establish processing-structure-property relationships for designing magnetically ordered MAX phases with potential applications in spintronics and functional devices.

1. Introduction

$\text{M}_{n+1}\text{AX}_n$ (MAX) phases are highly anisotropic hexagonal compounds possessing a number of unique properties, where n takes integer values of 1, 2, 3 и 4, M is a transition metal (e.g., Sc, Ti, V, Mn, Cr), A is an element from group 13 or 14 (Al, Ga, Ge, P, S); and X is carbon or nitrogen [1]. In recent years, theoretical and experimental searches for new MAX phases have been intensively conducted, along with the development of novel approaches for synthesizing bulk samples and thin films [2]. In addition to the mechanical and electronic properties of MAX materials, their magnetic properties are of significant interest. Both theoretically predicted and experimentally obtained MAX phases based on chromium and manganese, which exhibit long-range magnetic order, are of considerable fundamental and applied interest due to possible low-dimensional magnetism effects and the observed giant magnetostriction in Mn_2GaC [3]. This paper presents the results of a study on the growth features and electronic properties of thin films of MAX phases with various compositions, as well as theoretical calculations of atomic and electronic structures and spin states.

2. Experiment

Samples (Table 1) were synthesized via magnetron co-sputtering from elemental targets of Cr (99,95%), Mn (99,95%), Ge (99,99%) and C (99,95%) in an ultra-high vacuum (UHV) chamber with a base pressure of 10^{-9} Torr. Осаждение проводилось в режиме DC для мишеней Cr, Deposition was performed in DC mode for Cr, Mn, and C targets and in RF mode for the Ge target. The pressure of high-purity argon (99.99995%) was maintained at $7 \cdot 10^{-3}$ Torr. The average deposition rate, converted to volumetric density, was approximately 2.5 nm/min for all materials. A monocrystalline MgO (111) surface was used as the substrate. Deposition was carried out at a substrate temperature of 650°C . After deposition, all samples were additionally annealed for 30 minutes in UHV at 850°C . The

process was monitored in situ using reflection high-energy electron diffraction (RHEED) and Auger electron spectroscopy (AES).

X-ray diffraction (XRD) analysis was performed using a PANalytical X'Pert PRO diffractometer equipped with a PIXcel solid-state detector and $\text{Cu K}\alpha$ radiation. Film morphology was studied via atomic force microscopy (AFM) in semi-contact mode using a NanoInk DPN 5000 instrument. Transport properties were measured using the Van der Pauw method on $4 \times 4 \text{ mm}^2$ samples. A Keithley 2400 SourceMeter and a Keithley 2182A nanovoltmeter were used as the current source and voltage meter, respectively. Hall voltage measurements were conducted in an external magnetic field ranging from -9 to +9 T.

Table 1. Technological parameters of the synthesized Cr_2GeC and $\text{Cr}_{2-x}\text{Mn}_x\text{GeC}$ thin films.

#	atomic stoichiometry, %				D, nm
	Cr	Mn	Ge	C	
4	54.4	-	20.3	25.3	10
5	54.4	-	20.3	25.3	40
6	54.4	-	20.3	25.3	100
7	55	-	16.8	28.2	40
8	55	-	16.8	28.2	40
9	40.6	14.1	17	28.3	40
10	50.8	0	19.4	29.8	40
11	25.4	24.8	16.4	33.4	40
12	19.7	30	15.3	34.9	40
13	25.4	24.8	16.4	33.4	120

Density Functional Theory (DFT) within Periodic Boundary Conditions was employed for electronic structure calculations of crystalline structure and electronic properties of MAX and MXene phases using CRYSTAL 17 code [46].

3. Results and discussions

Initially, all samples were examined by AFM microscopy. It was found that increasing the C or Cr content led to an increase in grain height and size. For unsubstituted Cr_2GeC films, the surface is dominated by flat clusters with sizes of 100–500 nm and heights of 20–30 nm, along with small grains (10–20 nm) located directly on the cluster surfaces. The addition of manganese caused a significant change in crystallite size, indicating altered thermodynamics of film formation in Mn-substituted MAX phases compared to pure Cr_2GeC .

XRD analysis revealed the formation of a hexagonal $\text{P6}_3/\text{mmc}$ phase with a predominant $(00l)$ texture (Fig.1). However, impurity cubic phases corresponding to chromium germanides (CrGe and Cr_3Ge) were also detected in the films. Increasing the carbon content reduced the germanides concentration. Manganese addition further improved the phase composition. Moreover, our latest results (samples #11, #12, #13) demonstrated that further substituting Cr with Mn enhances phase formation stability. For samples with high manganese content, only peaks corresponding to the hexagonal MAX phase were observed (not shown here). According to AES data, the highest achieved manganese concentration was $x = 0.86$.

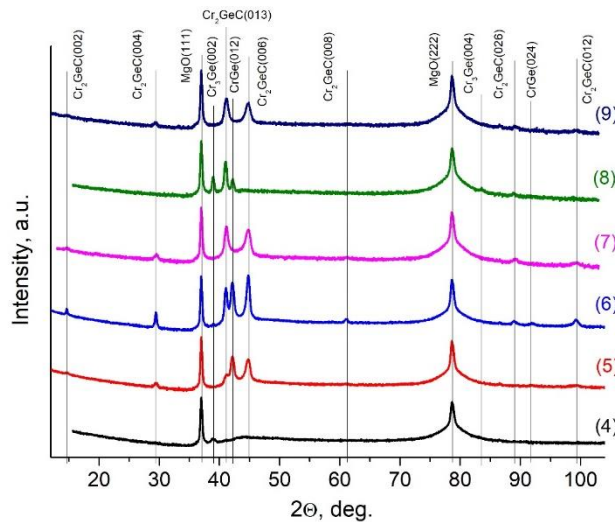


Fig. 1. XRD profiles for samples #4–#9.

Transport properties were investigated for a series of samples. Assuming that the mobility of electrons and holes equals the square root of the magnetoresistance (MR) $\mu_n = \mu_p = \sqrt{\alpha}$ ($\text{MR} \sim \alpha \cdot H^2$) [4]), the values of μ , N , and P were calculated for the samples with the best phase composition and conductivity. Carrier concentrations N and P were found to be in the range of 10^{26} – 10^{27} $1/\text{m}^3$ consistent with values reported for bulk polycrystalline Cr_2GeC [4] and single crystal Cr_2AlC [5]. The calculated mobility (Fig. 2) is one order of magnitude higher than that of bulk polycrystalline samples and comparable to the $\mu = 125 \text{ cm}^2/\text{V}\cdot\text{sec}$ reported for Cr_2AlC single crystals at room temperature [5]. This suggests that the high crystalline quality of the film positively impacts charge carriers' mobility. Notably, low-temperature data (below 50 K) in Fig. 2 may be distorted by the calculation method, which assumes MR is solely caused by the Lorentz force. At low temperatures, contributions from quantum corrections to conductivity (positive or negative) significantly affect the accuracy of determining α and, consequently, μ , N , and P .

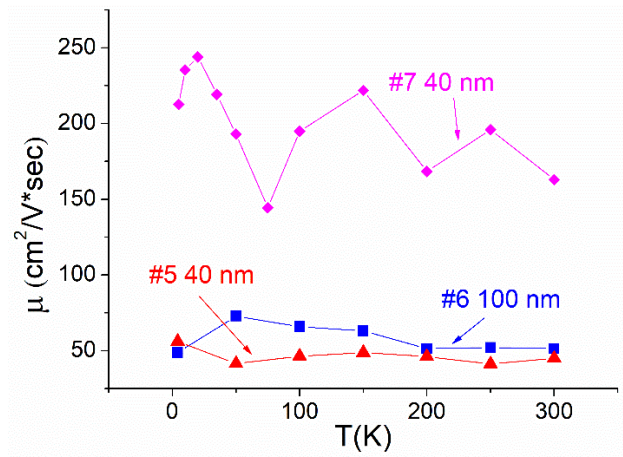


Fig. 2. Temperature dependences of μ for samples #5–#7.

To explore experimental realizations of magnetically ordered MAX phases, theoretical calculations of electronic properties were performed for $(\text{Cr}_{4-x}\text{Fe}_x)_{0.5}\text{AlC}$ ($\text{A} = \text{Ge}, \text{Si}, \text{Al}$), $(\text{Sc}_3\text{M}_1)_{0.5}\text{AlC}$ ($\text{M} = \text{Cr}, \text{Mn}, \text{Fe}$) and F -, Cl -, OH -, and O -terminated Mn_2C . It was found that $(\text{Cr}_{4-x}\text{Fe}_x)_{0.5}\text{GeC}$ and $(\text{Cr}_{4-x}\text{Fe}_x)_{0.5}\text{AlC}$ lattices adopt a ferrimagnetic state, in contrast to $(\text{Cr}_{4-x}\text{Fe}_x)_{0.5}\text{SiC}$, where ferromagnetic spin order dominates. Surface passivation of Mn_2C with F and Cl ions yields the maximum magnetic moments per unit cell (up to $5.63 \mu_B$), while hydroxylation results in half-metallicity. The substituted $(\text{Sc}_3\text{Mn})_{0.5}\text{AlC}$ structure exhibits stable magnetic moments per unit cell and individual ions, independent of their positions in the lattice.

4. Conclusions

Thin textured $\text{Cr}_{2-x}\text{Mn}_x\text{GeC}$ films with varying manganese content were synthesized. Increased carbon content was found to suppress the formation of impurity chromium germanide phases. Excess carbon combined with chromium substitution by manganese enabled stable growth of single-phase high-textured $\text{Cr}_{2-x}\text{Mn}_x\text{GeC}$ films with x up to 0.86. The Cr_2GeC films exhibited charge carrier mobility comparable to that of single crystals. Theoretical calculations demonstrated the feasibility of obtaining new magnetically ordered MAX phase compounds.

Acknowledgements

The research was supported by the grant of the Russian Science Foundation № 25-12-20012, <https://rscf.ru/project/25-12-20012/>, grant of the Krasnoyarsk Regional Science Foundation.

References

- [1] M. Dahlqvist, et al. *Materials Today* **72** (2024): 1-24.
- [2] B. Abhijit, V. Natu, A.B. Puthirath. *Oxford Open Materials Science* **1.1** (2021): itab020.
- [3] R. Dovesi, V.R. Saunders, C. Roetti, et al. *CRYSTAL17 User's Manual*, 2018. <http://tutorials.crystalsolutions.eu/>.
- [4] M.W. Barsoum, T.H. Scabarozi, S. Amini, et al. *J. Am. Ceram. Soc.* **94** (2011) 4123–4126.
- [5] T. Ouisse, L. Shi, et al. *Phys. Rev. B* **92** (2015) 045133.

Prospects of using hollow particles of oxide powders in thermal control systems of spacecraft

Mikhailov M.M.¹, Neshchimenko V.V.^{*2}, Morev N.G.², Lapin A.N.¹

¹ Tomsk State University of Control Systems and Radio-electronics, 40 pr. Lenin, Tomsk, Tomsk Region 634050, Russia.

² Amur State University, 21 hw. Ignatyevskoe, Blagoveshchensk, 675027, Russia

*e-mail: v1ta1y@mail.ru

Abstract. This study explores the potential of hollow oxide particles as advanced materials for thermal control systems in spacecraft engineering. Given their unique structural attributes, such as high surface area and low density, hollow particles of aluminum oxide, zinc oxide, titanium dioxide and silicon dioxide offer significant advantages in thermal management. We conducted a comparative analysis of the diffuse reflection and induced absorption spectra of coatings made from these hollow and solid microparticles after electron irradiation at 30 keV. The results demonstrate that coatings based on hollow ZnO particles exhibit the highest radiation stability, with a change in solar absorptance of only 0.03 at the maximum fluence of $5 \times 10^{16} \text{ cm}^{-2}$. This enhanced stability is attributed to the unique electronic properties of ZnO and its hollow structure, which effectively mitigate radiation-induced defects, making it a promising candidate for applications in harsh space environments.

1. Introduction

The ever-evolving field of spacecraft engineering continually seeks innovative materials and technologies to enhance the efficiency and performance of thermal control systems. Among the myriad of possibilities, hollow particles of oxide powders have emerged as a promising solution due to their unique structural attributes and functional properties. These lightweight materials, characterized by their high surface area and low density, offer substantial advantages in managing thermal dynamics within the challenging environments of space.

As thermal management becomes increasingly critical for the operational longevity and reliability of spacecraft, the exploration of advanced materials like hollow oxide particles gains urgency. Their ability to insulate, reflect, and dissipate heat can be pivotal in maintaining optimal temperatures for sensitive onboard equipment and systems. This article delves into the prospects of utilizing hollow particles of oxide powders within thermal control systems, examining their potential applications, benefits, and the challenges that must be addressed in the pursuit of next-generation thermal management solutions.

The purpose of this research is to conduct a comparative analysis of the diffuse reflection spectra and induced absorption spectra of coatings based on hollow and solid microparticles of Al_2O_3 , ZnO, TiO_2 and SiO_2 after irradiation by electrons.

2. Experiment

To obtain hollow aluminum oxide particles, the surfaces of polystyrene templates were coated with a chitosan solution (chitosan: acetic acid: water in a ratio of 2:1:40). Subsequently, aluminum oxide nanoparticles were deposited and mixed at high speed to facilitate the formation of a more compact $\text{PS}/\text{Al}_2\text{O}_3$ structure. This was followed by heating at 60°C until the solution was completely dried, and a stepwise thermal treatment was conducted at temperatures of 300, 900, and 1300°C for 2 hours at each stage in a vacuum.

Hollow ZnO particles were obtained using a hydrothermal method from a solution containing 2.5 moles of $\text{Zn}(\text{CH}_3\text{COO})_2 \cdot 2\text{H}_2\text{O}$, 1 mole of deionized water, and 7.5 moles of NH_4HCO_3 , which was transferred to an autoclave

with a Teflon cup and heated to 180°C for a duration of 15 hours [1]. After synthesis, the powders were washed by alcohol, dried at 60°C in air, and thermally treated at a temperature of 650°C .

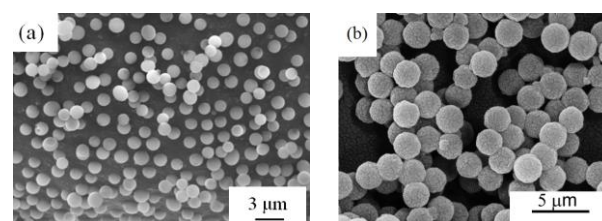


Fig. 1. SEM of hollow particles Al_2O_3 (a) and ZnO (b).

The synthesis of hollow TiO_2 particles was conducted as follows: the components were mixed on a magnetic stirrer for 30 minutes in the following molar ratios: 1 ($\text{Ti}(\text{OCH}(\text{CH}_3)_2)_4$):12($(\text{C}_4\text{H}_9)_4\text{NOH}$):43(H_2O):170($\text{C}_2\text{H}_5\text{O}$ H). The resulting solution was subsequently transferred to an autoclave, which was then heated to a temperature of 200°C for a duration of 6 hours [2]. This process yielded a solution containing a white precipitate, which was subjected to multiple washings by alcohol. The precipitate was dried at 60°C in air without undergoing any further thermal treatment.

Hollow SiO_2 particles were obtained through the deposition of $\text{Si}(\text{OC}_2\text{H}_5)_4$ onto solid substrates in the form of polystyrene microballs in a solution of alcohol and ammonia water, followed by thermal treatment at 600°C for a duration of 3 hours.

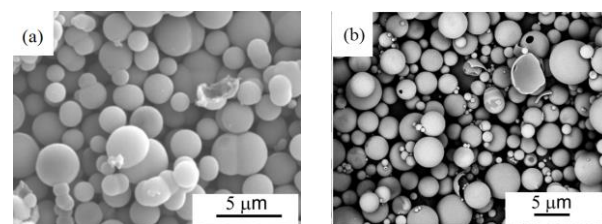


Fig. 2. SEM of hollow particles TiO_2 (a) and SiO_2 (b).

The coatings were prepared by mixing 50% by volume of hollow particles with 50% by volume of a silicone-based varnish. The resulting coatings were applied to AMG-6 aluminum substrates and dried at room temperature in air.

The thickness of the coatings was approximately 200-250 micrometers.

The surface morphology was analyzed using a Helios NanoLab 660 scanning electron microscope (SEM). The diffuse reflection spectra of the samples in the range of 0.2–2.2 micrometers were measured in vacuum at the irradiation site (*in situ*) using the space environment simulator “Spectrum” [3]. The solar absorptance (α_s) was calculated in accordance with international standards ASTM (E490-00a and E903-96). The samples were irradiated by electrons at an energy of 30 keV, with a fluence up to $5 \times 10^{16} \text{ cm}^{-2}$ at a flux density of $4 \times 10^{12} \text{ cm}^{-2} \cdot \text{s}^{-1}$.

3. Results and discussions

From the microphotographs obtained using a scanning electron microscope (SEM) (see Fig. 1 and 2), it can be observed that hollow particles of ZnO and TiO₂ with a spherical shape, ranging in size from 500 to 2000 nm, are formed through the hydrothermal synthesis method, with some particles being interconnected. The yield of spherical particles is approximately 90%. The particles of Al₂O₃ and SiO₂, synthesized based on polystyrene balls, exhibit a spherical shape with varying sizes up to 5000 nm.

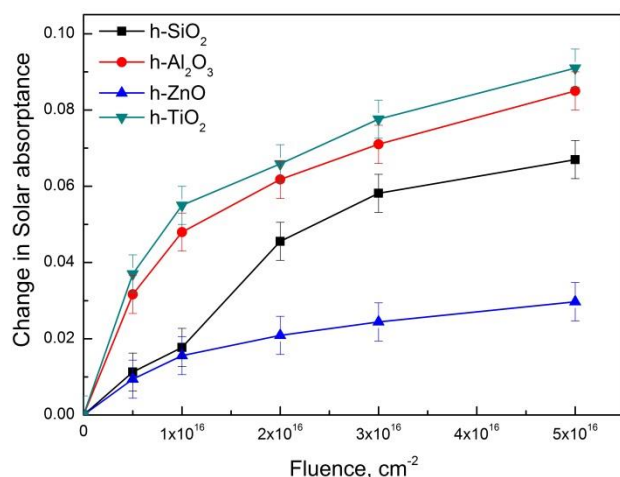


Fig. 3. Dependence of change in solar absorptance on the fluence of 30 keV electrons for coatings based on hollow particles.

From the dependence of the change in the solar absorptance on the electron fluence it follows (Fig. 3) that the coatings based on hollow ZnO particles have the highest radiation stability, so at the highest irradiation fluence of $5 \times 10^{16} \text{ cm}^{-2}$ the $\Delta\alpha_s$ value is 0.03, for hollow SiO₂ particles – 0.067, while for coatings based on Al₂O₃ and TiO₂ $\Delta\alpha_s = 0.085$ and 0.091. All curves show a stable upward trend, indicating an increase in change in the solar absorptance with increasing fluence. The improvement in radiation stability of coatings when using hollow ZnO particles compared to hollow TiO₂ particles reaches three times. The enhanced radiation stability of coatings based on hollow zinc oxide particles compared to hollow particles of aluminum oxide, silicon dioxide and titanium dioxide can be attributed to several intrinsic and extrinsic factors that govern the stability and structural integrity of these materials under radiation exposure. Firstly, the unique electronic properties of ZnO play a crucial role in its radiation resistance. ZnO possesses a wide bandgap and a high exciton binding energy, which allows it to effectively dissipate the energy deposited by ionizing radiation. This

characteristic minimizes the generation of defects within the crystal lattice, which can compromise the material's structural integrity. In contrast, TiO₂, Al₂O₃ and SiO₂, while also exhibiting some degree of radiation tolerance, tend to form more defects when exposed to similar radiation doses, leading to a decrease in their overall stability. Secondly, the hollow structure of ZnO particles contributes to their enhanced radiation resistance. The porous nature of these particles allows for better accommodation of radiation-induced stress, reducing the likelihood of catastrophic failure. The voids within the hollow particles can act as sinks for radiation-induced defects, effectively mitigating their impact on the overall material properties. In comparison, the hollow structures of Al₂O₃ and TiO₂ may not provide the same level of accommodation for defects, resulting in a higher susceptibility to radiation damage. Furthermore, the chemical stability of ZnO under radiation exposure is also a significant factor. ZnO is less prone to chemical reactions that can lead to degradation when subjected to radiation, whereas Al₂O₃, SiO₂ and TiO₂ may undergo chemical transformations that can weaken their structures. This stability is particularly important in applications where materials are exposed to harsh environments, such as in space applications. The increase in radiation stability of coatings based on hollow particles may be due to the fact that some of the free radicals present in the varnish before irradiation combine with uncompensated radicals in the hollow particles during irradiation to form complexes. This leads to a decrease in their concentration and to a decrease in the intensity of the absorption bands caused by such radicals. Crosslinking probably occurs for primary radiation defects on the surface of hollow aluminum oxide particles and radicals in the varnish. The rupture of bonds leads to the appearance of free radicals in the irradiated varnish. The radicals of the organosilicon varnish interact with radiation defects on the surface of hollow particles of aluminum oxide to form complexes, which leads to a decrease in the intensity of the absorption bands during irradiation.

4. Conclusions

Coatings based on hollow zinc oxide particles exhibit the highest radiation stability compared to coatings made from hollow silicon dioxide, aluminum oxide, and titanium dioxide. Overall, the findings highlight the advantages of using hollow ZnO particles in applications requiring high radiation tolerance, particularly in harsh environments such as space applications. The combination of intrinsic properties and structural characteristics makes ZnO a favorable choice for enhancing the performance and durability of coatings under radiation exposure.

Acknowledgements

The work was carried out with the financial support of the Ministry of Science and Higher Education of the Russian Federation (state assignment No. FZMU-2022-0007 и FEWM-2023-0012).

References

- [1] C. Yan, D. Xue J. Alloy. Compd.. **431**(2007) 241.
- [2] V.V. Neshchimenko, C. Li, M.M. Mikhailov. Dyes and Pigments. **145**(2017) 354.
- [3] L.G. Kositsyn, M.M. Mikhailov, N.Y. Kuznetsov, M.I. Dvoretzki. Instrum. Experim. Tech. **28**(1985) 929.

Ferroelectric nanocomposites on base of porous glasses with modified interfaces

Alekseeva O.A.¹, Koroleva E.Yu.¹, Molokov A.Yu.¹, Naberezhnov A.A.^{*1}, Sysoeva A.A.¹,
Gorshkova E.Yu.^{2,3}

¹ Ioffe Institute, 26 Polytekhnicheskaya, St.-Petersburg, 194021, Russia

² Frank Laboratory of Neutron Physics, Joint Institute for Nuclear Research, 6 Joliot-Curie, Dubna 141980, Russia

³ Kazan (Volga Region) Federal University, 18 Kremlyovskaya, 420008 Kazan, Russia

*e-mail: alex.naberezhnov@mail.ioffe.ru

Abstract. Mesoporous matrices with the surface of internal channels (pores) modified with carbon, TiO₂ and Al₂O₃ have been prepared based on mesoporous sodium borosilicate glasses with an average pore diameter of 7 nm (PG7). Then, using these matrices, nanocomposites have been formed, into the residual pore space of which the dielectric materials (NaNO₂, KNO₃, NaNO₃) were introduced. The macroscopic properties, crystal structure and spatial organization of these nanocomposites have been studied using dielectric spectroscopy, X-ray diffraction and small-angle X-ray scattering. It is shown, that modifiers form thin layers on the inner surface of the channels, in turn these layers organize a three-dimensional fractal structure. The introduction of dielectrics into the residual pore space leads to a significant change in the dielectric and structural properties of the obtained nanocomposites compared to unmodified samples. The sizes of the corresponding coherent scattering regions and fractal parameters of all produced nanocomposites have been determined.

1. Introduction

Size effect can fundamentally change the macroscopic physical properties of materials, especially when the characteristic sizes of the nanoparticles become comparable to the correlation length of critical fluctuations in the order parameter. There are various methods for obtaining nanocomposite materials (NCM), one of which is the introduction of substances into the pores of mesoporous alkali-borosilicate glasses [1]. It should be noted, that in addition to the size effect, the properties of NCMs are significantly dependent on the presence of an interface between the matrix and the embedded material. Changes in the interface can also be used to change the overall macroscopic properties of NCMs; this approach has been used in several studies [2-4]. The principle goal of this work has been to produce several types of matrices with a modified matrix-pore space interface, to create nanocomposites based on these matrices (containing embedded dielectrics including ferroelectrics), to study the influence of interfaces on the properties of produced nanocomposites and to clarify the role of interfaces in modifying the properties of these nanocomposites from a comparison with previously obtained data for unmodified nanocomposites of these types.

2. Samples and Experiment

As a basement of NCM we have used mesoporous alkali-borosilicate glasses manufactured at the Ioffe Institute using the conventional technology [1,5,6]. In these glasses, at special heat treatment, phase separation onto two components occurs: on a stable phase consisting of amorphous SiO₂, which forms the skeleton of the matrix, and the channels (in our glasses their diameter $D \sim 45 \pm 5$ nm) of chemically unstable phase (CUP) [5]. At chemical etching, the part of CUP is removed and a random dendrite 3D net of pores (connected channels) is formed. According to the mercury porosimetry the average pore diameter of empty glasses were 7(2) nm (PG7 or PG6) (Fig.1). Three types of PG7 with modified interfaces have been prepared: PG7+C, PG7+TiO₂ and PG7+Al₂O₃. Further the remnant porous spaces in these

matrices have been filled by NaNO₂, KNO₃ and NaNO₃ from the water solutions. The crystal structures and space organizations of all samples have been tested using X-ray diffraction (diffractometer DRON-8, Cu K α line, Ioffe Institute) and small-angle X-ray scattering (SAXS) (Xeuss 3.0 installation (JINR, Dubna), Mo K α radiation 0.71 Å) at three sample-detector distances: 550, 1825 and 4605 mm at room temperature. To carry out dielectric studies, gold electrodes about 80 nm thick with 4 nm chromium sublayer for better adhesion were deposited on the sample surfaces. The study of dielectric response has been carried out on the broadband dielectric spectrometer Novocontrol BDS80 in the frequency range of $0.1 - 3 \times 10^6$ Hz and in the temperature diapason 300–440 K on cooling at 1 K/min rate.

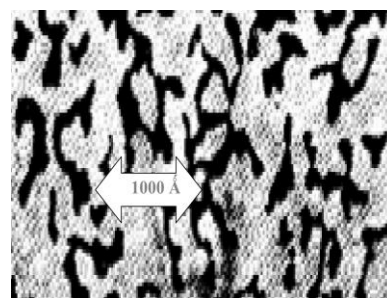


Fig. 1. TEM image of cross-section of empty PG7. Dark regions – pores, white regions – amorphous silica.

3. Results and discussions

Analysis of diffraction patterns has shown that the modifiers (C, TiO₂ and Al₂O₃) into PG7 in all modified matrices are in an amorphous state. The results of nitrogen sorption-desorption (BET procedure [7]) testing have confirmed a realization of thin (1-2 molecules) layers of modifiers on the inner surface of channels in PG7. Next, using SAXS data (Fig. 2), we have determined the parameters of the porous space organizations of empty PG7, PG7+C, PG7+TiO₂ and PG7+Al₂O₃, including gyration radii R_G (from the Guinier region at small momentum transfer Q) and fractal parameter α (a slope of $I(Q)$ vs. Q at large Q where $I(Q) \sim Q^{-\alpha}$) from Porod's region [8].

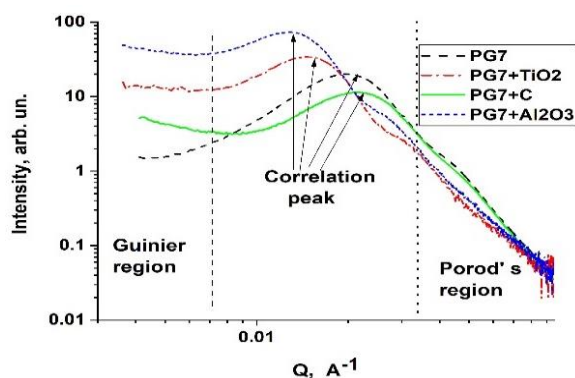


Fig. 2. Dependences of SAXS intensity $I(Q)$ vs. Q (momentum transfer) for PG7, PG7+C, PG7+TiO₂ and PG7+Al₂O₃ matrices.

R_G characterizes the average size of regions into the total porous space where the modifiers are localized. R_G values (29 ± 5 nm for PG7+TiO₂, 23 ± 3 nm for PG7+Al₂O₃ and 54 ± 4 nm for PG7+C) and the data of BET procedure indicate that modifiers have formed 3D random net of hollow quasi-cylindrical channels on the borders “matrix-porous space”. At large Q the scattering intensity follow to the Porod’s law $I(Q) \sim Q^{-\alpha}$ and $\alpha=4$ for scattering on a smooth surface [8]. In our matrices with modified interfaces parameter α at large Q is smaller than 4 and it corresponds to formation of surface fractal into the porous space. The introduction of dielectrics into the pore space of modified matrices leads to a significant change in the organization of the pore space and the fractal characteristics of the produced NCMs. Examples of the transformation of the internal organization for NCM PG6+C+KNO₃ and PG6+TiO₂+NaNO₂ are given in [9,10]. Firstly, SAXS intensity for all NCMs increases sharply due to the appearance of additional interfaces and scatterers, as well as due to the increase in both the scattering amplitude density and their difference (contrast) into modified matrices. Secondly, it has been shown, that the sizes of the coherent scattering regions (CSR) determined from the diffraction patterns are significantly smaller than the gyration radii R_G calculated from SAXS data analysis. It indicates the coexistence of crystalline and amorphous phases of embedded substances in the pore space of NCMs.

As for the studies of the dielectric response of these nanocomposites, to date, measurements of the temperature and frequency dependences of this response have been carried out for the nanocomposites PG6+C+KNO₃, PG6+TiO₂+NaNO₂, PG7+C+NaNO₃, PG7+TiO₂+NaNO₃ and PG7+Al₂O₃+NaNO₃. To clarify the role of the interface, studies of the dielectric properties of unfilled matrices with modified interfaces and unmodified matrices filled with NaNO₂, NaNO₃ and KNO₃ have been also performed. Fig. 3 shows the temperature dependences of the real (ϵ') part of the permittivity at 179 kHz (left) and 0.1 Hz (right) for empty PG6, PG6+C, PG6+KNO₃ and PG6+C+KNO₃. Analysis of temperature and frequency dependences of dielectric response reveals two relaxation processes. The first one provides the main contribution to the dielectric response of the carbon-free nanocomposite processes. We attribute this process to the charge polarization on the pores’ boundaries.

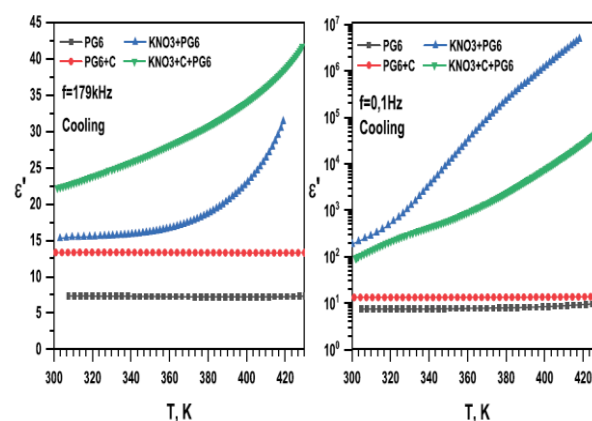


Fig. 3. Temperature dependences of permittivity on cooling at 179 kHz (left) and 0.1 Hz (right) for PG6, PG6+C, PG6+KNO₃ and PG6+C+KNO₃.

A similar relaxation process also exists in PG6+C+KNO₃, but it is much weaker and visibly slower, i.e. interface modification affects this process essentially. The second relaxation process in PG6+KNO₃ is weaker by three orders of magnitude. Relaxation times increase from 10^{-5} to 10^{-2} s on cooling. In PG6+C+KNO₃ the process becomes by six orders slower. We believe that this process corresponds to a hopping conductivity in KNO₃ clusters and between neighboring ones. This assumption is in good agreement with the peculiarities of the spatial organization of NCM, revealed from SAXS data.

4. Conclusions

A technology for producing mesoporous matrices with modified interfaces at the matrix-pore space boundary has been developed. Based on these matrices, nanocomposite materials (NCM) containing embedded dielectrics NaNO₂, KNO₃ and NaNO₃ have been obtained. Interface modification leads to a reorganization of spatial structure nanoparticles of embedded dielectrics and to a significant change in the macroscopic dielectric characteristics of nanocomposite materials compared to similar NCMs prepared on base of unmodified mesoporous glasses. It opens up the possibility of smart governing of macroscopic physical properties of NCMs by selecting appropriate interface modifiers.

References

- [1] D. Enke, F. Janowski, W. Schwieger, *Micropor. & Mesopor. Mat.* **60**(2003)19.
- [2] T. Kikukawa, K. Kuraoka K., K. Kawabe, K. Yashid, K. Hirao, T. Yazawa. *Jour. Amer. Cer. Soc.* **87**(2004)504.
- [3] T. Yazawa, S. Miyamoto, S. Yusa, T. Jin, A. Mineshige *Mat. Res. Bull.* **48**(2013)4267.
- [4] M. Dvoyashkin, E.E. Romanova, W.-D. Einicke, R. Gläser, J. Kärger, R. Valiulin. *Adsorption.* **17**(2011)93.
- [5] O.V. Mazurin, E.A. Porai-Koshits, *Phase Separation in Glass* (Elsevier, Amsterdam, North Holland, 1984).
- [6] H. Xihuai, J. Non-Cryst Solids. **112**(1989)58.
- [7] S. Brunauer, P.H. Emmett, E. Teller, *Jour. Amer. Chem. Soc.* **60**(1938)309.
- [8] L. A. Feigin, D. I. Svergun *Structure Analysis by Small-Angle X-Ray and Neutron Scattering* (Springer, New York, NY 1987).
- [9] O.A. Alekseeva, M.V. Tomkovich, A.A. Naberezhnov, A.A. Sysoeva, Yu.E. Gorshkova, *Tech. Phys. Lett.* **51**(2025)27 (in Russian).
- [10] P. Vanina, A. Naberezhnov, O. Alekseeva, Yu. Gorshkova, E. Lukin & A. Sysoeva *J. Porous Mater.* **32**(2025)425.

Hydrochemical synthesis of nanostructured metal-oxide compound of the Nb–Bi–Fe–O system

Gorokh G.G.^{*,1}, Fiadosenka U.S.¹, Chaeusky V.V.¹, Em M.¹, Taratyn I.A.²

¹ Belarusian State University of Informatics and Radioelectronics, 6 P.Brovki, Minsk, 220013, Belarus

² Belarusian National Technical University, 220013 Minsk, Belarus

*e-mail: gorokh@bsuir.by; Tel.: +375 29 3474903

Abstract. The metal oxide compound of the Nb–Bi–Fe–O system was obtained by successive ionic layer deposition from 0.05 M Bi(NO₃)₃ and 0.05 M Fe(NO₃)₂ solutions as sources of bismuth and iron on an array of anodic niobium oxide columnar nanostructures. The resulting composite was transformed into a homogeneous compound by thermal annealing at 600 °C. The nanostructured composite morphology was studied by scanning electron microscopy, its elemental composition by the EDX method, and its microstructure by the X-ray spectroscopy method. Phase transformations in the nanocomposite during annealing in the temperature range of 300 – 700 °C were studied. The synthesized composite was used as an active material in chemoresistive sensor. The results showed that the synthesized metal oxide composite is very promising for creating high-performance sensors.

1. Introduction

Mixed metal oxides of the compounds Bi–Ti–O; Bi–Fe–O; Nb–Te–O and others, depending on the composition, exhibit the properties of active smart materials — ferro- and piezoelectrics, thermoelectrics, or passive ones, such as gas-sensitive, photovoltaic and photocatalytic films [1,2]. In this regard, the development of methods for the formation of multicomponent spatially ordered planar metal oxide nanosystems with a three-dimensional architecture attractive for practical use is becoming relevant [3]. The paper presents a new technological approach to the synthesis of compounds of the Nb–Bi–Fe–O system, based on electrochemical anodization of a two-layer Al/Nb composition [4] and successive ionic layer deposition (SILD) onto the matrix of the formed metal oxide columns of iron and bismuth oxides. Comprehensive studies and phase transformations of the microstructure during high-temperature annealing were carried out. Bismuth-based composites exhibit ferromagnetic or antiferromagnetic properties depending on the crystal structure and composition. Bismuth is known for its ability to exhibit semiconductor and piezoelectric properties. Nb₂O₅ has good sensitivity to a number of gases and also has photocatalytic activity, which allows it to be used in light-activated sensors and makes it very promising for sensors. Niobium and iron oxides are very stable at high temperatures and have properties suitable for use in thermoelectric devices or high-temperature sensors. Bismuth ferrites exhibit both piezoelectric and ferroelectric properties, which makes them promising for piezoelectric devices such as pressure, vibration and sound sensors. Niobium additionally improves the structural stability and electrical characteristics of the material.

2. Experiment

Silicon substrates were used as initial samples, on which Nb and Al films were deposited by magnetron sputtering in vacuum at a thickness of 200 nm and 1.5 μm, respectively. Electrochemical anodizing of experimental samples was carried out in a combined mode. The upper aluminum layer was anodized in an aqueous solution in 0.4 M C₂H₂O₄ in the potentiostatic mode at 50 V. As a result, the upper aluminum layer was transformed into anodic alumina (AA) with hexagonally packed oxide cells with

vertical pores in the center. The subsequent anodization of the titanium sublayer through the AA pores was carried out in aqueous solution of 0.2 M C₄H₆O₆ at 250 V. On the second anodization stage, the nanosized columns of niobium oxide were formed under the AA pores and partially filled the lower part of the pores. After reanodization, the AA mask was removed in 50% H₃PO₄ aqueous solution at temperature of 323°K. After dissolving the AA mask, the ANOC array was annealed at a temperature of 600 °C for 30 minutes.

The electrical anodizing modes were set using a Keysight N5752A system DC power supply, and the process parameters were recorded and monitored in situ using a Keysight 34470A digital multimeter connected via a USB interface to a personal computer with the Bench Vue software installed. Composite Bi-Fe-O films was deposited on an array of vertically ordered anodic niobium oxide columns (ANOC) using SILD method from the cationic aqueous solution of 0.1 M Bi(NO₃)₃·5H₂O and 0,05 M Fe(NO₃)₂·9H₂O and the anionic solution – distilled water heated to 70 °C. Cyclic treatment of the initial samples was carried out alternately in a bismuth-containing solution and in water, and in an iron-containing solution and water for 15 s at temperature of 30 °C. The 30 cycles were conducted. After layering by SILD, all samples were subjected to heat treatment at temperature of 70 and 140 degrees for 20 and 40 min.

The surface morphology of the formed films was studied by scanning electron microscopy (SEM) in Hitachi S-806 at accelerating voltage of 7 kV and Hitachi S4-800 at accelerating voltage of 15 kV. The phase composition and microstructure of the formed films were determined based on the analysis of diffraction data obtained on the Bruker installation. The identification of chemical elements in the composition of the obtained films was determined using electron probe X-ray spectral microanalysis (EDX) using a Bruker QUANTAX 200.

3. Results and discussions

Figure 1a shows the electron microscopic images of ANOCs after AA dissolution. On the surface, there is a cluster of evenly distributed elongated columnar formations up to 350 nm high, about 50 nm in diameter, and a distance between columns of about 80 nm. Surface density of ANOC is 9,27×10⁹ cm⁻². During SILD process,

the Bi-Fe-O compound completely filled the gaps between the ANOCs and covered them to height of about 100 nm. However, after annealing at 600 °C, the compound was localized on the columns themselves along their entire length (Fig. 1, b).

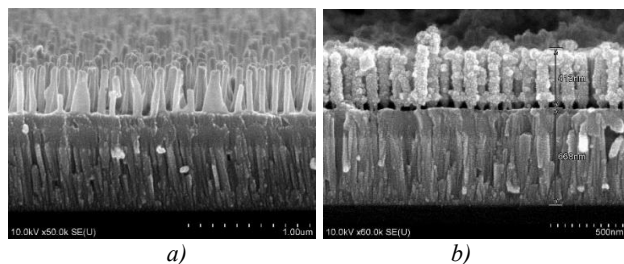


Fig. 1. SEM images of ANOC arrays after removal of the AA matrix (a); and ANOCs with the deposited composite Bi-Fe-O after annealing at 600 °C (b).

Figure 2 shows the diffraction pattern of ANOC annealed at 600 °C. The peaks (37.44°, 69.38°, 82.28°) characteristic of metallic niobium at temperature of 400 °C have practically disappeared. At the same time, modifications of the oxide phases Nb_2O_5 with peaks at 22.7°; 28.4°; 36.8° and 54.2°, as well as NbO_2 with peak at 43.8° appear.

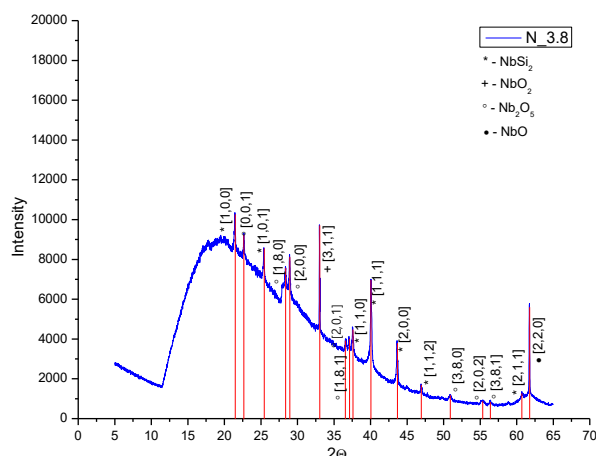


Fig. 2. X-ray diffraction patterns of ANOCs annealed in vacuum at 600 °C.

Analysis of the elemental and phase composition of ANOCs consisting of $\alpha\text{-Nb(O)}$ solid solution mixture and three stable modifications of oxides: NbO , NbO_2 and Nb_2O_5 , with a predominant content of the last phase at the top of the columns, as well as the nature of its modification from the tops to the base, allows us to predict and create pre-distributed growth centers in a given manner.

The atomic ratio of Nb; Bi, Fe and O determined by energy dispersive spectrometry, taking into account all the elements included in the nanocompound, was Nb – 18.67%; Bi – 7.10%; Fe – 5.49%; O – 49.38% (Fig 3).

Analysis of X-ray photoelectron spectroscopy (XPS) data indicates the formation of complex oxides after annealing, such as multicomponent oxides (e.g., $\text{Bi}_2\text{Fe}_4\text{O}_9$ or $\text{BiFeO}_3/\text{Nb}_2\text{O}_5$), since such compounds are usually characterized by a shift in binding energy and peak broadening.

Phase transformations in the nanocomposite as a result of high-temperature annealing were studied. At 300 °C the oxides retain their structures without significant phase

transformations, the composite remains mainly amorphous. At 500 °C the initial stages of complex compounds crystallization such as ferrites or complex oxides begin. The interaction between Fe and Bi leads to the formation of mixed phases such as BiFeO_3 . The Nb_2O_5 remains stable and begins to interact with Bi and Fe, forming the initial stages of niobates (BiNbO_4). At 700 °C active formation of crystalline phases occurs. Bismuth oxide transforms into a tetragonal phase ($\beta\text{-Bi}_2\text{O}_3$) and forms complex oxide phases with iron and niobium, such as bismuth ferrite and bismuth-iron niobate, which leads to the appearance of materials with interesting magnetic, ferroelectric and photocatalytic properties. At temperatures above 700 °C, BiFeO_3 and other complex ferrite structures become the dominant phases. High-temperature $\text{Bi}_4\text{Nb}_3\text{O}_{12}$ phases appear.

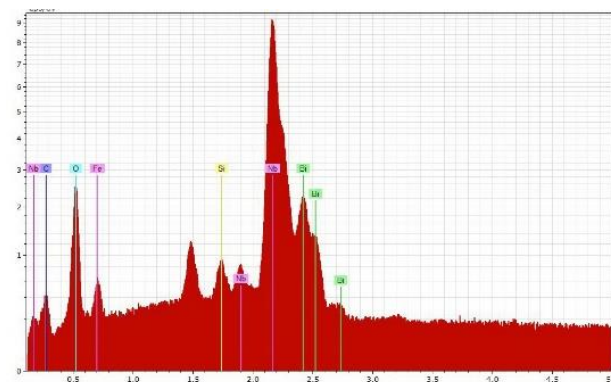


Fig. 3. EDX spectrum of composite metal oxide systems |Bi-Nb-Fe-O.

The synthesized composite was used as an active material in chemoresistive sensor. Studies of the gas-sensitive properties of metal oxide systems |Bi-Nb-Fe-O nanocomposite showed that for concentrations of 1 ppm and 10 ppm CO , the sensitivity was 0.16 and 0.45, and for H_2 concentrations of 5 and 40 ppm at 250°C was 0.22 and 0.40, respectively.

4. Conclusions

The fields of application of nanocomposites of the $\text{Bi}_x\text{Fe}_y\text{O}_z/\text{Nb}_2\text{O}_5$ system can be different. Compounds formed at 300–500 C can find application in gas sensors, where their electrical conductivity will change due to gas adsorption on their surface. Compounds annealed at temperatures of 700°C and above will be useful in photocatalysts, ferroelectric devices, supercapacitors, and in the creation of materials with magnetic properties.

Acknowledgements

The work was carried out with the financial support of the State Program of Scientific Research of the Republic of Belarus for 2021-2025 "Materials Science, New Materials and Technologies" (No. 1.14 and No. 2.19).

References

- [1] G. Gorokh, U. Fiadosenka, X. Wang, I. Taratyn. Next Nanotechnology **5**(2024)100038.
- [2] V. Fedosenko, M. Iji, A. Lozovenko, G. Gorokh. Doklady BGIR **21**(2023)89.
- [3] G. Gorokh, N. Bogomazova, A. Taleb, V. Zhyllinski, T. Galkovsky, A. Zakhlebayeva, A. Lozovenko, M. Iji, V. Fedosenko, V. Tolstoy. Sensors **21**(2021)4169.
- [4] G. Gorokh, A. Pligovka, A. Lozovenko. Technical Physics **64**(2019)1657.

Heterostructured TiO₂–CuO_x layers: electrophoretic deposition approach to efficient photocatalysis

Sorokina L.I.^{*1}, Volkova L.S.², Zhurina E.S.³, Dubkov S.V.¹, Gromov D.G.¹

¹ Institute of Advanced Materials and Technologies, National Research University of Electronic Technology—MIET, Bld. 1, Shokin Square, Zelenograd 124498, Russia

² Institute of Nanotechnology of Microelectronics RAS, 32A Leninsky Prospekt, Moscow 119991, Russia

³ Russia S.P. Kapitsa Scientific Technological Research Institute, Ulyanovsk State University, 42 Leo Tolstoy Street, Ulyanovsk 432017, Russia

*e-mail: larasork@gmail.com

Abstract. This work focuses on the development of a technology for the formation of TiO₂-based nanostructured layers by electrophoretic deposition (EPD) for photocatalytic applications. The effects of stabilizing additives on suspension stability, particle mobility, and layer morphology were studied to optimize EPD process. Composite TiO₂–CuO_x layers with CuO_x content ranging from 1.5 to 11 wt% were obtained. It was shown that increasing the CuO_x content decreases the optical band gap and enhances the photocatalytic performance in CO₂ reduction to methanol.

1. Introduction

The development of effective strategies for the fabrication of heterostructured photocatalysts is an urgent task for the production of renewable fuels (such as hydrogen, methanol, and methane) and the degradation of toxic pollutants [1,2]. One promising approach involves creating hybrid systems based on TiO₂ combined with semiconductors possessing narrower band gaps [3]. Such composites enable an extension of light absorption into the visible region and enhance photocatalytic performance by improving charge carrier separation. In particular, TiO₂–CuO_x composite structures have demonstrated high photocatalytic activity due to efficient interfacial charge transfer processes [4].

In parallel with the search for new materials, the development of low-cost fabrication technologies remains an important priority. EPD offers a cost-effective method for forming nanostructured layers from powder components without the need for expensive equipment. EPD is particularly effective for creating TiO₂-based layers with controlled morphology and composition [5,6]. However, the formation of composite layers presents challenges related to suspension stability and deposition reproducibility.

This study presents the results of forming TiO₂ and TiO₂–CuO_x layers by the EPD method, with controlled adjustment of their composition, thickness, and morphology, as well as an investigation of their photocatalytic activity in CO₂ reduction reactions.

2. Experiment

In this work, TiO₂ P25 with a particle size of 25 nm, CuO_x particles with sizes of 50–80 nm were used. Sodium lauryl sulfate (SDS) was employed as stabilizing additives. Chemically pure isopropyl alcohol (99.9%) was used as the solvent for suspension preparation. The loading of nanopowders was maintained at 1 g/L in all cases. The suspensions were processed using an immersion disperser at a power of 100 W for 1 hour at a temperature not exceeding 22 °C. The stability of the obtained suspensions was evaluated by sedimentation analysis.

Titanium foil was used as the substrate, while stainless steel foil served as the counter electrode. Prior to

deposition, the titanium foil was etched in an HF:HNO₃:H₂O solution (1:1:4 by volume) to remove impurities and the native titanium oxide layer. The foil was then washed with deionized water and dried in isopropyl alcohol vapor. The EPD process was performed in potentiostatic mode at an electric field strength ranging from 30 to 150 V/cm.

The obtained samples were characterized using a scanning electron microscope (SEM) equipped with an energy-dispersive X-ray spectroscopy (EDX) attachment and a transmission electron microscope (TEM). The photocatalytic activity of the samples was evaluated using a gas chromatograph.

3. Results and discussions

In the course of this study, a technology for the formation of TiO₂–CuO_x composite layers by EPD from isopropanol-based suspensions was developed and optimized. The effect of the SDS on the stability of the suspensions, electrophoretic deposition rate, and morphology of the formed layers was investigated.

It was shown that suspensions based on isopropanol and TiO₂ particles exhibit high stability; however, in the absence of surfactant, electrophoretic deposition practically does not occur due to the low surface charge of the particles. The dependence of the electrophoretic mobility of TiO₂ on the SDS content was obtained (Fig.1).

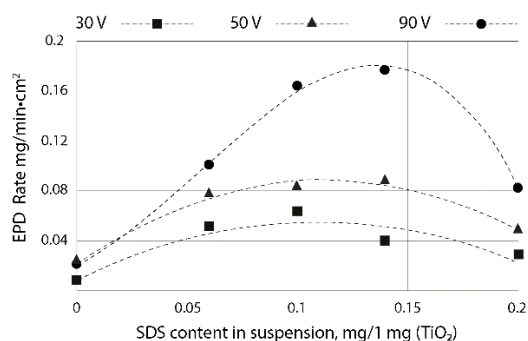


Fig. 1. EPD rate of TiO₂ particles as a function of SDS content per 1 mg of TiO₂ in suspension at different electric field strengths.

The addition of SDS significantly increases the electrophoretic deposition rate up to a certain limit: the optimal concentration of SDS was found to be in the range

of 0.1–0.14 mg per 1 mg of TiO_2 . When the concentration exceeds the critical value (0.2 mg/mg), particle coagulation occurs, leading to a decrease in the deposition rate.

Similar studies were carried out for suspensions containing mixtures of TiO_2 and CuO_x particles. In the absence of surfactant, CuO_x particles were predominantly precipitated in such systems. The addition of a small amount of SDS (0.04 mg per 1 mg of TiO_2 nanopowder) facilitated the co-electrophoretic deposition of both components, resulting in the formation of uniform composite layers.

The CuO_x content in the formed layers was determined using EDX analysis. The actual CuO_x content in the layers was found to be approximately half of its content in the original suspension. TEM analysis revealed the formation of TiO_2 - CuO_x heteroaggregates, where small TiO_2 particles (~25 nm) encapsulate larger CuO_x particles (50–80 nm). It is assumed that both individual TiO_2 particles and heteroaggregates migrate during the EPD process, which affects the final composition and morphology of the deposited layers.

The TiO_2 - CuO_x layer formed by electrophoretic deposition has a developed surface (Fig. 2).

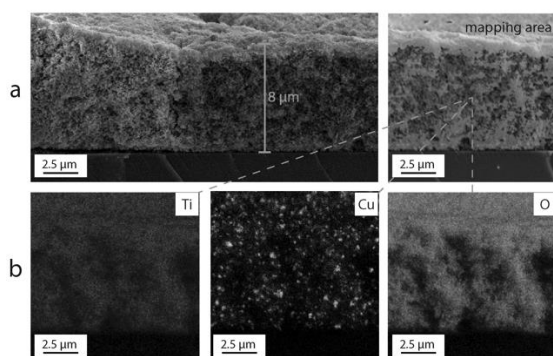


Fig. 2. SEM image of cross-section (a), cross-section element mapping (b) of TiO_2 - CuO_x deposited from suspension with 20 wt.% CuO_x .

All elements are distributed uniformly over the entire area. The approximate thickness of the TiO_2 - CuO_x layer with a specific mass of 1 mg/cm² is 8 μm.

The photocatalytic activity of TiO_2 - CuO_x composite layers electrophoretically deposited on titanium foil was investigated. The main product of CO_2 conversion under full-spectrum irradiation was methanol. It was found that the methanol yield increases almost linearly with the increasing copper oxide content in the composite material (Fig. 3.)

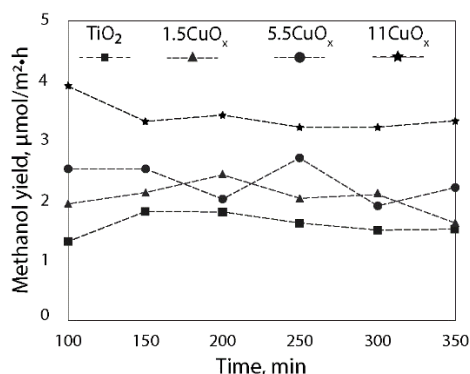


Fig. 3. Methanol yield over time TiO_2 - CuO_x composite layers.

The highest methanol yield, approximately 3.4 μmol/m²·h, was observed for the sample containing 11 wt.% CuO_x , which is twice as high as that of pure TiO_2 P25.

4. Conclusions

A technique for the formation of TiO_2 and composite TiO_2 - CuO_x layers by electrophoretic deposition from a suspension based on isopropanol with the addition of SDS was developed. Composite layers based on TiO_2 P25 and CuO_x in a certain ratio can be easily obtained by the EPD method. By varying the ratio of TiO_2 and CuO_x it is possible to adjust the optical and photocatalytic properties. Altering the quantity of CuO_x in the composite material allows for the manipulation of the proportion of free charge carriers (n and p), as evidenced by an open-circuit potential investigation. Thus, the catalytic properties of the material are controlled. The photocatalytic activity of the formed composite layers was investigated using the reaction of CO_2 reduction to methanol as a model reaction. It is found that the methanol yield increase linearly with increasing content of copper oxide in the composite material. The highest methanol yield is approximately 3.4 μmol/m²·h for the sample with 11 wt.% CuO_x , which is two times higher compared to pure TiO_2 P25. The increased photocatalytic activity of TiO_2 - CuO_x composite layers in comparison with pure TiO_2 is explained by the formation of a p-n heterojunction, which expands the spectral range of photoactivity, separates photogenerated charge carriers, and enhances the redox capacity.

Acknowledgements

This research was funded by State Assignment № FSMR-2023-0003.

References

- [1] E. Luévano-Hipólito, L.F. Garay-Rodríguez, L.M. Torres-Martínez. Handbook of Greener Synthesis of Nanomaterials and Compounds **1**(2021)593.
- [2] A. Shawky, R.M. Mohamed, N. Alahmadi, Z.I. Zaki. Colloids Surf. A Physicochem. Eng. Asp. **641**(2022)128564.
- [3] D. Cosma, A. Urda, T. Radu, M.C. Rosu, M. Mihet, C. Socaci. Molecules **27**(2022)5803.
- [4] Y. Wang, J. Tao, X. Wang, Z. Wang, M. Zhang, G. He, Z. Sun. Ceram. Int. **43**(2017)4866.
- [5] Y. Sun, Y. Wang, I. Zhitomirsky. Colloids Surf. A Physicochem. Eng. Asp. **418**(2013)131.
- [6] N. Parsi Benekohal, G.P. Demopoulos. J. Power Sources **240**(2013)667.

Electron spectroscopy of MAX phase $(\text{Cr}_{1-x}\text{Mn}_x)_2\text{GeC}$ and $\text{Cr}_2(\text{Ge}_{1-x}\text{Si}_x)\text{C}$ thin films

Andryushchenko T.A.^{*,1,2}, Lyaschenko S.A.¹, Yakovlev I.A.¹, Kriukov R.N.³, Lukyanenko A.V.¹, Solovyov L.A.⁴, Varnakov S.N.^{1,2}, Ovchinnikov S.G.¹

¹ Kirensky Institute of Physics, Federal Research Center KSC SB RAS, 50/38 Akademgorodok St., Krasnoyarsk 660036, Russia

² Krasnoyarsk Scientific Center, Federal Research Center KSC SB RAS, 50 Akademgorodok St., Krasnoyarsk 660036, Russia

³ National Research Lobachevsky State University of Nizhny Novgorod, 23 Gagarin Ave., Nizhny Novgorod 603022, Russia

⁴ Institute of Chemistry and Chemical Technology, Federal Research Center KSC SB RAS, 50/24 Akademgorodok St., Krasnoyarsk 660036, Russia

*e-mail: ata12@iph.krasn.ru

Abstract. Thin MAX films $(\text{Cr}_{1-x}\text{Mn}_x)_2\text{GeC}$ and $\text{Cr}_2(\text{Ge}_{1-x}\text{Si}_x)\text{C}$ were synthesized by magnetron co-deposition on MgO(111) substrates. Electron spectroscopy data indicate the presence of additional graphitic carbon in the films, which is associated with the technological features of the synthesis, competition between the carbothermic reduction of metals and carbon coalescence. Mixed $\text{sp}^2\text{-sp}^3$ hybridization of silicon and germanium, characteristic of two-dimensional materials, was found in silicon-containing samples.

1. Introduction

MAX phases ($\text{M}_{n+1}\text{AX}_n$, where $n = 1-4$) are nanolayered carbides or nitrides (X-element) of transition metals (M-element), alternating with atomic layers of an A-element, which is predominantly an element from groups XIII-XV of the periodic table. Due to different types of chemical bonds (covalent, ionic and metallic), these substances combine the properties of metals and ceramics, namely, they have high thermal and electrical conductivities, and demonstrate resistance to oxidation and high temperatures. The combination of these features makes these materials promising candidates for use as thermal barrier coatings, high-temperature ohmic contacts and solar cells [1].

MAX phases with chromium and manganese as an M-element have been found to have long-range magnetic order and the possibility of their magnetic properties being controlled by changing the parameters of the crystal lattice using deformation or substitution of elements [2-3]. Therefore, chromium- and manganese-containing MAX films with such properties can be used to obtain magnetically controlled heterostructures and coatings, in spintronics applications. MAX phases with silicon, in turn, have no less intriguing properties. Thin Ti_3SiC_2 films have a low coefficient of friction [4-5], and also have high values of hardness and Young's modulus [6]. However, among three-component MAX phases, only Ti-Si-C systems have an enthalpy of formation below zero and have been experimentally synthesized [7]. Other MAX phases with silicon as the A-element are predicted to be unstable compounds. Nevertheless, a possible way to obtain silicon-containing MAX phases is to substitute A-atoms with silicon in stable structures. For the above reasons, we synthesized thin substituted MAX $(\text{Cr}_{1-x}\text{Mn}_x)_2\text{GeC}$ and $\text{Cr}_2(\text{Ge}_{1-x}\text{Si}_x)\text{C}$ films and analyzed their properties by electron spectroscopy methods.

2. Experiment

Thin $(\text{Cr}_{1-x}\text{Mn}_x)_2\text{GeC}$ ($0 \leq x \leq 0.33$) and $\text{Cr}_2(\text{Ge}_{1-x}\text{Si}_x)\text{C}$ ($0 \leq x \leq 0.5$) films with a technological thickness of 40 nm were synthesized on MgO(111) substrates at a temperature of about 850°C by magnetron co-deposition in the

Laboratory of Magnetic MAX Materials of the Kirensky Institute of Physics SB RAS (created under the Megagrant project (agreement No. 075-15-2019-1886). For one of the samples with silicon, a gradient substitution from $x=0$ to $x=0.5$ was performed in the direction from the interface to the film surface. In situ, the crystal structure of the samples was analyzed by reflection high energy electron diffraction (RHEED), the chemical and phase composition was analyzed using Auger electron spectroscopy (AES). For more detailed analysis of the chemical composition and electronic structure of the samples, we used ex-situ X-ray photoelectron spectroscopy (XPS) with ion etching. Calculations of element concentrations based on electron spectroscopy data were made using the relative sensitivity factors of elements. X-ray diffraction analysis (XRD) and X-ray fluorescence analysis (XRF) were also used as ex-situ methods for analyzing the phase and chemical composition of the samples; the surface morphology of the samples was evaluated using atomic force microscopy (AFM).

3. Results and discussions

AES measurements show that the substituted films of both compositions, like the previously studied thin MAX Cr_2GeC films [8], accumulate an electronic charge, which is manifested by a positive shift of the Auger peaks of the film elements. Such phenomenon is typical for island conducting thin films on dielectric substrates [9-11]. At the same time, the oxygen Auger peak from the uncoated part of the substrate with an energy of about 510 eV does not shift, which is associated with the process of dynamic self-regulation in magnesium oxide under electron irradiation [10]. In turn, due to the shift it is possible to identify oxygen in the composition of the film itself.

According to XRD data, single-phase thin MAX $(\text{Cr}_{1-x}\text{Mn}_x)_2\text{GeC}$ films are formed at an increased technological concentration of carbon. Moreover, the carbon concentration increases along with the increase in the concentration of manganese. However, AES spectra (Fig. 1) and XPS data show that in addition to the carbide form of carbon, graphitic carbon is detected in the composition of MAX films.

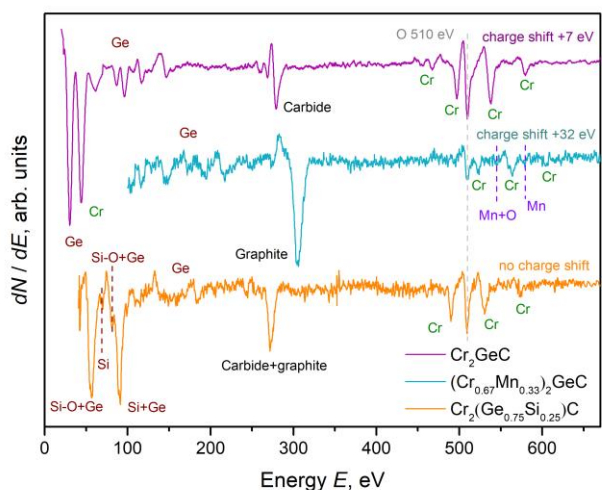


Fig. 1. Auger spectra of Cr_2GeC , $(\text{Cr}_{0.67}\text{Mn}_{0.33})_2\text{GeC}$ and $\text{Cr}_2(\text{Ge}_{0.75}\text{Si}_{0.25})\text{C}$ thin films on MgO substrates.

Additional research shows that excess carbon is required to reduce oxidized manganese. However, with an increase in the technological carbon concentration (and the power of the magnetron source), the concentration of individual graphite particles in the film increases. But the reduction of manganese occurs mainly due to the amorphous form of deposited carbon, and this process competes with the coalescence of graphite particles. These particles diffuse onto the film surface during annealing, and it may explain the presence of graphitic carbon on the surface of MAX films.

For the synthesis of MAX $\text{Cr}_2(\text{Ge}_{1-x}\text{Si}_x)\text{C}$ films, an increased technological concentration of carbon (about 30%) was also used. In this case, the excess carbon also may be involved in preliminary reduction of metals. RHEED and XRD patterns demonstrate that as the silicon concentration increases (from $x=0.125$ to $x=0.5$), crystallinity becomes worse and additional phases, like chromium monogermanide, Cr_3GeC with inverse-perovskite structure, Cr_3C_2 and/or Cr_3Si_5 , are formed. However, the sample with concentration gradient exhibits higher surface crystallinity and a smaller amount of secondary phases compared to the $\text{Cr}_2(\text{Ge}_{0.5}\text{Si}_{0.5})\text{C}$ sample. Electron spectroscopy data indicate that silicon in the samples is partially oxidized. In addition to the carbide, graphitic carbon is also present (Figure 1). The Si 2p and Ge 3d XPS lines contain peaks characteristic of sp^3 hybridization, as well as contributions from sp^2 hybridized bonds. Mixed $\text{sp}^2\text{-sp}^3$ hybridization is typical for two-dimensional layers of germanium and silicon – germanene and silicene [12]. This mixed hybridization in MAX film can be explained by its layered structure, where two-dimensional layers of silicon and germanium alternate with layers of chromium carbide. At the same time, the silicon concentration is higher closer to the substrate, which is explained by the possible segregation of silicon on defects and the growth surface [13], which leads to thermodynamically favorable conditions for the nucleation of the MAX phase.

4. Conclusions

The electron spectroscopy data of thin MAX $(\text{Cr}_{1-x}\text{Mn}_x)_2\text{GeC}$ and $\text{Cr}_2(\text{Ge}_{1-x}\text{Si}_x)\text{C}$ films demonstrate the presence of an additional graphite form of carbon, which is

explained by the technological features of the synthesis, the processes of carbothermic reduction of oxidized metals and carbon coalescence. In silicon-containing samples, mixed $\text{sp}^2\text{-sp}^3$ hybridization of silicon and germanium is found, probably associated with the layered structure of the MAX phase.

Acknowledgements

The research was supported by the grant of the Russian Science Foundation № 25-12-20012 (<https://rscf.ru/project/25-12-20012/>), grant of the Krasnoyarsk Regional Science Foundation.

References

- [1] J. Gonzalez-Julian. *J. Am. Ceram. Soc.* **104**(2021)659.
- [2] E.B. Thorsteinsson, et al. *APL Mater.* **11**(2023)121102.
- [3] Z. Liu, et al. *Phys. Rev. B* **89**(2014)054435.
- [4] A. Crossley, et al. *J. Phys. D: Appl. Phys.* **32**(1999)632.
- [5] S. Myhra, et al. *Mater. Lett.* **39**(1999)6.
- [6] J. Emmerlich, et al. *J. Appl. Phys.* **96**(2004)4817.
- [7] M. Dahlqvist, et al. *Mater. Today* **72**(2024)1.
- [8] T. Andryushchenko, et al. *Phys. Met. and Metall.* **124**(2023)1776.
- [9] P.J. Möller, J. He. *Nuc. Ins. and Meth. in Phys. Res. B.* **17**(1986)137.
- [10] J. Cazaux, et al. *J. Appl. Phys.* **70**(1991)960.
- [11] C. C. Chang. *Characterization of Solid Surfaces* (1974)509.
- [12] J. Beilstein. *Nanotechnol.* **9**(2018)2665.
- [13] J. Emmerlich, et al. *J. Appl. Phys.* **96**(2004)4817.

Stearic acid as green corrosion inhibitor of MA8 bioabsorbable magnesium alloy: *in vitro* coating characterization

Marchenko V.S.*, Gnedenkov A.S., Sinebryukhov S.L., Gnedenkov S.V.

Institute of Chemistry FEB RAS, 159 pr. 100-letiya Vladivostoka, Vladivostok 690022, Russia

*e-mail: filonina.vs@gmail.com

Abstract. This study investigates the structural characteristics and corrosion resistance of plasma electrolytic oxidation (PEO) coatings modified with polycaprolactone (CC-PCL) and stearic acid (CC-SA) on a MA8 magnesium alloy substrate. X-ray diffraction (XRD) analysis confirmed the presence of MgO, hydroxyapatite ($\text{Ca}_5(\text{PO}_4)_3(\text{OH})$), and sodium calcium silicate ($\text{Na}_2\text{CaSiO}_4$) in the PEO-layer, along with successful incorporation of PCL and stearic acid. The CC-SA coating exhibited calcium stearate formation due to interaction with the PEO matrix. Mass loss corrosion testing in minimum essential medium (MEM) revealed that hybrid coatings (coatings that include inhibitor and polymer in the PEO matrix, HC-1SP and HC-2SP) significantly enhanced degradation resistance. HC-2SP sample showed the lowest mass loss ($1.46 \pm 0.4\%$) and corrosion rate ($0.21 \pm 0.05 \text{ mg cm}^{-2} \text{ day}^{-1}$; $0.45 \pm 0.11 \text{ mm/year}$), representing an 80% reduction compared to the specimen with unmodified PEO-layer. These findings highlight the effectiveness of sequential polymer-inhibitor treatments in improving the long-term stability of biodegradable magnesium implants.

1. Introduction

Bioresorbable magnesium (Mg) alloys have garnered significant attention in biomedical applications due to their favorable mechanical properties, biocompatibility, and ability to degrade in physiological environments. However, their rapid corrosion rate in chloride-containing media, such as body fluids, limits their clinical utility [1–3]. To address this challenge, surface modification techniques and corrosion inhibitors were explored to enhance degradation resistance while maintaining biofunctionality.

Stearic acid, a long-chain fatty acid, has emerged as a promising corrosion inhibitor for Mg alloys due to its ability to form hydrophobic protective layers [4]. Furthermore, its non-toxic nature and biocompatibility make it suitable for medical applications [5], including implants [6,7]. Recent studies suggest that stearic acid coatings, significantly reduce corrosion rates in simulated physiological conditions.

In this study, the hybrid coatings were formed on a MA8 magnesium alloy using plasma electrolytic oxidation (PEO), polycaprolactone (PCL) and stearic acid (SA) treatment. The structural characteristics and corrosion resistance of the formed samples were studied. Future research should focus on optimizing deposition techniques, evaluating long-term degradation behavior, and assessing the *in vivo* performance of stearic acid-modified Mg alloys to advance their clinical translation.

2. Experiment

Sample preparation

For the experimental investigations, specimens were prepared from MA8 magnesium alloy plates with dimensions of $15 \times 20 \times 1.5 \text{ mm}$. The alloy composition (wt.%) was as follows: Mn (1.3–2.2), Ce (0.15–0.35), Mg balance. Prior to testing, the sample surfaces were standardized through sequential mechanical grinding using fine-grained silicon carbide (SiC) abrasive paper, with gradually decreasing grit sizes up to P1000 (corresponding to an abrasive particle size of 14–20 μm). Following mechanical treatment, the specimens were ultrasonically rinsed in isopropyl alcohol to remove residual

contaminants and subsequently dried in a desiccator at 40°C to ensure a contaminant-free surface. This standardized preparation protocol ensured consistent surface roughness and minimized oxide layer variations prior to further experimental treatments.

PEO-coating formation

The base oxide coatings were synthesized using a computer-controlled plasma electrolytic oxidation system. The electrolyte composition consisted of an aqueous solution containing calcium glycerol phosphate ($\text{C}_3\text{H}_7\text{CaO}_6\text{P}$, 25 g/L), sodium fluoride (NaF, 5 g/L), and sodium orthosilicate (Na_2SiO_3 , 7 g/L).

A bipolar polarization mode was employed, combining potentiostatic anodic polarization at a constant voltage of 400 V with galvanodynamic cathodic polarization, where the current was linearly reduced from 9 A to 6 A (corresponding to a current density range of 1.3–0.85 A/cm^2). The total process duration was maintained at 110 s with a duty cycle of 1. This optimized mode ensured controlled plasma discharge conditions for the formation of uniform, adherent oxide layers on the substrate surface.

Post-treatment with protective agents

Following plasma electrolytic oxidation, samples were rinsed with deionized water and dried at 40°C prior to subsequent surface modification. Inhibitor incorporation was achieved through exposure to a 0.1 M stearic acid solution prepared in a 1:1 ethanol-deionized water mixture. The SA solution was prepared via a two-stage process involving initial dissolution in ethanol followed by controlled addition of deionized water at 52°C under gentle mixing to ensure complete solubilization while minimizing foam formation. Samples were immersed for 60 min, slowly withdrawn, dried at 40°C , and subsequently heat-treated at 70°C for 15 min.

For pore sealing, a 6 wt.% polycaprolactone solution in dichloromethane (CH_2Cl_2) was applied using vacuum impregnation apparatus (Epovac, Struers) at reduced pressure (0.1–0.2 bar) to facilitate air removal and polymer penetration into the PEO matrix. After impregnation, samples were dried for 42 h at room temperature followed by heating at 65°C for 15 min, with the process repeated twice to ensure complete pore filling.

Various types of samples were investigated:

1. **PEO**: the sample with base PEO-layer;
2. **CC-SA**: the sample with a composite coating (CC) obtained by PEO followed by a stearic acid modification (0.1 M SA in ethanol/water);
3. **CC-PCL**: the sample with a CC obtained by PEO followed by dual polycaprolactone impregnation (6 wt.% in CH_2Cl_2);
4. **HC-2SP**: the sample with a hybrid coating (HC) obtained by CC-SA treatment with PCL;
5. **HC-1SP**: the sample with a HC obtained by PEO-treatment with following single-step co-impregnation with SA (0.1 M) and PCL (6 wt.%) in CH_2Cl_2 .

XRD analysis

The phase composition of MA8 magnesium alloy substrates with protective coatings was characterized by X-ray diffraction (XRD) using a SmartLab diffractometer (Rigaku, Japan) equipped with $\text{CuK}\beta$ radiation. Diffraction patterns were acquired in Bragg-Brentano geometry over a 2θ range of $4-90^\circ$ with a step size of 0.01° and a counting time of 1 s per step. The X-ray tube was operated at 42 kV accelerating voltage and 140 mA filament current under ambient temperature conditions.

Corrosion rate evaluation

The corrosion resistance of surface-modified magnesium alloy specimens was quantitatively evaluated through immersion testing according to standardized mass loss test methodology. Four samples (total exposed surface area = 28 cm^2) were immersed in 500 mL of corrosive medium (minimum essential medium, MEM [8]) under room temperature with continuous magnetic stirring for 7 days. Mass loss measurements were conducted following the protocol outlined in Russian GOST 9.908-85 (Section 2.1.1), with pre- and post-experimental mass determinations performed using an analytical balance (resolution $\pm 0.01 \text{ mg}$) after standardized cleaning procedures. The corrosion rate (CR) was calculated as:

$$\text{CR} = (\Delta m)/(A \cdot t) \quad (1)$$

where Δm – total mass loss (g), A – total exposed surface area (cm^2), and t – exposure duration (d).

3. Results and discussions

X-ray diffraction analysis of protective coatings (CC-PCL, CC-SA) confirmed the presence of magnesium oxide (MgO), hydroxyapatite ($\text{Ca}_5(\text{PO}_4)_3(\text{OH})$), and sodium calcium silicate ($\text{Na}_2\text{CaSiO}_4$) formed during plasma electrolytic oxidation. The diffraction patterns revealed characteristic peaks of the α -Mg substrate due to X-ray penetration through the coating layers.

For the CC-PCL coating, polycaprolactone ($[-(\text{CH}_2)_5\text{CO-O-}]_n$) was identified through its characteristic amorphous scattering profile. The CC-SA sample exhibited diffraction peaks corresponding to both stearic acid ($\text{C}_{18}\text{H}_{36}\text{O}_2$) and calcium stearate ($\text{Ca}(\text{C}_{17}\text{H}_{35}\text{COO})_2$), resulting from acid-base interaction between stearic acid and calcium-containing phases in the PEO-layer. The results demonstrate successful incorporation of organic components into the respective coating systems while maintaining the original PEO-derived ceramic phases.

The analysis of the immersion test results revealed significant mass loss in MEM after 7 days of exposure for the PEO ($8.43 \pm 0.6\%$), CC-SA ($6.70 \pm 0.3\%$), and CC-PCL ($5.30 \pm 0.4\%$) samples. Hybrid coatings demonstrated superior corrosion resistance, with HC-1SP ($1.96 \pm 0.6\%$)

exhibiting 4-fold lower mass loss than PEO, while HC-2SP ($1.46 \pm 0.4\%$) showed optimal performance, reducing degradation by 5-fold versus PEO.

Corrosion rates decreased sequentially: PEO ($1.08 \pm 0.10 \text{ mg cm}^{-2} \text{ day}^{-1}$; $2.27 \pm 0.22 \text{ mm/year}$) > CC-SA ($0.92 \pm 0.05 \text{ mg cm}^{-2} \text{ day}^{-1}$; $1.94 \pm 0.09 \text{ mm/year}$) > CC-PCL ($0.66 \pm 0.04 \text{ mg cm}^{-2} \text{ day}^{-1}$; $1.39 \pm 0.09 \text{ mm/year}$) > HC-1SP ($0.30 \pm 0.09 \text{ mg cm}^{-2} \text{ day}^{-1}$; $0.63 \pm 0.19 \text{ mm/year}$) > HC-2SP ($0.21 \pm 0.05 \text{ mg cm}^{-2} \text{ day}^{-1}$; $0.45 \pm 0.11 \text{ mm/year}$). The two-stage hybrid coating (HC-2SP) achieved maximal protection, suppressing corrosion rates by 80 % relative to PEO.

4. Conclusions

The modification of PEO-coatings with polycaprolactone (CC-PCL) and stearic acid (CC-SA) successfully enhanced the corrosion resistance of magnesium alloy substrates, as confirmed mass loss test analysis. The HC-2SP samples combining sequential inhibitor and polymer treatments proved most effective, reducing corrosion rates by 80 % compared to the base PEO-layer. These results demonstrate that hybrid coatings, particularly HC-2SP, offer a promising strategy for controlling the degradation of bioresorbable magnesium implants, ensuring prolonged structural integrity in physiological solution.

Acknowledgements

The study of the corrosion behavior of the coated samples were supported by the Russian Science Foundation (Grant No. 24-73-10008). The XRD analysis was performed under the government assignments from the Ministry of Science and Higher Education of the Russian Federation, Russia (project no FWFN-2024-0001).

References

- [1] S. Chatterjee, M. Saxena, D. Padmanabhan, M. Jayachandra, H.J. Pandya, *Biosens. Bioelectron.* 142 (2019).
- [2] A.S. Gnedenkov, S.L. Sinebryukhov, A.D. Nomerovskii, V.S. Marchenko, A.Y. Ustinov, S.V. Gnedenkov, *J. Magnes. Alloy.* 12 (2024) 2909–2936.
- [3] A.S. Gnedenkov, S.L. Sinebryukhov, A.D. Nomerovskii, V.S. Filonina, A.Y. Ustinov, S.V. Gnedenkov, *J. Magnes. Alloy.* 11 (2023) 3688–3709.
- [4] Y. Feng, S. Chen, Y. Frank Cheng, *Surf. Coatings Technol.* 340 (2018).
- [5] A.A. Öztürk, A. Aygöl, B. Şenel, *J. Drug Deliv. Sci. Technol.* 54 (2019).
- [6] S. Khalifeh, T.D. Burleigh, *J. Magnes. Alloy.* 6 (2018).
- [7] L. Zhang, E.A.A. Mohammed, A. Adriaens, *Surf. Coatings Technol.* 307 (2016).
- [8] A.S. Gnedenkov, S.L. Sinebryukhov, V.S. Filonina, V.S. Egorkin, A.Y. Ustinov, V.I. Sergienko, S.V. Gnedenkov, *J. Magnes. Alloy.* 10 (2022) 1326–1350.

Effects of silver nanoparticle array degradation on SERS and SICM measurements of living cells by ion-conducting nanopipette

Novikov D.V.^{*,1}, Chumachenko J.V.¹, Dubkov S.V.¹, Kolmogorov V.S.^{2,3}, Gorelkin P.V.², Erofeev A.S.², Parkhomenko Yu.N.², Volkova L.S.^{1,4}, Zheleznyakova A.V.¹, Popenko V.F.¹

¹ National Research University "MIET", 1 Shokin Square, Zelenograd, Moscow 124498, Russia

² National University of Science and Technology "MISiS", 4 Leninsky Prospekt, Moscow 119049, Russia;

³ M.V. Lomonosov Moscow State University, 1 Kolmogorova st., Moscow, 119991, Russia;

⁴ Institute of Nanotechnology Microelectronics, RAS, 32A Leninsky Prospekt, Moscow 115487, Russia

*e-mail: tororo@bk.ru

Abstract. This paper presents the results of a study of the degradation of the characteristics of nanopipettes with silver nanoparticles on the surface depending on the time and storage conditions. The geometric parameters of silver nanoparticle arrays were studied depending on the radius of the nanopipette tip. SEM studies showed a significant change in the morphology of the nanopipette surface when stored in air for 1 month. A decrease in the SERS activity of the nanopipettes was established regardless of the storage conditions in the first month, as well as the absence of a further decrease in the signal. It was shown that it is possible to use nanopipettes for SICM measurements when stored in a vacuum even 2 months after manufacture.

1. Introduction

Nanopipettes coated with silver nanoparticles provide the ability to simultaneously perform scanning ion-conductivity microscopy (SICM) of a living cell and study its individual elements (membranes, cytoplasm, organelles) using surface-enhanced Raman spectroscopy (SERS). The main problem for nanopipettes is the degradation of the nanoparticle array, which reduces the sensitivity of SERS, as well as the blocking of the hole in the pipette tip, which reduces or completely blocks the ion current, preventing SICM measurements.

In this work, the effect of storage conditions of ion-conducting nanopipettes with Ag NP arrays on the degradation of their performance characteristics was studied. It was found that the SERS signal and the internal radius of the nanopipette hole decrease during storage. The dependence of the tip radius on the SERS activity of the nanopipette was revealed.

2. Experiment

For the production of ion-conducting nanopipettes, borosilicate glass tubes with an internal diameter of 0.5 mm, an external diameter of 1.0 mm, and a length of 7.5 cm were used. Nanopipettes with a tip radius of 40, 50, and 60 nm were produced using a P-2000 CO₂ laser puller (Sutter Instrument, USA). Silver nanoparticle arrays on the surface of nanopipettes were formed by vacuum-thermal evaporation of 30 mg per pipette rotating at a speed of 14.4 rpm, similar to the previous work [1]. To obtain an array of dispersed nanoparticles, nanopipettes with a thin silver film were annealed in a vacuum at a pressure of 3×10^{-5} Torr at 230 °C for 30 min.

A Helios C4GX scanning electron microscope (SEM) (Thermo Fisher Scientific, Waltham, MA, USA) was used to study the morphology of the obtained nanopipettes with Ag nanoparticles. Visualization of the modified samples from the pipette was performed at an accelerating voltage of 1 kV and a current of 16 pA at a magnification of 160,000 times. The obtained SEM images were analyzed using ImageJ 1.49v.

After fabrication, some of the samples were stored in a vacuum desiccator at a pressure of 0.3 atm. The other part was stored in a Petri dish in an air atmosphere under normal conditions.

To study the SERS activity of the obtained nanopipettes, the samples were soaked in 10 μ M R6G solutions for 10 minutes. The measurements were performed on a Confotec MR200 confocal microscope-spectrometer at a wavelength of 532 nm and a laser power of 44 μ W in the mapping mode with a linear scanning area of $42 \times 1 \mu$ m and 21 points. The scanning area was positioned so that the scanning line coincided with the symmetry axis of the nanopipette, and the last point in the line was guaranteed to hit the pipette tip. The laser spot diameter was 1.5 μ m, the shooting duration at one point was 1 ms. After the mapping was completed, the total spectrum from all points was saved and used.

For contactless topographic scanning and assessment of the Young's modulus of living SH-SY5Y cells, a scanning ion-conducting microscope manufactured by ICAPPIC (ICAPPIC Limited, London, UK) was used. The scanning platform was mounted on an inverted optical microscope Nikon Ti-2 (Nikon, Tokyo, Japan). To estimate the Young's modulus of living cells, the pipette was moved towards the surface until the ion current through the tip decreased by 2% of its initial value during scanning. A non-contact topographic image was obtained when the ion current decreased by 0.5%.

3. Results and discussions

In the first stage of the work, the influence of the nanopipette tip radius on the geometric parameters and SERS activity of the silver nanoparticle array was investigated. Analysis of the SEM images of the pipettes showed that the densest array of about 250 particles/ μ m² with an average particle diameter of about 51 nm was demonstrated by a pipette with a curvature of 50 nm. At the same time, pipette's with a curvature of 40 and 60 nm demonstrated almost identical less dense arrays of about 185 and 181 particles/ μ m² with average diameters of about 64 and 57 nm, respectively. Analysis of the Raman spectra

obtained from the pipettes showed that the pipette with a tip radius of 50 nm demonstrated the highest signal enhancement factor, reaching 1.4×10^5 . At the same time, pipettes with radii of 40 and 60 nm demonstrated 18 times lower signal intensity (Fig. 1).

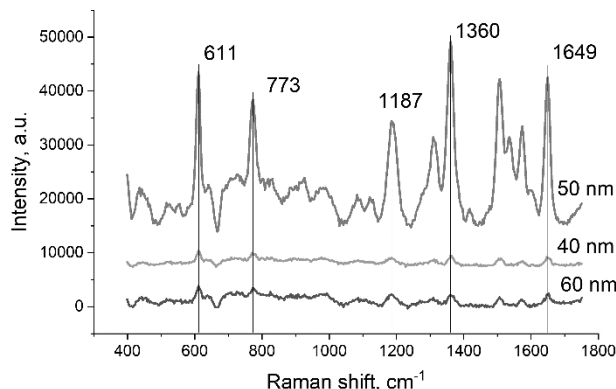


Fig. 1. Raman spectra of 10 μ M R6G on nanopipettes with different tip radii.

A study of the degradation of the nanopipette surface showed that within a few days of production, a dispersed array of silver nanoparticles with clear boundaries is observed (Fig. 2). However, after a month of storage in air, the array of nanoparticles degrades, turning into a continuous layer, probably due to sulfidization and adsorption of organic amine- and sulfur-containing molecules.

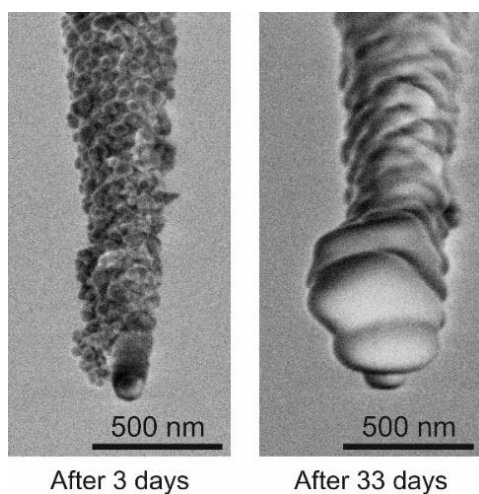


Fig. 2. SEM images of the morphology of nanopipettes with silver nanoparticles depending on the storage time in air.

The study of SERS activity of nanopipettes depending on time and storage conditions showed that practically regardless of storage conditions, in a vacuum desiccator or in air, after 1 month the pipettes provide approximately 3.5 times less intensity, demonstrating a drop in the SERS coefficient on average from 1.4×10^5 to 4×10^4 (Fig. 3). It is important to note that after 2 months of storage no further deterioration of the signal is observed, as can be seen from Fig. 3. Presumably, the main degradation of the nanoparticle array is achieved within 1 month, after which the changes cease.

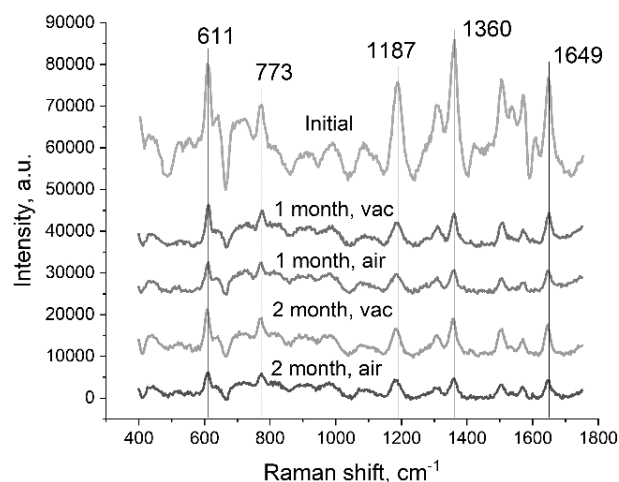


Fig. 3. Raman spectra of 10 μ M R6G on nanopipettes at different storage times and conditions.

SICM measurements of living SH-SY5Y cells, conducted in parallel with the assessment of SERS activity, showed that when stored in a vacuum, the tip radius gradually decreases from the initial 52 nm to 45 and 27 nm at 1 and 2 months of storage, respectively. When storing pipettes in the atmosphere, the tip radius decreases to 33 nm in the first month, and completely overlaps in the second month, preventing SICM measurements.

4. Conclusions

As a result of the work it was established that regardless of the storage conditions the gain of the nanopipette with silver nanoparticles decreases from 1.4×10^5 to 4×10^4 in the first month. It was determined that in the second month the drop in the gain is not observed. It was established that the radius of the pipette tip during storage in a vacuum decreases from 52 nm to 45 and 27 nm in the 1st and 2nd months of storage, respectively. When stored in the atmosphere the radius decreases to 33 nm in the first month, and in the second month the pipette tip overlaps, preventing SICM measurements.

Acknowledgements

The production of nanopipette, SERS and SICM studies were carried out within the framework of the grant of the Russian Science Foundation No. 22-19-00824.

The decoration of nanopipette by Ag NPs and SEM studies were carried out within the framework of the state assignment 2024-2026 FSMR-2024-0012.

References

- [1] S. Dubkov et al., Cells, **12** (2023) 2521.

Periodically spallated Ag+Au films for SERS-detection of polydopamine and chemosensing applications

Mitsai E.V.^{*}, Pilnik A.A., Borodaenko Yu.M., Kuchmizhak A.A.

Institute of Automation and Control Processes FEB RAS, 5 Radio St., Vladivostok 690041, Russia

^{*}e-mail: mitsai@dvo.ru

Abstract. This study focused on the development and optimization of a method for fast and dense nanotexturing of mixed composition metal films consisting of silver and gold to meet the demand for large quantities of single-use SERS substrates required in various chemo- and biosensing applications. SERS-detection of a number of practically significant analytes adsorbed on the produced surfaces in ultra-low concentrations, as well as detection of polydopamine at a concentration of at least 10^{-6} M using chemical functionalization of the surface, are demonstrated.

1. Introduction

Identification of organic pollutants, drugs and biogenic amines is a pressing issue in the areas of environmental monitoring, medical diagnostics and food quality control [1,2]. Often, such a task can be solved using optical sensor devices based on the effect of surface-enhanced Raman scattering (SERS), which enables identification of organic molecules in ultra-low concentrations, both adsorbed on the surface and dissolved in liquid [3]. SERS-substrates can be made of metal films with a high surface area, achieved through pre-processing by lithography methods. Metal nanotextures of such substrates support surface plasmon resonance (SPR), providing the local formation of intense electromagnetic fields enhancing the weak Raman signal of typical biological analytes. However, SERS technique usually require a large number of disposable substrates to reach the best possible performance with each measurement, which hinders the spread of slow and expensive lithography-based methods.

An alternative approach is pulsed laser-based nanotexturing allowing creation of substrates with large amount of electromagnetic "hot spots". It is possible to obtain various surface morphologies by controlling fabrication parameters [4]. But one of the drawbacks of pure metal-based SERS substrates is the limited set of suitable excitation wavelengths, since the spectral position of the SPR is specific to each commonly used SPR-supporting coinage metals. However, the creation of mixed-composition morphologies allows for effective tuning of the absorption peak position according to the relative ratio of metals [5,6]. Therefore, the flexibility of the approach enables the creation of suitable substrates for wide range of chemo- and biosensing applications. Here, we present a high-throughput method for the fast fabrication of nanotextured surfaces for SERS-detection of various chemical analytes at concentrations down to 10^{-7} M with an extended operating wavelength range due to hybrid silver-gold nature of the substrate.

Analytes presented in this work are rhodamine 6G (R6G), methylene blue (MB), doxorubicin (DOX), para-aminothiophenol (PATP) and dopamine (DA). R6G and MB are inexpensive and highly water-soluble organic dyes, which are mainly used as colorant in the textile industry and also in chemistry and medicine. Because of their carcinogenicity and toxicity to humans and animals, they are prohibited in the food industry [7]. Doxorubicin (DOX)

is an efficient drug used to treat a large number of cancers [8]. Recent developments in the delivery of DOX to cancerous internal organs involve numerous preliminary studies requiring large numbers of single-use test platforms [9]. PATP is an important probe molecule, fingerprint Raman features of which in SERS spectra have been widely used to measure plasmon-driven catalytic activities [10]. Dopamine is a biogenic amine that is an important neurotransmitter that may serve as a biological indicator of some neurological diseases. However, low affinity of dopamine for metal surfaces poses a challenge for SERS-based dopamine sensors [11]. The proposed solution is the functionalization of the metal surface adopting certain Raman peak shift or intensity variation resulting from the altered vibration mode of dopamine-bonded aptamer [12,13]. In this work we used a special functionalization protocol, as well as the tendency of dopamine to self-aggregate into polydopamine (PDA) in basic solutions [14]. PDA is also an attractive molecule gaining increasing attention in energy, catalytic, environmental and biomedical fields [15].

2. Experiment

To deposit noble metals films on glass we used electron beam evaporation method. The initial substrate composition consists of 500 nm of silver, on top of which a 50-nm thick layer of gold is deposited. These substrates were directly processed with a second-harmonic (515 nm) fs-laser (200 fs) pulses generated by a regeneratively amplified laser system (Pharos, Light Conversion) with pulse repetition rate of 10 Hz, scanning speed 5 $\mu\text{m/s}$ and energy 2.11 mW. The laser texturing was performed by a laterally expanded with an integrated mask stripe-shape laser beam with an in-plane size of $\approx 12 \times 0.6 \mu\text{m}$ focused onto the substrate surface with a dry microscope objective with numerical aperture (NA) of 0.95. This method enables fast and high-density surface texturing at millimeter scale. Morphological features of the laser-patterned surfaces demonstrated on Fig. 1 were characterized using scanning electron microscope (Ultra 55+, Carl Zeiss).

SERS spectroscopy measurements (Ntegra Spectra II, NT-MDT) were carried out with CW lasers ($\lambda = 473$ and 633 nm) that were focused by dry microscope objective (NA = 0.9, $\times 100$) after complete drying of the sample. Surface functionalization was performed using aqueous solution of TGA (thioglycolic acid), EDC (N-(3-(dimethylaminopropyl)-N'-ethylcarbodiimide

hydrochloride) and NHS (N-hydroxysuccinimide). Then, samples were incubated in formic-acetate buffer (FAB) solutions of dopamine (10^{-4} – 10^{-8} M) for 24 hours.

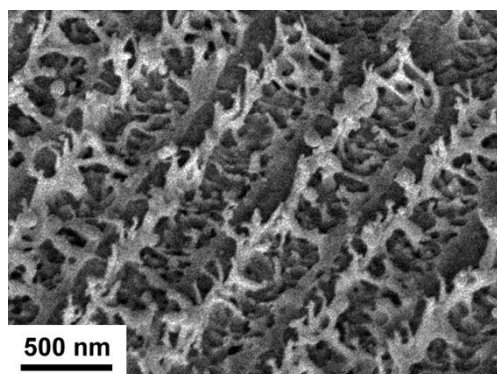


Fig. 1. SEM image of spallated lines on Ag+Au film.

3. Results and discussions

Figures 2a,b show the SERS spectra of R6G and MB adsorbed on the spallated surfaces from methanol solutions with a concentration of 10^{-7} and 10^{-5} M, respectively. Figure 2c shows the SERS spectrum of DOX at a concentration of 10^{-3} M, adsorbed onto the substrate in question from an aqueous solution, at an excitation wavelength of 473 nm. The detected peaks are consistent with previously reported results from other scientific groups [16,17]. For PATP at 10^{-6} M, an instantaneous catalytic dimerization to DMAB occurs, the bands of which (1140 , 1186 , 1387 и 1433 cm^{-1}) are detected after 1 second of laser irradiation at both wavelengths (Figure 2d), indicating a high chemical activity of the substrate [18].

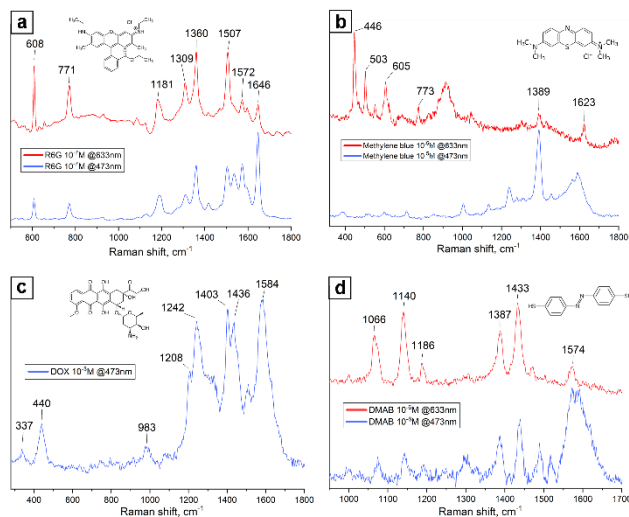


Fig. 2. SERS spectra and molecular structure of (a) rhodamine 6G, (b) methylene blue, (c) doxorubicin and (d) dimercaptoazobenzene adsorbed on produced surfaces. The red and blue lines represent the spectra obtained at excitation wavelengths of 633 and 473 nm, respectively.

Figure 3 shows a series of SERS spectra of polydopamine with increasing concentration at an excitation wavelength of 633 nm as well as reference spectrum measured after incubation of the sample in pristine FAB solution (gray line). From the presented spectra it is evident that with an increase in the concentration of dopamine, the intensity of D (~ 1390 cm^{-1}) and G (~ 1570 cm^{-1}) bands, typically observed in PDA [19], increases.

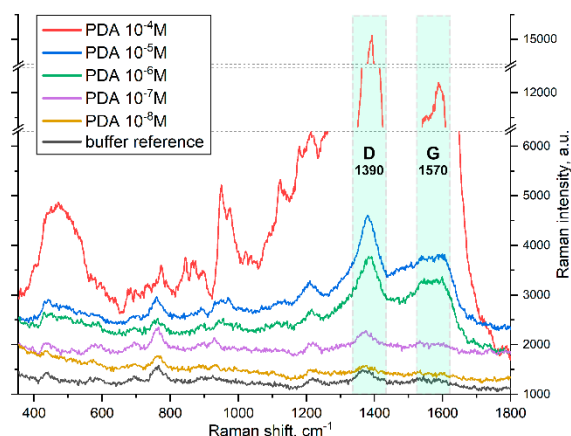


Fig. 3. SERS spectra of PDA adsorbed from corresponding FAB solutions of dopamine at molar concentrations from 10^{-8} to 10^{-4} , polymerized during incubation process. Integration time is 15s for all spectra, which are vertically shifted for better visibility.

4. Conclusions

This work demonstrates an optimized method for fast fs-laser processing of the metal films surface of mixed composition, allowing the creation of textured areas on a millimeter scale. Using such substrates, multi-wavelength detection of rhodamine 6G, methylene blue, doxorubicin, para-aminothiophenol and polydopamine adsorbed from corresponding solutions is demonstrated.

Acknowledgements

This research was supported by the Russian Science Foundation grant No. 24-19-00541 (<https://rscf.ru/en/project/24-19-00541/>).

References

- [1] L. Ding, Y. Fang. Chem. Soc. Rev. **39**(2010)4258.
- [2] G. Tırıs, R.S. Yanıkoğlu, B. Ceylan, D. Egeli, E.K. Tekkeli, A. Önal. Food Chem. **398**(2023)133919.
- [3] Z.A. Nima, A. Biswas, I.S. Bayer, F.D. Hardcastle, D. Perry, A. Ghosh, E. Dervishi, A.S. Biris. Drug Metab. Rev. **46**(2014)155.
- [4] F. Ruffino, M.G. Grimaldi. Nanomaterials **9**(2019)1133.
- [5] S. Link, Z.L. Wang, M.A. El-Sayed. J. Phys. Chem. B. **103**(1999)3529.
- [6] L.M. Liz-Marzán. Langmuir **22**(2006)32.
- [7] D. Zhang, H. Pu, L. Huang, D.W. Sun. Trends Food Sci. Technol. **109**(2021)690.
- [8] S. Rivankar. J. Cancer Res. Ther. **10**(2014)853.
- [9] N.A. Zhao, M.C. Woodle, A.J. Mixson. J. Nanomed. Nanotechnol. **9**(2018)519.
- [10] M. Sun, H. Xu. Small **8**(2012)2777.
- [11] Y. Bu, S. Lee. ACS Appl. Mater. Interfaces **4**(2012)3923.
- [12] L. Tang, S. Li, F. Han, L. Liu, L. Xu, W. Ma, H. Kuang, A. Li, L. Wang, C. Xu. Biosens. Bioelectron. **71**(2015)7.
- [13] Y. Choi, C.S. Jeon, K.B. Kim, H.J. Kim, S.H. Pyun, Y.M. Park. Talanta **260**(2023)124590.
- [14] M. Salomäki, L. Marttila, H. Kivelä, T. Ouvinen, J. Lukkari. J. Phys. Chem. B. **122**(2018)6314.
- [15] Q. Huang, J. Chen, M. Liu, H. Huang, X. Zhang, Y. Wei. J. Chem. Eng. **387**(2020)124019.
- [16] R. Zhang, J. Zhu, D. Sun, J. Li, L. Yao, S. Meng, Y. Li, Y. Dang, K. Wang. Micromachines **13**(2022)940.
- [17] J. Gautier, E. Munnier, L. Douziech-Eyrolles, A. Paillard, P. Dubois, I. Chourpa. Analyst **138**(2013)7354.
- [18] Y.F. Huang, M. Zhang, L.B. Zhao, J.M. Feng, D.Y. Wu, B. Ren, Z.Q. Tian. Angew. Chem. **126**(2014)2385.
- [19] R. Tejido-Rastrilla, G. Baldi, A.R. Boccaccini. Ceram. Int. **44**(2018)16083.

Structure and optical properties of epitaxial Cr₂AC MAX-films (A - Ge, Si, Al and Ga)

Lyaschenko S.A.^{*1}, Andryushchenko T.A.¹, Yakovlev I.A.¹, Lukyanenko A.V.^{1,2}, Varnakov S.N.¹,
Ovchinnikov S.G.^{1,2}

¹ Kirensky Institute of Physics of SB RAS, 50/38 Akademgorodok, Krasnoyarsk 660036, Russia

² Siberian Federal University, 79 Svobodny pr., Krasnoyarsk 660041, Russia

*e-mail: lisa@iph.krasn.ru

Abstract. A series of thin films of the stoichiometric composition Cr₂AC (A - Al, Ge, Si, Ga), including epitaxial MAX-phases was produced by magnetron co-deposition method. A significant influence of germanium substitution by silicon on the shape and size of MAX-phase crystallites was observed. The temperature dependences of the optical properties of MAX materials Cr₂GeC and Cr₂Ge_{0.75}Si_{0.25}C have been measured in the spectral range of 1.4–3.9 eV. The temperature boundaries of oxidation resistance, phase stability and optical properties of synthesized epitaxial Cr-containing MAX-phases were determined.

1. Introduction

In recent years, investigations of low-dimensional and anisotropic materials, in particular those with an atomic layer structure, have been continuously growing in popularity. Such objects demonstrate properties that are interesting for the creation of new electronic devices, various sensors and functional coatings. A broad class of atomic-layered materials are thin epitaxial films of MAX-phases (M is a transition metal, A is an element of the 13th and 14th groups, and X is carbon and/or nitrogen). Thin epitaxial MAX-films of the composition Cr₂AC, where A is Al, Ge, Si or Ga, have practically significant properties due to their high corrosion resistance, mechanical properties and non-trivial electronic structure [1]. Chromium-containing MAX-films with Al or Ge in the A-layer have hardness and chemical resistance, identical to that of single-crystal corundum, and high thermal resistance. At the same time, they have high reflection coefficient and good conductivity along the basal plane (00L), which makes them promising materials for creating anti-corrosion coatings, heat-resistant mirrors, and electrical contacts. The use of gallium in the A-layer allows both to realise an interesting electronic structure of MAX-films and to obtain exotic atomic-layer compounds with Au, Pt, Ir [2].

A popular and effective method for the synthesis of thin epitaxial MAX-films is magnetron co-deposition from elementary targets on a heated single-crystal MgO(111) or Al₂O₃(0001) substrate with in situ control of the surface by reflection high-energy electron diffraction (RHEED). It is convenient to analyse the optical properties of the obtained samples and study their oxidation resistance in air by non-destructive and fast spectral reflectance ellipsometry technique in the spectral range of 1.4–3.9 eV. This makes it possible to investigate the electronic structure and properties of stoichiometric compositions depending on the degree of substitution or synthesis technology, and also to observe phase transitions and solid-phase synthesis reaction at different temperatures.

2. Experimental results and discussions

A series of thin films of stoichiometric composition Cr₂AC (A - Al, Ge, Si, Ga), including epitaxial MAX phases, were synthesised by magnetron co-deposition from elementary targets on a heated MgO(111) substrate. The

crystal structure and phase composition were investigated by RHEED, X-ray structural analysis, Auger electron spectroscopy and X-ray fluorescence analysis. The surface morphology of the samples was investigated by atomic force microscopy. The epitaxy of planar crystallites in 40 nm MAX Cr₂GeC film was found to be enhanced with gradual gradient substitution of germanium by silicon during the deposition process. For the Cr₂GeC epitaxial film samples, both high surface hardness (single-crystal corundum writhes on the Cr₂GeC surface) and extraordinary chemical resistance are observed. In particular, no detectable traces of chemical damage after one-hour exposure in HF, HCl, KOH and aqua regia (including with added H₂O₂) at temperatures up to 90 °C were found. The detected properties are due to atomic alternation of Ge and Cr-C layers with cross-passivation properties and cermet-like composite structure.

High oxidative stability of the films was found by spectral reflectance ellipsometry, when Al- and Ge-containing samples were heated in air. The optical properties of MAX-films in the basal plane with pronounced optical anisotropy were found to be typical metallic, which agrees with ab initio calculations and expected uniaxial anisotropy.

4. Conclusions

The obtained results of the study of Cr-based thin epitaxial MAX films show their significance for the development of new materials with unique properties, which makes them promising for applications in anti-corrosion coatings, heat-resistant mirrors, and electrical contacts. The results of the analysis of composition and synthesis technology influence on the physicochemical properties of MAX-phases may contribute to the further development of research in the field of low-dimensional and anisotropic materials.

Acknowledgements

The research was supported by the grant of the Russian Science Foundation № 25-12-20012, <https://rscf.ru/project/25-12-20012/>, grant of the Krasnoyarsk Regional Science Foundation.

References

- [1] M. Dahlqvist, M. Barsoum, J. Rosen. *Materials Today* 72(2024)1-24.
- [2] Y. Shi, S. Kashiwaya, P. Helmer et al. *Results in Materials* 18(2023)100403.

Amorphous and crystallized tungsten trioxide: structural and optical responses in H₂-rich atmosphere

Kulikova D.P.^{*1}, Shelaev A.V.¹, Lotkov E.S.^{1,2}, Baburin A.S.^{1,2}, Rodionov I.A.^{1,2}, Baryshev A.V.¹

¹ Dukhov Automatics Research Institute (VNIIA), 22, Sushevskaya ul., Moscow 127030, Russia

² FMN Laboratory, Bauman Moscow State Technical University, 2/18, Rubtsovskaya emb., Moscow 105082, Russia

*e-mail: dp.kulikova@yandex.ru

Abstract. Thin films of amorphous tungsten trioxide, a prominent gasochromic material, were annealed in air within a temperature range of 300–400 °C. Crystallization of WO₃ into the monoclinic phase (m-WO₃) was observed above 400 °C. The optical absorption change in a hydrogen-rich atmosphere increased twofold as compared with the amorphous films, and maximum changes spectrally shifted towards the near-infrared spectral range. Raman scattering spectroscopy of m-WO₃ revealed a modification of W-O bonds and formation of tungstite (WO₃·H₂O) during interaction with hydrogen.

1. Introduction

The development of optical hydrogen gas sensors incorporating gas-sensitive elements based on gasochromic oxides represents a promising research direction. Tungsten trioxide WO₃ covered with catalytic metal (Pd, Pt) is widely used in such sensors due to its pronounced gasochromic properties, wherein optical absorption increases during reduction reaction in H₂. Despite extensive research on WO₃, enhancing its sensitivity and response rate remains a critical challenge [1]. Thus, the complex refractive index $n-ik$ of amorphous tungsten trioxide at all stages of its coloration in a hydrogen-rich atmosphere was retrieved, thoroughly analyzed and associated with the formation of oxygen vacancies on the surface and within the bulk of WO_{3-x} [2]. This raises the question of whether altering the ratio of surface-to-bulk oxygen vacancies could modulate the optical absorption characteristics of tungsten trioxide in a H₂-rich atmosphere. Additionally, the origin of degradation of gasochromic properties after repeated coloration/bleaching cycles is discussed as well [1].

2. Experiment

Amorphous WO₃/Pd films, with oxide and catalyst thicknesses of 150 and 1 nm, respectively, were deposited on fused silica substrates using electron beam evaporation. The fabricated nanofilms were annealed in air in a temperatures ranging from 300 to 400 °C for 2 hours. Transmittance and Raman scattering measurements in a gas were performed by placing the samples in a gas cell with parallel quartz windows, through which a gas mixture prepared with mass flow controllers was flowed.

3. Results and discussions

Annealing at ≥ 400 °C induced the crystallization of the tungsten trioxide film into the monoclinic phase m-WO₃ and reduced its thickness to 120 nm. Furthermore, refractive index n increased—from 1.93 to 2.1 at $\lambda = 1100$ nm. The maximum transmittance change ΔT_{H_2} induced by gasochromic coloration in H₂ was 0.24 for as-deposited film and 0.47 for m-WO₃. Notably, the spectral position of the maximum of ΔT_{H_2} shifted to longer wavelengths after annealing (1.1 $\mu\text{m} \rightarrow 2.5 \mu\text{m}$), while the response rate remained at ≈ 2 minutes. These observations are attributed to changes in the electronic structure of m-WO₃ and the distribution of surface and bulk oxygen vacancies. Raman scattering spectroscopy of the

m-WO₃/Pd film revealed that during coloration in H₂, Raman peaks at 712 cm⁻¹ and 803 cm⁻¹ exhibited significant reductions in intensity and shifts in spectral position (dashed lines, Fig. 1). These changes can be assigned to alterations in W-O bond lengths caused by the formation of oxygen vacancies. When H₂ was replaced with air, a slight return to the initial state of m-WO₃ occurred. Additionally, broad modes with maxima in the vicinity of 680 cm⁻¹ and 942 cm⁻¹ were detected exclusively during the reduction reaction (solid lines, Fig. 1). These peaks are associated with the formation of tungstite WO₃·H₂O [3], which is known to decompose at elevated temperatures, see a “before H₂” curve.

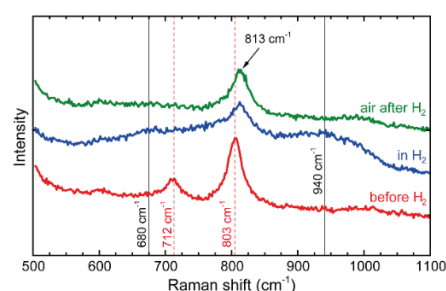


Fig. 1. Progression of Raman spectra of m-WO₃/Pd: before, during the reduction reaction in H₂, and at the oxidation in air.

4. Conclusions

The crystallization of WO₃ film under appropriate annealing conditions significantly enhances its performance as the hydrogen-sensitive material. The formation of tungstite during gasochromic coloration in H₂ was identified that may contribute to the degradation of response amplitude and rate upon repeated hydrogen exposure. These findings allow for overcoming limitations of sensing elements based on amorphous WO₃.

Acknowledgements

Samples were fabricated at the BMSTU Nanofabrication Facility (FMN Laboratory, FMNS REC, ID 74300).

References

- [1] D.P. Kulikova et al. Scientific Reports **13** (2023) 890.
- [2] D.P. Kulikova et al. International Journal of Hydrogen Energy **82** (2024) 767-775.
- [3] M.F. Daniel et al. Journal of Solid State Chemistry **67** (1987) 235-247.

Hybrid fumarate-containing protective coatings for MA8 magnesium alloy

Nomerovskii A.D.*, Gnedenkov A.S., Marchenko V.S., Sinebryukhov S.L., Gnedenkov S.V.
Institute of Chemistry, FEB RAS, 159 pr. 100-letiya Vladivostoka, Vladivostok, 690022, Russia

*e-mail: nomerovskii.ad@outlook.com

Abstract. This study investigates a novel hybrid coating system combining plasma electrolytic oxidation (PEO), treatment with sodium fumarate, and polycaprolactone (PCL) for enhancing the corrosion resistance of MA8 magnesium alloy in physiological solution. The hybrid coating demonstrated exceptional performance, reducing the corrosion rate of the material from 0.29 mm/year (bare alloy) to 0.12 mm/year. Electrochemical tests revealed a significant decrease in corrosion current density (from 33.0 $\mu\text{A}/\text{cm}^2$ to 0.16 $\mu\text{A}/\text{cm}^2$), while long-term immersion tests showed sustained corrosion protection. Microstructural analysis of the formed coating confirmed its three-layer architecture with uniform inhibitor distribution. The biocompatible coating system offers controlled degradation and self-healing properties, making it promising for biodegradable implant applications. This approach provides a synergistic solution combining active corrosion inhibition, and polymer-mediated protection for tailored implant degradation.

1. Introduction

Magnesium alloys have emerged as highly promising materials for biomedical implant applications owing to their exceptional biocompatibility, biodegradability, and favorable mechanical properties that closely match those of natural bone [1-3]. However, the rapid corrosion degradation of these alloys in chloride-containing physiological environments remains a critical challenge that limits their clinical implementation. The present study provides a comprehensive investigation of novel hybrid protective systems combining plasma electrolytic oxidation (PEO), environmentally benign inhibitor (sodium fumarate), and bioresorbable polymer (polycaprolactone, PCL) layers for enhanced corrosion protection of MA8 magnesium alloy.

Recent advances in materials science have highlighted the growing importance of developing multifunctional surface engineering solutions that combine corrosion protection with additional therapeutic capabilities for biomedical applications. While numerous coating strategies have been proposed for magnesium alloys, including conversion coatings, polymer films, and layered double hydroxides, most fail to address simultaneously the key requirements of long-term protection, controlled degradation kinetics, and biological functionality [4-8]. The particular innovation of our approach lies in the synergistic combination of three well-established technologies: PEO for creating a stable ceramic-like base layer with controlled porosity, sodium fumarate as a biocompatible corrosion inhibitor, and PCL as a biodegradable polymer matrix enabling both sustained inhibitor release and potential drug loading.

2. Experiment

The research methodology encompassed a multifaceted experimental approach. PEO-coatings were fabricated in an electrolyte containing calcium glycerophosphate (25 g/L), sodium fluoride (5 g/L), and sodium metasilicate (7 g/L). Subsequent modification involved PEO-coating impregnation with sodium fumarate solutions (0.05 M and 0.1 M concentration) followed by PCL deposition (CaP-Fum-PCL sample). The corrosion performance was systematically evaluated using hydrogen evolution measurements, electrochemical impedance

spectroscopy (EIS), potentiodynamic polarization, and hydrogen evolution test over 7-day exposure periods to 0.9 % NaCl solution. Advanced characterization techniques including scanning electron microscopy (SEM), energy-dispersive X-ray spectroscopy (EDS) provided detailed microstructural and compositional analysis.

3. Results and discussions

The experimental results revealed several critical aspects of the coating system's performance. Electrochemical testing demonstrated that the hybrid fumarate-containing coating reduced the corrosion current density by nearly an order of magnitude compared to uncoated samples, decreasing from 33.0 $\mu\text{A}/\text{cm}^2$ to just 0.16 $\mu\text{A}/\text{cm}^2$. According to the EIS data the hybrid CaP-Fum-PCL coating showed particularly stable behavior during prolonged immersion tests, maintaining its protective properties for over 168 h in simulated physiological conditions.

Microstructural analysis provided important insights into the coating formation mechanisms. Cross-sectional SEM imaging revealed a three-layer architecture: first is a dense 5-8 μm inner PEO-layer directly bonded to the magnesium substrate, second – a 15-20 μm porous intermediate layer containing fumarate reservoirs, and third – a 30-50 μm outer PCL polymer layer. Elemental mapping confirmed uniform distribution of inhibitor compounds on the coating surface, with particularly high concentrations at the metal-coating interface where corrosion initiation typically occurs.

Hydrogen evolution tests revealed exceptionally stable performance, with the coating maintaining over 85% of its initial protective efficiency after 30 days in Hank's balanced salt solution. This durability stems from the synergistic combination of: the ceramic PEO layer providing mechanical stability; the fumarate reservoirs ensuring continuous inhibitor supply; and the PCL topcoat controlling the release kinetics while preventing rapid electrolyte penetration.

The hybrid CaP-Fum-PCL coating demonstrated superior performance with corrosion rate of just 0.12 mm/year, representing a 2.4-fold improvement over bare alloy ($P_H = 0.29$ mm/year) and 1.5-fold enhancement compared to PEO coating with PCL layer ($P_H = 0.18$ mm/year).

4. Conclusions

The study has successfully demonstrated the effectiveness of hybrid protective coatings combining plasma electrolytic oxidation, sodium fumarate and polycaprolactone treatment for enhancing the corrosion resistance of MA8 magnesium alloy in physiological solution. The developed coating system achieved a remarkable reduction in corrosion rate to 0.12 mm/year while exhibiting self-healing properties through controlled inhibitor release. The complete biocompatibility of all coating components makes this technology particularly promising for biomedical applications.

These findings represent a significant advancement in surface engineering for biodegradable implants, offering both superior corrosion protection and functional performance. The combination of active corrosion inhibition with polymer-mediated protection provides a comprehensive solution to the challenge of controlling magnesium alloy degradation. Future work should focus on optimizing the coating parameters for specific clinical applications and conducting thorough preclinical evaluations to facilitate technology transfer to medical practice.

The proposed approach opens new possibilities for designing magnesium-based implants with precisely tailored degradation profiles that can match tissue regeneration timelines, potentially revolutionizing the field of temporary biomedical implants.

Acknowledgements

The study of the electrochemical properties and corrosion behavior of the coated samples were supported by the Russian Science Foundation (Grant No. 24-73-10008). The chemical composition of the coating was studied under the government assignments from the Ministry of Science and Higher Education of the Russian Federation, Russia (project no FWFN-2024-0001).

References

- [1] P. Babu, D.G. Solomon. *Mater. Today Proc.* (2023).
- [2] P. Rider, Ž.P. Kačarević, A. Elad, D. Tadic, D. Rothamel, G. Sauer, F. Bornert, P. Windisch, D.B. Hangyási, B. Molnar. *Bioact. Mater.* **14**(2022)152.
- [3] Y. Yang, X. Xiong, J. Chen, X. Peng, D. Chen, F. Pan. *J. Magnes. Alloy* **11**(2023)2611.
- [4] G.S. Pereira, O.M. Prada Ramirez, P.R.T. Avila, J.A. Avila, H.C. Pinto, M.H. Miyazaki, H.G. de Melo, W.W. Bose Filho. *Corros. Sci.* **206**(2022)110527.
- [5] X. Yang, X. Lu, Y. Zhou, Y. Xie, J. Yang, F. Wang. *Corros. Sci.* **215**(2023)111044.
- [6] A.S. Gnedenkov, S.L. Sinebryukhov, V.S. Filonina, S.V. Gnedenkov. *J. Magnes. Alloy* **11**(2023)4468.
- [7] S.V. Gnedenkov, V.S. Egorkin, S.L. Sinebryukhov, I.E. Vyaliy, A.S. Pashinin, A.M. Emelyanenko, L.B. Boinovich. *Surf. Coatings Technol.* **232**(2013)240.
- [8] A.S. Gnedenkov, S.L. Sinebryukhov, A.D. Nomerovskii, V.S. Filonina, A.Y. Ustinov, S.V. Gnedenkov. *J. Magnes. Alloy.* **11**(2023)3688.

Specifics of sample fabrication for studying high-resistivity thin films of phase-change materials

Al-Khadge L.A.^{*1}, Nikitin K.G.¹, Terekhov D.Yu.¹, Ermachikhin A.V.^{2,3}, Kiselev A.V.⁴,
Goroshko O.A.⁵, Goroshko D.L.⁵

¹ National Research University of Electronic Technology, 1 Shokin Sq., Moscow 124498, Russia

² Ryazan State Radio Engineering University, 59/1 Gagarin St., Ryazan 390005, Russia

³ Scientific-Manufacturing Complex Technological Centre, 1 Shokin Sq., Moscow 124498, Russia

⁴ Institute on Laser and Information Technologies of RAS, 1 Svyatoozerskaya St., Shatura 140700, Russia

⁵ Institute of Automation and Control Processes, 5 Radio St., Vladivostok 690041, Russia

*e-mail: allay.02@yandex.ru

Abstract. Phase-change materials are widely used in non-volatile memory elements, photonic devices, etc. However, the functional properties of thin films of phase-change materials have not yet been fully investigated, which significantly limits the development of devices based on them. The study of these properties is complicated by their high resistivity in the amorphous state and the structural sensitivity to external influences. We designed sample architectures and fabrication techniques enabling comprehensive investigation of different properties of phase-change thin films. Using the developed process flow, samples of various geometries were fabricated, and the electrophysical, thermoelectric and optical parameters of phase-change material thin films (using GeTe as an example) were investigated in the temperature range below -10°C and electric field strengths up to 10^5 V/cm^2 . The implemented multilayer thin-film PCM structures substantially simplify experimental procedures and improve measurement accuracy.

1. Introduction

Phase-change materials (PCM) have found wide application in the fields of creating elements of non-volatile electrical memory, integrated photonics, metasurfaces, etc. [1-3]. A special feature of such materials is the ability to control a rapid and reversible transition between the amorphous and crystalline phases, accompanied by a significant change in their electrophysical and optical properties [4, 5]. However, despite their active research and use in various applications in recent years, the properties of PCM thin films and the effects that directly affect their long-term stability are still not fully understood [6].

The main problem of studying the electrophysical properties of PCM thin films over a wide temperature range is related to their high resistivity in the amorphous state, which imposes a number of limitations on the measuring equipment and structures used [7, 8]. In addition, determining the structural and optical characterization of amorphous PCM thin films is difficult, since even low-energy analysis impact (laser radiation, electron beam, thermal effects) can induce structural changes.

Thus, an essential step for conducting further fundamental research aimed at continuing the optimization of PCMs and PCM-based devices is the development of design and technological solutions for fabricating multilayer structures. These structures must enable the study of electrophysical, optical, and thermoelectric parameters of amorphous-phase PCMs across a wide temperature range, utilizing modern metrological and analytical equipment. Data on the temperature dependences of optical, electrophysical, and thermoelectric properties will enable a more detailed analysis of possible charge carrier transport mechanisms, structural relaxation, switching and memory effects.

In this work, using phase-change GeTe thin films as an example - a material widely employed in thermoelectric devices, optical and electrical memory and reconfigurable photonics [9] - we demonstrate the possibility of studying

high-resistive thin films through variations in geometrical parameters of contact systems.

2. Experiment

Thin films of phase-change and contact materials were deposited by DC magnetron sputtering of targets with a purity of at least 99.99%. EDX analysis confirmed that the elemental composition of the deposited films matched the stoichiometric one. XRD measurements revealed that the PCM films were in an amorphous state immediately after deposition. Thickness of the fabricated GeTe thin films varied from 30 nm to 1 μm depending on the characterization method employed. Several samples were coated with a SiO_2 film to protect them from the oxidation process of the phase-changing material during exposure to air.

Multilayer thin-film structures were fabricated using display and contact photolithography with liquid (FP-3515) and dry film (AQUA MER 37 ME720) photoresist masks. Display photolithography was performed using a custom-developed portable lithography system featuring a liquid crystal display for digital photomask projection. This display lithography approach enabled patterning of structures with minimum feature sizes of 50 μm , corresponding to the display pixel size.

For higher-resolution patterning, contact metallized photomasks were fabricated. Mask production was conducted under both laboratory and industrial conditions. Laboratory mask fabrication employed laser ablation of 100 nm-thick Cr films deposited on Corning Glass 1737F substrates. The patterning process utilized a scanning laser beam with 15 μm spot diameter, which consequently limited the lithographic resolution. Industrial fabrication technology, however, achieved masks with minimum feature sizes of approximately 2 μm . Contact photolithography was performed using a laboratory setup equipped with a 405 nm wavelength UV LED exposure source.

3. Results and discussions

During this work, we optimized process parameters for both display and contact photolithography techniques. Optimal processing conditions were established, with additional technological steps implemented to improve the quality of fabricated structures. For instance, to enhance substrate surface quality after hard-baking, samples underwent additional oxygen plasma treatment (100 Pa pressure, 10 minute) with preliminary heating. All geometric parameters of the designed structures were selected according to the technological capabilities of the respective equipment and measurement system constraints.

To investigate the electrophysical properties of GeTe thin films across wide temperature and electric field ranges we prepared samples with various contact system geometries: classical planar structures with different interelectrode distances, vertical "sandwich" ones and structures with comb-shaped contacts. Using the manufactured structures, it was possible to determine the temperature dependences of resistivity in the range of electric field to 10^5 V/cm². To study the thermoelectric properties of GeTe thin films, two types of samples were prepared enabling measurements under different temperature gradients. In addition, samples were produced to study the Hall effect and electrophysical properties at low temperatures using the van der Pau method. To study the structural transformations and changes in the optical properties of thin films of amorphous GeTe during heating using Raman scattering and FTIR spectrophotometry, a set of samples with dimensions of 3×3 mm² was produced.

4. Conclusions

This study developed a fabrication technology and produced multilayer thin-film structures of amorphous GeTe PCM for comprehensive investigation of electrophysical, optical and thermoelectric properties across wide temperature ranges. These structures significantly simplify experiments and improve measurement accuracy.

Thus, within the framework of the presented work, the technology was developed and multilayer thin-film structures of amorphous PCM GeTe thin films were manufactured to conduct research on electrophysical, optical and thermoelectric properties over a wide temperature range, which greatly simplify experiments and increase their accuracy.

Acknowledgements

The authors are grateful to P. Lazarenko, Yu. Vorobyov, A. Yakubov and A. Sherchenkov for useful discussions. The work was performed in the laboratory "Active Photonic Materials and Devices" (Agreement 075032025266/1 dated 03/25/2025, FSMR-2025-0002).

References

- [1] Kim H. et al. Hybrid Plasmonic-GeTe Active Metasurfaces with High Tunability // *Advanced Photonics Research*. – 2024. – C. 2400132.
- [2] Reddy V. J., Ghazali M. F., Kumarasamy S. Advancements in phase change materials for energy-efficient building construction: A comprehensive review // *Journal of Energy Storage*. – 2024. – T. 81. – C. 110494.
- [3] Prabhathan P. et al. Roadmap for phase change materials in photonics and beyond // *Iscience*. – 2023. – T. 26. – №. 10.
- [4] Burtsev A. A. et al. Physical properties' temperature dynamics of GeTe, Ge₂Sb₂Te₅ and Ge₂Sb₂Se₄Te₁ phase change materials // *Materials Science in Semiconductor Processing*. – 2022. – T. 150. – C. 106907.
- [5] Lee J. et al. Phase purity and the thermoelectric properties of Ge₂Sb₂Te₅ films down to 25 nm thickness // *Journal of Applied Physics*. – 2012. – T. 112. – №. 1.
- [6] Wintersteller S. et al. Unravelling the amorphous structure and crystallization mechanism of GeTe phase change memory materials // *Nature Communications*. – 2024. – T. 15. – №. 1. – C. 1011.
- [7] Bertelli M. et al. Stable chalcogenide Ge–Sb–Te heterostructures with minimal Ge segregation // *Scientific Reports*. – 2024. – T. 14. – №. 1. – C. 15713.
- [8] Burr G. W. et al. Recent progress in phase-change memory technology // *IEEE Journal on Emerging and Selected Topics in Circuits and Systems*. – 2016. – T. 6. – №. 2. – C. 146-162.
- [9] Kuznetsov V. G. et al. Flexoelectric effect in GeTe // *Fizika Tverdogo Tela*. – 2024. – T. 66. – №. 12. – C. 2311-2316.

Features of the formation SERS-substrates as a result of the combustion of multilayer thermite structures Al/CuO + Ag

Novoselcev A.I.^{*1}, Novikov D.V.¹, Ryazanov R.M.², Kruzhalina M.D.¹, Dubkov S.V.¹, Lebedev E.A.¹

¹ National Research University "MIET", Shokin Square 1, Moscow, Zelenograd, 124498, Russia

² Scientific-Manufacturing Complex "Technological Centre", Shokin Square, 1, building 7, Moscow, Zelenograd 124498, Russia

*e-mail: aleks.novoselcev1999@gmail.com

Abstract. The paper considers a method for creating SERS substrates by self-forming particles due to the introduction and melting of an additional layer of Ag as a result of the combustion multilayer thermite structures Al/CuO_x. To study the process of self-formation of Ag particles, several sets of samples with different positions of the embedded layer relative to the multilayer structure were prepared. The geometric parameters of the Ag structure and particles were studied using SEM, and the elemental analysis was performed using EDX. The amplification of the Raman spectroscopy signal on self-formed Ag particles relative to the silicon substrate in the study of malachite green was 5×10^4 .

1. Introduction

Currently, research areas aimed at studying metal particles ranging in size from several nanometers to several micrometers have become widespread. An important place in these studies is occupied by scientific works related to the methods of forming noble metal particles for their use in Raman surface-enhanced spectroscopy.

However, most of the studies on the methods of forming metal particles for SERS substrates are aimed at studying traditional methods of their synthesis. These methods include hydrothermal and chemical synthesis, as well as chemical and physical vapor deposition. [1] The particles produced with them quickly become unusable when stored outside an inert atmosphere. This is due to the presence of a large number of free bonds on their surface, which leads to their rapid oxidation and loss of properties. [2]

The solution to this problem can be the methods of self-formation of metal particles immediately before their application. [3] One of these techniques is the introduction of an additional Ag layer into multilayer thermite structures (MTS). In this case, the particles will be formed from the molten Ag layer, which will turn into a liquid state as a result of the combustion MTS.

In this paper, MTS based on Al/CuO_x with an embedded Ag layer formed by magnetron sputtering are considered. The features of Ag particle formation are investigated depending on their location in MTS. The degree of signal amplification was 5×10^4 of the malachite green (MG) concentration of 10 μ M.

2. Experiment

During the study, several sets of samples were formed with the location of the embedded silver layer with a planned thickness of 250 nm at the bottom, in the middle and on top of the MTS. The planned thickness of the layers of the multilayer structure was 50 nm, and the total thickness of the entire structure was 4.25 microns. A rectangular-shaped citall measuring 30×15 mm was used as a substrate. The substrates were cleaned before the layers were formed. Mechanical impurities were removed from the surface using an ultrasonic bath and a 1 : 1 solution of isopropyl alcohol with acetone. Organic pollutants were removed with a heated CARO solution. Moisture removal

from the cleaned substrates was carried out in vapors of isopropyl alcohol.

The layers of the multilayer structure and the embedded Ag layer were deposited on the IMS-026 installation in an argon atmosphere at a pressure of 3 mTorr. The spray power for the Al, CuO_x, and Ag targets was 500, 250, and 500 Watts, respectively. Before deposition, ion stripping of the surface was carried out at a pressure of 0.5 mTorr for 2 minutes using an ion source.

The initiation of combustion in the formed MTS with embedded Ag layers was performed using a piezoelectric element. The study of surface morphology, self-formed Ag particles, and elemental composition was carried out on SEM Jeol JSM - 6010 Plus/LA. The spectrum of malachite green (MG) was studied using the MR-200 installation on a laser with a wavelength of 633 nm. Before the study, the substrates were initiated and soaked in a solution of malachite green (MG) with a concentration of 10 μ M and a volume of 4 ml for 30 minutes. The remaining liquid was removed from the surface of the substrate using an air stream.

3. Results and discussions

After the formation of the MTS, studies of the embedded Ag layer were carried out, and a study of the chipping of the structure using SEM was carried out. The results of the SEM study of a sample with a silver layer located in the middle of the structure are shown in Fig. 1A, the results of the EDX are shown in Fig. 1B.

The SEM image shows a layered structure with a clearly distinguishable layer boundary. The embedded Ag layer is clearly visible in the middle of the MTS. And from the EDX study, it can be seen that the silver layer is located only in the center of the structure.

A SEM study of the substrate surface was also performed after initiation and the combustion process of a multilayer thermite structure. The image shows an array of particles of various sizes, self-formed during the combustion process. Part of the particles consists of Ag, and the rest of the surface is made up of products of combustion of MTS Al/CuO_x. The results of the SEM study are shown in Fig. 2A, and the EDX study in Fig. 2B.

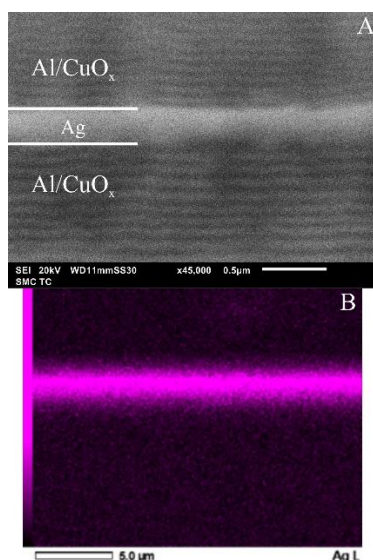


Fig. 1. SEM images and EDX sample studies.

To study the occurrence of the SERS effect in self-phosphored Ag particles, after initiation of combustion of MTS Al/CuOx + Ag. Malachite green (MG) concentration of 10 microns was analyzed by Raman spectroscopy with a laser with a wavelength of 633 nm. Before the study, the samples were soaked in a solution of MG with a concentration of 10 μ M and a volume of 4 ml for 30 minutes. The results of Raman spectroscopy are shown in Fig. 3.

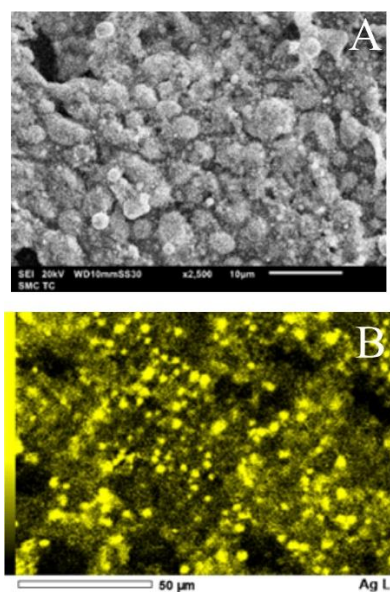


Fig. 2. SEM image of Ag particles and a map of the particle distribution over the surface.

The samples showed 10 characteristic malachite green peaks out of 10, with a 5×10^4 fold signal amplification relative to silicon substrates without the SERS effect.

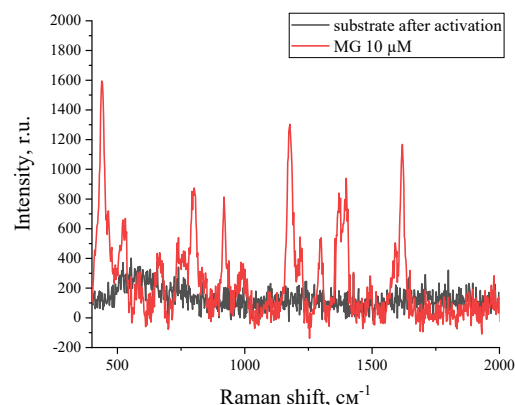


Fig. 3. MTS Raman Spectroscopy with embedded Ag layer

4. Conclusions

This article demonstrates a successful approach to the creation of SERS-active substrates by introducing an additional layer of silver (Ag) into multilayer thermite structures (MTS) based on Al/CuOx.

The results of Raman spectroscopy demonstrated a significant signal amplification for the studied samples when analyzing malachite green (MG) at a concentration of 10 μ M. Substrates with self-formed Ag particles provided a 5×10^4 increase in the Raman spectroscopy signal relative to silicon substrates.

The use of multilayer thermite structures embedded with a Ag layer is an innovative and effective solution for creating materials suitable for the ultra-sensitive analysis of substances using Raman spectroscopy.

Acknowledgements

The research was carried out in the scientific research laboratory "Photonic Sensors and Plasmonic Materials" at the National Research University "MIET" within the framework of the state assignment FSMR-2024-0012.

References

- [1] S. Dubkov, D. Novikov, A. Overchenko, V. Kolmogorov. Cells **12**(2023)21.
- [2] T. Grishin, A. Overchenko, S. Dubkov, St. Petersburg Polytechnic University Journal, Conference materials **15**(2020)3.1.
- [3] Patent RU 2806842 C1. A method for manufacturing a substrate with rapid self-forming of nanoparticles for obtaining giant RAMAN spectra of light. Applicant: Gromov D.G., Lebedev E.A. and others; published on 11/08/2023.

Electron paramagnetic resonance of Fe-doped NASICON

Saritsky D.A.^{*}, Grishchenko D.N., Medkov M.A., Ziatdinov A.M.

Institute of Chemistry FEB RAS, 159, Pr-t 100-letiya Vladivostoka, Vladivostok, 690022, Russia

*e-mail: denissaricki@mail.ru

Abstract. The sodium superionic conductor NASICON, doped with iron ions, was investigated using electron paramagnetic resonance (EPR). Based on the analysis of experimental data, it was concluded that, in addition to isolated Fe³⁺ ions in weakly distorted octahedra, the samples also contain these ions in crystal fields with strong rhombic distortion (in the glassy phase of the sample). By approximating the Fe³⁺ EPR spectrum, the distributions of fine structure parameters in the ordered and glassy phases of the sample were obtained.

1. Introduction

The development of energy storage technologies is of particular importance given the need to reduce greenhouse gas emissions and ensure reliable energy supply. Solid-state sodium-ion batteries are of particular interest, surpassing lithium-ion counterparts in terms of raw material availability, safety, and lifespan [1]. A key element of such batteries is the solid electrolyte, which determines their ionic conductivity and stability. Sodium superionic conductors NASICON (Na_{1+x}Zr₂Si_xP_{3-x}O₁₂, 0 < x < 3) are considered promising materials for sodium-ion batteries [2]. To improve their characteristics, doping methods are employed, among others, allowing for the modification of the crystal structure and enhancement of sodium ion mobility [3]. In this work, some aspects of the structure of NASICON doped with iron ions according to the formula: Na_{3+y}Fe_yZr_{2-y}Si₂PO₁₂, at y=0.1, were investigated using the electron paramagnetic resonance (EPR) method. The synthesis method was pyrolysis of organic solutions [2].

2. Experiment

The electron paramagnetic resonance (EPR) spectra of iron-doped NASICON powders were recorded using a JES-X330 spectrometer (JEOL, Japan) in the X-band frequency range. The power of the microwave field during the recording of the spectra was 1.00 mW, and the static magnetic field (*B*) was swept within the 0-800 mT range, modulated at a frequency of 100 kHz. Temperature-dependent measurements were conducted in a continuous flow of gaseous nitrogen using an ES-13060 DVT5 variable temperature controller (JEOL, Japan).

For the analysis of the experimental spectra, custom MATLAB programs were developed, utilizing functions from the EasySpin software package for EPR spectrum simulation and analysis.

Fig. 1 illustrates the electron paramagnetic resonance (EPR) spectra of iron-doped NASICON powder at three distinct temperatures. A broad and intense component with *g* ~ 2.0 dominates in all spectra. A wider line is also present, with the peak of its low-field wing characterized by *g* ~ 2.8. In the low-field region, a line with a complex lineshape is observed at *g* ≈ 4.3. Lines with these *g*-factor values are characteristic of Fe³⁺ (3d⁵) ions in crystal fields with a significant rhombic component [4]. In addition to the resonances described, a "step-like" increase in intensity is observed at *g* ≈ 9.2 in the low-field region. This spectral feature is typical for EPR spectra of glasses containing Fe³⁺ ions [5], and may be associated with the

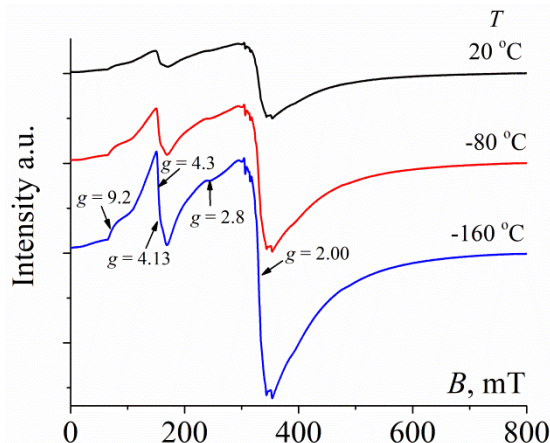


Fig. 1. EPR spectrum of iron-doped NASICON powder at different temperatures.

presence of a glassy phase in the samples. Superimposed on the central broad line of the spectrum is a low-intensity sextet with *g* ~ 2.0. This spectrum is characteristic of ions with a nuclear spin *I* = 5/2, and may belong to Mn²⁺ (3d⁵, *I* = 5/2) ions, which enter the sample from precursors during synthesis.

3. Results and discussions

The complex structure of the electron paramagnetic resonance (EPR) spectra of iron-doped NASICON powders indicates the presence of iron ions in significantly different positions within the samples. The broad line with *g* ~ 2.0 is observed in the EPR spectra of various iron-doped oxide powders [6]. In the literature, it is considered to consist of two components: one belonging to exchange-coupled Fe³⁺ ion clusters, and the other to isolated Fe³⁺ ions in weakly distorted octahedra [7]. The complex appearance of the spectrum in the low-field region may be attributed to the presence of broad distributions of crystal field parameters at the impurity ions, which is characteristic of glasses [8]. Taking into account all of the above, the theoretical analysis of the EPR spectra of iron-doped NASICON powders was performed using the spin Hamiltonian:

$$\hat{H} = g\beta(\vec{B}, \vec{S}) + D\left(\hat{S}_z^2 - \frac{S(S+1)}{3}\right) + \lambda(\hat{S}_x^2 - \hat{S}_y^2)$$

where β is the Bohr magneton, \vec{B} is the applied magnetic field, *g* is the spectroscopic splitting factor, \vec{S} is the spin angular momentum vector of the system, \hat{S}_x , \hat{S}_y , and \hat{S}_z are the spin angular momentum operators along the *x*, *y*, and *z* axes, respectively, *S* is the spin quantum number of the

electron system, D is the axial component of the crystal field, $\lambda = E/D$, where E is the rhombic component of the crystal field. Theoretical EPR spectra were calculated within a specific range of D and λ values, corresponding to strongly and weakly distorted crystal fields.

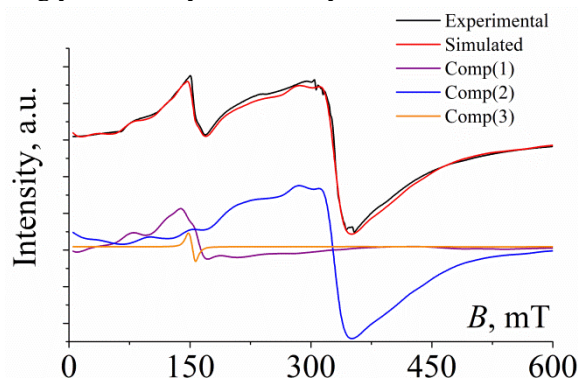


Fig. 2. Experimental (black) and theoretical (red) EPR spectra of iron-doped NASICON powder. Comp(i) ($i = 1, 2, 3$) - components of the theoretical spectrum. $T = -160^\circ\text{C}$.

To calculate the weight w of each individual spectrum $f(B, D, \lambda)$ a double normal distribution was used for the parameters D and λ . The weights w were calculated using the formula

$$w(D, \lambda) = \frac{1}{2\pi\sigma_D\sigma_\lambda} e^{-\left[\frac{(D-D_0)^2}{2\sigma_D^2} + \frac{(\lambda-\lambda_0)^2}{2\sigma_\lambda^2}\right]},$$

where σ_D and σ_λ are the standard deviations of parameters D and λ , D_0 and λ_0 – are the mean values of parameters D and λ in the distribution. Subsequently, the theoretical spectrum $F(B)$ was computed, taking into account the distributions of the fine structure parameters:

$$F(B) = \int \int f(B, D, \lambda) \cdot w(D, \lambda) dD d\lambda.$$

Following the initial calculation of a set of spectra $f(B, D, \lambda)$ and the computation of the weights w , the experimental spectrum was approximated. To improve the agreement between theory and experiment, the weights w were varied in subsequent calculations using the gradient descent method. The final calculated spectrum is presented in fig. 2, and the distribution of the fine structure parameters in fig. 3.

The comparison of the experimental and theoretical spectra confirms the hypothesis that the low-field part of the spectrum belongs to a group of Fe^{3+} ions located in positions with strong environmental distortion, while the high-field part belongs to a group of Fe^{3+} ions located in weakly distorted octahedra. The latter is possible if the impurity Fe^{3+} ions substitute for the matrix Zr^{4+} ions.

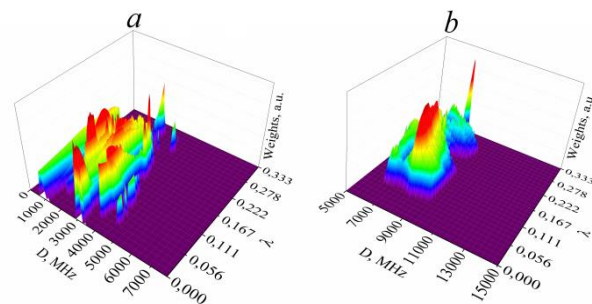


Fig. 3. Distributions of the fine structure parameters D and λ of the NASICON EPR spectrum, obtained from the approximation of the main (a) and low-field (b) components of the spectrum. $T = -160^\circ\text{C}$.

4. Conclusions

The EPR spectra of iron-doped NASICON, recorded at various temperatures, exhibit a similar appearance. The theoretical calculations of the spectra indicate that the majority of the impurity Fe^{3+} ions are located in weakly distorted octahedra, while a smaller part resides in sites with strongly distorted environments. The nature of the crystal field parameter distributions, obtained from the numerical simulation of the spectra, suggests the presence of a glassy phase and allows for the refinement of the fine structure parameter ranges.

Acknowledgements

This work was carried out within the framework of the state assignment to the Institute of Chemistry FEB RAS (project FWFN-2025-0005).

References

- [1] K. M. Abraham. ACS Energy Letters **5**(2020)3544.
- [2] D. N. Grishchenko, M. A. Medkov. Russ. J. Inorg. Chem. **68**(2023)972.
- [3] A. G. Jolley, G. Cohn, G. T. Hitz, E. D. Wachsman. Ionics **21**(2015)3031.
- [4] T. Castner, G. S. Newell, W. C. Holton, C. P. Slichter. J. Chem. Phys. **32**(1960)668.
- [5] M. V. S. Rao, A. S. Kumar, G. C. Ram, Ch. Tirupataiah, D. K. Rao. Phase Transitions **91**(2017)92.
- [6] G. Alvarez. Electron paramagnetic resonance of transition metal ions in glasses: Recent progress. Kerala, India: Transworld Research Network. 2010. 181-202pp.
- [7] D. Karmakar, S. K. Mandal, R. M. Kadam, P. L. Paulos, A. K. Rajarajan, T. K. Nath, A. K. Das, I. Dasgupta, G. P. Das. Phys. Rev. B **75**(2007)144404.
- [8] C. Legein, J. Y. Buzare, J. Emery, C. Jacoboni. J. Phys.: Condens. Matter. **7**(1995)3853.

Investigation of electric current influence on properties and morphology of SERS-active Ag-Nb-N-O film for photonic sensorics

Chumachenko J.V.^{*,1}, Novikov D.V.¹, Dubkov S.V.¹, Gromov D.G.¹, Volkova L.S.^{1,2}, Gavrilov S.A.¹

¹ National Research University "MIET", Shokin Square, House 1, Zelenograd, Moscow 124498, Russia

² Institute of Nanotechnology Microelectronics, RAS, Leninsky Prospekt, 32A, Moscow 115487, Russia

*e-mail: julia.chumachenko@mail.com

Abstract. Surface-enhanced Raman scattering (SERS) is a highly sensitive analytical method that allows the detection of trace amounts of substances due to their interaction with plasmonic nanostructures. Substrates based on them are an indispensable tool for medical, biological, chemical and environmental studies. A significant disadvantage of SERS-active substrates is their limited lifetime due to oxidation of plasmonic material and adsorption of substances by the surface from the atmosphere. The main purpose of the work was to study the activation (formation of an array of nanoparticles on the surface) of Ag-Nb-N-O thin film by electric current. This alloy has a high resistance to the atmosphere, as well as the possibility of carrying out the activation process immediately before the study. In this work, the results of electric current exposure in galvanostatic and potentiostatic modes on Ag-Nb-N-O thin film were investigated. The relationship between the temperature of the structure and its volt-ampere characteristics were investigated. The intensities of the SERS-spectra when the thin film was exposed to different modes of electricity were compared. The analyzed substance was rhodamine 6G solutions of different concentrations.

1. Introduction

SERS-active substrates based on silver nanoparticles (Ag NPs) have prospects of wide application in biomedical diagnostics, food quality control and environmental monitoring. However, their practical use is hindered by the rapid degradation of the properties of SERS-active substrates due to oxidation of nanoparticles and surface contamination.

Alloy films, in which the plasmonic material is uniformly distributed in the volume of the thin film, are a promising solution to this problem. Our previous studies have shown that the Ag-Nb-N-O film remains stable for more than 60 days and can be activated by microwave radiation to form SERS-active silver nanoparticles [1].

In the present work, a new method for energetic activation of Ag-Nb-N-O films by DC current flow is proposed. This approach provides rapid formation of silver nanoparticles and opens up the possibility of creating portable SERS sensors for off-laboratory studies.

2. Experiment

An oxidized monocrystalline silicon wafer was used as an initial substrate for deposition of the metal alloy film. Silicon dioxide layer had a thickness of 300 nm. The oxidized Si wafer was subsequently cleaned in the Caro's acid ($\text{H}_2\text{SO}_4\text{:H}_2\text{O}_2$) and an ammonia-peroxide solution ($\text{H}_2\text{O}_2\text{:NH}_4\text{OH:H}_2\text{O}$) followed by washing in deionized water. The Ag-Nb-N-O alloy film was deposited on the unheated substrate by magnetron sputtering of Ag and Nb targets in an atmosphere of Ar and N_2 gas mixture at a ratio of 1:6. The targets were sputtered simultaneously at a power of 1000 W for Nb and 150 W for Ag. The residual atmosphere of 5×10^{-5} Torr in the vacuum chamber is the source of oxygen in the film due to the getter properties of niobium.

Exposure to direct electric current was performed using an Instek GPR-30H100 laboratory power supply unit in two modes: galvanostatic at a current of 160-440 mA and potentiostatic at 30-40 V.

The surface morphology was investigated using a Helios G4 CX scanning electron microscope. A Confotec MR 200 confocal microscope-based Raman spectrometer was used to obtain the SERS-spectra of the activated substrates. Rhodamine 6G solutions were used as analyzed substance.

3. Results and discussions

The galvanostatic mode was chosen as the first mode of exposure to electric current. The effect of the current passed through the sample on the intensity of the SERS signal was studied using an R6G solution with a concentration of 10 μM . To analyze the intensity value, the peak of the Raman shift characteristic of R6G was 1360 cm^{-1} [2], (bending of the C-H ring in the plane). From the data obtained, it follows that with a current transmission of more than 280 mA, the intensity of the peaks of the SERS-spectra decreases slightly. This decrease in intensity may be due to the evaporation of nanoparticles from the surface when sufficiently high energy is applied to the substrate. It follows from the SEM images that at a low impact current, mainly large particles with an average size of about 400 nm and small particles with a size of about 140 nm are formed on the substrate, while with an increase in current, the number of small nanoparticles begins to increase, with an average size of about 70 nm. The nature of the dependence of the parameters of the nanoparticle array on the exposure current allows us to assert that after a certain current value, namely 280 mA, the NPs array weakly changes its characteristics. This means that for a given composition of a thin film, it is sufficient to activate when a current of 280 mA is passed through the substrate.

The second studied mode of exposure to electric current was the potentiostatic mode. Based on previous studies, the galvanostatic activation process is accompanied by a voltage change in the range from 30 to 40 V. Accordingly, activation is guaranteed to occur in this voltage range. SEM images were obtained showing that at 30 and 35 V, mainly large nanoparticles with an average diameter of 190 nm with sharp edges are formed on the surface of the film. At

the same time, at 40 V, the appearance of small particles with an average diameter of approximately 4 nm was observed in the space between large nanoparticles (Fig. 1). This may be due to strong heating of the substrate and evaporation of large silver nanoparticles at a given voltage value. If at 30 and 35 V the current did not rise above 25 and 14 mA, respectively, then at 40 V the current reached 1 A, the limit that the power supply could provide. You can also notice that the small NPs are located mainly between the large NPs. Probably, this voltage value is sufficient to heat up the substrate so that the medium-sized NPs are broken down into smaller ones. In addition, it should be noted that when exposed to a voltage of 40 V, the nanoparticles have a smooth shape, unlike faceted particles with other activation parameters. This indicates the melting of the NPs surfaces. We can also talk about coalescence, as evidenced by an increase in particle size.

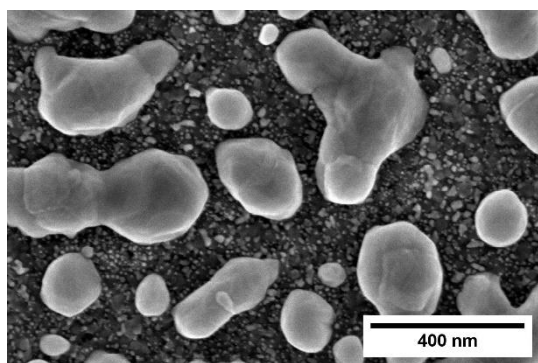


Fig. 1. SEM image of an activated thin film Ag-Nb-N-O in a potentiostatic mode at 40 V.

To verify the obtained nanoparticle arrays as a SERS-active substrate, as well as the subsequent calculation of the enhancement factor, the standard rhodamine 6G dye was used, which has the following characteristic modes: 617 cm^{-1} , 774 cm^{-1} , 1187 cm^{-1} , 1314 cm^{-1} , 1360 cm^{-1} , 1506 cm^{-1} , 1572 cm^{-1} , 1650 cm^{-1} [2]. Fig. 2 shows the SERS-spectra of an activated thin film in galvanostatic mode with applied R6G of different concentrations. The detection limit of R6G was 10^{-8} or 10 nM, at which a characteristic peak of R6G was observed in the region of 774 cm^{-1} . The enhancement factor of the activated SERS-active substrate for the peak was 2.2×10^6 .

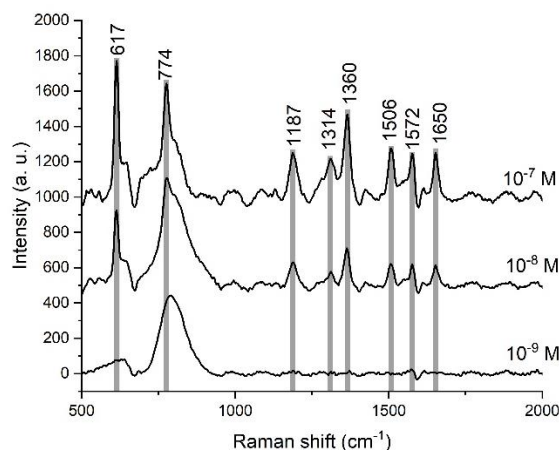


Fig. 2. SERS-spectra of activated thin film Ag-Nb-N-O with applied R6G of different concentrations with reduction to the baseline.

A comparison of the activation modes showed that the highest intensity of the SERS signal is shown by samples activated in galvanostatic mode at an activation current of 280 mA. When the thin film is activated in the potentiostatic mode, the peak intensity is about 3 times less than when activated in the galvanostatic mode.

4. Conclusions

The present study demonstrates a fast and effective way to activate an Ag-Nb-N-O thin film using an electric current. It is shown that the formation of an array of nanoparticles from a thin film is possible in galvanostatic and potentiostatic modes, however, in a comparative analysis, the galvanostatic mode with an activation current of 280 mA showed the highest intensity of the SERS signal. The detection limit of the resulting structure was 10^{-8} or 10 nM, and the enhancement factor was 2.2×10^6 . Based on the data obtained, it can be said that the method of activating the Ag-Nb-N-O thin film by galvanostatic action of current makes it possible to obtain a SERS-active substrate suitable for use in analytical studies.

Acknowledgements

This research was funded by the Russian Science Foundation (Project No. 24-19-00610), <https://rscf.ru/project/24-19-00610/>.

References

- [1] S. Dubkov, D. Novikov, H. Bandarenka, A. Burko, A. Trifonov, L. Volkova, P. Edelbekova. *Applied Surface Science* **645**(2024)158682.
- [2] R. Lu, A. Konzelmann, F. Xu, Y. Gong, J. Liu, Q. Liu, M. Xin, R. Hui, J. Wu. *Carbon* **86**(2015)78.

Synthesis of boron and aluminium-based ligatures in a low-frequency arc discharge plasma

Churilov G.N.^{*1,2}, Glushenko G.A.¹, Nikolaev N.S.¹, Shalygina T.A.^{1,3}, Elesina V.I.^{1,2}, Lopatin V.A.¹, Vnukova N.G.^{1,2}, Zhyzhaev A.M.^{1,4}, Ivaneeva A.D.^{1,4}, Loktev A.N.¹, Tomashevich Y.V.^{1,4}

¹ Kirensky Institute of Physics, FSBSI "Federal Research Center "Krasnoyarsk Science Center SB RAS", 50/38 Akademgorodok St., Krasnoyarsk 660036, Russia

² Institute of Engineering Physics and Radio Electronics, Siberian Federal University, 28 Academician Kirensky St., Krasnoyarsk 660074, Russia

³ Reshetnev Siberian State University of Science and Technology, 31 Krasnoyarskiy Rabochiy Av., Krasnoyarsk 660037, Russia

⁴ Institute of Chemistry and Chemical Technology of the Siberian Branch of the Russian Academy of Sciences, FSBSI "Federal Research Center "Krasnoyarsk Science Center SB RAS", 50/24 Akademgorodok St., Krasnoyarsk 660036, Russia

*e-mail: churilov@iph.krasn.ru

Abstract. In this research work, a novel technology for the production of boron and aluminium-based ligatures processed in a low-frequency arc discharge plasma (66 kHz) is described. Also presents data of the morphology, microstructure, and distribution of boron particles within the aluminium ingot. Boron is uniformly distributed throughout the volume of the aluminium ingot, as confirmed by scanning electron microscopy images. It was demonstrated that the method of treating micron-sized boron particles with arc discharge plasma significantly reduces particle size. Also the proposed technology makes it possible to destroy the oxide film on the surface of the melt and produce ligatures based on boron and aluminium with a uniform distribution of boron over the entire volume of the ingot.

1. Introduction

In the synthesis of ligatures and nanocomposite materials, achieving a uniform distribution of the introduced substance within the matrix is crucial [1]. Proper selection of its dimensions simplifies this task. The smaller the size, the easier it is to achieve a uniform distribution of additive.

Composite materials with an aluminium matrix are of significant interest. [2,3]. It is known that the properties of alloys can be modified through additives (alloying) [4,5]. The most problematic aspect is the introduction of boron into aluminium, which is one of the most attractive alloying elements [6]. This is due to the differences in their physical and chemical properties. At temperatures above the melting point of aluminium, boron does not penetrate into its melt due to the presence of a stable oxide film on the surface of the melt, as well as due to the agglomeration and flotation of nanosized boron particles (caused by poor wetting by the liquid metal) [7].

The destruction of oxide film is necessary when introducing alloying substances in the form of powder, especially when introducing powder in the nanoscale state. In addition to chemical methods for breaking down these film, there exists a plasma method. However, when introducing the alloying substance directly under the mirror of the melt, the alloying substance is often impossible to achieve uniform distribution in the resulting ingot. This, in turn, prevents obtaining material with the required characteristics.

Agglomeration of powder particles is another one of the main challenges in the synthesis of nanocomposites. The introduction of powder using a plasma-forming gas, which also serves as a transport gas, may help address this issue. The plasma-forming gas facilitates particle dispersion and prevents their agglomeration, ensuring a more uniform distribution within the matrix.

Known methods do not demonstrate sufficiently high levels of boron content and uniform distribution throughout the volume of the melt [8,9].

2. Experiment

In this study, we investigated the possibility of addressing the aforementioned challenges based on a previously developed single-jet alternating current plasma generator (66 kHz). We used argon simultaneously as both the plasma-forming and transport gas [10]. The treatment was conducted in a chamber under a buffer gas atmosphere—helium. The generator was utilized in two modifications. In the first case, the discharge occurred between the melt and a hollow copper electrode, through which the powder was also supplied along with a flow of plasma-forming gas. In the second case, the powder was supplied with a tangentially swirling flow of argon. The discharge took place between the melt and a tungsten rod positioned along the axis of the vortex flow.

We have investigated the influence of plasma on the introduced boron powder. Using emission X-ray microscopy method with the mapping method, we examined and compared the initial boron powder (before introduction into the plasma) and boron powder after plasma treatment.

The same method was used to study samples of molten aluminium obtained as a result of treatment with a plasma flow containing boron. The metal was initially melted under induction heating. The results obtained through optical emission spectroscopy qualitatively confirmed those obtained via emission X-ray spectroscopy.

Using X-ray phase analysis (XPA) and X-ray photoelectron spectroscopy (XPS) methods, data were obtained on the structural and chemical composition of the molecular compounds formed in the ingots.

3. Results and discussions

Statistical processing of images obtained through mapping indicated that the boron powder consists of particles whose average size is an order of magnitude smaller, Fig. 1, 2 [11].

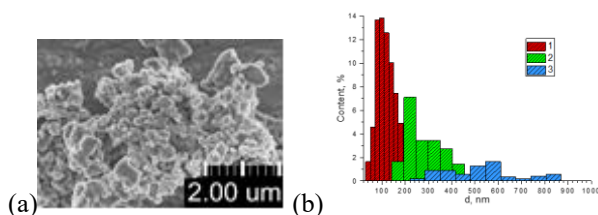


Fig. 1. Initial boron powder: image obtained in mapping mode (a); particle size distribution diagram where (1) is powder with low-size (2) – with medium-size and (3) – with large size particles (b).

Processing ingots with boron in a plasma generator with a copper electrode allowed for mapping to establish the presence of uniformly distributed boron (7.5 ± 2.5 wt%), which is comparable to results previously obtained by us [11]. At this point, the content of impurities remains virtually unchanged. The silicon content slightly decreases while the content of ubiquitous carbon increases.

In contrast, in the case of treatment with plasma from an arc discharge using a tungsten electrode, both the average amount of boron and its distribution uniformity decrease. We noted an important fact that plasma treatment using tungsten electrodes significantly contaminates the resulting alloys with tungsten itself and impurities contained within it (such as copper). This seemingly unexpected result can be explained by different methods of plasma generation. As is known, both types of discharges are arc discharges; however, they differ in that the first involves cold and hot electrodes, while the second involves two hot electrodes. For discharges with cold electrode, the initial part of the discharge is characterized by the emergence of electrode (cathode) spots that rapidly move across the surface of the electrode [12]. Subsequently, these electrode spots merge into one. This process is repeated every period of the current and is repeated every time the current passes through zero.

When current passes through the oxide film, it evaporates due to the large amount of thermal energy released in accordance with Joule's law. Through the rupture of the oxide film, particles of the alloying substance powder enter the melt.

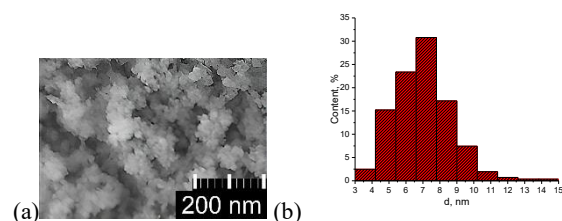


Fig. 2. Plasma-treated boron powder: image obtained in mapping mode (a); particle size distribution diagram (b).

For discharges with a tungsten electrode, the effect of multi-strand structure formation is suppressed by the thermal stabilization effect of the discharge. With the tungsten electrode, there is a significant reduction in the phase shift between the voltage on the electrodes and the

current in the arc circuit compared to discharges with a hollow copper electrode.

4. Conclusions

It has been shown that the introduction of boron powder into the argon flow, which is both plasma forming and transport, leads to a decrease in particle size by more than an order of magnitude. Combining the process of introducing boron powder with a plasma flow made it possible to obtain an aluminium alloy with boron evenly distributed in it. For plasma introduction of refractory substance powder (boron) into a melt having a refractory film on its surface (e.g. aluminum oxide), one of the electrodes must be cooled (e.g. a water-cooled copper electrode can be used).

Acknowledgements

The authors would like to express their special thanks to Center for Common Use of the FSBSI "Federal Research Center "Krasnoyarsk Science Center SB RAS" for providing equipment to ensure the accomplishment of this research.

Funding

The research was carried out at the expense of a grant Russian Science Foundation № 25-29-00794, <https://rscf.ru/project/25-29-00794/>.

References

- [1] K.Yu. Chervyakova, M.E. Samoshina, N.A. Belov. Non-ferrous Metals **2**(2016)34.
- [2] R. Ramanjaneyulu, K. Raja Gopal, B. Durga Prasad. Mater. Today Proc. (2023) <https://doi.org/10.1016/j.matpr.2023.05.564>.
- [3] J. Korzekwa. Rev Adv Mater Sci. **62(1)** (2023)20230108.
- [4] W. Zhai, L. Bai, R. Zhou, X. Fan, G. Kang, Y. Liu, K. Zhou. Adv. Sci. **8**(2021) 2003739.
- [5] P. Cornette, S. Zanna, A. Seyeux, D. Costa, P. Marcus, Corros. Sci. **174**(2020)108837.
- [6] A.I. Malkin, A.D. Aliev, V.A. Klyuev, V. Savenko, A. Shiryayev, A.A. Ryazantseva. Colloid J. **82**(2020)403.
- [7] V.V. Sanin, M.R. Filonov, Yu.A. Anikin, V.I. Yukhvid, D.M. Ikornikov. International Symposium on Self-Propagating High-Temperature Synthesis XV **402**(2019)DOI: 10.24411/9999-0014A-2019-10147.
- [8] K. Yu. Chervyakova, M. E. Samoshina, N. A. Belov. Non-ferrous Metals **2**(2016)34.
- [9] L. Yuan, J. Han, J. Liu, Z. Jiang. Tribol. Int. **98**(2016)41.
- [10] G.N. Churilov, N.S. Nikolaev, G.A. Glushenko, V.I. Elesina, V.G. Isakova, Ye.V. Tomashevich. Int. J. Hydrogen Energy **47**(2022) 7299.
- [11] G.N. Churilov, G.A. Glushenko, A.M. Zhyzhaev, N.S. Nikolaev, V.I. Elesina, N.G. Vnukova, A. Tokmin, V. Lopatin, M. Kastyuk, A.N. Loktev, A.D. Ivaneeva. Uniform alloying of aluminum with boron // Pramana – Journal of Physics. 2025(in press).
- [12] Yu.P. Raiser. Physics of Gas Discharge (Book: 2nd edition, revised and supplemented). Moscow: Nauka Publishing House (1992) 536 p.(in Russ).

Obtaining and investigation of properties of C, Ni and Pd-based nanocomposites

Churilov G.N.^{*1,2}, Elesina V.I.^{1,2}, Isakova V.G.¹, Vnukova N.G.^{1,2}, Glushenko G.A.¹, Nikolaev N.S.¹, Tomashevich Y.V.^{1,4}, Lopatin V.A.¹

¹ Kirensky Institute of Physics, FSBSI "Federal Research Center "Krasnoyarsk Science Center SB RAS", 50/38 Akademgorodok St., Krasnoyarsk 660036, Russia

² Institute of Engineering Physics and Radio Electronics, Siberian Federal University, 28 Academician Kirensky St., Krasnoyarsk 660074, Russia

³ Reshetnev Siberian State University of Science and Technology, 31 Krasnoyarskiy Rabochiy Av., Krasnoyarsk 660037, Russia

⁴ Institute of Chemistry and Chemical Technology of the Siberian Branch of the Russian Academy of Sciences, FSBSI "Federal Research Center "Krasnoyarsk Science Center SB RAS", 50/24 Akademgorodok St., Krasnoyarsk 660036, Russia

*e-mail: churilov@iph.krasn.ru

Abstract. In this research work, nickel/carbon and palladium/carbon nanocomposites obtained in a low-frequency arc discharge plasma (66 kHz). Comparative characteristics of nanocomposites are given. The study also presents the results of the electrochemical behavior of nanocomposite palladium/carbon materials. The dependence of their electrochemical behavior on the composition of the composite has been established.

1. Introduction

Composite materials possess numerous advantages associated with the combination of heterogeneous structural components within a single material. This opens up extensive possibilities for varying their properties by leveraging the benefits of each material type while minimizing their drawbacks [1].

It is known that metals are used as substances with chemical reaction accelerating activity to accelerate the oxidation of various carbon-based products. Transition metals (e.g. Ni) and more expensive platinum group metals exhibit high electrochemical activity [2,3].

Particular attention is drawn to particles containing palladium oxides due to their interesting properties regarding potential applications. Oxygen-containing groups at carbon sites play a crucial role on the reduction of Pd(II) to Pd(0) and in controlling nanoparticle growth [4].

The synthesis of nanocomposite materials with desired properties can be achieved through various methods. Our research focuses on the development of plasma-chemical methods for producing powdered nanocomposite materials in a low-frequency arc discharge plasma based on carbon, nickel, and palladium, characterized by their ability to accelerate electrochemical reactions.

2. Experiment

In this study, synthesis was carried out in an arc discharge plasma (with a current of 240 A and an arc frequency of 66 kHz) using a setup designed for synthesizing carbon-based nanomaterials [5]. Hollow graphite rods were used in both syntheses, with metal in powdered form placed in the axial hole. The nickel content was 19 wt.%, while palladium constituted 28 wt.% (see Fig. 1) [6,7].

In Fig. 1, metal particles (nickel, palladium) are visible, distributed within the carbon matrix. The metal particles exhibit a core-shell structure.

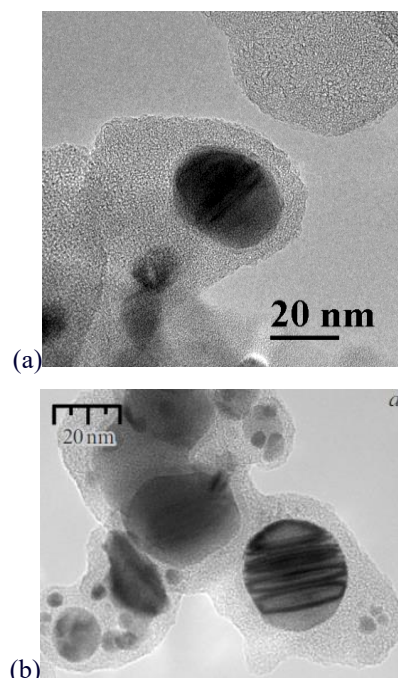


Fig. 1. TEM images: nickel/carbon nanopowder obtained on a JEOL JEM-2100, accelerating voltage 200 kV (a); palladium/carbon nanopowder obtained on a electron microscope TEM HT7700, Hitachi (b).

Studies were conducted on the changes occurring in the synthesized nanopowders using differential thermal analysis (DTA) on a NETZSCH STA 449C thermal analyzer with a QMS 403C mass spectrometer in an argon flow containing 20 wt.% oxygen.

As observed in Fig. 2(a) [6], all phases present in the nickel/carbon nanopowder undergo combustion within the temperature range of 400 to 600°C.

In contrast to the nickel-containing powder, after 600°C, a slow mass decrease is observed during the combustion of the palladium-containing powder (Fig. 2(b)) [7]. At a temperature of 830°C, an endothermic reaction occurs, as known from the literature [8]. This phenomenon

was utilized for the separation of palladium/carbon nanopowder into components [7].

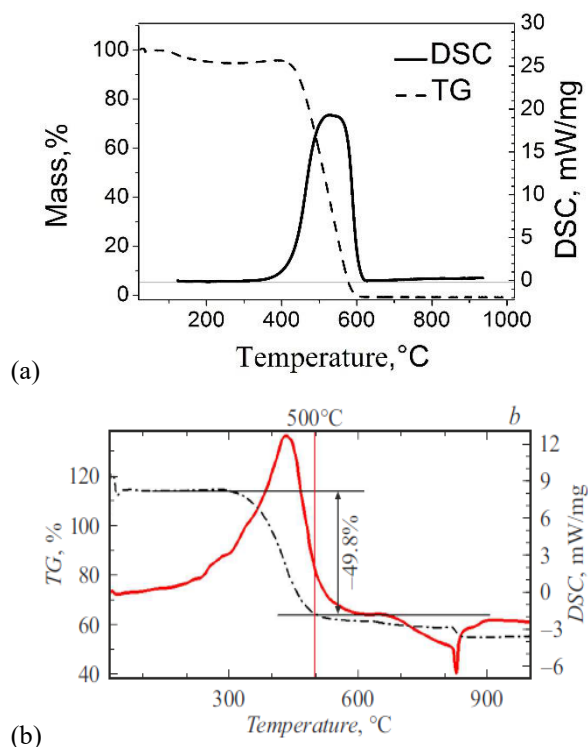


Fig. 2. Thermograms: nickel/carbon nanopowder (a), palladium/carbon nanopowder (b).

For this purpose, during the heating process, we employed a crucible with a height of 5 cm, placed in a gradient thermal field within an argon-oxygen mixture flow. The bottom of the crucible was heated to 1000°C, while the upper part reached 700°C (the decomposition temperature of palladium oxide is around 830°C). The heating was maintained for 20 minutes. As a result, the substance separated into two parts: the lower part exhibited a black color characteristic of carbon materials, while the upper part displayed a light gray color.

Both parts were analyzed using powder X-ray diffraction, transmission electron microscopy (TEM), X-ray photoelectron spectroscopy (XPS), X-ray fluorescence analysis, and cyclic voltammetry (CV).

It was found that the electrode made from the powder from the upper part of the crucible (which contained palladium and palladium oxides) exhibited significantly higher activity in the ethanol oxidation reaction.

4. Conclusions

As research has shown, the selected parameters of the arc discharge plasma in the kilohertz frequency range enabled the synthesis of composite nanomaterials, consisting of powders with nickel or palladium particles distributed within a carbon matrix.

The study of the behavior of the obtained nanopowder which contained palladium in the electrochemical oxidation reaction of ethanol in an alkaline electrolyte using cyclic voltammetry demonstrated high electrochemical activity, attributed to the elevated concentration of the mixture of metallic palladium and its oxides. Consequently, the resulting palladium-containing nanocomposite powder can be effectively utilized for the development of electrode materials.

Acknowledgements

The authors would like to express their special thanks to Center for Common Use of the FSBSI "Federal Research Center "Krasnoyarsk Science Center SB RAS" for providing equipment to ensure the accomplishment of this research.

Funding

The research was carried out within the state assignment of Kirensky Institute of Physics, FSBSI "Federal Research Center "Krasnoyarsk Science Center SB RAS".

References

- [1] L. Huang, L. Geng, H. Peng. *Progr. Mater. Sci.* **71**(10) (2015), 93.
- [2] O.V. Krylov *Technology of catalysts* (Book: 3rd edition, edited by I.P. Mukhlenov) L.: Chemistry (1989). 328 p.(in Russ).
- [3] B. Chen, D. Chao, E. Liu, M. Jaroniec, N. Zhao, S.-Z. Qiao. *Energy Environ. Sci.* **13**(2020)1096.
- [4] W. Zhao, T. Wang, B. Wang, R. Wang, Y. Xia, M. Liu, L. Tian. *Colloids Surf. A: Physicochem. Eng. Aspects*, **658**(2023)130677.
- [5] G.N. Churilov, W. Krätschmer, I.V. Osipova, G.A. Glushenko, N.G. Vnukova, A.L. Kolonenko, A.I. Dudnik. *Carbon* **62**(2013)389.
- [6] G.N. Churilov, N.S. Nikolaev, A.V. Cherepakhin, A.I. Dudnik, E.V. Tomashevich, M.V. Trenikhin, N.G. Bulina. *Technical Physics. The Russian Journal of Applied Physics* **63**(2) (2018)216.
- [7] G. N. Churilov, V. G. Isakova, V. I. Elesina, N. G. Vnukova, N. S. Nikolaev, E. V. Tomashevich, G. A. Glushchenko, V. A. Lopatin. *Journal of Technical Physics* (special issue based on the materials of the International Conference "Nanocarbon and Diamond" 2024) **95**(2) (2025)398.(in Russ).
- [8] P.K. Gallagher, M.E. Gros. *J. Thermal Analysis* **31**(1986)1231.

Development of technology for formation of SERS-active nanostructures on Ag/Mo and Ag/Nb alloys

Dubkov S.V.^{*1}, Tarasov A.M.¹, Medenkov G.A.¹, Gromov D.G.¹, Novikov D.V.¹,
Chumachenko J.V.¹, Volkova L.S.², Gavrilov S.A.¹

¹ National Research University of Electronic Technology "MIET", 124498 Moscow, Russia

² Institute of Nanotechnology of Microelectronics of the Russian Academy of Sciences, 115487 Moscow, Russia

*e-mail: i@dubkov.ru

Abstract. This work presents the results on the formation of plasmonic Ag nanoparticles on the surface of SERS substrate from multicomponent thin films of Ag/Mo and Ag/Nb composition. The thin films were formed by magnetron and ion-plasma deposition. Ag nanoparticles were formed by heat treatment in air. Dependences of nanoparticle morphology as a function of exposure temperature and film thickness were obtained. The obtained SERS substrates showed signal enhancement factors of the order of 2×10^6 and 6×10^5 for Ag₃₀Nb₇₀ and Ag₆₀Nb₄₀ films, and Ag₂₀Mo₈₀ of the order of 1.5×10^6 .

1. Introduction

SERS structures are promising for application in several analytical studies, including environmental, pharmacological and medical applications. These structures are based on the enhancement of Raman light scattering near plasmonic metal nanoparticles. SERS enables the detection of ultra-small concentrations of substances, down to single molecules.

The highest enhancement is observed for SERS structures based on silver plasmonic silver nanoparticles. One of the disadvantages of such structures is their short lifetime. As a result of interaction between silver and air atmosphere, sulfidization of the surface occurs [1]. This leads to a decrease in gain.

One solution to this problem may be the use of multicomponent thin films consisting of mutually insoluble components. Usually, such systems consist of a plasmonic component and a metallic base. The role of the plasmonic component can be Ag, and the role of the base film can be Nb and Mo. The plasmonic component does not form stable chemical compounds with the metal film-base, which allows the plasmonic component to be in the form of individual particles inside the film. Energy impact on the substrate leads to the release of plasmonic nanoparticles from the volume of the thin film and the formation of an array of nanoparticles on the surface. Thermal treatment of the substrate can act as an energetic influence. It is possible to control the density of the array and morphology of plasmonic nanoparticles by changing the concentration of the plasmonic component, thickness, and heat treatment mode.

2. Experiment

Ag-Nb-N-O and Ag-Mo-N-O thin films were obtained by magnetron and ion-plasma sputtering, respectively. Ag-Nb-N-O thin films of Ag₃₀Nb₇₀ nm and Ag₆₀Nb₄₀ composition were formed on silicon substrate at N₂ pressure of about 5×10^{-4} Torr and Ar pressure of about 3×10^{-3} Torr. The composition of the initial film was changed by varying the applied power to the magnetrons with Ag and Nb mixtures.

The films of Ag-Mo-N-O system were formed on silicon substrate. The Ar:N₂ flow rate ratio was 5:1. The concentration of Ag in the formed layer was varied by changing the ratio of Ag and Mo areas of the composite

target. Thin film formation was carried out for 5, 10 and 20 minutes.

Heat treatment of thin films was carried out in air at 100 to 600 °C for 10 min.

The morphology of Ag nanoparticle arrays was investigated using a Helios G4 CX scanning electron microscope. The activity of CERS substrates was investigated on a Confotec MR200 Raman microscope. Methylene blue solutions were used as analytical material.

3. Results and discussions

Ag nanoparticles were observed on the surface of Ag-Nb-N-O film of Ag₆₀Nb₄₀ composition with a thickness of about 250 nm. The average size of nanoparticles varied from 20 to 200 nm with a spacing of about 500 nm. The density of the nanoparticles was about $3 \mu\text{m}^{-2}$. In addition to spherical nanoparticles, single rod-shaped particles were observed.

After the formation of a thin film of Ag₃₀Nb₇₀ composition with a thickness of about 250 nm, formed nanoparticles with diameters ranging from 20 to 170 nm were observed on the surface. The distance between the particles is of the order of 150 nm with a particle density of the order of $21 \mu\text{m}^{-2}$.

Thin films of Ag₂₀Mo₈₀ composition obtained for 5, 10 and 20 minutes had thicknesses of the order of 44, 83 and 180 nm. The films with thicknesses of the order of 44 and 83 nm have no Ag nanoparticles on the surface. In the film with a thickness of about 180 nm, particles with a diameter of about 110 nm are observed.

After heat treatment on the surface of a thin film of Ag₆₀Nb₄₀ composition with a thickness of about 250 nm at a temperature of 100°C for 10 minutes, the distance between the particles decreases to 310 nm. The number of nanoparticles increases to $6 \mu\text{m}^{-2}$ with an average diameter of about 140 nm. As the annealing temperature increases, the number of nanoparticles per unit surface area decreases and the average diameter increases. At the same time, the distance between the particles changes insignificantly. Thus, after heat treatment at 600 °C, the average diameter of nanoparticles is about 300 nm, the distance between particles is about 305 nm at a particle density of about $3 \mu\text{m}^{-2}$. A similar trend is maintained for thin films of Ag₃₀Nb₇₀ composition. It is worth noting that the diameter

of nanoparticles decreases as the amount of Ag in the film decreases.

As a result of thermal treatment of thin films of $\text{Ag}_{20}\text{Mo}_{80}$ composition in air at a temperature of about $400\text{ }^{\circ}\text{C}$ for 10 min, Ag nanoparticles are formed on the surface. In films with thicknesses of about 44, 83 and 180 nm, the average diameter of nanoparticles is about 195, 520 and 710 nm with the distance between the particles about 1300, 1000 and 500 nm, respectively.

The signal enhancement factor of the heat-treated thin film of $\text{Ag}_{60}\text{Nb}_{40}$ and $\text{Ag}_{30}\text{Nb}_{70}$ composition was of the order of 2×10^6 and 6×10^5 , respectively. The heat treatment of $\text{Ag}_{20}\text{Mo}_{80}$ thin film achieved the gain of 1.1×10^6 , 1.5×10^6 , and 9×10^5 for the 44, 83, and 180 nm thick films, respectively.

4. Conclusions

SERS substrates based on thin multicomponent films of $\text{Ag}_{30}\text{Nb}_{70}$, $\text{Ag}_{60}\text{Nb}_{40}$ and $\text{Ag}_{20}\text{Mo}_{80}$ composition were obtained. The obtained films had thicknesses of about 250 nm for $\text{Ag}_{30}\text{Nb}_{70}$ and $\text{Ag}_{60}\text{Nb}_{40}$ films, and $\text{Ag}_{20}\text{Mo}_{80}$ of 44, 83, and 180 nm.

On the surface of the formed $\text{Ag}_{60}\text{Nb}_{40}$ films, the average diameter of the nanoparticles was of the order of 398 nm. $\text{Ag}_{30}\text{Nb}_{70}$ films had about 153 nm. Ag nanoparticles were not formed on the surface of $\text{Ag}_{20}\text{Mo}_{80}$ composition films at film thicknesses of the order of 44 and 83 nm. Ag particles with an average diameter of about 110 nm were observed on the surface of the film with a thickness of about 180 nm.

The heat treatment resulted in the formation of arrays of plasmonic Ag nanoparticles. As the annealing temperature increased, the distance between the particles decreased, the number per unit surface area increased while the average diameter decreased.

The obtained SERS substrates showed signal enhancement factors of about 2×10^6 and 6×10^5 for $\text{Ag}_{30}\text{Nb}_{70}$ and $\text{Ag}_{60}\text{Nb}_{40}$ films, and $\text{Ag}_{20}\text{Mo}_{80}$ of about 1.5×10^6 .

Acknowledgements

The study was supported by the Russian Science Foundation grant No. 24-19-00610, <https://rscf.ru/project/24-19-00610/>.

References

- [1] C. Thota, J.K.R. Modigunta, M. Reddeppa, Y.H. Park, H. Kim, H. Kang, S. Kokkiligadda, S. Lee, G. Murali, S.Y. Park, I. In.

Thermal annealing of ultrathin Ag films on SiO₂ for morphology-optimized SERS substrates

Grishin T.S.^{*1,2}, Volkova L.S.^{1,2}, Dudin A.A.¹, Dubkov S.V.², Medenkov G.A.², Gromov D.G.²

¹ Institute of Nanotechnology of Microelectronics of RAS, 32A Leninsky Prospekt, Moscow 119334, Russia

² National Research University of Electronic Technology - MIET, 1 Shokin Square, Zelenograd, Moscow 124498, Russia

*e-mail: Grishin.t@outlook.com

Abstract. We report a reproducible method for creating high-performance SERS substrates via thermal annealing of ultrathin Ag films on SiO₂. By adjusting the film thickness (2 – 12 nm) and annealing temperature (80 – 300 °C), we achieve controlled nanoparticle arrays. SEM analysis identifies optimized morphological features, notably particle radii of 12 – 25 nm, interparticle spacing of 40 – 50 nm, and sphericity exceeding 0.8, which maximize SERS enhancement factors to 10⁴ – 10⁵ using malachite green as an analyte

1. Introduction

The development of reproducible and highly sensitive substrates for Surface-Enhanced Raman Scattering (SERS) is of considerable interest due to the wide range of applications in chemical analysis, biomedicine, environmental monitoring, and other fields requiring trace-level detection. Arrays of silver (Ag) nanoparticles on solid-state substrates are among the most commonly used systems for SERS. Ag exhibits strong localized surface plasmon resonance (LSPR) in the visible range, leading to significant enhancement of the Raman signal from target molecules. Despite the well-known advantages of Ag as plasmonic material, controlling the morphology of Ag nanoparticles (particularly their size, shape, density, and interparticle spacing) is crucial for obtaining high SERS enhancement factors (EF).

One of the simplest and most reproducible approaches to create arrays of metallic nanoparticles on a solid substrate involves the thermal annealing of ultrathin metal films [1]. When a thin Ag film on a substrate (e.g., silicon with an oxide layer) is heated to moderate temperatures (well below the melting point of the bulk metal), the film breaks into discrete islands or nanoparticles due to the reduced melting temperature at the nanoscale and to surface energy minimization. As these discrete particles form, their size distribution, shape, and spacing can be tuned by varying the initial film thickness and the annealing temperature. These morphological features directly influence the optical properties, including the position and intensity of the LSPR peaks, and thus the SERS response [2].

Despite the simplicity of the method, several questions remain. The evolution of nanostructures at low temperatures (80–300 °C) for varying film thicknesses is not fully understood [3]. While nanoparticle uniformity and array density are known to enhance SERS, the relationships between radius, spacing, coverage, and sphericity require systematic study. Clear guidelines are needed to optimize these parameters for reproducible and strong SERS signals in practical sensing applications.

In this work, we present a systematic examination of how annealing temperature (from 80 to 300 °C) and the volume (or “equivalent thickness”) of a sputtered silver layer (ranging from 2 nm to 12 nm) affect the evolution of array of Ag nanoparticles on a thermally oxidized silicon substrate. By assessing particle size, shape (in terms of

sphericity), coverage, and interparticle spacing using scanning electron microscopy SEM, we identify key morphological factors that lead to strong SERS enhancement. Raman measurements were carried out using malachite green (MG) as a probe molecule to quantify enhancement factors. Our findings yield a set of optimized morphological conditions that produce significant improvements in SERS activity.

2. Experiment

We used silicon (100) wafers with a thermally grown SiO₂ layer of approximately 300 nm thickness. The wafers were cleaned to remove any organic and ionic contaminants prior to silver deposition. Ag was deposited using a magnetron sputtering system (Q300T D Plus, Quorum, UK) with a high-purity (99.995%) Ag target. The base pressure in the chamber was around 10⁻⁵ mbar, and argon was introduced at a working pressure of 10⁻² mbar during sputtering. A calibrated quartz crystal microbalance monitored the nominal thickness of the deposited silver film. In the range of very thin Ag layers (up to ~15 nm), the film is discontinuous (island-like), and thus the indicated thickness from the quartz sensor is understood as the “equivalent thickness” if it were spread as a continuous film of the same volume.

After deposition, the silicon wafers (with their newly formed ultrathin Ag layers) were cut into multiple pieces, which were then annealed at various target temperatures (80 – 300 °C) for 10 minutes in a nitrogen atmosphere. Samples were allowed to cool naturally once the heating was finished. Through these annealing conditions, Ag nanoparticles of varying size and shape were formed on the surface.

SEM images (Helios G4CX, TFS, USA) provided a top-view assessment of nanoparticle size, shape, and coverage. Analysis of these images was performed with Gwyddion software. Each particle on the images was delineated by a watershed mask, and the area, perimeter, equivalent disc radius and centroid were determined for each particle.

For Raman spectroscopy, a inVia Qontor system (Renishaw, UK) was employed, calibrated to the 520 cm⁻¹ Si peak. A 532 nm laser was used as the excitation source, typically at low laser power to avoid photodegradation of the analyte. Malachite green was chosen as the probe molecule: droplets of its aqueous solution (with concentrations from 10⁻⁶ M down to 10⁻⁸ M) were placed

onto the Ag nanoparticle arrays. After drying, SERS spectra were collected. For reference and calculation of enhancement factors (EF), spectra of a 10^{-2} M malachite green solution deposited on plain glass were also acquired. Enhancement factors were estimated using the ratio of intensities from the SERS substrate to the reference substrate, normalized by the difference in analyte concentration.

3. Results and discussions

The as-deposited layers with nominal thicknesses up to 3 nm already appeared as discrete clusters with relatively high sphericity. For slightly thicker films (3.5 – 6 nm), the structures displayed both spherical particles and some “merged” particle or “dimers” features. At higher equivalent thicknesses (7–12 nm), the as-deposited layers formed more complex island shapes or “blots” (fig. 1).

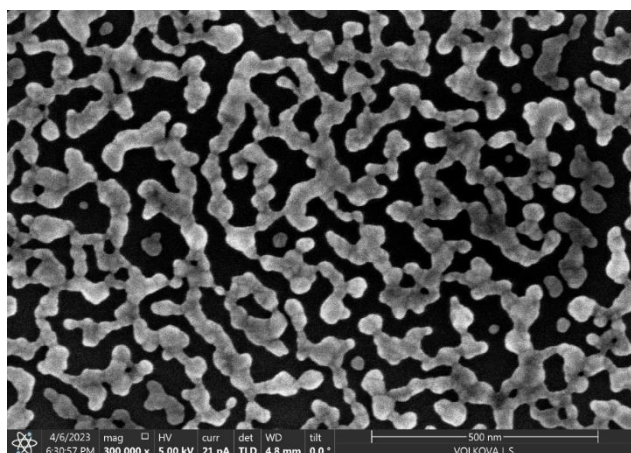


Fig. 1. Initial layer of Ag, equivalent thickness is 10 nm.

Upon heating above 100 °C, the larger, irregular islands tended to break into smaller nanoparticles. This resulted in a significant increase in the total number of particles and an increase in their average sphericity. The of this depended on the initial thickness of the Ag layer. For the thickest layers (10 – 12 nm), it took temperatures of 140 – 180 °C to completely break large islands into separate particles. Furthermore, with increasing temperature, smaller particles merge via meniscus formation, creating dimers that would than form single larger spherical particles.

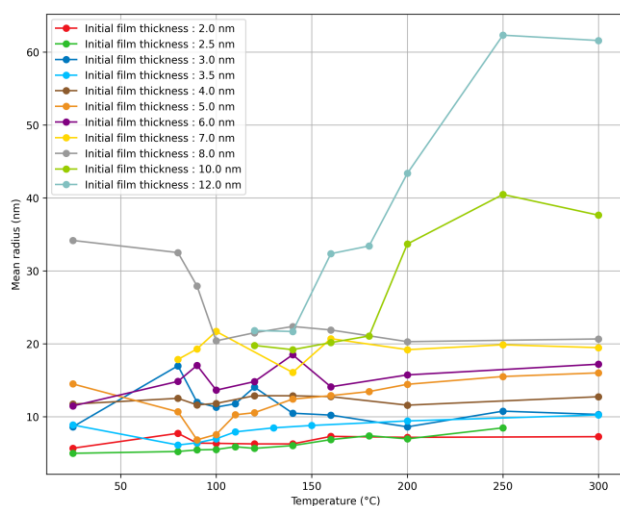


Fig. 2. Dependence of average radius of NPs on annealing temperature.

We used a sphericity coefficient S (ranging from 0 to 1, with 1 being a perfect circle in top view) to categorize the shapes. At lower temperatures (for thick initial layers), the sphericity could be < 0.7 , indicating very irregular islands. As temperature rise, sphericity generally reaches or exceeds 0.8, marking nearly spherical particles. However, when two particles coalesced, there could be brief dips in the average sphericity, followed by a return to more spherical shapes as the merged particle relaxed into a single domain.

The SERS enhancement was found to peak for average nanoparticle radii in the range of 12 – 25 nm. The spacing between neighboring nanoparticles is critical for “hot spot” formation, where intense local electromagnetic fields boost Raman signals. We observed that SERS signals were highest when the average interparticle spacing is about 20 nm. Larger distances (> 30 nm) lead to a rapid decrease in SERS enhancement because the collective plasmonic coupling between particles is weakened.

While shape alone is not the sole determinant of high enhancement, large deviations from spherical shapes tend to reduce the overall uniformity of the array. Thus, arrays characterized by sphericity values above 0.8 typically outperformed arrays with more irregular particles.

We calculated EF from the ratio of a characteristic Raman peak intensity (the 1616 cm^{-1} band in MG) on the Ag nanoparticle substrate to that on a glass substrate, accounting for the difference in concentration. EFs in the range of 10^4 – 10^5 were achieved, enabling detection of malachite green at concentrations down to 10^{-8} M.

4. Conclusions

We have demonstrated a reproducible method of fabricating SERS-active substrates via thermal annealing of sputtered ultrathin Ag films on Si/SiO₂ supports. By varying the initial film thickness (2 – 12 nm) and the annealing temperature (80 – 300 °C), it is possible to control crucial morphological parameters. Arrays with quite spherical ($S > 0.8$) NPs with radii in the range of 12 – 25 nm and interparticle spacing of about 20 nm exhibit the highest SERS response for malachite green under 532 nm laser excitation.

The interplay of initial film thickness and annealing temperature controls the morphological evolution of Ag nanoparticles, which in turn governs their plasmonic properties and SERS performance. By tuning these parameters, one can reproducibly achieve substrates with exceptionally high sensitivity to trace-level analytes.

Acknowledgements

This research was funded by the Russian Science Foundation (Project No. 24-19-00610), <https://rscf.ru/project/24-19-00610>.

References

- [1] Gromov, D. G. et al. Applied Surface Science **489**(2019)701.
- [2] Dubkov, S. V. et al. Defect and Diffusion Forum **386**(2018)250.
- [3] Gafner, Yu. Ya. et al. Surfaces and Interfaces **54**(2024)105165.

Sol-gel derived nanostructured materials for luminescence and photocatalytic applications

Khoroshko L.S.^{*,1,2}, Baglov A.V.^{1,2}, Yauseichyk M.A.², Korolik O.V.¹

¹ Belarusian State University, Faculty of Physics, 4 Nezavisimosti Av., Minsk 220030, Belarus

² Belarusian State University of Informatics and Radioelectronics, 6 P. Browka St., Minsk 220013, Belarus

*e-mail: l.s.khoroshko@gmail.com

Abstract. Sol-gel technology is a promising complex of processes for obtaining various composites for a wide range of applications. For example, luminescent and photocatalytic active materials can be obtained by the sol-gel method with different form factors, such as powders or coatings. In this work, the structure and luminescent properties of lanthanide-doped sol-gel derived perovskite powders, as well as titania coatings obtained with an organic template, are described. BaTiO₃:Eu^{2+/3+} and SrTiO₃:Tb³⁺ powders with the average crystalline size of 30-90 nm demonstrate strong photoluminescence at room temperature with characteristic lines of dopant ions. Sol-gel derived carbon-enriched TiO₂ coatings on the monocrystalline silicon possess a high UV-activated photocatalytic activity, depending on the phase composition of titania. The prospects of the application of these materials are discussed.

1. Introduction

Sol-gel technology is saving its actuality for the obtaining of different types of materials with various form-factors during the last decades. Particularly, the well-quality nanostructured luminophores and sorbent could be obtained through the sol-gel synthesis in the form of powders or porous materials, including aerogels [1]. Further, using the sol-gel process, thin and thick films of coatings with various structure, porosity, roughness, etc., can be fabricated. That coatings have a wide area of application: from anti-corrosion protection to safety luminescent marks and photocatalytic active surfaces [2]. In this work, we provide a brief overview of the work of sol-gel technology for obtaining luminescent and photocatalytically active materials. The structure and luminescence characteristics of Tb- and Eu-doped nanostructured perovskite powders are analyzed. The photocatalytic activity of sol-gel derived nanocomposites based on TiO₂ with carbon is investigated.

2. Experiment

Nanostructured perovskite luminophore powders were obtained by sol-gel technology with a multi-step annealing process. Titanium isopropoxide (C₁₂H₂₈O₄Ti), barium or strontium acetates, europium or terbium oxides were used as starting materials to obtain BaTiO₃:Eu and SrTiO₃:Tb sols, the concentration of dopant was 0,01 % to preserve the initial crystalline structure and to prevent excessive formation of the additionally lanthanide oxide phases. Both of the sols were annealed under a multi-step process during which the temperature was raised by 100 °C withholding for 30 min in every step, and final annealing was carried out at 1000 °C for 1 h. Then powders were kept in the furnace for cooling up to room temperature (about 24 h). The structure of luminophores was examined by X-ray diffraction (XRD, Rigaku Ultima IV, Japan). Photoluminescence (PL) of powders was registered using Nanofinder HE (LOTIS TII, Belarus–Japan) confocal spectrometer at room temperature.

Photocatalytically active coatings were obtained using non-acidic sol based on titanium isopropoxide prepared as described in [3]. To obtain carbon-enriched TiO₂, we used the modification of the classical sol-gel synthesis – template sol-gel synthesis. This variant assumes the

possibility of complete thermal decomposition of the so-called "sacrificial" template to form a porous material of a photocatalyst. Thiocarbamide CS(NH₂)₂ was suspended in TiO₂ sol as a template with concentrations from 0.012 to 0.096 g per 1 ml of sol. Suspensions (1 ml) were applied onto the monocrystalline silicon plates and annealed on air at 550 or 850 °C. Phase composition was investigated using Raman spectroscopy on Nanofinder HE. Photocatalytic activity was estimated according to the reduce of adsorption of test pollutant Rhodamine B in water solution (10 mg/L) after the UV exposure with the presence of TiO₂ samples. Absorption spectra were registered at room temperature using Proscan MC 122 (SOL Instruments, Belarus). Absorption intensities were normalized to concentration change according to the calibration line as described in [4].

3. Results and discussions

Luminescence of BaTiO₃:Eu powder under UV excitation demonstrates bands characteristic of Eu³⁺ ions and a broadband due to Eu²⁺ ions (Fig. 1). According to XRD, the powder forms from the monophasic phosphor with average crystalline sizes 30–50 nm [5]. Divalent Eu ion can be found in one compound of this oxide system - europium titanate, which requires further investigation, particularly XPS analysis.

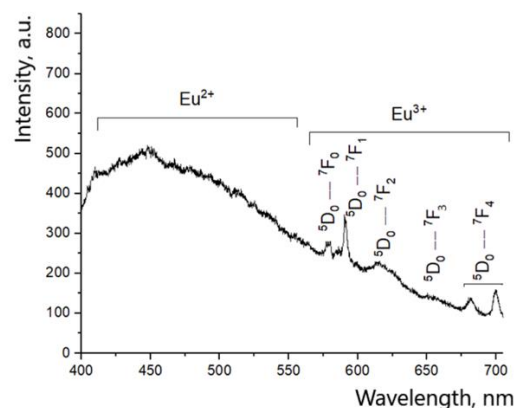


Fig. 1. PL spectrum of BaTiO₃:Eu nanostructured powder under the 355 nm excitation registered at room temperature.

Strontium titanate powder is characterized as a pure oxide phase with a small addition of extra phases from Sr-

Ti-Tb oxide system, average crystalline sizes according to XRD are 50–90 nm [6]. In the PL spectra the typical luminescence of trivalent Tb ions associated with optical transitions from the 5D_4 level is observed. The band related with $^5D_3 \rightarrow ^7F_n$ transitions is also well-resolved, and its intensity depends on the power of the excitation radiation. This indicates the good quality and low-defect matrix of the Tb environment in the powder.

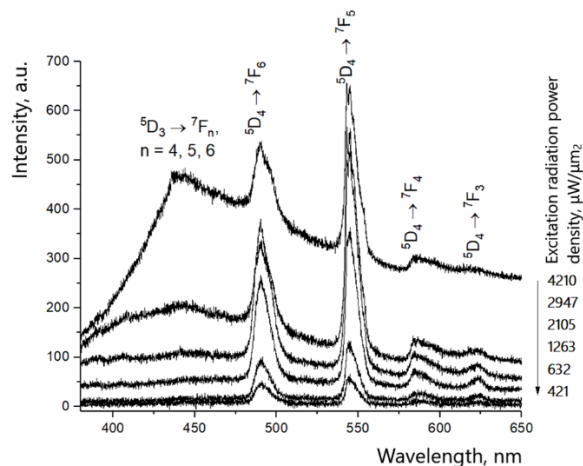


Fig. 2. Excitation radiation ($\lambda = 355$ nm) power depended photoluminescence of SrTiO₃:Tb powder.

TiO₂ films formed on single-crystal silicon are characterized by a developed surface texture with quasi-uniform macro graining and a typical size of homogeneous regions (up to 50 nm, Fig.3).

For all samples, a characteristic set of Raman peaks for anatase and rutile phases is observed, and the rutile content increases consistently during annealing [3].

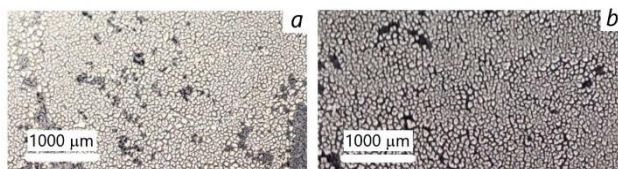


Fig. 3. Appearance of the surface of the samples formed from suspensions with 0.096 g/ml of thiocarbamide on mono-Si substrate after annealing at 550 (a) and 850 °C (b) for 1 h.

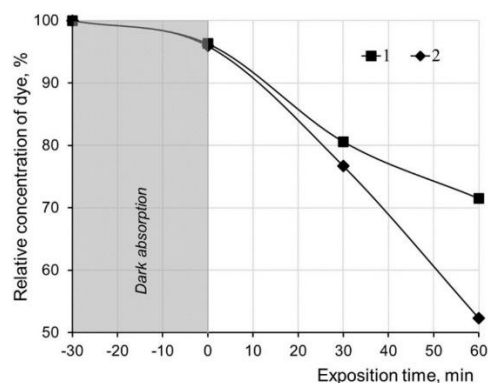


Fig. 4. Kinetic of photocatalytic destruction of Rhodamine B in the aqueous solution under the UV-irradiation in the presence of the TiO₂/Si samples fabricated by annealing at 550 °C (1) and 850 °C (2).

The maximum destruction of the test pollutant dye (48%) was observed in the presence of a film obtained from the suspension with a thiocarbamide content of 0.096 g/ml

after annealing at the temperature of 850 °C (Fig.4). This is due to the optimal ratio of anatase and rutile phases in the TiO₂ film for these conditions, as well as the formation of a developed relief due to template combustion.

4. Conclusions

Thus, sol-gel derived materials have a strong position and great prospects in the synthesis of powder and film phosphors. Obtaining multi-cationic substituted crystals, such as described BaTiO₃:Eu^{2+/3+}, is a perspective for white light-emitting sources and security marks. The obtained in SrTiO₃:Tb power dependence of the luminescence intensity allows the analysis of a dopant concentration in crystalline systems with gradient doping, e.g., during the growth of single crystals, and can be used as a method for non-destructive testing of phosphors. A wide range of sol-gel derived thin film photocatalysts' compositions offers the prospect of designing portable water purifiers and flow purification systems.

Acknowledgements

Investigation supported by SPSR "Material Science, New Materials and Technologies" in frame of the assignments 2.14.3 (reg. № 20212445) and 2.25 (reg. № 20240603).

The authors are grateful to professor V.E. Borisenko for the rewarding discussion of the photocatalyst research results.

References

- [1] D. Bokov, A.T. Jalil, S. Chupradit, W. Suksatan, M.J. Ansari, I.H. Shewael, G.H. Valiev, E. Kianfar. *Advances in Materials Science and Engineering* **1**(2021)5102014.
- [2] W.K. Tan, H. Muto, G. Kawamura, Z. Lockman, A. Matsuda. *Nanomaterials* **11**(2021)181.
- [3] M.A. Yauseichyk, S.E. Maksimov, L.S. Khoroshko, A.V. Baglov, O.V. Korolik, D.V. Yakimchuk, O.N. Ruzimuradov, Sh.I. Mamatkulov. *Journal of the BSU. Physics* **2**(2023) 58.
- [4] O. Alisiyonak, A. Lavitskaya, L. Khoroshko, A.L. Kozlovskiy, M. Zdorovets, I. Korolkov, M. Yauseichuk, E. Kaniukov, A. Shumskaya. *Membranes* **13**(2023)733.
- [5] L.S. Khoroshko, A.V. Baglov, I.A. Svito, O.V. Korolik. *Proc. of XIII Int. Conf. on Phys. Techn. of Nanoheterostruct. Microwave Electron. Mokerov's Readings. Moscow* (2022)106.
- [6] L. Khoroshko, A. Baglov, O. Korolik. *Proc. of 15th Int. Conf. Interaction of Radiation with Solids. Minsk* (2023)464.

The effect of deposition potential on the electrodeposition of platinum particles on highly-doped silicon wafer for ethanol electrooxidation

Volovlikova O.V.¹, Goroshko D.L.², Lazorkina E.N.^{*1}, Dubovitsky A.A.¹, Gavrilov S.A.¹

¹ National Research University of Electronic Technology, 1 Shokin Square, Zelenograd, Moscow 124498, Russia

² Institute of Automation and Control Processes, 5 Radio St., Vladivostok 690041, Russia

*e-mail: Lena.lazorkina.00@mail.ru

Abstract. The effect of the deposition potential of Pt nanoparticles on a highly-doped p-type silicon wafer on the catalytic activity to ethanol oxidation in an acidic solution has been studied. It is shown that the highest specific activity was observed for particles deposited at -0.3 V. The values of current density, the number of changing electrons and the diffusion coefficient was calculated.

1. Introduction

Particles of precious metals, in particular platinum, are of great interest for the creation of various electrodes [1]. Due to the catalytic properties of Pt, functional layers can be synthesized for biosensors and fuel cells for direct electrooxidation of ethanol [2]. The cost of platinum anodes is high, and this is a significant limitation for their industrial applications.

One of the ways to reduce the cost of fuel cell electrodes is to apply Pt nanoparticles to less expensive materials [3], for example, on a silicon substrate. By changing the deposition parameters, it is possible to increase the effective surface of the catalyst and form more electroactive centers on the substrate, which will significantly increase the efficiency of ethanol electrooxidation.

2. Experiment

Platinum particles were formed on the surface of monocrystalline p-type silicon with a resistivity of 0.01 Ohm·cm (highly doped-HD) by electrochemical deposition from a solution containing 2 mM H₂PtCl₆ and 0.5 M H₂SO₄. Deposition was carried out at 25 °C and constant potential from -0.25 V to -0.4 V. The counterelectrode was a platinum mesh electrode, the reference electrode was a silver chloride electrode. The catalytic activity for ethanol were determined by CV in the solution containing 0.5 mol·L⁻¹ H₂SO₄ and different concentration of C₂H₅OH at 50 mV/s. Particle deposition and investigation of catalytic activity of ethanol three-electrode cell were carried out using Autolab Potentiostat equipment with Nova 2.1 software.

3. Results and discussions

The results of the ethanol catalytic activity investigation are shown in Figure 1.

The appearance of anodic forward peak confirming ethanol electrooxidation and the oxidation of freshly adsorbed ethanol pieces. Hence the forward and reverse peak potential and peak current density were used to evaluate the EOR catalytic activity.

The value of the forward peak potential does not depend on the concentration of ethanol in the solution. The lowest potential is observed for particles deposited at -0.35 and -0.4 V, while the highest specific activity of particles deposited at -0.3 V. Anodic forward peak is not

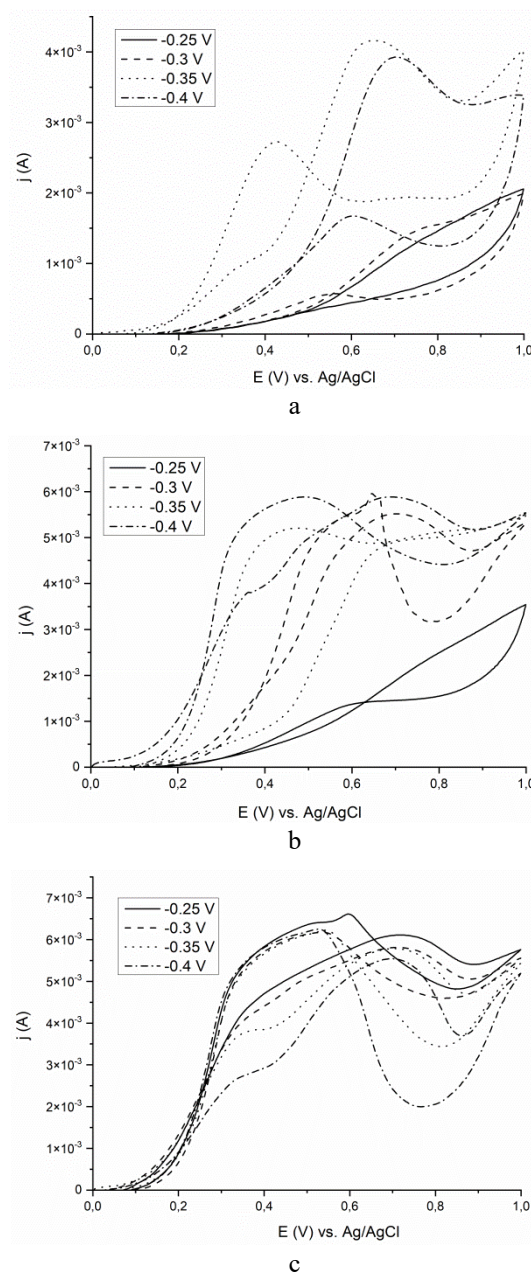


Fig. 1. CV curves of electrodeposited Pt catalysts in solution containing: 0.1 M (a), 0.5 M (b), 1 M (c). Pt particles deposited on surface at -0.25 V, -0.3 V, -0.35 V and -0.4 V during 500 s.

observed for Pt/Si surface in solution contained 0.1 M and 0.5 M of C_2H_5OH . With increasing ethanol concentration, the anodic forward peak current density increases.

During the reverse sweep process above 0.43-0.6 V the oxidation peak is often attributed to the further oxidation of the adsorbed intermediate species of ethanol [4].

Chronoamperograms of ethanol electrooxidation at the potential of 0.5 V in acid solution for samples formed at -0.4 V were also measured. The results of the maximum current I_{max} and stable current I_{ss} values are shown in Table I. Each of the next four cycles shows a lower current density, due to the accumulations of poisonous carbonaceous species [5].

Table I. The value of current density.

Cycles	0.1 M	0.5 M	1 M
	$I_{max}, \cdot 10^{-4} \text{ A/cm}^2$		
1	7.94	3.46	4.45
2	1.92	1.54	1.17
3	2.67	2.32	0.76
4	0.76	1.27	0.55
	$I_{ss}, \cdot 10^{-4} \text{ A/cm}^2$		
	0.1 M	0.5 M	1 M
1	2.95	0.81	0.78
2	7.92	0.39	0.43
3	0.33	0.21	0.31
4	0.13	0.14	0.23

It should be noted that the oxidation peak current density for the first cycle is about ten times higher than that for fourth cycle in 0.1M, three times higher than that for fourth cycle in 0.5M, eight times higher than that for fourth cycle in 1M. The charge values calculated based on the results of chronoamperometry are shown in Figure 2.

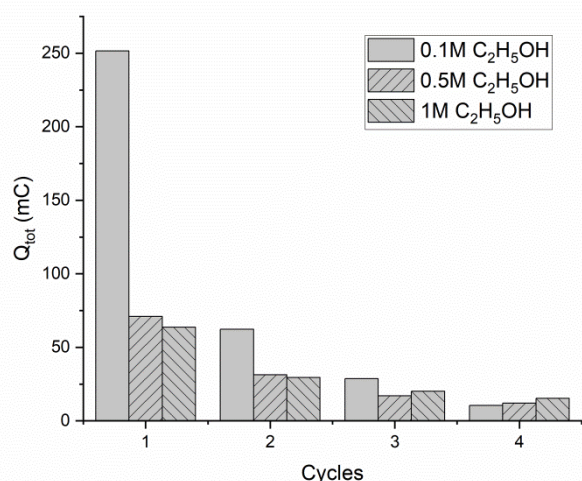


Fig. 2. Diagram of charge values for each measurement cycle.

The effect of the concentration of electrolyte on the peak and stable current density at the electrodes is most noticeable at 0.1M. On the base of chronoamperometric and coulometry data (equation 1) and cyclic voltamperograms curve Randles–Sevcik (equation 2) the average number of exchanged electrons n and diffusion

coefficient D of ethanol on the Pt/Si electrode was obtained.

$$\frac{dQ}{dt} = \frac{2nFD^2C}{\pi^2} \quad (1)$$

Q – charge, t – time, F – Faraday constant, D – the diffusion coefficient, n – the charge electron number, C – ethanol concentration.

$$j_p = 0.4463 \left(\frac{F^3}{RT} \right)^{\frac{1}{2}} \cdot n^{\frac{3}{2}} C (Dv)^{\frac{1}{2}} \quad (2)$$

j_p – anode peak current, v – the scan rates of CV.

The calculation results for the first cycle are presented in Table II.

Table II. Average number of exchanged electrons n and diffusion coefficient D .

Cycles	0.1 M	0.5 M	1 M
	n		
1	14	28	24
	$D, \text{ cm}^2/\text{s}$		
	0.1 M	0.5 M	1 M
1	$1.54 \cdot 10^{-10}$	$1.66 \cdot 10^{-12}$	$7.83 \cdot 10^{-13}$

4. Conclusions

The catalytic activity of platinum particles deposited on c-Si potentials of -0.25 V, -0.3 V, -0.35 V and -0.4 V. The results of the study by the CV method show the lowest potential electrooxidation is observed for particles deposited at -0.35 and -0.4 V, and highest specific activity of particles deposited at -0.3 V. According to the measurement results of the chronoamperograms, the values of the maximum current and stable electrooxidation current for the sample formed at -0.4 V was shown. Based on these data, the diffusion coefficients and the average number of exchanged electrons was calculated. It was shown that for 0.1 M ethanol solution diffusion coefficient is $D = 1.54 \cdot 10^{-10}$, for 0.5 M solution is $D = 1.66 \cdot 10^{-12}$ and for 1 M solution is $D = 7.83 \cdot 10^{-13}$.

Acknowledgements

The work was carried out within the framework of the state assignment 2023-2025, agreement FSMR-2023-0003.

References

- [1] H. A. Huy, T. V. Man, H. T. Tai, V. T. T Ho. Journal of Science and Technology **54**(2016)472.
- [2] K. M. Hassan, A. A. Hathoot, R. Maher, M. A. Azzem. RSC Adv. **8**(2018)15417.
- [3] G. Foti, C. Mousty, K. Novy, Ch. Comminellis, V. Reid. J. Appl. Electrochem. **30**(2000)147.
- [4] P. Bommersbach, M. Mohamedi, D. Guay. J. Electrochem. Soc. **154**(2007)B876.
- [5] H. Gao, S. Liao, Z. Liang, H. Liang, F. Luo. J. Power Sources **196**(2011)6138.

Morphology control of Al-CuO_x thermite materials combustion products due to variation of geometrical characteristics of initial multilayer structure

Novoselcev A.I.¹, Ryazanov R.M.², Volkova L.S.³, Dubkov S.V.¹, Gromov D.G.¹, Lebedev E.A.^{*,1,2,3}

¹ National Research University of Electronic Technology, 1 Shokin Sq., Zelenograd 124498, Russia

² Scientific-Manufacturing Complex "Technological Centre", 1 (7) Shokin Sq., Zelenograd 124498, Russia

³ Institute of Nanotechnology of Microelectronics of the RAS, 32A Leninsky Prospekt, Moscow 119334, Russia

*e-mail: dr.beefheart@gmail.com

Abstract. Al-CuO_x multilayer thermite materials are a striking representative of the metastable intermolecular composite, which is characterized by outstanding energy and combustion properties. In this paper, we investigated the effect of the total thickness of a multilayer thermite Al-CuO_x material formed on the surface of siall substrates on the morphology of the reaction products. High-speed video shooting from different angles allowed us not only to estimate the propagation velocity of the combustion front, but also to visually assess the intensity of gas emission.

1. Introduction

Metastable intermolecular composites, which include multilayer thermite materials, have gained a second life in recent years due to the emergence of new unique applications in various fields of engineering and technology. Such materials are capable of storing thermal energy for a long time and, if necessary, releasing it in fractions of seconds. Almost always, multilayer thermite materials are considered as a source of thermal energy and their characteristics are optimized in order to increase its specific values. In this paper, the influence of changes in the geometric parameters of the multilayer structure of Al-CuO_x on the morphology of combustion products is considered

2. Experiment

Multilayer Al-CuO_x structures were formed on the surface of citall substrates as a result of sequential magnetron sputtering of Al and CuO_x targets in vacuum. The surface of the substrates was subjected to preliminary bombardment with argon ions using an ion source. The thicknesses of the Al and CuO_x layers were 50 nm, and the total thickness of the multilayer structure was 2, 3, and 4 microns (20, 30, and 40 bilayers, respectively).

The control of the elemental composition and thickness of individual layers, the total thickness of the multilayer structure and morphology of combustion products, including cross-sections formed using a focused ion beam, was carried out using a scanning electron microscope equipped with an energy dispersive X-ray spectroscopy attachment.

The features of the combustion process of multilayer thermite materials were studied using a high-speed video camera with a video recording speed from 10,000 to 15,000 frames per second.

3. Results and discussions

The combustion process of multilayer Al-CuO_x structures of various thicknesses has been studied experimentally. It was found that with a change in the overall thickness of the multilayer structure, not only the combustion regime changed, but also the morphology and geometry of the combustion products (Figure 1 shows a

characteristic image of the combustion product). With an increase in the total thickness of the multilayer structure, more intense gas emission was observed.

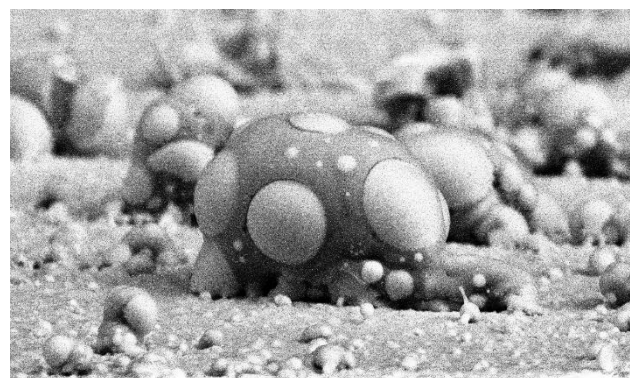


Fig. 1. SEM image of the combustion product of the multilayer structure Al-CuO_x.

The results of the study of the elemental composition of combustion products indicate that the body of the object consists of aluminum oxide, and the inclusions are made of copper. The structure of the combustion products allowed an indirect assessment of the reaction temperature.

4. Conclusions

The features of combustion of multilayer Al-CuO_x thermite structures with different total thicknesses formed on the substrate surface have been studied. It has been found that with a change in the overall thickness of the structure, the combustion mode changes – the intensity of gas release and expansion of heated combustion products increases. As a result of the study of the morphology and composition of the combustion products, it was found that for all thicknesses, the combustion products were formed in the form of drop-shaped structures of complex shape, consisting of an aluminum oxide matrix with copper inclusions. As the overall thickness of the multilayer structure changes, the characteristic size of the reaction products changes non-linearly

Acknowledgements

This work was supported by State Assignment № FSMR-2024-0012.

Application of silicon anode materials in lithium-ion full cells

Pustovalova A.A.*, Morozov A.V., Nedoluzhko A.I.

Skolkovo Institute of Science and Technology, 30 bld. 1 Bolshoy Boulevard, Skolkovo Innovation Center, Moscow, 121205, Russia

*e-mail: a.pustovalova@skoltech.ru

Abstract. The structures of two commercially available silicon materials, non-stoichiometric Si oxide with added Mg (Mg-SiO_x) and silicon-carbon composite (Si/C), were studied. Both materials consist of Si nanoparticles surrounded by inactive buffer media. Then, these two Si materials were tested as the active anode materials of the lithium-ion full cells. The much superior electrochemical performance of Si/C compared to Mg-SiO_x correlates well with the structural features of the materials, which include the size of Si nanoparticles, their oxidation state, and the homogeneity of the samples.

1. Introduction

The application of silicon (Si) as an anode active material in a lithium-ion battery (LIB) is attractive due to its high capacity (up to the theoretical limit of 3579 mAh/g for lithiated $\text{Li}_{14}\text{Si}_5$ phase) and abundance in the Earth's crust determining the potential low cost. The major problems associated with the Si anode materials include the following:

(1) enormous volume change (by 300%) during the reversible lithiation, causing fast degradation of the silicon electrodes;

(2) low initial Coulombic efficiency (ICE), resulting in the withdrawal of active lithium from the cell;

(3) poor conductivity, leading to difficulties in the fabrication of thick electrodes and insufficient rate capability of the cells.

The solutions to these problems involve the synthesis of nanostructured materials. Success, albeit partial, in the development of sufficiently stable silicon anode materials led to their commercialization around 2015 when battery manufacturers started to employ silicon in the anodes of their cylindrical 18650 cells. However, the main component of the anode material in those cells was graphite, and the silicon content was only about 5 wt% [1]. Modern commercial silicon anode materials are divided into two groups: silicon oxide materials (SiO_x) and silicon-carbon composites (Si/C). SiO_x materials were the first successful commercial materials. They are particles of non-stoichiometric silicon oxide, which is the homogeneous mixture of Si and SiO_2 domains with a few nanometers in size [2]. The other group of anode materials is composites of silicon and carbon (Si/C materials). These composites differ greatly in their structures, synthesis procedures, and the resulting electrochemical properties.

In this study, we compared the structures and properties of commercially available silicon anode materials belonging to these two groups. Our study aimed at the practical application of these materials in the anodes of LIB cells.

2. Experiment

The Si/C and Mg-SiO_x materials were commercially purchased and used as the anode active materials.

Transmission electron microscopy (TEM, Titan Themis Z, Thermo Fisher Scientific) was applied to characterize the structure and chemical composition of the composites. The

phase composition was analyzed by a Huber G670 Guinier diffractometer with $\text{Co-K}_{\alpha 1}$ radiation ($\lambda = 1.78892 \text{ \AA}$, curved Ge (111) monochromator, transmission geometry image plate detector) in the $15\text{--}100^\circ$ 2θ range with an angular step of 0.005° .

The electrode slurry was prepared by mixing the active material (70 wt%), carbon black (17 wt%), Na-CMC (7 wt%), CNT (3 wt%), and SBR (3 wt%) in distilled water using a SPEX 8000M ball mill. The slurry was deposited onto a carbon-coated copper foil using an automatic film applicator ZAA 2300 (Zehntner) with a thickness of 200 μm , dried at 80°C in a vacuum oven for 12 h, and then rolled with a roller press. The full coin cells including the Si-based anodes and the $\text{LiNi}_{0.6}\text{Mn}_{0.2}\text{Co}_{0.2}\text{O}_2$ (NMC622) cathodes were subjected to prolonged cycling at 0.2C in the range of 2.5–4.2 V.

3. Results and discussions

The structural data of the Mg-SiO_x material are shown in Fig. 1. As revealed by the energy-dispersive X-ray (EDX), selected area electron diffraction (SAED), and powder X-ray diffraction (PXRD) data, the sample contained the crystalline phases of Si and SiO_2 as well as a significant amount of magnesium in the form of MgSiO_3 . The magnesium is usually added to increase the material ICE [3]. According to the EDX elemental maps (Fig. 1a), the Si nanocrystals around 20 nm in size are surrounded by MgSiO_3 inside the particle. The polycrystalline nature of Si is clearly observed in the SAED pattern (Fig. 1b). On the basis of the PXRD and electron energy loss spectroscopy (EELS) data (Fig. 1c,d), we assume that the Si crystals are strongly oxidized on the surface. Therefore, the SiO_x component of the material is not a uniform mixture of Si and SiO_2 domains; rather, it is Si oxidized on the surface.

The structural data of the Si/C material are presented in Fig. 2. The EDX elemental map (Fig. 2a) displays Si particles of several nanometers surrounded by nanostructured carbon. This structure is highly uniform within a particle. The SAED (Fig. 2b) and PXRD (Fig. 2c) patterns exhibit a diffuse halo and broad peaks, respectively, which are attributed to largely amorphous Si.

Overall, the comparison of Mg-SiO_x and Si/C structures shows that the Si/C material has a better uniformity and contains much smaller and less oxidized Si particles. These structural differences affect the electrochemical properties summarized in Table 1.

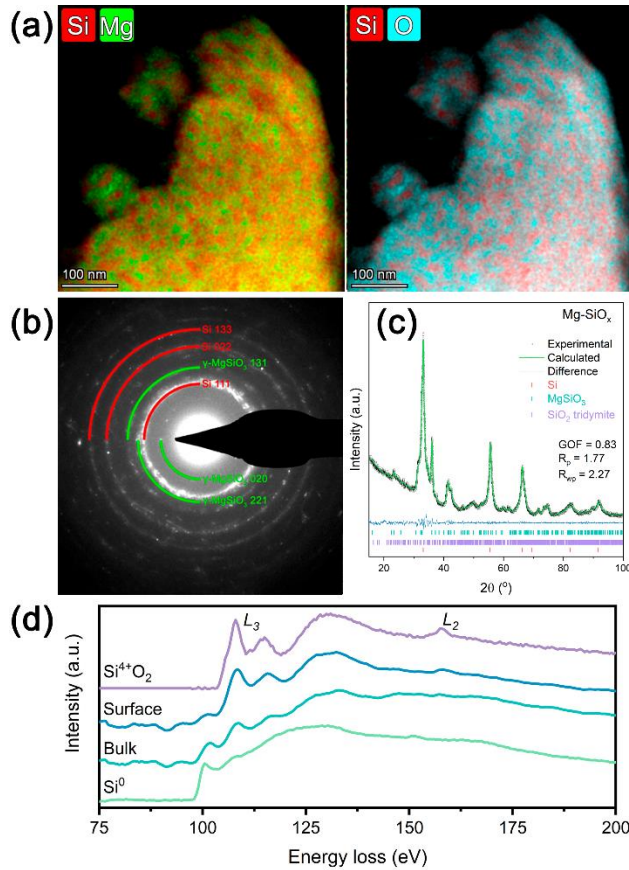


Fig. 1. Mg-SiO_x material: (a) STEM-EDX elemental maps of Si-Mg and Si-O, (b) SAED pattern, (c) PXRD pattern, and (d) STEM-EELS spectrum.

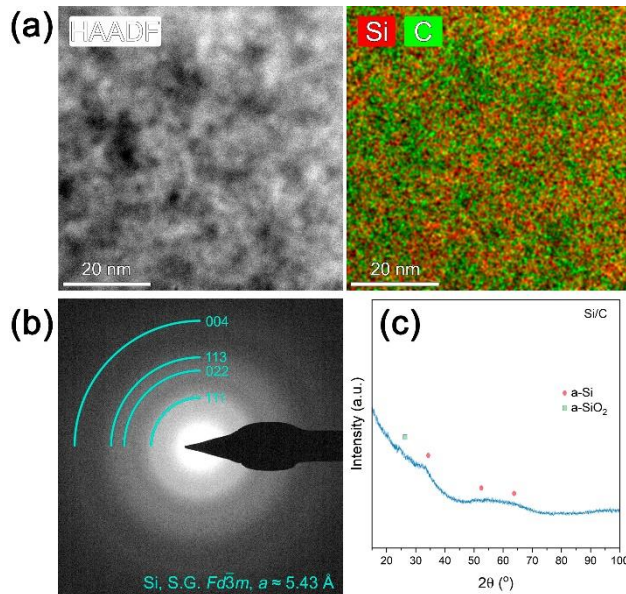


Fig. 2. Si/C composite material: (a) HAADF-STEM image and elemental map of Si-C, (b) SAED pattern, and (c) PXRD pattern.

As seen in Table 1, the Si/C sample demonstrates much superior electrochemical properties compared to the Mg-SiO_x. These include: (1) 62% higher delithiation capacity at low current and (2) higher ICE, both correlate with less oxidized Si particles, (3) much better rate capability, (4) higher Coulombic efficiency (CE) of the later cycles, and (5) greater cycle life, all three consistent with smaller Si particles and more uniform structure. Our experiments

demonstrate that the Si/C is a much better anode material overall.

However, the practical application of these materials is still limited because it seems difficult to achieve stable electrodes of sufficient thickness and areal capacity. Our attempts to prepare the electrodes of 2 mAh/cm² or higher resulted in the fast degradation of the cells.

Table 1. The electrochemical properties of Mg-SiO_x and Si/C, measured in full cells with NMC622 cathode and electrolyte containing 1M LiPF₆ in EC:DEC (1:1 vol.).

	Mg-SiO _x	Si/C
Areal capacity, 0.1C (mAh/cm ²)	1.04	1.35
Specific delithiation capacity, 0.1C (mAh/g)	593	963
Specific delithiation capacity, 0.5C (mAh/g)	490	899
ICE (%)	71.4	78.6
CE of 100 th cycle (%)	98.5	99.8
Capacity retention, C ₆ /C ₁₀₀ (%)	61.5	94.9

4. Conclusions

For the application in practical LIBs, the silicon anode material should possess sufficient cycling stability. A successful example of a structure that is stable toward reversible lithiation is Si nanoparticles embedded in an electrochemically inactive buffer matrix. This buffer matrix alleviates the severe stresses emerging from the changes in the silicon volume and prevents the aggregation of Si nanoparticles. Examples of the buffer media include carbon, SiO₂, and MgSiO₃. Both materials studied in our research have this complex structure design. As demonstrated in our study, the important factors to obtain a stable material include its high uniformity and ultrafine Si domains, preferably of a few nanometers because the nanocrystalline Si in a buffer matrix degrades more rapidly.

The cycling stability alone is not sufficient for the practical application of Si anode material. High ICE and good conductivity are also important. The latter determines the maximum areal capacity of the electrode. In our experiments, the electrodes with Si/C active material cycled well if the areal capacity did not exceed 1.4 mAh/cm². This is 3 times less than the value needed for the application of Si anode materials in high-capacity LIBs. For the anodes of practical LIBs, mixtures of Si materials with graphite are still preferred as active materials.

Acknowledgements

The research has been supported by the Russian Science Foundation, grant 23-73-30003.

References

- [1] T.M.M. Heenan, A. Jnawali, M.D.R. Kok, T.G. Tranter, C. Tan, A. Dimitrijevic, R. Jervis, D.J.L. Brett and P.R. Shearing. *J. Electrochem. Soc.* **167**(2020)140530.
- [2] K. Schulmeister, W. Mader. *J. Non-Cryst. Solids* **320**(2003)143.
- [3] J. Han, S. Jo, I. Na, S. Oh, Y. Jeon, J. Park, B. Koo, H. Hyun, S. Seo, D. Lee, H. Kim, J. Kim, J.-C. Lim, J. Lim. *ACS Appl. Mater. Interfaces* **13**(2021)52202.

Electron paramagnetic resonance of Fe-doped $\text{Na}_2\text{Ti}_6\text{O}_{13}$

Saritsky D.A.^{*}, Zheleznov V.V., Ziatdinov A.M.

Institute of Chemistry FEB RAS, 159, Pr-t 100-letiya Vladivostoka, Vladivostok, 690022, Russia

^{*}e-mail: denissaricki@mail.ru

Abstract. The structural features of iron-doped sodium hexatitanate ($\text{Na}_2\text{Ti}_6\text{O}_{13}$) were investigated using electron paramagnetic resonance (EPR). In the low-field region, the EPR spectrum of this compound exhibits features at g -factor values of ≈ 17 , ≈ 8.4 , ≈ 5.6 , and ≈ 4.3 . The spectral signals at $g \approx 4.3$ and $g \approx 5.6$ originate from Fe^{3+} centers in crystal fields with strong rhombic and strong axial distortions, respectively. Consideration of the dispersion of crystal field parameters across the Fe^{3+} ions allowed for the refinement of the D and λ value ranges for all low-field signals and the determination of the nature of the spectral features at $g \approx 8.4$ and ≈ 17 . The temperature dependence of the main signal at $g \approx 2$ indicates the presence of both paramagnetic and superparamagnetic resonance contributions. The paramagnetic component is attributed to Fe^{3+} ions substituting for matrix Ti^{4+} ions in a weakly distorted oxygen octahedron. The superparamagnetic resonance component may be associated with iron oxide clusters.

1. Introduction

In recent years, there has been a significant surge in interest in sodium-ion batteries due to their low cost and environmental safety [1]. Sodium hexatitanate ($\text{Na}_2\text{Ti}_6\text{O}_{13}$) has attracted considerable attention from researchers due to its framework structure, which facilitates rapid sodium ion diffusion [2]. Its high cycling stability makes it a promising material for application in sodium-ion batteries [3]. However, a key limitation is its low capacity [3]. The pursuit of methods to enhance this capacity is a critical research objective. One effective approach to modify material properties is through doping. In this study, electron paramagnetic resonance (EPR) spectroscopy was employed to investigate structural aspects of iron-doped sodium hexatitanate.

2. Experiment

EPR spectra of iron-doped sodium hexatitanate powders were recorded using a JES-X330 spectrometer (JEOL, Japan) in the X-band frequency range. The power of the microwave field during the recording of the spectra was 2.00 mW, and the static magnetic field (B) was swept from 0 to 800 mT, modulated at a frequency of 100 kHz. Temperature-dependent measurements were conducted in a continuous flow of gaseous nitrogen using an ES-13060 DVT5 variable temperature controller (JEOL, Japan).

For the analysis of the experimental spectra, custom MATLAB programs were developed, utilizing functions from the EasySpin software package for EPR spectrum simulation and analysis.

Fig. 1 illustrates the electron paramagnetic resonance (EPR) spectra of the iron-doped $\text{Na}_2\text{Ti}_6\text{O}_{13}$ sample at three distinct temperatures. At each temperature, a broad resonance is observed, characterized by a g -factor of ≈ 2.05 at -160°C . Its shape and position are temperature-dependent. Specifically, as the temperature increases to 20°C , the g -factor value rises to 2.25. The intensity of this resonance remains relatively constant with temperature variation. In the low-field region of the spectrum, narrower features are observed at $g \approx 17$, ≈ 8.4 , ≈ 5.6 , and ≈ 4.3 . In the literature [4], the feature at $g \approx 4.3$ is attributed to the resonance of the high-spin configuration of the Fe^{3+} ion in a crystal field with strong rhombic distortion. The feature at $g \approx 5.6$ is characteristic of ions residing in crystal fields with a strong axial component [5]. However, the origin of

the maxima at $g \approx 8.4$ and ≈ 17 remains a subject of debate in the literature.

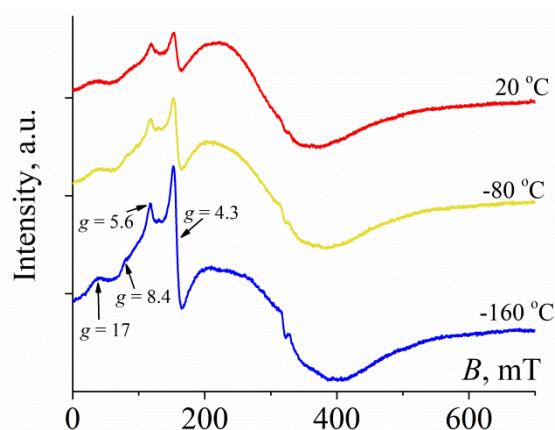


Fig. 1. EPR spectra of iron-doped $\text{Na}_2\text{Ti}_6\text{O}_{13}$ powder at various temperatures.

3. Results and discussions

Superparamagnetic resonance is characterized by temperature-dependent variations in its shape, intensity, and g -factor value. Specifically, a shift of the superparamagnetic resonance towards higher fields is expected with decreasing temperature, accompanied by a reduction in its intensity [6]. The observed behavior of the main resonance in $\text{Na}_2\text{Ti}_6\text{O}_{13}:\text{Fe}^{3+}$ can be attributed to its composite nature, arising from the superposition of two distinct resonances: paramagnetic and superparamagnetic. The superparamagnetic resonance may originate from iron oxide clusters or nanoparticles, while the paramagnetic resonance is associated with isolated Fe^{3+} ions subjected to a weakly distorted octahedral crystal field, such as in the substitution site of the matrix Ti^{4+} ion.

The low-field maxima in the spectrum are evidently generated by several groups of individual Fe^{3+} ions residing in strongly distorted crystal fields. The contour shapes of these maxima do not correspond to isolated Fe^{3+} centers, suggesting the presence of a distribution of crystal field parameters across these ions.

For the theoretical analysis of the EPR spectra of iron-doped $\text{Na}_2\text{Ti}_6\text{O}_{13}$ powders, a spin Hamiltonian was utilized:

$$\hat{H} = g\beta(\vec{B}, \vec{S}) + D\left(\hat{S}_z^2 - \frac{S(S+1)}{3} + \lambda(\hat{S}_x^2 - \hat{S}_y^2)\right),$$

where β is the Bohr magneton, \vec{B} is the applied magnetic field, g is the spectroscopic splitting factor, \vec{S} is the spin angular momentum vector of the system, \hat{S}_x , \hat{S}_y , and \hat{S}_z are the spin angular momentum operators along the x , y , and z axes, respectively, S is the spin quantum number of the electron system, D is the axial component of the crystal field, $\lambda = E/D$, where E is the rhombic component of the crystal field.

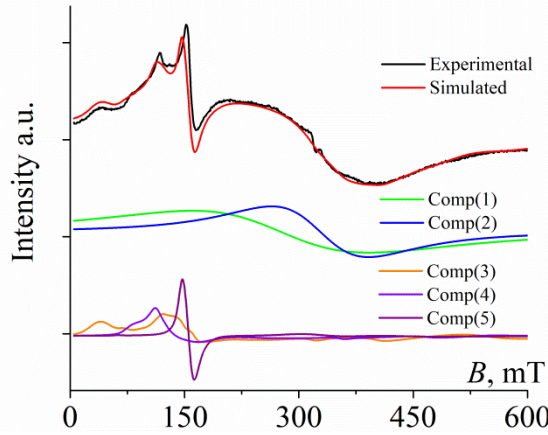


Fig. 2. Experimental (black) and theoretical (red) EPR spectra of iron-doped $\text{Na}_2\text{Ti}_6\text{O}_{13}$ powder. Comp(i) ($i=1-5$) - components of the theoretical spectrum. $T = -160^\circ\text{C}$.

To account for the dispersion of crystal field parameters during the simulation of the low-field signals, a double normal distribution was employed for the D and λ parameters, as follows:

$$w(D, \lambda) = \frac{1}{2\pi\sigma_D\sigma_\lambda} e^{-\left[\frac{(D-D_0)^2}{2\sigma_D^2} + \frac{(\lambda-\lambda_0)^2}{2\sigma_\lambda^2}\right]},$$

where σ_D and σ_λ are the standard deviations of parameters D and λ , D_0 and λ_0 – are the mean values of parameters D and λ in the distribution.

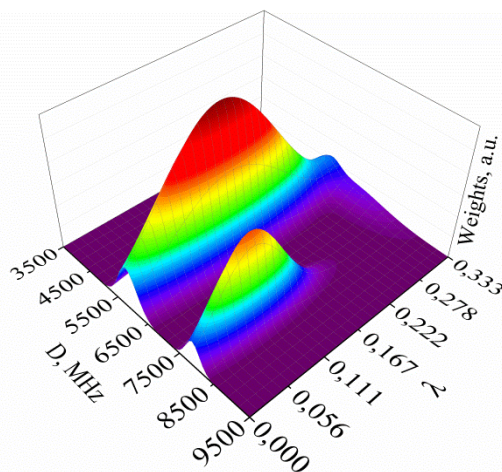


Fig. 3. Distributions of the fine structure parameters D and λ of the $\text{Na}_2\text{Ti}_6\text{O}_{13}$ EPR spectrum, obtained from the fitting of the low-field spectral components.

Since the main maxima in the low-field region at $g \approx 17$, ≈ 5.6 , and ≈ 4.3 correspond to different types of iron centers, three distinct lines were selected for their simulation, each with its own set of parameters and their

distribution. To describe the main resonance, two broad lines of Lorentzian shape were used. The result of the fitting is shown in Fig. 2. The distribution of the D and λ parameters is presented in Fig. 3. The distribution parameters for the simulated EPR spectra 3, 4 and 5 are shown in table 1. Analysis of the temperature dependence of the main resonance component parameters confirmed the superparamagnetic nature of one of them.

Table 1. Distribution parameters of low-field simulated EPR spectra

Comp(i)	D_0 , (MHz)	λ_0	σ_D , (MHz)	σ_λ
3	5700	0.1	300	0.09
4	7900	0.08	200	0.05
5	6500	0.33	1000	0.02

4. Conclusions

The EPR data of $\text{Na}_2\text{Ti}_6\text{O}_{13}:\text{Fe}^{3+}$ indicate a heterogeneous crystal structure. The most intense high-field resonance of Fe^{3+} with $g \approx 2$ represents a superposition of two signals, attributed to different types of Fe^{3+} centers. One of these centers corresponds to superparamagnetic particles, while the other corresponds to Fe^{3+} ions substituting for the matrix Ti^{4+} ions in a weakly distorted oxygen octahedron. The low-field spectral maxima at $g \approx 4.3$ and $g \approx 5.6$ originate from Fe^{3+} centers in crystal fields with strong rhombic and strong axial distortions, respectively. Accounting for the dispersion of crystal field parameters across the Fe^{3+} ions allowed for the refinement of the D and λ value ranges for all low-field maxima and the determination of the nature of the spectral features at $g \approx 8.4$.

Acknowledgements

This work was carried out within the framework of the state assignment to the Institute of Chemistry FEB RAS (project FWFN-2025-0004).

References

- [1] A. M. Skundin, T. L. Kulova, A. B. Yaroslavl'tsev. Russ. J. Electrochem. **54**(2018)113.
- [2] D. M. De Carolis, D. Vrankovic, S. A. Kiefer, E. Bruder, M.T. Durrschnabel, M. T. Molina-Luna, M. Graczyk-Zajac, R. Riedel. Energy Technology **9**(2020)2000856.
- [3] Z. Wang, R. Zhang, L. Chen, L. Cao, X. Guo, Z. Wu, B. Liang, D. Luo. J. Electroanal. Chem. **972**(2024)118621
- [4] T. Castner, G. S. Newell, W. C. Holton, C. P. Slichter. J. Chem. Phys. **32**(1960)668.
- [5] A. A. Jahagirdar, N. Dhananjaya, D. L. Monika, C. R. Kesavulu, H. Nagabhushana, S. C. Sharma, B. M. Nagabhushana, C. Shivakumara, J. L. Rao, R. P. S. Chakradhar. Spectrochim. Acta A **104**(2013)512.
- [6] R. Berger, J.-C. Bissey, J. Kliava, H. Daubric, C. Estournes. J. Magn. Magn. Mat. **234**(2001)535.

Self-cleaning SERS substrates based on TiO₂ nanopillars decorated with Ag and Cu nanoparticles

Volkova L.S.^{*1,2}, Grishin T.S.^{1,2}, Dudin A.A.¹, Nazarkina Yu.V.², Dubkov S.V.², Gromov D.G.²

¹ Institute of Nanotechnology of Microelectronics of RAS, 32A Leninsky Prospekt, Moscow 119334, Russia

² National Research University of Electronic Technology - MIET, 1 Shokin Square, Zelenograd, Moscow 124498, Russia

*e-mail: Lidiya.Volkova.96@outlook.com

Abstract. We report highly sensitive, self-cleaning SERS platforms based on vertically oriented TiO₂ nanopillars decorated with Ag and Cu nanoparticles. The UV-photocatalytic activity of TiO₂ enables the degradation of residual organic analytes and thus permits repeated usage of the substrate. Ag nanoparticle coatings deliver strong Raman signal enhancement in the blue-green visible range, while Cu broadens the detection window into the red/NIR region. SERS measurements with malachite green as an analyte show enhancement factors (EF) up to 10⁶ at concentrations down to 10⁻⁸ M. After measurements, the substrate can be cleaned of residual analyte concentrations through photocatalysis and reused without loss of sensitivity.

1. Introduction

Surface-Enhanced Raman Scattering (SERS) is one of the most sensitive analytical techniques, capable of analyte detecting at concentrations down to the single-molecule level. Conventional SERS substrates utilize arrays of plasmonic nanoparticles that create localized electromagnetic “hot spots” on their surfaces, resulting in substantial amplification of Raman signals [1]. Such substrates are effectively single-use because trace amounts of analyte remain detectable due to sensitivity of the method.

A promising route to reusability involves coupling plasmonic nanoparticles with a photocatalyst such as TiO₂, which degrades organics under UV irradiation and effectively “resets” the substrate. Vertically oriented TiO₂ nanopillars decorated with Ag and Cu nanoparticles can be used as such a hybrid substrate. This combination leads to a synergy between two key attributes. First, the high aspect ratio TiO₂ nanopillars provide a significantly enlarged surface area for analyte adsorption and for the dense deposition of metal nanoparticles, leading to abundant hot spots and enhanced SERS signals. Second, the plasmonic metal nanoparticles reinforce the photocatalytic activity of TiO₂ by promoting electron–hole separation and enhancing light absorption through localized surface plasmon resonance. Under UV illumination, TiO₂ photocatalytically degrades adsorbed organic residues [2], thus regenerating the substrate. This dual functionality provides strong SERS enhancement and UV-driven self-cleaning, which paves the way for robust, reusable SERS platforms.

2. Experiment

Vertically oriented TiO₂ nanopillars were obtained by a two-stage anodization procedure applied to TiN/Al bilayers (300 nm / 1000 nm). In the first stage, the aluminum layer was oxidized to create a nanoporous Al₂O₃ template. In the second stage, the underlying TiN layer was anodized through this Al₂O₃ template, producing TiO₂ nanopillars with an average diameter of about 25 nm, a center-to-center spacing near 65 nm, and a typical height of 200 nm. These high-aspect-ratio structures offer a large surface area for subsequent decoration with plasmonic metals.

Arrays of TiO₂ nanopillars were decorated with plasmonic nanoparticles by depositing thin layers of Cu or Ag by magnetron sputtering. For Cu, process was followed

by mild annealing at 300 °C, inducing dewetting into discrete nanoparticles that predominantly formed at the nanopillar tops. In the case of Ag, no additional thermal treatment was applied, since the deposited thin layer already formed a nanoparticle array covering the nanopillars. Both metals provided dense coverage critical for achieving strong near-field enhancements in SERS.

3. Results and discussions

SEM and TEM analyses confirmed that two-stage anodization produces uniform arrays of vertically oriented TiO₂ nanopillars. These high-aspect-ratio structures significantly increase the active surface area available for analyte adsorption, which is critical for achieving strong SERS signals. Selected-area electron diffraction (SAED) patterns indicate that the as-grown pillars are primarily amorphous. Mild annealing at 300 °C leads to weak crystallization, whereas higher temperatures (500 °C and 800 °C) induce predominantly anatase or mixed anatase–rutile phases, both exhibiting notable photocatalytic activity [3].

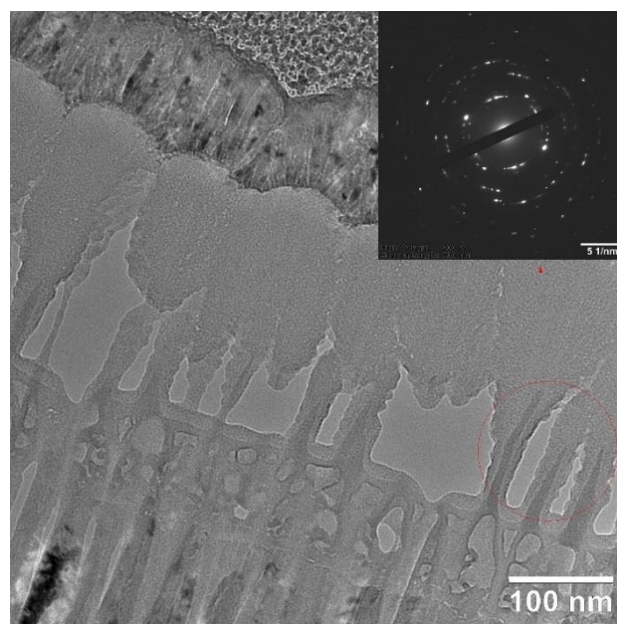


Fig. 1. TEM image of cross-sectional lamella of the TiO₂ nanopillar array after annealing at 800 °C. Inset shows SAED pattern representing polycrystalline mixture of rutile and anatase phases.

SEM images revealed that sputtered Cu films undergo thermal dewetting at 300 °C, yielding discrete, spherical nanoparticles primarily located at the tops of the TiO₂ nanopillars.

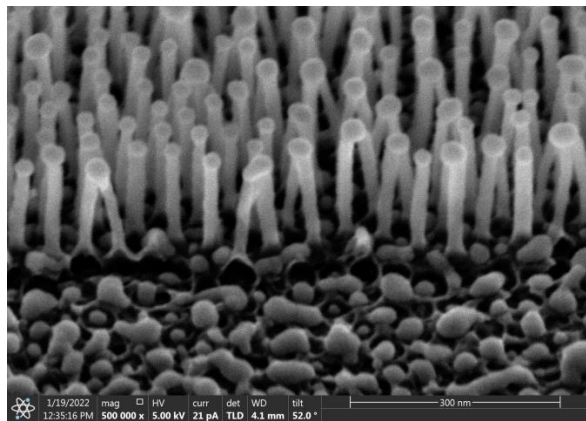


Fig. 2. SEM image of Cu-decorated TiO₂ nanopillars showing spherical NP formation after annealing at 300 °C.

In contrast, Ag naturally formed dense nanoparticle clusters upon deposition without requiring further annealing. This three-dimensional coverage of plasmonic metals created abundant local “hot spots” for Raman signal amplification, significantly enhancing the SERS response on both Cu- and Ag-coated pillars.

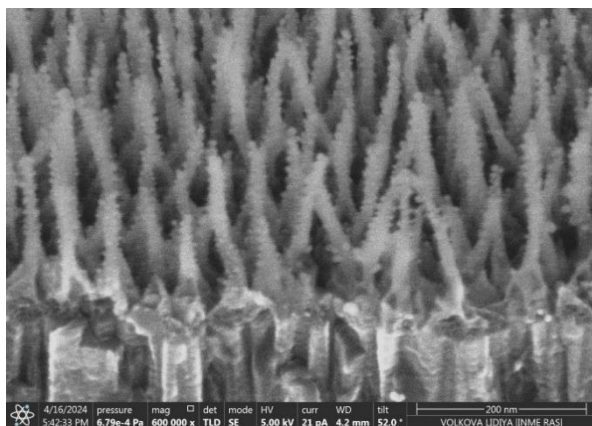


Fig. 3 SEM image of Ag-decorated TiO₂ nanopillars with dense nanoparticle coverage.

SERS measurements on malachite green (MG) solutions at concentrations of 10⁻⁶ – 10⁻⁸ M revealed substantial enhancement relative to a 10⁻² M reference on plain glass. Under 532 nm excitation, Ag-decorated substrates achieved enhancement factors (EF) up to 10⁶ at 10⁻⁸ M, whereas Cu-coated samples showed somewhat lower EFs at 532 nm yet comparable or stronger signals under 633 nm excitation. The dual decoration of Ag and Cu broadened the operational window, demonstrating consistent signal intensity across visible region.

Beyond high sensitivity, another major advantage of these hybrid platforms is their UV-driven self-cleaning behavior. TiO₂ photocatalysis was demonstrated by rinsing used substrates and then exposing them to UV for 30 min. Subsequent Raman scans revealed a complete disappearance of MG peaks, confirming that residual analytes had been effectively oxidized. This is critical for applications demanding repeated sensing cycles. Conventional SERS substrates often become unusable after a single measurement, because trace analytes remain

detectable on their surfaces even after rinsing. Here, TiO₂ nanopillars eliminate that limitation by offering a “reset” mechanism via photocatalysis.

Overall, the synergy between the high-aspect-ratio TiO₂ nanopillars and the plasmonic nanoparticles ensures both enhanced Raman scattering and UV-induced degradation of adsorbed contaminants. The 3D geometry greatly amplifies the density of hot spots, boosting the SERS signal, while the plasmonic metals also facilitate light absorption and electron–hole separation, further accelerating the photocatalysis.

4. Conclusions

A reusable SERS platform was successfully developed by integrating high-aspect-ratio TiO₂ nanopillars with plasmonic Ag and Cu nanoparticles. The 3D nanopillar morphology, coupled with the localized surface plasmon resonance of the metal nanoparticles, provides strong Raman signal enhancements – reaching up to 10⁶ for malachite green at 10⁻⁸ M. At the same time, the photocatalytic properties of TiO₂ enable UV-driven degradation of organic residues, allowing repeated usage without signal carryover. This dual functionality – a high SERS response combined with self-cleaning capability – represents a step toward practical sensing applications that require both extreme sensitivity and robust, long-term operability.

Acknowledgements

The specimens were obtained in the laboratory “Photonic Sensorics and Plasmonic Materials” of the National Research University MIET under State Assignment FSMR-2024–0012.

References

- [1] Dubkov, S. Et al. IOP Conference Series: Materials Science and Engineering **1093**(2021)1.
- [2] R. Ratshiedana et al. Materials Today Communications **41**(2024).
- [3] Y. Qu et al. ChemPlusChem **79**(2017)7.

Raman scattering of sp^2 -hybridized carbon clusters in graphite oxide

Ziatdinov A.M.*

Institute of Chemistry of FEB RAS, 159, Pr-t 100-letiya Vladivostoka, Vladivostok 690022, Russia

*e-mail: ziatdinov@ich.dvo.ru

Abstract. The first-order (G , D and D' bands) and second-order ($2D$, $G+D$ and $2D'$ bands) Raman spectra of a graphite oxide (GO) film are analyzed. The presence of an analogue of the graphite band G in the spectrum of GO film indicates the presence of, at least, clusters of non-oxidized sp^2 -hybridized carbon atoms (“ sp^2 -islands”). The presence of D band in the GO spectrum confirms the presence of oligomers of six-membered aromatic rings in it. The ability of describing the D , D' , $2D$ and $2D'$ bands with separate Lorentzians favors a predominantly turbostratic structure of the domains consisting of several non-oxidized regions. The analysis of the intensity ratios for different bands indicates the presence of many fractures (cracks) at the boundaries of the “ sp^2 -islands”, some of which have zigzag-shaped sections. The presence of the $G+D$ overtone indicates a large size of the k -space region, determined by the quantum uncertainty of the wave vector magnitude for the “ sp^2 -islands”.

1. Introduction

Raman spectra of carbon materials are very sensitive to their structural organization [1]. This paper presents new data on the structure of graphite oxide (GO) films, obtained with Raman spectroscopy. The advantages and disadvantages of known methods for acquiring information on the structure of GO from the Raman spectra are also discussed.

2. Experiment

The first-order Raman spectrum of the GO film is observed in the range from 800 to 2100 cm^{-1} and contains two intense, partially resolved peaks (Fig. 1). It is well approximated by the sum of the Lorentzians: G , D and D' (Fig. 1). Several additional low-intensity partially resolved peaks, corresponding to the overtones of the main spectrum, are observed at Raman shift values from 2100 to 3600 cm^{-1} (Fig. 2). This spectrum is well approximated by the sum of Lorentzians $2D$, ($D+G$) and $2G$ (Fig. 2).

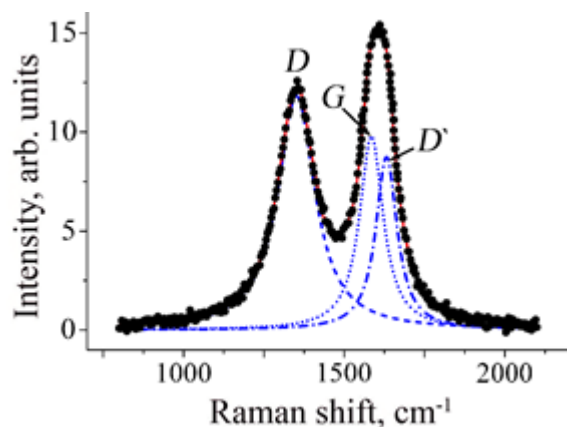


Fig. 1. Raman spectrum of the GO film (dots) and its decomposition into Lorentzians G , D and D' . Solid line corresponds to the sums of all components of the spectral decomposition.

For the GO film the full width at half maximum and the Raman shift of the single-phonon band G are equal to 89 and 1585 cm^{-1} , respectively (Fig. 1). The value of the Raman shift allows to consider this band as an analogue of the band of the same name in crystalline graphite [2]. Its presence in the spectrum of GO film indicates the presence

of clusters of non-oxidized sp^2 -hybridized carbon atoms. The noticeable differences in the width and Raman shift of the G band for the GO film and those for crystalline graphite can be accounted for by the small length of the layer coherence of the structure (L_a) in the former. For example, in the Raman spectrum of activated carbon fibers, whose structural blocks are nanographites with $L_a \sim 3$ nm, the G band, at the same laser excitation energy as in the experiments under consideration, is observed at ~ 1590 cm^{-1} and has a full width at half-height of ~ 82 cm^{-1} [3].

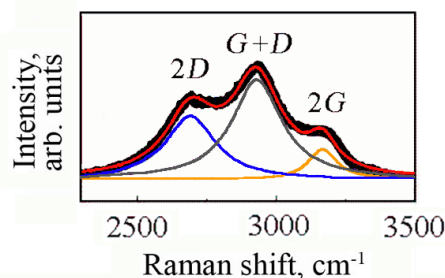


Fig. 2. Raman spectrum overtones of the GO film (dots) and its decomposition into Lorentzians $2D$, $D+G$ and $2G$. Red solid line corresponds to the sums of all components of the spectral decomposition.

3. Results and discussions

The presence of intense D band in the Raman spectrum of the GO film indicates, on the one hand, a high content of defects in the samples, and on the other hand, the presence of oligomers of six-membered aromatic carbon rings in them. In other words, in GO films there are non-oxidized regions (“ sp^2 -islands”) of the carbon framework (Fig. 3), adjacent to structural defects, which may also be the boundaries of these regions. The ability of describing the D and D' bands by separate Lorentzians favors a predominantly turbostratic structure of the packs (domains) consisting of several non-oxidized regions.

In the Raman spectra of the GO film under consideration the peak intensity ratio $I_D/I_{D'} < 3.5$. Consequently, the “defective” bands D and D' are activated predominantly near the boundaries of non-oxidized regions of the carbon framework [4]. Therefore, in them the average length of in-layer structural coherence can be identified with the average lateral size of the

“sp²-islands”, i.e. with L_a . Since the phase boundaries of “sp²-islands” in adjacent carbon layers are located randomly relative to each other, the probability of the formation of loop-shaped configurations of σ -bonds between them is, obviously, insignificant. This circumstance suggests that the reason for the small values of $I_D/I_{D'}$ (~ 1.2) in the Raman spectrum of the GO film is not these edge bonds. A more plausible assumption is that it is caused by the presence of numerous fractures (cracks) on the boundaries of the “sp²-islands”, some of which have zigzag shape or contain such regions. It has been shown experimentally [5] that such edges do not participate in the activation of the D band, but activate only the D' band. In the context of the problem under discussion, it is appropriate to note that in the activated carbon fibers, whose structural blocks are nanographites, the value of $I_D/I_{D'}$ is also small (~ 1.6) [3]. According to EPR and magnetic susceptibility data the structural elements of these materials exhibit anomalously high values of the density of states at the Fermi level, which is a characteristic feature of zigzag edges of honeycomb carbon structures [6].

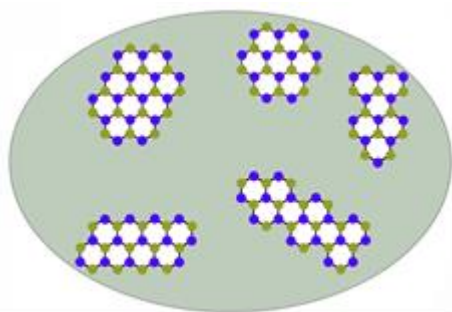


Fig. 3. Schematic representation of “sp²-islands” in the GO film. The dots and gray background correspond to carbon atoms in the sp²-hybridization state and to the regions of matrix (oxidized) sp³-carbon, respectively.

The significant widths of the single-phonon bands G , D and D' in the Raman spectrum of the GO film indicate the small lateral sizes of the “sp²-islands”. Indeed, at small coherence lengths, excitation light is scattered by phonons with slightly different energies due to its dispersion in the k -space region, determined by the quantum uncertainty of the wave vector [7]. The smaller the size of the sample, the larger the size of the light dispersion region in k -space, and, therefore, the width of the single-phonon bands in the Raman spectrum becomes larger.

In the studied GO film the ratio of integrated intensities $A_D/(A_G + A_{D'}) = 0.9$. According to [8], it corresponds to $L_a \sim 18.3$ nm, and according to [9], this value of the ratio corresponds to $L_a \sim 1$ nm. The value of L_a , determined from the full width at half maximum of the G band, is equal to 4.1 nm. Of all the presented values of L_a , only the one determined by the formula from [8] is acceptably close to the value of $L_a \sim 17.2$ nm found from the X-ray diffraction data of GO films [10]. Nevertheless, all L_a values found are in the nanometer range.

The spectral positions of the $2D$ and $2G$ overtones correspond to approximately doubled Raman shifts of the D and G bands (Figs. 1 and 2). Similar overtones are observed in the Raman spectra of many honeycomb sp²-carbon structures [1]. They do not require structural defects to be activated. For graphene and turbostratic graphites they have no inner structure [9] and are well approximated by

Lorentzians. Therefore, the ability of a good approximation of $2D$ and $2G$ overtones using individual Lorentzians to describe them (Fig. 2) can be considered as an argument in favor of the predominantly turbostratic structure of non-oxidized GO domains. Note that this explanation of the homogeneity of the $2D$ and $2G$ overtones coincides with the previously proposed respective explanation for the D and D' bands. The reasons for the large widths of the overtones under consideration are the same as the respective reasons for the bands of the main spectrum of the GO.

In small-sized samples some new phenomena are possible when the overtone Raman spectrum is activated. For example, whereas in a large sample the requirement of conservation of the wave vector excludes the possibility of light scattering at a frequency equal to the sum of the frequencies of two maxima of the density of vibrational states, in a small sample such scattering can be realized due to the large size of the k -space region determined by the quantum uncertainty of the magnitude of the wave vector. This can account for the presence of the $D+G$ overtone in the GO spectrum, whose position corresponds approximately to the sum of the Raman shifts of the D and G bands.

4. Conclusions

Thus, Raman spectroscopy of graphite oxide indicates the presence of clusters of non-oxidized sp²-hybridized carbon (“sp²-islands”) in it. At the boundaries of these areas there are many fractures (cracks), some of which have a zigzag shape. Domains consisting of several “sp²-islands” have a predominantly turbostratic structure. The presence of the $D+G$ overtone in the second-order Raman spectrum indicates the large dimensions of the k -space region determined by the quantum uncertainty of the magnitude of the wave vector for small-sized “sp²-islands”.

Acknowledgements

The work was carried out within the framework of the State Assignment for the Institute of Chemistry of the Far Eastern Branch of the Russian Academy of Sciences (project FWFN-2025-0005).

References

- [1] A. Jorio, M.S. Dresselhaus, R. Saito, G. Dresselhaus. Raman spectroscopy in graphene related systems. Weinheim, Germany: Wiley-VCH, 2011. 368 pp.
- [2] F. Tuinstra, J.J. Koenig. Chem. Phys. **53**(1970)1126.
- [3] A.M. Ziatdinov, N.S. Saenko, P.G. Skrylnik. Russ. Chem. Bull. **66**(2017)837.
- [4] A. Eckmann, A. Felten, A. Mishchenko et al. Nano Lett. **12**(2012)3925.
- [5] L.G. Cancado, M.A. Pimenta, B.R.A. Neves et al. Phys. Rev. Lett. **93**(2004)247401.
- [6] K. Nakada, M. Fujita, G. Dresselhaus, M.S. Dresselhaus. Phys. Rev. **B 54**(1996)17954.
- [7] R.J. Nemanich, S.A. Solin. Phys. Rev. **B 20**(1979)392.
- [8] L.G. Cancado, K. Takai, T. Enoki et al. Appl. Phys. Lett. **88**(2006)163106.
- [9] A.C. Ferrari. Solid St. Commun. **143**(2007)47.
- [10] A.M. Ziatdinov, N.S. Saenko, P.G. Skrylnik. Russ. J. Inorg. Chem. **65**(2020)131.

Magneto-optical ellipsometry for experimental studies of functional thin films of atomic-layered carbon-based MAX phases

Maximova O.A.^{*,1}, Lyaschenko S.A.¹, Yakovlev I.A.¹, Shevtsov D.V.¹, Tarasov A.S.¹, Varnakov S.N.^{1,2}, Ovchinnikov S.G.¹

¹ Kirensky Institute of Physics, Federal Research Center KSC Siberian Branch Russian Academy of Sciences, bld. 38, 50 Akademgorodok, Krasnoyarsk 660036, Russia

² Federal Research Center KSC Siberian Branch Russian Academy of Sciences, bld. 50 Akademgorodok, Krasnoyarsk 660036, Russia

*e-mail: maximo.a@mail.ru

Abstract. $M_{n+1}AX_n$ -materials are promising anisotropic systems, and algorithms for their synthesis and study are of scientific interest. In this paper, we propose to use the magneto-optical ellipsometry technique to obtain information about their optical and magneto-optical properties.

1. Introduction

Nowadays, there is an urgent need to reduce the consumption of minerals and energy worldwide. The development of technologies for synthesis of anisotropic multilayer coatings and thin films, in which the layered structure is thermodynamically stable, can help reduce the costs of producing functional coatings, solar batteries, and nanoelectronic devices. One example of such anisotropic multilayer systems are hexagonal structures $M_{n+1}AX_n$, where n takes integer values 1, 2, 3 or 4, M is a transition metal, A is an element from group 13 or 14, X is carbon or nitrogen [1-3]. The condition of thermodynamic stability of such multilayer systems is the alternation of types of chemical bonds between the atomic sublayers $M-X-M$ and $M-A-M$. Various properties of these structures, including optical, magnetic and magneto-optical, are of interest. The problem of non-destructive experimental analysis of the listed physical properties can be solved using the magneto-optical ellipsometry technique, which combines the classical ellipsometry and measuring the magneto-optical Kerr effect [4, 5].

2. Experiment and discussion

The key difficulty in applying the proposed technique is the need to interpret the results for a limited number of measured parameters. In ellipsometry, only two parameters ψ and Δ are measured. These data are used to obtain the values of the diagonal components of the tensor of permittivity, which are responsible for the optical properties of the material. In magneto-optical ellipsometry, an external magnetic field is applied to the sample, so, two magneto-ellipsometric angles $\delta\psi$ and $\delta\Delta$ are added to the measured values, allowing one to analyze the non-diagonal components of the permittivity tensor, and, therefore, to obtain the values of the magneto-optical parameter Q , and, accordingly, to analyze the magneto-optical properties [6].

There are many scientific groups in the world [7] working on the development of the method, but not every algorithm can be applied to a specific experimental setup without its technological re-equipment. Accordingly, in order to process the data obtained on the UHV ellipsometric complex [4], we have been developing the methodology of the magneto-optical ellipsometry, which resulted in the

new algorithms for processing data from anisotropic structures, allowing calculations to be carried out without additional measurements and without upgrading the setup.

The first algorithm is a solution to the basic equation of magneto-optical ellipsometry under the assumption that the magnetic contribution is of such a magnitude that $Q \ll I$, which allows calculations to be carried out analytically. The second algorithm deals with data from films with the thickness that significantly exceeds the light penetration depth, which also significantly simplifies calculations, though already requires the use of numerical methods. The third algorithm allows calculating thin anisotropic films with magnetic properties, taking into account the optical response from the substrate.

3. Conclusions

Thus, we have carried out serious methodological work aimed at ensuring the possibility of non-destructive analysis of optical and magneto-optical properties of anisotropic structures such as functional thin films of atomic-layered carbon-based MAX phases.

Acknowledgements

The research was supported by the grant of the Russian Science Foundation No 25-12-20012, <https://rscf.ru/project/25-12-20012/>, grant of the Krasnoyarsk Regional Science Foundation.

References

- [1] Barsoum M.W., Radovic M., Annu. Rev. Mater. Res. **41** (2011) 195.
- [2] Barsoum M.W., in *Ceramics Science and Technology*, ed. R. Riedel and I.-W. Chen, Wiley-VCH Verlag GmbH & Co. KGaA, Weinheim, Germany, **2** (2010) 299.
- [3] Sun Z. M., Int. Mater. Rev. **56** (2011) 143.
- [4] Shevtsov D.V., Lyaschenko S.A., Varnakov S.N. *Instruments and Experimental Techniques* **60** (2017) 759.
- [5] Maximova O. A., Lyaschenko S. A., Varnakov S. N., et al. *Physics of Metals and Metallography* **124** (2023) 1654.
- [6] Maximova O. A., Lyashchenko S. A., Tarasov I. A., et al. *Phys. Solid State*. **63**. Is. 10 (2021) 1485.
- [7] Fujiwara H., *Spectroscopic Ellipsometry. Principles and Applications*. Wiley, Chichester, UK (2007) 369pp.

VI. Biomaterials and biosensors on their base, gas sensors

Aptamer-conjugated biosensors

Kichkailo A.S.^{*1,2}, Zamay T.N.^{1,2}, Zamay G.S.^{1,2}, Moryachkov R.V.¹, Shabalina A.V.^{3,4}, Lapin I.N.⁴, Svetlichnyi V.A.⁴, Zamay S.S.¹

¹ Federal Research Center "Krasnoyarsk Science Center of SB RAS," 50 Akademgorodok, Krasnoyarsk 660036, Russia

² Prof. V.F. Voyno-Yasenetsky Krasnoyarsk State Medical University, 1 Partizana Zheleznyaka, Krasnoyarsk 660022, Russia

³ Prokhorov General Physics Institute RAS, 38 Vavilova, Moscow 119333, Russia

⁴ Tomsk State University, 36 Lenina, 634050 Tomsk, Russia

*e-mail: annazamay@yandex.ru

Abstract. Aptamers are promising biomolecular tools for development of the high-effective biosensors due to their ability to bind with high specificity and affinity to the targets such as proteins, viruses, bacteria and even cells and tissues. Widely developed methods of chemical modification of nucleic acids allow the construction of various types of conjugates with aptamers, using them as active molecules that recognize molecular targets. This paper presents various types of surface modification with DNA aptamers, as well as examples of biosensors that use aptamers as conjugates that react to the desired analytes. Examples of the use of such biosensors in the diagnostics of socially significant diseases are given.

1. Introduction

Aptamers are single-stranded short DNA or RNA oligonucleotides (10-100 bases), generated from the ssDNA libraries using the systematic evolution of ligands by exponential enrichment (SELEX). Aptamers can be used as independent agents for targeted drug delivery, as they have a unique spatial structure that ensures their high affinity for the molecular targets for which they were selected.

2. Biosensors based on immobilized DNA aptamers for detection of bacteria, viruses and tumor cells

One of the main advantages of aptamers is their ability to distinguish between microbial and viral strains and target cells without prior knowledge of membrane-associated antigenic determinants or molecular biomarkers of a particular microorganism. One of the most promising methods for identifying pathogens using aptamers is an electrochemical biosensor. An electrochemical biosensor is a device that combines an electrochemical transduction unit and a detector, where aptamers are a recognition element. Work has been carried out on the development and application of electrochemical sensors based on DNA aptamers for the detection of circulating tumor cells, pathogens of microbial and viral origin, assessment of the viability of microorganisms, bacterial typing, identification of epitope-specific aptamers, assessment of the degree of protection of oncolytic viruses by aptamers from neutralizing antibodies for therapeutic purposes.

3. Assessing the viability of microorganisms and viruses using aptasensors

Standard methods for assessing the number of viable microorganisms (bacteria and viruses), such as culturing in nutrient media, are time-consuming and require specially equipped rooms with a high degree of operator protection. The most popular methods for assessing the viability of bacteria are based on counting colony-forming units. For viruses, counting the number of foci of infection in cell cultures is used. In addition, methods for detecting prokaryotic mRNA are used, ultra-sensitive radiofrequency sensors. However, further work is required to improve the accuracy of data measurement. Electrochemical detection methods have a number of advantages, such as rapid

response, ease of measurement, and inexpensive miniature commercial detectors.

4. Electrochemical aptasensor for lung cancer-related protein detection in crude blood plasma samples

The development of an aptamer-based electrochemical sensor for lung cancer detection is presented in this part. A highly specific DNA-aptamer, selected to postoperative lung cancer tissues was immobilized onto a gold microelectrode and electrochemical measurements were performed in a solution containing the redox marker ferrocyanide/ferricyanide. The aptamer protein targets were harvested from blood plasma of lung cancer patients by using streptavidin paramagnetic beads and square wave voltammetry of the samples was performed at various concentrations. In order to enhance the sensitivity of the aptasensor, silica-coated iron oxide magnetic beads grafted with hydrophobic C8 and C4 alkyl groups were used in a sandwich detection approach. Addition of hydrophobic beads increased the detection limit by 100 times. The detection limit of the aptasensor was enhanced by the beads. The formation of the aptamer – protein – bead sandwich on the electrode surface was visualized by electron microscopy. As a result, the electrochemical aptasensor was able to detect cancer-related targets in crude blood plasma of lung cancer patients [1].

5. Detection of circulating tumor cells in the blood of lung cancer patients using DNA aptamers

Lung cancer (LC) is one of the most common oncological diseases, with mortality rates reaching a quarter among all deaths from malignant neoplasms. Most patients are diagnosed at stage IV of the disease, when the chances of successful treatment are minimal. Standard methods of LC diagnostics are expensive, labor-intensive, and highly invasive in the case of taking biopsy material. In this regard, attention in oncology is focused on liquid biopsy, based on taking blood samples to identify circulating tumor cells (CTCs) that enter the bloodstream during the development of a malignant tumor.

A method for isolating and identifying CTCs in the peripheral blood of LC patients using DNA aptamers has been developed.

Magnetic particles decorated with gold and thiolated aptamers specific to lung cancer cells were used to isolate proteins. A hybrid of a thiol primer and a non-specific DNA sequence consisting of repeats of two nucleotides AG was used as a control. Mass spectrometric analysis, determination of the number of CTCs after triple staining, and fluorescence microscopy for visualization of CTCs were performed.

As a result, probable protein targets of aptamers were determined, using which CTCs were isolated from the blood of LC patients, which were identified by flow cytometry and fluorescence microscopy. The method of searching for CTCs using magnetic separation and flow cytometry allows for quantitative analysis of the desired analyte using high affinity and LC cell-specific aptamers. [2].

6. Development of electrochemical aptasensor for lung cancer diagnostics in human blood

In this stage the preparation and characterization of an aptamer-based electrochemical sensor to lung cancer tumor markers in human blood is described. The highly reproducible aptamer sensing layer with a high density (up to 70% coverage) on the gold electrode was made. Electrochemical methods and confocal laser scanning microscopy were used to study the stability of the aptamer layer structure and binding ability. A new blocking agent, a thiolated oligonucleotide with an unrelated sequence, was applied to fill the aptamer layer's defects. Electrochemical aptasensor signal processing was enhanced using deep learning and computer simulation of the experimental data array. It was found that the combinations (coupled and tripled) of cyclic voltammogram features allowed for distinguishing between the samples from lung cancer patients and healthy candidates with a mean accuracy of 0.73. The capacitive component from the non-Faradic electrochemical impedance spectroscopy data indicated the tumor marker's presence in a sample. These findings allowed for the creation of highly informative aptasensors for early lung cancer diagnostics [3].

7. Conclusions

The possibility of using single-stranded DNA or RNA oligonucleotides for bioanalysis as aptasensors has been studied relatively recently. Numerous studies conducted in this area have already shown broad prospects for the use of aptamers for the identification of various types of targets, including for the diagnosis of various diseases. One of the main reasons why nucleic acids have become widely used in scientific research is that they can be easily synthesized, amplified and modified.

This study describes the application of aptamers to several typical targets (cells, bacteria, viruses, proteins) for various detection methods, including optical, cytometric, and electrochemical.

Electrochemical aptasensors have virtually no limitations in use and can be applied for various purposes. For the first time, the possibility of using electrochemical sensors based on aptamers for typing bacteria, measuring the viability of bacteria and viruses, quantitative and qualitative analysis of aptamer sequences, determining the affinity, specificity of aptamers, determining the epitopes of aptamer binding, identifying circulating cancer cells was demonstrated.

Acknowledgements

The study was carried out with the financial support of the Ministry of Education and Science of Russia within the framework of a state assignment (FWES-2025-0012).

References

- [1] Zamay G.S., Zamay T.N., Kolovskii V.A., Shabanov A.V., Glazyrin Y.E., Veprintsev D.V., ... & Zamay A.S. *Sci. Rep.* **6(1)**(2016)34350.
- [2] Shabalina A.V., Sharko D.O., Glazyrin Y.E., Bolshevik E.A., Dubinina O.V., Kim A.M., ... & Berezovski M.V. *Sensors*. **21(23)**(2021)7851.
- [3] Krat A.V., Kirichenko D.A., Zamay G.S., Zukov R.A., Kolovskaya O.S., Zamay T.N., ... & Kichkailo A.S. *Rus. J. of Onc.* **29(4)**(2025)295.

Laser-assisted fabrication of magnetic biosensors

Dzhun I.O.^{1,2}, Shuleiko D.V.¹, Nesterov V.Yu.¹, Presnov D.E.¹, Perova N.N.¹, Mineev Ya.S.¹,
Nazarov A.V.^{1,2}, Romashkina I.L.², Kozin M.G.², Chechenin N.G.^{1,2}, Zabotnov S.V.^{*,1}

¹ Faculty of Physics, Lomonosov Moscow State University, 1/2 Leninskie Gory, Moscow 119991, Russia

² Skobeltsyn Institute of Nuclear Physics, Lomonosov Moscow State University, 1/2 Leninskie Gory, Moscow 119991, Russia

*e-mail: zabotnov@physics.msu.ru

Abstract. Designing modern magnetic biosensors means applying micro- and nanotechnologies to fabricate magnetic labels with desirable size and properties, as well as controlling the magnetization and relief configuration in ferromagnet/antiferromagnet structures, which are active elements of spin-valve sensors. To solve these problems, we suggest using laser pulse irradiation of thin magnetic films. The pulsed laser ablation technique of cobalt and iron thin-film targets in water and acetone, respectively, allowed fabricating magnetic nanoparticles of various sizes. The nanoparticles are nanocomposites: the cobalt-based particles predominantly consist of Co₃O₄ and pure Co in the form of a disordered alloy, while the iron-based particles possess the core-shell structure of Fe@FeO. Femtosecond laser irradiation showed opportunities to produce a periodic (~1.2 μm) relief with similarly modulated magnetization in a multilayer structure of Si/Ta30nm/NiFe10nm/IrMn10nm/Ta15nm, as well as micromagnetic patterning without accompanying surface modification in a Si/Ta30nm/NiFe10nm/IrMn10nm/Ta15nm structure.

1. Introduction

Active development of technologies to create portable personal «lab-on-chip» devices for in vitro diagnostics is driven by the need to health monitoring and early diagnostics of diseases. A promising basis for such devices might be magnetic biosensors (MBS) that detect biomolecules conjugated with magnetic labels [1]. To improve the detection limit of MBS, it is necessary to both improve fabrication technologies of magnetic labels and increase efficiency of their capture and retention on the sensor surface.

In this paper, we propose to apply laser nano- and microstructuring for this purpose in three directions: (i) fabrication of magnetic nanoparticles (MNPs) using pulsed laser ablation in liquids (PLAL) of thin cobalt and iron films; (ii) creating laser-induced periodic surface structures (LIPSS) in a ferromagnet/antiferromagnet (F/AF) thin-film exchange biased multilayer based on NiFe/IrMn, which is an active element of a magnetoresistive sensor; (iii) local modulation of a micromagnetic structure of F/AF sample using heating with femtosecond laser pulses in the presence of an external magnetic field.

2. Experiment

Thin films for PLAL were fabricated by magnetron sputtering of Co and Fe targets on glass slide substrates with an AJA ATC ORION-5 sputtering system. The thickness of cobalt films were varied from 5 nm to 500 nm. The thickness of an iron film was 250 nm.

The PLAL was performed using picosecond pulses of an EKSPLA PL 2143A laser (1064 nm, 34 ps, 10 Hz, 5 mJ) in a cuvette filled with distilled deionized water or acetone for the Co and Fe films, respectively [2, 3].

Size distributions and morphological features of the prepared MNPs were analyzed by scanning (SEM) and transmission (TEM) electron microscopy with a Carl Zeiss Supra 40 SEM and a Libra 200 FE HR TEM microscopes, respectively. Additionally, size distributions of the MNPs in suspensions were analyzed by the dynamic light scattering (DLS) technique using a Malvern Zetasizer NANO-ZS analyzer.

The Raman spectroscopy measurements were performed with a Horiba Jobin Yvon HR800 Raman microscope using excitation by laser radiation with 633 nm wavelength. The Mössbauer spectroscopy studies that allowed a more detailed analysis of the iron-based MNPs phase composition were carried out at room temperature on a remote access spectrometer of the SINP MSU.

To better understand the ablation mechanisms leading to MNP formation, laser ablation craters were analyzed by atomic force microscopy (AFM) and optical microscopy (OM) with a Vega NT-MDT scanning probe microscope and an Olympus BX41 microscope, respectively.

LIPSS were fabricated on a silicon substrate under action of femtosecond laser pulses generated by an Avesta Cr:Forsterite laser system (1250 nm, 150 fs, 0.1 mJ, 10 Hz) [3]. After that, a multilayer structure of Ta30nm/NiFe10nm/IrMn10nm/Ta15nm was deposited by magnetron sputtering over the LIPSS formed on a silicon substrate.

The micromagnetic structuring of a Si/Ta30nm/NiFe10nm/IrMn10nm/Ta15nm sample was performed by irradiation with laser pulses in the presence of an external magnetic field applied perpendicular to the sample plane. The laser pulses were generated by a femtosecond laser Avesta TEMA-DUO (1050 nm, 150 fs, 130 nJ, 78 MHz) which was purchased within the framework of the Lomonosov Moscow State University Program of Development and the National Project «Science and Universities» No. DS/45-pr on 28.12.2023 under contract No. 0784-44-2024 on 12.07.2024.

The relief of both types of the F/AF structures were analyzed by SEM and OM. Magnetic properties were studied by magnetic force microscopy (MFM) and magneto-optical Kerr effect (MOKE) microscopy using the mentioned above Vega NT-MDT scanning probe microscope and an Evico magnetics GmbH Magneto-Optical Kerr Microscope based on a Carl Zeiss polarizing microscope, respectively.

3. Results and discussions

All cobalt- and iron-based nanoparticles exhibit magnetic response at applying an external magnetic field.

PLAL of cobalt films with the various thicknesses leads to formation of MNPs with average sizes in the range of 70–1000 nm with different size dispersion. The results are presented in Table I and are based on DLS data analysis. SEM data analysis confirms the observed trends.

Table I. Average size and dispersion for MNPs produced by PLAL of thin Co films of various thicknesses in water.

Sample	Film thickness, (nm)	Average size of MNPs, (nm)	Relative size dispersion, (%)
1	5	150	19
2	10	550	19
3	15	1000	19
4	25	950	20
5	35	70	38
6	50	95	37
7	100	70	39
8	150	100	40
9	250	85	39
10	500	75	38

The non-monotonic dependence of the MNPs size distribution on the film thickness can be explained by features of laser-induced heat distribution and ablation mechanisms. At the film thicknesses of less than 35 nm (i.e. the skin-layer depth) the ablation process corresponds to the phase explosion; in the thicker samples, the ablation occurs in the spallation mode. This hypothesis is supported by both the corresponding ablation craters profiles and the values of ablation thresholds calculated by analyzing a dependence of the crater diameter on the laser pulse energy.

The results of the analysis of MNPs by Raman spectroscopy indicate the presence of cobalt oxide Co_3O_4 . The magnetic response and TEM analysis of the particles also indicates the presence of random inclusions of pure cobalt.

The MNPs obtained from the iron film via PLAL have an average size ~ 90 nm, an iron core and an oxide shell (Fe@FeO) according to SEM, TEM (Fig. 1), Raman and Mössbauer spectroscopy studies.

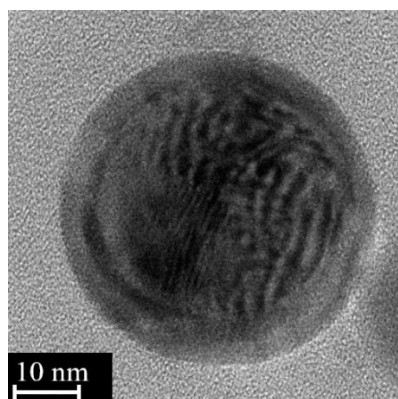


Fig. 1. Typical SEM image of MNP obtained by laser ablation in acetone of a 250-nm-thick Fe film.

The period of as-formed LIPSS on a silicon substrate was ~ 1.2 μm that was not changed after the Ta/NiFe/IrMn/Ta multilayer deposition. MFM analysis

revealed a periodic magnetic contrast attributed to an appearance of the out-of-plane magnetization component with the same period. According to SEM analysis, such patterning facilitates the capturing and retention of the MNPs after their deposition on the surface.

Additionally, an irradiation mode was implemented that made it possible to obtain micromagnetic patterning without accompanying surface modification (Fig. 2).

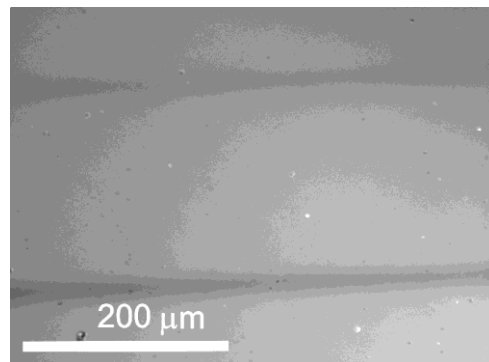


Fig. 2. MOKE image of irradiated surface of the Si/Ta/NiFe/IrMn/Ta multilayer structure. Dark lines correspond to a changed magnetization component within tracks of the femtosecond laser beam.

4. Conclusions

We demonstrate that PLAL of cobalt and iron thin films makes it possible to fabricate MNPs with size distributions depending on the film thickness, since the latter affects the heat distribution in a thin layer under the laser action and, consequently, the ablation mechanisms. The comprehensive study of structural properties of the MNPs using TEM, Raman and Mössbauer spectroscopy revealed the presence of oxides in the nanoparticles: the MNPs made of cobalt films predominantly consist of Co_3O_4 with unoxidized Co inclusions, while the iron-based particles possess the core-shell structure of Fe@FeO . The MNPs obtained look promising as magnetic labels for MBS.

Femtosecond laser irradiation of the Si wafer and F/AF structures leads to micromagnetic patterning in the form of LIPSS or separate laser tracks. Such surface relief and micromagnetic modification has the potential to improve capturing and retention of the MNPs on the F/AF sensor element surfaces.

Acknowledgements

This investigation was supported by the Russian Science Foundation grant # 25-29-00176, <https://rscf.ru/en/project/25-29-00176/>.

References

- [1] H.T. Huang, P. Garu, C.H. Li, W.C. Chang, B.W. Chen, S.Y. Sung, C.M. Lee, J.Y. Chen, T.F. Hsieh, W.J. Sheu, H. Ouyang, W.C. Wang, C.R. Chang, C.L. Wang, M.S. Hsu, Z.H. Wei. *SPIN* **9**(2019)1940002.
- [2] I.O. Dzhun, V.Yu. Nesterov, D.V. Shuleiko, S.V. Zabolotnov, D.E. Presnov, Yu.A. Alekhina, E.A. Konstantinova, N.S. Perov, N.G. Chechenin. *Bull. Russ. Acad. Sci.: Phys.* **88**(2024)540.
- [3] I.O. Dzhun, D.V. Shuleiko, A.V. Nazarov, D.E. Presnov, V.Yu. Nesterov, N.N. Perova, I.L. Romashkina, M.G. Kozin, N.G. Chechenin, S.V. Zabolotnov. *Bull. Russ. Acad. Sci.: Phys.* **88**(2024)S166.

Diffractive Pd/PdO nanostructures as a hydrogen sensor element

Shelaev A.V.^{*}, Kulikova D.P. and Baryshev A.V.

Dukhov Automatics Research Institute (VNIIA), 22, ul. Sushchevskaya, Moscow 127055, Russia

*e-mail: artem.shelaev@yandex.ru

Abstract. A method for the laser oxidation of palladium nanofilms is presented for the rapid fabrication of diffractive Pd/PdO nanostructures. Changes in their optical responses were analyzed when subjected to hydrogen-containing gas. Interaction with hydrogen resulted in the reduction of palladium oxide, which affected the physical and chemical properties of the nanostructures. By considering the catalytic role of palladium in accelerating the autocatalytic reaction, we demonstrate optimal structural parameters to achieve enhanced sensitivity. The influence of humidity and oxygen in the gas mixture on the sensor element response was investigated in detail.

1. Introduction

The transition to hydrogen energy on a large scale necessitates the development of cost-effective and highly precise H₂ sensors to detect leaks and mitigate potential hazards posed by high hydrogen concentrations. Optical sensors are inherently safer than electrical ones, as they lack electrical contacts and eliminate the risk of sparking, which could have catastrophic consequences in hydrogen-rich environments. While it is well-established that PdO is reduced by hydrogen, the response times are typically long, and sensitivity to hydrogen in air remains low (on the order of a few volume percent). Therefore, there is a critical need to identify methods for improving both the speed and magnitude of the sensor response, as well as enhancing its sensitivity to hydrogen.

It has been shown that the catalytic decomposition of molecular hydrogen into atomic hydrogen on the surface of palladium (Pd) significantly enhances sensitivity and accelerates the reduction reaction of PdO [1]. Consequently, alternating structures of Pd and PdO, created using a CW laser, can markedly improve response times.

2. Experiment

In our study, we propose employing a focused beam from a CW laser with a wavelength of 405 nm and an optical power of 40 mW to form PdO on the surface of a 20 nm-thick Pd film. In an air atmosphere, this laser heats the Pd to temperatures exceeding 400°C, inducing localized oxidation. By tracing a predetermined path, the laser effectively "writes" periodic PdO stripes onto the Pd surface. The widths of the PdO and Pd stripes were 2 μm and 8 μm respectively, forming a periodic structure over an area of 250 × 400 μm. The presence of PdO in the oxidized regions was verified using Raman spectroscopy, which detected the characteristic PdO peak at 641 cm⁻¹.

A 633 nm laser was utilized to detect the optical response to hydrogen. To enhance the amplitude of the response, it was proposed to employ a structured nanofilm with a period of 10 μm as a reflective diffraction grating. The sensor element was positioned at an angle such that the diffracted radiation of the first diffraction order propagated back along the optical axis. The intensity of the reflected light was measured under exposure to varying concentrations of H₂ in synthetic air. Additionally, the influence of humidity and oxygen concentration on the sensor response rate was investigated.

3. Results and discussions

For 0.2 vol.% H₂ in dry synthetic air, the 100%-to-50% response time was 29 sec (green curve, Fig. 1). Hydrogen exposure began at 50 sec for all curves. The initial delay before reduction depends significantly on oxygen concentration: absent at 0% O₂, 24 sec at 40%. A similar trend is seen with humidity—no delay below 25%, but 15 seconds at 50% humidity. In dry air, sensor responses were measured for H₂ concentrations from 0.05% to 4%. Over 5 min, responses ranged from 40% (0.05% H₂) to 90% (≥0.5% H₂). Reaction speeds (100%-50%) varied from 300 sec (0.05% H₂) to 3 sec (1%-4% H₂), likely limited by gas exchange in the cell.

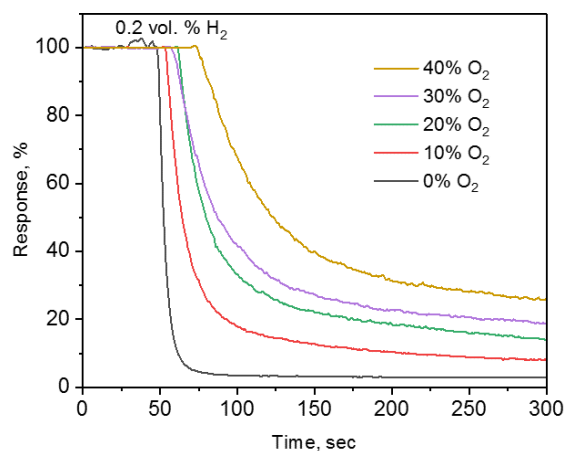


Fig. 1. Sensor response to 0.2 vol. % H₂ in the N₂ / O₂ mixture.

4. Conclusions

The proposed optical sensor element, based on diffractive Pd/PdO nanostructures fabricated through laser-induced oxidation, demonstrates significant advancements in hydrogen detection capabilities. This research establishes Pd/PdO diffraction gratings as a highly promising approach for hydrogen sensing, offering rapid, reliable, and sensitive detection. Further optimization of these techniques could lead to even more robust hydrogen detection systems.

References

- [1] A.V. Shelaev, D.P. Kulikova, A.Sh. Amiraslanov, A.S. Baburin, I.A. Rodionov, A.V. Baryshev. Nano-Structures & Nano-Objects **39** (2024) 101234.

Fe₃O₄-SiO₂-Au nanoparticles for combined radiation therapy and phototherapy

Markin N.S.^{*,1,5}, Gordeev I.S.^{2,6}, Fu H.E.³, Lapidas V.S.⁴, Shevlyagin A.V.⁴, Kuchmizhak A.A.⁴, Ivannikov S.I.⁵, Kim Y.B.³, Samardak A.Yu.¹, Samardak A.S.¹, Kim Y.K.³, Ognev A.V.¹

¹ Far Eastern Federal University, 10 Ajax Bay, Russky Island Vladivostok 690922, Russia

² Laboratory of Radiation Biology, Joint Institute for Nuclear Research, 6 Joliot-Curie, Dubna 141980, Russia

³ Department of Materials Science and Engineering, Korea University, Seoul 02841, Republic of Korea

⁴ Institute of Automation and Control Processes, 5 Radio St., Vladivostok 690041, Russia

⁵ Institute of Chemistry, 159 prosp. 100-letiya Vladivostoka, Vladivostok 690022, Russia

⁶ Dubna State University, 19 Universitetskaya St., Dubna 141982, Russia

*e-mail: markkin.ns@gmail.com

Abstract. The paper presents the results of evaluating the effectiveness of using Fe₃O₄-SiO₂-Au composite nanoparticles with a "core-shell-satellite" type structure for the tasks of both radiation therapy for cancer and an agent of photothermal therapy with near-infrared laser radiation. The effects of the structure (number of gold particles on the surface of the adhesive layer) of nanoparticles on the dose increase factor in an aqueous phantom have been studied using the Monte Carlo method. The efficiency of photothermal conversion of laser radiation with a wavelength of 808 nm has been experimentally determined. The results obtained indicate a high potential for the applicability of the analyzed nanoparticles to the tasks of tumor therapy.

1. Introduction

The increasing incidence of cancer necessitates the search for innovative treatment methods. Radiation therapy is the most common therapeutic strategy, but it has several limitations. The main one is the inability to deliver a dose sufficient for complete destruction of the tumor [1]. However, the efficiency of irradiation can be improved by using radio sensitizers based on metal with a high atomic number of nanoparticles, such as gold, which enhance the absorbed radiation dose in the vicinity of the nanoparticle due to avalanche generation of secondary electrons, leading to a local enhancement of the effects of radiation therapy and reducing the load on healthy tissues[2,3].

The expansion of gold's application is possible through the creation of gold-containing nanocomposites that can be customized for specific tasks. For example, the combination of gold with magnetic materials allows for a significant expansion of the scope of application of composites due to their potential use in magnetic resonance imaging or magnetic hyperthermia[4]. A promising material for creating such composites is magnetite, which, along with its high saturation magnetization, has high biocompatibility and stability. Magnetite is also suitable for radio sensitization tasks due to the release of Auger electrons[5]. Finally, the presence of a light absorption band in the near-infrared wavelength range allows magnetite to be used as an agent for photodynamic therapy[6].

This work evaluates the physical factors determining the applicability of Fe₃O₄-SiO₂-Au composite nanoparticles to the tasks of radiation therapy radiosensibilization and photothermal therapy.

2. Experiment

Nanoparticles were synthesized via a modified multi-step procedure. In the first stage, Fe₃O₄ nanoparticles were obtained using a modified polyol method. Next, the surface of the particles was functionalized with an amino-silica shell for the attachment of gold nanoparticles (AuNPs). The resulting composite particles were obtained by directly

attaching AuNPs of a specified size (d-10 nm) to the silica shell (type 1 - low density nanoparticles (LD NPs) or by attaching seed particles to the surface of SiO₂, followed by the deposition of gold onto the seed particle until the desired size was reached (type 2 – high density nanoparticles (HD NPs)).

Simulation of radiation transport processes was conducted using the Monte Carlo code for radiation transport PHITS version 3.33 [7]. To implement the physical model of the experimentally obtained "core-shell-satellite" nanoparticles, an approach based on a Fibonacci spherical lattice [8] was used. Several different particle configurations were analyzed, namely: 67, 331, 661, and 921 AuNPs on the surface of SiO₂, and the case with a solid Au shell on SiO₂. A single target placed in a water phantom with a diameter of 20 μm was irradiated with a parallel monoenergetic X-ray beam. The photon energy was 50, 100, and 150 keV. The flat circular radiation source was positioned so that its axis coincided with the centre of the nanoparticle. Another series of simulations were performed under the same geometric conditions to evaluate the effect of increasing the dose, but water was used as the target material. Dose enhancement factor (DEF) was calculated using the formula (Eq. 1)

$$DEF = \frac{D^+}{D^W} \quad (1)$$

where: D^+ , D^W – the dose of electrons in the volume of the phantom when a particle is introduced into it and without it, respectively.

To quantitatively assess the effectiveness of photothermal conversion by nanoparticles, a series of experiments on laser irradiation of nanoparticle suspensions in water at various concentrations (6.25, 12.5, 25, 50, 100 μg mL⁻¹) was performed. The heating process for HD NPs, LD NPs and for the same particles coated with an additional stabilizing polyethylene glycol (PEG) shell. Suspensions (1 mL volume) were placed in a quartz cuvette (1×1 cm²) and aligned coaxially with a laser beam from a diode emitting at 808 nm (5.1 W) such that the beam entered the cuvette from below. The temperature on the

surface of the suspensions was recorded using an infrared camera at specified time intervals.

3. Results and discussions

The results of transmission electron indicate that the analysed nanoparticles have a core-shell structure. The average size of the iron-containing core was 62 ± 10 nm for both systems. The size of the gold nanoparticles on the adhesive layer surface was 13.7 ± 1.9 nm and 9.5 ± 1.8 nm for the first (Fig. 1a, b) and second (Fig. 1e, f) systems, respectively. Additionally, the first and second systems differed in the concentration of AuNPs on the surface of the silicon oxide layer. The average number of AuNPs per $\text{Fe}_3\text{O}_4\text{-SiO}_2$ nanoparticle was 16 ± 4 for the first system and 40 ± 12 for the second.

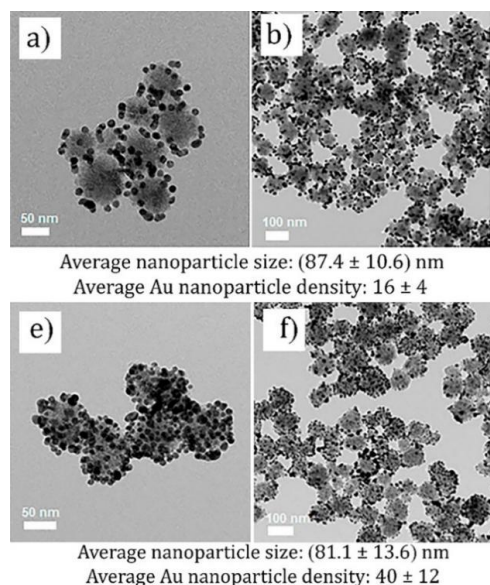


Fig. 1. TEM images of LD NPs (a,b) and HD NPs (e, f).

The results of the dose enhancement factor (DEF) determination for various types of nanoparticles indicate that the structure of the nanoparticles has a minimal impact on the efficiency of radiosensitization with an equal thickness of the gold layer on SiO_2 shell.

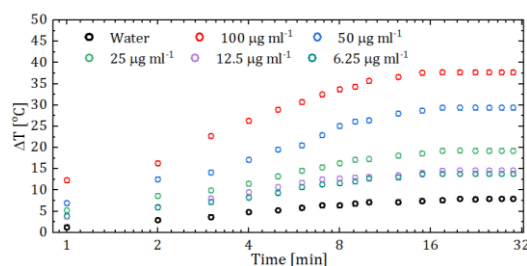


Fig. 2. Dependence of the temperature of colloid of the HD NPs on the duration of its irradiation with by 808 nm laser.

The mechanisms of dose formation by secondary electrons were described in detail, and it was determined that the photoelectric effect and the Auger effect on gold are the predominant processes of formation of an additional component of the absorbed dose. The influence of the structure and composition of nanoparticles on the uniformity of dose distribution over the depth of the phantom is estimated [9].

Conversely, the results of the study on the relationship between the temperature of nanoparticle colloids in water

and the duration of laser irradiation indicate that analyzed materials are promising agents for infrared hyperthermia. It was established that magnetite plays a crucial role in the efficiency of photothermal conversion for 808 nm laser ray (Fig. 2). This is evidenced by a decrease in the rate of temperature change in solutions as the density of gold nanoparticles deposited on the surface of SiO_2 increases, while maintaining a constant solid phase content in the suspension. Additionally, we observed that nanoparticles cover by a polyethylene glycol shell, the efficiency of photothermal conversion decreases by 1.5-3.0% compared to unstabilized particles.

4. Conclusions

The results of the Monte Carlo simulation of secondary electrons dynamic from the surface of X-ray irradiated nanoparticles, and experiments to determine the effectiveness of photothermal conversion of laser radiation by the studied nanoparticles, indicate a high potential for using nanocomposite for cancer therapy cases. The introduction of a nanoparticle into an aqueous phantom enhances the physical component of the dose in this volume by 1.06-4.96 times, depending on both the energy of the incident radiation and the target chemical composition. The main dose-forming component is gold. On the contrary, laser heating of nanoparticles is mainly caused by magnetite, which has a strong absorption line in the near-infrared range. Conversion efficiency decreases in a row: LD NPs, LD-PEG NPs, HD NPs, HD-PEG NPs.

Acknowledgements

The work of Markin N.S., Samardak A.Yu., Ogneva A.V. was carried out with the financial support of the Ministry of Science and Higher Education of the Russian Federation (project No. FZNS-2023-0012). The Monte Carlo calculation was performed using the servers of the JINR Laboratory of Radiation Biology. This study was supported by the National Research Foundation of Korea (NRF) (RS-2024-00347718). The work of Lapidis V.S., Shevlyagina, A.V. Kuchmizhak, A.A. was carried out with the financial support of the Russian Science Foundation (project No. 25-79-20016)

References

- [1] J.M. Straub, J. New, C.D. Hamilton, C. Lominska, Y. Shnayder, S.M. Thomas. *J Cancer Res Clin Oncol* **141**(2015)1985.
- [2] S. Bayda, M. Hadla, S. Palazzolo, P. Riello, G. Corona, G. Toffoli, F. Rizzolio. *Curr Med Chem* **25**(2018)4269.
- [3] X. Zhao, J. Li, Q. Wang, Z. Zhang, J. Liu, C. Zhang, J. Shi. *Chin J Chem* **41**(2023)2545.
- [4] D. Stanicki, T. Vangijzegem, I. Ternad, S. Laurent, *Expert Opin Drug Deliv* **19**(2022)321.
- [5] S. Klein, M. Kızaloğlu, L. Portilla, H. Park, T. Rejek, J. Hümmer, K. Meyer, R. Hock, L.V.R. Distel, M. Halik, C. Krysch, *Small* **14**(2018) 1704111.
- [6] R. Yang, X. Yu, C. Wei, C. Wu, W. Zhang, *Chem Eng J* **504** (2025)159045.
- [7] T. Sato, Y. Iwamoto, S. Hashimoto, T. Ogawa, T. Furuta, S.-I. Abe, T. Kai, Y. Matsuya, N. Matsuda, Y. Hirata, T. Sekikawa, L. Yao, P.-E. Tsai, H. N. Ratliff, H. Iwase, Y. Sakaki, K. Sugihara, N. Shigyo, L. Sihver and K. Niita, *J Nucl Sci Technol* **61**(2024)127.
- [8] A. González. *Math geosci* **42**(2010)49.
- [9] N.S. Markin, I.S. Gordeev, H.E. Fu, S.I. Ivannikov, Y.B. Kim, A.Yu. Samardak, A.S. Samardak, Y.K. Kim, A.V. Ognev. *Nanoscale* (2025).

SERS-based biosensors for drug resistance testing

Mushenkov V.A.¹, Nechaev A.N.², Kukushkin V.I.³, Zavyalova E.G.^{*,1}

¹ Chemistry Department of Lomonosov Moscow State University, 1 Leninskie gory, Moscow 119991, Russia

² Joint Institute for Nuclear Research, Dubna 141980, Russia

³ Osipyan Institute of Solid State Physics RAS, 2 str. Akad. Osipyan, Chernogolovka 142432, Russia

*e-mail: zlenka2006@gmail.com

Abstract. Antimicrobial resistance (AMR) is one of the top global health threats. Antimicrobial resistance is associated with millions of deaths per year. Traditional and most commonly used antibiotic susceptibility tests are based on detection of bacterial growth and its inhibition in the presence of an antimicrobial. These tests typically take over 1-2 days to perform, so empirical therapy schemes are often administered before the proper testing. Rapid tests for antimicrobial resistance are necessary to optimize the treatment of bacterial infection. A combination of MTT test with Raman spectroscopy to provide 1.5-hour long test for minimal inhibitory concentrations determination using 10^6 - 10^8 cfu/mL of *E.coli* strains inhibited with ampicillin, kanamycin and levofloxacin. The test provided the same minimal inhibitory concentrations as traditional Etest confirming its robustness. Bacterial titer can be decreased using gold nanoparticles and silver coated membranes as SERS (surface enhanced Raman spectroscopy) -substrates.

1. Introduction

Antimicrobial resistance (AMR) is one of the top global health threats. In 2019, antimicrobial resistance was associated with 4.95 million deaths, of which 1.97 million were caused by drug resistant infections directly [1]. The main subset of AMR is the antibiotic resistance, that is resistance of bacteria to antibiotic treatment. The significant decline in new antibiotic discoveries exacerbates the problem even more. Most antibiotics were discovered in 1950-1970s, in the “Golden Age of antibiotics”, and since 1987 no new class of antibiotics has been discovered for use as treatment [2].

In drug resistant infections treatment, fast therapy appointment is crucial. For life – threatening conditions, such as sepsis, appropriate therapy needs to be applied within the first hours after diagnosis [3]. Traditional and most commonly used antibiotic susceptibility tests (ASTs) are based on detection of bacterial growth and its inhibition in the presence of an antimicrobial [4]. These ASTs typically take over 1-2 days to perform, so empirical therapy schemes are often administered before the results of AST. Because of the delay, AST results are often not used at all. The delayed appropriate antibiotic therapy can result in prolonged hospital length of stay and higher mortality rate.

MTT assay is based on the enzymatic reduction of tetrazolium salts, commonly MTT (3-(4,5-dimethylthiazol-2-yl)-2,5-diphenyltetrazolium bromide) to violet insoluble formazan [5]. The reaction rate depends on cell metabolic activity; therefore, only living and active cells will sustain efficient MTT reduction. While MTT assay was originally designed as an assay for eukaryotic cells, this method was also used for microbial cells viability estimation [6].

Raman spectroscopy (RS) is a label-free, noninvasive technique, which is based on nonelastic light scattering. RS provides unique fingerprints for substances. Surface-enhanced Raman spectroscopy (SERS) intensifies signal due to surface plasmon resonance effect. This effect occurs on rough metal surfaces, such as surfaces of nanoparticles, the most commonly used SERS-active substrate [7].

In this study, we developed a rapid AST that is based on a combination of RS or SERS and MTT assay. The method has turnaround time of about 1.5 hours having low

labor intensity. We used the method on antibiotic resistant and susceptible strains of *E. coli* to estimate minimal inhibitory concentrations (MICs). The estimated MICs were compared with MICs obtained by a common technique, broth dilution.

2. Experiment

MTT bromine salt was obtained from Dia-M (Russia). Antibiotics (levofloxacin, kanamycin, ampicillin) were purchased from Sigma-Aldrich (U.S.). All chemicals were analytical grade reagents.

Strains of *E.coli* were obtained from own collection of the laboratory of Olga Dontsova. 532 nm wavelength Raman spectra were obtained on the Enspectr RaPort spectrometer (Enspectr, Russia) and 637 nm spectra were obtained on the Photon-Bio RL637 spectrometer (Photon-Bio, Russia).

Bacterial strains were obtained from overnight cultures, diluted with media to 2 MFU (McFarland Units, around $6 \cdot 10^8$ cells/ml. Then 50 μ L of cell culture (1x, 10x, 100x, 1000x dilution of the overnight culture) was added to 350 μ L of PBS or a mix of PBS with gold nanoparticles with the required amount of antibiotic and incubated at 37°C for another 1h. After the incubation, 100 μ L MTT was added to the samples, and after the incubation for 20 minutes, samples with total volume of 500 μ L were placed into glass vials and measured with a spectrometer.

Intensity of formazan peak at 967 cm^{-1} were collected from each spectrum from samples with antibiotic and related to those of the control sample without antibiotic. The final intensity values were presented as a percentage of the intensity of the control sample.

3. Results and discussions

Two pairs of antibiotic susceptible and resistant *E.coli* strains were chosen to test the performance of novel AMR test. The intensities of two formazan bands, 722 and 967 cm^{-1} (Figure 1), were followed in both samples varying concentration of kanamycin. Both bands provided similar concentration dependencies. MIC can be estimated taking 50% of Raman intensity as a reference value of susceptibility to the antibiotic. The MICs were 6 and 9 μ g/mL for 967 and 722 cm^{-1} dependencies, respectively, for the kanamycin susceptible *E.coli* strain (Δ tolC-GyrA-D87Y). These values are in good agreement with MIC of 5

µg/mL that was determined with Etest [8]. The kanamycin resistant *E.coli* strain (Δ tolC-KanR) had MIC larger than 1000 µg/mL.

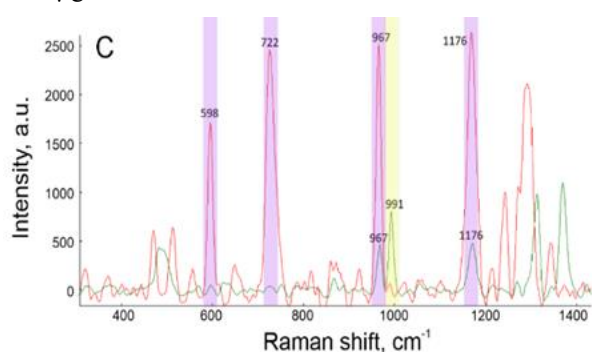


Fig. 1. Raman spectra of *E.coli* after incubation with MTT reagent. Spectra were collected with 532 nm and 637 nm excitation wavelengths of Raman spectrometer (green and red colors, respectively). Characteristic bands are signed; MTT band is shown in yellow; formazan bands are shown in purple [9].

Direct comparison with conventional techniques in MIC determination, namely, Etest, revealed that with these two techniques were the same demonstrating good performance of the novel test. The detailed research is shown in [9].

The technique can be improved using gold nanoparticles. Approximately 50-fold signal enhancement was recorded for formazan. Isopropanol effectively released formazan from *E. coli* cells inducing SERS effect. The minimal *E. coli* concentration determined with gold nanoparticles was 10^5 cfu/mL that is 100-fold lower compared to RS. The detailed research is shown in [10].

Alternatively, track-etched membranes coated with silver nanoparticles were used for cell filtration after MTT-assay. The formazan-labeled cells were identified with a microscope at the concentration as low as 10^3 cfu/mL that is 10,000-fold lower compared to RS (these data are not published).

4. Conclusions

Direct comparison with conventional techniques in MIC determination, namely, Etest, revealed that with these two techniques were the same demonstrating good performance of the novel test. SERS-substrates, such as gold nanoparticles and silver-coated membranes, provide additional enhancement decreasing the minimal bacterial titer 100- and 10,000-fold, respectively. This means that the MTT assay can now be used to analyze the viability of samples with a low content of bacterial cells without their prior accumulation by cultivation.

Acknowledgements

This study was supported by the Russian Science Foundation, project no. 24-65-00015, <https://rscf.ru/project/24-65-00015/>.

References

- [1] C.J.L. Murray, K.S. Ikuta, F. Sharara, L. Swetschinski, G.R. Aguilar, A. Gray, C. Han, C. Bisignano, P. Rao, E. Wool. *Lancet*. **399**(2022)629.
- [2] G.A. Durand, D. Raoult, G. Dubourg. *Int. J. Antimicrob. Agents*. **53**(2019)371.
- [3] J.D. Dickinson, M.H. Kollef. *Curr. Infect. Dis. Rep.* **13**(2011)399.

- [4] K. Syal, M. Mo, H. Yu, R. Iriya, W. Jing, S. Guodong, S. Wang, T.E. Grys, S.E. Haydel, N. Tao. *Theranostics*. **7**(2017)1795.
- [5] J. Van Meerloo, G.J.L. Kaspers, J. Cloos. *Methods Mol. Biol.* **731**(2011)237.
- [6] E. Grela, J. Kozłowska, A. Grabowiecka. *Acta Histochem.* **120**(2018)303.
- [7] P.A. Mosier-Boss. *Nanomaterials* **7**(2017)142.
- [8] K. Shapovalova, G. Zatonsky, N. Grammatikova, I. Osterman, E. Razumova, A. Shchekotikhin, A. Tevyashova. *Pharmaceutics*. **15**(2023)1177.
- [9] V. Mushenkov, K. Zhigalova, P. Denisov, A. Gordeev, D. Lukyanov, V. Kukushkin, T. Priputnevich, E. Zavyalova. *Open Biology*. (2025).
- [10] V.A. Mushenkov, D.A. Lukyanov, N.F. Meshcheryakova, V.I. Kukushkin, E.G. Zavyalova. *Mol. Biol.* **58**(2024)1148.

Improving the sensitivity of a gas sensor based on anodic titanium oxide nanotubes

Dronova D.A.*, Savchuk T.P., Butmanov D.D., Zheleztssov A.D.

National Research University of Electronic Technology, Zelenograd 124498, Russia

*e-mail: demetpatakai@gmail.com

Abstract. This work aims to investigate the insulating characteristics of different an insulating sublayer and their effect on the sensitivity of a gas sensor based on an array of anodic titanium oxide nanotubes (TiO₂ NTs).

1. Introduction

The development of low-temperature gas sensors functioning at temperatures below 150°C is an important task for the development of portable devices. Most metal-oxide sensors require heating of the sensitive element up to 200-600 °C to overcome the energy barrier of activation of the surface redox reaction [1, 2], which increases energy consumption, leads to rapid degradation of the sensor [3] and limits its application in autonomous systems. This motivated the study of new sensitive nanoscale metal-oxide materials with high specific surface area and photocatalytic activity that allow the sensor to operate at low temperatures while maintaining high sensitivity and selectivity.

Meanwhile, arrays of anodic titanium oxide nanotubes (TiO₂ NTs) obtained in a fluorine-containing electrolyte based on ethylene glycol have an ordered vertical structure with high adhesion to a conducting substrate and a potential height of up to several hundred micrometers [4]. The combination of these factors makes arrays of TiO₂ NTs a promising platform for gas sensing [5]. The top contacts required to measure the electrical performance of the sensor can lead to noise interference and short circuits due to the titanium conductive substrate. The formation of an insulating sublayer under the nanotubes could play a key role in the design of gas sensors based on an array of TiO₂ NTs, affecting their sensitivity, selectivity, stability, and power consumption. Such a sublayer would serve as an insulating base between the sensing layer and the substrate, providing electrical isolation and thermal stability.

2. Experiment

TiO₂ NTs were formed on titanium foil (0.89 mm thick, 99.7% metal basis, Alfa Aesar). Prior to anodization, substrates were chemically polished in HNO₃:HF solution during 120 s, then washed in deionized water and dried in an argon stream. The electrochemical growth of titanium oxide was carried out in a potentiostatic mode (60 V) and a temperature of 20°C. A platinum grid was used as a counter electrode. Anodizing for one hour has carried out in ethylene glycol 98 vol.% C₂H₅O₂ with the addition of 0.3 vol.% NH₄F and 2 vol.% H₂O. After this, the array of anodic titanium oxide nanotubes was thermally treated at a temperature of 450°C for 1 hour.

The formation of an insulating sublayer of dense titanium oxide was carried out by anodizing in a solution of orthophosphoric acid, and the porous one was formed by anodizing in a fluorine-containing electrolyte based on ethylene glycol for 30 minutes.

The top contacts were deposited using vacuum thermal deposition.

3. Results and discussions

Comparison of the current-voltage characteristics of an array of TiO₂ NTs on a titanium substrate without an insulating sublayer and an array of TiO₂ NTs with a dense and porous titanium oxide sublayer showed that the porous sublayer gives better insulating properties (Figure 1).

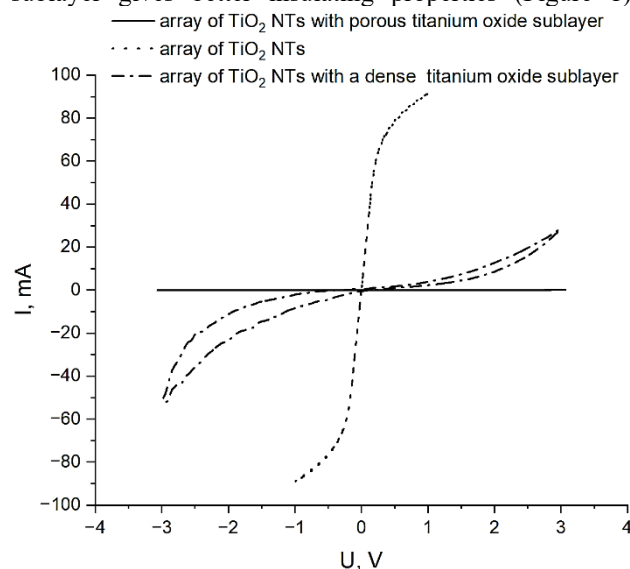


Fig. 1. Current-voltage characteristics of an array of TiO₂ NTs without an insulating sublayer, with a sublayer of dense titanium oxide, and with a sublayer of porous titanium oxide.

The presence of a porous insulating sublayer in the sensor structure increases the resistance from 4 Ohm to 29 MOhm.

4. Conclusions

The study of the insulation characteristics of dense and porous titanium oxide under the nanotube array showed a significant increase in resistance to 29 MOhm. The sublayer will serve as an insulating base between the sensitive layer and the substrate, providing electrical insulation and thermal stability. The presence of an insulating sublayer will improve the characteristics of the gas sensor based on an array of anodic titanium oxide nanotubes, such as sensitivity, selectivity, stability and power consumption.

Acknowledgements

This work was supported by State Assignment № FSMR-2023-0003.

References

- [1] Barsan, N.; Schweizer-Berberich, M.; Göpel, W. Fundamental and practical aspects in the design of nanoscaled SnO₂ gas sensors: a status report / Barsan, N.; Schweizer-Berberich, M.; Göpel, W. // *Fresenius' Journal of Analytical Chemistry*, 1999, 365(4), 287–304. doi:10.1007/s002160051490.
- [2] Ghosh, A.; Majumder, S. B. Modeling the sensing characteristics of chemi-resistive thin film semi-conducting gas sensors / Ghosh, A.; Majumder, S. B. // *Physical Chemistry Chemical Physics*, 2017, 19(34), 23431–23443. doi:10.1039/c7cp04241h.
- [3] Srinivasan, P.; et al. Room temperature chemiresistive gas sensors: challenges and strategies—a mini review / Srinivasan, P.; Eswaramoorthy, M.; Chandiramouli, R. // *Journal of Materials Science: Materials in Electronics*, 2019, 30, 15825-15847.
- [4] Macak, J. M.; Albu, S. P.; Schmuki, P. High-aspect-ratio TiO₂ nanotubes by anodization of titanium / Macak, J. M.; Albu, S. P.; Schmuki, P. // *Phys. Status Solidi RRL*, 2007, 1, 181-183.
- [5] Bouktif, B.; et al. Synthesis and Characterization of TiO₂ Nanotubes for High-Performance Gas Sensor Applications / Bouktif, B.; Zahed, M. A.; El-Yadri, M.; Lahbabi, F. Z.; Belmokhtar, I.; El Khessaimi, Y.; El Hamidi, A.; El Ouahabi, M.; Kaya, S.; Bouachrine, M. // *Crystals*, 2024, 14(11).

Development of MEMS resistive gas sensors for smart nose technology

Kondrateva A.S.^{*1,2}, Enns Y.B.^{1,2}, Kazakin A.N.², Komarevtsev I.M.², Karaseov K.P.²,
Bakanova M.D.², Karaseov P.A.²

¹ Alferov University, 8/3 Khlopina St., St. Petersburg, 195220, Russia

² Peter the Great St. Petersburg Polytechnic University, 29 Politechnicheskaya St., St. Petersburg, 195251, Russia

*e-mail: a.s.kondrateva@yandex.ru

Abstract. Development of a MEMS-based resistive gas sensor is presented. This study investigates the response of a resistive MEMS gas sensor with an NiO-sensitive layer to benzene and toluene within a temperature range of 40-230°C. The vapour detection properties of both substances are examined, and an approach to describing the differences in interaction with the oxide surface is proposed. Recognition of a benzene-toluene mixture using a trained CNN is demonstrated.

1. Introduction

The development of advanced gas detection systems has become a critical area of research due to the increasing demand for accurate environmental monitoring, industrial safety and medical diagnostics [1]. Microelectromechanical systems (MEMS) technology has emerged as a promising platform for creating highly sensitive and selective gas sensors capable of mimicking human olfactory capabilities [2]. Recent studies have demonstrated significant progress in integrating MEMS-based platforms with various sensing materials to detect hazardous gases, volatile organic compounds and other target analytes [3].

The current state of the art in MEMS gas sensing technology involves the use of thin-film platforms with ultra-thin dielectric membranes, which enable fast thermal response and low power consumption [2]. Innovative approaches, such as the integration of nanostructured sensitive layers based on metal oxides and metal nanoparticles, have shown great potential for improving sensor performance [4]. These advances are paving the way for the development of multifunctional electronic noses capable of detecting complex gas mixtures and identifying minimal concentrations of target substances [2].

The integration of MEMS technology with advanced materials science offers a unique opportunity to create compact, energy-efficient and highly sensitive gas detection systems. The development of such devices is particularly relevant for applications in environmental monitoring, industrial safety, healthcare diagnostics and food quality control, where accurate and rapid detection of various gases is critical [5].

The main objective of this thesis is to develop a MEMS-based resistive gas sensor for Smart Nose application. The response of a resistive MEMS gas sensor with NiO sensitive layer to benzene and toluene is investigated.

2. Experiment

The functional scheme and fabrication of MEMS gas sensors with a heating element and a sensing layer based on a gas sensitive semiconductor has been discussed in [6].

The study of the gas sensitivity of MEMS sensors was carried out using a home-made setup. The MEMS sensor was placed in the measuring chamber in front of the sensor to be tested. The concentration of the analytes (ethyl and

isopropyl alcohol vapours, acetic acid, acetone, ammonia alcohol, hexane and arenas) (Neva Reactive LLC, analytical grade) was varied by temperature. The change in resistance of the layer heated by the MEMS chip when the analyte was introduced into the gas phase was considered as the response. The response of the sensing layer was measured at 40-220 °C.

3. Results and discussions

The sensitive layer of the gas sensor used for the smart nose should be able to detect the presence of a wide range of substances. The first step was to study the effect of introducing hydrogen sulphide vapour into the gas mixture on the response of a resistive MEMS with a nickel oxide sensing layer.

The response of the MEMS resistive gas sensor with a nickel oxide sensing layer at 130 ppm of benzene was 0.94 a.u.. Response and recovery time was 44 and 90 s (fig. 1).

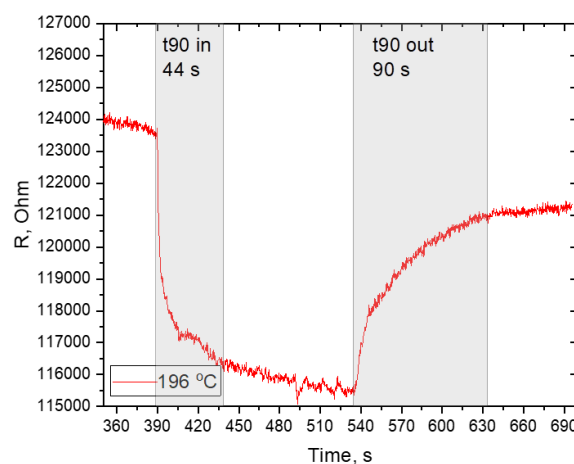


Fig. 1. Relative MEMS resistive gas sensor response to 130 ppm benzene vapor.

The response of the MEMS resistive gas sensor with a nickel oxide sensing layer at 45 ppm of toluene was 0.97 a.u.. Response and recovery time was 12 and 19 s (fig.1). It is possible that the decrease in the response times of the MEMS system indicates a weaker interaction between toluene and the nickel oxide surface.

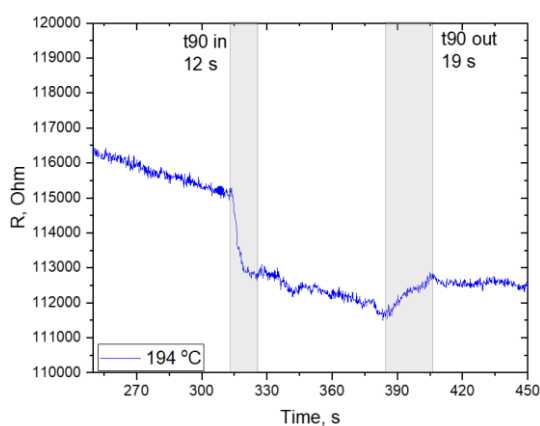


Fig. 2. Relative MEMS resistive gas sensor response to 45 ppm toluene vapor.

The temperature dependence of the sensor response was also investigated. Figure 3 shows the temperature dependence of the sensor response to the introduction of benzene vapours. It can be seen that it is dome-shaped (Fig.3). This means that by controlling the temperature, response and recovery time of the MEMS, it is possible to increase the selectivity of benzene detection in gas mixtures.

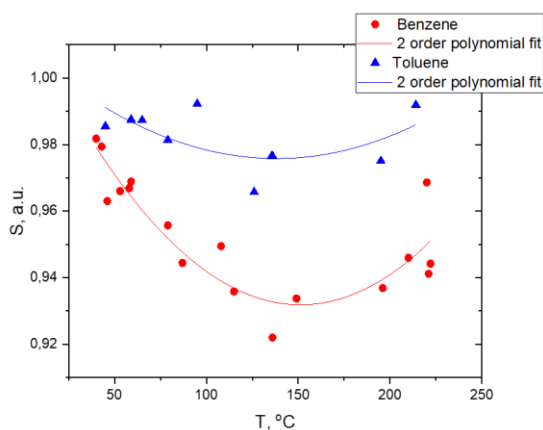


Fig. 3. Relative NiO MEMS resistive gas sensor response to benzene and toluene saturated vapors.

Arrhenius plot (Fig.4) allow us to infer the change in the character of the interaction of benzene with the surface at a temperature of about 150°C. The changes are probably related to the change in the dominant oxygen ion on the surface from O^{2-} to O^- [4]. The value of the apparent activation energy of the process is 0.5 kJ/mol. Taking into account that the apparent activation energy is lower than the real one by the value of the heat of adsorption of the reacting substance, the activation energy of the process is 48.6 kJ/mol [7], indicating that not physical adsorption but surface interaction between benzene and NiO was contributing factor [8].

In the case of toluene, a decrease in detection efficiency is observed compared to benzene. At the same time, the apparent activation energy of the process decreases to a value of 0.2 kJ/mol. The thermochemical properties of the substances are similar. The difference is probably due to the presence of a dipole moment in toluene, which increases the contribution of orientational interactions on the oxide surface.

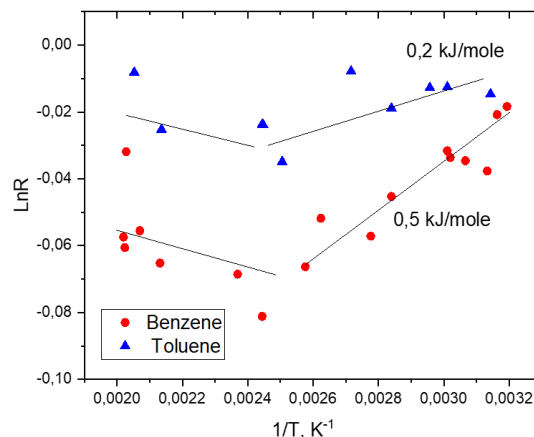


Fig. 4. Arrhenius plot of NiO MEMS resistive gas sensor response to benzene saturated vapors.

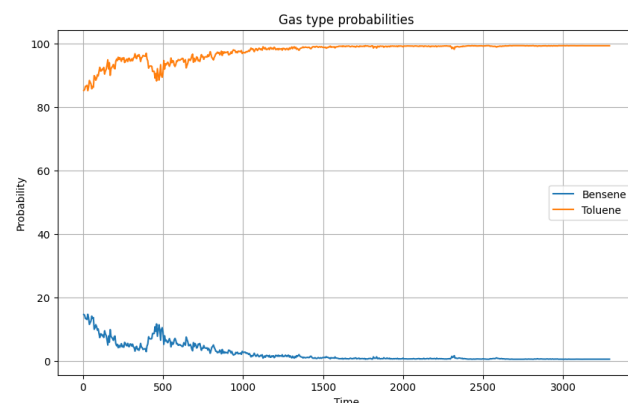


Fig. 5. The result of a CNN's recognition of an unknown mixture.

To confirm the applicability of the developed MEMS sensor as a sensing element of the Smart Nose, a fully connected four-layer neural network (CNN) was trained. A mixture of benzene and toluene was used as a test sample, which showed the recognition result.

4. Conclusions

In conclusion, a MEMS resistive gas sensor was proposed for utilisation in Smart Nose applications. This study investigates the response of a resistive MEMS gas sensor with an NiO-sensitive layer to benzene and toluene within a temperature range of 40-230°C. The vapour detection properties of both substances are examined, and an approach to describing the differences in interaction with the oxide surface is proposed. CNN was used for vapour recognition.

References

- [1] P. Saxena, P. Shukla. *Env.Prog.Sust.En.* 42 (2023)e14126.
- [2] D.Li, H. Zhou, Z. Ren, C. Lee. *Small Science* 5(2025)2400250.
- [3] P. B.Shinde, U. D. Shiurkar. *Mat. Tod.Proc.* 44(2021)615.
- [4] H. Ji, Z. Wen, Y.Li. *Nanoscale* 11.47 (2019): 22664.
- [5] I. A. Casalnuovo, D. Di Pierro, M. Coletta, P.Di Francesco. *Sensors* 6(2006)1428.
- [6] I. M. Komarevtsev, A. S. Kondrateva, A. N. Kazakin, Y.B. Enns, P. A. Karaseov, U. D. Akulshin. *Mat. Phys. Mech.* 52(2024)9.
- [7] A. M. Rubinstein, K. I. Solovetskaya, T. P. Brueva. *USSR AS Rep.* 151(1963)580.
- [8] J. A. Brundage, G. Parravano. *J. Cat.* 2(1963) 380.

Led-based compact illuminator design for effective photodynamic therapy

Sain A.Yu.^{*,1}, Abdurashitov A.S.^{1,2}, Proshin P.I.^{1,2}, Terentyeva D.A.^{1,3}, Sukhorukov G.B.^{1,2} and Sindeeva O.A.¹

¹ Vladimir Zelman Center for Neurobiology for Brain Rehabilitation, Skolkovo Institute of Science and Technology, 30 Bolshoy Boulevard, Moscow 121205, Russia

² Life Improvement by Future Technologies (LIFT) Center, 5 Nobel St, Moscow 143025, Russia

³ Center for Photonic Science and Engineering, Skolkovo Institute of Science and Technology, 30 Bolshoy Boulevard, Moscow 121205, Russia

*e-mail: Alexandra.Sain@skoltech.ru

Abstract. The growing request for miniaturized LED-based illuminators in modern photodynamic therapy, particularly for parameter optimization and the screening of new photosensitive agents, calls for the development of innovative design strategies. This study presents the development of a tunable LED illuminator operated at 660 nm engineered to scan-less provide uniform irradiation across an area of 110.25 cm², with power outputs ranging from 1 to 140 mW/cm². We assessed the temporal stability of the output power, emission spectrum, and temperature of the illuminator to ensure consistent and reproducible light dosages. The practical efficacy of the compact LED illuminator was evaluated through experiments involving CT26, U-87, 4T1, N2A, 22RV1+ and B16F10 cell cultures, utilizing photodynamic dyes Photoditazine (PD) and aluminum tetrasulfophthalocyanine chloride (PS), an analogue of Photosens.

1. Introduction

Photodynamic therapy (PDT) presents a promising strategy for solid tumor treatment, enabling precise, light-activated photosensitizer activation to induce localized cytotoxicity. Advances in optical technologies have enhanced light delivery and tissue penetration; however, the effectiveness and reproducibility of PDT is still constrained by suboptimal light delivery. Recent advancements in LED-based devices for PDT highlight their potential as effective and accessible alternatives to traditional laser systems [1,2]. Compared to lasers, LED systems are more cost-effective and portable, making them more practical for widespread clinical use. Moreover, the development of automated systems with programmable light exposure has further optimized treatment protocols [3]. For instance, a split-face study comparing an LED system with a high-pressure lamp showed similar remission rates for actinic keratoses, demonstrating that LEDs can effectively deliver the required light doses for PDT. These devices have proven versatile in clinical applications, successfully treating superficial tumors and other conditions [4]. However, at the research stage, there is a need for specialized equipment capable of supporting large series of experiments aimed at optimizing PDT parameters, characterizing novel photosensitizers, and conducting extensive *in vitro* screening studies.

2. Experiment

LED based illuminator design. For PCB design an open source software KiCad 7.0 was utilized. For parts design a commercially available software KOMPAS 3D V22 was used. 3D printing was performed using VS3D mini printer and UNI printer. As printing material carbon filled ABS and neet PLA was used. As a light source, the TDS-P003L4N03 light emitting diode was chosen. For optical power measurements Thorlabs PM100A power meter and S121C detector was used. To monitor spectral stability Thorlabs CCS200 fiber spectrometer was utilized. To access thermal dynamics, a UNI-T UT325 thermometer was used.

Table I. Parameters of light emitting diode.

Central wavelength, nm	660
Light flux, lm	70
Viewing angle, deg	140
Forward voltage, V	2.6
Current, A	0.7

Phototoxicity in vitro experiments. Photosense analogue was synthesized. Photoditazine was purchased from LLC Veta-Grand (Russia). Dulbecco's Modified Eagle's Medium (DMEM), Roswell Park Memorial Institute medium (RPMI-1640), Fetal Bovine Serum, PenicillinStreptomycin, Dulbecco's Phosphate Buffered Saline without Ca and Mg, and Trypsin-EDTA (0.25 %) with phenol red were purchased from Gibco (Paisley, UK). AlamarBlue (Cell Viability Reagent) was obtained from Invitrogen (Waltham, MS, USA). Phosphate-buffered saline (PBS) was purchased from Thermo Fisher Scientific.

To evaluate the stability of irradiation, dark and light toxicity assessment of photosensitizers was conducted, various cell lines (CT-26, U-87, N2A, 22RV1+, 4T1, and B16F10) were seeded into 96-well plates (10,000 cells per well). Following 12 hours of incubation at 37 °C in a humidified atmosphere containing 5% CO₂, the culture medium was replaced with solutions of the respective photosensitizers. After 3 hours of incubation, cells were irradiated for 20 minutes at energy densities of 10, 15, and 20 J/cm². Dark toxicity was assessed to validate the specific effect of irradiation; in these experiments, cells were treated identically but not exposed to light. After 24 hours, cell viability was measured using the Alamar Blue assay and a Tecan Infinite M Nano+ multifunctional microplate reader (Tecan Trading AG, Männedorf, Switzerland).

3. Results and discussions

Fifty-four LEDs were placed in a rectangular grid to cover the whole area of a standard 96-well plate. LEDs were connected as follows: 9 rows, of 6 LEDs each, were

connected in parallel. This series-parallel connection allows the LED array to operate at 15 V DC. For compactness an air-based cooling system was applied. To enable the pulse width modulation (PWM) control of the LED's intensity a metal-oxide-semiconductor field-effect transistor (MOSFET, IPD060N03LG) was added to the circuit board. To monitor the temperature of the LED array a B57621-C5103-J62 was incorporated into the board design.

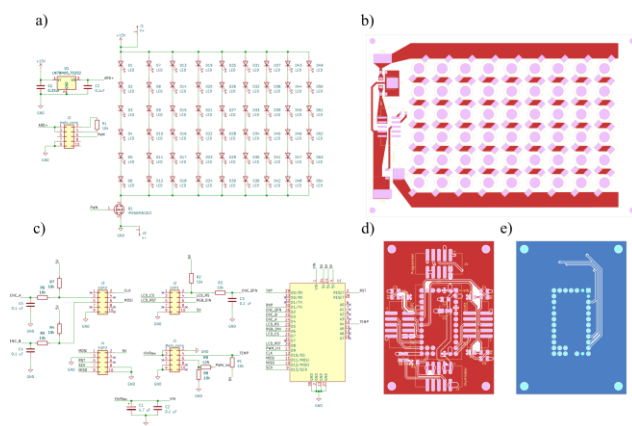


Fig. 1. a) Principle electrical scheme of the LED array PCB. b) Layout of the LED array PCB. c) Principle electrical scheme of the main control board. d) and e) are layouts of the front and back layers of the main control board respectively.

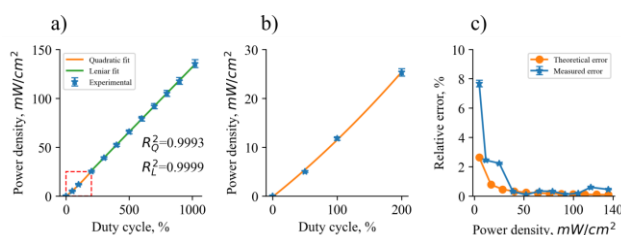


Fig. 2. a) Two-component calibration curve for the proposed illuminator design. b) Enlarged quadratic fit for low power densities marked as red rectangle on a). c) Relative error between set and measured values for both experimental data and theoretical predictions.

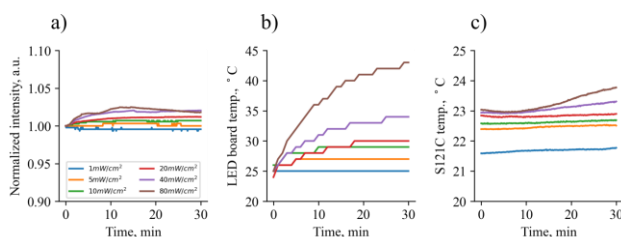


Fig. 3. a) Normalized temporal behavior of the power output for different power densities. b) Temperature of the LED array board accessed via the NTC thermistor. c) Temperature of the S121C power sensor during measurements.

Cells viability assay of light and dark toxicity experiments allows to detect the concentration considerably affecting cells viability for each irradiation parameters (Fig. 4.).

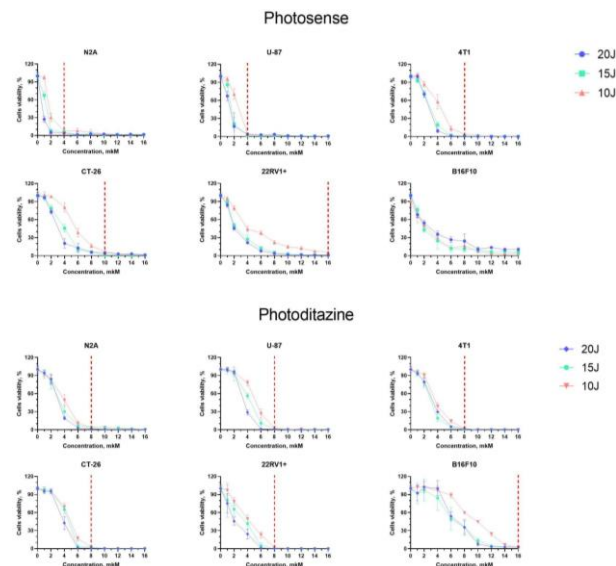


Fig. 4. Cells viability assay for photosensitizers irradiated at three energy densities - 10, 15, and 20 J/cm².

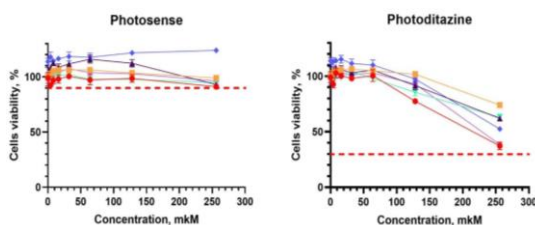


Fig. 5. Cells viability assay without photosensitizers irradiation.

4. Conclusions

Phototoxicity *in vitro* experiments display stability and reproducibility of results obtained with LED based illuminator designed. Relative error in power setting was 6%±2%. Temporal stability of power density within the operation range was estimated to be ~1.5%. Within the operational power densities the PCB temperature did not exceed 30 °C and the temperature within the well of the black-walled 96-well plate did not exceed 37 °C which ensured safe operation.

Acknowledgements

This work was supported by a grant from the Russian Science Foundation (RSF grant 23-75-10070).

References

- [1] M.M. Kim, A. Darafsheh. Light Sources and Dosimetry Techniques for Photodynamic Therapy. *Photochem. Photobiol* **96:2**(2020)280.
- [2] J.F. Algorri, M. Ochoa, P. Roldán-Varona, et al. Light Technology for Efficient and Effective Photodynamic Therapy: A Critical Review. *Cancers (Basel)* **13:14**(2021)3484.
- [3] K. Zhang, S. Timilsina, M. Waguespack, et al. An open-source LED array illumination system for automated multiwell plate cell culture photodynamic therapy experiments. *Sci. Rep.* **12**(2022)19341.
- [4] P. Babilas, R. Travník, A. Werner, et al. Split-face-study using two different light sources for topical PDT of actinic keratoses: non-inferiority of the LED system. *J. Dtsch. Dermatol. Ges. J. Ger. Soc. Dermatol. JDDG.* **6:1**(2007)25.

Author Index

A

Abdurashitov A.S. 15, 238
 Afremov L.L. 36
 Agekyan V.F. 125
 Akopian N. 70
 Alekseev P.A. 66
 Alekseeva O.A. 176
 Al-Khadge L.A. 68, 194
 Andryushchenko T.A. 172, 182, 190
 Anikin A.V. 138

B

Babich A.V. 72
 Baburin A.S. 130, 191
 Baglov A.V. 210
 Bakanova M.D. 236
 Balashev V.V. 98
 Bandarenka H.V. 64
 Banniy D.E. 115, 119
 Baretin D. 70
 Baryshev A.V. 130, 191, 229
 Bazrov M.A. 161
 Bezruk M.N. 136
 Bogdanov A.A. 18
 Bolshakov A.D. 125
 Bondarenko L.V. 32, 56
 Bondarev I.A. 76, 172
 Bondarev M.A. 172
 Borgardt N.I. 47, 138
 Borodaenko Yu.M. 115, 188
 Bozhok A.V. 115, 119
 Bronnikov K.A. 111
 Burkovskaya P.V. 42, 58
 Butmanov D.D. 234
 Buzaverov K.A. 130

C

Chaeusky V.V. 178
 Chechenin N.G. 227
 Chepak A.K. 40
 Cherepakhin A.B. 104, 109, 119
 Chernev I.M. 78, 80, 100
 Chernodub M.N. 40
 Chernousov N.N. 147, 149, 167
 Chernov A.I. 135
 Chumachenko J.V. 186, 200, 206
 Churilov G.N. 202, 204
 Cirlin G.E. 66, 70
 Cora I. 86

D

Davydenko A.V. 147, 149, 167
 Demidov E.V. 26
 Denisov N.V. 32
 Dostovalov A.V. 111
 Dou S. 119
 Dozmorov S.A. 135
 Dronova D.A. 234

Dubkov S.V. 47, 140, 180, 186, 196,
 200, 206, 208, 214, 219

Dubovitsky A.A. 212
 Dudin A.A. 78, 208, 219
 Durakov D.E. 38
 Dyakov S.A. 26, 131, 133
 Dzhun I.O. 227

E

Efimov T.A. 136
 Elesina V.I. 202, 204
 Em M. 178
 Enns Y.B. 236
 Eremkin E.V. 123
 Ermachikhin A.V. 82, 96, 142, 194
 Erofeev A.S. 186

F

Fedorov A.S. 123
 Fedorova N.A. 172
 Fedyaj V.E. 111
 Fedyanina M.E. 140
 Feng Y. 157
 Fiadosenka U.S. 178
 Fogarassy Z. 86
 Fomin D.V. 90, 92, 94
 Fu H.E. 230

G

Galkin K.N. 84, 86, 90, 92, 94, 127
 Galkin N.G. 80, 84, 86, 90, 92, 94, 100
 Gavrilov S.A. 200, 206, 212
 Gerasimenko A.V. 78
 Gerasimov V.S. 123
 Gippius N.A. 26, 131
 Gladush Yu.G. 135
 Glushenko G.A. 202, 204
 Gnedenkov A.S. 184, 192
 Gnedenkov S.V. 184, 192
 Goldt A.E. 135
 Goltsman G.N. 106
 Golyashov V.A. 43
 Gordeev I.S. 230
 Gorelkin P.V. 186
 Gorin D.A. 22
 Gorkusha O.A. 51
 Gorokh G.G. 178
 Goroshko D.L. 80, 84, 100, 194, 212
 Goroshko O.A. 84, 194
 Gorshkova E.Yu. 176
 Gostishchev P.A. 102
 Gouralnik A.S. 78
 Gren D.A. 102
 Gridchin V.O. 66, 70
 Grishchenko D.N. 198
 Grishin T.S. 47, 208, 219
 Gromov D.G. 47, 138, 140, 180, 200,
 206, 208, 214, 219
 Gromov V.D. 138
 Gruznev D.V. 32, 56
 Gumbarg V.V. 34, 49
 Guoqin Cao 23, 74

Gurbatov S.O. 115

I

Ignatieva L.N. 127
 Ignatovich K.V. 98
 Il'yaschenko V.M. 119
 Ilicheva E.A. 102
 Iliushin I.G. 36
 Ilkiv I.V. 66, 70
 Isaenko L.I. 109
 Isakova V.G. 204
 Ivaneva A.D. 202
 Ivannikov S.I. 230
 Ivanova M.S. 165

J

Jianrong Xin 105
 Jinjin Ban 75
 Jiupeng Zhao 105
 Junhua Hu 23, 74, 75

K

Kabachkov E.N. 170
 Kadinskaya S.A. 125
 Kalachikova P.M. 135
 Kamzin A.S. 145
 Kaneva M.V. 113
 Kapitan V.Yu. 55
 Karaseov K.P. 170, 236
 Karaseov P.A. 170, 236
 Karpinsky D.V. 163
 Kashkarov P.K. 107
 Kazakin A.N. 236
 Khairullina E.M. 113
 Khoroshilov D.A. 80, 100
 Khoroshko L.S. 210
 Khrebrov A.I. 70
 Kichkailo A.S. 225
 Kim Y.B. 230
 Kim Y.K. 230
 Kiselev A.V. 72, 194
 Kitan S.A. 78
 Kitsyuk E.P. 106, 121
 Kokh K.A. 43
 Kolmogorov V.S. 186
 Komarevtsev I.M. 236
 Komlenok M.S. 138
 Komogortsev S.V. 159
 Kondratev V.M. 125
 Kondrateva A.S. 236
 Koroleva E.Yu. 176
 Korolik O.V. 210
 Kotlyar K.P. 70
 Kotlyar V.G. 42, 58
 Kovalyuk V.V. 106
 Kozin M.G. 227
 Kozlov A.G. 78, 80, 100, 147, 149,
 151, 155, 157
 Kozyreva Z.V. 15
 Kozyukhin S.A. 106
 Krasilnik Z.F. 26
 Kraynova G.S. 159

Kriukov R.N. 182
Kropachev O.V. 84, 86
Kruzhalina M.D. 140, 196
Kryzhanovskaya N.V. 70
Kuchmizhak A.A. 104, 109, 111, 113,
115, 117, 119, 188, 230
Kukushkin V.I. 232
Kulikova D.P. 191, 229
Kunkel T.S. 142
Kurochitskiy N.D. 138
Kurus N.N. 38
Kuzmin E.V. 107
Kuznetsova M.A. 151, 155, 157

L

Labzovskaya M.E. 125
Lapidas V.S. 117, 230
Lapin A.N. 174
Lapin I.N. 225
Latushka S.I. 163
Latyshev A.V. 34, 38, 43, 49
Lazarenko P.I. 68, 106, 111, 121
Lazorkina E.N. 212
Le T.S. 102
Lebedev E.A. 138, 196, 214
Lei Pan 105
Levshakova A.S. 113
Li Y. 119
Lisenkov O.E. 80, 100
Litvinov V.G. 82
Lobanova E.A. 153
Loktev A.N. 202
Lopatin V.A. 202, 204
Lotkov E.S. 191
Luchnikov L.O. 102
Lukyanenko A.V. 76, 172, 182, 190
Luniakov Yu.V. 45
Luponosov Yu.N. 102
Lyaschenko S.A. 172, 182, 190, 223

M

Makarov A.G. 55, 153
Makeeva A.A. 38
Maksimov F.M. 135
Mararov V.V. 88, 98
Marchenko V.S. 184, 192
Marchenko Yu.V. 127
Markin N.S. 230
Martyshov M.N. 107
Mashchenko V.A. 127
Matveeva T.G. 165
Maximova O.A. 172, 223
Medenkov G.A. 206, 208
Medkov M.A. 198
Meng F.Y. 157
Menshikov E.V. 106
Migas D.B. 24, 86
Mihalyuk A.N. 32, 42, 56
Mikhailov M.M. 174
Mikhailova M.S. 163
Mikhalevsky V.A. 72
Mikushev S.V. 125
Milekhin A.G. 38
Mineev Ya.S. 227
Mitsai E.V. 188

Molochkov A.V. 40
Molokov A.Yu. 176
Morev N.G. 174
Morozov A.V. 135, 215
Moryachkov R.V. 225
Mushenkov V.A. 232
Mushtuk P.S. 36

N

Naberezhnov A.A. 176
Nakamura Y. 21
Namsaraev Zh.Zh. 155
Nasibulin A.G. 135
Nasimov D.A. 43
Nazarkina Yu.V. 219
Nazarov A.V. 227
Nechaev A.N. 232
Nedoluzhko A.I. 215
Nefedev K.V. 55, 153
Neshchimenko V.V. 174
Nesterov V.Yu. 227
Nevzorov A.A. 106
Nikiforov D.F. 38
Nikitin K.G. 194
Nikolaev N.S. 202, 204
Ninayan R. 113
Nomerovskii A.D. 192
Novikov A.V. 26, 131, 133
Novikov D.V. 47, 186, 196, 200, 206
Novoselcev A.I. 196, 214

O

Ognev A.V. 161, 167, 230
Olyanich D.A. 56, 58
Ovchinnikov S.G. 172, 182, 190, 223

P

Pakholchuk P.P. 107
Pankratov E.L. 26
Parkhomenko Yu.N. 186
Pashenko A.S. 147, 149, 167
Pavlikov A.V. 138
Pavlov D.V. 100, 104, 119
Pécz B. 86
Peretokin A.V. 26, 131, 133
Perova N.N. 227
Pestov G.N. 121
Pestova V.B. 121
Petrov A.S. 34, 38, 49
Pikalov D.O. 127
Pilnik A.A. 188
Pinchuk K.E. 159
Pisarenko T.A. 88, 98
Plusnin N.I. 29, 51
Pochinok A.S. 40
Poliakov M.V. 78
Polyakov A.V. 90, 92, 94
Polyantsev M.M. 127
Ponomarev S.A. 43
Popenko V.F. 186
Presnov D.E. 227
Prihodchenko A.V. 80, 151, 157
Prokhotdov A.I. 106
Prokopeva G.A. 80, 100

Proshin P.I. 238
Proshin P.P. 15
Pukha V.E. 170
Pustovalova A.A. 215

R

Rakhmatullaev T.R. 159
Rautskii M.V. 76, 172
Revin L.S. 26
Reznik R.R. 66, 70
Rodionov I.A. 130, 191
Rodyakina E.E. 133
Rogachev K.A. 161
Rogilo D.I. 34, 38, 43, 49
Romashkina I.L. 227
Romashko R.V. 136
Ryabov I.A. 92
Ryazanov R.M. 196, 214
Rybin N.B. 142
Rybina N.V. 142
Ryzhkova M.V. 53

S

Sain A.Yu. 238
Sakurai Y. 62
Samardak A.S. 161, 230
Samardak A.Yu. 161, 230
Sapovskii I.M. 159
Saranin A.A. 32, 42, 56, 58
Saranin D.S. 102
Saritsky D.A. 198, 217
Satymov E.T. 113
Saurov M.A. 121
Savchenko N.N. 127
Savchuk T.P. 234
Serdobintsev A.A. 107
Serov A.Yu. 125
Sevryukov D.K. 56
Sgibnev Y.M. 130
Shabalina A.V. 225
Shakhmin A.L. 170
Shaleev M.V. 26, 131, 133
Shalygina T.A. 202
Sheglov D.V. 26, 34, 38, 43, 49
Shelaev A.V. 130, 191, 229
Shemetov D.A. 92
Shengurov D.V. 26, 133
Sherchenkov A.A. 68, 72
Shevlyagin A.V. 109, 115, 119, 230
Shevtsov D.V. 223
Shishelov A.F. 161
Shmagin V.B. 26
Shmyrin D.A. 26
Sholygin I.O. 90, 92, 94
Shtrom I.V. 66, 125
Shuleiko D.V. 107, 227
Sibirev N.V. 66, 125
Silibin M.V. 163
Silina S.K. 149
Simanchuk A.E. 111
Sindeeva O.A. 15, 238
Sinebryukhov S.L. 184, 192
Sinev I.S. 106
Sinotova S.A. 80, 100
Sitnikov S.V. 26

Smagin I.A. 131
 Smagina Zh.V. 131, 133
 Smayev M.P. 121
 Sokolovskaya O.I. 107
 Solovyev V.G. 165
 Solovyov L.A. 172, 182
 Sorokina L.I. 140, 180
 Soshnikov I.P. 66
 Stepikhova M.V. 26, 131, 133
 Storozhenko D.V. 136
 Strizhkin D.A. 170
 Subbotin E.Yu. 78, 80, 84, 100
 Suemasu T. 19
 Sukhorukov G.B. 15, 238
 Sukhorukova P.K. 102
 Svetlichnyi V.A. 225
 Svetukhin V.V. 106
 Sysoeva A.A. 176
 Syubaev S.A. 109

T

Takahashi T. 62
 Tananaev P.N. 130
 Tarasov A.M. 206
 Tarasov A.S. 76, 172, 223
 Taratyn I.A. 178
 Tatsuka H. 60
 Teplinskaia A.S. 123
 Terai Y. 62
 Terekhov D.Yu. 68, 194
 Terentyeva D.A. 238
 Tikhodeev S.G. 131
 Tomashevich Y.V. 202, 204
 Tomilin F.N. 172

Trusov E.P. 82, 96
 Tsukanov D.A. 53, 88, 98
 Tupchaya A.Y. 32, 56
 Turpak A.A. .. 147, 149, 151, 155, 167

U

Udilov A.D. 100
 Udono H. 63
 Ustinov A.Yu. 78
 Utas T.V. 32, 42, 58
 Utkin D.E. 131

V

Varnakov S.N. 76, 172, 182, 190, 223
 Vasiliev E.V. 55
 Vekovshinin Yu.E. 32, 56
 Venig S.B. 107
 Vildanova A.R. 135
 Vnukova N.G. 202, 204
 Volkov N.V. 76
 Volkov R.L. 47, 138
 Volkova L.S. 78, 180, 186, 200, 206,
 208, 214, 219
 Volkovoyanova L.D. 107
 Voloshchuk I.A. 72
 Volovlikova O.V. 212
 Vorobyov Y.V. 82, 96, 142

W

Wang Y. 155, 157

Y

Yablonskiy A.N. 26
 Yakovlev A.A. 88, 98
 Yakovlev I.A. 76, 172, 182, 190, 223
 Yakubov A.O. 68, 111, 140
 Yao Li. 105
 Yauseichyk M.A. 210
 Yurasov D.V. 26, 131, 133

Z

Zabotnov S.V. 107, 227
 Zaharov V.E. 26
 Zamay G.S. 225
 Zamay S.S. 225
 Zamay T.N. 225
Zavodinsky V.G. 51
 Zavyalova E.G. 232
 Zhaludkevich D.V. 163
 Zhdanov V.S. 56
 Zheleznov V.V. 217
 Zheleznyakova A.V. 186
 Zheleztsov A.D. 234
 Zhizhchenko A.Yu. 104, 111, 117
 Zhou H. 119
 Zhurina E.S. 180
 Zhyzhaev A.M. 202
 Ziatdinov A.M. 198, 217, 221
 Zotov A.V. 32, 42, 56, 58

**The Seventh Asian School-Conference on
Physics and Technology of
Nanostructured Materials
(ASCO-NANOMAT 2025)**

International School-Conference
Vladivostok, Russia, July 11 – 15, 2025

PROCEEDINGS

In charge of publication: N.G. Galkin

Design and layout: S.V. Chusovitina

**Седьмая азиатская школа-
конференция по физике и технологии
наноструктурированных материалов**

Международная школа-конференция
Владивосток, Россия, 11 – 15 июля 2025

Редактор: Н.Г. Галкин

Дизайн и вёрстка: С.В. Чусовитина

СБОРНИК ТРУДОВ
(на англ. яз.)

Отпечатано с оригинал-макета,
подготовленного в Институте автоматики и процессов управления ДВО РАН,
минуя редподготовку в издательстве «Дальнаука»

Подписано к печати 30.06.2025 г.

Отпечатано в ООО «Дальнаука»
690106, г. Владивосток, пр-т Красного знамени, 10